

JUL -- 1966

ELMER H. SCHEIBE

UNCLASSIFIED

AD 255 509

DESIGN CRITERIA FOR MICROWAVE FILTERS
AND COUPLING STRUCTURES

G. L. Matthaei, et al

Stanford Research Institute
Menlo Park, California

January 1961

Processed for . . .

DEFENSE DOCUMENTATION CENTER
DEFENSE SUPPLY AGENCY



U. S. DEPARTMENT OF COMMERCE / NATIONAL BUREAU OF STANDARDS / INSTITUTE FOR APPLIED TECHNOLOGY

UNCLASSIFIED

NOTICE TO DEFENSE DOCUMENTATION CENTER USERS

This document is being distributed by the Clearinghouse for Federal Scientific and Technical Information, Department of Commerce, as a result of a recent agreement between the Department of Defense (DOD) and the Department of Commerce (DOC).

The Clearinghouse is distributing unclassified, unlimited documents which are or have been announced in the Technical Abstract Bulletin (TAB) of the Defense Documentation Center.

The price does not apply for registered users of the DDC services.

255509

DESIGN CRITERIA FOR MICROWAVE FILTERS AND COUPLING STRUCTURES

By: G. L. Matthaei S. B. Cohn E. M. T. Jones
P. S. Carter, Jr. W. J. Getsinger J. T. Bellhorn
C. C. Flammer J. K. Shimizu B. M. Schiffman

Prepared for:

U.S. ARMY SIGNAL RESEARCH AND DEVELOPMENT LABORATORY
FORT MONMOUTH, NEW JERSEY

STANFORD RESEARCH INSTITUTE

MENLO PARK, CALIFORNIA

* SRI

\$ 26.00

XEROX



January 1961

Final Report**DESIGN CRITERIA FOR MICROWAVE FILTERS
AND COUPLING STRUCTURES**

By: G. L. Matthaei S. B. Cohn E. M. T. Jones
P. S. Carter, Jr. W. J. Getsinger J. T. Bolljahn
C. C. Flammner J. K. Shimizu B. M. Schiffman

SRI Project 2326

Prepared for:

U.S. ARMY SIGNAL RESEARCH AND DEVELOPMENT LABORATORY
FORT MONMOUTH, NEW JERSEY

Contract DA 36-039 SC-74862
Sub-Task 3-26-01-701
DA Project 3-26-01-000

Objective: To improve design criteria for microwave filters and
strip-line components by theoretical and experimental investigation.

Approved:

R. L. TANNER, MANAGER, ELECTROMAGNETICS LABORATORY

D. R. SCHEUCH, DIRECTOR, ELECTRONICS AND RADIO SCIENCES

Copy No. 27

ABSTRACT

This report discusses a wide variety of topics, investigated during a three-year contract for the Signal Corps, some of which concern the theory and design of specific microwave devices, while others concern design data and methods for various configurations of lines and discontinuities that form building blocks for microwave devices.

The topics discussed include:

A wide-band, strip-line Magic-T

A ferrite-loaded non-reciprocal TEV-mode structure for wide-band gyrator and isolator applications

A forward-coupling hybrid junction in strip line

A forward-coupling hybrid junction in trough guide

Broadside-coupled strip transmission lines

Interleaving, printed-circuit, parallel-coupled strip transmission lines

Parallel-coupled strip-transmission-line circuits in a cylindrical transmission-line configuration

The design of thick, capacitive obstacles for microwave circuits

The junction effect of strip-line T-junctions

A waveguide filter having unusually broad stop bands

Tables of lumped-element, low-pass, prototype element values for use in designing Tchebyscheff or maximally flat filters

A generalization of Cohn's method for design of direct-coupled, band-pass filters having narrow or moderate bandwidth.

The design of several types of wideband, band-pass filters from lumped-element, low-pass prototypes.

The design of diplexers

The effects of dissipation loss and design for minimum midband dissipation loss.

The design of high-power filters

Electronically tunable microwave filters

Impedance-matching networks.

FOREWORD

The material presented in this report has been extracted from the progress reports issued quarterly on this contract, and combined with new material written since the last progress report was issued. Because of the nature of this investigation, and the method chosen herein for presenting the results, assembling the conclusions of each investigation into a separate chapter of conclusions seems inappropriate.

In all references to equations and figures, the chapter number has been printed in boldface to facilitate finding the item referred to. The diversity of the subjects covered made it seem advisable to print all bibliographic references at the end of the chapter that contains them. While this may lead to repetition, it makes it possible to use particular sections of the report in handbook fashion.

It is expected that most of the material contained in this report, along with material from preceding contracts on this same subject, will be assembled and revised for later publication as a handbook.

The Signal Corps technical monitor for this work is Mr. Nathan Lipetz.

CONTENTS

| | |
|--|-------|
| ABSTRACT | iii |
| FOREWORD | v |
| LIST OF ILLUSTRATIONS. | xv |
| LIST OF TABLES | xxvii |
| TECHNICAL PAPERS RESULTING FROM THIS CONTRACT. | xxix |
| | |
| CHAPTER 1 - INTRODUCTION | 1 |
| CHAPTER 2 - WIDE-BAND STRIP-LINE MAGIC-T | 7 |
| CHAPTER 3 - A NONRECIPROCAL, TEM-MODE STRUCTURE FOR WIDE-BAND GYRATOR AND ISOLATOR APPLICATIONS | 23 |
| A. General | 23 |
| B. Qualitative Description of Operation | 23 |
| 1. Gyrator Network | 23 |
| 2. Isolator | 25 |
| C. Perturbation Analysis of Nonreciprocal Coupling Between a Pair of Shielded Conductors | 26 |
| D. Detailed Description of Operation | 31 |
| 1. Gyrator | 31 |
| 2. Wide-Band Isolator | 32 |
| E. Measured Performance | 33 |
| 1. Gyrator Experimental Results | 33 |
| 2. Isolator Experimental Results | 36 |
| CHAPTER 4 - FORWARD-COUPLING HYBRID JUNCTIONS IN STRIP LINE | 43 |
| A. General | 43 |
| B. Types of Hybrids to be Considered | 43 |
| C. Design Considerations | 44 |
| 1. Design Problems | 44 |
| 2. Power Division | 45 |
| 3. Power Division Flatness | 47 |
| 4. Reflected Waves | 48 |
| 5. Changes in Reflected Voltages with Frequency | 48 |
| D. Design of Zero-Order-Mode Hybrid Junction | 49 |
| 1. Configuration | 49 |
| 2. Simple Theory: Design Relations | 49 |
| E. Experimental Results | 57 |
| CHAPTER 5 - HIGHER-ORDER-MODE FORWARD-COUPLING HYBRID | 65 |
| A. General | 65 |
| B. Propagation Constants in the Coupling Region | 67 |
| 1. TEM Mode | 67 |
| 2. Higher-Order Mode | 67 |
| C. Transition from Coupling Region to Trough Guide | 68 |

CONTENTS

| | | |
|------------|---|-----|
| D. | Design Considerations | 71 |
| 1. | General | 71 |
| 2. | Length of the Coupling Region | 72 |
| 3. | Width of the Conducting Strip in the Coupling Region | 72 |
| 4. | Even-Mode Tuning with Central Capacitance | 73 |
| a. | Effect of Capacitance on Insertion Phase Length of the TEM Mode | 73 |
| b. | Effect on Input VSWR | 74 |
| c. | Effect on Odd Mode | 74 |
| 5. | Flat Power Division | 75 |
| E. | Measured Results | 77 |
| F. | Discussion | 81 |
| CHAPTER 6 | FORMULAS FOR BROADSIDE-COUPLED STRIP TRANSMISSION LINES | 87 |
| A. | Formulas for Broadside-Coupled Strips Parallel to Ground Planes | 88 |
| 1. | Simplification for $(\omega/b)/(1 - s/b) \geq 0.35$ | 90 |
| 2. | Effect of a Small Thickness of the Strips | 91 |
| B. | Formulas for Broadside-Coupled Strips Perpendicular to Ground Planes | 92 |
| C. | Comments on the Derivations | 93 |
| CHAPTER 7 | A COUPLED STRIP-LINE CONFIGURATION USING PRINTED-CIRCUIT CONSTRUCTION THAT ALLOWS VERY CLOSE COUPLING | 97 |
| A. | General | 97 |
| B. | Proposed Configuration | 97 |
| C. | Technical Description | 98 |
| D. | Use of the Graphs | 107 |
| E. | Considerations of Accuracy | 109 |
| F. | Applications | 111 |
| G. | Derivation of Fringing Capacitances | 121 |
| 1. | Preliminary | 121 |
| 2. | Odd-Mode Fringing Capacitance—Strip a | 126 |
| 3. | Odd-Mode Fringing Capacitance—Strip c | 129 |
| 4. | Even-Mode Fringing Capacitance—Strip a | 130 |
| 5. | Even-Mode Fringing Capacitance—Strip c | 131 |
| 6. | Definition of Parallel-Plate Capacitance of Strip a | 132 |
| 7. | Derivation of $C'_{c\omega}/\epsilon$ | 132 |
| 8. | Summary of Equations | 133 |
| H. | Summary | 136 |
| CHAPTER 8 | NON-PLANAR COUPLED TRANSMISSION LINE CIRCUITS | 139 |
| A. | General | 139 |
| B. | Analysis | 139 |
| CHAPTER 9 | EFFECT OF THICKNESS OF CAPACITIVE OBSTACLES | 145 |
| A. | General | 145 |
| B. | The Thickness Correction Term | 148 |
| C. | Example of Thick Capacitive Iris in Waveguide | 150 |
| D. | Derivation | 153 |
| CHAPTER 10 | TECHNIQUES FOR COMPENSATING STRIP-LINE T-JUNCTIONS | 157 |

CONTENTS

| | |
|--|------------|
| CHAPTER 11 - MEASURED EQUIVALENT CIRCUITS OF COMPENSATED AND UNCOMPENSATED STRIP-LINE T-JUNCTIONS | 163 |
| A. General | 163 |
| B. Equivalent Circuit Data | 165 |
| C. Compensation of B_1 | 169 |
| CHAPTER 12 - WAVE-STOP-BAND WAVEGUIDE FILTERS | 173 |
| A. General | 173 |
| B. Filter Specifications | 173 |
| C. Practical Considerations | 174 |
| 1. Scaling | 174 |
| 2. Physical Structure | 174 |
| 3. Choice of Number of Longitudinal Slots | 176 |
| 4. Limitations on Width of Slots | 176 |
| D. Electrical Design | 177 |
| 1. Theory | 177 |
| 2. Design Procedure for Middle Sections | 180 |
| 3. Design of Transforming End Sections | 182 |
| 4. Design of Stepped Transformers | 184 |
| 5. Effect of Longitudinal Slots in the Transformers and Terminating Waveguide | 184 |
| E. Experimental Model of Filter | 188 |
| 1. Description | 188 |
| 2. Adjustment of Gap for Optimum Performance in Pass Band | 188 |
| 3. Adjustment of Slot Depth to Extend Stop Band; Change of Impedance Level | 189 |
| 4. Redesign of Stepped Transformers | 191 |
| 5. Adjustment of Length of Filter-Terminating Waveguide Sections | 192 |
| 6. Performance of Scale Model with Higher Modes Incident | 194 |
| F. Filters I and II | 194 |
| CHAPTER 13 - EXTENSION OF TABLE FOR TCHEBYSCHIEFF AND MAXIMALLY FLAT LOW-PASS-FILTER ELEMENT VALUES | 201 |
| A. General | 201 |
| B. Use of the Tables | 201 |
| CHAPTER 14 - PHASE-SHIFT AND TIME-DELAY RESPONSE OF MICROWAVE NARROW-BAND FILTERS | 207 |
| A. General | 207 |
| B. Time-Delay and Phase-Shift Relationship | 210 |
| C. Calculated Results | 212 |
| D. Formulas Used for Phase-Shift Calculations | 217 |
| E. Conclusions | 219 |
| CHAPTER 15 - A GENERALIZED APPROACH FOR DIRECT-COUPLED FILTER DESIGN | 221 |
| A. General | 221 |
| B. Review of an Example from Ref. 1 | 221 |
| C. A Generalized Statement of Cohn's Design Method | 225 |
| 1. Design Relations with Mapping Unspecified | 225 |
| 2. Selection of a Mapping Function $F(\omega)$ | 228 |
| 3. Determination of the Resonator Constants a_k or b_k | 231 |

CONTENTS

| | | |
|-------------------|--|------------|
| CHAPTER 16 | DESIGN OF BAND-PASS FILTERS WITH VERY WIDE STOP BANDS | 233 |
| A. | General Properties of the Resonators and Filter Circuit | 233 |
| B. | Properties of the Interior Coupling | 239 |
| C. | Properties of the End Couplings | 240 |
| D. | Design Using Bar Transmission Line Construction | 242 |
| E. | Results of Some Trial Designs | 248 |
| CHAPTER 17 | A METHOD FOR DESIGNING WIDE-PASS-BAND, MICROWAVE FILTERS FROM LUMPED-ELEMENTS PROTOTYPES | 255 |
| A. | General | 255 |
| B. | A Modified Low-Pass Prototype and its Bandpass Equivalent | 255 |
| C. | The General Basis for this Wideband Design Procedure | 260 |
| D. | Quantitative Relations Between Prototype and Microwave Filter Sections | 261 |
| 1. | The Mapping Function | 261 |
| 2. | The End Sections | 262 |
| 3. | The Interior Sections | 264 |
| E. | A Design Example | 265 |
| F. | Discussion of General Application of These Methods | 273 |
| CHAPTER 18 | DESIGN OF WIDE-BAND (AND NARROW-BAND) BANDPASS MICROWAVE FILTERS USING STUBS OR PARALLEL-COUPLED LINES | 277 |
| A. | General | 277 |
| B. | Practical Applications of the Design Equations | 281 |
| 1. | Equivalence of the Networks in Figs. 18-1(a) to 18-1(d) | 281 |
| 2. | Use of Mapping Functions, and Selection of Appropriate Lumped-Element Prototypes | 283 |
| 3. | A Design Procedure Especially Suited to Filters Realized in the Form in Figs. 18-1(a) and 18-1(b) | 291 |
| 4. | A Design Procedure Especially Suited to Filters Realized in the Form in Figs. 18-1(c) and 18-1(d) | 295 |
| 5. | Design of Filters in the Form in Fig. 18-2 | 297 |
| 6. | Design of Filters in the Form in Fig. 18-3 | 300 |
| 7. | Suggested Ways for Fabricating the Filters Under Consideration | 302 |
| C. | Theoretical Basis for the Filter Equations and Mapping Functions | 305 |
| 1. | Modified Prototypes as a Basis for Design | 305 |
| 2. | Procedure for Deriving the Equations in Table 18-1 | 308 |
| 3. | Procedure for Deriving the Equations in Table 18-2 | 310 |
| 4. | Procedure for Deriving the Equations in Table 18-3 | 311 |
| 5. | Selection of Mapping Functions | 313 |
| CHAPTER 19 | AN EXPERIMENTAL WIDE-BAND, BAND-PASS FILTER | 317 |
| A. | General | 317 |
| B. | Computations of Filter Element Values | 318 |
| C. | Junction Effect and Choice of Physical Construction | 319 |
| D. | Experimental Results | 324 |
| CHAPTER 20 | MATHEMATICAL ANALYSIS OF DIPLEXER DESIGN | 329 |
| A. | General | 329 |
| B. | A Viewpoint for Diplexer Design | 329 |
| C. | Filter Circuits for the Required Diplexers | 331 |

CONTENTS

| | | |
|------------|--|-----|
| D. | Simplified Filters for use in Mathematical Analysis of Diplexer . . . | 334 |
| E. | Computed Response of Simplified Diplexer | 339 |
| F. | Physical Construction of the Series-Connected Diplexer | 343 |
| CHAPTER 21 | DESIGN OF A LOW-PASS FILTER FOR THE 1- TO 4-kMc DIPLEXER | 347 |
| CHAPTER 22 | DIPLEXERS FOR THE 1- TO 4-kMc AND 4- TO 12.4 kMc RANGES AND THEIR MEASURED RESPONSES | 355 |
| A. | General | 355 |
| B. | Diplexer for the 1- to 4-kMc Range | 355 |
| C. | Diplexer for the 4- to 12.4-kMc Range | 364 |
| CHAPTER 23 | DISSIPATION LOSS IN MULTIPLE-RESONATOR FILTERS | 383 |
| A. | General | 383 |
| B. | Computation Methods | 385 |
| 1. | Center-Frequency Loss | 386 |
| 2. | Exact Calculation Using Low-Pass Prototype | 387 |
| C. | Minimum Loss for Symmetrical Designs | 388 |
| 1. | Approximate Minimum Loss Design | 388 |
| 2. | Exact Minimum Loss Design for Symmetrical Filter with $n = 3$ | 390 |
| D. | Comparative Performance of Different Designs | 391 |
| 1. | Pass-Band Response | 391 |
| 2. | Center-Frequency Loss | 394 |
| E. | Derivation of Formulas | 396 |
| 1. | Low-Pass Equivalence of Dissipative Band-Pass Filter | 396 |
| 2. | Center Frequency Loss Formula | 399 |
| 3. | Stop-Band Loss Formula | 400 |
| CHAPTER 24 | DESIGN CRITERIA FOR HIGH-POWER FILTERS | 403 |
| A. | General | 403 |
| B. | Power-Handling Formulas for Multiple-Resonator Filters | 404 |
| C. | Calculated Examples | 408 |
| D. | System Considerations for High-Power Filters | 409 |
| E. | Derivation of Field-Strength Formula for Multiple- Resonator Filter | 411 |
| CHAPTER 25 | PERTURBATION ANALYSIS OF THE RESONANT FREQUENCY AND Q OF CAVITIES LOADED WITH SMALL FERRITE SAMPLES | 417 |
| A. | General | 417 |
| B. | Variation of the Resonance Frequency of a Cavity by Means of Ferrites | 418 |
| 1. | The Perturbation Formulae | 419 |
| 2. | Fields in a Ferrite | 421 |
| 3. | Illustrative Examples | 423 |
| a. | Small Spherical Sample | 424 |
| b. | Thin Rectangular Slabs, I | 425 |
| c. | Thin Rectangular Slabs, II | 427 |
| C. | Discussion of the Accuracy of the Assumed Mathematical Model of the Ferrite | 429 |
| D. | Discussion of Results | 431 |

CONTENTS

| | |
|--|------------|
| CHAPTER 26 - TWO FERRITE-LOADED FILTER STRUCTURES | 433 |
| A. Ferrite-Loaded Cavities with Multiple Resonances | 433 |
| 1. Description of System | 433 |
| 2. Experimental Measurements on Ferrite Phase Shifter | 434 |
| 3. Utilization of Data | 439 |
| B. Ferrite Tunable Filters Operating Near Ferromagnetic Resonance | 442 |
| 1. Theory of Proposed Filter | 442 |
| 2. Theoretical Investigation of a Ferrite Phase Shifter | 443 |
| 3. Calculation of Response Based on Foregoing Theory | 446 |
| CHAPTER 27 - TUNING OF RESONATORS BY DIODE BARRIER CAPACITANCE | 451 |
| A. General | 451 |
| B. Transmission-Line Resonator Case | 453 |
| 1. Resonance Equations | 453 |
| 2. The Effect of Capacitor Loss | 454 |
| 3. Correction for Transmission-Line Losses | 459 |
| C. Use of Shunt Capacitance for Enhancing the Diode Q | 460 |
| D. Use of Series Capacitance for Enhancing the Diode Q | 464 |
| E. Some Numerical Examples | 468 |
| F. Physical Realization of a Resonator Using C_j | 472 |
| G. Conclusions | 474 |
| CHAPTER 28 - MAGNETICALLY TUNABLE MICROWAVE FILTERS USING SINGLE-CRYSTAL YTTRIUM-IRON-GARNET RESONATORS | 475 |
| A. Introduction | 475 |
| B. Basic Principle of Operation | 476 |
| C. Analysis and Measurement of Coupling Characteristics and Equivalent Circuits of Ferrite Resonators in Lumped-Element Circuits, Transmission-Lines, and Waveguides | 478 |
| 1. Basic Relations | 478 |
| 2. Development of Equivalent Circuit Representations | 480 |
| 3. Measurement of Equivalent Circuit Quantities, Q_e and Q_u | 487 |
| D. DC Magnetic Field Required for Resonance | 492 |
| E. Development of Single-Resonator Tunable Filter | 496 |
| F. Development of a Two-Resonator Filter | 502 |
| G. Possible Future Developments | 507 |
| CHAPTER 29 - DESIGN THEORY OF UP-CONVERTERS FOR USE AS ELECTRONICALLY TUNABLE FILTERS | 513 |
| A. General | 513 |
| 1. Description of the Proposed Devices | 513 |
| 2. Factors Permitting Large Tuning Range | 514 |
| B. Definition of Diode Parameters | 516 |
| C. Definition of Filter Parameters | 518 |
| D. An Up-Converter Model for Purposes of Analysis and Discussion | 522 |
| E. Determination of Signal-Input and Sideband-Output Circuit Parameters for Upper-Sideband Up-Converters | 528 |
| F. Pump Circuit Impedance Matching Filter | 533 |
| G. Determination of Signal Input and Sideband Output Circuit Parameters for Lower-Sideband Up-Converters | 537 |
| H. Estimated Performance of Some Design Examples | 540 |

CONTENTS

| | | |
|------------|--|-----|
| I. | Results of a Preliminary Electronic Tuning Experiment with an Up-Converting Filter Circuit | 544 |
| 1. | Description of the Device and Its Performance | 544 |
| 2. | Theoretical Performance Assuming Diode Inductance is Zero | 548 |
| 3. | Theoretical Performance Including Effects of L_d | 549 |
| J. | The Admittance Parameters of a Variable-Capacitance Diode Having Appreciable Series Inductance | 551 |
| K. | Conclusions | 554 |
| 1. | Theory of Up-Converters as Electronically Tunable Filters | 554 |
| 2. | Insights Obtained from the Electronic Tuning Experiment | 555 |
| 3. | Admittance Parameters of a Diode Having Appreciable Series Inductance | 556 |
| CHAPTER 30 | LUMPED-ELEMENT PROTOTYPES FOR IMPEDANCE-MATCHING NETWORKS | 559 |
| A. | General | 559 |
| B. | Element Values for Impedance-Matching Networks Giving Minimum Reflection | 560 |
| C. | Impedance-Matching Network Prototypes with a Specified Pass-Band Tchebyscheff Ripple | 571 |
| D. | Computation of Element Values that Minimize $(L_A)_{max}$ | 575 |

ILLUSTRATIONS

| | | |
|--------------|---|----|
| Fig. 2- 1 | Schematic Diagram of a Wide-Band Strip-Line Magic-T | 7 |
| Fig. 2- 2 | Magic-T Equivalent Circuit Used in Computing Voltages at Ports 1 and 4 | 10 |
| Fig. 2- 3 | Magic-T Equivalent Circuit Used in Computing Voltages at Ports 1 and 3 | 12 |
| Fig. 2- 4 | Magic-T Equivalent Circuit Used in Computing Voltages at Ports 1 and 2 | 12 |
| Fig. 2- 5 | Input Impedance of Magic-T 1 | 14 |
| Fig. 2- 6 | Input Impedance of Magic-T 2 | 15 |
| Fig. 2- 7 | Input Impedance of Magic-T 3 | 16 |
| Fig. 2- 8 | Input Impedance of Magic-T 4 | 17 |
| Fig. 2- 9 | Input Impedance of Magic-T 5 | 18 |
| Fig. 2-10 | Isolation Between Ports 1 and 4 and Between Ports 2 and 3 for Magic-T's 2 and 5 | 20 |
| Fig. 3- 1 | Wide-Band Gyrator | 24 |
| Fig. 3- 2 | Wide-Band Isolator | 25 |
| Fig. 3- 3 | Photograph of the Wide-Band Gyrator | 34 |
| Fig. 3- 4 | Measured Performance of Wide-Band Gyrator | 35 |
| Fig. 3- 5 | Measured Response of a TEM Mode Gyrator Using a 0.147-Inch-Diameter R-1 Ferrite Rod, 5.70 Inches in Over-All Length with Each End Tapered to a Point in a Distance of 1.2 Inches | 37 |
| Fig. 3- 6 | Difference Between Reverse and Forward Loss for the Isolator in Fig. 3-5 when at Each Frequency the Solenoid Current is Adjusted to Give Peak Reverse Loss | 39 |
| Fig. 3- 7 | Measured Performance of a TEM Mode Isolator Using a 0.100-Inch Diameter R-1 Ferrite Rod 6.00 Inches in Over-All Length with Each End Tapered to a Point in a Distance of 0.5 Inch | 41 |
| Fig. 4- 1 | Basic Coupler Circuit | 45 |
| Fig. 4- 2 | Phase Difference—Even and Odd Mode | 47 |
| Fig. 4- 3 | View of Zero-Order-Mode Forward Coupler | 49 |
| Fig. 4- 4(a) | Even-Mode Electric Field | 50 |
| Fig. 4- 4(b) | Odd-Mode Electric Field | 50 |
| Fig. 4- 5 | Zero-Order-Mode Maximally Flat Forward-Coupling Hybrid Phase Lengths for Even and Odd Modes | 54 |
| Fig. 4- 6 | Predicted Performance vs Frequency for Zero-Order-Mode Maximally Flat Forward-Coupling Hybrid | 55 |
| Fig. 4- 7 | Dimensions of Zero-Order-Mode Forward-Coupling Hybrid | 58 |

ILLUSTRATIONS

| | | |
|--------------|--|-----|
| Fig. 4- 8 | Theoretical and Measured Performance vs Frequency for a Zero-Order-Mode Maximally Flat Forward-Coupling Hybrid | 59 |
| Fig. 4- 9 | Measured Performance vs Frequency for a Zero-Order-Mode Maximally Flat Forward-Coupling Hybrid Tuned with Lumped Inductances | 61 |
| Fig. 4-10 | Photograph of the Zero-Order-Mode Maximally Flat Forward-Coupling Hybrid | 62 |
| Fig. 5- 1 | Electric Field Patterns in Higher-Order-Mode Forward Coupling Hybrid | 65 |
| Fig. 5- 2 | Trough Guide Configuration | 66 |
| Fig. 5- 3 | View of Higher-Order-Mode Forward-Coupling Hybrid | 66 |
| Fig. 5- 4 | Propagation Incident on Semi-Infinite Parallel Plates | 69 |
| Fig. 5- 5(a) | Locations of Terminal Planes T and T' with Respect to Ends of Coupling Region | 70 |
| Fig. 5- 5(b) | Circuit Showing Equivalent Electrical Lengths for Mode Conversion from Trough-Guide Even-Mode to TEM Mode in the Coupling Region | 70 |
| Fig. 5- 6 | Equivalent Circuit for Even-Mode Propagation when a Tuning Screw is Inserted in the Coupling Region | 73 |
| Fig. 5- 7 | Hybrid Performance Without Capacitive Tuning | 78 |
| Fig. 5- 8 | Performance of Short Hybrid Using Capacitive Tuning | 79 |
| Fig. 5- 9 | Performance of Tuned Hybrid Having Flat Power Division | 80 |
| Fig. 5-10 | Pertinent Dimensions of Forward-Coupling Higher-Order-Mode Hybrid Junction | 80 |
| Fig. 5-11 | Calculated and Measured Performance of Higher-Order Mode Hybrid | 82 |
| Fig. 5-12 | Calculated and Measured Performance of Higher-Order Mode Hybrid | 83 |
| Fig. 6- 1 | Three Useful Configurations of Very Thin Coupled Strips Between Parallel Ground Planes | 87 |
| Fig. 6- 2 | Cross-Section Dimensions of Broadside-Coupled Strips Parallel to the Ground Planes | 89 |
| Fig. 6- 3 | Even- and Odd-Mode Fringing Capacitances for Broadside-Coupled Very Thin Strips Parallel to the Ground Planes | 91 |
| Fig. 6- 4 | Thick Strips in the Broadside-Coupled Parallel Arrangement | 91 |
| Fig. 6- 5 | Cross-Section Dimensions of Broadside-Coupled Strips Perpendicular to the Ground Planes | 93 |
| Fig. 6- 6 | Thick Strips in the Broadside-Coupled, Perpendicular Arrangement. | 93 |
| Fig. 6- 7 | Boundaries Considered for the Broadside-Coupled Parallel Case | 94 |
| Fig. 6- 8 | Boundaries Considered for the Broadside-Coupled Perpendicular Case | 95 |
| Fig. 7- 1 | Proposed Strip-Line Configuration | 98 |
| Fig. 7- 2 | Generalized Schematic Diagram | 99 |
| Fig. 7- 3 | Capacitances and Dimensions of Proposed Strip-Line Configuration | 100 |
| Fig. 7- 4 | Inter-Strip Capacitance | 101 |
| Fig. 7- 5 | Fringing Capacitance of Offset Thin Strip | 102 |
| Fig. 7- 6 | Even-Mode Fringing Capacitance of Strip c | 103 |
| Fig. 7- 7 | Odd-Mode Fringing Capacitance of Strip c | 104 |

ILLUSTRATIONS

| | | |
|------------|--|-----|
| Fig. 7- 8 | Even-Mode Fringing Capacitance of Strip a | 105 |
| Fig. 7- 9 | Odd-Mode Fringing Capacitance of Strip a | 106 |
| Fig. 7-10 | Details of Construction of 200-Mc, 3-db Backward Coupler | 112 |
| Fig. 7-11 | Performance of 200-Mc, 3-db Backward Coupler | 114 |
| Fig. 7-12 | Details of Construction of 1000-Mc, 3-db Backward Coupler | 115 |
| Fig. 7-13 | Performance of 1000-Mc, 3-db Backward Coupler | 116 |
| Fig. 7-14 | 1000-Mc, 3-db Backward Coupler | 117 |
| Fig. 7-15 | Details of Construction of 30 Percent Band-Pass Filter | 118 |
| Fig. 7-16 | Performance of 30 Percent Band-Pass Filter | 120 |
| Fig. 7-17 | Cross Section of Proposed Configuration on z-Plane | 122 |
| Fig. 7-18 | Intermediate Transformations from z-Plane | 123 |
| Fig. 7-19 | Final Configurations on w-Planes | 126 |
| Fig. 8- 1 | Two Non-Planar, Parallel-Coupled Transmission-Line Circuits | 139 |
| Fig. 8- 2 | Image Impedance of the Structure in Fig. 8-1(a) and its Pass Band | 141 |
| Fig. 8- 3 | Image Transfer Function for Circuit Shown in Fig. 8-1(b) | 143 |
| Fig. 9- 1 | Examples of Capacitive Obstacles of Moderate Thickness in Waveguide and Coaxial Line | 146 |
| Fig. 9- 2 | Meta-Strip Artificial Dielectric Medium | 146 |
| Fig. 9- 3 | Effect of Strip Thickness on Odd Mode in Parallel-Coupled Strip Transmission Line | 146 |
| Fig. 9- 4 | Semi-Infinite-Plate Geometries Analyzed Exactly in this Report | 147 |
| Fig. 9- 5 | Plot of Capacitance Correction per Unit Length | 149 |
| Fig. 9- 6 | Capacitive Obstacle in Rectangular Waveguide for Very Thin, Moderately Thick, and Very Thick Cases | 150 |
| Fig. 9- 7 | Semi-Infinite-Plate Boundary in z Plane | 153 |
| Fig. 10- 1 | Equivalent Circuit of an Uncompensated Strip-Line T-Junction | 157 |
| Fig. 10- 2 | Compensated Strip-Line T-Junctions | 158 |
| Fig. 10- 3 | Equivalent Circuit of a Strip-Line T-Junction Compensated with a $\lambda/4$ Transformer | 158 |
| Fig. 10- 4 | Measured Performance of an Uncompensated Strip-Line T-Junction | 159 |
| Fig. 10- 5 | Measured Performance of a Strip-line T-Junction Compensated with a $\lambda/4$ Transformer | 161 |
| Fig. 11- 1 | Equivalent Circuit of an Uncompensated Strip-Line T-Junction | 163 |
| Fig. 11- 2 | Compensated Strip-Line T-Junctions | 164 |
| Fig. 11- 3 | Reference-Plane Locations Versus Z_{02} | 166 |
| Fig. 11- 4 | Measured Transformer Turns Ratio of 16 Uncompensated Strip-Line T-Junctions | 167 |
| Fig. 11- 5 | Measured Discontinuity Susceptance of 16 Uncompensated Strip-Line T-Junctions | 168 |
| Fig. 11- 6 | Measured Equivalent Circuit of a Compensated Strip-Line T-Junction with $Z_{01} = Z_{02} = 35$ ohms | 171 |

ILLUSTRATIONS

| | | |
|------------|---|-----|
| Fig. 11- 7 | Measured Equivalent Circuit of a Compensated Strip-Line T-Junction with $Z_{01} = Z_{02} = 100$ ohms | 172 |
| Fig. 12- 1 | Photographs of Filter Having 15-21 kMc Pass Band and 30-63 kMc Stop Band | 175 |
| Fig. 12- 2 | A Single Filter Section of the Corrugated Waveguide Filter | 176 |
| Fig. 12- 3 | Exact Equivalent Network of a Corrugated Waveguide Filter Section for the Dominant Mode | 177 |
| Fig. 12- 4 | Equivalent Network of the Half-Section | 178 |
| Fig. 12- 5 | Graph of Quantities Which Determine Critical Frequencies | 179 |
| Fig. 12- 6 | Graph Showing Relation of Frequency of Infinite Attenuation to Slot Proportions for Filter with no Longitudinal Slots | 180 |
| Fig. 12- 7 | Graph of Susceptance b_{oc} and b_{sc} of Equivalent Network of Filter I with no Longitudinal Slots | 182 |
| Fig. 12- 8 | Sketch of Normalized Image Admittance vs Frequency of Middle and End Sections for Filter I | 183 |
| Fig. 12- 9 | Sketch of Filter II Giving Dimensions | 186 |
| Fig. 12-10 | Measured Performance of Experimental Filter Showing Progressive Development | 190 |
| Fig. 12-11 | Measured VSWR of Final Experimental Filter Design Showing Improvement Obtained by Reducing Terminating Guide Lengths Between Filter and Each Transformer | 193 |
| Fig. 12-12 | Measured Performance of Experimental Filter Showing Effect of Artificially Generated Higher Modes | 195 |
| Fig. 12-13 | Measured VSWR of Filter I | 196 |
| Fig. 12-14 | Measured Performance of Filter II | 198 |
| Fig. 13- 1 | A Low-Pass Filter Having $n = 4$ Reactive Elements | 204 |
| Fig. 13- 2 | A Filter Circuit Which Can Be Obtained from That in Fig. 13-1 by use of the Principle of Duality | 204 |
| Fig. 14- 1 | Low-Pass Prototype Filter | 208 |
| Fig. 14- 2 | Connection of Filter to its Terminations | 210 |
| Fig. 14- 3 | Correspondence Between Frequency Scales for Low-Pass-Prototype Filter and Equivalent Band-Pass Filter | 211 |
| Fig. 14- 4 | Insertion-Phase-Shift Response of Five-Element Equal-Ripple and Maximally Flat Insertion-Loss Prototype Filters | 213 |
| Fig. 14- 5 | Normalized Time Delay Versus ω'/ω'_{3db} for Various Prototype Filters | 214 |
| Fig. 14- 6 | Normalized Time Delay Versus ω'/ω'_{60db} for Various Prototype Filters | 215 |
| Fig. 15- 1 | A Tchebyscheff Low-Pass Filter Response for the Case of $n = 5$, and the Resulting Band-Pass Filter Response Which Would be Obtained by a Low-Pass to Band-Pass Transformation | 222 |
| Fig. 15- 2 | Transformations from a Low-Pass Prototype to a Band-Pass Filter Containing Impedance Inverters | 223 |
| Fig. 15- 3 | Two Circuits Suitable for Use as Impedance Inverters | 225 |
| Fig. 15- 4 | A Generalized, Band-Pass Filter Circuit Using Impedance Inverters | 226 |
| Fig. 15- 5 | A Generalized, Band-Pass Filter Circuit Using Admittance Inverters | 227 |
| Fig. 15- 6 | Two Circuits Suitable for Use as Admittance Inverters | 228 |

ILLUSTRATIONS

| | | |
|---------------|---|-----|
| Fig. 16- 1 | Wide-Stop-Band Filter | 234 |
| Fig. 16- 2 | Resonator Susceptance Characteristics for the Circuit in Figure 16-1(c) when $C_L = 0$ | 235 |
| Fig. 16- 3 | Chart for Design of Resonators to Suppress the Spurious Pass Band in the Vicinity of $3\omega_0$ | 237 |
| Fig. 16- 4 | Chart for Design of Resonators to Suppress the Spurious Pass Band in the Vicinity of $5\omega_0$ | 238 |
| Fig. 16- 5 | Definition of Parameters Associated with the Wide-Stop-Band Filter Couplings | 239 |
| Fig. 16- 6 | A Bar Transmission Line Construction for the Filter in Fig. 16-1(a) | 242 |
| Fig. 16- 7 | Charts of Estimated Values of the Capacitances Associated with the Couplings for the Construction in Fig. 16-6 | 244 |
| Fig. 16- 8 | Definition of the Junction Reference Planes for the Construction in Fig. 16-6 | 245 |
| Fig. 16- 9 | Basic Dimensions of a Four-Resonator, Wide-Stop-Band Filter Design | 249 |
| Fig. 16-10 | Photograph of the Filter Whose Dimensions are Given in Fig. 16-9 | 249 |
| Fig. 16-11 | The Measured Response of the Filter in Fig. 16-10 in the Vicinity of the Pass Band | 250 |
| Fig. 16-12 | The Stop-Band Response of the Filter in Fig. 16-10 | 252 |
| Fig. 17- 1 | The Low-Pass Prototype in Fig. 15-2(a) Modified to Include Impedance Inverters | 256 |
| Fig. 17- 2 | The Low-Pass Prototype Used for the Wide-Pass-Band Filter Example Discussed Herein | 257 |
| Fig. 17- 3 | Arrangement for Fixing the Parameters of the Prototype End Sections | 259 |
| Fig. 17- 4 | A Band-Pass Filter Model Derived from the Prototype in Fig. 17-2 | 259 |
| Fig. 17- 5 | Arrangement for Determining the Parameters of the Microwave Filter End Sections | 263 |
| Fig. 17- 6 | A Symmetrical, Lossless, Microwave Filter Section $S_{k,k+1}$ with Image Parameters as Discussed in the Text | 264 |
| Fig. 17- 7 | A Filter Structure Suitable for "High-Pass" Microwave Filter Applications | 265 |
| Fig. 17- 8 | Definition of Parameters for the End Sections in Fig. 17-7 | 269 |
| Fig. 17- 9 | Definition of Parameters for the Interior Sections in Fig. 17-7 | 270 |
| Fig. 17-10(a) | Calculated Pass-Band Response for the Filter Defined by Fig. 17-7 and Table 17-2 | 272 |
| Fig. 17-10(b) | Computed Attenuation Characteristic for the Filter Defined by Fig. 17-7 and Table 17-2, and the Response Predicted by Mapping the Attenuation of the Low-Pass Prototype | 272 |
| Fig. 17-11 | Exploded View of a Possible Printed-Circuit, Strip-Transmission-Line Construction for the Filter Defined by Fig. 17-7 and Table 17-2 | 273 |
| Fig. 18- 1(a) | Parallel-Coupled, Strip-Transmission-Line Filter with Open-Circuited Sections | 278 |
| Fig. 18- 1(b) | Parallel-Coupled, Strip-Transmission-Line Filter with Short-Circuited Sections | 278 |
| Fig. 18- 1(c) | Bandpass Filter Using Quarter-Wavelength Series Stubs and Quarter-Wavelength Connecting Lines | 279 |

ILLUSTRATIONS

| | | |
|---------------|--|-----|
| Fig. 18- 1(d) | Bandpass Filter Using Quarter-Wavelength Shunt Stubs and Quarter-Wavelength Connecting Lines | 279 |
| Fig. 18- 2 | Bandpass Filter with Half-Wavelength Shunt Stubs and Quarter-Wavelength Connecting Lines | 280 |
| Fig. 18- 3 | Bandpass Filter with Quarter-Wavelength Shunt Stubs, Quarter-Wavelength Connecting Lines, and Half-Wavelength Series Stubs at the Ends | 280 |
| Fig. 18- 4 | Equivalence Between Parallel-Coupled Strip-Line Sections and Sections Consisting of Stubs with Connecting Lines | 282 |
| Fig. 18- 5 | Definition of the Low-Pass Prototype Parameters $g_0, g_1, \dots, g_n, g_{n+1}$ | 284 |
| Fig. 18- 6 | Equations and Parameters for Maximally Flat Response | 285 |
| Fig. 18- 7 | Equations and Parameters for Tchebyscheff Response | 290 |
| Fig. 18- 8(a) | Computed Response of Filters Designed as in Table 18-1 to Have 5-Percent Bandwidth | 292 |
| Fig. 18- 8(b) | Computed Response of Filters Designed as in Table 18-1 to Have 30-Percent Bandwidth | 293 |
| Fig. 18- 8(c) | Computed Response of Filters Designed as in Table 18-1 to Have Approximately 2 to 1 Bandwidth | 294 |
| Fig. 18- 9 | Computed Response of a Filter Designed as in Table 18-2 to Have Approximately 2 to 1 Bandwidth | 296 |
| Fig. 18-10 | Computed Response of a 30-Percent Bandwidth Bandpass Filter Designed in the Form in Fig. 18-2 | 298 |
| Fig. 18-11 | Computed Response of a Filter as in Fig. 18-3 with Approximately 2 to 1 Bandwidth | 301 |
| Fig. 18-12 | Possible Means for Fabricating Wide-Band Filters of the Type in Fig. 18-1(a) | 302 |
| Fig. 18-13 | Possible Means for Fabricating Wide-Band Filters of the Type in Fig. 18-1(b) in Bar-Transmission Line Construction | 303 |
| Fig. 18-14 | Possible Way for Fabricating Wide-Band Filters of the Type in Fig. 18-3 in Split-Block Construction | 304 |
| Fig. 18-15 | Definitions of Impedance Inverters and Admittance Inverters | 306 |
| Fig. 18-16 | Low-Pass Prototypes Modified to Include Impedance Inverters or Admittance Inverters | 307 |
| Fig. 18-17 | Modified Prototype for Deriving the Design Equation in Table 18-1 | 308 |
| Fig. 18-18 | Modified Prototype for Deriving the Equations in Table 18-2 | 311 |
| Fig. 18-19 | Modified Prototype for Deriving the Equations in Table 18-3 | 311 |
| Fig. 19- 1 | Open-Wire Transmission Line Representation of the Wide-Band Band-Pass Filter Under Discussion | 319 |
| Fig. 19- 2 | Equivalent Circuit of a Strip-Line T-Junction | 320 |
| Fig. 19- 3 | Layout of Strip Transmission Line Band-Pass Filter with Upper Ground Plane Removed | 321 |
| Fig. 19- 4 | Some Construction Details of the Band-Pass Filter | 322 |
| Fig. 19- 5 | Details of Transition from Filter to Type-N Connector | 323 |
| Fig. 19- 6 | Photograph of Wide-Band Band-Pass Filter | 323 |

ILLUSTRATIONS

| | | |
|------------|---|-----|
| Fig. 19- 7 | Estimated Equivalent Circuit for Typical Plus-Junction in the Filter of Figs. 19-3 to 19-6 | 325 |
| Fig. 19- 8 | Measured Response of the Filter Shown in Fig. 19-6 | 327 |
| Fig. 19- 9 | Equivalent Circuit of the Filters in Fig. 19-1 at Frequencies in the Vicinity of $2f = 2f_0$ where f_0 is the Pass-Band Center | 328 |
| Fig. 20- 1 | Filters Connected in Series | 330 |
| Fig. 20- 2 | Low-Pass Filter Circuit for Diplexer | 332 |
| Fig. 20- 3 | Band-Pass Filter with Series Stubs at the Ends | 333 |
| Fig. 20- 4 | Response of the Simplified Version of the Filter in Fig. 20-2 and Table 20-1 | 335 |
| Fig. 20- 5 | Normalized Input Impedance Z_a/Z_0 of the Simplified Version of the Filter in Fig. 20-2 | 336 |
| Fig. 20- 6 | Response of the Simplified Version of the Filter in Fig. 20-3 and Table 20-2 | 337 |
| Fig. 20- 7 | Normalized Input Impedance Z'_a/Z_0 of the Simplified Version of the Filter in Fig. 20-3 | 338 |
| Fig. 20- 8 | Modification and Connection of the Filters in Figs. 20-2 and 20-3 to Form a Series-Connected Diplexer | 340 |
| Fig. 20- 9 | The Normalized Real Parts of the Impedances Z_b and Z'_b (and their sum) for the Simplified Versions of the Filters in Figs. 20-2 and 20-3 | 340 |
| Fig. 20-10 | The Normalized Imaginary Parts of the Impedances Z_b and Z'_b (and their sum) for the Simplified Versions of the Filters in Figs. 20-2 and 20-3 | 341 |
| Fig. 20-11 | The Normalized Reactance X/Z_0 and the Resultant Total Normalized Reactance in Z_c/Z_0 (See Fig. 20-8) | 342 |
| Fig. 20-12 | The Power Reflection Loss for Transmission into the Junction Port of the Simplified Diplexer | 343 |
| Fig. 20-13 | A Partial View of a Series-Connected Diplexer Construction | 344 |
| Fig. 21- 1 | Low-Pass Filter | 348 |
| Fig. 21- 2 | Dimensions of the Filter in Fig. 21-1 | 350 |
| Fig. 21- 3 | Modified Type-N Connector used with the Filter in Figs. 21-1 and 21-2 | 350 |
| Fig. 21- 4 | Measured Response of the Filter in Fig. 21-1 | 351 |
| Fig. 22- 1 | Band-Pass Filter Structure for 1- to 4-kMc Diplexer | 356 |
| Fig. 22- 2 | Band-Pass Filter Structure for 1- to 4-kMc Diplexer | 357 |
| Fig. 22- 3 | Connector Mount for Band-Pass Filter for 1- to 4-kMc Diplexer | 358 |
| Fig. 22- 4 | Details of Diplexer Junction for 1- to 4-kMc Diplexer | 359 |
| Fig. 22- 5 | Further Details of Diplexer Junction for 1- to 4-kMc Diplexer | 360 |
| Fig. 22- 6 | Photograph of the 1- to 4-kMc Band Diplexer with the Cover Plates Removed | 361 |
| Fig. 22- 7 | Measured Transmission Characteristics of the Low-Pass Channel of Diplexer in Fig. 22-6 | 362 |
| Fig. 22- 8 | Measured Transmission Characteristics of the Band-Pass Channel of the Diplexer in Fig. 22-6 | 363 |
| Fig. 22- 9 | VSWR at Junction Port of the Diplexer in Fig. 22-6, and Cut-Off Characteristics of the Low-Pass and Band-Pass Channels Superimposed | 366 |

ILLUSTRATIONS

| | | |
|---------------|---|-----|
| Fig. 22-10 | Diplexer for the 4- to 12.4-kMc Range | 367 |
| Fig. 22-11 | Band-Pass Filter Structure for Diplexer for the 4- to 12.4-kMc Range | 368 |
| Fig. 22-12 | Band-Pass Filter Structure for Diplexer for the 4- to 12.4-kMc Range | 369 |
| Fig. 22-13 | Low-Pass Filter Structure for Diplexer for the 4- to 12.4-kMc Range | 370 |
| Fig. 22-14 | Details of Junction for Diplexer for the 4- to 12.4-kMc Range | 371 |
| Fig. 22-15 | Further Details of Junction for Diplexer for the 4- to 12.4-kMc Range | 372 |
| Fig. 22-16 | Cover Plate for Band-Pass Filter Structure for Diplexer for the 4- to 12.4-kMc Range | 373 |
| Fig. 22-17 | Transition for Junction Port for Diplexer for the 4- to 12.4-kMc Range | 374 |
| Fig. 22-18 | Transition for Band-Pass Filter Port for Diplexer for the 4- to 12.4-kMc Range | 375 |
| Fig. 22-19 | Modified Type-N Connector for Diplexer for the 4- to 12.4-kMc Range | 376 |
| Fig. 22-20(a) | Photograph of Diplexer for the 4- to 12.4-kMc Range | 377 |
| Fig. 22-20(b) | Photograph of Diplexer in Fig. 22-20(a) with Cover Plates Removed | 378 |
| Fig. 22-21 | Measured Transmission Characteristics of the Low-Pass Channel of the Diplexer in Figs 22-20(a,b) | 379 |
| Fig. 22-22 | Measured Transmission Characteristics of the Band-Pass Channel of the Diplexer in Figs 22-20(a,b) | 380 |
| Fig. 22-23 | VSWR at Junction Port of Diplexer in Figs. 22-20(a,b) and Low-Pass and Band-Pass Channel Cut-Off Characteristics Superimposed | 381 |
| Fig. 23- 1 | Correspondence Between Low-Pass Prototype Response and Equivalent Band-Pass Response | 386 |
| Fig. 23- 2 | Nondissipative Low-Pass Prototype Filter | 387 |
| Fig. 23- 3 | Dissipative Low-Pass Prototype Filter | 387 |
| Fig. 23- 4 | Comparison of Mid-Band Insertion Loss of Exact Maximally Flat Design of Taub and Bogner and Minimum-Loss Design of Shiffman | 390 |
| Fig. 23- 5 | Pass-Band Insertion-Loss Curves for Three Different Three-Resonator Filter Designs | 392 |
| Fig. 23- 6 | Pass-Band Insertion-Loss Curves for Four Different Five-Resonator Filter Designs | 393 |
| Fig. 23- 7 | Center-Frequency Dissipation Loss and Relative Bandwidth for Various Symmetrical Multiple-Resonator Filters | 395 |
| Fig. 23- 8 | Nondissipative Lumped-Element Band-Pass Filter (a), and Equivalent Low-Pass Prototype Filter (b) | 397 |
| Fig. 23- 9 | Dissipative Lumped-Constant Band-Pass Filter (a), and Equivalent Low-Pass Prototype Filter (b) | 398 |
| Fig. 24- 1 | Typical Output Spectrum of a Magnetron | 403 |
| Fig. 24- 2 | E-Plane View of High-Power Filter Structure Proposed by J. H. Vogelman | 404 |
| Fig. 24- 3 | Correspondence Between Low-Pass Prototype Response and Equivalent Band-Pass Response | 405 |
| Fig. 24- 4 | Low-Pass Prototype Filter and Equivalent Waveguide-Cavity Filter | 405 |
| Fig. 24- 5 | Insertion-Loss-Versus-Frequency Response of Multiple-Cavity Filter with $R_1 = 1$ | 406 |

ILLUSTRATIONS

| | | |
|---------------|---|-----|
| Fig. 24- 6 | Effect of Frequency on Electric Field Strengths in Multiple-Cavity Filter with $g_1 = 1$ | 407 |
| Fig. 24- 7 | Connection of Filters in Cascade to Eliminate Spurious Responses | 410 |
| Fig. 24- 8 | Suggested Means for Dissipating Energy Reflected from Filter | 410 |
| Fig. 24- 9 | Leaky-Waveguide Techniques for Dissipating Unwanted Energy Above the Desired Signal Frequency | 411 |
| Fig. 24-10 | Equivalent Circuit of a Multiple-Resonator Filter | 412 |
| Fig. 24-11 | Voltage and Current Magnitudes in the Equivalent Multiple-Resonator Filter | 412 |
| Fig. 25- 1 | A Wide-Band Magnetically Tunable Filter Composed of Cascaded Directional Filters | 418 |
| Fig. 25- 2 | Rectangular Cavity Coordinate System | 423 |
| Fig. 26- 1 | Multiple Responses of a Transmission-Line Resonator | 433 |
| Fig. 26- 2 | Cascade of Filter Resonators Showing Method of Eliminating Unwanted Modal Response | 434 |
| Fig. 26- 3 | Schematic Diagram of Phase Comparison Circuit | 435 |
| Fig. 26- 4(a) | Differential Phase Constant vs Applied Magnetic Field | 436 |
| Fig. 26- 4(b) | Dissipation Loss vs Applied Magnetic Field | 437 |
| Fig. 26- 5 | Insertion Phase Shift vs Frequency for Zero Applied Magnetic Field | 438 |
| Fig. 26- 6 | Phase Shift Hysteresis Loop at 9.6 kMc | 439 |
| Fig. 26- 7 | ω - β Curves for 1/4-inch Ferrite Rod in Standard X-Band Waveguide | 441 |
| Fig. 26- 8 | Schematic Diagram for Ferromagnetic Resonance Band-Separation Filter | 443 |
| Fig. 26- 9 | Theoretical Phase Shift vs Normalized Frequency Curves for Two Ferromagnetic Resonance Ferrite Phase Shifters | 447 |
| Fig. 26-10 | Theoretical Attenuation vs Normalized Frequency Curves for Two Ferromagnetic Resonance Ferrite Phase Shifters | 448 |
| Fig. 26-11 | Theoretical Insertion Loss vs Normalized Frequency of Band-Separation Filter | 449 |
| Fig. 27- 1 | A Transmission Line Resonator Tuned by the Barrier Capacitance of a Back-Biased Diode | 452 |
| Fig. 27- 2 | A Resonator with Diode-Capacitance Tuning and an Extra Capacitance C_p to Enhance the Q of the Diode | 452 |
| Fig. 27- 3 | A Resonator with Diode-Capacitance Tuning and an Extra Capacitance C_d to Enhance the Q of the Diode | 452 |
| Fig. 27- 4 | Design-Parameter Chart for the Circuit in Fig. 27-1, for the case where $n = 0$ | 455 |
| Fig. 27- 5 | Design-Parameter Chart for the Circuit in Fig. 27-1, for the case where $n = 1$ | 456 |
| Fig. 27- 6 | Design-Parameter Chart for the Circuit in Fig. 27-1, for the case where $n = 2$ | 457 |
| Fig. 27- 7 | Chart for Determining Q_o , the Q of the Over-all Circuit in Fig. 27-1 in Terms of Q_d , the Q of the Diode | 458 |
| Fig. 27- 8 | Design-Parameter Chart for the Circuits in Figs. 27-2 and 27-3 | 463 |
| Fig. 27- 9 | Chart for Determining Q_o , the Over-all Q of the Circuits in Figs 27-2 and 27-3, in Terms of Q_d , the Diode Q | 465 |

ILLUSTRATIONS

| | | |
|---------------|--|-----|
| Fig. 27-10 | Chart for Determining Q_o , the Over-all Q in the circuits of Figs. 27-2 and 27-3, in Terms of Q_d , the Diode Q | 466 |
| Fig. 27-11(a) | A Possible Form for a UHF, Diode-Tuned Resonator Using Semi-Lumped Elements and a Series Capacitor C_s to Enhance the Diode Q | 472 |
| Fig. 27-11(b) | An Equivalent Circuit for the Resonator in Fig. 27-11(a) | 473 |
| Fig. 28- 1 | Magnetic Resonance Filter | 477 |
| Fig. 28- 2 | Equivalent Circuit of Magnetic Resonance Filter | 481 |
| Fig. 28- 3 | External- Q of Ferromagnetic Resonator in Various Waveguide Geometries. | 482 |
| Fig. 28- 4 | Q_e of Spherical YIG Resonator in S-Band Rectangular Waveguide | 483 |
| Fig. 28- 5 | Q_e of Spherical YIG Resonator in G-Band Rectangular Waveguide | 485 |
| Fig. 28- 6 | Q_e of Spherical YIG Resonator in X-Band Rectangular Waveguide | 486 |
| Fig. 28- 7 | Theoretical and Experimental Q_e of YIG Resonators in Reduced (One-Quarter) Height, Standard Width X-Band Waveguide at 10,000 Mc. | 488 |
| Fig. 28- 8 | Theoretical and Experimental Values of Q_e of YIG Resonator Using Strip-Transmission-Line | 489 |
| Fig. 28- 9 | Measured Unloaded Q of 0.064-Inch-Diameter YIG Resonator | 491 |
| Fig. 28-10 | Nomenclature of Directions and Planes in Cubic Crystal | 494 |
| Fig. 28-11 | Resonant Frequency of YIG Sphere vs Applied DC Field with Field Along Principal Axes | 495 |
| Fig. 28-12 | Coupling Principle of Single Resonator Waveguide Filter | 496 |
| Fig. 28-13 | Construction of Half-Section of Single-Resonator Filter | 498 |
| Fig. 28-14 | Photograph of Single-Resonator Filter | 499 |
| Fig. 28-15 | Single Resonator Filter Response Curves | 500 |
| Fig. 28-16 | Amplitude and Phase of Output of X-Band Single Resonator Filter vs Input Power | 502 |
| Fig. 28-17 | Two-Resonator Filter | 503 |
| Fig. 28-18 | Disassembled Two-Resonator Filter | 504 |
| Fig. 28-19 | Measured Responses of Two-Resonator Filter | 505 |
| Fig. 28-20 | Response of Two-Resonator Filter Tuned to 12 kMc Showing Polarized Slot Leakage at 15 kMc | 506 |
| Fig. 28-21 | Measured Response of Two-Resonator Filter Tuned to 11 kMc | 508 |
| Fig. 28-22 | Tunable Band-Rejection Filter Using Quarter-Wave-Spaced YIG Resonators | 509 |
| Fig. 28-23 | Strip-Transmission-Line-Coupled Two-Resonator Filter | 509 |
| Fig. 29- 1 | Low-Pass Prototype Filter and a Typical Tchebyscheff Response | 519 |
| Fig. 29- 2 | Summary of Relations for Design of Lumped-Element Band-Pass Filters from Low-Pass Prototype | 520 |
| Fig. 29- 3 | General Description of Band-Pass Filters in Terms of Resonator Slope Parameters | 521 |
| Fig. 29- 4 | A Possible Circuit for an Up-Converter for Electronically Tunable Filter Applications | 523 |
| Fig. 29- 5 | A Circuit Which is Approximately Equivalent to that in Fig. 29-4 for Energy Components at the Input Frequency for the Sideband Frequency f | 524 |

ILLUSTRATIONS

| | | |
|---------------|---|-----|
| Fig. 29- 6 | A Circuit Approximately Equivalent to that in Fig. 29-4 for Energy at the Pump Frequency f^p | 525 |
| Fig. 29- 7(a) | Approximate Equivalent Circuit for the Diode Resonator | 526 |
| Fig. 29- 7(b) | Reactance Properties of the Resonator in Fig. 29-7(a) | 526 |
| Fig. 29- 8 | A Possible Strip-Transmission-Line Embodiment of the Circuit in Fig. 29-4 | 527 |
| Fig. 29- 9 | Chart for Determining the Gain of Upper-Sideband Up-Converters | 532 |
| Fig. 29-10 | Chart for Use in Determining the Reflection Loss Required in the Pump Circuit when Using an Optimum Tchebyscheff Impedance Matching Filter . . | 536 |
| Fig. 29-11 | Charts for Determining the Gain of Lower-Sideband Up-Converters | 539 |
| Fig. 29-12(a) | Photograph of a Strip-Transmission-line Structure (with cover plate removed) Used for Electronically Tunable, Upper-Sideband Up-Converter Experiments | 545 |
| Fig. 29-12(b) | Equivalent Circuit for the Structure in Fig. 29-12(a) | 546 |
| Fig. 29-13 | Electronic Tuning Properties of the Circuit in Fig. 29-12(a) | 547 |
| Fig. 30- 1 | Definition of $(L_A)_{\max}$ and $(L_A)_{\min}$ for Tchebyscheff Impedance Matching Networks Discussed Herein | 561 |
| Fig. 30- 2 | $(L_A)_{\max}$ vs δ for the Impedance Matching Networks Whose Element Values are Given in Figs. 30-4(a), (b), (c), (d) | 562 |
| Fig. 30- 3 | Tchebyscheff Ripple in Db vs δ for the Impedance Matching Networks Whose Element Values are Given in Figs. 30-4(a), (b), (c), (d) | 563 |
| Fig. 30- 4(a) | Element Values vs δ for Tchebyscheff Impedance Matching Networks Which Minimize $(L_A)_{\max}$ | 564 |
| Fig. 30- 4(b) | Element Values vs δ for Tchebyscheff Impedance Matching Networks Which Minimize $(L_A)_{\max}$ | 565 |
| Fig. 30- 4(c) | Element Values vs δ for Tchebyscheff Impedance Matching Networks Which Minimize $(L_A)_{\max}$ | 566 |
| Fig. 30- 4(d) | Element Values vs δ for Tchebyscheff Impedance Matching Networks Which Minimize $(L_A)_{\max}$ | 567 |
| Fig. 30- 5 | $(L_A)_{\max}$ vs δ for Impedance Matching Networks Having a Specified Tchebyscheff Ripple (See Sec. C) | 573 |

TABLES

| | | |
|------------|--|-----|
| Table 2-1 | ABCD Matrices of the Individual Networks in the Magic-T | 9 |
| Table 2-2 | Electrical Parameters of Various Strip-Line Magic T's | 13 |
| Table 4-1 | Solutions to Design Equations for Maximally Flat Zero-Order-Mode Forward-Coupling Hybrid | 56 |
| Table 10-1 | Dimensions of Compensated Strip-Line T-Junction | 160 |
| Table 11-1 | Dimensions of Uncompensated Strip-Line T-Junction | 165 |
| Table 12-1 | Specifications for the Two Waveguide Filters | 174 |
| Table 12-2 | Experimental-Filter Frequency Range | 188 |
| Table 12-3 | Steps in the Development of the Experimental Filter of Table 12-2 | 189 |
| Table 13-1 | Element Values for Tchebyscheff Filters | 202 |
| Table 13-2 | Element Values for Maximally Flat Filters | 203 |
| Table 17-1 | Image Parameters of Low-Pass Maximally Flat and Tchebyscheff Filters of Form in Fig. 17-2 with $n = 9$ Reactive Elements and $R_1 = R_9 = 1$ | 261 |
| Table 17-2 | Design Parameters for Filters in Fig. 17-7 for Specifications: $\omega_1/\omega_0 = 0.656$, $\omega_2/\omega_0 = 1.397$, and $R_1 = R_6 = 1$ | 271 |
| Table 18-1 | Design Equations Especially Suited for Filters of the Form in Figs. 18-1(a) and 18-1(b) | 286 |
| Table 18-2 | Design Equations for Filters Especially Suited for Realization in the Form in Figs. 18-1(c) and 18-1(d) | 287 |
| Table 18-3 | Design Equations for Filters of the Form in Fig. 18-3 | 288 |
| Table 18-4 | Computed Response of Filters Designed as in Table 18-1 to Have Approximately 2 to 1 Bandwidth | 294 |
| Table 18-5 | Computed Response of a Filter Designed as in Table 18-2 to Have Approximately 2 to 1 Bandwidth | 296 |
| Table 18-6 | Element Values for the Filter of Fig. 18-10 Realized as Shown in Fig. 18-2 | 299 |
| Table 18-7 | Element Values for the Filter of Fig. 18-11 Realized as Shown in Fig. 18-3 | 301 |
| Table 19-1 | Element Values for a Band-Pass Filter of the Form in Fig. 19-1 Having $n = 13$, a Band-Edge Ratio of $f_2/f_1 = 2.175$, and Approximately 0.1 db Tchebyscheff Pass-Band Ripple | 319 |
| Table 20-1 | Normalizing Element Values for Low-Pass Filter in Fig. 20-2 | 332 |
| Table 20-2 | Line Impedances for the Band-Pass Filter in Fig. 20-3 | 333 |
| Table 27-1 | Comparison of Resonator Q 's Obtained with the Circuits of Figs. 27-1 to 27-3 | 471 |
| Table 28-1 | Performance of Single-Resonator Filter | 497 |
| Table 29-1 | Low-Pass Prototype Parameter d for Various Amounts of db Tchebyscheff Pass-Band Ripple and n (Number of Reactive Elements) | 535 |
| Table 29-2 | Up-Converter Filter, Operation with Variable Bias | 548 |

TECHNICAL PAPERS RESULTING FROM THIS CONTRACT

1. E. M. T. Jones, S. B. Cohn, J. K. Shimizu, "A wide-band nonreciprocal TEM-transmission-line network" 1958 WESCON Convention Record pt 1, pp 131-135.
2. S. B. Cohn, "Design Considerations for High-Power Microwave Filters," *IRE Trans PGMT-7*, pp. 149-153 (January 1959).
3. S. B. Cohn, "Dissipation Loss in Multiple-Coupled-Resonator Filters," *Proc. IRE* 47, pp 1342-1348 (August 1959).
4. E. M. T. Jones, G. L. Matthaei, S. B. Cohn, "A nonreciprocal, TEM-mode structure for wide-band gyrator and isolator applications" *IRE Trans MIT*, Vol 7 No. 4 pp 453-460 (October 1959).
5. E. M. T. Jones "Wide-Band Strip-Line Magic-T" *IRE Trans. MIT* Vol. 8, No. 2 pp 160-168 March 1960.
6. P. S. Carter, Jr., "Magnetically Tunable Microwave Filters Employing Single Crystal Garnet Resonators," 1960 *IRE International Convention Record*, Part 3, pp 130-135.
7. G. L. Matthaei, "Band-Pass Microwave Filter Design—A New Method and Its Relation to Other Methods," 1960 *International Convention Record*, Part 3, pp 95-122.
8. P. S. Carter, Jr. and Carson Flammer, "Unloaded Q of Single Crystal Yttrium-Iron-Garnet Resonator as a Function of Frequency," *IRE Trans. PGMTT*, Vol MIT-8, No. 5, pp 570-571 (September 1960).
9. S. B. Cohn, "Phase-Shift and Time-Delay Response of Microwave Narrow-Band Filters," *The Microwave Journal* 3, pp 47-51 (October 1960).
10. S. B. Cohn, "Thickness Corrections for Capacitive Obstacles and Strip Conductors," *IRE Trans. PGMTT* 8, pp. 638-644 (November 1960).
11. S. B. Cohn, "Characteristic Impedances of Broadside-Coupled Strip Transmission Lines," *IRE Trans. PGMTT*, Vol 8, pp 633-637 (November 1960).
12. G. L. Matthaei, "Design of Wide-Band (and Narrow-Band) Band-Pass Microwave Filters on the Insertion Loss Basis," *IRE Trans. PGMTT*-8, pp 580-593 (November 1960).
13. P. S. Carter, Jr., "Magnetically Tunable Microwave Filters Employing Single Crystal Yttrium Iron Garnet Resonators," accepted for publication in *IRE Trans. PGMTT*.
14. G. L. Matthaei, "Design Theory of Up-Converters for Use as Electronically Tunable Filters," scheduled for presentation at the 1961 PMMT National Symposium to be held in Washington, D.C. on May 15 to 17, 1961.

CHAPTER 1

INTRODUCTION

This report presents the results of a three-year research contract carried out for the Signal Corps. This research, and that of two preceding contracts,^{1,2} has been concerned, both theoretically and experimentally, with new types of microwave filters and coupling structures, and with developing more precise methods of design for various previously known structures. A major goal has been the eventual preparation of a handbook for microwave filter design.

Although the major emphasis of this research has been directed toward the microwave filter design problem, various coupling structures have also been considered that have applications independent from filters. The structures discussed in Chapters 2 to 5 fall in this category. Among the structures discussed are a wide-band, strip-line, Magic-T; a ferrite-loaded nonreciprocal TEM-mode structure for wide-band gyrator and isolator applications; and two types of forward-coupling hybrid junction, one in strip-line and one in trough guide. The forward-coupling hybrid junctions have an advantage for some applications over the common 3-db backward couplers, in that the balance arms of the hybrid junctions are adjacent.

Work has also been directed toward preparing data to give designers quantitative information about the electrical effects of various discontinuities and about the coupling between various types of parallel-coupled lines. The material in Chapters 6 to 11 is of this sort. This material should prove valuable for precision design of microwave filters and a variety of other types of microwave devices.

To aid in the design of circuits such as 3-db backward couplers and wide-band filters using parallel-coupled lines, design data are presented in Chapter 6 for broadside-coupled strip transmission lines, and in Chapter 7 for an interleaving, printed-circuit, parallel-coupled, strip-transmission-line construction. Both of these constructions permit very tight coupling between lines while maintaining reasonable tolerances. In Chapter 8, some parallel-coupled line circuits in a nonplanar (cylindrical) transmission-line configuration are considered.

In precise microwave circuit design, it is often necessary to determine the capacitive effect of various discontinuities. Design data have previously existed for thin capacitive obstacles, and in Chapter 9 design data are presented which permit accurate design of thick capacitive obstacles. Data are presented in Chapters 10 and 11 which show the junction effect of strip-line T-junctions. These latter data are useful in correcting for the junction effects in filters or other strip-line devices using stubs with connecting lines.

The material in Chapters 12 to 30 deals specifically with various aspects of microwave filter design.

In Chapter 12, design theory and experimental results are presented for a type of waveguide filter having unusually broad stop bands. This type of filter uses a "waffle-iron" form of interior structure, and has been constructed to give stop bands free of spurious responses between two and three times the cutoff frequency of the filter.

Tables of lumped-element, low-pass, prototype-element values are presented in Chapter 13 for use in the design of Tchebyscheff or maximally flat filter, and in Chapter 14 a discussion is presented of the comparative time-delay characteristics of these various filter types. It has been found that Tchebyscheff filters with small amounts of pass-band ripple have more uniform time-delay characteristics than do maximally flat filters.

Chapter 15 presents a generalized description of Cohn's method for design of direct-coupled, band-pass filters. Using this approach with the lumped-element, low-pass prototype-element values discussed above, the design of filters using any kind of resonators can be readily carried out to give band-pass filters of narrow or moderate bandwidth having a prescribed response characteristic (i.e., such as a Tchebyscheff response). This approach is illustrated in Chapter 16, in the development of design data for a type of transmission-line filter having very wide stop bands. This filter uses quarter-wavelength resonators with capacitive couplings located at points that will be voltage-null points in the higher-order pass bands. Detailed design data are presented for strip-line filters of this sort, and the measured response of a trial design is shown which is free of spurious responses up to five times the frequency of the primary pass band.

In Chapter 17 a method is presented for the design of wide-band, band-pass filters from lumped-element, low-pass prototypes and is applied to filters consisting of transmission lines with series-capacitance couplings. In Chapter 18 this same method is applied to filters using parallel-coupled lines, and to filters using various arrangements of stubs with connecting lines. A number of trial Tchebyscheff filter designs are worked out having bandwidths ranging from 5 percent to wideband filters with 2-to-1 band-edge ratios. In the case of the filters of 30-percent bandwidth or less, the computed responses of the trial designs were almost exactly as specified, while for the octave bandwidth designs there were some noticeable deviations. However, the deviations were small, and of little practical consequence. Chapter 19 reports on a Tchebyscheff filter using stub construction that was designed and built to give a 2.2-to-1 bandwidth; the measured response was found to be very close to the theoretical

Chapter 20 presents a mathematical study of the design of diplexers. Theory is presented, along with the computed impedances and the response of a trial design. Chapter 21 discusses the design of a low-pass filter for use in a diplexer. Two complete diplexers were built, one with a crossover at 2 kMc and another with a crossover at 8.2 kMc. In Chapter 22 their measured responses and constructions are shown.

The results of a study to determine the effects of dissipation loss in filters are presented in Chapter 23. Easy-to-use methods for computing filter loss are discussed, and it is shown that in many narrow-band filter situations where losses are critical, neither the common Tchebyscheff nor the maximally flat types of filters give the best results. Methods for optimum design are shown. Design principles for high-power filters are discussed in Chapter 24, along with means for computing the field strengths in cavities so that the power rating of filters can be estimated. Means are suggested for designing high-power filters which absorb rather than reflect the unwanted signal components.

Mr. Nathan Lipetz, the Signal Corps technical monitor for this contract, asked that special attention be given to possible methods for the design of electronically tunable microwave filters, and various approaches to this problem are presented in Chapters 25 to 29. Chapters 25 and 26 discuss the use of cavities with ferrite loading to give magnetically-tunable filters; Chapter 27 discusses the use of voltage-variable-capacitor diodes to vary the tuning of filter resonators; Chapter 28 discusses the use of single-crystal yttrium-iron-garnet spheres as

magnetically-tunable ferrimagnetic resonators; and Chapter 29 discusses the use of pumped, variable-capacitance diodes in up-converters to form filters whose pass-band frequency is controlled by a voltage-tunable pump oscillator. Although completeness required that all of the various tuning methods studied be discussed, it is the opinion of the authors that the electronically tunable up-converter (Chapter 29) offers most promise at this time for electronic tuning in frequency ranges up to around 3 kMc, while the garnet filters (Chapter 28) offer most promise for use at higher frequencies.

Finally, in Chapter 30, lumped-element, low-pass prototype data are given for impedance-matching networks. Since impedance-matching networks are necessarily filter-type structures, these data can be used with the previously mentioned filter design techniques in order to design microwave impedance-matching networks.

The theory, design data, and experimental results obtained during the course of this research project should be useful in a wide variety of applications. Some of the applications will be concerned with the precision design of filters or coupling structures as system components, while others will be of the nature of precision design of sub-structures of large components. Examples of the latter type of application are the design of an impedance-matching structure which is to be an integral part of a microwave amplifying tube, and the design of impedance-matching discontinuities to become an integral part of an antenna feed structure.

REFERENCES

1. S. B. Cohn, J. K. Shimizu, P. M. Sherk, and E. M. T. Jones, "Strip Transmission Lines and Components," Final Report, SRI Project 1114, Contract DA 36-039 SC-63232, Stanford Research Institute, Menlo Park, California, (February 1957).
2. S. B. Cohn, E. M. T. Jones, O. Heinz, J. K. Shimizu, B. M. Schiffman, and F. S. Coale, "Research on Design Criteria for Microwave Filters," Final Report, SRI Project 1331, Contract DA 36-039 SC-64625, Stanford Research Institute, Menlo Park, California (June 1957).

CHAPTER 2

WIDE-BAND STRIP-LINE MAGIC-T *

This chapter of the report contains a theoretical analysis of a new type of wide-band strip-line Magic-T. A schematic diagram of this device is shown in Fig. 2-1. It is seen that Ports 4 and 3 and 4 and 2 are connected by means of transmission lines of characteristic impedance Z and electrical length θ . Port 1 is connected to Port 2 by means of a band-pass filter[†] having image impedance Z_0 and image phase shift β , while Port 1 is connected to Port 3 by a band-pass filter which is the dual of that connecting Port 1 and 2. It has image impedance Z_1 and an image phase shift $\beta + 180$ degrees.[†] The definitions of these quantities are:

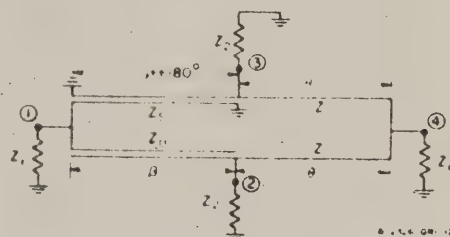


FIG. 2-1

SCHEMATIC DIAGRAM OF A WIDE-BAND
STRIP-LINE MAGIC-T

- | | |
|--|---|
| $Z_1 = \frac{2Z_{oe} Z_{oo} \sin \theta}{[(Z_{oe} - Z_{oo})^2 - (Z_{oe} + Z_{oo})^2 \cos^2 \theta]}$ | The image impedance of the filter with the pair of shorted strips |
| Z_{oe} | Characteristic impedance of one coupled strip, measured with respect to ground, with equal currents flowing in the same direction. |
| Z_{oo} | Characteristic impedance of one coupled strip, measured with respect to ground, with equal currents flowing in opposite directions. |
| $Z_2 = Z_{oe} Z_{oo} Z_1$ | The image impedance of the filter with the pair of open circuited strips |
| θ | Electrical length of each band-pass filter and each line of characteristic impedance Z . |
| $\beta = \cos^{-1} \left[\frac{(Z_{oe} + Z_{oo})}{(Z_{oe} - Z_{oo})} \cos \theta \right]$ | image phase shift of the filter with the pair of open-circuited strips |

* This chapter has been published. See E. M. T. Jones "Wide-Band Strip-Line Magic-T" IRE Trans. MTT Vol. 8, No. 2 pp 160-168 March 1960.

† The subscript e applies to the filter with the pair of shorted strips while the subscript o applies to the filter with the pair of open-circuited strips.

$\beta + 180^\circ$ = image phase shift of the filter with the pair of short-circuited strips.

At midband, where $\theta = 90^\circ$, it is seen that β is always equal to 90° for arbitrary values of Z_{oe} and Z_{oo} . If one chooses Z_{oe} and Z_{oo} as

$$\begin{aligned} Z_{oe} &= Z(\sqrt{2} + 1) \\ Z_{oo} &= Z(\sqrt{2} - 1) \end{aligned} \quad (2-1)$$

$Z_0 = Z_1 = Z$ at midband. If, in addition one sets

$$2Z_1 = Z_2 = Z \quad (2-2)$$

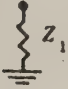

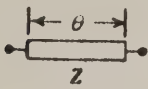
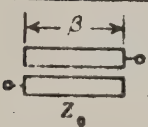
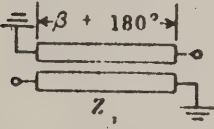
The Magic-T is perfectly matched at midband at all ports and hence has perfect midband isolation between Ports 1 and 4 and Ports 2 and 3. Inspection of Fig. 2-1 shows that Ports 2 and 3 are equivalent to the through arms of a waveguide Magic-T while Ports 1 and 4 are equivalent to the ports on the series and shunt arms, respectively, of a waveguide Magic-T. At frequencies other than the midband frequency the various ports will not be perfectly matched and the isolation between opposite ports will not be infinite. Nevertheless, as will be shown later, the calculated performance of this Magic-T is quite good over a 2:1 frequency band. Calculations are also presented for cases when the various impedances are different from those defined by Eqs. (2-1) and (2-2). It is shown that optimum performance over the 2:1 frequency band is obtained when $Z_1/Z = Z_2/Z = 0.8024$ and $Z_0/Z = 1.0785$ at midband.

The performance of these Magic-T's as a function of frequency is analyzed here in terms of the well-known ABCD matrices of the individual networks within a particular Magic-T. These matrices are listed in Table 2-1 for reference.

The techniques used to compute the input impedance of any port and the output voltages at the other ports will now be illustrated for the case when Port 1 is energized. Figure 2-2 shows the Magic-T of Fig. 2-1 redrawn in a convenient form for computation of the input impedance of Port 1 and the isolation between Ports 1 and 4. Here the matrix elements of the upper network are given by

TABLE 2-1

ABCD MATRICES OF THE INDIVIDUAL NETWORKS IN THE MAGIC-T

| NETWORK | MATRIX |
|--|--|
|  | $\begin{vmatrix} 1 & 0 \\ \frac{1}{Z_1} & 1 \end{vmatrix} = M_1 $ |
|  | $\begin{vmatrix} 1 & 0 \\ \frac{1}{Z_2} & 1 \end{vmatrix} = M_2 $ |
|  | $\begin{vmatrix} \cos \theta & j Z \sin \theta \\ j \frac{\sin \theta}{Z} & \cos \theta \end{vmatrix} = M_3 $ |
|  | $\begin{vmatrix} \cos \beta & + j Z_0 \sin \beta \\ j \frac{\sin \beta}{Z_0} & \cos \beta \end{vmatrix} = M_4 $ |
|  | $\begin{vmatrix} -\cos \beta & - j Z_1 \sin \beta \\ - j \frac{\sin \beta}{Z_1} & -\cos \beta \end{vmatrix} = M_5 $ |
| $\begin{vmatrix} A_u & B_u \\ C_u & D_u \end{vmatrix} = M_5 \times M_2 \times M_3 \quad (2-3)$ | |

while those in the lower network are given by

$$\begin{vmatrix} A_L & B_L \\ C_L & D_L \end{vmatrix} = |M_4| \times |M_2| \times |M_3| \quad (2-4)$$

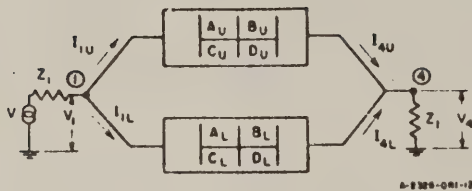


FIG. 2-2

MAGIC-T EQUIVALENT CIRCUIT USED IN
COMPUTING VOLTAGES AT PORTS 1 AND 4

The voltages and currents at the
two ports are related by

$$\begin{aligned} V_1 &= A_U V_4 + B_U I_{4U} \\ I_{1U} &= C_U V_4 + D_U I_{4U} \end{aligned} \quad (2-5)$$

and

$$\begin{aligned} V_1 &= A_L V_4 + B_L I_{4L} \\ I_{1L} &= C_L V_4 + D_L I_{4L} \end{aligned} \quad (2-6)$$

The currents I_{4U} and I_{4L} are related as

$$(I_{4U} + I_{4L}) Z_1 = V_4 \quad (2-7)$$

When Eq. (2-7) is substituted into Eqs. (2-6) and (2-5) one finds
that the input impedance $Z_{in(1)}$ at Port 1 is

$$Z_{in(1)} = \frac{V_1}{I_{1U} + I_{1L}} = \frac{A_U B_L + B_U A_L + \frac{B_U B_L}{Z_1}}{-2 + B_U C_L + B_L C_U + D_U A_L + D_L A_U + \frac{B_U D_L + D_U B_L}{Z_1}} \quad (2-8)$$

The input impedance at Port 4 when Port 1 is terminated in Z_1 is easily
determined by replacing, in Eq. (2-8), A_U by D_U , D_U by A_U , A_L by D_L ,
and D_L by A_L .

It is easy to show that the ratio of V_1/V_4 when Port 1 is energized
is given as

$$\frac{V_1}{V_4} = \frac{\frac{B_U B_L}{Z_1} + A_U B_L + A_L B_U}{B_L + B_U} \quad (2-9)$$

The ratio V_4/V_1 when Port 4 is energized is determined by replacing, in Eq. (2-9), A_U by D_U and A_L by D_L , which shows that in general these ratios are slightly different. The actual insertion loss, *I. L.*, between Terminals 1 and 4 is independent of the direction of propagation through the network and is given by

$$I.L. = \frac{1}{|1 + \Gamma_{in(1)}|} \cdot \frac{\frac{B_U B_L}{Z_1} + A_U B_L + A_L B_U}{B_L + B_U} \quad (2-10)$$

or

$$I.L. = \frac{1}{|1 + \Gamma_{in(4)}|} \cdot \frac{\frac{B_U B_L}{Z_1} + D_U B_L + D_L B_U}{B_L + B_U}$$

where

$$\Gamma_{in(1)} = \frac{Z_{in(1)} - Z_1}{Z_{in(1)} + Z_1}$$

$$\Gamma_{in(4)} = \frac{Z_{in(4)} - Z_1}{Z_{in(4)} + Z_1}$$

Equation (2-10) predicts that the insertion loss between Ports 1 and 4 is infinite only when $Z_1 = Z_0 = Z$.

The voltage at Port 3 when Port 1 is energized is determined with the aid of the circuit in Fig. (2-3). The matrices in this circuit have the values

$$\begin{bmatrix} A' & B' \\ C' & D' \end{bmatrix} = |M_4| \times |M_2| \times |M_3| \times |M_1| \times |M_5|$$

and

$$\begin{bmatrix} A_5 & B_5 \\ C_5 & D_5 \end{bmatrix} = |M_5|$$

(2-11)

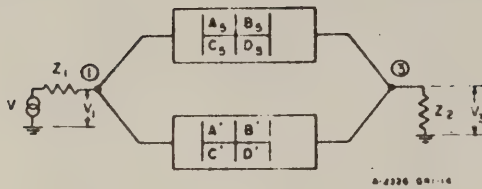


FIG. 2-3

MAGIC-T EQUIVALENT CIRCUIT USED IN
COMPUTING VOLTAGES AT PORTS 1 AND 3

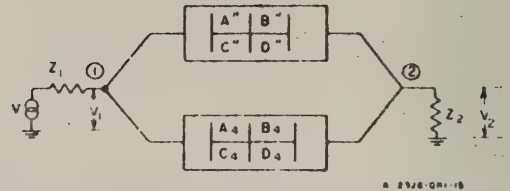


FIG. 2-4

MAGIC-T EQUIVALENT CIRCUIT USED IN
COMPUTING VOLTAGES AT PORTS 1 AND 2

The voltage ratio V_3/V_1 is

$$\frac{V_3}{V_1} = \frac{B' + B_5}{\frac{B'B_5}{Z_2} + A'B_5 + A_5B'} \quad (2-12)$$

The voltage at Port 2 when Port 1 is energized is determined with the aid of Fig. 2-4. The matrices in this circuit have the values

$$\begin{bmatrix} A'' & B'' \\ C'' & D'' \end{bmatrix} = |M_5| \times |M_2| \times |M_3| \times |M_1| \times |M_3|, \quad (2-13)$$

and

$$\begin{bmatrix} A_4 & B_4 \\ C_4 & D_4 \end{bmatrix} = |M_4|$$

The voltage ratio V_2/V_1 is

$$\frac{V_2}{V_1} = \frac{B'' + B_4}{\frac{B''B_4}{Z_2} + A''B_4 + A_4B''} \quad (2-14)$$

The input impedance of the other ports and the voltage transfer coefficients between the various ports when a particular port is energized may be written by inspection using the above technique. One interesting result of such a procedure is the fact that the insertion loss between Ports 2 and 3 is infinite only when $Z_1 Z_0 = Z^2$ and $\theta = \beta = 90^\circ$. This condition is satisfied at midband for all the Magic T's discussed here.

The electrical performances of five Magic T's have been computed on a high-speed digital computer using the above formulas. The important electrical parameters of these structures are listed in Table 2-2.

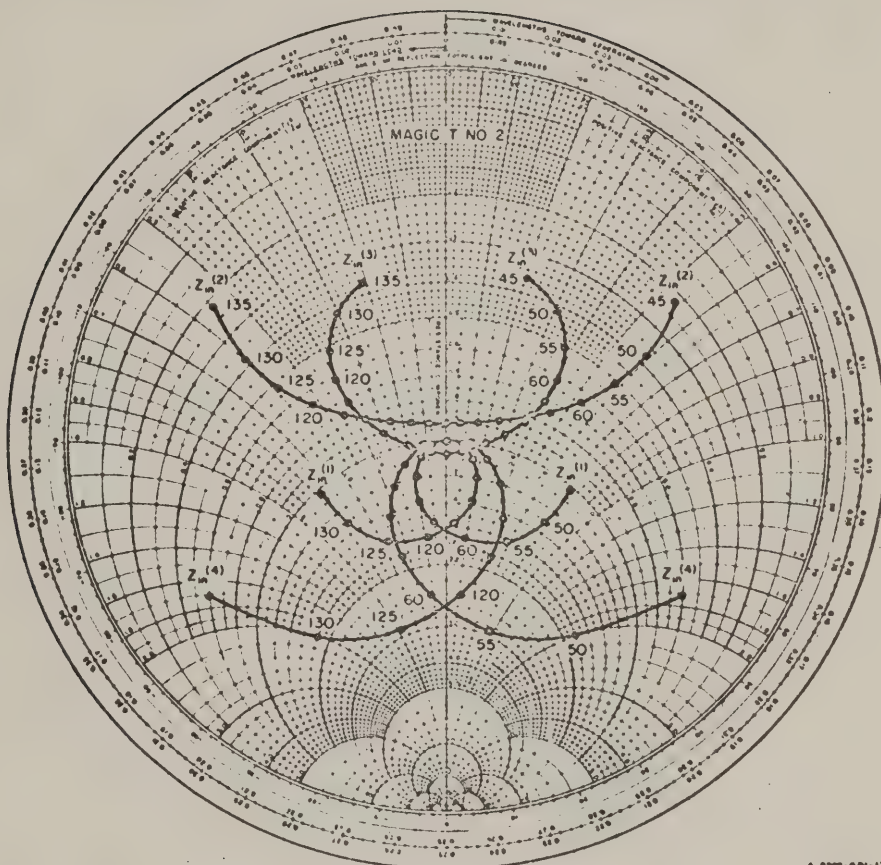
TABLE 2-2
ELECTRICAL PARAMETERS OF VARIOUS STRIP LINE MAGIC-T'S

| | MAGIC-T NO. 1 | MAGIC-T NO. 2 | MAGIC-T NO. 3 | MAGIC-T NO. 4 | MAGIC-T NO. 5 |
|----------------------------------|------------------|---------------------------|---------------------------|---------------------------|---------------------------|
| Z_{oo}/Z | 2.414 | 2.550 | 2.550 | 2.550 | 2.550 |
| Z_{oo}/Z | 0.414 | 0.392 | 0.392 | 0.392 | 0.392 |
| Z_1/Z | 0.500 | 0.500 | 0.6350 | 0.7407 | 0.8024 |
| Z_2/Z | 1.000 | 1.000 | 1.000 | 0.8696 | 0.8024 |
| Z_0/Z (Midband) | 1 | 1.0785 | 1.0785 | 1.0785 | 1.0785 |
| Z/Z (Midband) | 1 | 0.9272 | 0.9272 | 0.9272 | 0.9272 |
| θ (when $Z_1/Z = Z_0/Z$) | 90° | $90^\circ \pm 30.7^\circ$ | $90^\circ \pm 30.7^\circ$ | $90^\circ \pm 30.7^\circ$ | $90^\circ \pm 30.7^\circ$ |
| θ (when $Z_1/Z = Z_0/Z$) | 90° | $90^\circ \pm 22^\circ$ | $90^\circ \pm 22^\circ$ | $90^\circ \pm 22^\circ$ | $90^\circ \pm 22^\circ$ |

The input impedance at the four ports of these Magic T's are plotted in Figs. 2-5 through 2-9. It is observed that in all cases the real part of the input impedance of a port is a symmetrical function of frequency while the imaginary part is an antisymmetrical function of frequency. Furthermore, the input impedance at each of the various ports of any one Magic T has a different variation with frequency since this device has no electrical plane of symmetry.

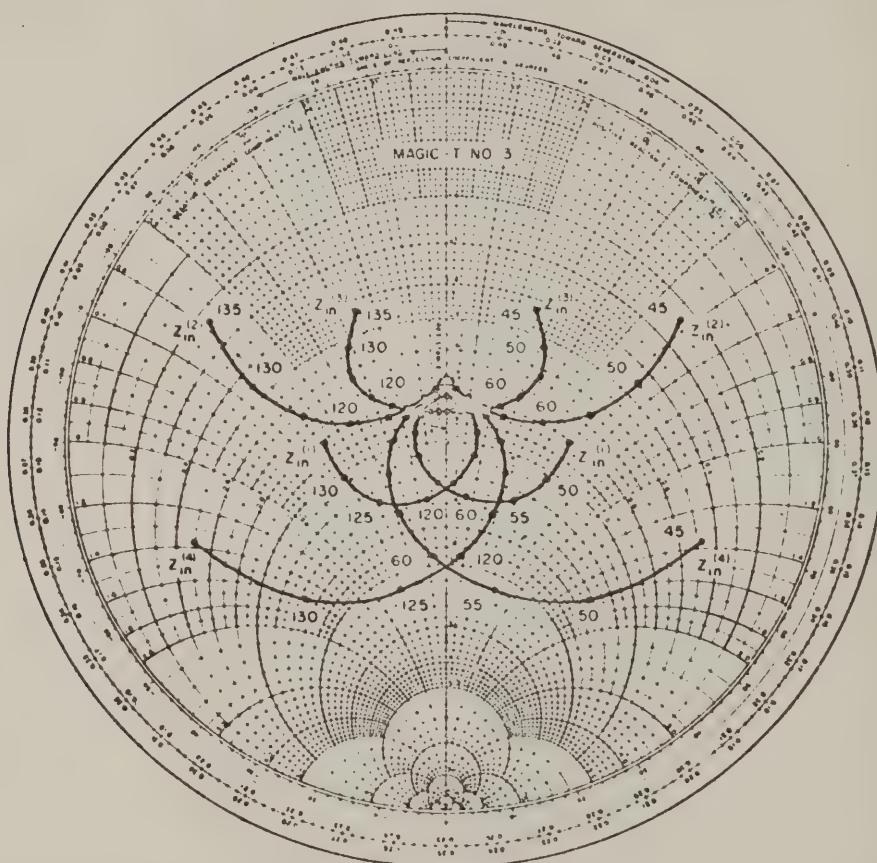
Magic T 1 is designed to be matched at all ports at midband. It also has infinite isolation between Ports 1 and 4 and Ports 2 and 3 at midband. The input match at the various ports deteriorates at frequencies above and below midband. At the edges of a 2:1 frequency band the VSWR at Port 4 rises to 2.55.

Magic-T 2 was designed to have perfect isolation between Ports 1 and 4 at $\theta = 90^\circ \pm 22^\circ$ and approximately equal isolation between these



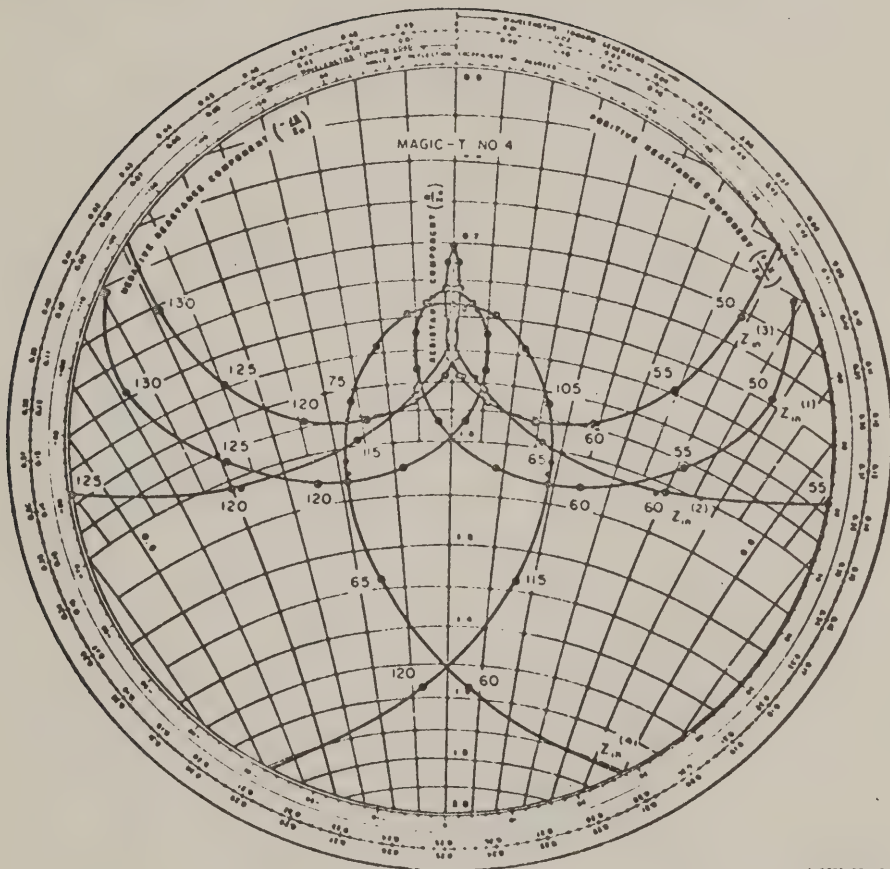
6-2205-0R1-17

FIG. 2-6
INPUT IMPEDANCE OF MAGIC-T 2



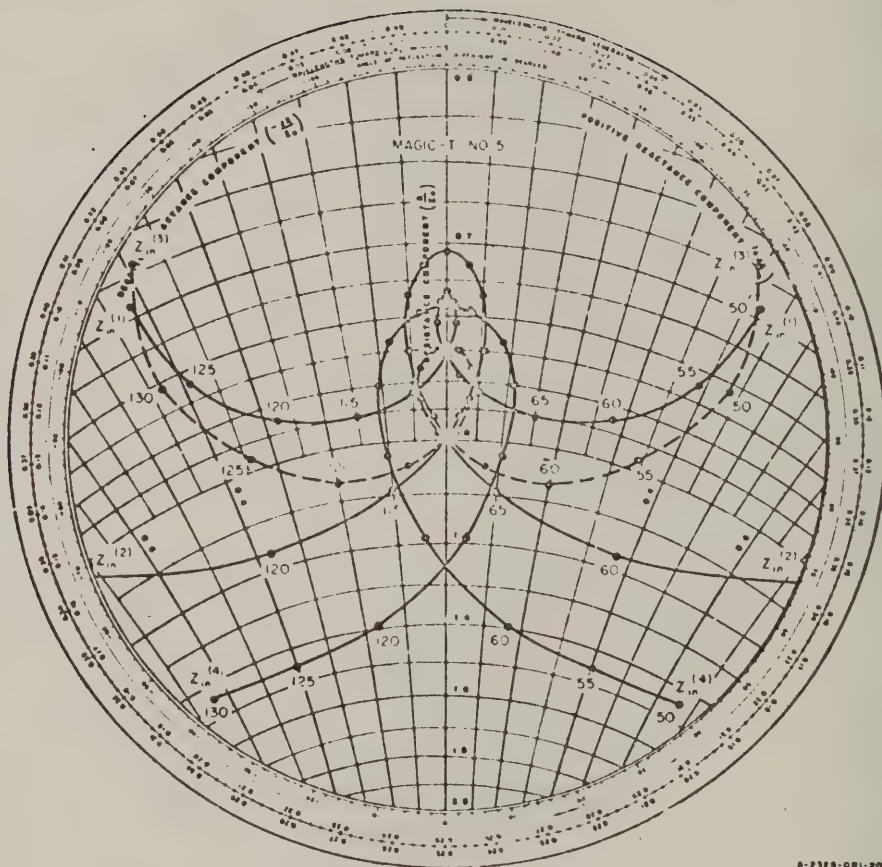
A-7229-001-10

FIG. 2-7
INPUT IMPEDANCE OF MAGIC-T 3



6-2380-001-10

FIG. 2-8
INPUT IMPEDANCE OF MAGIC-T 4



A-2528-QR1-20

FIG. 2-9
INPUT IMPEDANCE OF MAGIC-T 5

ports at the center and at the edges of a 2:1 frequency band. As mentioned before it also has perfect isolation between Ports 2 and 3 at $\theta = 90^\circ$. The frequency variation of the isolation between these pairs of ports is shown in Fig. 2-10. It is observed that over a 2:1 frequency band the isolation between Ports 1 and 4 is always greater than 24.8 db. While the isolation between Ports 2 and 3 drops to 22.2 db at the edges of a 2:1 frequency band. The input impedance of the various ports is quite similar to that of Magic-T 1 and at the edges of a 2:1 frequency band the VSWR at Port 4 rises to 2.45.

The internal structure of Magic-T 3 is the same as that of Magic-T 2, however, the terminating impedance Z_1 at Ports 1 and 4 has been changed to improve the match at these ports. The input impedance of this Magic-T is shown in Fig. 2-7. The VSWR at the various ports of this filter is less at the edges of a 2:1 band than in Magic-T 2. The highest VSWR at the edge of the band is 1.93 measured at Port 4.

The internal structure of Magic-T 4 is the same as that of Magic-T's 2 and 3. The impedances Z_1 and Z_2 have been chosen to give a perfect match at Port 1 when $\theta = 90^\circ \pm 22^\circ$. The input impedance plot of this Magic-T in Fig. 2-8 shows that this technique considerably improves the match at all ports. The maximum VSWR of 1.58 at the edges of a 2:1 band occurs at Port 4.

Magic-T 5 is the same as Magic-T 4 except that it has equal impedances at all the ports whose value is the geometric mean of the values of Z_1 and Z_2 in Magic-T 4. The input impedance of this Magic-T is shown in Fig. 2-9. Its frequency variation of input impedance is less than that of any of the other Magic-T's. Furthermore, the total impedance excursion at each port as a function of frequency is quite similar over a 2:1 frequency band. Hence, it is believed that the parameters of Magic-T 5 are essentially optimum for a 2:1 frequency band of operation. The isolation between diagonally opposite ports is plotted in Fig. 2-10. It is seen that the isolation is quite similar to that of Magic-T 2.

In many applications the most pertinent parameters of a Magic-T are the input impedance of the various ports and the isolation between opposite ports (i.e., between Ports 1 and 4 and Ports 2 and 3). However, it is sometimes desirable to know approximately the ratio, R , of wanted to unwanted voltages at Ports 2 and 3 when Ports 1 or 4 are energized, or the ratio of wanted to unwanted voltages at Ports 1 and 4 when Ports 2 or 3

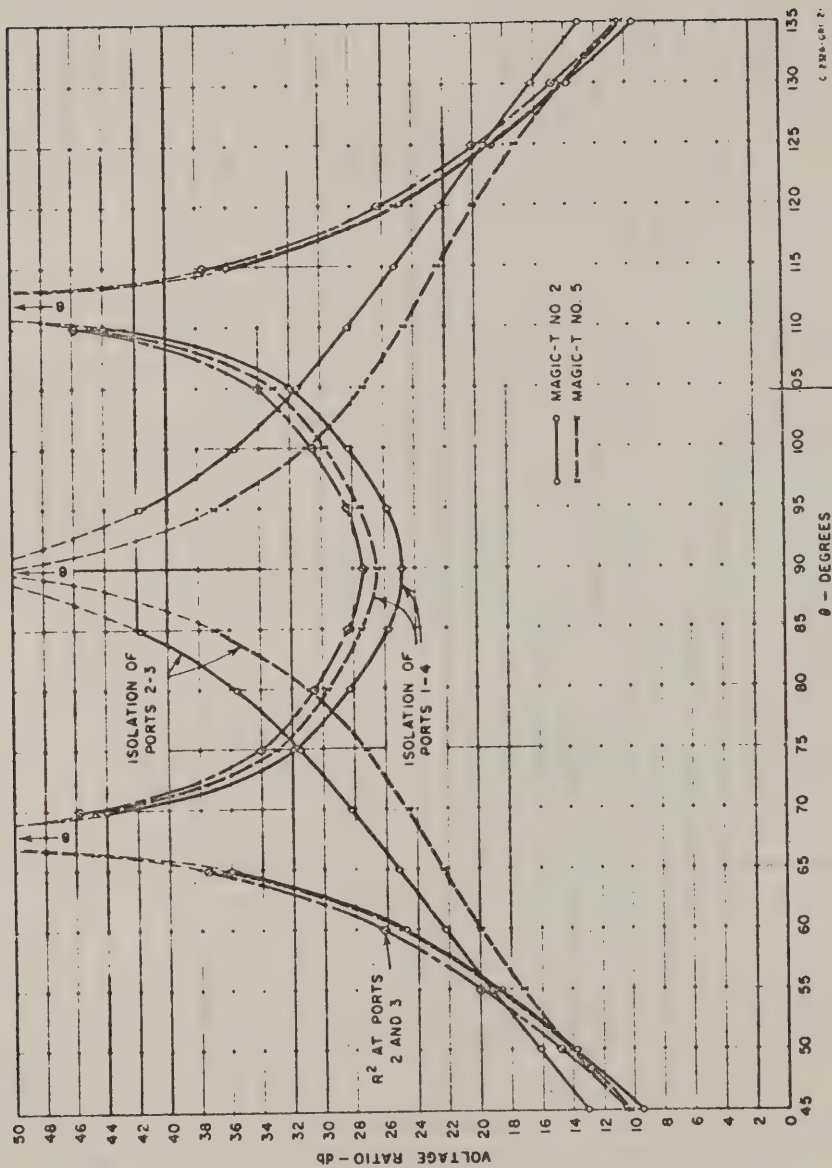


FIG. 2-10

ISOLATION BETWEEN PORTS 1 AND 4 AND BETWEEN PORTS 2 AND 3 FOR MAGIC-T'S 2 AND 5

are energized. This ratio R is V_b/V_u when Ports 1 or 3 are energized and V_u/V_b when Ports 4 or 2 are energized. Here V_b is the balanced voltage and V_u the unbalanced voltage.* An approximation to R can be obtained by the simple procedure outlined below. Inspection of Fig. 2-1 shows that when Port 1 is energized

$$\frac{V_1^2}{Z_1} \approx \frac{V_2^2}{Z_2} + \frac{V_3^2}{Z_2} + \frac{V_4^2}{Z_1} \quad (2-15)$$

or

$$\frac{V_1^2}{Z_1} \approx \frac{2V_b^2}{Z_2} + \frac{2V_u^2}{Z_2} + \frac{4Z_1}{Z^2} V_u^2 \quad (2-16)$$

In deriving Eq. (2-16) use has been made of the fact that

$$V_2^2 + V_3^2 = 2V_u^2 + 2V_b^2$$

and it is assumed that $\theta \approx \beta - \pi/2$ and $Z_1 \approx Z_2 \approx Z_0 \approx Z$ over the operating band. Recalling that the insertion loss (I.L.) is approximately V_1^2/V_4^2 it is seen that

$$\frac{V_1^2}{V_4} \approx \text{I.L.} \approx \frac{V_b^2 Z^2}{2V_u^2 Z_1 Z_2} + \frac{1}{2Z_1 Z_2} + 1 \approx \frac{V_b^2 Z^2}{2V_u^2 Z_1 Z_2} \quad (2-17)$$

and

$$R^2 \approx \text{I.L.} \left(\frac{2Z_1 Z_2}{Z^2} \right) \quad (2-18)$$

It is easy to show that Eq. (2-18) also applies to Ports 2 and 3 when Port 4 is energized and to Ports 1 and 4 when either Port 2 or 3 is energized.

* When Port 1 or 4 is energized $V_b = |V_3 - V_2|/2$ and $V_u = |V_3 + V_2|/2$. When Port 2 or 3 is energized $V_b = |V_1 - V_4|/2$ and $V_u = |V_1 + V_4|/2$.

Application of Eq. (2-18) to Magic-T 2 shows that the insertion loss between opposite ports is numerically equal to R^2 at the other two ports. In Fig. 2-10 is plotted the correct value of R^2 calculated from Eqs. (2-12) and (2-14) at Ports 2 and 3 when Port 1 is energized. It is seen to agree very closely with the approximate value of R^2 computed by Eq. (2-18). In Magic-T 5, Eq. (2-18) predicts that R^2 is about 4 db greater than the insertion loss between opposite ports.

REFERENCES

1. S. B. Cohn, O. Heinz, B. M. Schiffman, E. M. T. Jones, J. K. Shimizu, and F. S. Coale, "Research on Design Criteria for Microwave Filters," SRI Project 1331, Contract DA 36-039 SC-64625, Stanford Research Institute, Menlo Park, California (June 1957).

CHAPTER 3

A NONRECIPROCAL, TEM-MODE STRUCTURE FOR WIDE-BAND GYRATOR AND ISOLATOR APPLICATIONS *

A. GENERAL

This chapter describes the theoretical and experimental operation of a novel form of TEM transmission-line network. This network consists basically of a parallel arrangement of two conductors and a ferrite rod within a grounded outer conductor. The conductors may be connected in a two-port configuration which provides, in the absence of the ferrite rod, complete isolation from zero frequency to the cut-off frequency of the first higher mode. With an unmagnetized ferrite rod properly inserted, the broadband isolation is virtually unaffected. When the rod is magnetized by an axial magnetic field, coupling occurs between the two ports by a process analogous to Faraday rotation.

The device may be used as a broad-band gyrator, switch, or modulator, and with the addition of a resistance load, as an isolator. The bandwidth of these components is inherently limited only by the bandwidth capability of the ferrite material itself.

B. QUALITATIVE DESCRIPTION OF OPERATION

1. GYRATOR NETWORK

The form of the nonreciprocal TEM transmission-line network that functions as a wide-band gyrator, switch, or modulator is illustrated in Fig. 3-1. It is seen to consist of a pair of shielded, coupled transmission lines and an axially oriented ferrite pencil. In a general study of many different filter circuits utilizing coupled transmission lines, Jones and Bolljahn¹ have shown that the circuit of Fig. 3-1 behaves, in the absence of the ferrite rod, as an all-stop filter; that is, infinite attenuation theoretically exists between the two ports at all frequencies. One of the conditions that must be satisfied in order that the network be an all-stop filter is that one of the coupled lines be open-circuited and the other short-circuited in the manner shown in the figure. The other condition is that the phase velocity of the even and odd modes on the coupled lines be the same. Both these conditions can be satisfied when

* Condensed versions of this chapter have been published, see: E. M. T. Jones, G. L. Matthaei, S. B. Cohn "A nonreciprocal, TEM-mode structure for wide-band gyrator and isolator applications" IRE Trans MTT, Vol 7 No. 4 pp 453-460 (October 1959) also E. M. T. Jones, S. B. Cohn, J. K. Shimizu "A wide-band nonreciprocal TEM-transmission-line network" 1958 WESCON Convention Record pt 1, pp 131-135.

the ferrite is properly oriented in the plane of symmetry between the coupled lines. It is found that the proper position of the rod is quite independent of frequency so that the composite structure has high attenuation over a wide band of frequencies.

When an axial magnetic field is applied to the ferrite rod, it rotates the plane of polarization of the linearly polarized transverse RF magnetic field existing along the ferrite rod, and energy is coupled between the input and output ports. When the axial field is increased to the point where the RF magnetic field is rotated by 90 degrees, virtually all the energy is transferred. When the cross section of the ferrite rod is small in terms of wavelength, and the operating frequency is far removed from the ferromagnetic resonance frequency, the rotation of the plane of polarization per unit length by the ferrite is essentially independent of frequency. Therefore, low insertion loss is experienced over a wide frequency range. Because the plane of polarization of the RF magnetic field is rotated in the same sense with respect to the positive direction of the

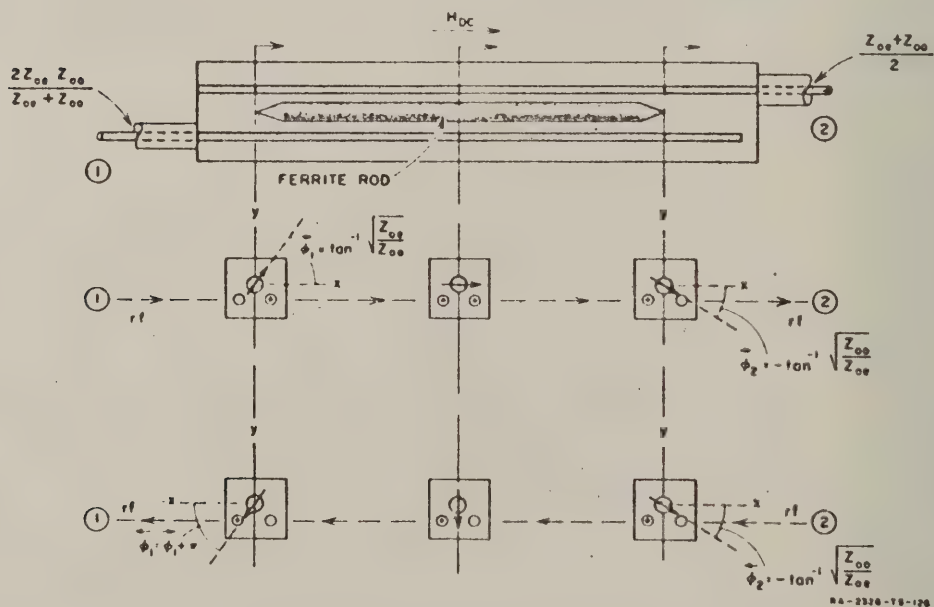


FIG. 3-1

WIDE-BAND GYRATOR

biasing magnetic field, independent of the direction of propagation through the device, it can be seen that the signal undergoes 180 degrees more phase shift while passing through in one direction than it does while passing through in the opposite direction. Thus the device functions as a gyrator. It may also be used as a switch by abruptly changing the magnetizing field from zero to the strength that gives full transfer of energy, or it can be used as a modulator by continuously varying the field.

2. ISOLATOR

The configuration of the network that is most suitable for use as an isolator is shown in Fig. 3-2. The diagrams at the bottom of the figure illustrate the manner in which the RF magnetic field at the axis of the ferrite rod is rotated in passing through the device in either direction. It can be seen that when a signal travels from left to right the RF magnetic field is initially oriented at an angle, ϕ_1 , somewhat greater than 45 degrees to the horizontal. Since there is no voltage induced in the short-circuited line on the upper left, the resistive termination placed behind this line does not attenuate the signal. The RF magnetic field on passing through the ferrite is rotated through an angle ϕ_1 so that at the output it is horizontal. A signal entering from the right also has its RF magnetic field

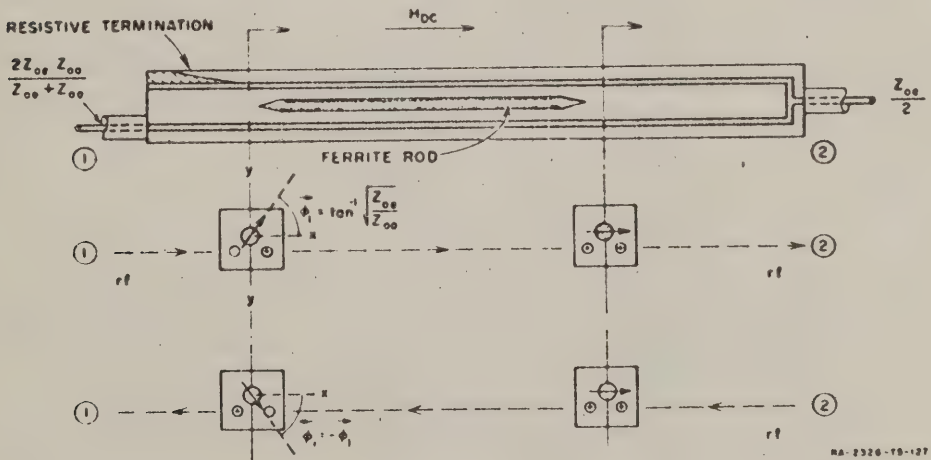


FIG. 3-2
WIDE-BAND ISOLATOR

rotated ϕ_1 degrees as it passes through the ferrite so that all the power is transferred to the upper line where it is attenuated by the resistive termination at the left-hand end of the network.

C. PERTURBATION ANALYSIS OF NONRECIPROCAL COUPLING BETWEEN A PAIR OF SHIELDED CONDUCTORS

A more detailed picture of the behavior of the various forms of the device may be obtained by analyzing the nonreciprocal coupling between shielded conductors using perturbation theory. This theory is exact for ferrite rods having infinitesimal cross-section areas, and is qualitatively correct for the ferrite rods used in practice. The first-order perturbation expression for the propagation constant Γ of uniformly loaded transmission line is²

$$\Gamma - k_1 = \frac{j\omega \int_{\Delta_1} (\epsilon_0 : \vec{X}_e^{eff} : \mathbf{E}_1 \cdot \mathbf{E}_1^* + \mu_0 \vec{X}_m^{eff} : \mathbf{H}_1 \cdot \mathbf{H}_1^*) d\tau}{\int_S \mathbf{i}_z (\mathbf{E} \wedge \mathbf{H}_1^* + \mathbf{E}_1^* \wedge \mathbf{H}) d\tau} \quad (3-1)$$

In this expression

- k_1 = the propagation constant of the unperturbed system, which will be assumed to be lossless
- ω = angular frequency of the RF field
- Δ_1 = cross-section area of the ferrite—in square meters
- S = cross-section area of the transmission line—in square meters
- \vec{X}_e^{eff} = effective tensor electric susceptibility of the ferrite
- \vec{X}_m^{eff} = effective tensor magnetic susceptibility of the ferrite
- \mathbf{E}, \mathbf{H} = electric and magnetic fields everywhere across the section of the transmission line with the ferrite in place
- $\mathbf{E}_1, \mathbf{H}_1$ = electric and magnetic fields everywhere across the section of the transmission line in the absence of the ferrite

\mathbf{i}_z = unit vector in the direction of propagation

* = symbol denoting the complex conjugate

ϵ_0 = $10^{-9}/36\pi$ farads per meter

μ_0 = $4\pi \times 10^{-7}$ henries per meter.

In evaluating Eq. (3-1) one customarily assumes that $\mathbf{E} = \mathbf{E}_1$ and that $\mathbf{H} = \mathbf{H}_1$.

When the ferrite is unmagnetized, the effective electric susceptibility is a scalar, and if the ferrite is cylindrical in cross section χ_e^{eff} has a value $2(\epsilon - 1)/(\epsilon + 1)$, where ϵ is the relative dielectric constant of the ferrite. Likewise the effective magnetic susceptibility of an unmagnetized ferrite is a scalar and if the ferrite is cylindrical in cross section χ_μ^{eff} has a value of $2(\mu - 1)/(\mu + 1)$, where μ is the relative initial permeability of the ferrite. In the following discussion it will be assumed that both ϵ and μ are real. With the ferrite rod in position and unmagnetized, the propagation constant β_e' of the even mode as determined from Eq. (3-1) is

$$\beta_e' - k_1 = \frac{a\mu_0\Delta sH_e^2 \left[2\left(\frac{\epsilon - 1}{\epsilon + 1}\right) + 2\left(\frac{\mu - 1}{\mu + 1}\right) \right]}{4I_o^2 Z_{oe}} \quad (3-2)$$

Similarly the propagation constant β_o' of the odd mode is related to the unperturbed odd-mode propagation constant, k_1 , as

$$\beta_o' - k_1 = \frac{a\mu_0\Delta sH_o^2 \left[2\left(\frac{\epsilon - 1}{\epsilon + 1}\right) + 2\left(\frac{\mu - 1}{\mu + 1}\right) \right]}{4I_o^2 Z_{oo}} \quad (3-3)$$

In these expressions

H_e = RF field existing at the axis of the ferrite, in the absence of the ferrite when the device is excited in the even mode (i.e., equal in-phase currents I_o flow on the conductors)

H_o = RF magnetic field existing at the axis of the ferrite, in the absence of the ferrite, when the device is excited in the odd mode (i.e., equal out-of-phase currents I_o flowing in the center conductors)

Z_{oe} = characteristic impedance of one center conductor to ground with equal in-phase current I_o flowing in the center conductors

Z_{oo} = characteristic impedance of one center conductor to ground with equal out-of-phase currents I_o flowing in the center conductors.

In order that there be no reciprocal coupling between the conductors the ferrite rod must be oriented so that the phase velocities of perturbed even and odd modes are equal. That is,

$$\beta'_e = \beta'_o = \beta \quad (3-4)$$

Substitution of Eqs. (3-2) and (3-3) into Eq. (3-4) shows that

$$\frac{H_e}{I_o Z_{oe}} = \frac{H_o}{I_o Z_{oo}} \quad (3-5)$$

Thus it is seen that if the even and odd modes carry equal power they will produce equal RF magnetic fields at the center of the ferrite rod. However equal even and odd mode currents do not produce equal fields at the center of the rod

The amount of nonreciprocal rotation per unit length θ of the plane of polarization of the wave at the axis of the ferrite rod as well as the attenuation per unit length α can be determined by first resolving the wave into right- and left-hand circularly polarized components. Then from the propagation constants $\alpha_+ + j\beta_+$ and $\alpha_- + j\beta_-$ of the right- and left-circularly polarized waves one computes the nonreciprocal rotation per unit length θ from the well known relation

$$\theta = \frac{\beta_- - \beta_+}{2} \quad (3-6)$$

and the attenuation α from

$$\alpha = \frac{\alpha_+ + \alpha_-}{2} \quad (3-7)$$

The expression for the propagation constants of the two waves as determined by perturbation theory is

$$\beta_{\pm} - \beta = \frac{\omega \mu_0 \Delta S (H_e^2 + H_o^2) \left[2 \left(\frac{\epsilon - 1}{\epsilon + 1} \right) + X_{\pm}'^{eff} \right]}{4I_e^2 Z_{oe} + 4I_o^2 Z_{oo}} \quad (3-8)$$

and

$$\alpha_{\pm} = \frac{\omega \mu_0 \Delta S (H_e^2 + H_o^2) X_{\pm}''^{eff}}{4I_e^2 Z_{oe} + 4I_o^2 Z_{oo}} \quad (3-9)$$

In these expressions

$$X_{\pm}'^{eff} = \frac{\omega_a (\omega_{res} \mp \omega)}{(\omega_{res} \mp \omega)^2 + \left(\frac{\omega_{res}}{\omega_0 \tau} \right)^2} \quad (3-10a)$$

$$X_{\pm}''^{eff} = \frac{\frac{\omega_a \omega}{\omega_0 \tau}}{(\omega_{res} \mp \omega)^2 + \left(\frac{\omega_{res}}{\omega_0 \tau} \right)^2} \quad (3-10b)$$

where

$$\omega_a = \gamma 4\pi M$$

$$4\pi M = \text{saturation magnetization—gauss}$$

$$\gamma/2\pi = 2.8 \text{ Mc/oersted}$$

$$\omega_0 = \gamma H_{DC}$$

$$H_{DC} = \text{applied internal field in the ferrite rod—in oersteds}$$

$$\omega_{res} = \omega_0 + \omega_a/2$$

$$\tau = 2/\gamma \Delta H = T \omega/\omega_0$$

$$T = \text{phenomenological relaxation time as defined by Lax}^2$$

$$\Delta H = \text{ferrite linewidth measured to the one half amplitude points.}$$

If one substitutes Eq. (3-10a) into Eq. (III-8) and makes the usual approximation that $(\omega_{res}/\omega_0\tau)^2 \ll (\alpha_{res} \pm \alpha)^2$ one finds that

$$\theta l = \frac{(\beta_- - \beta_+)l}{2} = \frac{\omega l \mu_0 \Delta s (H_r^2 + H_o^2) \omega \alpha_{\pm}}{(4I_{res}^2 Z_{oo} + 4I_{oo}^2 Z_{oo}) (\omega_{res}^2 - \omega^2)} \quad (3-11)$$

To the same approximation substitution of Eq. (3-10b) into Eq. (3-9) yields

$$\alpha l = \left(\frac{\alpha_+ + \alpha_-}{2} \right) l = \frac{\omega l \mu_0 \Delta s (H_r^2 + H_o^2) \omega \alpha_{\pm}}{(4I_{res}^2 Z_{oo} + 4I_{oo}^2 Z_{oo}) \omega_0 \tau} \left[\frac{\omega_{res}^2 + \omega^2}{(\omega_{res}^2 - \omega^2)^2} \right] \quad (3-12)$$

combining Eqs. (3-11) and (3-12) yields

$$\alpha l = \frac{1}{\omega_0 \tau} \left(\frac{\omega_{res}^2 + \omega^2}{\omega_{res}^2 - \omega^2} \right) \theta l \quad (3-13)$$

Equation (3-13) shows that for a given total rotation θl the total attenuation αl experienced by a signal is independent of the cross-section geometry. In the experimental gyrator and isolator described later in this section the ferrite used is Ferramic R-1. This material has a line-width ΔH of about 500 oersteds at an operating frequency of 9000 Mc. This value of line width yields $\alpha_0 \tau = \alpha T$ of about 12.7 over a wide band of frequencies centered at 9000 Mc. Hence it is seen that far from resonance the theoretical attenuation through the gyrator, which has a $\theta l = \pi/2$ radians is about 1.07 db. The theoretical minimum forward attenuation through the isolator which has a θl of about 0.91 radian is 0.62 db. Inspection of Eq. (3-11) reveals that at frequencies removed from the ferromagnetic resonance frequency, the rotation θl is independent of the operating frequency. It is also seen that θl increases with the ferrite length l , the saturation magnetization $4\pi M_s$, and the cross-section area of the ferrite rod Δs . Also θl increases when the operating frequency approaches the resonance frequency; however, it is seen that operating near resonance also increases the attenuation. For a given size of ferrite the amount of rotation is proportional to the ratio $H_o^2 + H_r^2$ (the square of the total unperturbed RF field at the axis position of the ferrite) to $4I_{res}^2 Z_{oo} + 4I_{oo}^2 Z_{oo}$.

(twice the total power transmitted along the ferrite-loaded structure). In general it is very difficult to determine this ratio quantitatively; however, it has been done for the case of thin, flat, co-planar coupled strips using a conformal mapping technique. The results of this analysis show that this ratio increases as the gap between the coupled strips is decreased. At the same time it is found that the position where the magnetic fields of the even and odd mode are equal for equal power in the two modes moves closer to the plane of the coupled strips as the gap between the strips is decreased. It seems likely that this behavior will obtain for other conductors having different cross-section shapes.

D. DETAILED DESCRIPTION OF OPERATION

1. GYRATOR

When the correct biasing field for gyrator action is applied to the ferrite rod shown in Fig. 3-1, perfect transmission is achieved through the network, assuming a reflectionless and lossless ferrite* when the terminating impedances at Port 1 and Port 2 are equal to the input impedances at each of these ports when the opposite port is terminated in a matched load. The input impedance at Port 1 under these conditions can be readily computed by noting that a signal entering Port 1 excites even and odd modes on the coupled lines, having equal voltages $V/2$ since it is necessary to have zero voltage on the shorted line. Hence the current flowing on the coupled line connected to Port 1 is $V/2 [1/Z_{oe} + 1/Z_{oo}]$ while that induced on the shorted line is $V/2 [1/Z_{oe} - 1/Z_{oo}]$. Therefore, the input impedance at Port 1 is $2Z_{oe}Z_{oo}/(Z_{oe} + Z_{oo})$. In a like manner it is seen that a signal entering Port 2 excites even and odd modes having equal currents, I . Hence the voltage on the line connecting to Port 2 is $I(Z_{oe} + Z_{oo})$ while that induced on the open-circuited line is $I(Z_{oe} - Z_{oo})$. Therefore, the input impedance at Port 2 is $(Z_{oe} + Z_{oo})/2$.

The inclination angle ϕ of the RF magnetic field along the axis of the ferrite as a signal passes through the gyrator can be computed in the following fashion. When a signal is incident on Port 1** with voltage amplitude V , the amplitude of the even current I_{1e} is $V/2Z_{oe}$ on the coupled lines while the amplitude of the odd current I_{1o} is $-V/2Z_{oo}$. Referring to

* Part C of this section.

** The arrows indicate the direction of power flow through the device with reference to Fig. 3-1.

Fig. 3-1 and remembering the condition of Eq. (3-5), it is seen that the even current produces an x-directed component of magnetic field $H_{1x} = H_{1e}$ at the axis of the ferrite rod having an amplitude proportional to $1/\sqrt{Z_{oe}}$. The odd-mode current produces a y-directed component of magnetic field $H_{1y} = H_{1o}$ at the axis of the ferrite rod having an amplitude proportional to $1/\sqrt{Z_{oo}}$. Thus

$$\tan \psi_1 = \frac{H_{1y}}{H_{1x}} = \sqrt{\frac{Z_{oe}}{Z_{oo}}} \quad (3-14)$$

As the signal passes through the magnetized ferrite the plane of polarization of the field at the center of the ferrite rod rotates clockwise, however its magnitude $\sqrt{H_x^2 + H_y^2}$ is unchanged. When the wave reaches the end of the ferrite rod adjacent to Port 2 it is necessary that $I_{2e} = I_{2o} = 1/\sqrt{2Z_{oe}Z_{oo}}$ in order that all the signal power will pass out Port 2. Therefore the inclination angle ψ_2 is

$$\tan \psi_2 = \frac{H_{2y}}{H_{2x}} = -\sqrt{\frac{Z_{oe}}{Z_{oo}}}$$

showing that the plane of polarization of the wave at the center of the ferrite is rotated 90 degrees in passing once through the gyrator. When a signal passes through the device from Port 2 to Port 1 the plane of polarization of the RF magnetic field is rotated in the same sense with respect to the biasing field as shown in Fig. 3-1. Hence, as explained above this device functions as a gyrator, since a signal undergoes 180 degrees more phase shift in going through the device in one direction than the other.

2. WIDE-BAND ISOLATOR

When the correct biasing field is applied to the ferrite rod shown in Fig. 3-2 for isolator action, it is seen that zero forward loss is achieved, again assuming a lossless and reflectionless ferrite when the characteristic impedances of the lines connected to Port 1 and Port 2 are $2Z_{oe}Z_{oo}/(Z_{oe} + Z_{oo})$ and $Z_{oe}/2$, respectively. Furthermore it is necessary that the termination within the isolator perturb the phase velocities of the even and odd modes equally

When a signal is incident on Port 1 the inclination angle $\bar{\phi}_1$ of the RF magnetic field at the axis of the ferrite rod is $\bar{\phi}_1 = \tan^{-1} \sqrt{Z_{oe}/Z_{oo}}$. As the signal passes through the isolator the plane of polarization of the field at the axis of the rod is rotated until $\bar{\phi}_2$ is zero at Port 2. When a signal is incident on Port 2 the angle of inclination $\bar{\phi}_2$ of the field at Port 2 is again zero. As the signal passes through the device the RF magnetic field is rotated in the same direction with respect to the biasing magnetic field so that the inclination angle $\bar{\phi}_1$ of the magnetic field at the center of the ferrite rod nearest Port 1 is $\bar{\phi}_1 = -\bar{\phi}_1$. This orientation of the magnetic field corresponds to zero RF voltage on the line connecting to Port 1 and maximum voltage on the line containing the termination, which is the optimum condition for a large absorption in the termination.

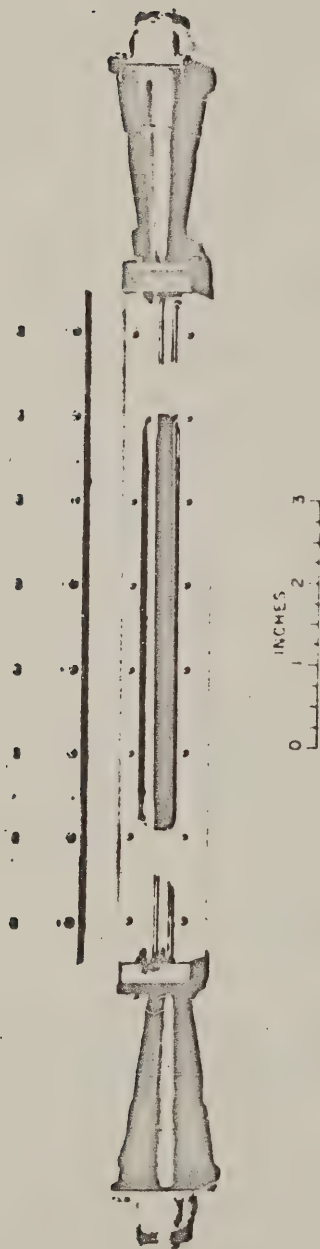
It is interesting to note that should the direction of the biasing magnetic field be reversed, a signal incident on Port 2 will propagate through the isolator and emerge unattenuated from Port 1. However it can be seen that a signal incident on Port 1 after passing through the isolator will set up both even and odd mode currents on the lines adjacent to Port 2. The energy in the even mode will pass out of Port 2 while the energy in the odd mode will be reflected at the T-junction and later after retraversing the network be absorbed in the termination. Thus, other factors being the same, the reverse loss is less for this orientation of biasing field than for the correct orientation of the biasing field shown in Fig. 3-1.

However, as discussed in Part F, measurements made on an isolator indicated only a small difference in attenuation when the H field was reversed.

F MEASURED PERFORMANCE

I GYRATOR EXPERIMENTAL RESULTS

A photograph of the experimental model of the wide band gyrator is shown in Fig. 3-3. Its measured performance is shown in Fig. 3-4. The cross-section dimensions of the coupled strip lines and the Ferramic R-1 ferrite rod are also shown in the figure. The over-all length of the coupled lines is 8 inches. The over-all length of the ferrite rod is 5.75 inches and each end is tapered over a length of 0.625 inch. The theoretical values of Z_{oe} and Z_{oo} are 139 and 88 ohms respectively.



P-2326-TB-120

FIG. 3-3
PHOTOGRAPH OF THE WIDE-BAND GYRATOR

These values were computed from Eqs. (24) and (25) of Ref. 1 suitably modified to account for the increased self-capacitance of the lines caused by the presence of the vertical side walls of the outer conductor of the network. Tapered transitions were employed at either end of the gyrator to match it to the 50-ohm impedance level of the measuring equipment. The transition at Port 1 transformed between 50 ohms and $2Z_{00}Z_{00}/(Z_{00} + Z_{00}) = 108$ ohms while the transition at Port 2 transformed between 50 ohms and $(Z_{00} + Z_{00})/2 = 114$ ohms.

It is seen that with no DC biasing field applied, the insertion loss through the gyrator is greater than 20 db except near the highest frequencies measured where it drops to 16 db. When the magnetic field is applied to obtain gyrator action the insertion loss decreases to less than 2 db except at a few isolated points in the band. At the upper end of the band the insertion loss averages about 1 db in agreement with the results of the perturbation analysis. Although the data were not recorded it is believed that the gyrator shown would operate satisfactorily down to frequencies as low as 5.5 kMc since one of the experimental isolators described in the next section operated down to this frequency:

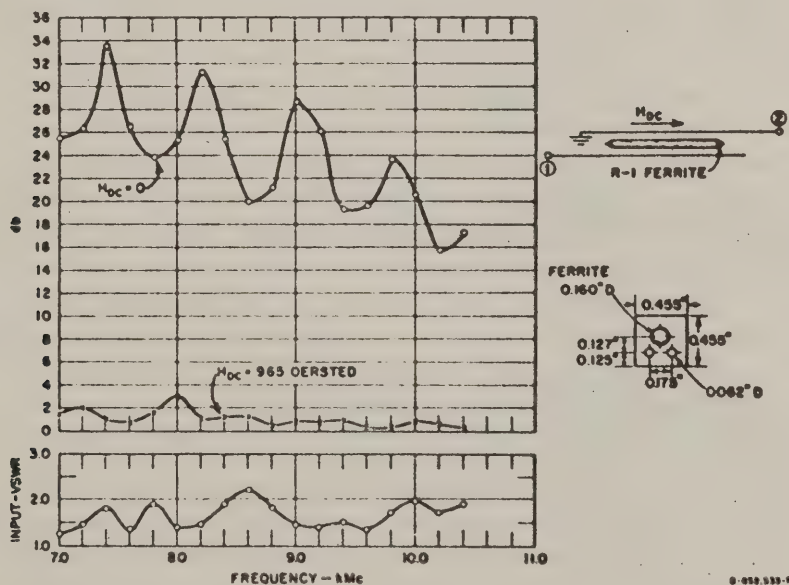


FIG. 3-4

MEASURED PERFORMANCE OF WIDE-BAND GYRATOR

It is believed that the insertion loss of the gyrator could be reduced by a factor of 10 by employing a yttrium iron garnet rod which has a line width of about 50 oersteds, rather than the Ferramic R-1 which has a line width of about 500 oersteds. No extended effort was made to perfect the gyrator shown in Fig. 3-3; doubtless with further work it could be improved considerably.

2. ISOLATOR EXPERIMENTAL RESULTS

An experimental isolator design was constructed having cross-sectional dimensions as shown in Fig. 3-5. In this case the even and odd mode impedances are approximately $Z_{oe} = 148$ and $Z_{oo} = 90.4$ ohms. Then, by Part F-2, the input impedance at Port 1 in Fig. 3-2 is $Z_{oe}Z_{oo}/(Z_{oe} + Z_{oo}) = 112.5$ ohms while the input impedance at Port 2 is $Z_{oe}/2 = 74$ ohms. In order to match the 112.5-ohm impedance at Port 1 to 50 ohms, a 2.4-inch taper section was used at that end. At Port 2 it was possible to achieve a good match by adjusting the position of the Y-junction with respect to the end wall, and by altering the diameter of the conductor between the junction and the end of the box. In order to test the VSWR of the transitions, long tapered sections of Polyrion were placed beside the conductors to act as terminations inside the box.

The isolator whose cross section is shown in Fig. 3-5 used a 0.147-inch diameter rod of Ferramic R-1 ferrite, 5.70 inches in over-all length with each end tapered to a point in a distance of 1.2 inch. In order to determine the optimum position of the ferrite rod, the rod was suspended in the box by threads with metal pull rods and calibrated adjusting nuts. In this manner it was possible to adjust the position of the ferrite rod while the isolator was in operation. Since the reverse loss is the most sensitive test of proper operation, the rod was positioned in such a way as to optimize the reverse loss characteristic. Because the thread system used for holding the rod was not very rigid, the rod position indicated in Fig. 3-5 can be regarded only as a close approximation.

Before the perturbation analysis in Part C was completed it was thought to be theoretically correct for the forward loss to be measured from Port 1 of the isolator with the field as shown in Fig. 3-2, while to obtain the reverse loss characteristic one could either keep the H -field fixed and feed power in Port 2, or one could continue to feed the power in Port 1 and simply reverse the direction of the H -field. Since the thread supports for the ferrite rod were not rigid, it was desirable to reverse the solenoid

current rather than disturbing the set-up to reverse the direction of power flow. Tests showed that reversing the H -field and reversing the direction of power flow appear to give the same results within what appeared to be experimental error, so the data in Fig. 3-5 were taken with power fed in Port 1 with the H -field as in Fig. 3-2 for the forward loss characteristic, and with the H -field reversed to measure the reverse loss characteristic. Later, the perturbation analysis of Part C

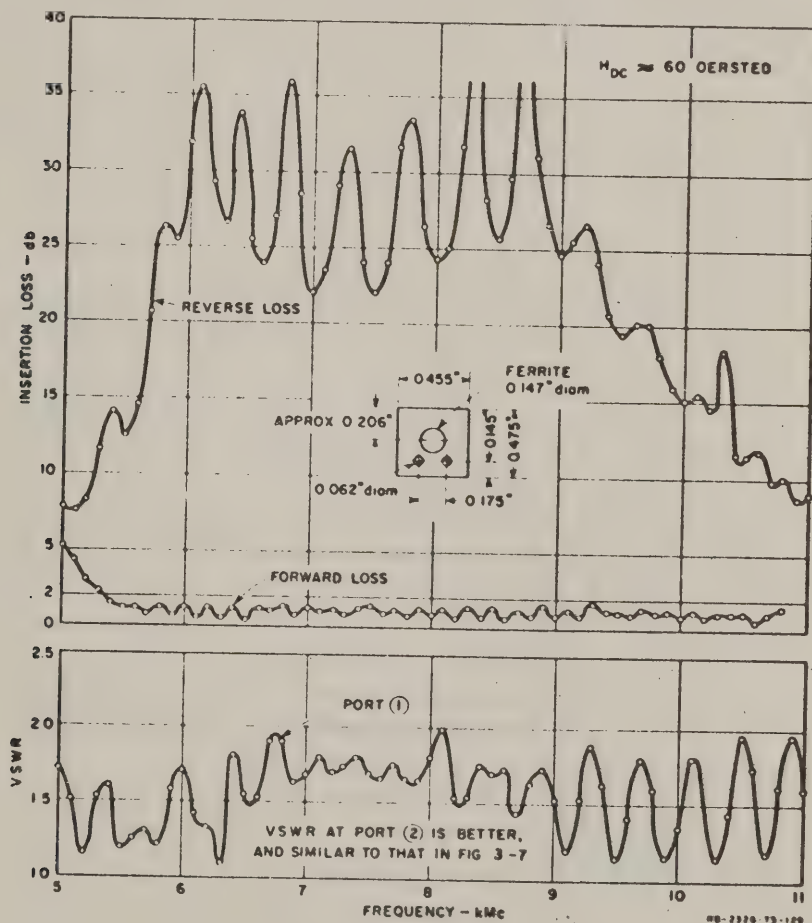


FIG. 3-5

MEASURED RESPONSE OF A TEM MODE ISOLATOR USING A 0.147-INCH-DIAMETER R-1 FERRITE ROD, 5.70 INCHES IN OVER-ALL LENGTH WITH EACH END TAPERED TO A POINT IN A DISTANCE OF 1.2 INCHES

was completed, and it showed that the amount of field rotation in the device should not be 45 degrees but somewhat greater than 45 degrees. This implied that a reverse loss characteristic measured by reversing the H -field should not be quite the same for this device as that obtained by reversing the direction of power flow. Consequently, the later data of Fig. 3-7 were taken by reversing the direction of power flow. However in that case the difference between the reverse loss measured by reversing the H -field and that measured by reversing the direction of power flow was found to be small.

As can be seen from Fig. 3-5, the device had quite high isolation (i.e., reverse loss) over a considerable bandwidth. The forward loss was around 1.0 db over most of the band with a few peaks reaching a maximum of 1.6 db. It is interesting to note that the VSWR at Port 1 ranged as high as 2:1, while spot checks taken at Port 2 consistently indicated VSWR of considerably lower values. These two observations appear to be consistent with the hypothesis that due to some extraneous effects such as higher-order modes or reciprocal coupler action caused by the presence of the ferrite rod, the optimum rotation angle for the forward and reverse loss characteristics is not quite the same. Since the H -field and ferrite rod position was so selected as to optimize the reverse loss characteristic, the forward loss characteristic would not be optimum if there were any such extraneous effects. The VSWR at Port 1 was the same regardless of the H -field direction, and the same was true for the VSWR at Port 2. The fact that the VSWR at Port 1 is higher than that at Port 2 is logical since, for example, if the amount of forward-direction rotation were not exactly correct, power fed in Port 1 would be partially reflected at the Y-junction near Port 2. However, consideration of Fig. 3-2 will show that when power is being fed into Port 2, the direction and amount of the rotation will primarily control the division of power between the power sent to the termination at Port 1 and the power sent to the adjacent internal termination. Thus, an error in rotation angle should have little or no effect on the VSWR seen looking in Port 2.

In order to obtain a better understanding of the response in Fig. 3-5, the data in Fig. 3-6 were taken. In this case the solenoid current was adjusted at each frequency so as to peak the reverse loss. These data show

that at both the relatively low and the relatively high frequencies less solenoid current (and less H -field) is required. A possible explanation of this is that less H -field is required at the lower frequencies due to the proximity of ferrimagnetic resonance. The perturbation analysis of Part C is consistent with this view. Also, it has been noted in waveguide ferrite rotator sections that for a given field strength the amount of rotation will increase with frequency due to increased concentration of energy in the ferrite rod.³ This appears to be a logical explanation for the decrease in field strength required to give the desired rotation at high frequencies for the case of Fig. 3-6. It is probable that the rotation could be kept more constant with frequency for a given H -field

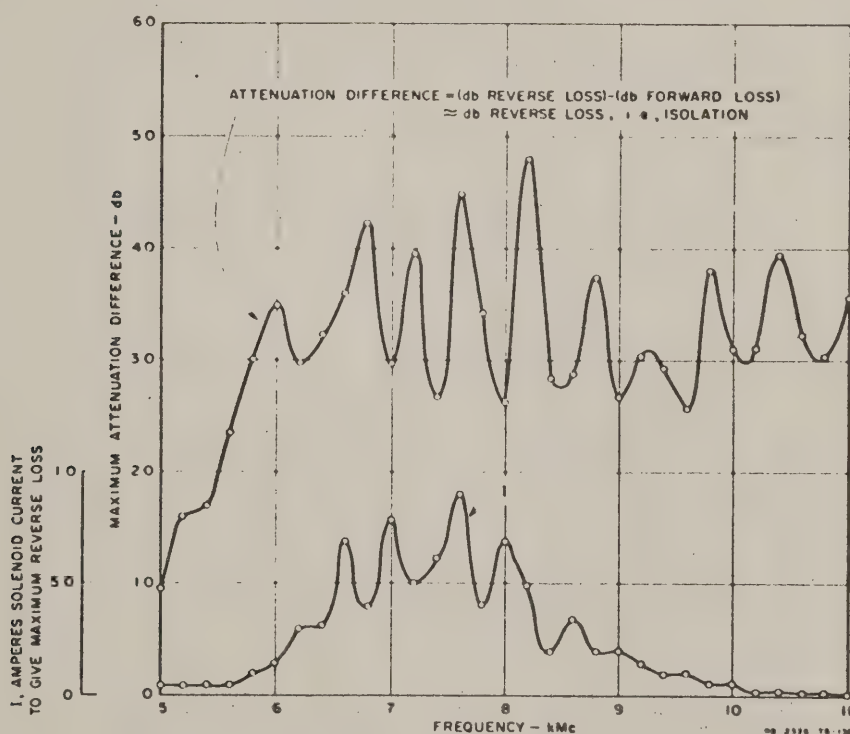


FIG. 3-6
 DIFFERENCE BETWEEN REVERSE AND FORWARD LOSS FOR THE ISOLATOR
 IN FIG. 3-5 WHEN AT EACH FREQUENCY THE SOLENOID CURRENT IS
 ADJUSTED TO GIVE PEAK REVERSE LOSS
 (The solenoid current used to give peak reverse loss is also plotted.)

by introducing dielectric loading in the isolator box. By this technique some of the energy can be drawn away from the ferrite rod at the higher frequencies.³

In hopes of reducing any possible higher-order mode effects, tests were made with a ferrite rod of smaller diameter, and metallic inserts were placed in the roof of the isolator box in order to constrict the cross section of the isolator. The inserts were tapered at the ends so as not to disturb the end impedance matches. The cross section was then as shown in Fig. 3-7. The ferrite rod was Ferramic R-1, 0.100 inch in diameter, 6.00 inches in over-all length, with each end tapered to a point in a distance of 0.5 inch. The distance x in the cross-section drawing in Fig. 3-7 was approximately 0.070 inch, and from measurement of the ferrite support thread lengths after disassembling the isolator, it appears that the rod may have had a small amount of vertical tilt in its position. Once again, the position of the rod was arrived at by adjusting for optimum reverse loss.

The isolator of Fig. 3-7 apparently should have had a longer ferrite rod, since for frequencies beyond midband it was not possible to peak the reverse loss at a definite solenoid current as was possible in the case of Fig. 3-6. Using the isolator of Fig. 3-7, an attempt was made to see if the forward loss could be optimized at some definite solenoid current so as to give a minimum loss. Once again it was possible to attain a definite optimum point only at the lower frequencies which again indicates that the rod was not long enough to give sufficient rotation at the higher frequencies. At frequencies in the 7- to 8-kMc band the optimum loss values ran around 0.5 db, or somewhat less, which agrees fairly well with the perturbation analysis and should be indicative of what optimum performance of the isolator would be. As seen from Fig. 3-7, the VSEP at Port 1 of the isolator is rather high, just as in the case of Fig. 3-6, while the VSI at Port 2 is quite low. In this case insertion loss data were taken for both directions of the H -field and for both directions of power flow. The differences in the measured data were quite small although operation with the H -field as shown was slightly better in the forward loss characteristic.

It is interesting to note that in the case of Fig. 3-7 there appears to be insufficient rotation at the higher frequencies regardless of the applied H -field, while for the case of Fig. 3-5, there is too much

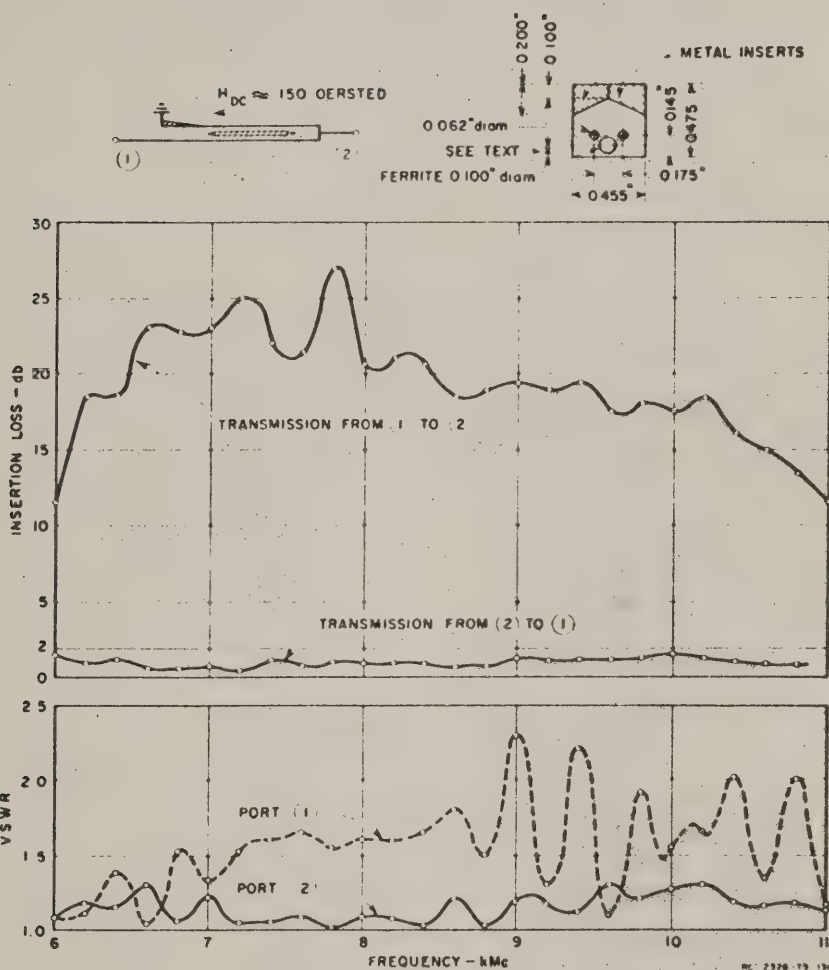


FIG. 3-7

MEASURED PERFORMANCE OF A TEM MODE ISOLATOR USING A 0.100-INCH DIAMETER R-1 FERRITE ROD 6.00 INCHES IN OVER-ALL LENGTH WITH EACH END TAPERED TO A POINT IN A DISTANCE OF 0.5 INCH
(Metal inserts were introduced in the roof of the box in order to reduce the possibility of higher-order modes.)

rotation at the higher frequencies unless the H -field is reduced. The adequate rotation achieved at the lower frequencies for the case of Fig. 3-7 may be due to the proximity of ferromagnetic resonance, while the high frequency energy concentration effect discussed with reference to Figs. 3-5 and 3-6 may not be sufficient in this case to overcome the effect of a ferrite rod which is too short for its diameter.

REFERENCES

1. E. M. T. Jones, J. T. Bolljahn, "Coupled-Strip-Transmission-Line Filters and Directional Couplers," Trans. IRE, Vol. MTT-4, pp 75-81 (April 1956).
2. B. Lax, "Frequency and Loss Characteristics of Microwave Ferrite Devices," *Proc. IRE* 44, 10 pp 1368-1386, (October 1956).
3. E. A. Ohm, "Broad-Band Microwave Circulator," Trans. IRE, Vol. MTT-4, pp 210-217 (October 1956).

CHAPTER 4

FORWARD-COUPLING HYBRID JUNCTIONS IN STRIP LINE

A GENERAL

Hybrid junctions are familiar components of many microwave systems. The term *hybrid junction* is used here to mean a four port device that accepts RF power at any one port, divides the power more or less equally between two of the other ports, and maintains a relatively high isolation between the remaining port and the input port. The increasing use of strip line in microwave applications has led to a number of strip line structural configurations capable of hybrid performance.^{1,2,3} The choice of configuration for a particular application must often be made on physical considerations, such as size, shape, and locations of ports. For instance, when balanced output is required over a very broad band, the backward-coupling hybrid described by Shimizu⁴ can be recommended. However, the balanced output ports of this coupler are diagonally opposite each other, and separated by the length of the coupler. In another instance, such broad-band performance may not be required, while a closer arrangement of the output ports may be very desirable. This can be accomplished by a forward coupling hybrid.

B. TYPES OF HYBRIDS TO BE CONSIDERED

Hybrid performance directional couplers with adjacent output ports are forward-coupling. A familiar example of this in waveguide is the short-slot hybrid.^{5,6} With only one of the input ports excited, this type of coupler is characterized by two propagating orthogonal modes of different phase velocities in the coupling region. These modes, designated the odd mode and the even mode, combine to match the input boundary conditions of applied voltage at one port and zero voltage at the adjacent port. In traveling down the coupling region, they undergo phase delay at different rates, and combine at the output ports to yield voltages in quadrature, whose amplitudes depend on the length of the coupling region.

The forward-coupling hybrid to be described in this chapter uses the even and odd zero-order orthogonal modes which can exist on a pair of conducting strips separated from each other by an air gap, and from parallel

ground planes by a solid dielectric. Chapter 5 will describe the performance of a forward coupling hybrid which uses the TEM mode and the first higher order mode which can propagate along a single flat strip between parallel ground planes.

C. DESIGN CONSIDERATIONS

1. DESIGN PROBLEMS

Certain considerations apply to all forward-coupling hybrids, independent of the particular construction used.

Performance of the hybrid is defined by power division, isolation, and VSWR, each given over some band of frequencies. It is assumed here that the hybrid is lossless, bilateral, linear, passive, and in this case, symmetrical. From a consideration of the scattering matrix of a perfectly symmetrical forward coupler, Biblet⁵ has shown that complete isolation implies perfect match. It can also be shown that reflection in either the odd or even mode, but not both, scatters equal-amplitude voltages out the input port and the adjacent, or isolated, port. Therefore, if the hybrid has low VSWR over a band of frequencies, it implies a high isolation. The major design problems reduce to the following.

- (1) Power accepted at one port to be equally divided between two other ports. This is the condition of balance.
- (2) Power division to be as flat as possible over the broadest possible band.
- (3) Reflected voltage from each mode to be zero at center of coupling band.
- (4) Change in reflected voltage for each mode to be as small as possible over the coupling band.

It would be desirable to satisfy all these requirements simultaneously. In practice they are not independently adjustable, and so compromise is made where necessary.

The basic circuit to be considered is pictured in Fig. 4-1. It consists of two arbitrary, lossless, coupled transmission lines with each end terminated in a real impedance, Z_L . When the generators produce equal-amplitude, in phase voltages, even-mode voltages appear at Ports 1, 2, 3, and 4. When the generators produce oppositely phased equal-amplitude voltages, odd mode voltages appear at the four ports. The effects of any

other excitations can be found by adding the resulting even and odd mode voltages at each of the four ports. The even and odd mode characteristics of each of the two lines can be expressed in terms of the $ABCD$ parameters, or other convenient parameters, for any specific structure. In a forward coupler the even and odd modes have different phase velocities, and different characteristic impedances, of which one is equal to the terminating-line characteristic impedance, Z_L . By even- or odd-mode characteristic impedance is meant the characteristic impedance of a single one of the lines to ground when operating in that mode. For non-uniform lines, image impedances apply rather than characteristic impedances, but, as used in this analysis, the two impedance designations are analytically equivalent.

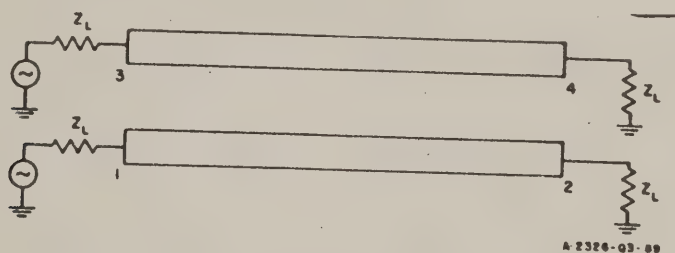


FIG. 4-1
BASIC COUPLER CIRCUIT

In the frequency range where power division is near balance, relatively simple working relations can be used to describe the performance of forward coupling hybrids.

2 POWER DIVISION

Approximate relations among input and output voltages can be established with the aid of Fig. 4-1 by assuming that the coupler is perfectly matched. The results can be applied to slightly mismatched couplers by using insertion phase delays for θ_e and θ_o , rather than image phase shifts. Under these conditions, and assuming appreciable mismatch exists in only one mode, the following formulas give results within about 0.005 db of an exact formula for the divided output powers within 1 0. db of each other and for a voltage transmission coefficient greater than 0.9 (input VSWR, typically, less than about 1.55). All are exact at $\theta_e - \theta_o = 90^\circ$. For power division greater than 1.0 db, the tangent formula [Eq. (4-4)] is

much more accurate than the linear one [Eq. (4-5)]. Neither should be used for voltage transmission coefficients less than about 0.9, except very close to equal power division. Numeric subscripts refer to the port involved, and e and o subscripts refer to even and odd modes. Signal is applied at Port 1. The derivation is as follows.

$$\text{Voltage at Port 1} = V_1 = V_{e1} + V_{o1} = 1$$

$$\text{Voltage at Port 2} = V_2 = V_{e2} + V_{o2} = \frac{1}{2} (e^{-j\theta_e} + e^{-j\theta_o}) \quad (4-1)$$

$$\text{Voltage at Port 3} = V_3 = V_{e3} + V_{o3} = 0$$

$$\text{Voltage at Port 4} = V_4 = V_{e4} + V_{o4} = \frac{1}{2} (e^{-j\theta_e} - e^{-j\theta_o})$$

Voltages at Ports 2 and 4, the output ports, can be written as

$$V_2 = e^{-j(\theta_e + \theta_o)/2} \cos \left[\frac{\theta_e - \theta_o}{2} \right] \quad (4-2)$$

$$V_4 = j e^{-j(\theta_e + \theta_o)/2} \sin \left[\frac{\theta_e - \theta_o}{2} \right]$$

$$\text{Power division is now defined as } 20 \log_{10} \frac{|V_4|}{|V_2|} \quad (4-3)$$

$$\text{Power division} = 20 \log_{10} \tan \left[\frac{|\theta_e - \theta_o|}{2} \right] \text{ decibels} \quad (4-4)$$

This relation is plotted in Fig. 4-2. Of specific interest is the information that the phase difference between modes must be 90 degrees for balanced output.

For small deviations from $|\theta_e - \theta_o| = 90^\circ$ degrees, the following approximation holds.

$$\text{Power division} = 0.15 (|\theta_e - \theta_o| - 90^\circ) \text{ decibels} \quad (4-5)$$

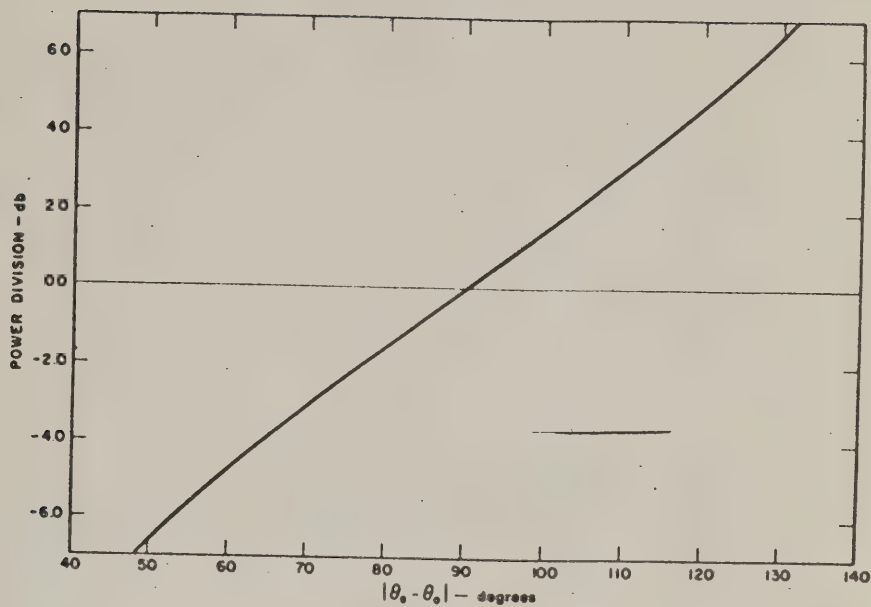


FIG. 4-2

PHASE DIFFERENCE - EVEN AND ODD MODE

3. POWER DIVISION FLATNESS

The phase shift curves for even and odd modes are such that the simplest approach to constancy of equal power division is to try for maximally flat performance. This requires setting the power division to give balance at band-center, and then setting the rate of change in power division with frequency to equal zero at band-center. For flatness of power division

$$\frac{d|\theta_e - \theta_o|}{df} = 0$$

or

(4-6)

$$\frac{d\theta_e}{df} = \frac{d\theta_o}{df}$$

at band center. That is, graphs drawn of θ_r and θ_o as functions of frequency should have equal slopes where their difference is 90 degrees. This will be illustrated when actual structures are discussed.

4 REFLECTED WAVES

The two modes in the coupling region have different characteristic impedances. In practice, the input and output lines, assumed identical, are matched to one of the coupling region modes in magnitude and in variation with frequency. The reflection from the other mode is set to zero at bandcenter by adjusting the coupling region length to be resonant. Thus, the match to this mode is length- and frequency-sensitive.

5 CHANGES IN REFLECTED VOLTAGES WITH FREQUENCY

If the transition from input and output lines to the coupling region is made smoothly enough, the nonresonant mode suffers negligibly small reflected waves. The other mode produces a VSWR varying with frequency periodically from unity to some value dependent on the ratio of the feeding line characteristic impedance to the resonant mode characteristic impedance. Off resonance it causes an input arm reflection in accordance with

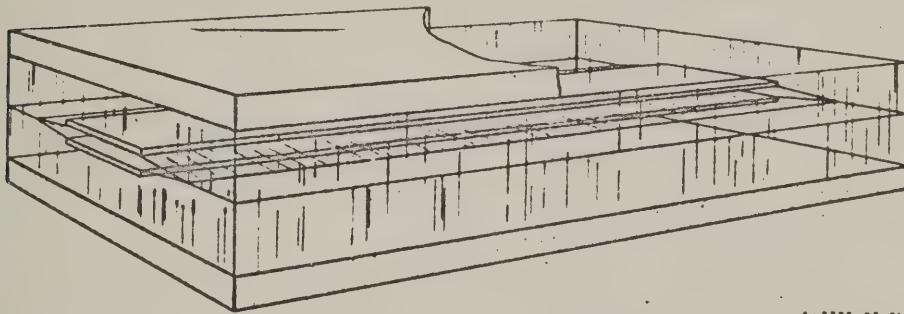
$$\frac{1}{2} \frac{1 - Z/Z_L}{1 + Z/Z_L} \quad (4-7)$$

for perfect balance, where ρ is the ratio of reflected-to-incident voltage in the input port, and Z/Z_L is the ratio of the input impedance of the resonant mode to the characteristic impedance of the single mode existing in the input port. An equal voltage is scattered into the normally decoupled port and this determines the isolation. The factor $\frac{1}{2}$ allows for the division of incident power into the two coupling region modes, and the subsequent division of reflected power between input port and its adjacent isolated port. It is obviously desirable to operate near resonance, in order to keep the reflected voltages low in magnitude.

D. DESIGN OF ZERO-ORDER-MODE HYBRID JUNCTION

1. CONFIGURATION

The hybrid configuration of this report uses flat, parallel strips stacked between ground planes, as shown in Fig. 4-3. The strips are surrounded by a dielectric of relative dielectric constant greater than unity, but are separated from each other by an air-filled gap. Even and odd modes have electric field patterns as shown in Figs. 4-4(a) and 4-4(b). For wide strips spaced close together these sketches indicate that the gap has little effect on the even mode, which thus travels very nearly at the velocity of light in the dielectric, but does substantially



A-5326-09-01

FIG. 4-3

VIEW OF ZERO-ORDER-MODE FORWARD COUPLER

affect the odd mode, causing it to travel at a greater velocity. The dielectric of higher constant is used outside the strips rather than between them to reduce the unavoidable initial difference in characteristic impedances, resulting ultimately in better performance than would be obtained with the dielectric between the two strips.

2. SIMPLE THEORY: DESIGN RELATIONS

The structure is filled with a dielectric of constant ϵ_r , except for the air gap between strips.

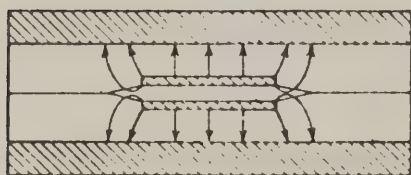
Let

C = Even-mode strip capacitance per unit length to ground
for a single strip

- C_s = That part of the odd mode strip capacitance per unit length to the effective ground plane between strips, for a single strip, when the air gap is filled with dielectric of constant ϵ_r
 L_e = Even-mode inductance per unit length for a single strip
 L_o = Odd-mode inductance per unit length for a single strip
 Z_{oe} = Even-mode characteristic impedance for a single strip, assumed to be the same when gap between strips is filled with either air or dielectric
 Z'_{oo} = Odd-mode characteristic impedance for single strip
 Z_{oo} = Odd-mode characteristic impedance for a single strip when air gap is filled with dielectric of constant ϵ_r
 v_e = Even-mode phase velocity
 v'_{oo} = Odd mode phase velocity
 c = Velocity of light in free-space

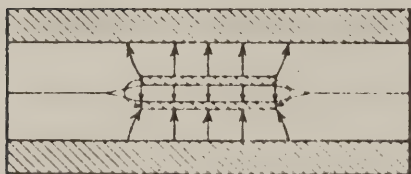
Then the following approximate

formulas hold.



A-2376 Q3 92b

FIG. 4-4(a)
EVEN-MODE ELECTRIC FIELD



A-2376 Q3 92b

FIG. 4-4(b)
ODD-MODE ELECTRIC FIELD

$$Z_{oe} = \sqrt{\frac{L_e}{C}} \quad (a)$$

$$Z_{oo} = \sqrt{\frac{L_o}{C + C_s}} \quad (b)$$

$$Z'_{oo} = \sqrt{\frac{L_o}{C + C_s/\epsilon_r}} \quad (c)$$

$$v_e = \frac{1}{\sqrt{L_e C}} = \frac{c}{\sqrt{\epsilon_r}} \quad (d)$$

$$v_o = \frac{1}{\sqrt{L_o (C + C_s)}} = \frac{c}{\sqrt{\epsilon_r}} \quad (e)$$

$$v'_o = \frac{1}{\sqrt{L_o (C + C_s/\epsilon_r)}} \quad (f)$$

$$\frac{Z_{oe}}{Z_{oo}} = \frac{C + C_s}{C} \quad (g)$$

$$\frac{Z_{oe}}{Z'_{oo}} = \frac{v_o}{v'_o} = \sqrt{\frac{C + C_s/\epsilon_r}{C + C_s}} \quad (h)$$

(4-8)

Use of an averaged static capacitance in the composite structure along which the odd mode propagates is a simplifying approximation. The actual fields in such a composite structure are not purely transverse. However, as long as strip width and plate spacing remain small compared to wavelength, it is reasonable to assume that the over-all effect of the composite structure is the same as a similar line having a homogeneous "averaged-out" dielectric. In addition to frequency and coupling-region length, hybrid performance is determined by Z_{oe} , Z'_{oe} , and ϵ_r . However, it is convenient to relate Z'_{oe} to Z_{oe} so that design data for strips immersed in homogeneous dielectrics (given in Chapter 6), can be used to find physical dimensions.

As an initial step in making a directional coupler of this device, the characteristic impedance of the even mode is set equal to the characteristic impedance of the input and output lines. The odd mode is thus unmatched, until the length of the structure is set to an integral number of half-wavelengths for that mode. That is, for odd-mode match,

$$L = \frac{n\lambda'_o}{2} \quad (4-9)$$

where λ'_o is the wavelength of the odd mode, and L is the length of the coupling region. This defines n as the length of the coupling section in half wavelengths of the odd mode at the design frequency.

For balanced output, the phase difference between modes over the length of the coupling region must be $\pi/2$ radians. Other output ratios are also possible for this type of coupler. For instance n phase difference transfers all the input power to the diagonally opposite arm, and $\pi/5$ gives an output power division of -9.8 db. For the general coupler, phase difference will be specified as π/m . For hybrid performance, $m = 2$. The phase difference between modes over a coupling length L for specified coupling is given by

$$\frac{2\pi L}{\lambda_e} - \frac{2\pi L}{\lambda'_o} = \frac{\pi}{m}$$

if the odd mode is matched. From this,

$$L = \frac{\lambda_e \lambda'_o}{2m(\lambda'_o - \lambda_e)} \quad (4-10)$$

If this length is set equal to the length for odd-mode match, and rearranged, there results

$$\frac{\lambda'_o}{\lambda_e} = \frac{mn + 1}{mn} \quad (4-11)$$

Substitution in Eq (4-10) gives

$$\frac{L}{\lambda_1} = \frac{mn + 1}{2m \sqrt{\epsilon_r}} \quad (4-12)$$

where λ_1 is the free-space design center wavelength

Equations (4-4) and (4-5) showed power division to be a function of $|\theta_e - \theta_o|$, the absolute difference of insertion phase lengths of the two modes over the coupling region. Through a standard ABCD matrix analysis of the circuit of Fig. 4-1, subject to the conditions discussed in this section, even- and odd mode insertion phase shifts are determined to be

$$\theta_e = \frac{2\pi L \sqrt{\epsilon_r}}{\lambda}$$

and

$$\theta_o = \arctan \left[\left(\frac{\frac{Z'_{oo}}{Z_{oe}} + \frac{Z_{oe}}{Z'_{oo}}}{2} \right) \tan \frac{2\pi L}{\lambda'_o} \right] \quad (4-13)$$

where the value of the arctangent taken is that nearest $2\pi L/\lambda'_o$. The term $2\pi L/\lambda'_o$ is the same as nm/f_1 , where f_1 is the design center frequency. Also, at f_1 the even mode phase length is π/m greater than that of the odd mode, so that

$$\theta_e = \left(nm + \frac{\pi}{m} \right) \frac{f}{f_1} \quad (4-14)$$

Making these substitutions, the phase difference between modes can be written as

$$\theta_e - \theta_o = \pi \frac{mn+1}{m} \frac{f}{f_1} - \arctan \left(\frac{\frac{Z'_{oe}}{Z_{oe}} + \frac{Z_{oe}}{Z'_{oe}}}{2} \tan \frac{n\pi f}{f_1} \right) \quad (4-15)$$

where the value of the arctangent taken is that nearest $n\pi f/f_1$.

This equation gives a phase difference of π/m at band-center for any Z_{oe}/Z'_{oe} , as the term containing Z_{oe}/Z'_{oe} is zero there. However, the change in phase difference is dependent on Z_{oe}/Z'_{oe} , and it will now be found and set to zero to give the value of Z_{oe}/Z'_{oe} required for flat coupling response. In order to investigate the behavior around band center, $\tan n\pi f/f_1$ will be replaced by $n\pi(f/f_1 - 1)$ and the arctangent function will be replaced by its argument. This gives

$$\theta_e - \theta_o = \frac{f}{f_1} \left(\frac{mn+1}{m} \pi - \frac{\frac{Z_{oe}}{Z'_{oe}} + \frac{Z'_{oe}}{Z_{oe}}}{2} n\pi \right) + \left(\frac{\frac{Z_{oe}}{Z'_{oe}} + \frac{Z'_{oe}}{Z_{oe}}}{2} - 1 \right) \quad (4-16)$$

for $(2n-1)/2n < f/f_1 < (2n+1)/2n$. The derivative of this function is the first term in brackets. Setting it to zero,

$$\frac{\frac{Z_{oe}}{Z'_{oe}} + \frac{Z'_{oe}}{Z_{oe}}}{2} = \frac{mn+1}{mn} \quad (4-17)$$

Now the equation set in Eq. (4-13) may be written as

$$\begin{aligned} \theta_e &= \frac{mn+1}{m} \frac{\pi f}{f_1} \\ \theta_o &= \arctan \left(\frac{mn+1}{mn} \tan \frac{n\pi f}{f_1} \right) \end{aligned} \quad (4-18)$$

where the value of the arctangent taken is that nearest $n\pi f/f_1$.

Using $m = n = 2$, values chosen from the hybrid junction actually constructed, θ_e and θ_o are plotted against f/f_1 in Fig. 4-5. Substituting the quantities of Eq. (4-18) in Eq. (4-4) gives power division as a function of frequency in terms of m and n . This is plotted in Fig. 4-6(a) for hybrids of $n = 1$ and $n = 2$.

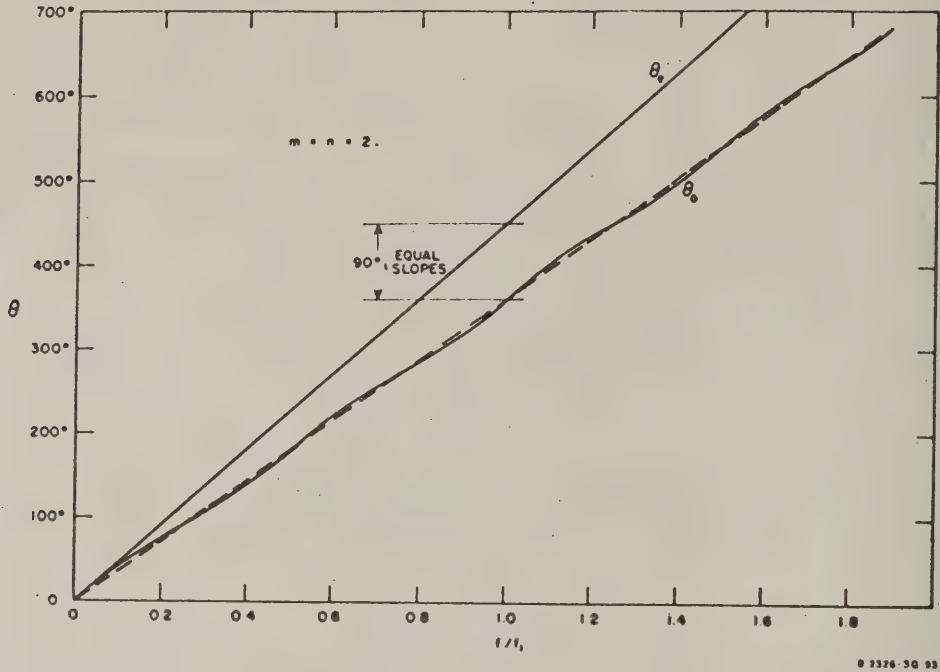


FIG. 4-5

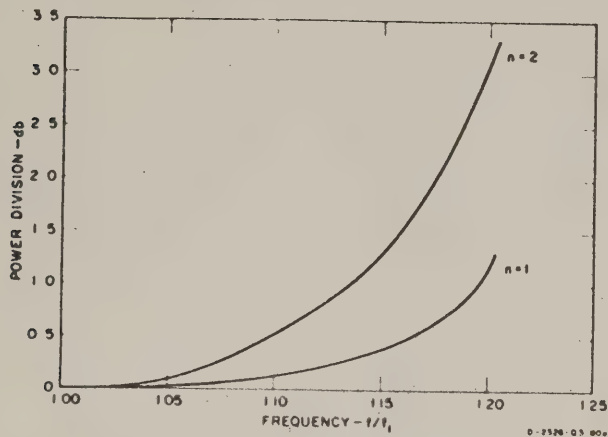
ZERO-ORDER-MODE MAXIMALLY FLAT FORWARD-COUPLING HYBRID PHASE LENGTHS
FOR EVEN AND ODD MODES

To design an actual coupler giving the performance described above, the quantity Z_{oe}/Z_{oo} must be found in terms of m and n . This is done by solving Eq. (4-17) for

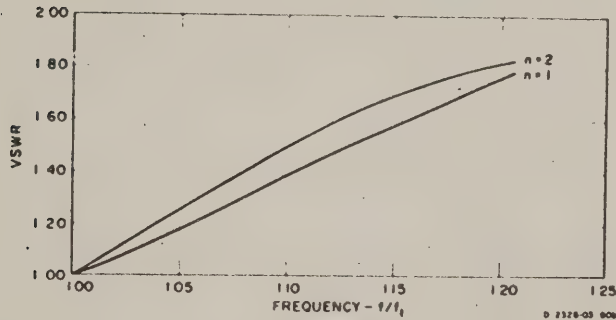
$$\frac{Z_{oe}}{Z'_{oo}} = \frac{mn + 1}{mn} + \sqrt{\left(\frac{mn + 1}{mn}\right)^2 - 1} \quad (4-19)$$

Equation (4-8h) and Eq. (4-11) taken together show that

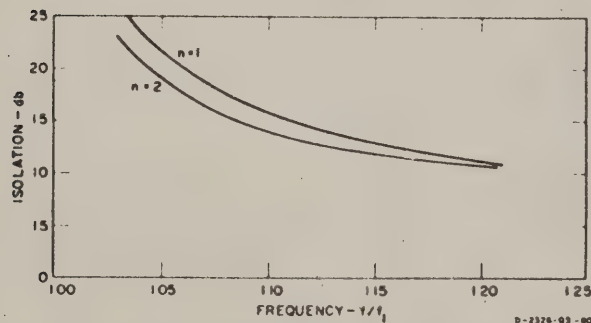
$$\frac{Z'_{oo}}{Z_{oo}} = \frac{mn + 1}{mn} \quad (4-20)$$



(a)



(b)



(c)

FIG. 4-6
PREDICTED PERFORMANCE VS. FREQUENCY FOR ZERO-ORDER-MODE
MAXIMALLY FLAT FORWARD-COUPLING HYBRID

Equations (4-19) and (4-20) multiplied give the desired design quantity:

$$\frac{Z_{oe}}{Z_{oo}} = \frac{mn + 1}{(mn)^2} (mn + 1 + \sqrt{2mn + 1}) \quad (4-21)$$

It will now be shown that in these couplers having maximally flat coupling response, the relative dielectric constant ϵ_r is numerically equal to Z_{oe}/Z_{oo} . This can be done by combining Eq (4-8g) with Eq. (4-8h) to yield

$$\epsilon_r = \frac{\frac{Z_{oe}}{Z_{oo}} - 1}{\left(\frac{Z_{oe}}{Z_{oo}}\right)^2 \frac{Z_{oe}}{Z_{oo}} - 1} \quad (4-22)$$

Substituting Eqs. (4-20) and (4-21) in Eq. (4-22) gives, after simplification,

$$\epsilon_r = \frac{mn + 1}{(mn)^2} (mn + 1 + \sqrt{2mn + 1}) \quad (4-23)$$

Comparing this [Eq. (4-23)] with Eq. (4-21), it is seen that

$$\epsilon_r = \frac{Z_{oe}}{Z_{oo}} \quad (4-24)$$

All the basic design quantities have now been specified solely in terms of m and n for maximally flat coupling at band-center

For hybrid performance, the above design relations are

$$\frac{L}{\lambda_1} = \frac{2n + 1}{4\sqrt{\epsilon_r}} \quad (4-25)$$

$$\epsilon_r = \frac{Z_{oe}}{Z_{oo}} = \frac{2n + 1}{4n^2} (2n + 1 + \sqrt{4n + 1}) \quad (4-26)$$

These relations are shown in Table 4-1 for interesting values of n .

TABLE 4-1

SOLUTIONS TO DESIGN EQUATIONS FOR
MAXIMALLY FLAT ZERO ORDER MODE
FORWARD COUPLING HYBRID

| n | $\epsilon_r = \frac{Z_{oe}}{Z_{oo}}$ | $\frac{L}{\lambda_1}$ |
|-----|--------------------------------------|-----------------------|
| 1 | 3.920 | 0.378 |
| 2 | 2.500 | 0.792 |
| 3 | 2.065 | 1.220 |
| 4 | 1.845 | 1.650 |

The relations in Chap. 6, Eqs. (6-4) and (6-5), can be used to translate a given Z_{00}/Z_{00} into physical cross-sectional dimensions.

Following the method of Part C, 4 and 5, and assuming that all reflected waves are the result of odd-mode mismatch, it is relatively straightforward to compute the VSWR and isolation. This has been done and plotted in Fig. 4-6(b) and (c) for hybrids of $n = 1$ and $n = 2$.

E. EXPERIMENTAL RESULTS

In order to test the validity of the foregoing theory, a coupler was made in accordance with the design data for hybrid performance using $n = 2$, as this allowed the convenience of using polystyrene for the dielectric. Figure 4-7 shows some details of the construction. Z_{00} was chosen as 50 ohms to match the coaxial feed line, and in accordance with Table 4-1, this required Z_{00} to be 20 ohms. These characteristic impedances were calculated from the formulas for broadside coupled strips parallel to ground planes, given by Cohn in Chap. 6, Eqs. (6-4) and (6-5) on this contract. The design-center frequency used in determining length was 1500 Mc. Initial results are shown in Fig. 4-8, (a) and (b), along with curves computed from the theory.

The experimental curve of VSWR is in good agreement with the theoretical one except near the minimum, where residual effects become prominent. Some of this residual VSWR is due to mechanical asymmetry, as VSWR measurements on separate terminals differed by as much as 0.04 at the center frequency, although all external conditions were held the same. It is not unlikely that some residual VSWR was introduced through mismatches of the even mode to the feed lines, and junction susceptances where coaxial line joined strip line. The effective length of the coupler was assumed to be end-to-end length. No effort was made to locate the effective terminal planes, nor to eliminate junction effects. This may be the reason that the measured center frequency was found at 1590 Mc rather than the computed 1500 Mc. It is probable too, that the assumed "averaged-out" dielectric constant was not, in fact, achieved exactly. However, allowing for the existence of such residual effects, the theoretical curve gives an adequate prediction of the measured VSWR.

The measured power division curve has about the proper shape, but it undercoupled by about 2.3 db. This represents about 73 degrees difference in the phase length of the two modes, rather than 90 degrees. If the

0.312 dia

0.136 dia

1.000

POLYSTYRENE 6 220 LONG

AIR 0.063

0.029

0.100

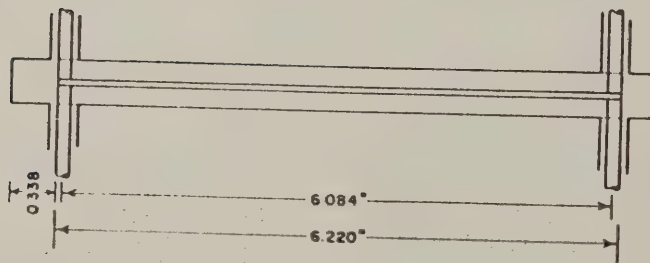
0.227

0.150

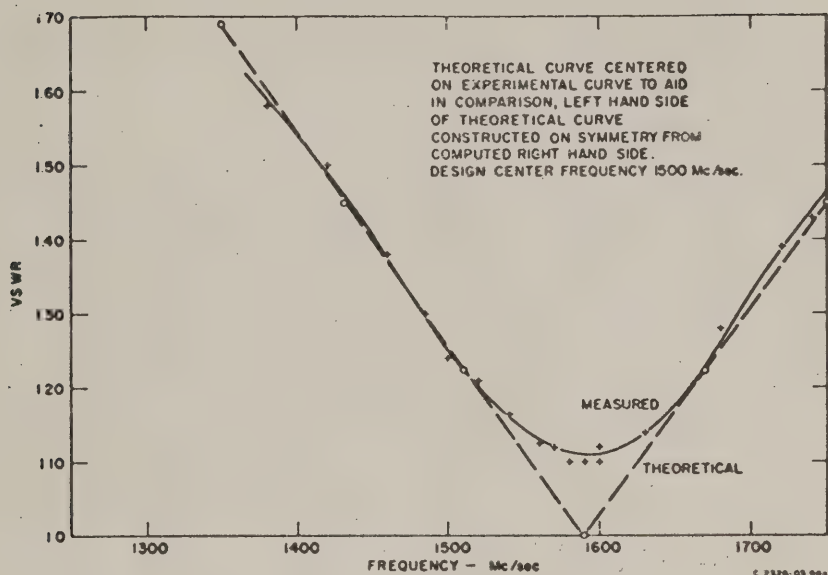
0.550

2 STRIPS
0.227 x 0.020 x 6 220
COPPER OR BRASS

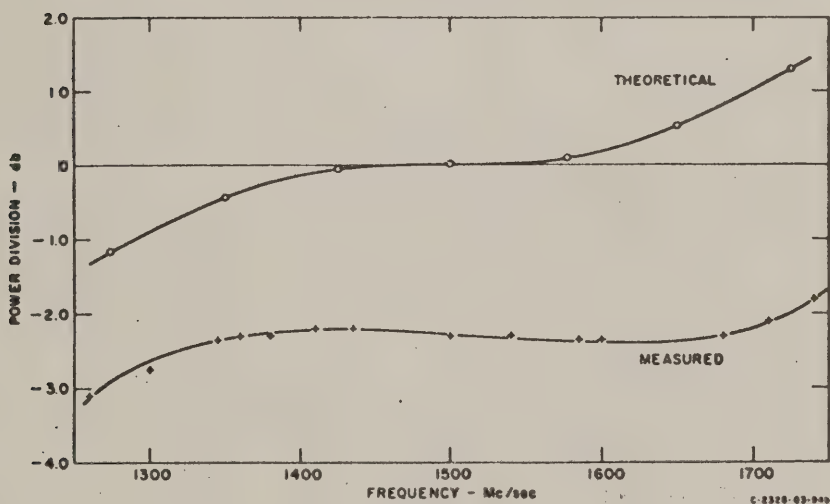
UG-1187/U, MODIFIED



9-2326-30-21



(a)



(b)

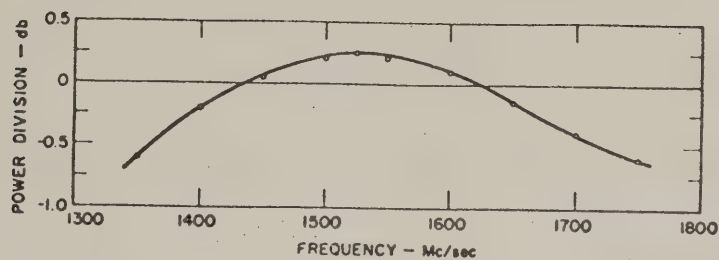
FIG. 4-8
THEORETICAL AND MEASURED PERFORMANCE VS. FREQUENCY
FOR A ZERO-ORDER-MODE MAXIMALLY FLAT
FORWARD-COUPLING HYBRID

dielectric constant of the even mode could be increased without affecting the odd mode, then, according to this hypothesis, the coupler should perform more nearly as designed.

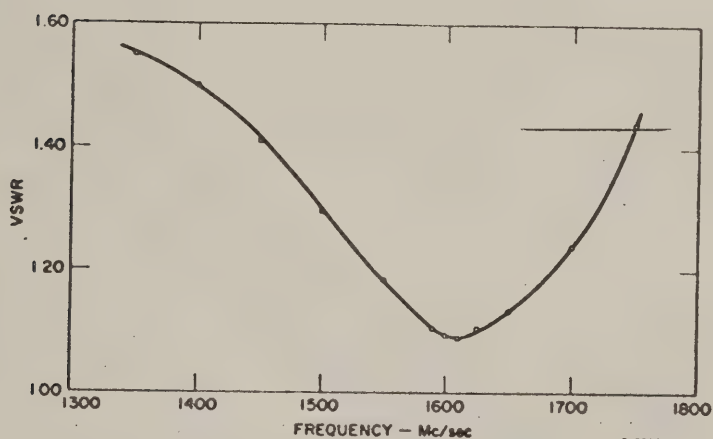
Actually, a different approach was followed in hopes of realizing a better VSWR characteristic than predicted by the theory for the simple structure, while obtaining a flat, balanced output. The first step in this effort was to reduce the spacing between the strips by making them thicker (reducing the gap from 0.065 to 0.048 inch) holding all other dimensions of the coupler unchanged. This increased the power division to around -3 db, but the flatness deteriorated. Power division was then brought in to around zero db and flattened somewhat by tuning the odd mode with two one-turn 0.005-inch-diameter wire inductances wrapped on polystyrene slugs and placed between strips about one-quarter wavelength from each end of the structure. Test results for this device are shown in Fig. 4-9(a), (b), and (c). Over a 17.5 percent band, power division is flat within 1/4 db, VSWR is less than 1.50, and isolation is 13 db or better.

This performance is somewhat better than predicted from the theoretical curves of the simpler coupler allowing for the unexplained frequency displacement of the maximum of isolation. The coupler performance could be improved further by using the $n = 1$ design, using better matched junctions to the coaxial line, or improving the mechanical design. Figure 4-10 is a photograph of the device.

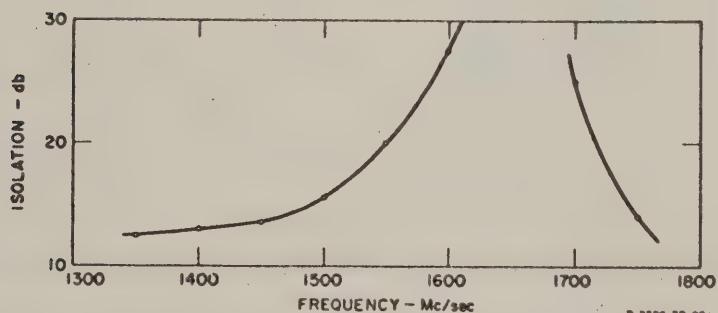
It might be noted, too, that this design procedure can be used for couplers in the range between large coupling and small coupling. For less coupling than required for hybrid performance, the bandwidth of coupling, VSWR and isolation should be better than predicted for the hybrid



(a)



(b)



(c)

FIG. 4-9

MEASURED PERFORMANCE VS. FREQUENCY FOR A ZERO-ORDER-MODE
MAXIMALLY FLAT FORWARD-COUPLING HYBRID
TUNED WITH LUMPED INDUCTANCES

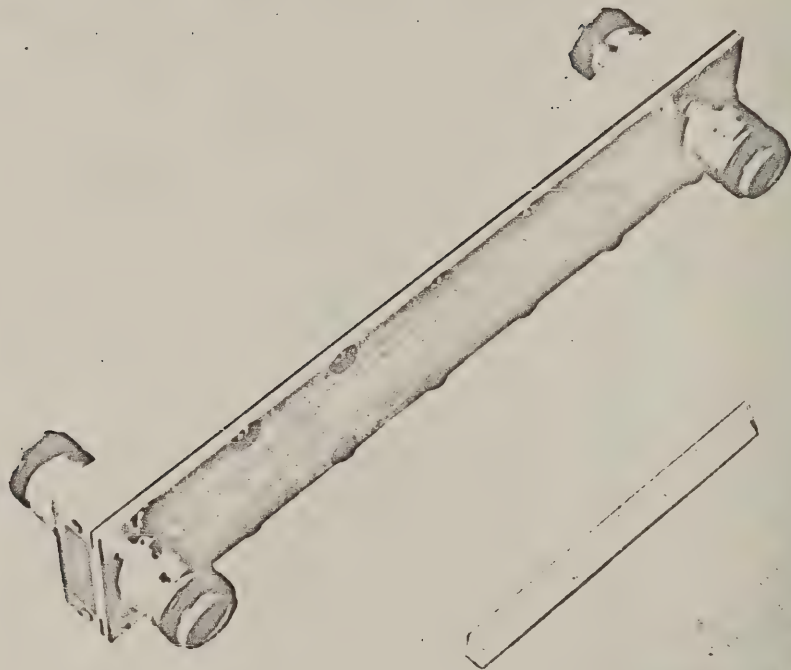


FIG. 4-10

PHOTOGRAPH OF THE ZERO-ORDER-MODE MAXIMALLY FLAT FORWARD-COUPLING HYBRID

REFERENCES

1. S. B. Cohn, P. M. Sherk, J. K. Shimizu, E. M. T. Jones, "Strip Transmission Lines and Components," Final Report, SRI Project 1114, Contract DA-36-039 SC-63232, Stanford Research Institute, Menlo Park, California (February 1957).
2. Herbert G. Pascalar, "Strip Line Hybrid Junction," Trans. IRE, Vol. MTT-5, No. 1, p. 23 (January 1957).
3. J. Reed and G. J. Wheeler, "A Method of Analysis of Symmetrical Four-Port Networks," Trans. IRE, Vol. MTT-4, No. 4, p. 246 (October 1956).
4. James K. Shimizu, "Strip Line 3-db Directional Couplers," IRE WESCON Convention Record, Part I, on Microwaves, Antennas, and Propagation, p. 4 (1957).
5. Henry J. Riblet, "The Short-Slot Hybrid Junction," Proc. IRE 40, 2, p. 180 (February 1952).
6. Henry J. Riblet, Waveguide Hybrid Junctions, U.S. Patent 2739287, issued March 20, 1956, and Waveguide Hybrid, U.S. Patent 2739288, March 20, 1956.

CHAPTER 5

HIGHER-ORDER-MODE FORWARD-COUPLING HYBRID

A. GENERAL

This section describes a forward-coupling balanced-output hybrid junction that uses the TEM mode and the first higher-order mode that can exist on a flat, wide, conducting strip between parallel ground planes. Figure 5-1 shows the electric field patterns of a strip line designed to support these modes. The

higher-order mode has a plane of zero electric field along the center of the strip, so that a thin metal wall can be placed in this plane without disturbing the mode, although the TEM mode then no longer propagates. With the wall in

place, each half of the line is identical to a section of trough guide, the configuration of which is shown in

Fig. 5-2. These properties are used as the basis for the higher-order-mode forward-coupling hybrid shown in Fig. 5-3. As shown there, two adjacent trough guides are separated from each other

by a thin metal wall. The separating wall is partly cut away in a section which forms the coupling region. The odd trough-guide mode (corresponding to the case where the two trough guides in Fig. 5-3 are excited with equal amplitudes but opposite phases) maintains the higher-order mode form shown in Fig. 5-1 when passing through the coupling region; hence passes the coupling region without reflection if the dividing walls are thin. The even trough-guide mode (corresponding to the case where the two trough guides in Fig. 5-3 are excited with equal amplitudes and the same phase) converts to the TEM mode (Fig. 5-1) in the coupling region because of

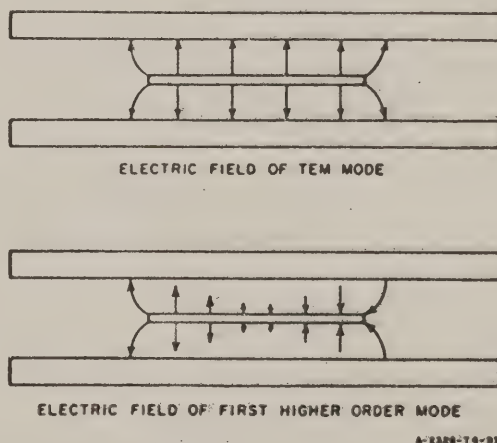
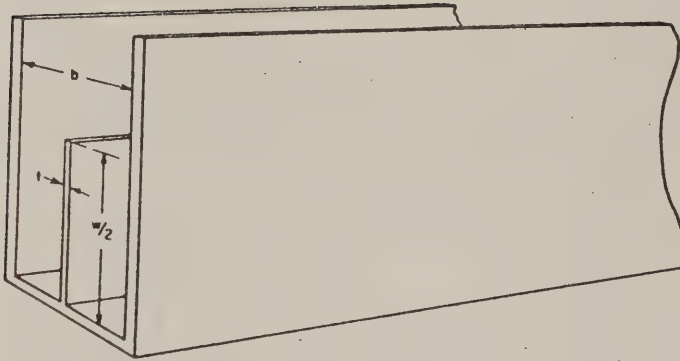


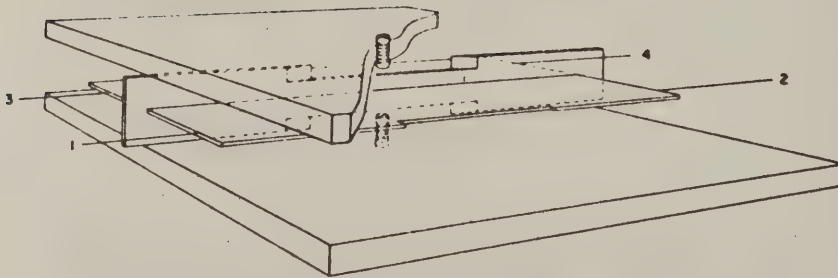
FIG. 5-1

ELECTRIC FIELD PATTERNS IN HIGHER-ORDER-MODE FORWARD-COUPLING HYBRID



A-2326-74-00

FIG. 5-2
TROUGH-GUIDE CONFIGURATION



A-2326-74-00

FIG. 5-3
VIEW OF HIGHER-ORDER-MODE FORWARD-COUPLING HYBRID

the absence of the dividing wall. It is necessary to know the phase constants of the higher-order mode and the TEM mode in the coupling region in order to relate the physical dimensions of the coupler to its electrical properties. Further discussion of the operation of forward-coupling hybrids was presented in Sections A, B, and C of Chapter 4.

B. PROPAGATION CONSTANTS IN THE COUPLING REGION

1. TEM MODE

The TEM mode propagates at the velocity of light, and thus its phase constant is

$$k = \frac{2\pi}{\lambda} \quad (5-1)$$

where λ is the free-space wavelength.

2. HIGHER-ORDER MODE

For the higher-order-mode transmission line, it is necessary to determine cut-off wavelength before the phase constant can be found. Keen¹ gives formulas communicated by Jasik relating cut-off wavelength, λ_c , to the trough-guide dimensions. His tabulation of values has been corrected by Cohn,² who applied them to the determination of the cut-off wavelength of the first higher-order mode on strip line. These formulas and tabulations, which assume the ratio of strip thickness to ground-plane spacing to be approximately zero, are approximations of the transverse resonance equation,

$$\lambda_c = \pi (b - t) \frac{C_f'}{\epsilon} \tan \frac{\pi w}{\lambda_c} \quad (5-2)$$

where b is the ground plane spacing, t is the strip thickness, and w is the width of the strip in the coupling region or twice the trough-guide fin width. The fringing capacity, C_f' , is one-half the total fringing capacity per unit length from the edges of the strip to both ground planes, and is given as a function of t/b by formulas and graphs in Cohn's articles.^{2,3} The permittivity, ϵ , has the same dimensions as C_f' , farads

per meter in the MKS system. The ratio C'_f/ϵ is independent of the relative dielectric constant. An approximation for wide strips of appreciable thickness is

$$\lambda_c = 2w + 2(b - t) \frac{C'_f}{\epsilon} \quad (5-3)$$

For $t = 0$, this formula gives values of λ_c 2.20 percent larger than Eq. (5-2) for $w/b = 1.0$, and 0.46 percent larger than Eq. (5-2) for $w/b = 2.0$. For $w/b < 1.0$ an additional error due to interaction of the fringing fields becomes appreciable. For $w/b > 2.0$ the difference between the exact and approximate formulas becomes negligible for this application. Guide wavelength, λ_g , is found from the well-known relation,

$$\lambda_g = \lambda \left[1 - \left(\frac{\lambda}{\lambda_c} \right)^2 \right]^{-1/2} \quad (5-4)$$

and the higher-order-mode phase constant is $2\pi/\lambda_g$.

At this point, it is necessary to examine the nature of the transition from TEM mode in the coupling region to even trough-guide mode in the terminating lines

C. TRANSITION FROM COUPLING REGION TO TROUGH GUIDE

An array of semi-infinite parallel plates is sketched in Fig. 5-4. A plane wave with its electric field vector parallel to the edges of the plates is traveling normal to the plane separating free space from the parallel-plate region. The upper view of Fig. 5-4 shows where magnetic walls might be placed without disturbing the fields, and the lower view shows the manner in which electric walls might be placed without disturbing the fields. The magnetic walls must lie in planes perpendicular to the magnetic field lines. This requires the walls to be exactly half-way between adjacent parallel plates. No limitation is imposed on the positions of the electric walls other than that they be perpendicular to the lines of electric field. If the guide wavelength in the parallel-plate region is the same as the guide wavelength in the trough-guide of the higher-order-mode coupler at the same frequency, the region bounded by the electric and magnetic walls pictured is very similar to the transition region of the higher-order-mode coupler. It may be expected then, that the results of an investigation of the parallel-plate problem can be applied,

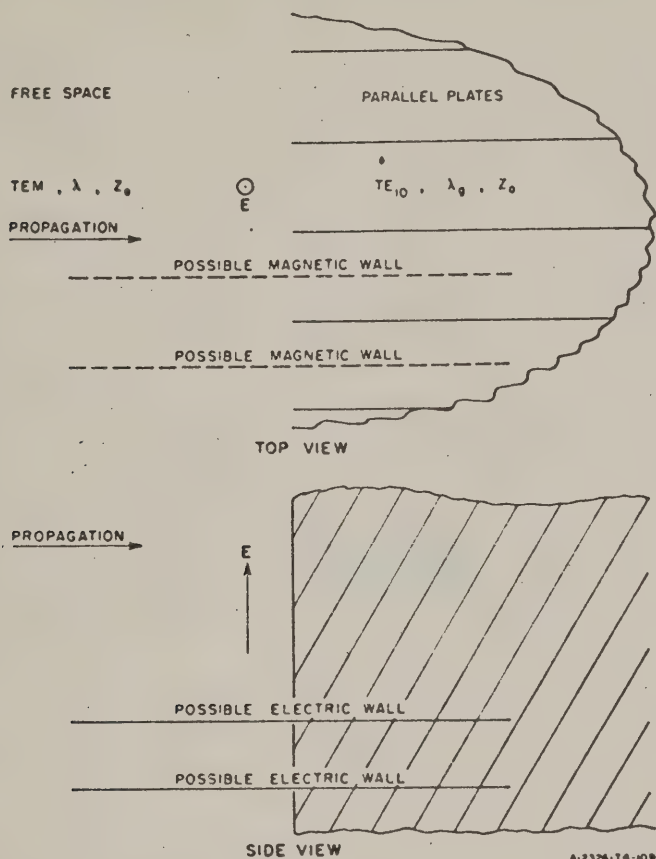
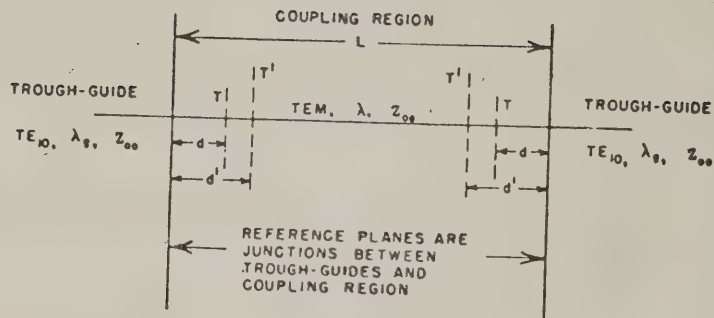


FIG. 5-4

PROPAGATION INCIDENT ON SEMI-INFINITE PARALLEL PLATES

at least qualitatively, to the higher-order-mode coupler. Carlson and Heins,⁴ Lengyel,⁵ and Marcuvitz,⁶ have published results of work in this area. This report will follow Marcuvitz, since his results are in a particularly useful form.

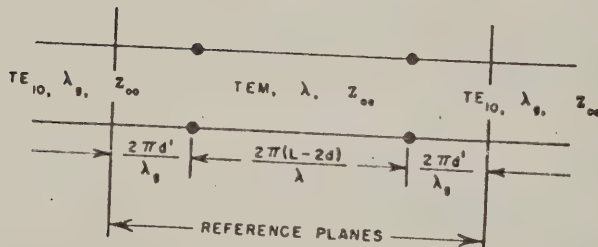
The plane wave in Fig. 5-4 has a real-impedance terminal plane at T , a distance d from the plates, in the region where only the plane wave exists. According to Marcuvitz, at this plane the normalized impedance presented to the plane wave by a matched parallel-plate structure is λ_g/λ . The real-impedance terminal plane for the TE_{10} mode is at T' , a distance d out from the edges of the plates in the free-space region. Now, in reference to the hybrid coupling region of length L , as indicated in Fig. 5-5(a) and Fig. 5-5(b), these results will be applied to the



NA-5326-T6-1066

FIG. 5-5(a)

LOCATIONS OF TERMINAL PLANES T AND T' WITH RESPECT TO ENDS OF COUPLING REGION



NA-5326-T6-1109

FIG. 5-5(b)

CIRCUIT SHOWING EQUIVALENT ELECTRICAL LENGTHS FOR MODE CONVERSION FROM TROUGH-GUIDE EVEN MODE TO TEM MODE IN THE COUPLING REGION

even mode, which exists inside the coupling region only as a TEM wave, and exists outside the coupling region as TE_{10} waves of identical phase and magnitude in adjacent lines. Electric field lines of the TEM mode in the hybrid lie between a ground plane and the wide center strip very much in the same manner as they lie between possible electric walls of the parallel plate structure. The end of the dividing wall at the start of the coupling region in the hybrid corresponds to the edge of one of the parallel plates in the parallel plate array.

If the center conducting strip is increased in width from w to $\lambda_c/2$, as computed by Eq. (5-2) or Eq. (5-3), magnetic walls can be placed at the edges of the center conducting strip, parallel to the dividing wall, and the propagation will be undisturbed. These magnetic walls are analogous to the possible magnetic walls of the parallel plate array. With the acceptance of these points of similarity, it follows that the effective length of the coupling region is $L - 2d$ for the TEM mode existing only inside the coupling region, and the even trough-guide higher-order mode appears to extend a distance d' into the coupling region. In the particular hybrid constructed, d and d' were found by experiment to be about 30 percent greater than predicted by this analysis, but were only about 15 percent greater than predicted by the work of Primich⁷ on semi-infinite parallel plates of finite thickness. No obvious differences in terminal plane locations were noticed for couplers with the dividing walls cut off square (analogous to the thick plates of Primich's analysis) and for those with the dividing walls ending in a short ($0.11\lambda_g$) taper.

D. DESIGN CONSIDERATIONS

1. GENERAL

The discussions in Sections A, B, and C of Chapter 4 apply to this hybrid also. To summarize:

$$(1) \text{ Power division} = 20 \log_{10} \tan \left(\frac{\theta_e - \theta_o}{2} \right) \\ \approx 0.15 [|\theta_e - \theta_o| - 90^\circ] \quad (5-5)$$

decibels, for small reflections and power divisions less than about one decibel, where θ_e and θ_o are the even- and odd-mode insertion phase-shifts through the coupling region

$$(2) \text{ Power division is flat when } \frac{d\theta_c}{df} = \frac{d\theta_o}{df} \quad (5-6)$$

- (3) One mode is matched to the input lines at all frequencies within the coupling band.
- (4) The other mode is matched to the input lines only when the coupling region has a resonant length for that mode.
- (5) Low VSWR implies high isolation.

2. LENGTH OF THE COUPLING REGION

The physical length, L , of the coupling region is selected to be resonant to the TEM mode at the design center frequency, so that this mode appears matched at that frequency. For a uniform coupling region, the apparent electrical length to the TEM mode must be an integral number of half-wavelengths long:

$$L = 2d = n \frac{\lambda_1}{2} \quad (5-7)$$

where d is the terminal plane location for the TEM mode, as discussed in Section C, while λ_1 is the design-center free-space wavelength, and n is an integer. Experience shows that the coupling region should be about one wavelength long for hybrid performance between, and not too near, the first two higher-order-mode cut-off frequencies. Thus,

$$n = 2 \quad , \quad \text{and} \quad L = \lambda_1 + 2d \quad (5-8)$$

3. WIDTH OF THE CONDUCTING STRIP IN THE COUPLING REGION

For equal power division, the insertion phase length of the higher-order mode must be $\pi/2$ less than that of the TEM mode, as is seen from Eq. (5-5). At match, the insertion phase length for the TEM mode is 2π , and so

$$\frac{2\pi(L - 2d')}{\lambda_g} = 2\pi - \frac{\pi}{2} \quad (5-9)$$

or

$$\lambda_g = \frac{4}{3} (L - 2d') \quad (5-10)$$

where λ_g is the higher-order-mode guide wavelength, and d' the terminal plane location for the higher-order mode, as discussed in Section C. Equations (5-4) and (5-2) or (5-3) can be used to find w , the width of the strip in the coupling region.

4. EVEN-MODE TUNING WITH CENTRAL CAPACITANCE

a. EFFECT OF CAPACITANCE ON INSERTION PHASE LENGTH OF THE TEM MODE—Lumped shunt capacitance at the center of the coupling region affects only the TEM mode, since no electric field exists there for the higher-order mode. When such capacitance has been added to an existing hybrid, it has been observed that it is possible to reduce the coupling region length and still operate over the same frequency band. That is, when the coupling region is shortened, its electrical length to both the TEM and the higher-order mode is of course reduced, as is the phase difference between modes. Capacitive tuning increases the phase shift in the TEM mode, and allows the phase difference between modes to be restored to its original value at the same frequency, thus restoring the original value of power division. The effect of the capacitance on insertion phase length can be analyzed by using an ABCD matrix for the even-mode circuit shown in Fig. 5-6.

The ratio of the terminating conductance to the characteristic conductance of the even mode is designated as Y_{oo}/Y_{oe} , which is the ratio of the characteristic conductance of the odd mode to that of the even mode. The transmission phase constant of a uniform even-mode line is given by k ,

and the centrally located shunt susceptance is jB , normalized to the even mode characteristic admittance, Y_{oe} . The general solution for the insertion phase shift of the even mode is

$$\theta_e = \arctan \left\{ \frac{\left(\frac{Y_{oo}}{Y_{oe}} + \frac{Y_{oe}}{Y_{oe}} \right) - \left(\frac{B}{2} \right) \left[\left(\frac{Y_{oo}}{Y_{oe}} \right) \tan \frac{kl}{2} - \left(\frac{Y_{oe}}{Y_{oe}} \right) \cot \frac{kl}{2} \right]}{2 - B \tan kl} \tan kl \right\} \quad (5-11)$$

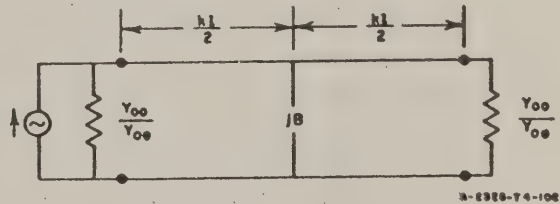


FIG. 5-6

EQUIVALENT CIRCUIT FOR EVEN-MODE PROPAGATION
WHEN A TUNING SCREW IS INSERTED
IN THE COUPLING REGION

where, for small B , the value of the arctangent taken is that nearest kl .

Equation (5-11) is applied to the structure being considered by substituting $L - 2d$ for l , this substitution being allowed by the arguments of Sec. C, and then letting $k = 2\pi/\lambda_1$, from Eq. (5-1). For shunt susceptance, B , small, and $(L - 2d)/\lambda$ near unity, appropriate simplifications yield the approximation

$$\theta_e \approx \arctan \left[\frac{1}{2} \left(\frac{Y_{oo}}{Y_{oe}} + \frac{Y_{oe}}{Y_{oo}} \right) \tan 2\pi \left(\frac{L - 2d}{\lambda} \right) + \frac{B}{2} \frac{Y_{oe}}{Y_{oo}} \right] \quad (5-12)$$

Inspection of Eq. (5-12) shows that the addition of a small, positive shunt susceptance increases θ_e . That is, a small, centrally located, shunt capacitance acts as though it were a short length of line for the TEM mode. Notice that the length of the coupling region and the width of the strip in the coupling region discussed in Sec. D-2 and -3 are for the case where $B = 0$.

b. EFFECT ON INPUT VSWR—If the coupling region of a matched, balanced hybrid junction having no shunt susceptance is reduced in length, and central capacitance is then added until equal power division is again obtained at the original frequency, it will be found that the frequency of best match is also practically unchanged. This fortunate tendency for equal power division and match to occur at about the same frequency for reduced coupling region lengths with appropriate even-mode tuning can be checked on a Smith chart and shown to be a practical approximation, until the shunt capacity becomes large.

c. EFFECT ON ODD MODE—The tuning capacitors used are wide screws threaded through the ground planes. They are usually physically large enough to perturb the magnetic field of the higher-order mode, introducing a small but undesirable reflection. The effect of this reflection, which occurs as a small shunt inductance at the center of the coupling section, is to increase the purely real conductance at the ends of the coupling section. This is compensated for by having the trough-guide feedlines match the increased conductance.

With the dividing wall completely removed in the coupling region, the trough-guide fin widths are made exactly one-half the width of the strip in the coupling region in order to maintain the same cut-off

wavelength and characteristic conductances in both feed line and coupling region for the trough-guide mode. The thickness of the dividing wall in the trough-guide region, and its absence in the coupling region then requires a step in the edge of the strip of half the dividing wall thickness, occurring at the junctions of the coupling region with the feed lines. This step is shown on the completed hybrid sketched in Fig. 5-3. Now, in order to make the feed line conductances slightly greater at the junctions, the dividing walls are tapered to narrow edges at the junctions, increasing the electrical width of the trough-guide fins in those regions. The resulting small increase in feedline conductance is sufficient to reduce the effect of odd-mode reflections from the tuning screws to a very small level.

5. FLAT POWER DIVISION

It is reasonable to expect that the widest bandwidth for nearly equal power division will be obtained when the slope of the power division with frequency curve is zero at band center. This is equivalent to the statement of Eq. (5-6). A qualitative analysis can be made from the power-division formula, Eq. (5-5), using approximations suitable for use near the frequency where power division is equal, and letting the even-mode shunt susceptance be zero, for simplicity.

$$2\pi \left(\frac{L - 2d}{\lambda_g} \right) \quad (5-13)$$

$$\approx \arctan \left[\frac{1}{2} \left(\frac{Y_{oe}}{Y_{os}} + \frac{Y_{oe}}{Y_{os}} \right) \tan 2\pi \left(\frac{L - 2d}{\lambda} \right) \right] \quad (5-14)$$

Equation (5-14) is equivalent to Eq. (5-12) with $B = 0$. At band center, $(L - 2d)/\lambda$ is unity, and so, around band center, $\tan 2\pi(L - 2d)/\lambda$ may be replaced by the linear approximation $2\pi[(L - 2d)/\lambda - 1]$. A similar linear simplification may be made for the arctangent function. After making the above substitutions in Eq. (5-14), using Eqs. (5-13) and (5-14) in Eq. (5-5), one obtains

$$\text{Power division} = 0.3\pi \left[\frac{3}{4} + \frac{1}{2} \left(\frac{Y_{oe}}{Y_{os}} + \frac{Y_{oe}}{Y_{os}} \right) \left(\frac{L - 2d}{\lambda} - 1 \right) - \frac{L - 2d}{\lambda_g} \right] \quad (5-15)$$

At band center, where $(L - 2d)/\lambda$ is unity, the value of power division is independent of Y_{oo}/Y_{oe} . The rate of change of power division with frequency is

$$\frac{d(\text{power division})}{df} = \frac{0.3\pi}{c} \left[\frac{1}{2} \left(\frac{Y_{oo}}{Y_{oe}} + \frac{Y_{oe}}{Y_{oo}} \right) (L - 2d) - \frac{(L - 2d')\lambda_g}{\lambda} \right] \quad (5-16)$$

where c is the velocity of light. From Eq. (5-16), it can be seen that a change in $Y_{oe}/Y_{oo} + Y_{oe}/Y_{oo}$ at the design center frequency will change the slope of the power division curve without changing the value of the power division itself. For flat coupling at band center, Eq. (5-16) must be zero. In the actual coupler, as illustrated in Fig. 5-3, if only a very small part of the dividing wall were cut away to form the coupling region, it is evident that the characteristic conductance of the TEM mode would be much higher than that of the higher-order, or $Y_{oe} \gg Y_{oo}$. Then the first term in Eq. (5-16) would predominate, and the slope of the power division curve would be positive. If the dividing-wall is now completely cut away, leaving only the flat, wide strip in the coupling region, the approximation of Sec. C, that $Y_{oo} = Y_{oe} = \lambda/\lambda_g$, can be substituted in Eq. (5-16), which gives

$$\frac{d(\text{power division})}{df} = \frac{0.3\pi}{c} \left[\frac{1}{2} \left(\frac{\lambda}{\lambda_g} + \frac{\lambda_g}{\lambda} \right) (L - 2d) - \frac{(L - 2d')\lambda_g}{\lambda} \right] \quad (5-17)$$

Because only the sign is being determined, the order of accuracy is such that $L - 2d \approx L - 2d'$ may be allowed. This simplifies Eq. (5-17) to

$$\frac{d(\text{power division})}{df} = \frac{0.3\pi}{c} (L - 2d) \frac{\left(\frac{\lambda}{\lambda_g} - \frac{\lambda_g}{\lambda} \right)}{2} \quad (5-18)$$

Since $\lambda_g > \lambda$, Eq. (5-18) predicts a negative slope to the power-division curve when all the dividing wall is removed in the coupling region. This simple investigation implies that there exists some height of the dividing-wall at which the slope of the power-division curve is zero at band center. In the experimental hybrid, it was found that removal of slightly less than half the height of the dividing wall gave flat power division

E. MEASURED RESULTS

The design principles in the preceding sections were verified with an engineering model. The ground planes of the model were one-half inch apart, and the conducting center strip was one-sixteenth inch thick, as was the dividing wall. The first objective was to achieve equal power division at the frequency of matched input, without using central tuning capacitance. As a first approximation, Eqs. (5-8) and (5-10) were used to find the length and width of the conducting strip in the coupling region. Values of the effective terminal plane distances (d and d') as discussed in Sec. C) that were more accurate than those given by Marcuvitz⁶ were obtained for the model by measuring the frequency of match and the power division obtained at that frequency, and then using Eqs. (5-8), (5-5), and (5-13). [It must be recognized that in Eq. (5-5), $\phi_c = 2\pi$ at match.] All measurements apply to trough guide only, and do not include effects of transitions to strip or coaxial line. However, an initial investigation has indicated that it would be possible to make such transitions to have a VSWR < 1.05 over the frequency band of interest for this hybrid.

The frequency and the length of the coupling region were then both adjusted to achieve equal power division with impedance match. Measured power division and input VSWR were plotted in Fig. 5-7. Length of the coupling region was 3.940 inches and width of the strip in the coupling region was 2.30 inches. The dividing wall was completely removed in the coupling region, leaving a broad flat strip there.

The next objective was to shorten the coupling region and compensate with central tuning capacitance, as discussed in Sec. D-4. The coupling-region length of the hybrid constructed was shortened to 3.500 inches and then the hybrid was tuned with the central tuning capacitance for match at the same frequency at which the hybrid was matched without capacitance. Touch-up tuning was necessary to bring about equal power division, which changed the frequency of match slightly. Power division, VSWR, and isolation for this hybrid are shown in Fig. 5-8. Notice that the 11-percent change in coupling-region length caused the frequency of match and equal power division to change by less than 2 percent.

The final objective was to flatten the power division curve at band center. In Sec. D-5 it was indicated that a height could be found for the dividing wall in the coupling region which would give flat coupling. In the model, the height was found by experiment to be 0.125 inches above

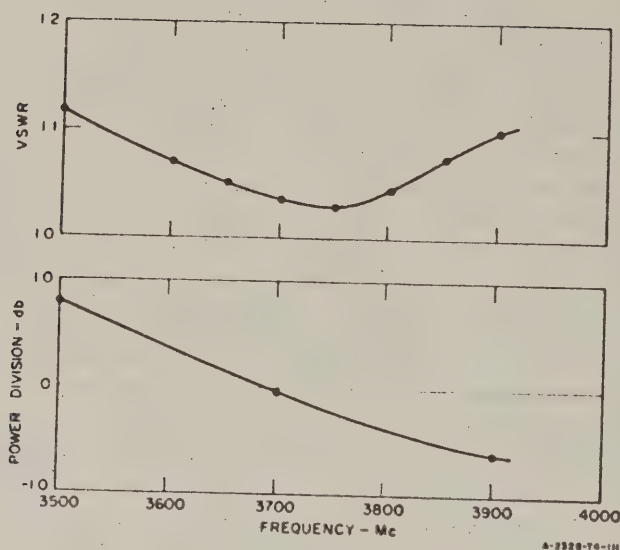
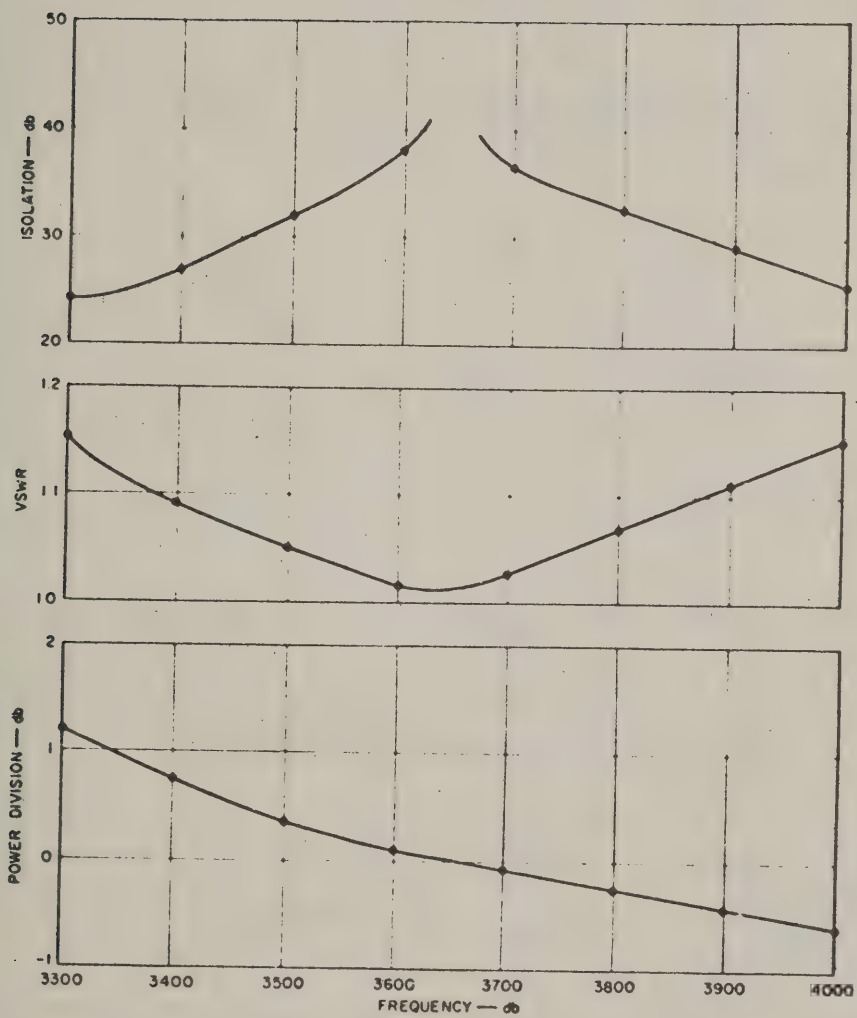


FIG. 5-7
HYBRID PERFORMANCE WITHOUT CAPACITIVE TUNING

the conducting center strip. With the $\frac{3}{8}$ -inch-diameter tuning screws set so that 0.031-inch gaps existed between the flat bottoms of the screws and the tops of the dividing walls, the coupling on this hybrid was 0.25 db less than the equal power division condition at band center. This was done in order to maintain an arbitrary ± 0.25 db specification, allowing for the power division increase on either side of band center. Power division, VSWR, and isolation are plotted in Fig. 5-9 for this coupler. The power division is within ± 0.25 db over a 19-percent band. VSWR is under 1.15 over a 16-percent band. VSWR curves are given for both blunt and tapered ends (taper $\frac{1}{2}$ inch long) of the dividing walls as they approach the coupling region. The smaller VSWR with tapered ends illustrates the discussion in Sec. D-4 concerning cancellation of the odd-mode reflections from the tuning screws. That this probably does not give complete cancellation of odd-mode reflections is indicated by the difference between the measured isolation of the device and the isolation computed from the VSWR on the basis that reflections exist only in the even mode. However, the two isolation curves are close enough to show that reflections from the odd mode are residual in comparison with those from the even mode, as assumed.

A sketch showing the pertinent physical dimensions for the final version of this device is shown in Fig. 5-10.



DA-2526-T4-112

FIG. 5-8
PERFORMANCE OF SHORT HYBRID USING CAPACITIVE TUNING

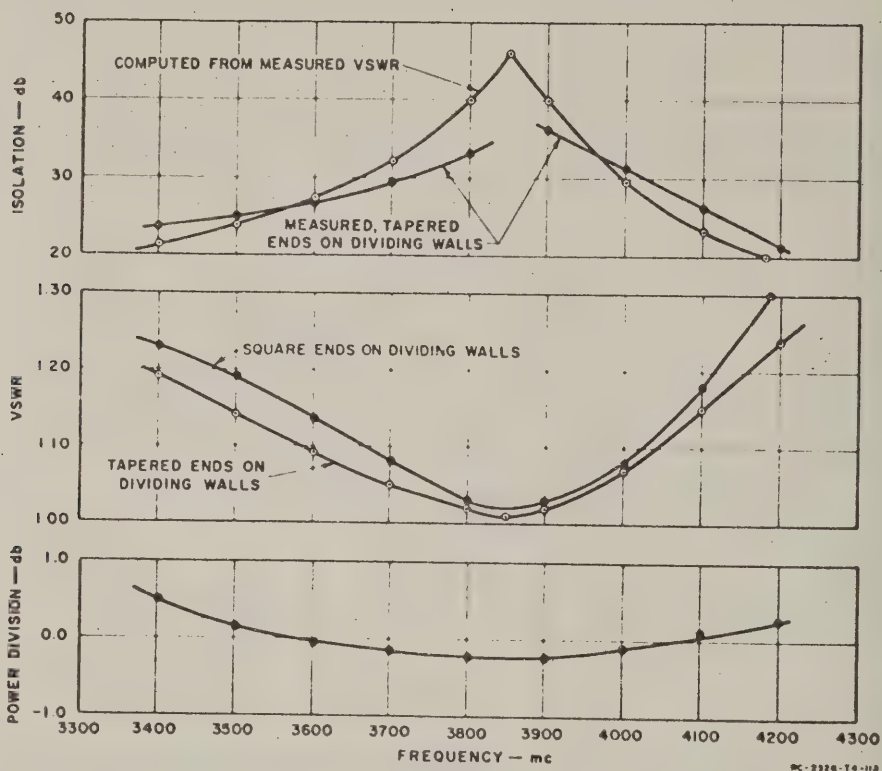


FIG. 5-9
PERFORMANCE OF TUNED HYBRID HAVING FLAT POWER DIVISION

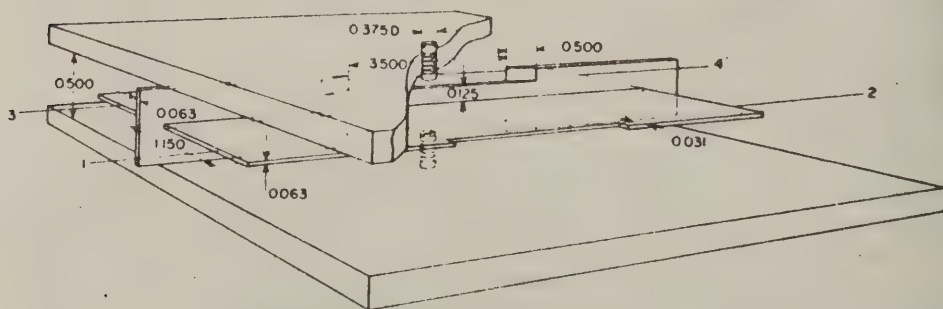


FIG. 5-10
PERTINENT DIMENSIONS OF FORWARD-COUPLING HIGHER-ORDER-MODE HYBRID JUNCTION

F. DISCUSSION

If the formulas developed in preceding sections are used to predict the behavior of the hybrid, it is necessary to assume values for certain parameters. It was mentioned previously that measurement at one frequency showed a 15 percent discrepancy from theory for the terminal plane distances. These distances are assumed fixed in making calculations. The characteristic impedance in the coupling region for the even mode can be determined for thin walls,⁸ but this was not known when the work on the forward-coupling hybrid was being done. The ratio of the characteristic impedances of the odd and even mode is not known for the case of a fin along the center of the coupling region. The capacitance from tuning screw to finned center-conductor is not known. It is possible to make reasonable rough estimates of the values of the above parameters, however, and substitute these values in the formulas given previously to determine coupling and mismatch. Adjustments can then be made in the assumed values in order to make the calculated performance agree with the measured performance. This has been done, and the results are shown in Figs. 5-11 and 5-12. Figure 5-11 shows measured and computed curves for the case of no fin in the central section and no tuning capacitance. Measured values were used for terminal-plane distances and it was assumed that they did not change with frequency. No other assumptions were necessary. Agreement between theory and measurement is considered to be good for this case.

For the structure with a fin along the center of the coupling region, and in which large-diameter tuning screws are used, many sample calculations have been made of balance and input VSWR. Various values of even-mode admittance and shunt capacitance were chosen and adjusted in an attempt to obtain calculated performance curves similar to the measured performance curves. Calculated performance for a typical set of parameters, and the measured performance curves are shown in Fig. 5-12. The shapes of the measured curves are predicted by the theory. In particular, the slope of the balance curve passes from negative to positive, in agreement with the measurements, and then, beyond the range of the measured points, the calculated balance curve resumes negative slope. The original structure is now in the possession of the Signal Corps; for this reason, it has not been verified that the measured balance curve would eventually resume negative slope at higher frequencies.

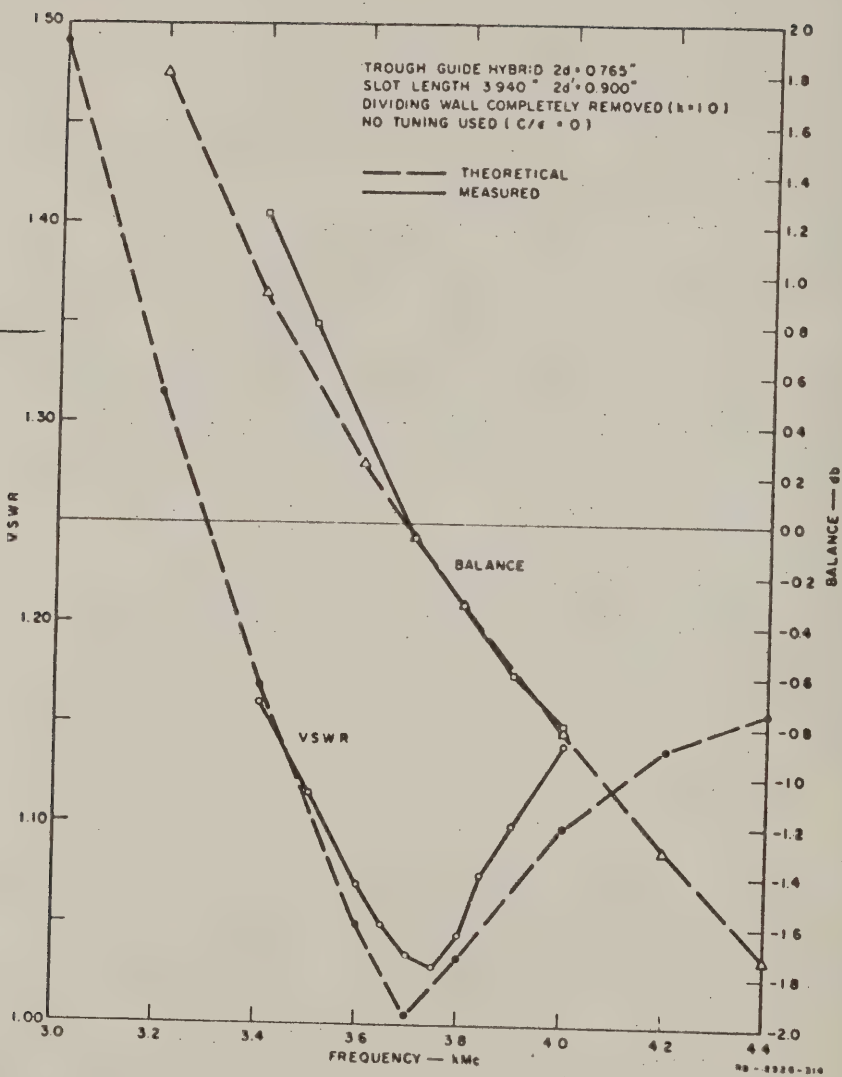


FIG. 5-11
 CALCULATED AND MEASURED PERFORMANCE OF HIGHER-ORDER MODE HYBRID

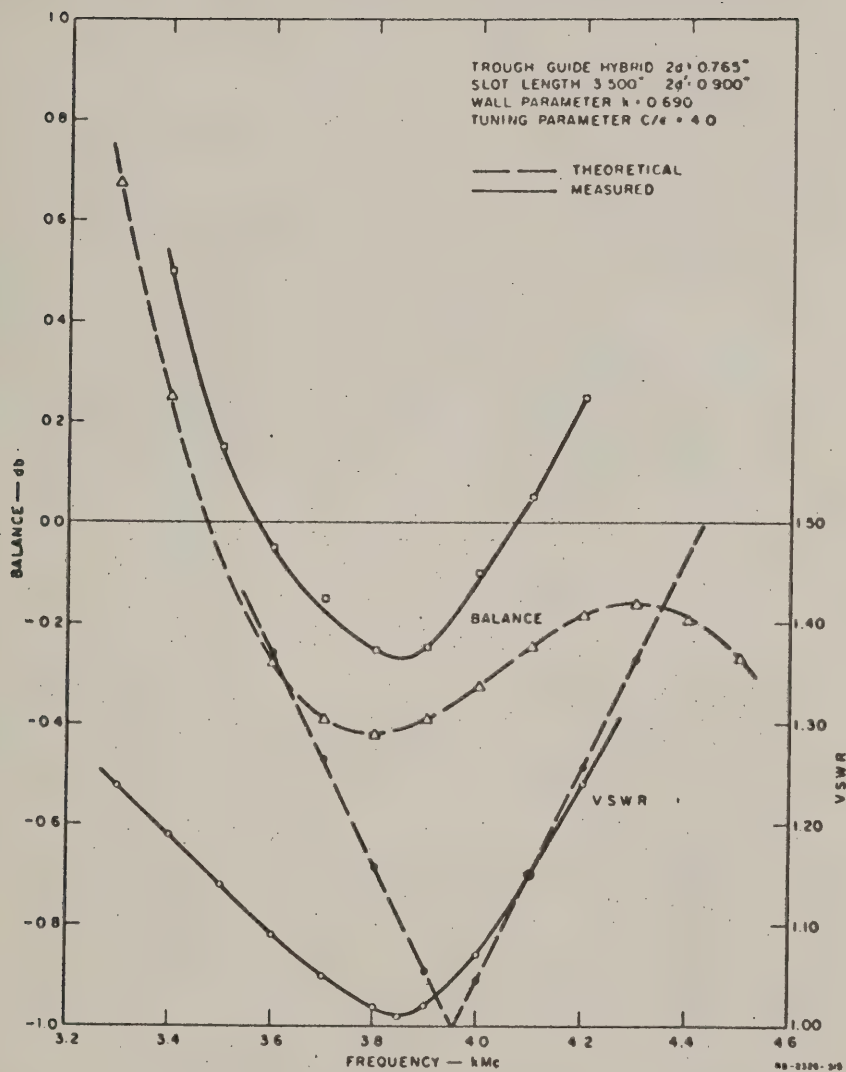


FIG. 5-12
 CALCULATED AND MEASURED PERFORMANCE OF HIGHER-ORDER MODE HYBRID

The curves of Fig. 5-12 also show that the theory predicts a narrower VSWR-bandwidth and a wider balance-bandwidth than measured. It is doubtful if this can be explained simply on the basis of having chosen incorrect values of even-mode admittance and shunt capacitance, because the calculated VSWR-bandwidth is so much smaller than the measured VSWR-bandwidth. Inasmuch as good agreement was found for the no-fin, no-tuning-screw case, it is reasonable to assume that the different results are somehow connected with the introduction of the fin and the screws. The following paragraph concerns a possible, but uninvestigated, source of the discrepancy.

The strip conductor in the coupling region must be wide enough to support the first higher-order mode that can exist on strip-line. This mode has a voltage minimum along the centerline of the strip. The introduction of a fin (providing ridge loading), and the proximity to the fin of a large-diameter screw ensures that the next higher-order mode, which has a voltage maximum along the strip centerline, not only will be excited, but will be propagating as a ghost mode⁹ in the vicinity of the tuning screws. Although this mode is reactively terminated, it can exert a large influence on the susceptance of the tuning screws, making the lumped capacitance assumption inappropriate. If the effect of this coupled, second-higher-order mode is to decrease the rate of change with frequency of the even-mode phase-length of the coupling region, then it would have the effect of broadening the VSWR-bandwidth while simultaneously decreasing the balance-bandwidth. It is felt that this is the case, although only an extensive theoretical investigation would prove it.

The many side effects in the theory, as described above, make a truly precision synthesis procedure quite complicated. A design method using educated trial and error methods appears to be preferable, using the theory to describe only the qualitative performance of the device, and to serve as a guide for the empirical design.

REFERENCES

1. H. S. Keen, "Scientific Report on Study of Strip Transmission Lines," Report 2830-2, Contract AF 19(604)-780, Airborne Instruments Laboratory, Inc., Mineola, New York (December 1955).
2. S. B. Cohn, et al., "Strip Transmission Lines and Components," Final Report, SRI Project 1114, Contract DA 36-039 SC 63232, DA Project 3-26-00-600 SC Project 2006A, Stanford Research Institute, Menlo Park, California (February 1957).
3. S. B. Cohn, "Characteristic Impedance of Shielded-Strip Transmission Line," *Trans. IRE*, Vol. MTT-2, No. 2 (July 1954).
4. J. F. Carlson, and A. E. Heins, "The Reflection of an Electromagnetic Plane Wave by an Infinite Set of Plates," *Quart. Appl. Math.* 4, 4, pp. 313-329 (January 1947).
5. B. A. Lengyel, "Reflection and Transmission at the Surface of Metal-Plate Media," *Jour. Appl. Phys.* 22, 3, p. 265-276 (March 1951).
6. N. Marcuvitz, *Waveguide Handbook*, Vol. 10, Sec. 5.23 (McGraw-Hill Book Company, Inc., New York, N.Y. 1951).
7. R. I. Primich, "A Semi-Infinite Array of Parallel Metallic Plates of Finite Thickness for Microwave Systems," *Trans. IRE*, Vol. MTT-4, No. 3, pp. 156-166 (July 1956).
8. C. A. Hachemeister, "The Impedances and Fields of Some TEM Mode Transmission Lines," Research Report R-623-57, PIB-551 for Air Force Cambridge Research Center, Contract No. AF-19(604)-2031, April 16, 1958.
9. E. T. Jaynes, "Ghost Modes in Imperfect Waveguides," *Proc. IRE*, 46, 2, (February 1958).

CHAPTER 6

FORMULAS FOR BROADSIDE-COUPLED STRIP TRANSMISSION LINES*

Coupling effects between parallel transmission lines have useful applications in the design of many components, such as filters,^{1,2} directional couplers,³ baluns,⁴ and differential-phase-shift networks.⁵ Three useful coupled-strip-line configurations are shown in Fig. 6-1. The coplanar strip cross section of Fig. 6-1(a) was analyzed previously and design data are conveniently available,^{3,6} while the broadside-coupled strip-line cross sections of Fig. 6-1(b) and (c) are treated in this section. In all three cases, the theory applies to strips of zero thickness, which may be approximated by metal-foil conductors sandwiched between dielectric plates filling the cross section. If air dielectric is desired, the strips must be given a moderate thickness to provide mechanical strength. In this case, adequate computational accuracy has been obtained by suitably modifying the zero-thickness formulas

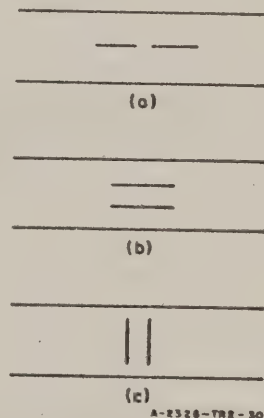


FIG. 6-1

THREE USEFUL CONFIGURATIONS
OF VERY THIN COUPLED STRIPS
BETWEEN PARALLEL GROUND
PLANES

The coplanar configuration of Fig. 6-1(a) is particularly well suited to photo-etched strip-line circuits, but cannot be used where very close coupling is required. For example, in directional couplers having couplings greater than about -8 db, the spacing between the strips becomes prohibitively small. However, closer coupling may be obtained with a reasonable spacing if thick strips are used in the arrangement of Fig. 6-1(a). This is clear if one considers that a sizable parallel-plate capacitance is added to the fringing capacitance between the two strips. To achieve close coupling with thin strips, a broadside coupling arrangement as in Fig. 6-1(b) and (c) is necessary. Both of these configurations have been used successfully at Stanford Research Institute

* The material in this chapter has been published. See S. B. Cohn, "Characteristic Impedances of Broadside-Coupled Strip Transmission Lines," *IRE Trans. PGWTT*, Vol. 8, pp. 633-637 (November 1960).

in directional couplers having midband couplings as great as -2.7 db.^{3,7} The formulas used in the design of those directional couplers were judged to be too approximate for general use, and therefore a more precise analysis has been carried out and the results are given in this section.

The details of the analysis of the two broadside-coupled strip configurations are not given here, since they involve a fairly routine application of the well-known Schwartz-Christoffel transformation method. However, the specific transformation geometries are described at the end of this section, where they reveal a simplifying approximation that was made in each derivation. It is believed that the error in computed values of characteristic impedance due to these approximations will not be greater than about 0.1 percent in close-coupling applications. The error increases as the coupling is decreased, but is not likely to exceed 1 percent in any practical application for which a broadside-coupled strip arrangement would be preferred over a coplanar arrangement. The advantage gained by these approximations is that the elliptic functions necessary in exact solutions are avoided, thus simplifying the use of the formulas, as well as their derivation. However, rigorous solutions have been carried out by C. A. Hachmeister⁸ of Polytechnic Institute of Brooklyn.

A FORMULAS FOR BROADSIDE-COUPLED STRIPS PARALLEL TO GROUND PLANES

Two orthogonal TEM modes can propagate on a pair of parallel-coupled transmission lines. These are the *even* mode, for which the respective voltages and currents on the two conductors are equal and of the same sign, and the *odd* mode, for which the respective voltages and currents are equal but of opposite sign. All other voltage, current, and field conditions on the conductors can be expressed as a linear combination of these two modes and, therefore, the complete performance of the coupled conductors in a circuit may be computed in terms of the characteristic impedances and propagation constants of these modes. It will be assumed that losses are small and that the cross sections are uniformly filled with a medium of relative dielectric constant ϵ_r , so that the characteristic impedances are essentially real, the attenuation is small, and the phase velocities are equal to $c/\sqrt{\epsilon_r}$, where c is the velocity of light in free space.

The following formulas give the even-mode characteristic impedance, Z_{oe} , and the odd-mode characteristic impedance, Z_{oo} , of each conductor with respect to ground for the cross section of Fig. 6-2. These formulas hold for any ratio of w/b and s/b , as long as w/s is greater than about 0.35:

$$Z_{oe} = \frac{188.3}{\sqrt{\epsilon_r}} \frac{K(k')}{K(k)} \quad (6-1)$$

$$Z_{oo} = \frac{296.1}{\sqrt{\epsilon_r} \frac{b}{s} \tanh^{-1} k} \quad (6-2)$$

where

k is a parameter

$$k' = \sqrt{1 - k^2}$$

$K(k)$ and $K(k')$ are complete elliptic integrals of the first kind.

The ratio w/b is given by

$$\frac{w}{b} = \frac{2}{\pi} \left\{ \tanh^{-1} \sqrt{\frac{\frac{b}{s} - 1}{\frac{1}{k} \frac{b}{s} - 1}} - \frac{s}{b} \tanh^{-1} \left[\frac{1}{k} \sqrt{\frac{\frac{b}{s} - 1}{\frac{1}{k} \frac{b}{s} - 1}} \right] \right\} \quad (6-3)$$

The quantity $K(k')/K(k)$ has been tabulated versus k by Oberhettinger and Magnus.⁹ With the aid of their table, a cross section may be designed in a straightforward process to have the desired characteristic impedances Z_{oe} and Z_{oo} , as follows. First, from Eq. (6-1), solve for $K(k')/K(k)$. Next determine k from the above-mentioned table.* Then, obtain b/s from Eq. (6-2). Finally, calculate w/b from Eq. (6-3).

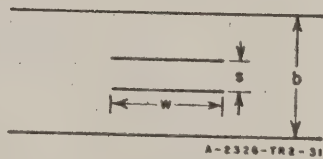


FIG. 6-2
CROSS-SECTION DIMENSIONS OF
BROADSIDE-COUPLED STRIPS
PARALLEL TO THE GROUND PLANES

* For k small, one may use

$$\frac{K(k')}{K(k)} = \frac{2}{\pi} \log_2 \frac{4}{k}$$

The error in this formula increases with k , being about 4 percent for $k = 0.2$, and 1 percent for $k = 0.3$.

1. SIMPLIFICATION FOR $(w/b)/(1 - s/b) \geq 0.35$

If, in addition to the condition $w/s \geq 0.35$, one imposes the condition

$$\frac{w/b}{1 - s/b} \geq 0.35,$$

the fringing fields at opposite edges of the strips will be sufficiently isolated that fringing capacitances can be specified that are essentially independent of the strip width. Then, the characteristic impedances are given by

$$Z_{oe} = \frac{188.3/\sqrt{\epsilon_r}}{\frac{w/b}{1 - s/b} + \frac{C'_{fe}}{\epsilon}} \quad (6-4)$$

and

$$Z_{oo} = \frac{188.3/\sqrt{\epsilon_r}}{\frac{w/b}{1 - s/b} + \frac{w}{s} + \frac{C'_{fo}}{\epsilon}} \quad (6-5)$$

where the fringing capacitance, C'_{fe} , is the capacitance per unit length that must be added at each edge of each strip to the parallel-plate capacitance so that the total capacitance to ground for the even-mode field distribution will be correct. C'_{fo} is the corresponding quantity for the odd mode, and ϵ is the absolute dielectric constant, equal to 8.85ϵ , $\mu\mu\text{f}$ per meter. The fringing capacitances are functions only of s/b , and are given by

$$\frac{C'_{fe}}{\epsilon} = 0.4413 + \frac{1}{\pi} \left[\log_e \left(\frac{1}{1 - s/b} \right) + \frac{s/b}{1 - s/b} \log_e \frac{b}{s} \right] \quad (6-6)$$

$$\frac{C'_{fo}}{\epsilon} = \frac{b/s}{\pi} \left[\log_e \left(\frac{1}{1 - s/b} \right) + \frac{s/b}{1 - s/b} \log_e \frac{b}{s} \right] \quad (6-7)$$

Equations (6-6) and (6-7) are plotted versus s/b in Fig. 6-3.

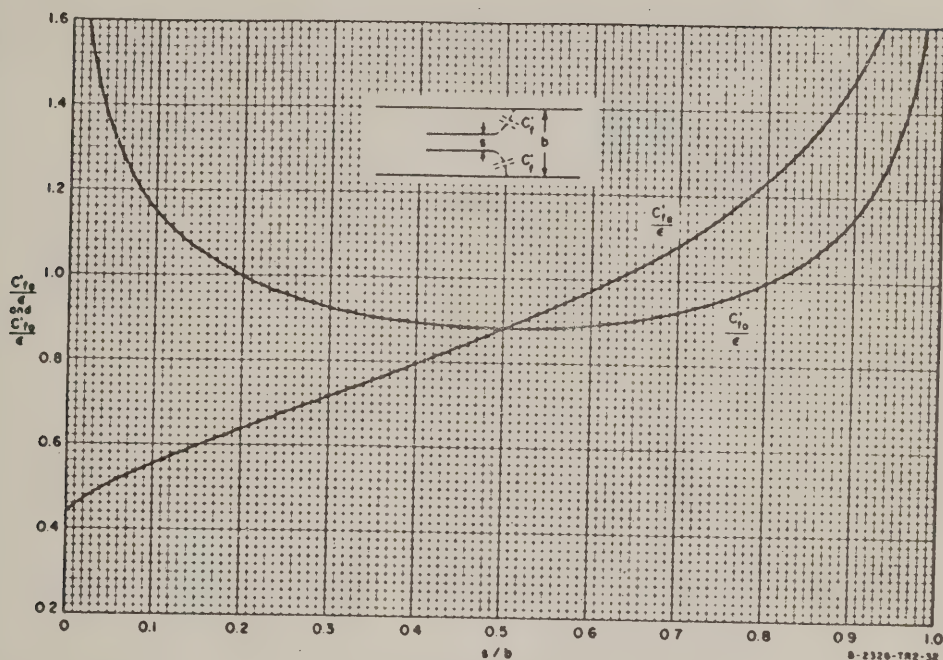


FIG. 6-3

EVEN- AND ODD-MODE FRINGING CAPACITANCES FOR BROADSIDE-COUPLED VERY THIN STRIPS PARALLEL TO THE GROUND PLANES

2. EFFECT OF A SMALL THICKNESS OF THE STRIPS

When foil strips are used in the cross section of Fig. 6-2, the strip thickness of about 0.0015 inch is usually not great enough to affect seriously the zero-thickness values of C'_{fe}/ϵ and C'_{fo}/ϵ , but it can have an appreciable effect on the parallel-plate capacitance between the strips in the odd-mode case, depending on how the dimension s is defined. In the usual case of $s/b < 0.5$, s should be taken to be the spacing between the strips, as in Fig. 6-4. Then Eqs. (6-1), (6-2) and (6-3) or Eqs. (6-4), (6-5), (6-6) and (6-7) may be used with good accuracy. For greater strip thickness, the fringing capacitances will be larger than the values given by Eqs. (6-6) and (6-7) and Fig. 6-3. The parallel-plate capacitance

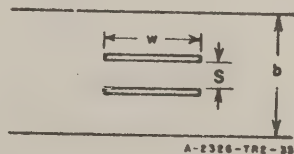


FIG. 6-4

THICK STRIPS IN THE BROADSIDE-COUPLED PARALLEL ARRANGEMENT

between each strip and its adjacent ground plane will also be increased. Formulas accurate for this case have not yet been derived.

B. FORMULAS FOR BROADSIDE-COUPLED STRIPS PERPENDICULAR TO GROUND PLANES.

The even- and odd-mode characteristic impedances of the cross section of Fig. 6-5 are given by these formulas:

$$Z_{oe} = \frac{188.3}{\sqrt{\epsilon_r}} \frac{K(k)}{K(k')} \quad (6-8)$$

$$Z_{oo} = \frac{296.1/\sqrt{\epsilon_r}}{\frac{b}{s} \cos^{-1} k + \log_e \frac{1}{k}} \quad (6-9)$$

where k is a parameter and k' , $K(k)$, and $K(k')$ are as defined in Sec. A. The ratio w/b is given by

$$\frac{w}{b} = \frac{2}{\pi} \left\{ \tan^{-1} \left[\frac{k'}{k} \sqrt{\frac{1 - \frac{k}{k'} \frac{s}{b}}{1 + \frac{k}{k'} \frac{s}{b}}} \right] - \frac{s}{b} \tanh^{-1} \sqrt{\frac{1 - \frac{k}{k'} \frac{s}{b}}{1 + \frac{k}{k'} \frac{s}{b}}} \right\} \quad (6-10)$$

The inverse cosine and tangent functions in Eqs. (6-9) and (6-10) are evaluated in radians between 0 and $\pi/2$. As in the case of broadside strips parallel to the ground planes, the dimension ratios may be determined in a straightforward manner for given values of Z_{oe} and Z_{oo} . With the aid of the table of $K(k)/K(k')$ versus k in Oberhettinger and Magnus,⁹ the parameter k is determined from Eq. (6-8). Then b/s is obtained from Eq. (6-9), and finally w/b from Eq. (6-10).

Equations (6-8), (6-9), and (6-10) are accurate for all values of w/b and s/b , as long as w/s is greater than about 1.0. As s/b is made small compared to 1.0, the formulas remain accurate for smaller values of w/s . This range of validity covers all practical cases except that of very loose coupling.

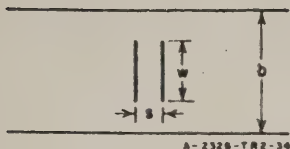


FIG. 6-5

CROSS-SECTION DIMENSIONS OF
BROADSIDE-COUPLED STRIPS
PERPENDICULAR TO THE GROUND
PLANES

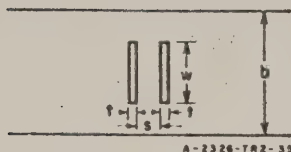


FIG. 6-6

THICK STRIPS IN THE
BROADSIDE-COUPLED,
PERPENDICULAR
ARRANGEMENT

Effect of a Small Thickness of the Strips—In the case of foil strips, the effect of strip thickness can be neglected if s is defined to be the spacing between the strips, as shown in Fig. 6-6. With thicker strips, a parallel-plate capacitance equal to $2\epsilon t/(b-w)$ may be added at each edge to improve the accuracy. The resulting formulas for the characteristic impedances are

$$Z_{ee} = \frac{188.3 \sqrt{\epsilon_r}}{\frac{K(k')}{K(k)} + \frac{2t}{b-w}}$$

and

$$Z_{oo} = \frac{94.15 \sqrt{\epsilon_r}}{\frac{1}{\pi} \left(\frac{b}{s} \cos^{-1} k + \log_e \frac{1}{k} \right) + \frac{t}{b-w}}$$

(6-11)

These formulas should have very good accuracy if $2t/(b-w) \ll 1$, and should have an error of no more than a few percent for any strip thickness.

C. COMMENTS ON THE DERIVATIONS

The formulas in this section were derived by the Schwartz-Christoffel conformal-transformation method.^{10,11} This method enables one to evaluate the capacitance and characteristic impedance between straight-sided conductors when the problem can be reduced to two dimensions, as in the cross-section plane of a transmission line. By means of one or more transformations in the complex plane, the boundary of the cross section is transformed into a simpler boundary for which the solution is known. Then because of the special properties of the conformal transformation,

the capacitance and characteristic impedance of the original boundary are equal to the respective quantities of the transformed boundary.

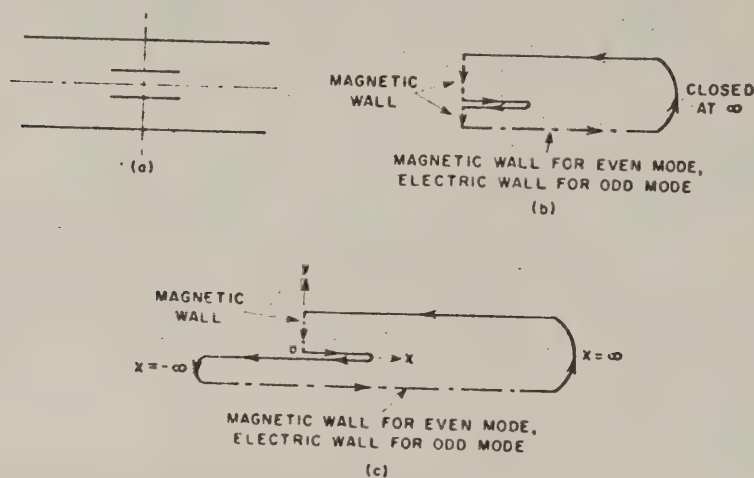


FIG. 6-7
BOUNDARIES CONSIDERED FOR THE BROADSIDE-COUPLED PARALLEL CASE

Figure 6-7(a) shows the cross section of broadside-coupled strips parallel to the ground planes. Vertical and horizontal planes of symmetry are indicated, and because of this symmetry the solution can be obtained from the geometry of Fig. 6-7(b), which is the upper right-hand quarter of the complete cross section. The boundary in Fig. 6-7(b), consists of half of the upper ground plane, the two sides of half of the upper strip, two vertical magnetic-wall segments, and a horizontal plane which is a magnetic wall for the even-mode case and an electric wall for the odd-mode case. In addition, the open end of the boundary is assumed to be closed at infinity. An exact solution of Fig. 6-7(b) requires elliptic functions. In order to avoid these functions, it is necessary to reduce the number of right-angle corners in the boundary. One way of doing this is shown in Fig. 6-7(c), where the lower vertical segment of magnetic wall is shifted to minus infinity. The new boundary is not exactly equivalent to Fig. 6-7(a) but the approximation is excellent in the usual case of $w > s$. In that case it is clear that for the even mode very little electric-field energy penetrates into the region on the left of the $x = 0$ plane in the

lower left-hand part of Fig. 6-7(c), while for the odd mode, the electric field is virtually uniform in that region. Thus very good accuracy is obtained in the even-mode case by evaluating the total capacitance between the conductors of Fig. 6-7(c) and assuming it to be equal to the capacitance of Fig. 6-7(b), and in the odd-mode case by calculating the total capacitance minus the parallel-plate capacitance between $x = 0$ and $x = -\infty$. This procedure has been followed in the derivation of Eqs. (6-1), (6-2), and (6-3), and no further approximations were made. Experience with other geometries of strip conductors indicates that an accuracy of the order of one percent should be provided for w/s as low as 0.35, and of the order of 0.1 percent for w/s greater than 1.0.

A similar approximation was made in the analysis of broadside-coupled strips perpendicular to the ground planes. The cross section is shown with its symmetry planes in Fig. 6-8(a), and the exact quarter model is shown in Fig. 6-8(b). As in the previous case, elliptic functions are needed in the solution of Fig. 6-8(b), but are avoided in the solution of Fig. 6-8(c), which is the geometry that was used in the derivation of Eqs. (6-8), (6-9), and (6-10). The total even-mode capacitance in Fig. 6-8(c) is assumed equal to the even-mode capacitance in Fig. 6-8(b), while the total odd-mode capacitance minus the parallel plate capacitance from $y = 0$ to $y = -\infty$ is assumed equal to the odd-mode capacitance in Fig. 6-8(b). The considerations about accuracy are the same as in the previous case, but it is believed that w/s should not be made smaller than 1.0 unless further evidence justifies a lower limit.

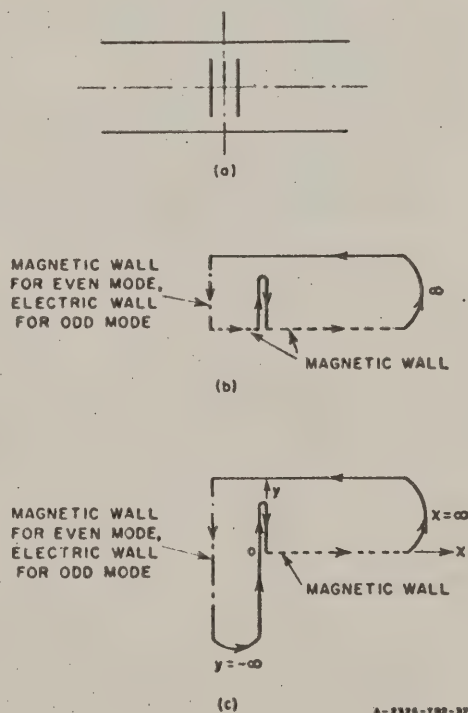


FIG. 6-8

BOUNDARIES CONSIDERED FOR THE BROADSIDE-
COUPLED PERPENDICULAR CASE

REFERENCES

1. S. B. Cohn, O. Heinz, B. M. Schiffman, E. M. T. Jones, J. K. Shimizu, and F. S. Coale, "Research on Design Criteria for Microwave Filters," Final Report, SRI Project 1331, Contract DA 36-039 SC-64625, Stanford Research Institute, Menlo Park, California (June 1957).
2. E. M. T. Jones and J. T. Bolljahn, "Coupled Strip-Transmission-Line Filters and Directional Couplers," *IRE Trans., MTT-4*, pp. 75-81 (April 1956).
3. S. B. Cohn, P. M. Sherk, J. K. Shimizu, E. M. T. Jones, "Strip Transmission Lines and Components," Final Report, SRI Project 1114, Contract DA-36-039 SC-63232, Stanford Research Institute, Menlo Park, California (February 1957).
4. J. K. Shimizu and E. M. T. Jones, "A Wide-Band Strip-Line Balun," Scientific Report 3 on SRI Project 1592, Contract AF 19(604)-1571, Stanford Research Institute, Menlo Park, California (To be published).
5. B. M. Schiffman, "A New Class of Broadband Microwave 90-Degree Phase Shifters," Scientific Report 2 on SRI Project 1592, Contract AF 19(604)-1571, Stanford Research Institute, Menlo Park, California (July 1957).
6. S. B. Cohn, "Shielded Coupled-Strip Transmission Lines," *IRE Trans., MTT-3*, pp. 29-38 (October 1955).
7. J. K. Shimizu, "A Strip-Line 3-db Directional Coupler," Scientific Report 1 on SRI Project 1592, Contract AF 19(604)-1571, Stanford Research Institute, Menlo Park, California (June 1957).
8. C. A. Hachemeister, "The Impedances and Fields of Some TEM Mode Transmission Lines," Research Report B-623-57, PIB-551 for Air Force Cambridge Research Center, Contract No. AF-19(604)-2031, April 16, 1958.
9. F. Oberhettinger and W. Magnus, "Anwendung der Elliptischen Functionen in Physik und Technik," (Springer-Verlag (Berlin) 1949).
10. W. R. Smythe, "Static and Dynamic Electricity," First ed., p. 80 ff. (McGraw-Hill Book Co., Inc., New York, 1939).
11. E. Weber, "Electromagnetic Fields, Vol. 1," p. 325 ff. (John Wiley & Sons, Inc., New York, 1950).

CHAPTER 7

A COUPLED STRIP-LINE CONFIGURATION USING PRINTED-CIRCUIT CONSTRUCTION THAT ALLOWS VERY CLOSE COUPLING

A. GENERAL

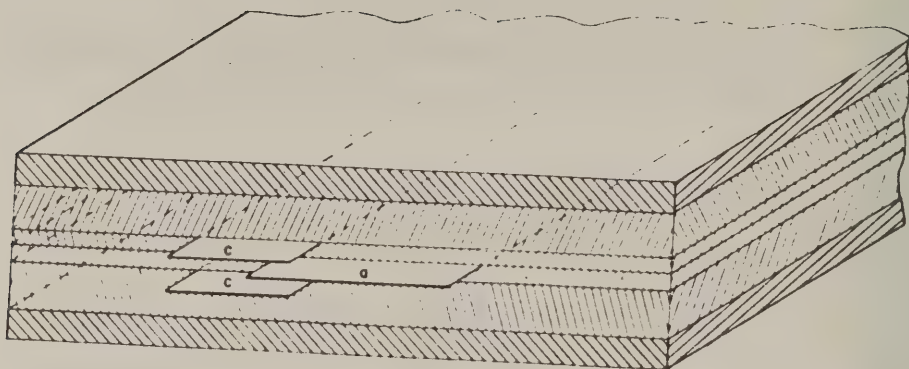
In working with shielded strip line, the need for closely coupled strips arises in designing 3-db couplers¹ and broad-band filters.^{2,3} The typical printed-circuit coupled strip-line configuration consists of two slabs of dielectric sandwiched between parallel ground planes. One of the slabs has two parallel copper strips printed on it. Coupling is achieved by bringing adjacent edges of the two strips close enough to cause appreciable capacitance to exist between the strips. Very close coupling requires that the strips be brought very near each other. For the 3-db coupler, and even more for very broad-band parallel-coupled filters, the spacing between strips becomes too small to be made accurately using practical construction techniques because the allowable tolerance on the spacing decreases as the spacing decreases. Thus, there is a practical limit to the inter-strip capacitance that can be achieved with edge coupled thin strips.

One solution to this problem has been to orient the coupled strips face-to-face and perpendicular to the ground planes. While this achieves large inter-strip capacitance, it is not always a desirable configuration, because it is difficult to build and it does not interconnect easily with more conventional strip-line circuits in which the strip is parallel to the ground planes. Also, current tends to concentrate at the thin edges of the strips in this construction, causing higher losses.

It is also possible to use thick bars for strips in order to achieve sufficient inter-strip capacitance, but this possibility precludes the use of printed-circuit materials and techniques.

B. PROPOSED CONFIGURATION

A cross section of coupled strip-lines using the proposed construction is shown in Fig. 7-1. The two strips denoted by c' are tied together at the ends of the microwave component in which they are used, while in the coupling region Strips c overlap the strip denoted by a . Thus, Strips c



RA-2326-276

FIG. 7-1

PROPOSED STRIP-LINE CONFIGURATION

form a single transmission line coupled to the transmission line formed by Strip *a*. Large coupling between these two lines is achieved by using the parallel-plate capacitance caused by the overlapping. This configuration uses thin strips parallel to the ground planes, and thus is amenable to the use of printed-circuit techniques and materials. It connects easily with conventional strip-line circuits, and does not require critical tolerances. This construction will be denoted by the term *interleaving*.

It is necessary to use a symmetrical construction with respect to the ground planes, requiring two outer center-strips for one line, in order to prevent radiation into a parallel-plate mode between the ground planes.

C TECHNICAL DESCRIPTION

The characteristic impedance, Z_0 , of a lossless uniform transmission line operating in the TEM mode is related to its shunt capacitance by:

$$Z_0 \sqrt{\epsilon_r} = \frac{\eta}{(C/\epsilon)} \text{ ohms} \quad (7-1)$$

where

$\sqrt{\epsilon_r}$ is the relative dielectric constant of the medium in which the wave travels

η is the impedance of free space = 376.7 ohms per square

C/ϵ is the ratio of the static capacitance per unit length between conductors to the permittivity (in the same units) of the dielectric medium. This ratio is independent of the dielectric constant.

The even and odd mode impedances of coupled TEM lines⁴⁵ can be found by substituting even and odd-mode capacitances of the lines into Eq. (7-1).

A generalized schematic diagram of shielded coupled-strip transmission line is shown in Fig. 7-2. The circles represent the coupled conductors. The capacitance to ground for a single conductor when both conductors are at the same potential is C_{oe} , the even-mode capacitance. The capacitance to ground when the two conductors are

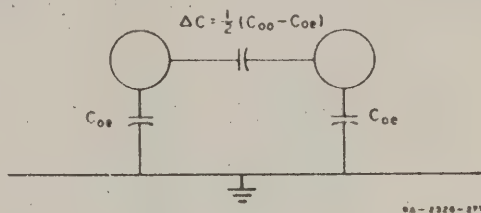


FIG. 7-2

GENERALIZED SCHEMATIC DIAGRAM

oppositely charged with respect to ground is C_{oo} , the odd-mode capacitance. It is assumed that the physical arrangement is such that the even mode capacitances of the two conductors are the same, thus implying that the odd mode capacitances are also the same. This chapter relates these capacitances to the physical dimensions of the strips.

The structure of Fig. 7-1 is composed of parallel planar surfaces. This makes it practical to consider the total capacitance of a given strip to be composed of parallel-plane capacitances plus appropriate fringing capacitances. (Fringing capacitances take into account the distortion of the field lines in the vicinity of the edges of the plane strips.) Figure 7-3 relates the various capacitances to the geometry of the structure under consideration. Two diagrams are shown to clarify the definitions for Strip a inserted in and withdrawn from Strips c . All capacitances are defined on the basis of unit depth into the paper. The parallel plane capacitances to one ground plane are given by:

$$\frac{C_{ap}}{\epsilon} = \frac{2a}{b} \quad (7-2)$$

(7-3)

Capacitance ΔC , between the center strips, has been plotted as a function of g/b and d/g in Fig. 7-4. The fringing capacitance were found by conformal mapping techniques. The derivations are given in Sec. E. Graphs of the fringing capacitances as functions of g/b and d/g are given in Figs. 7-5 through 7-9. Notice that the parallel plate and fringing capacitances are defined to apply from one side of the center line to the nearest ground plane, as shown in Fig. 7-3.



CAPACITANCES AND DIMENSIONS OF PROPOSED STRIP-LINE CONFIGURATION

The total even-mode capacitance for either strip is given by the sum of all of the capacitances to ground associated with that strip when operating in the even mode:

(7-4)

Equation (7-4) imposes the condition that the even-mode capacitances be the same for the two transmission lines. Similarly,

(7-5)

When the strips are operating in the odd mode, they are oppositely charged, one positive and one negative, and thus a surface of zero potential exists somewhere between them. The odd mode fringing capacitances include the capacitance (ΔC) to this wall of zero potential, as well as the capacitances to the actual ground plane.

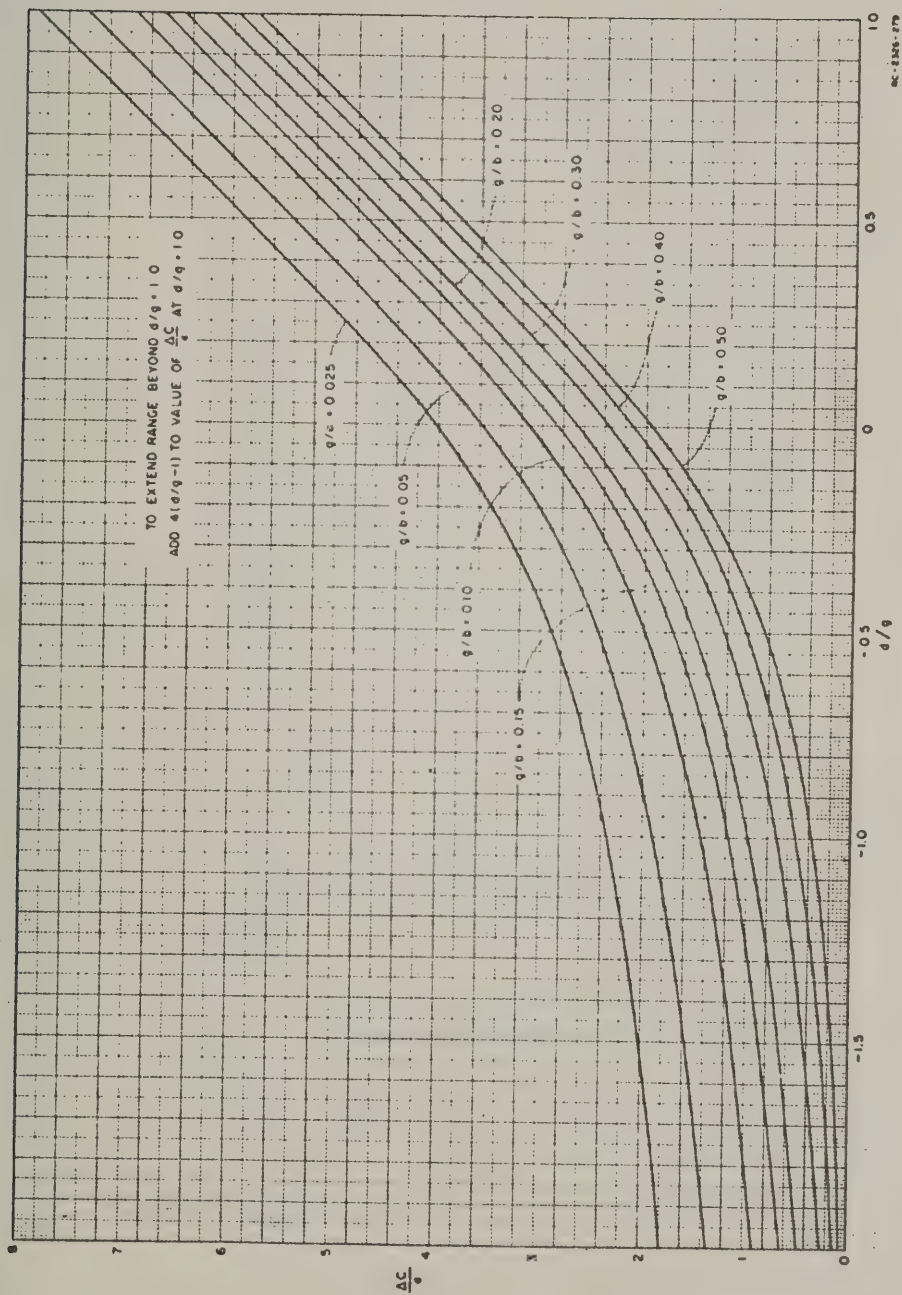


FIG. 7-4
INTER-STRIP CAPACITANCE

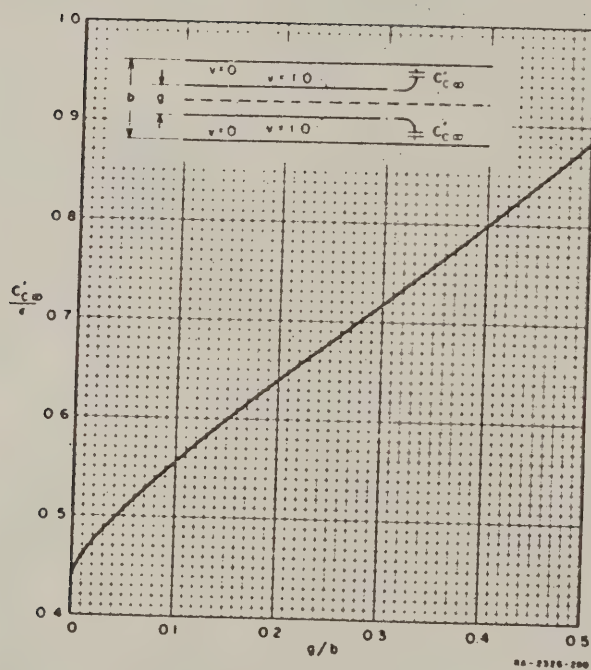


FIG. 7-5
FRINGING CAPACITANCE OF OFFSET THIN STRIP

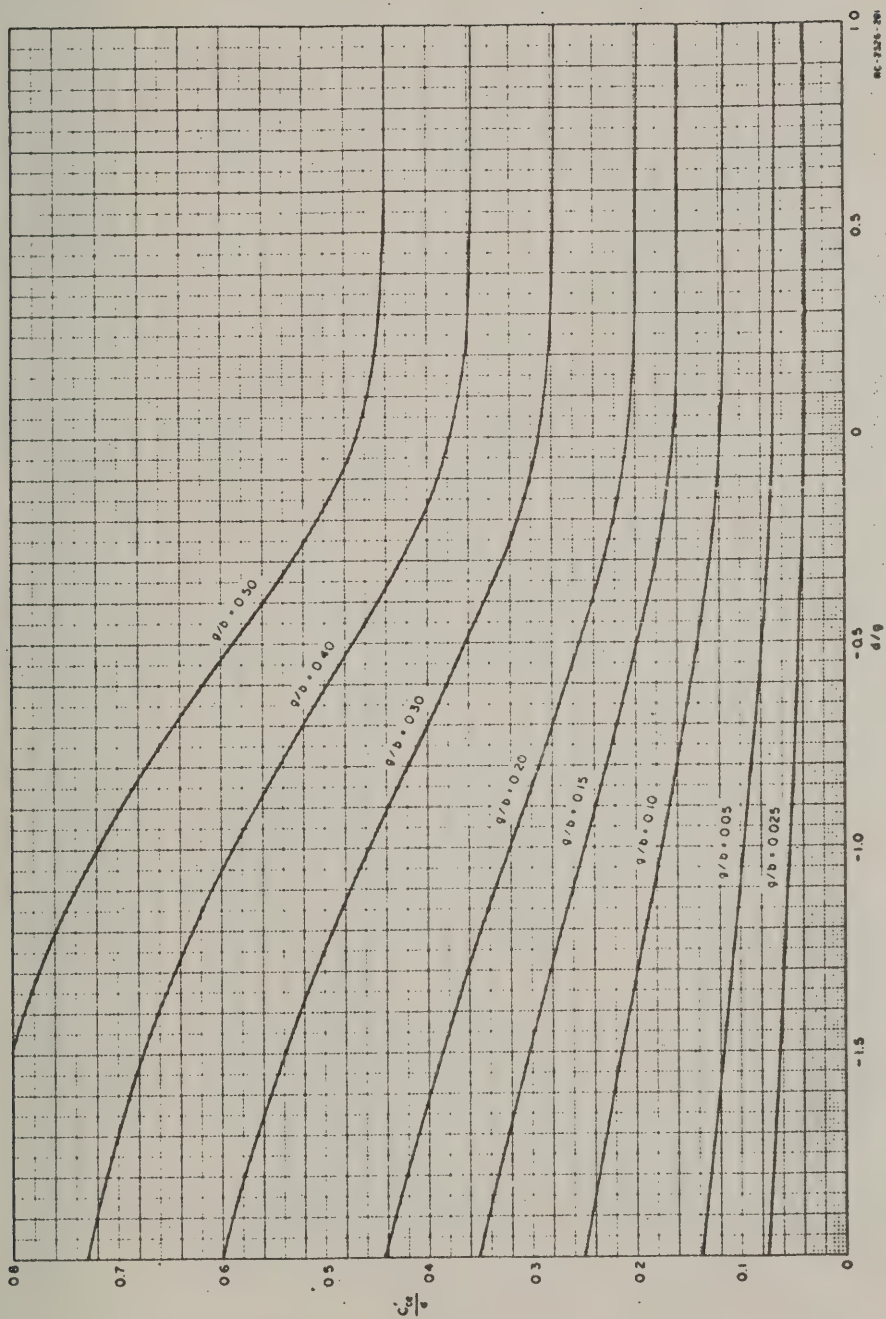


FIG. 7-6
EVEN-MODE FRINGING CAPACITANCE OF STRIP c

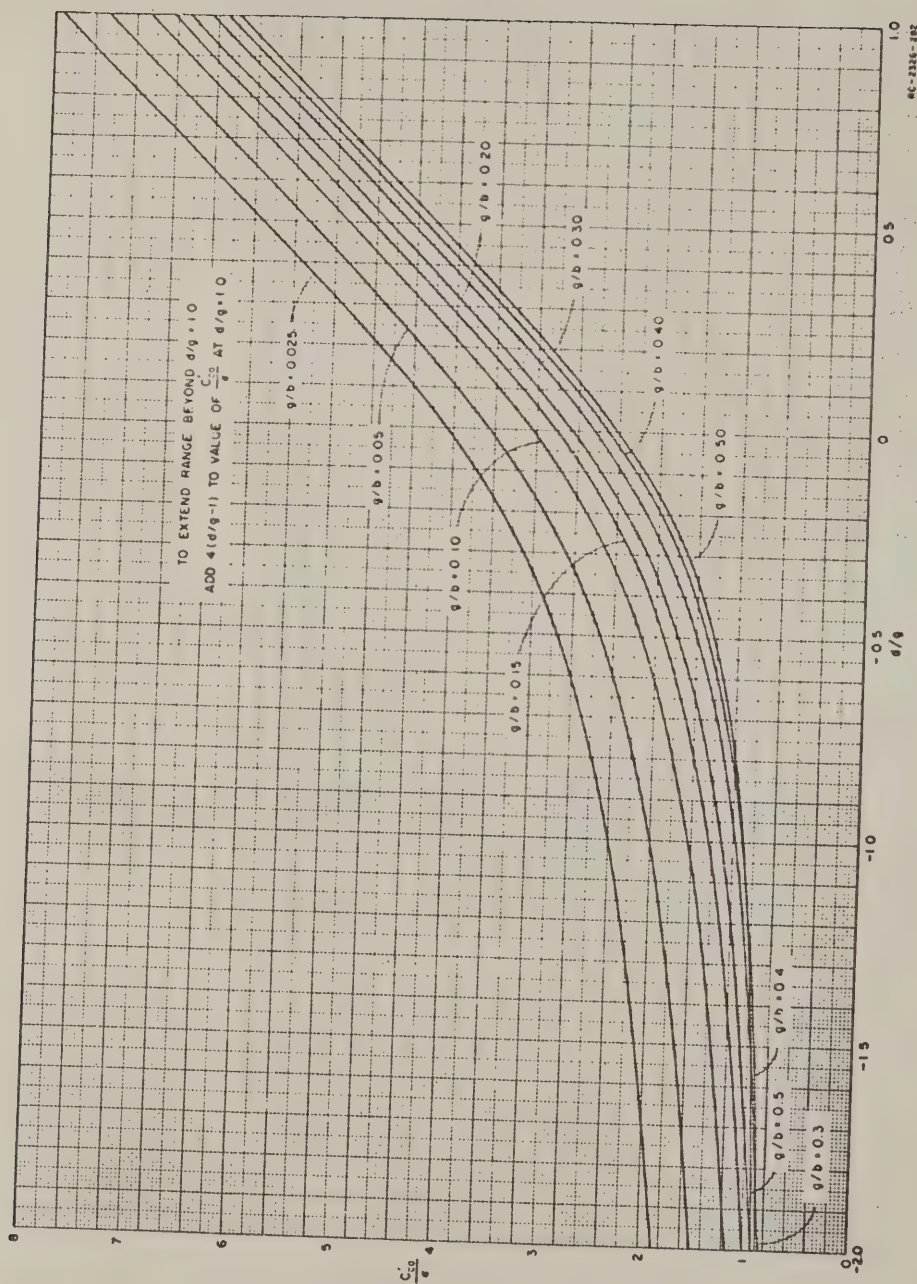


FIG. 7-7
ODD-MODE FRINGING CAPACITANCE OF STRIP ϵ

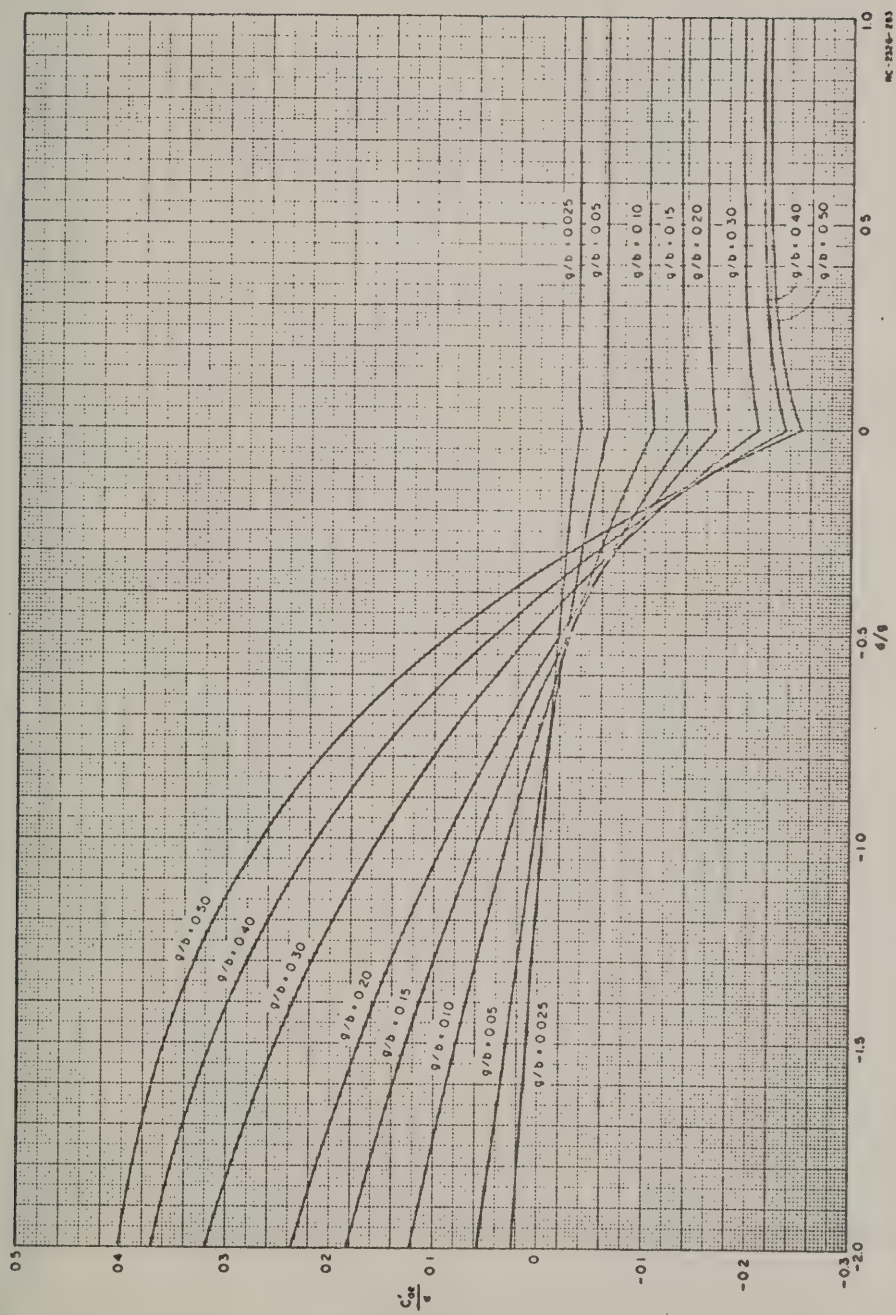


FIG. 7-8
EVEN-MODE FRINGING CAPACITANCE OF STRIP

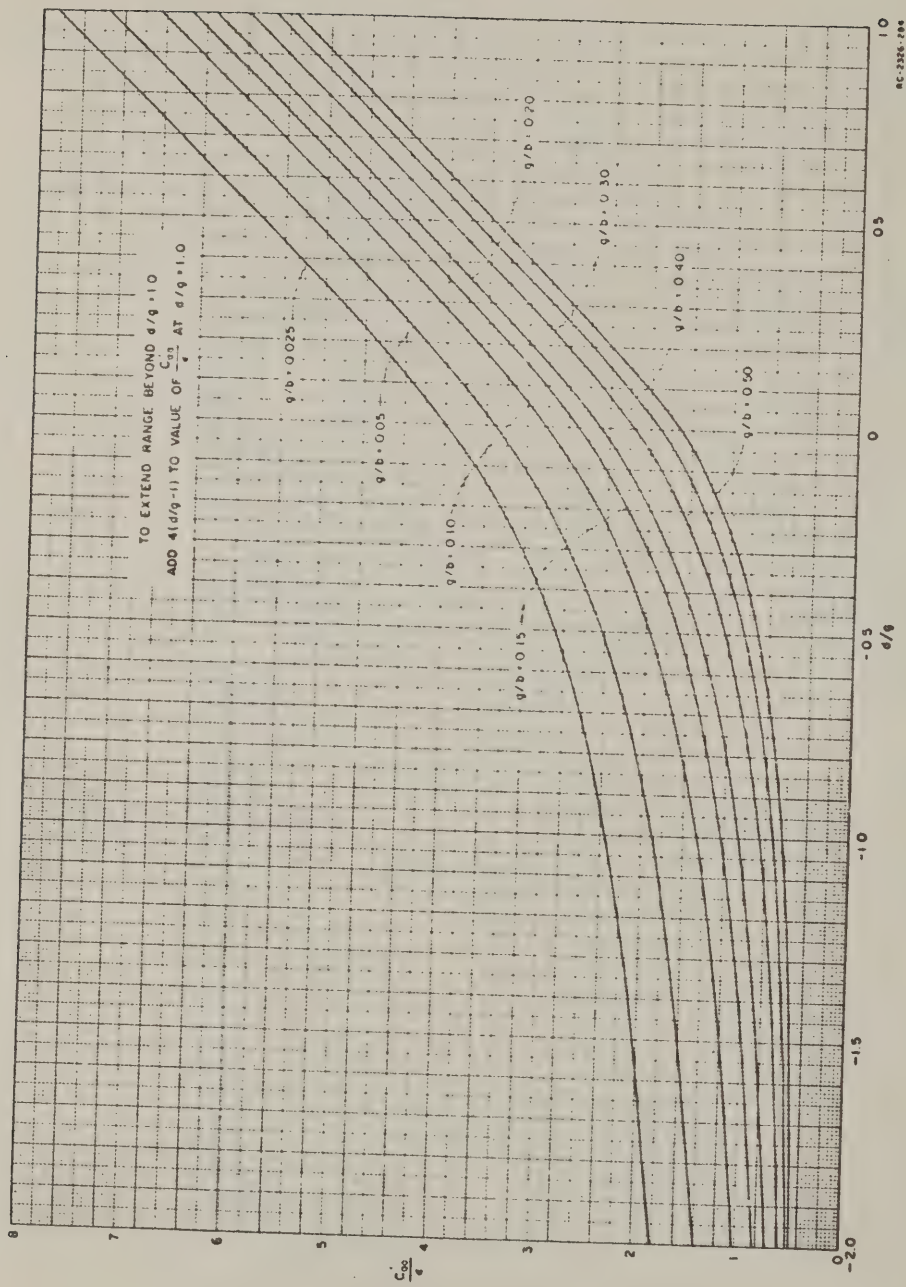


FIG. 7.9
 ODD-MODE FRINGING CAPACITANCE OF STRIP a

When identical even-mode capacitances have been imposed on the two lines, it can be shown that the odd-mode capacitances are also the same. Subtraction of Eq. (7-4) from Eq. (7-5) gives

$$C_{oe} - C_{oe} = 2(C'_{oe} - C'_{oe}) = 2(C'_{oe} - C'_{oe}) \quad (7-6)$$

The total capacitance between the two lines is denoted ΔC and is given by

$$\Delta C = (1/2) (C_{oe} - C_{oe}) \quad (7-7)$$

This follows from consideration of the definitions of even- and odd-mode capacitances, as indicated on Fig. 7-2. The quantity $\Delta C/\epsilon$ is given as a function of d/g and g/b in Fig. 7-4. The capacitance C'_f is the same as $C'_{f\infty}$ at $g/b = 0$, and its value is given by

$$\frac{C'_f}{\epsilon} = 0.441 \quad (7-8)$$

Through the use of the above relations and figures, it is possible to relate physical dimensions of the given configuration to even- and odd-mode capacitances or impedances.

D. USE OF THE GRAPHS

Usually an engineer has already determined values of even- and odd-mode impedances, Z_{oe} and Z_{oe} , or even- and odd-mode capacitances, C_{oe} and C_{oe} , and wishes to determine the corresponding physical parameters. A simple procedure accomplishes this. Equation (7-7) can be written

$$\Delta C/\epsilon = \frac{1}{2} \left(\frac{C_{oe}}{\epsilon} - \frac{C_{oe}}{\epsilon} \right) \quad (7-9)$$

Using Eq. (7-1) gives

$$\Delta C/\epsilon = \frac{\eta}{2\sqrt{\epsilon}} \left(\frac{1}{Z_{oe}} - \frac{1}{Z_{oe}} \right) \quad (7-10)$$

Values of b and g are selected, and then used with the value of $\Delta C/\epsilon$ found by Eq. (7-9) or (7-10) to determine d/g directly from the graph of Fig. 7-4. Next, having determined C_{oe}/ϵ from Z_{oe} and Eq. (7-1), it is possible to find C'_{ea}/ϵ and C'_{ce}/ϵ from Figs. 7-5 and 7-6. These quantities are substituted in Eq. (7-11) to give c/b :

$$c/b = \frac{1 - g/b}{2} \left[\frac{1}{2} C_{oe}/\epsilon - C'_{ea}/\epsilon - C'_{ce}/\epsilon \right] \quad (7-11)$$

Finally, C'_{oe}/ϵ is found from Fig. 7-8 and substituted in Eq. (7-12) to give a/b :

$$a/b = \frac{1}{2} \left[\frac{1}{2} C_{oe}/\epsilon - C'_{oe}/\epsilon - 0.441 \right] \quad (7-12)$$

Thus, all the physical dimensions are determined. These formulas are accurate for $a/b > 0.35$ and $(c/b)(1 - g/b) > 0.35$. For narrower widths, simple corrections are possible which will be given in the next section.

Equations (7-11) and (7-12), used to determine c/b and a/b , were derived from Eq. (7-4) and use no odd-mode capacitances. Similar equations for determining a/b and c/b could have been derived using Eq. (7-5), and then no even-mode capacitances would have been involved. Both methods are equally valid. This report includes graphs of both even- and odd-mode capacitances for completeness and for possible applications in which one mode may be of greater interest than another, although only the even-mode graphs, Figs. 7-6 and 7-8 will be used in the examples to follow.

In a specific device, the feeding lines connected to the coupled region may be constructed of single and dual strips in isolation from each other. The characteristic impedance of a single thin strip between parallel ground planes⁶ is either the even- or odd-mode characteristic impedance of Strip a when widely separated from Strips c . Adding the fringing capacitances from the edges of a thin strip [see Eq. (7-8)] to the parallel plate capacitances from its surfaces [see Eq. (7-2)], and then substituting in Eq. (7-1) gives the following formula for the relative strip width, a/b in terms of the characteristic impedance, Z_{oe} , for an isolated single strip between parallel ground planes:

$$a/b = \frac{\eta}{4Z_{0d}\sqrt{\epsilon_r}} = 0.441 \quad (7-13)$$

for $a/b > 0.35$.

Similarly, for thin dual strips between parallel ground planes, the fringing capacitances (Fig. 7-5) are added to the parallel-plate capacitances [Eq. (7-3)] and substituted in Eq. (7-1) to yield

$$c/b = (1 - g/b) \left(\frac{\eta}{4Z_{0d}\sqrt{\epsilon_r}} + C'_{ex} \right) \quad (7-14)$$

for $(c/b)(1 - g/b) > 0.35$, as the relation between relative strip width, c/b , and the characteristic impedance, Z_{0d} . Corrections for narrow strips will be given in the next section.

E. CONSIDERATIONS OF ACCURACY

If the strip widths g and c are allowed to become too small, then there is interaction of the fringing fields from the two edges, and the decomposition of total capacitance into parallel plane capacitance and fringing capacitances (which are based on infinite strip widths), no longer is accurate. Cohn¹⁶ shows that for a single strip centered between parallel planes, the error in total capacitance from this cause is about 1.24 percent for $w/(b - t) = 0.35$, where w is the width of the strip, t is its thickness, and b is again the ground-plane spacing. If maximum error in total capacitance of approximately this magnitude is allowed, then it is necessary that $a/b > 0.35$ and $[(c/b)/(1 - g/b)] > 0.35$.

Should these inequalities be too restricting, it is possible to make approximate corrections based on increasing the parallel-plate capacitance to compensate for the loss of fringing capacitance due to interaction of fringing fields. If an initial value, a_1/b is found to be less than 0.35, a new value, a_2/b can be used, where

$$a_2/b = (0.07 + a_1/b)/1.20 \quad (7-15)$$

provided $0.1 \leq a_2/b \leq 0.35$. A similar formula for correcting an initial value c_1/b , gives a new value, c_2/b as

$$c_2/b = [0.07(1 - g/b) + c_1/b]/1.20 \quad (7-16)$$

provided g/b is fairly small and $0.1 < (c_2/b)/(1 - g/b) < 0.35$. These formulas are based on a linear approximation to the exact fringing capacitance of a single thin strip for a width to plate-spacing ratio between 0.1 and 0.35. As the relative strip width becomes narrower than 0.35, the fringing capacitance, defined as total capacitance less parallel plate capacitance, decreases from the value C'_f or $C'_{f\infty}$ used in the derivations and graphs. The total capacitance is given by substituting into Eq. (7-1) the exact thin-strip formula for Z_0 given in Ref. 6. Equations (7-15) and (7-16) add sufficient parallel-plate capacitance to compensate for the loss of fringing capacitance. The loss of fringing is assumed to vary linearly below a relative width of 0.35, and it is also assumed that $C'_{f\infty}$ decreases by the same amount as does C'_f . Although the formulas are analytically only approximate for coupled strips, they are sufficiently accurate for practical use because they do no more than give a small correction to a quantity that is reasonably close to the exact value. They can be used with both isolated and coupled strips.

The discontinuity in the slope of C'_{af}/ϵ in Fig. 7-8 at $d/g = 0$ is not a physical phenomenon, but is a mathematical result of considering dimension a to extend to the edge of Strips c for positive d , while for negative d , dimension a extends to the edge of Strip a , as shown in Fig. 7-3. The only practical effect of this situation is that the width of Strip a is equal to dimension a when d is negative, but when d is positive the width of Strip a is equal to the sum of dimensions a and d . This is shown clearly in Fig. 7-3.

In deriving the fringing capacitance, one of the assumptions made was that the strip was infinitely thin. Investigation of a graph given by Cohn^{1,6} shows that the fringing capacitance, C'_f/ϵ from a strip centered between parallel ground planes increases by about 2 percent for a 1 percent increase in the ratio of strip thickness to plate spacing, for a very thin strip. Fringing capacitance is usually only part of the total capacitance involved in a strip-line circuit, so that for many situations, a strip no thicker than 1 or 2 percent of the associated parallel-plate separation can be considered thin without serious error.

The derivations for the fringing capacitances are exact for infinitely thin strips with dimension a (see Fig. 7-3) extending infinitely far to the right while dimension c extends infinitely far to the left. The computed values from which the curves were plotted were accurate to three places after the decimal, although the curves themselves cannot be relied on to be closer than about ± 5 in the third significant figure, as plotted.

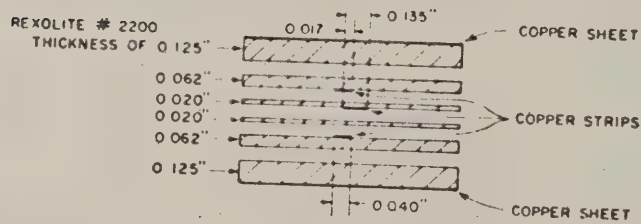
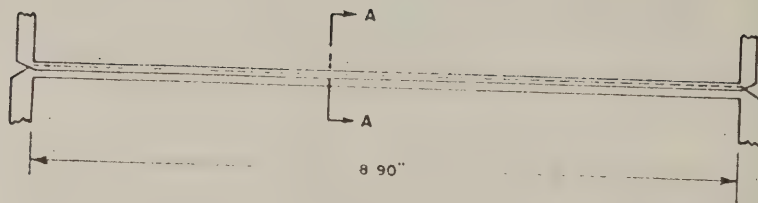
For insertion of the Strip a between Strips c beyond the maximum plotted, $d/g = 1.0$, the even-mode values C'_{oe}/ϵ and C'_{eo}/ϵ do not change from their values at $d/g = 1.0$, while $\Delta C/\epsilon$ and the odd-mode values C'_{oo}/ϵ and C'_{eo}/ϵ , can be found simply by adding $4(d/g - 1)$ to their values at $d/g = 1$. For spacing between Strips c greater than $g/b = 0.5$, or for a separation $d/g < -2.0$, probably some different strip-line construction would be more suitable.

Finally, it should be noted that if these curves predict a value of d positive and approximately equal to or greater than c , the result is not valid. When Strip a protrudes all the way between Strips c in this manner, it merely means that too great a value of g/b was selected to realize the odd-mode capacitance. This restriction may be expressed mathematically by requiring that $d < c - (g/2)$. If this condition is not met for a desired set of capacitances, then it is necessary to make g/b smaller and determine new dimensions.

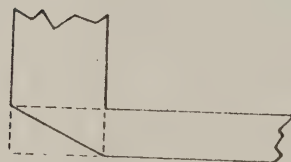
F. APPLICATIONS

The graphs and procedures described above have been used to design strip-line 3-db couplers,^{1,5} and a strip-line parallel-coupled filter.^{2,3}

A 3-db coupler was designed to have an input impedance of 50 ohms. Figure 7-10 shows pertinent details of its construction. The dielectric material used, Rexolite #2200, has a published dielectric constant of 2.77. This material is commercially available with sheets of 0.001-inch copper bonded to the sides.



EXPLODED VIEW OF SECTION A-A



DETAIL SHOWING METHOD
OF MITERING CORNERS

NA - 2326-292

FIG. 7-10
DETAILS OF CONSTRUCTION OF 200-Mc, 3-db BACKWARD COUPLER

A center-frequency coupling value of -2.8 db, rather than -3.0 db, was chosen to allow for an expected decrease in coupling at frequencies away from the center frequency. Use of the formulas of Refs. 1 or 5 gave values of 125.15 ohms for Z_{01} and 19.95 ohms for Z_{02} . Substitution of these values in Eq. (7-1) gave $C_{01} = 1.81$ and $C_{02}/\epsilon = 11.34$. Using the laminate thicknesses shown on Fig. 7-10, it was found that $g/b = 0.0964$. Equation (7-9) and Fig. 7-4 showed the required value of d/g to be 0.445. Then, use of the procedure described in the preceding section, including Eqs. (7-11) and (7-12), gave $a/b = 0.284$ and $c/b = 0.107$. (In the coupler constructed, a value of 0.097 was used for c/b because Fig. 7-5 had not been prepared, and an approximate method was used to find C'_{c0}/ϵ . The coupler was made one-quarter wavelength long in the dielectric at the center frequency of 200 Mc.

Performance curves for this coupler are shown in Fig. 7-11. The behavior of the coupler is typical of 3-db backward couplers made in other configurations.

A second 3-db coupler was made on another project for parametric amplifier work. This coupler was designed to have a center frequency of 1000 Mc. In this design the strip widths were widened in accordance with Eqs. (7-15) and (7-16) for correcting narrow strips. The dimensions are shown in Fig. 7-12. The bulk of input reflections were caused by reactance of the right-angle bends joining the feed lines to the coupling region. The purely capacitive tuning screws shown were much more effective in cancelling the reflections than were modifications of the structure of the bend or tabs on the feed lines at the bends. The greater effect of the bend reactance as frequency increases is shown in the performance curves for this coupler, Fig. 7-13. Figure 7-14 is a photograph of the coupler.

A parallel-coupled filter³ was made in interleaved construction, also. This filter was designed to have a 30 percent pass band, with a center frequency of 1000 Mc. A sketch giving pertinent dimensions is shown in Fig. 7-15, and the frequency response of the filter is shown

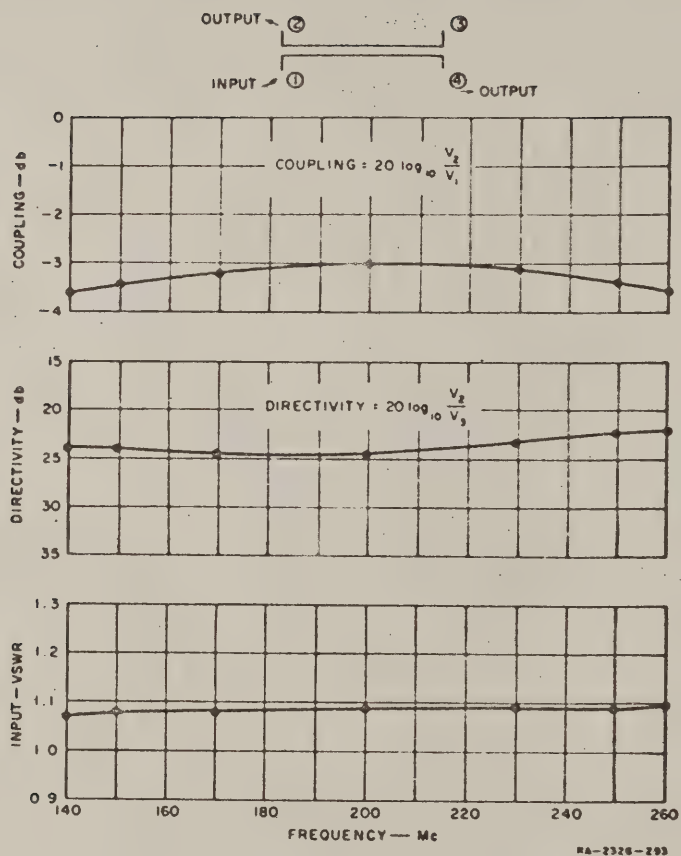


FIG. 7-11
PERFORMANCE OF 200-Mc, 3-db BACKWARD COUPLER

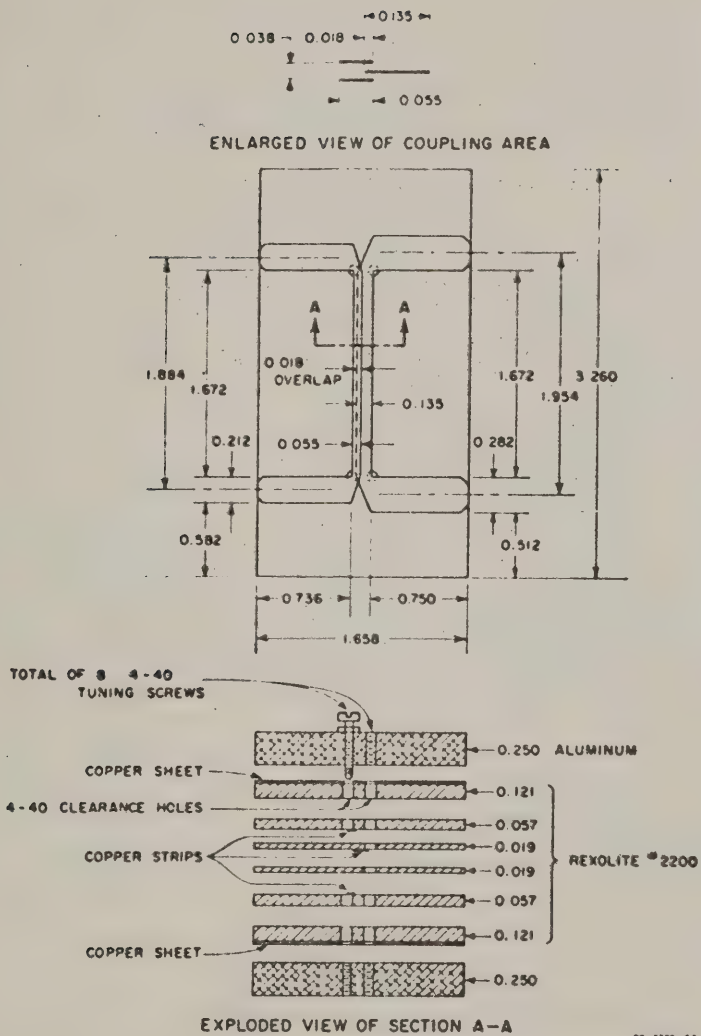


FIG. 7-12
DETAILS OF CONSTRUCTION OF 1000-Mc 3-db BACKWARD COUPLER

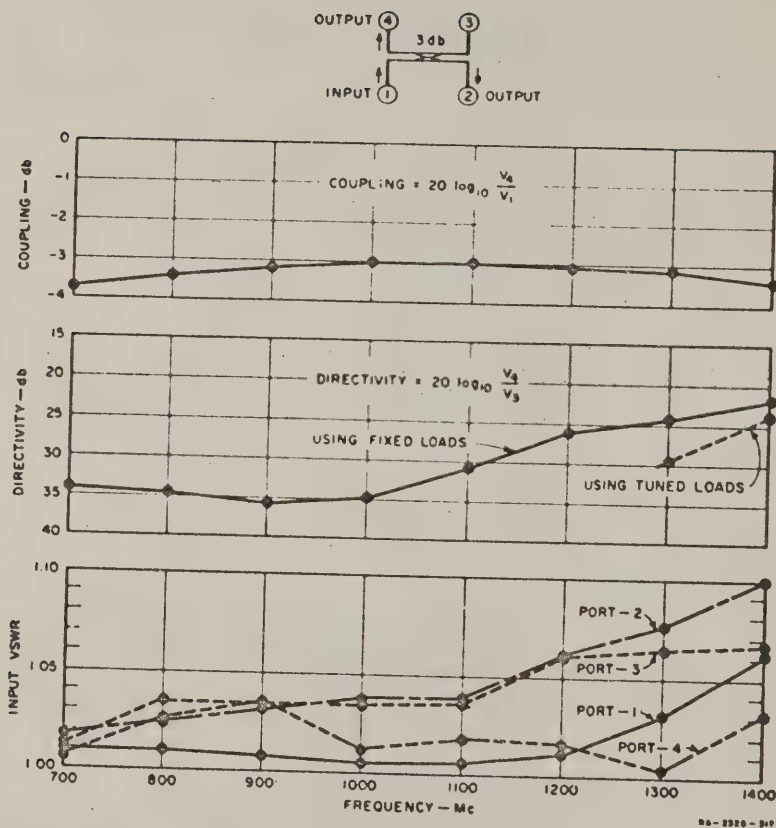


FIG. 7-13
 PERFORMANCE OF 1000-Mc 3-db BACKWARD COUPLER

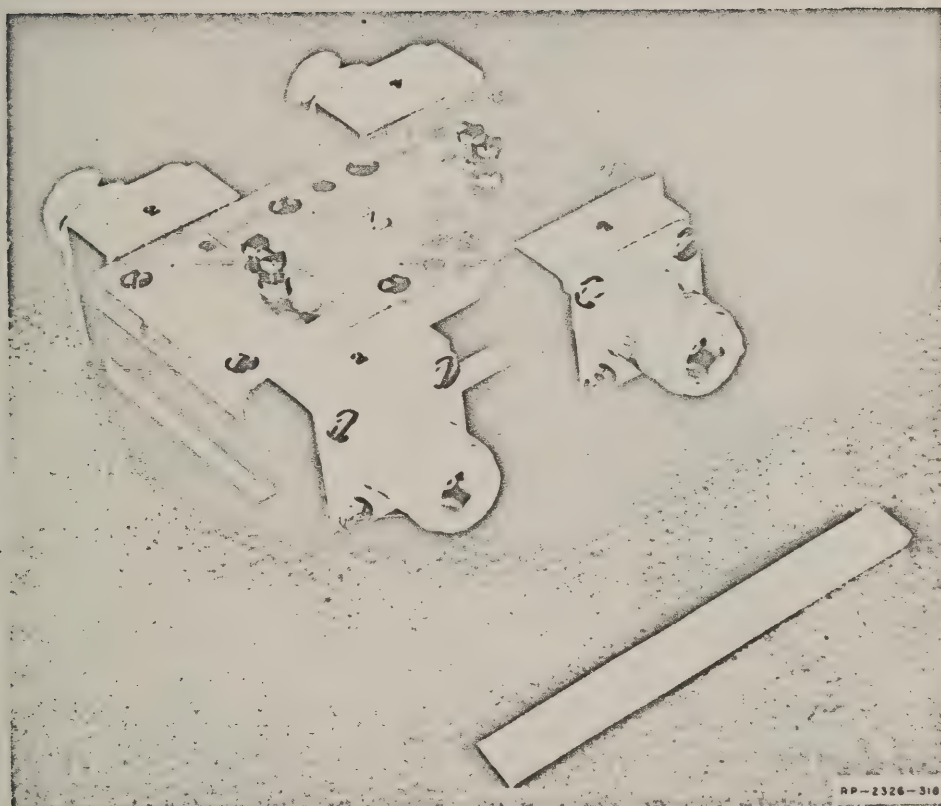
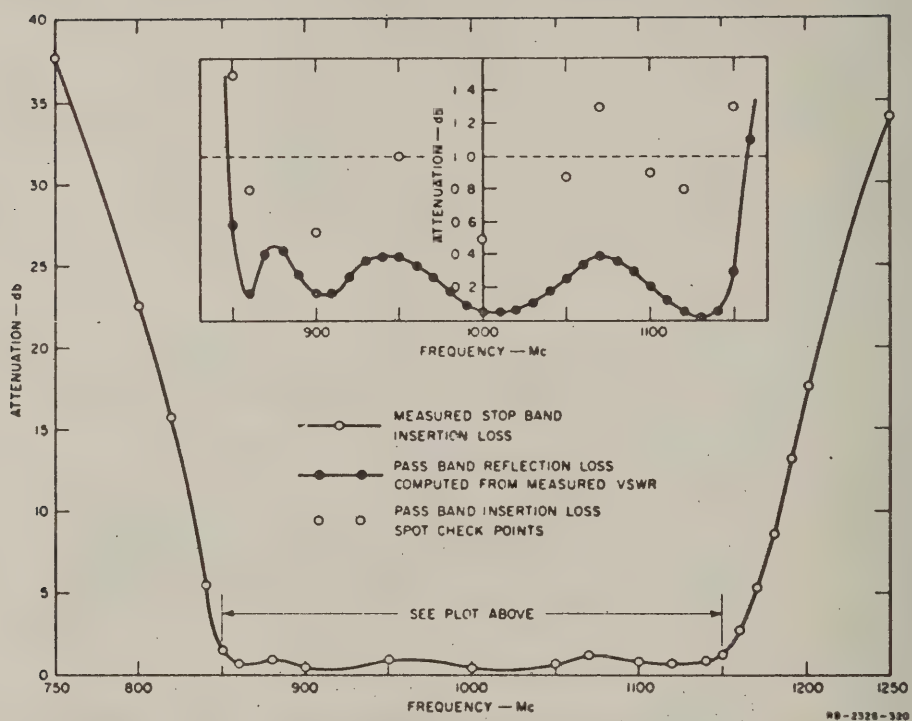


FIG. 7-14
1000-Mc 3-db BACKWARD COUPLER

in Fig. 7-16. The bandwidth is very close to the design value, but the shape of the pass-band response and the pass-band loss are not in close agreement with intended pass-band response, which is shown in Fig. 18-8(b) in Chapter 18 of this report. The most important cause of the pass-band discrepancies was that the coupled strips were not all exactly the proper electrical length. The fringing capacitances from the ends of the single strips differ from those of equivalent dual strips, and these fringing capacitances greatly influence the electrical length of each strip. Thus, different compensation is required for the two types of strips, and unfortunately, no reliable analytical method is presently available for determining the end-fringing for either case. Some improvement in the pass-band response was realized by using capacitive tuning for each section, but it was not possible to compensate each section exactly, and the tuning for each section was influenced by the tuning of the preceding sections.

For a 30-percent bandwidth filter, such as that in Fig. 7-15, the only places where interleaved construction is really necessary are at the coupled strips on each end. The tuning difficulties could have been largely eliminated if the main body of the filter had been designed to use parallel-coupled single strips^{1,2,11} with interleaved construction only at the end sections. For a two-to-one or three-to-one bandwidth filter to be used, say, as a high-pass filter, tight couplings (and thus overlapping strips) would be needed for all sections. However, for a filter of such wide bandwidth, the tuning errors would have a much less disrupting effect on the shape of the pass-band response.

The filter and the couplers used a simple transition to coaxial line devised by J. Shimizu. In this transition the coaxial-line center conductor is machined to a flat tongue extending into the strip-line device, such that one or both flat surfaces of the tongue make contact with the single or dual strip-line conductors. The tongue is made thick enough to be a very tight fit when the strip-line device is assembled. The VSWR for this type of connector is typically less than 1.025, using mechanical pressure alone to give good electrical contact.

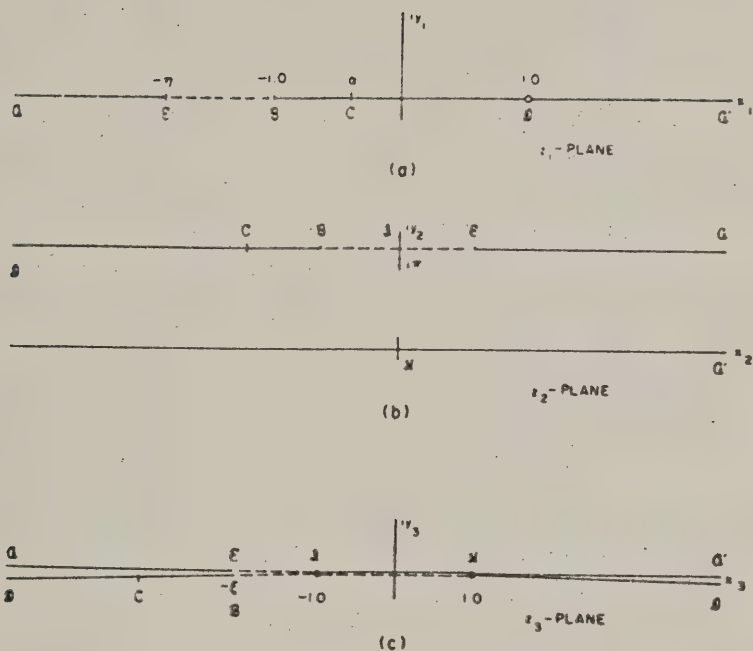


G. DERIVATION OF FRINGING CAPACITANCES

1. PRELIMINARY

It is desired to determine the static fringing capacitances shown on the structure of Fig. 7-3 by means of conformal mapping techniques.^{7,8} This can be done by subjecting the boundaries of the structure to transformations under which capacitance is invariant, and that lead to a new structure for which capacitance is known. Subtraction of parallel plate capacitances of the original structure from the total capacitance then leaves the fringing capacitances. The analysis will be limited to structures in which Strips *c* and *a* are so wide that interaction between fringing fields of the two edges of a single strip are negligible. As discussed in Section E, this requires that the approximate relations $a/b > 0.35$ and $[(c/b)/(1 - g/b)] > 0.35$ be held. Under these conditions it is possible to let Strip *c* extend infinitely far to the left, and Strip *a* infinitely far to the right without disturbing the fringing fields appreciably in the region where the two strips interact. Also, the electric field can lie parallel to the horizontal centerline where no conductor exists, but cannot cross it because of the symmetry of the structure, assuming the two conducting Strips *c* are always at the same potential with respect to each other. Therefore a magnetic wall can be placed along the centerline extending infinitely far to the left from the left edge of Strip *a*. These modifications allow analysis of only half of the total symmetrical structure, as shown in Fig 7-17(a). The mathematical model is shown in Fig. 7-17(b). Conductors are indicated by solid lines and the magnetic wall is indicated by a dashed line. The upper-case script letters of Fig 7-17(b) denote pertinent points of the structure and will serve as references when transformations to different complex planes are made. The values chosen for the various points on the *z*-plane will prove convenient under transformation.

The analysis consists essentially in transforming the contours of the structure on the *z*-plane into a parallel-plate representation on the *w*-plane, where capacitance can be computed directly. This procedure is



NA-2726-200

FIG. 7-18

INTERMEDIATE TRANSFORMATIONS FROM z -PLANE

As a first step, the interior of the polygon $CEC\alpha'$ will be mapped onto the upper half of a z_1 -plane as shown in Fig. 7-18(a). The mapping is given by Kober⁹ as

$$z = \frac{1 - \alpha}{2} \ln(z_1 - 1) + \frac{1 + \alpha}{2} \ln(z_1 + 1) \quad (7-17)$$

The points noted on the z -plane are related to points on the real axis of the z_1 -plane by

$$z(0) = i \frac{\pi}{2} (1 - \alpha)$$

$$z(\alpha) = \frac{1 - \alpha}{2} \ln(1 - \alpha) + \frac{1 + \alpha}{2} \ln(1 + \alpha) + i \frac{\pi}{2} (1 - \alpha) \quad (7-18)$$

$$z(\eta) = \frac{1 - \alpha}{2} \ln(1 + \eta) + \frac{1 + \alpha}{2} \ln(\eta - 1) + i\pi$$

Notice that

$$\eta > 1.0$$

$$(7-19)$$

$$-1.0 < \alpha < 1.0$$

The small circle at point \mathcal{D} indicates an infinitely small gap at that point, such that the conductors on either side may be different potentials. Point \mathcal{D} is removed to ∞ under the next transformation, which is to a z_2 -plane. This transformation will place points \mathcal{E} and \mathcal{E} equidistant from the y_2 axis, as shown in Fig. 7-18(b). The transformation is

$$z_1 = 1 + \sqrt{2(\eta + 1)} e^{z_2} \quad (7-20)$$

The source of this transformation, as with most transformations used in this chapter, is a combination of experience and the use of references.⁷⁻¹⁰ However, although the derivations of the transformations may not be obvious, they may be checked at points of interest simply by substituting values of the independent variable and observing that the transformation gives the correct result for the dependent variable.

The structure on the z_2 -plane will now be related to the given structure. The conductor between \mathcal{A} and \mathcal{D} corresponds to the ground plane on the given structure. The conductor between \mathcal{A} and \mathcal{E} corresponds to Strip a in the given structure, and the conductor between \mathcal{E} and \mathcal{D} corresponds to one of the Strips c in the given structure. The z_2 -plane structure is symmetrical about the y_2 axis. Under even-mode excitation both conducting Strips a and c are at the same potential, and thus no electric field lines cross the y_2 -axis. Therefore, a magnetic wall can be placed along the y_2 -axis and left and right halves may be analyzed separately. Under odd-mode excitation the conducting Strips a and c are oppositely charged with

respect to the ground plane, and thus all electric field lines crossing the y_2 -axis must cross normal to that axis to preserve symmetry. Therefore, an electric wall at zero potential may be placed along the y_2 -axis and left or right half only need be analyzed. Notice that script letters \tilde{A} and \tilde{B} have been assigned to the end points of the line of symmetry.

By means of the transformation

$$z_2 = \text{arc cosh } z_3 \quad (7-21)$$

The interior of the polygon $\tilde{A}\tilde{B}\tilde{A}'$ goes into the upper half of the z_3 -plane, and the polygon $\tilde{B}\tilde{A}\tilde{B}'$ goes into the lower half of the z_3 -plane, as shown in Fig. 7-18(c). Only that portion of the x_3 axis between \tilde{A} and \tilde{B} is common to both upper and lower half-planes, and for this reason the x_3 axis is shown split beyond \tilde{A} and \tilde{B} . The solid line (conductor) between \tilde{A} and \tilde{B} is to be used for odd-mode analysis, while the dashed line (magnetic wall) is to be used for even-mode analysis.

On the z_3 -plane \tilde{A} and \tilde{B} fall at $+1.0$ and -1.0 , as can be determined by substituting the known values of \tilde{A} and \tilde{B} on the z_2 -plane into Eq. (7-21). In order to find $z_3(\xi)$ it is necessary to work from the z_1 plane, where Kober⁹ shows that $z_1(\tilde{B}) = -1.0$. Then, by successive substitution and manipulation of Eqs. (7-20) and (7-21), it is found that

$$z_3(\xi) = -\frac{1}{2} \left[\frac{2}{\sqrt{2(\eta+1)}} + \frac{\sqrt{2(\eta+1)}}{2} \right] = -\xi \quad (7-22)$$

where $-\xi$ is the value of $z_3(\xi)$ on the z_3 -plane. Notice that

$$\xi > 1.0 \quad (7-23)$$

By the symmetry of the z_2 -plane with respect to the imaginary axis and the nature of the transformation, Eq. (7-21),

$$z_3(\mathcal{E}) = z_3(\mathcal{B}) = -\xi \quad (7-24)$$

although it should be noted that \mathcal{E} and \mathcal{B} are on opposite sides of a branch cut on the z_3 -plane.

2. ODD-MODE FRINGING CAPACITANCE—STRIP a

Now consider the odd mode, and investigate the fringing capacitance of Strip a, which is associated with point E. The upper half of the z_3 -plane is transformed to a parallel plate region on the w_1 -plane by

$$z_3 = (1/2)[(\xi - 1) \cosh \pi w_1 - (\xi + 1)] \quad (7-25)$$

as shown on Fig. 7-19(a).

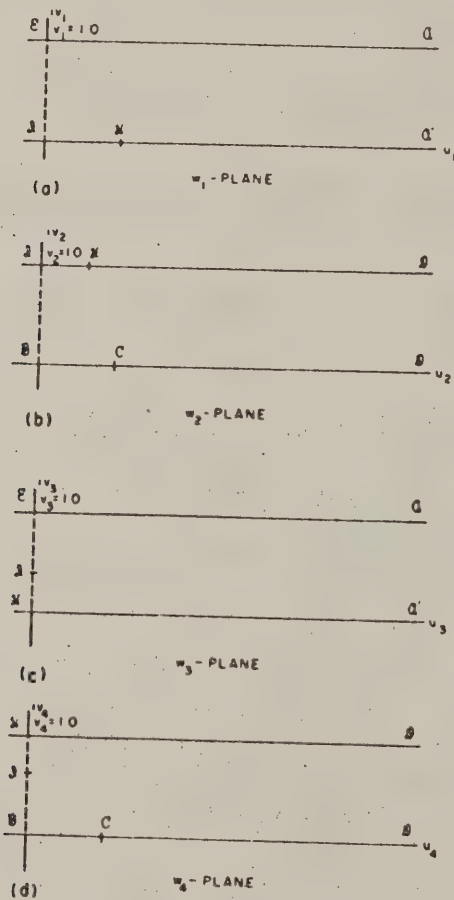


FIG. 7-19
FINAL CONFIGURATIONS ON w -PLANES

The total capacitance on the w_1 -plane is parallel-plate capacitance. The amount of capacitance per unit permittivity between the w_1 -plane origin and some location $u_1 > 0$ is equal to u_1 , for unit depth into the paper, because there is unit spacing between the conducting planes. This is the odd-mode capacitance to one ground plane from Strip a . The corresponding capacitance for Strip a on the z -plane is the fringing capacitance from the vicinity of \mathcal{E} plus the parallel-plate capacitance, which will be defined as the amount of parallel-plate capacitance from Strip a to ground, measured between $z(\alpha)$ (Edge \mathcal{C}) and the mapping of u_1 mentioned above onto the z -plane. Mathematically, the z -plane parallel-plate capacitance, relevant to some value u_1 on the w_1 -plane, has the value $(1/\pi)\text{Re}[z(u_1) - z(\alpha)]$, as can be deduced from Fig. 7-17(b). Alternatively this defines the fringing capacitance in the odd mode from Strip a to one ground plane as the difference between the total capacitance to some value u_1 on the w_1 -plane and the parallel-plate capacitance out to the mapping of u_1 on the z -plane, as u_1 approaches infinity. This odd-mode fringing capacitance from Strip a will be denoted by C'_{ao}/ϵ . From the above discussion,

$$C'_{ao}/\epsilon = \lim_{u_1 \rightarrow \infty} \{u_1 - \text{Re} \frac{1}{\pi} [z(u_1) - z(\alpha)]\} \quad (7-26)$$

From a physical point of view, this definition of parallel-plane capacitance assumes that Strips a and c always overlap. Mathematically, the definition of parallel-plane capacitance is wholly arbitrary, so that this physical defect in definition need not be ameliorated until the mathematical derivation is complete.

The bracketed term of Eq. (7-26) will be expanded separately:

$$\lim_{u_1 \rightarrow \infty} \text{Re}[z(u_1) - z(\alpha)] = \lim_{u_1 \rightarrow \infty} \text{Re}[z\{z_1\{z_2[z_3(u_1)]\}\} - z(\alpha)] \quad (7-27)$$

This can be handled factor by factor. From Eq. (7-24),

$$\lim_{u_1 \rightarrow \infty} z_3(u_1) = \frac{1}{4} (\xi - 1) e^{\pi u_1} \quad (7-28)$$

Substituting in Eq. (7-21), and selecting the positive branch,

$$\lim_{u_1 \rightarrow \infty} z_2(u_1) = \ln \left[\frac{1}{2} (\xi - 1) e^{\pi u_1} \right] \quad (7-29)$$

Further substitution into Eq. (7-20) gives

$$\lim_{u_1 \rightarrow \infty} z_1(u_1) = \sqrt{2(\eta + 1)} \left[\frac{1}{2} (\xi - 1) e^{\pi u_1} \right] \quad (7-30)$$

Then, substitution into Eq. (7-17) gives

$$\lim_{u_1 \rightarrow \infty} z(u_1) = \pi u_1 + \ln \left\{ \frac{1}{2} (\xi - 1) \sqrt{2(\eta + 1)} \right\} \quad (7-31)$$

This result, Eq. (7-31), will be substituted back into Eq. (7-26) to find C'_{∞}/ϵ .

$$C'_{\infty}/\epsilon = \lim_{u_1 \rightarrow \infty} \left\{ u_1 - Re \frac{1}{\pi} \left[\pi u_1 + \ln \left\{ \frac{1}{2} (\xi - 1) \sqrt{2(\eta + 1)} \right\} - z(\alpha) \right] \right\} \quad (7-32)$$

which gives

$$C'_{\infty}/\epsilon = Re \frac{1}{\pi} \left\{ z(\alpha) - \ln \left[\frac{1}{2} (\xi - 1) \sqrt{2(\eta + 1)} \right] \right\} \quad (7-33)$$

The term in brackets can be simplified somewhat by eliminating ξ in favor of η , using Eq. (7-22). The result is

$$\frac{1}{2} (\xi - 1) \sqrt{2(\eta + 1)} = \frac{1}{4} [\eta + 3 - 2\sqrt{2(\eta + 1)}] \quad (7-34)$$

The final expression for C'_{∞}/ϵ is

$$C'_{\infty}/\epsilon = Re \frac{1}{\pi} \left[z(\alpha) - \ln \frac{(\eta + 3) - 2\sqrt{2(\eta + 1)}}{4} \right] \quad (7-35)$$

3. ODD-MODE FRINGING CAPACITANCE--STRIP c

Strip c is associated with points BCD . Equation (7-21) mapped the polygon $ABCD$ of the z_2 -plane onto the lower half of the z_3 -plane (Fig. 7-18). The lower half of the z_3 -plane is next mapped onto the w_2 -plane by means of the transformation

$$z_3 = -\frac{1}{2}[(\xi + 1) + (\xi - 1) \cosh \pi w_2] \quad (7-36)$$

assuming unit depth into the paper, the total capacitance per unit permittivity as a function of u_2 is equal to u_2 . The parallel-plate capacitance to the adjacent ground plane of one of the Strips c may be defined as

$$\frac{Re[z(\alpha) - z(u_2)]}{(\pi/2)(1 - \alpha)}$$

from Fig 7-17, in a manner similar to that defined for Strip a. The difference between total capacitance and parallel-plate capacitance, relevant to some value of u_2 approaching infinity, is the odd-mode fringing capacitance of Strip c, and will be denoted by C'_{eo}/ϵ . Therefore, from the above discussion,

$$C'_{eo}/\epsilon = \lim_{u_2 \rightarrow \infty} \left\{ u_2 - Re \frac{[z(\alpha) - z(u_2)]}{(\pi/2)(1 - \alpha)} \right\} \quad (7-37)$$

The term in brackets may be evaluated for $u_2 \rightarrow \infty$ in a manner similar to that used in determining C'_{ao}/ϵ , except that in this case the negative branch of the arc $\cosh z_3$ is the appropriate choice to satisfy the mappings described:

$$\lim_{u_2 \rightarrow \infty} z(u_2) = z(z_1\{z_2[z_3(u_2)]\}) \quad (7-38)$$

From Eq. (7-36)

$$\lim_{u_2 \rightarrow \infty} z_3(u_2) = -\frac{1}{4}(\xi - 1)e^{\pi u_2} \quad (7-39)$$

From Eq. (7-21)

$$\lim_{u_2 \rightarrow \infty} z_2(u_2) = -\ln \frac{1}{2}(\xi - 1)e^{\pi u_2} - i\pi \quad (7-40)$$

From Eq. (7-20)

$$\lim_{u_2 \rightarrow \infty} z_1(u_2) = 1 - \sqrt{2(\eta + 1)} \left(\frac{1}{(1/2)(\xi - 1)e^{\pi u_2}} \right) \quad (7-41)$$

or

$$\lim_{u_2 \rightarrow \infty} z_1(u_2) = 1 - \frac{2\sqrt{2(\eta + 1)}}{\xi - 1} e^{-\pi u_2} \quad (7-42)$$

Substituting in Eq. (7-17) gives

$$\lim_{u_2 \rightarrow \infty} z(u_2) = \frac{1 - \alpha}{2} \ln \left[-\frac{2\sqrt{2(\eta + 1)}}{\xi - 1} e^{-\pi u_2} \right] + \frac{1 + \alpha}{2} \ln \left[2 - \frac{2\sqrt{2(\eta + 1)}}{\xi - 1} e^{-\pi u_2} \right] \quad (7-43)$$

which becomes

$$\lim_{u_2 \rightarrow \infty} z(u_2) = -\frac{1 - \alpha}{2} \pi u_2 + \frac{1 - \alpha}{2} \ln \left[\frac{2\sqrt{2(\eta + 1)}}{\xi - 1} \right] + \frac{1 + \alpha}{2} \ln 2 + i \frac{\pi}{2} (1 - \alpha) \quad (7-44)$$

Substitution of Eq. (7-44) into Eq. (7-37) gives

$$C'_{eo}/\epsilon = \lim_{u_2 \rightarrow \infty} \left\{ u_2 - Re \frac{2z(\alpha)}{\pi(1 - \alpha)} - u_2 + \frac{1}{\pi} \ln \frac{2\sqrt{2(\eta + 1)}}{\xi - 1} + \frac{1}{\pi} \frac{1 + \alpha}{1 - \alpha} \ln 2 \right\} \quad (7-45)$$

or

$$C'_{eo}/\epsilon = \frac{1}{\pi} \left\{ \frac{1 + \alpha}{1 - \alpha} \ln 2 + \ln \frac{2\sqrt{2(\eta + 1)}}{\xi - 1} - Re \frac{2z(\alpha)}{1 - \alpha} \right\} \quad (7-46)$$

Eliminating ξ in favor of η gives the final result,

$$C'_{eo}/\epsilon = Re \frac{1}{\pi} \left[\frac{1 + \alpha}{1 - \alpha} \ln 2 + \ln \frac{8(\eta + 1)}{(\eta + 3) - 2\sqrt{2(\eta + 1)}} - \frac{2}{1 - \alpha} z(\alpha) \right] \quad (7-47)$$

4. EVEN-MODE FRINGING CAPACITANCE—STRIP a

In analyzing the even mode, the two strips, a and c are at the same potential, as previously discussed, and the plane ab may be considered

as a magnetic wall. For Strip a, associated with point ξ , the transformation from the upper half of the z_3 -plane, Fig. 7-17(c) to a w_3 -plane, Fig. 7-18(c), is

$$z_3 = (1/2)[(\xi + 1) \cosh \pi u_3 - (\xi - 1)] \quad (7-48)$$

The definition and discussion of parallel-plate capacitance for Strip a given in connection with odd-mode capacitance holds for this case also. The even-mode fringing capacitance is given by the difference between total capacitance and parallel-plate capacitance, so that by analogy with Eq. (7-26), the even-mode fringing capacitance for Strip a is

$$C'_{ae}/\epsilon = \lim_{u_3 \rightarrow \infty} \{u_3 - \operatorname{Re} (1/\pi) [z(u_3) - z(\alpha)]\} \quad (7-49)$$

The algebraic manipulations are simplified by noting that $\lim_{u_3 \rightarrow \infty} z_3(u_3)$ of Eq. (7-48) differs from $\lim_{u_1 \rightarrow \infty} z_3(u_1)$ of Eq. (7-28) only in that $(\xi - 1)$ and u_1 must be replaced in Eq. (7-28) by $(\xi + 1)$ and u_3 , respectively. Then, because subsequent transformations are the same in both cases, it is possible to go directly to Eq. (7-33), replace C'_{ao}/ϵ by C'_{ae}/ϵ and $(\xi - 1)$ by $(\xi + 1)$, yielding

$$C'_{ae}/\epsilon = \operatorname{Re} (1/\pi) \{z(\alpha) - \ln [(1/2)(\xi + 1) \sqrt{2(\eta + 1)}]\} \quad (7-50)$$

Eliminating ξ in favor of η by use of Eq. (7-22) gives the final result,

$$C'_{ae}/\epsilon = \operatorname{Re} \frac{1}{\pi} \left[z(\alpha) - \ln \frac{(\eta + 3) + 2\sqrt{2(\eta + 1)}}{4} \right] \quad (7-51)$$

5. EVEN-MODE FRINGING CAPACITANCE—STRIP c

The same reasoning and procedure may be used in finding the even-mode fringing capacitance from Strip c as were used for the other three fringing capacitances and, in fact, this was done in the original work on this problem. However, only three capacitances are required to describe a parallel coupled TEM structure, as in Fig. 7-2, and this indicates the possibility that if three fringing capacitances are known, the fourth may be related to them by a function which is independent of the geometry of the structure. This geometry-independent function, applicable to any parallel-coupled TEM structure that can be represented schematically by Fig. 7-2, is given by Eq. (7-6), which upon manipulation, may be written as

$$C_{ce}/\epsilon = C'_{co}/\epsilon - C'_{so}/\epsilon + C'_{oe}/\epsilon = C'_{co}/\epsilon - \Delta C/\epsilon \quad (7-52)$$

using Eq. (7-7) for the definition of $\Delta C/\epsilon$. Thus, the unknown fringing capacitance, C'_{ee}/ϵ , can be written as a linear combination of the other three fringing capacitances. Substitution of Eqs. (7-35), (7-17), and (7-51) into Eq. (7-52) yields

$$C'_{ee}/\epsilon = \operatorname{Re} \frac{1}{\pi} \left[\frac{1+\alpha}{1-\alpha} \ln 2 - \frac{2}{1-\alpha} z(\alpha) + \ln \frac{8(\eta+1)}{(\eta+3) + 2\sqrt{2(\eta+1)}} \right] \quad (7-53)$$

This result agrees with that found for C'_{ee}/ϵ directly from the mapping.

6. DEFINITION OF PARALLEL-PLATE CAPACITANCE OF STRIP a

In mathematically determining the fringing capacitances for the centered center-strip, Strip a , the equivalent parallel-plate capacitor on the z -plane, Fig. 7-17, is extended to the right from $z(\alpha)$ for all cases. In considering the physics of the situation, it is apparent that a more realistic definition would have the parallel-plate capacitance for Strip a computed from the edge of Strip a , $z(\eta)$, except when Strip a is shielded by Strip c , and then the parallel-plate capacitance would be computed from the edge of the shielding Strip c at $z(\alpha)$. In order for the plotted curves to agree with this physical definition, it was necessary to add a parallel-plate capacitance to computed values of C'_{ao}/ϵ and C'_{as}/ϵ . This parallel-plate capacitance was added only when $z(\eta) > z(\alpha)$, and simply replaced that subtracted in the derivation. The value added to C'_{ao}/ϵ and C'_{as}/ϵ was equal to $[z(\eta) - z(\alpha)]/\pi$. In terms of dimensions, this additional capacitance per unit permittivity can be expressed as $|2d/b|$ for $d < 0$. The plotted curves for Strip a , Figs. 7-8 and 7-9, incorporate this term

7. DERIVATION OF C'_{eo}/ϵ

The fringing capacitance C'_{eo}/ϵ is that from the edge of a strip located between a parallel magnetic wall and a parallel electric wall, as indicated on the graph, Fig. 7-5. It can be specified mathematically as

$$C'_{eo}/\epsilon = \lim_{d \rightarrow -\infty} C'_{eo}/\epsilon \quad \text{or} \quad C'_{es}/\epsilon \quad (7-54)$$

From Fig. 7-17 it can be seen that $z(\eta) \rightarrow \infty$ as $d \rightarrow \infty$, and on Fig. 7-18(a) this corresponds to $\eta \rightarrow \infty$. Thus, using Eq. (7-47),

$$C'_{e\infty}/\epsilon = \lim_{\eta \rightarrow \infty} \operatorname{Re} \frac{1}{\pi} \left[\frac{1+\alpha}{1-\alpha} \ln 2 + \ln \frac{8(\eta+1)}{(\eta+3) - 2\sqrt{2}(\eta+1)} - \frac{2}{1-\alpha} z(\alpha) \right] \quad (7-55)$$

or

$$C'_{e\infty}/\epsilon = \frac{1}{\pi} \left[\frac{1+\alpha}{1-\alpha} \ln 2 + \ln 8 - \frac{2}{1-\alpha} \operatorname{Re} z(\alpha) \right] \quad (7-56)$$

The real part of $z(\alpha)$ is given in Eq. (7-14), and from Fig. 7-17, α is found to be related to g/b by

$$\alpha = 2g/b - 1 \quad (7-57)$$

Thus, $C'_{e\infty}/\epsilon$ can be expressed in terms of g/b by

$$C'_{e\infty}/\epsilon = \frac{1}{\pi} \left[2 \ln 2 - \ln(1 - g/b) - \frac{g/b}{1 - g/b} \ln g/b \right] \quad (7-58)$$

This is plotted in Fig. 7-5. The fringing capacitance C'_f/ϵ is the value of $C'_{e\infty}/\epsilon$ for $g/b = 0$, and is

$$C'_f/\epsilon = \frac{2}{\pi} \ln 2 = 0.4413 \quad (7-59)$$

8. SUMMARY OF EQUATIONS

A schematic diagram, showing even and odd mode capacitances for coupled strips in uniform TEM line is given in Fig. 7-2.

The geometry analyzed and the specifications of fringing capacitances are given in Fig. 7-3. The parallel plate capacitance for Strip a is given by

$$C_{ap}/\epsilon = \frac{2a}{b} \quad (7-2)$$

Notice from Fig. 7-3 that dimension a is defined differently for $d > 0$ and $d < 0$.

The parallel plate capacitance for Strip c is given by

$$C_{cp}/\epsilon = \frac{2c/b}{1 - g/b} \quad (7-3)$$

The mathematical model of the structure analyzed is given in Fig. 7-17. The dimensions of the structure are related to the coordinates on the z -plane of Fig. 7-17 and the z_1 -plane of Fig. 7-18 by

$$g/b = \frac{1 + \alpha}{2} \quad (7-60)$$

$$d/g = \frac{z(\alpha) - z(\eta)}{\pi(1 + \alpha)} \quad (7-61)$$

The z -plane functions are related to the locations on the z_1 -plane real axis by

$$z(\alpha) = \frac{1 - \alpha}{2} \ln(1 - \alpha) + \frac{1 + \alpha}{2} \ln(1 + \alpha) \quad (7-18)$$

$$z(\eta) = \frac{1 - \alpha}{2} \ln(\eta + 1) + \frac{1 + \alpha}{2} \ln(\eta - 1)$$

where

$$\begin{aligned} -1.0 < \alpha < 1.0 \\ \eta > 1.0 \end{aligned} \quad (7-19)$$

The fringing capacitances are given by

$$C'_{eo}/\epsilon = \operatorname{Re} \frac{1}{\pi} \left[z(\alpha) - \ln \frac{(\eta + 3) - 2\sqrt{2(\eta + 1)}}{4} \right], \quad (7-35)$$

which is plotted in Fig. 7-9,

$$C'_{eo}/\epsilon = \operatorname{Re} \frac{1}{\pi} \left[\frac{1 + \alpha}{1 - \alpha} \ln 2 + \ln \frac{8(\eta + 1)}{(\eta + 3) - 2\sqrt{2(\eta + 1)}} - \frac{2}{1 - \alpha} z(\alpha) \right], \quad (7-47)$$

which is plotted in Fig. 7-7,

$$C'_{a\omega}/\epsilon = Re \frac{1}{\pi} \left[z(\alpha) - \ln \frac{(\eta + 3) + 2\sqrt{2(\eta + 1)}}{4} \right], \quad (7-51)$$

which is plotted in Fig. 7-8,

$$C'_{c\omega}/\epsilon = Re \frac{1}{\pi} \left[\frac{1+\alpha}{1-\alpha} \ln 2 + \ln \frac{8(\eta + 1)}{(\eta + 3) + 2\sqrt{2(\eta + 1)}} - \frac{2}{1-\alpha} z(\alpha) \right] \quad (7-53)$$

which is plotted in Fig. 7-6,

$$C'_{e\omega}/\epsilon = \frac{1}{\pi} \left[2 \ln 2 - \ln (1 - g/b) - \frac{g/b}{1 - g/b} \ln g/b \right], \quad (7-58)$$

which is plotted in Fig. 7-5. Also,

$$C'_f/\epsilon = \frac{2}{\pi} \ln 2 = 0.4413. \quad (7-59)$$

The total coupling capacitance between strips is given by

$$\Delta C/\epsilon = \frac{1}{2} (C_{\omega\omega}/\epsilon - C_{\omega\omega}/\epsilon) \quad (7-9)$$

or

$$\Delta C/\epsilon = C'_{a\omega}/\epsilon - C'_{c\omega}/\epsilon = C'_{e\omega}/\epsilon - C'_{f\omega}/\epsilon, \quad (7-62)$$

which is plotted in Fig. 7-4.

A formula relating dimensions to characteristic impedance for an isolated single strip is

$$a/b = \frac{\eta}{4Z_{0\omega}\sqrt{\epsilon_r}} = 0.441 \quad (7-13)$$

and for an isolated dual strip is

$$c/b = \left(1 - \frac{g}{b} \right) \left(\frac{\eta}{4Z_{0\omega}\sqrt{\epsilon_r}} - \frac{C'_{e\omega}}{\epsilon} \right). \quad (7-14)$$

Approximate correction formulas for narrow strips, either isolated or coupled are

$$a_2/b = \frac{(0.07 + a_1/b)}{1.20} \quad (7-15)$$

for an initially determined value a_1/b , and a corrected value a_2/b , such that $0.1 < a_2/b < 0.35$, and

$$c_2/b = \frac{[0.07(1 - g/b) + c_1/b]}{1.20} \quad (7-16)$$

for an initially determined value c_1/b , and a corrected value c_2/b , such that $0.1 < (c_2/b)/(1 - g/b) < 0.35$.

II. SUMMARY

A new strip-line configuration has been presented, applicable to printed circuit construction, that allows very close coupling to be achieved without resorting to very small coupling gaps and excessively critical dimensions. Graphs of even- and odd-mode fringing capacitances have been given. These graphs can be used with simple formulas, which also are given, to determine the dimensions of the configuration that will give specified even- and odd-mode characteristic impedances or shunt capacitances.

The usefulness of the graphs and formulas was demonstrated by using them to design 3-db backward-couplers and a filter. The performance of the couplers in this new configuration was typical of similar couplers made in more conventional configurations, as expected. However, the devices shown have an advantage in that they can be manufactured by relatively inexpensive and rapid printed-circuit methods and, since the region between the conductors is solid dielectric, they are unusually rugged.

REFERENCES

1. S. B. Cohn et al., "Strip Transmission Lines and Components," Final Report, SRI Project 1114, Contract DA 36-039 SC-63232, Stanford Research Institute, Menlo Park, California (February 1957).
2. S. B. Cohn et al., "Research on Design Criteria for Microwave Filters," Final Report, SRI Project 1331, Contract DA 36-039 SC-64625, Stanford Research Institute, Menlo Park, California (June 1957).
3. See Chapter 18 of this report.
4. B. M. Oliver, "Directional Electromagnetic Couplers," *Proc. IRE* **42**, 11, p. 1686 (November 1954).
5. E. M. T. Jones and J. T. Bolljahn, "Coupled-Strip-Transmission-Line Filters and Directional Couplers," *IRE Trans. PGWTT-4*, 2, p. 75 (April 1956).
6. S. B. Cohn, "Problems in Strip Transmission Lines," *IRE Trans. PGWTT-3*, 2, pp. 119-126 (March 1955).
7. W. R. Smythe, *Static and Dynamic Electricity*, Chap. IV (McGraw-Hill Book Company, Inc., New York City, 1939).
8. Ernst Weber, *Electromagnetic Fields: Theory and Applications*, Vol. I, "Mapping of Fields," (John Wiley and Sons, New York City, 1950).
9. H. Kober, *Dictionary of Conformal Representations*, Sec. 12.5, p. 155 (Dover Publications, Inc., New York City, 1952).
10. R. V. Churchill, *Introduction to Complex Variables and Applications*, Appendix II (McGraw-Hill Book Company, Inc., New York City, 1948).
11. S. B. Cohn, "Shielded Coupled-Strip Transmission Line," *IRE Trans. PGWTT-3*, pp. 29-38 (October 1955).

CHAPTER 8

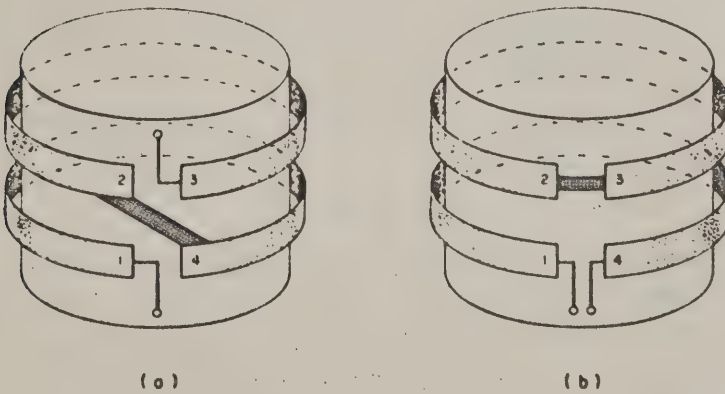
NON-PLANAR COUPLED TRANSMISSION LINE CIRCUITS

A. GENERAL

Jones and Bolljahn¹ consider the ten possible planar circuits that may be formed using a single pair of coupled transmission lines with different terminal connections. This section extends the earlier study by adding the analyses for two non-planar circuits. The non-planar configurations are found to have properties similar to certain of the planar circuits described in Ref. 1.

B. ANALYSIS

The two configurations of interest are illustrated as coupled conductors wrapped around a cylindrical ground plane in Fig. 8-1. In each case, two terminals are available to serve as input and output ports of a symmetrical two-port network.



NA-2326-TN-242

FIG. 8-1

TWO NON-PLANAR, PARALLEL-COUPLED TRANSMISSION-LINE CIRCUITS

The network equations for the coupled line system may be written, taking due account of all the symmetries involved, as

$$\left. \begin{aligned} V_1 &= I_1 Z_{11} + I_2 Z_{12} + I_3 Z_{13} + I_4 Z_{14} \\ V_2 &= I_1 Z_{12} + I_2 Z_{11} + I_3 Z_{14} + I_4 Z_{13} \\ V_3 &= I_1 Z_{13} + I_2 Z_{14} + I_3 Z_{11} + I_4 Z_{12} \\ V_4 &= I_1 Z_{14} + I_2 Z_{13} + I_3 Z_{12} + I_4 Z_{11} \end{aligned} \right\} \quad (8-1)$$

where

$$\left. \begin{aligned} Z_{11} &= -j(Z_{\infty} + Z_{\infty}) \frac{\cot \theta}{2} \\ Z_{12} &= -j(Z_{\infty} - Z_{\infty}) \frac{\cot \theta}{2} \\ Z_{13} &= -j(Z_{\infty} - Z_{\infty}) \frac{\csc \theta}{2} \\ Z_{14} &= -j(Z_{\infty} + Z_{\infty}) \frac{\csc \theta}{2} \end{aligned} \right\} \quad (8-2)$$

and where

Z_{∞} = Characteristic impedance of one wire to ground with equal currents in the same direction in the two wires

Z_{∞} = Characteristic impedance of one wire to ground with equal currents in opposite directions in the two wires

θ = Electrical length of each wire.

The properties of the two-port network shown in Fig. 8-1(a) may be developed by setting $V_4 = V_2$ and $I_4 = -I_2$ in Eq. (8-1). When this is done, the elements of the impedance matrix for this network are found to be

$$\begin{aligned} z_{11} &= Z_{11} + \frac{(Z_{12} - Z_{14})^2}{2(Z_{13} - Z_{11})} \\ z_{13} &= Z_{13} - \frac{(Z_{12} - Z_{14})^2}{2(Z_{13} - Z_{11})} \end{aligned} \quad (8-3)$$

and the image impedance is

$$Z_I = \sqrt{z_{11}^2 - z_{13}^2} = \sqrt{\frac{Z_{11} + Z_{13}}{Z_{11} - Z_{13}}} [(Z_{11} - Z_{13})^2 - (Z_{12} - Z_{14})^2]. \quad (8-4)$$

Substituting the expressions for the matrix elements from Eq. (8-2) and reducing, one obtains finally

$$Z_I = \sqrt{Z_{oe} Z_{oo}} \sqrt{\frac{\cos \theta + \left(\frac{Z_{oe} - Z_{oo}}{Z_{oe} + Z_{oo}} \right)}{\cos \theta - \left(\frac{Z_{oe} - Z_{oo}}{Z_{oe} + Z_{oo}} \right)}} \quad (8-5)$$

The salient features of this function are illustrated in Fig. 8-2. Note that $Z_{oe} > Z_{oo}$.

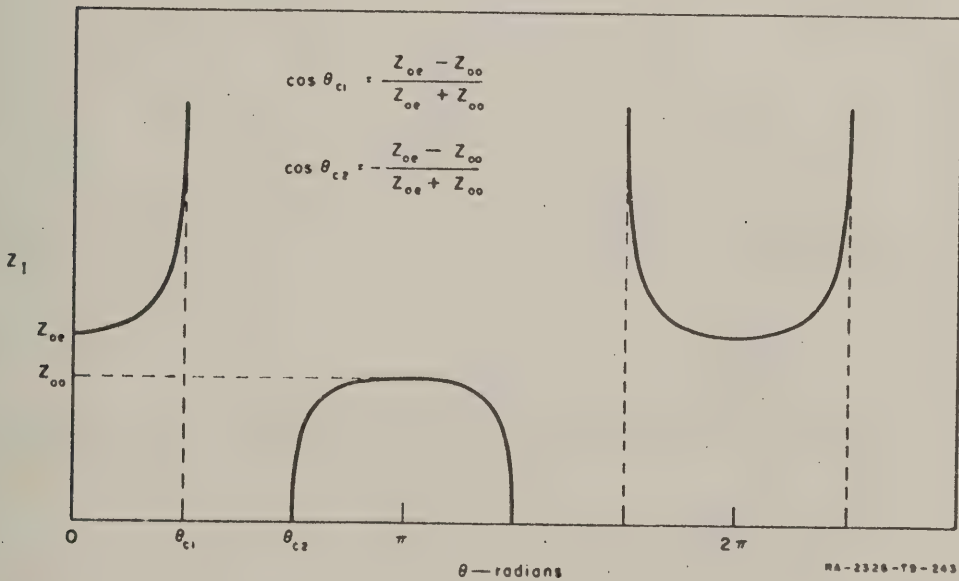


FIG. 8-2

IMAGE IMPEDANCE OF THE STRUCTURE IN FIG. 8-1(a) IN ITS PASS BAND

The image transfer function for this circuit may be calculated from the relationship $\cosh (\alpha + j\beta) = (z_{11} / z_{12})$. Substituting values for z_{11} and z_{12} from Eqs. (8-3) and (8-2) this expression reduces to

$$\cosh (\alpha + j\beta) = \frac{1 + \left[\frac{Z_{oe} - Z_{oo}}{Z_{oe} + Z_{oo}} \right]^2 - 2 \cos^2 \theta}{(2 - \cos^2 \theta) \left(\frac{Z_{oe} - Z_{oo}}{Z_{oe} + Z_{oo}} \right)^2 - 1} \quad (8-6)$$

The circuit shown in Fig. 8-1(b) may be analyzed by setting $V_3 = V_2$, $I_3 = -I_2$ in Eq. (8-1). Following the same procedure as above, we find that this circuit is an all-pass network with

$$Z_I = \sqrt{Z_{oe} Z_{oo}} \quad (8-7)$$

and

$$\cos \beta = \frac{2 \cos \theta + \left(\frac{Z_{oe} - Z_{oo}}{Z_{oe} + Z_{oo}} \right)^2 (1 - \cos \theta)}{2 - \left(\frac{Z_{oe} - Z_{oo}}{Z_{oe} + Z_{oo}} \right)^2 (1 - \cos \theta)} \quad (8-8)$$

Graphs of β as a function of θ for the case of zero coupling ($Z_{oe} = Z_{oo}$) and for a tightly coupled case ($Z_{oe} = 0.1 Z_{oo}$) are shown in Fig. 8-3.

REFERENCES

1. E. M. T. Jones and J. T. Bolljahn, "Coupled Strip Transmission Line Filters and Directional Couplers," *IRE Trans., PGMT-4*, pp. 75-81 (April 1956).

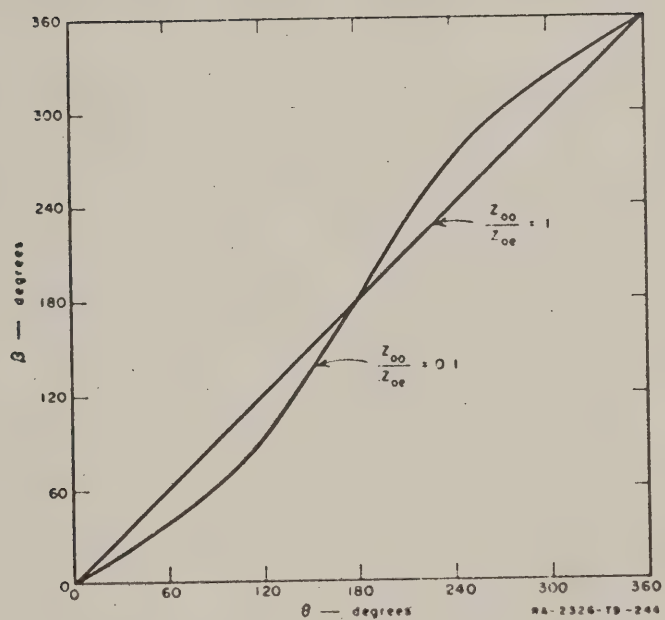


FIG. 8-5
IMAGE TRANSFER FUNCTION FOR CIRCUIT SHOWN IN FIG. 8-1(b)

CHAPTER 9

EFFECT OF THICKNESS OF CAPACITIVE OBSTACLES*

A. GENERAL

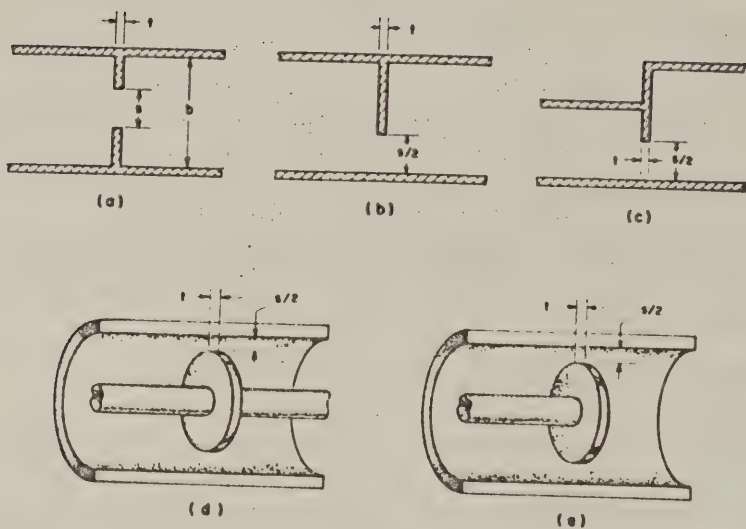
Capacitive obstacles are frequently used as matching elements in microwave circuits, and as reactive elements in filters and slow-wave structures. Figure 9-1 shows examples of commonly used capacitive-obstacle configurations in waveguide and coaxial line, while Fig. 9-2 shows the application of capacitive obstacles to an artificial dielectric medium. Still another case where the capacitance between parallel strips is important is that of the odd mode in a parallel-coupled strip transmission line (Fig. 9-3).

Because of the usefulness of capacitive obstacles, they have been given much theoretical attention. The theoretical treatment is particularly detailed for zero-thickness obstacles (or irises) in waveguide and coaxial line.^{1,2} For very thick irises, the obstacle may be treated as two isolated step discontinuities separated by lengths of waveguide or coaxial line. Theoretical formulas and curves for isolated step discontinuities in waveguide and coaxial line are available.^{3,4,5}

In most practical cases, capacitive obstacles are neither thin enough to be treated accurately as having zero thickness, nor thick enough for the isolated step-discontinuity approximation to be precise. Yet, the theoretical information available for obstacles of moderate thickness is relatively incomplete. Marcuvitz treats two cases in waveguide. In the first case,⁶ less than 5 percent error is obtained when $s/b > 0.5$ and $t/s < 0.5$ [see Fig. 9-1(a) for notation]. In the second case,⁷ less than 5 percent error is obtained when $s/b < 0.5$, for any t . Aside from the disadvantage of this amount of error, the formulas for these two cases are very complex, and the graphical data are incomplete.

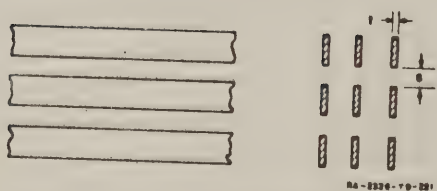
Because of the greater simplicity of analyzing obstacles of zero-thickness rather than finite thickness, and because many zero-thickness configurations have already been treated, it is convenient to take account of thickness as a correction to the zero-thickness case. Correction terms suited for this purpose are derived in this report. In general, thickness adds an increment to the shunt capacitance in the

* This material has been published. See S. B. Cohn, "Thickness Corrections for Capacitive Obstacles and Strip Conductors," *IRE Trans. PGWT* 8, pp. 638-644 (November 1960).



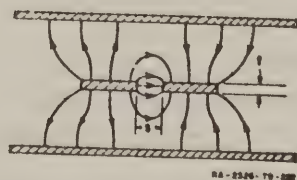
RA-2326-Y9-229

FIG. 9-1
EXAMPLES OF CAPACITIVE OBSTACLES OF MODERATE THICKNESS
IN WAVEGUIDE AND COAXIAL LINE



RA-2326-Y9-221

FIG. 9-2
METAL-STRIP ARTIFICIAL DIELECTRIC
MEDIUM



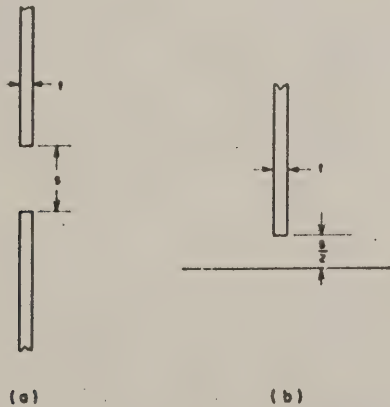
RA-2326-Y9-222

FIG. 9-3
EFFECT OF STRIP THICKNESS
ON ODD MODE IN PARALLEL-
COUPLED STRIP
TRANSMISSION LINE

equivalent circuit, and also requires the insertion of a small series inductance (or, alternatively, a small change in the reference planes). As will be made clear, the same numerical correction to the shunt capacitance may be made with good accuracy for all the examples of Figs. 9-1, 9-2, and 9-3, as well as for many other capacitive structures. The small inductances or reference-plane shifts may usually be determined very easily from considerations of the effect of thickness on magnetic stored energy.

The point of view taken in this report is that the electric field distribution in the vicinity of a capacitive obstacle is affected appreciably by thickness only near the edge or edges of the obstacle. Thus, although the structures of Figs. 9-1, 9-2, and 9-3 are different far from these edges, the incremental change in capacitance due to thickness is, in all cases, very closely the same when the dimensions t and s are the same. More specifically, the capacitance change due to thickness per unit length of edge is, to a good approximation, a function only of the ratio t/s .

Figure 9-4(a) shows a cross section through the simplified configuration analyzed in this report. It consists of two semi-infinite coplanar plates of thickness t separated by spacing s . Figure 9-4(b)



NO. 2320-10-003

FIG. 9-4

SEMI-INFINITE-PLATE GEOMETRIES
ANALYZED EXACTLY IN THIS REPORT

shows an equivalent configuration for which the field distribution is the same, and the capacitance is exactly doubled. The total capacitance per unit length of edge is infinite in both cases, but nevertheless, the increase in capacitance when the thickness is increased from zero to a value t is a finite quantity. This capacitance increment is evaluated in this report, and may be used directly as a thickness correction for structures like those in Figs. 9-1, 9-2, and 9-3.

B. THE THICKNESS CORRECTION TERM

Consider the pair of semi-infinite plates shown in cross section in Fig. 9-4(a). Let $C'(t/s)$ be the total capacitance between the plates per unit depth into the figure. Then,

$$\Delta C'(t/s) = C'(t/s) - C'(0) \quad (9-1)$$

is the increase in capacitance per unit length of edge when the plate thickness is increased from zero to a finite value t . As derived in Sec. D, the formula for $\Delta C'(t/s)$ is

$$\Delta C'(t/s) = \frac{2\epsilon}{\pi} \ln \left[\frac{E(k) - (1/2)k'^2 K(k)}{\sqrt{k}} \right] \quad (9-2)$$

where the parameters k and k' are evaluated from the following equations functions of t/s :

$$\frac{t}{s} = \frac{\frac{1+k^2}{2} K(k') - E(k')}{2 \left[E(k) - \frac{k'^2}{2} K(k) \right]} \quad (9-3)$$

$$k' = \sqrt{1 - k^2} \quad (9-4)$$

The units of $\Delta C'(t/s)$ are the same as those of the permittivity ϵ , which for free space has the value $8.85 (10)^{-12}$ farads per meter, $0.0885 \mu\text{mf}$ per cm, or $0.225 \mu\text{mf}$ per inch. $K(k)$ and $E(k)$ are complete elliptic integrals of the first and second kinds, respectively.

Equations (9-2), (9-3), and (9-4) have been computed, and the resulting curve is given in Fig. 9-5. The procedure used was first to

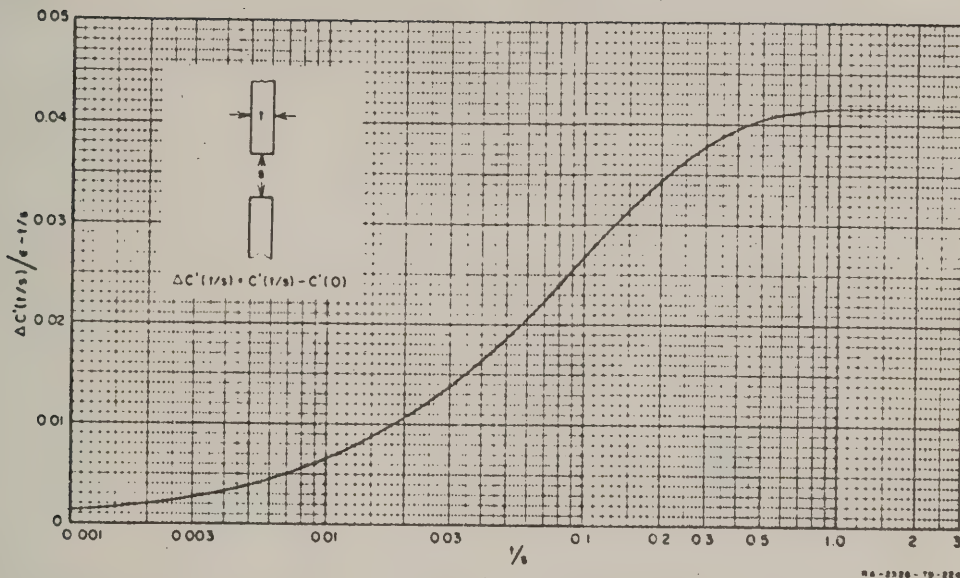


FIG. 9-5

PLOT OF CAPACITANCE CORRECTION PER UNIT LENGTH

select values of t/s , and then to calculate the corresponding values of $\Delta C'$ and t/s . The quantity plotted is $[\Delta C'(t/s) - \epsilon t/s]/\epsilon$, in which the term $\epsilon t/s$ is the parallel-plate capacitance per unit length, neglecting fringing. By subtracting this parallel-plate term from $\Delta C'$, the curve is made to approach a constant value as t/s is made large enough so that the fringing fields on the two sides of the configuration become independent. It is seen that this occurs for $t/s \geq 1$. The limiting value of $\Delta C'$ for $t/s \geq 1$ is of interest. With the aid of limiting values of the elliptic integrals, one may show this to be

$$\frac{\Delta C'}{\epsilon} = \frac{t}{s} + \frac{2}{\pi} \left(1 + \ln \frac{\pi}{8} \right) = \frac{t}{s} + 0.0415. \quad (9-5)$$

The curve approaches zero as t/s goes to zero. For $t/s < 0.001$ the correction is very small, so that zero-thickness-obstacle calculations are highly accurate. For $t/s > 0.5$, the correction is essentially constant, so that data for isolated step discontinuities may be applied accurately.

The range $0.001 < t/s < 0.5$ is, therefore, the region of interest for which the thickness correction presented here is needed. Almost all practical capacitive-iris structures fall within this range.

Equations (9-2), (9-3), and (9-4), or Fig. 9-5, are exact only for the zero-frequency, semi-infinite-plate cases of Fig. 9-4(a) and (b). In order for the correction to apply accurately in other cases, it is necessary that $s/\lambda_g \ll 1$ and $s/r \ll 1$, where λ_g is the guide wavelength and r is the distance from the center point to the nearest extraneous surface. It is believed that the correction will yield good results for s/λ_g as large as $1/4$, and s/r as large as $1/2$.

C. EXAMPLE OF THICK CAPACITIVE IRIS IN WAVEGUIDE

The manner in which the thickness correction may be applied to practical configurations will be illustrated by the example of a thick capacitive iris in waveguide. Figure 9-6(a) shows a longitudinal E -plane section through a rectangular waveguide containing a zero-thickness, perfectly conducting, symmetrical, capacitive iris. It is assumed that only the TE_{10} mode is propagating. In the limiting case of $b/\lambda_g \rightarrow 0$, the equivalent normalized susceptance of the iris¹ is

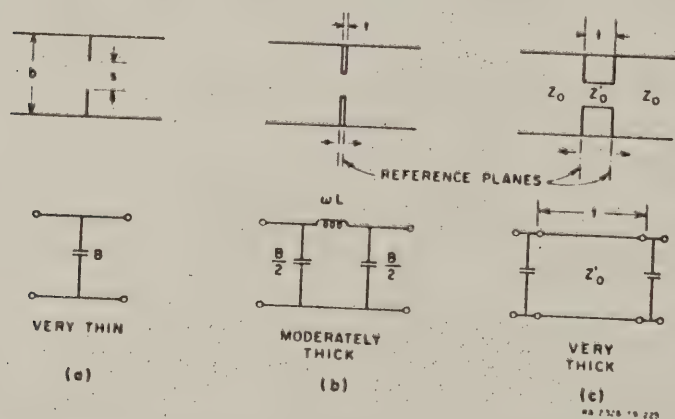


FIG. 9-6

CAPACITIVE OBSTACLE IN RECTANGULAR WAVEGUIDE FOR VERY THIN, MODERATELY THICK, AND VERY THICK CASES

$$\frac{B}{Y_0} = \frac{4b}{\lambda_g} \ln \csc \left(\frac{\pi s}{2b} \right) \quad (9-6)$$

where B is the susceptance of the iris, Y_0 is the characteristic admittance of the waveguide, λ_g is the guide wavelength, and b and s are dimensions defined in Fig. 9-6(a).

In applying the capacitive thickness correction, it is necessary to employ an equivalence theorem between E -plane structures in TE_{10} -mode rectangular waveguide and in TEM-mode parallel-plane transmission line. If the structure has the same boundary in all longitudinal E -plane sections in both cases, then the normalized element values of the waveguide equivalent circuit are identical to those of the parallel-plane equivalent circuit, if λ_g of the TE_{10} mode is used in place of λ of the TEM mode.⁸ The normalized susceptance increment due to thickness may therefore be evaluated in terms of $\Delta C'$ as follows. Assume a parallel-plane TEM-mode transmission line with E -plane dimension b and H -plane dimension a . The characteristic admittance is $Y_0 = (a/b) \sqrt{\epsilon/\mu}$ mhos, where ϵ and μ are the permittivity and permeability of the filling medium in MKS units. The susceptance increment is $\Delta B = a \omega \Delta C' = 2\pi a \Delta C' / \lambda \sqrt{\epsilon\mu}$. Hence, the normalized susceptance increment due to thickness is

$$\frac{\Delta B}{Y_0} = \frac{2\pi b}{\lambda} \cdot \frac{\Delta C'}{\epsilon}$$

By virtue of the equivalence theorem, the corresponding quantity in rectangular waveguide is

$$\frac{\Delta B}{Y_0} = \frac{2\pi b}{\lambda_g} \cdot \frac{\Delta C'}{\epsilon} \quad (9-7)$$

where $\Delta C'/\epsilon$ is obtained as a function of t/s from Eqs. (9-2), (9-3), and (9-4), or from the graph in Fig. 9-5.

In addition to the increase in capacitive susceptance, thickness also requires a series inductive reactance to be added to the equivalent circuit, as shown in Fig. 9-6(b). This reactance represents the magnetic-field energy in the gap region of the thick iris. In the parallel-plane case, the inductance of this region is simply $L = \mu t s/a$, while the

characteristic impedance is $Z_0 = \sqrt{\mu/\epsilon} (b/a)$. Therefore, the normalized reactance is $\omega L/Z_0 = 2\pi ts/\lambda b$. In waveguide, this becomes,

$$\frac{\omega L}{Z_0} = \frac{2\pi ts}{\lambda_g b} \quad (9-8)$$

Equations (9-7) and (9-8) are also valid for the very thick iris case of Fig. 9-6(c), if $t/\lambda_g \ll 1$. (For $t/\lambda_g = 0.1$, $\omega L/Z_0$ is in error by 7 percent, and $\Delta B/Y_0$ by about 3.5 percent.) For larger t/λ_g , the obstacle must be treated as a waveguide of length t and characteristic impedance $Z_0' = (s/b)Z_0$ with step-discontinuity susceptances at each end.

An interesting check on the thickness correction may be obtained in the very thick iris case of Fig. 9-6(c). If $t/\lambda_g \ll 1$ and $t/s \gg 1$, the total shunt susceptance is obtained by adding Eqs. (9-6) and (9-7), with the aid of Eq. (9-5):

$$\frac{B}{Y_0} = \frac{4b}{\lambda_g} \left[\ln \csc \left(\frac{\pi s}{2b} \right) + \frac{\pi t}{2s} + 1 + \ln \frac{\pi}{8} \right] \quad (9-9)$$

In the limit $s/b \rightarrow 0$ this reduces to

$$\frac{B}{Y_0} = \frac{4b}{\lambda_g} \left(\ln \frac{b}{4s} + 1 + \frac{\pi t}{2s} \right) \quad (9-10)$$

The total susceptance for this case may also be evaluated by adding the parallel-plate capacitance to two times the step-discontinuity capacitance. The normalized shunt susceptance appropriate to the parallel-plate capacitance is $(2\pi t/\lambda_g) (b/s)$, while the normalized step-discontinuity susceptance³ in the limit $s/b \rightarrow 0$ is $(2b/\lambda_g) [\ln (b/4s) + 1]$. The total shunt susceptance is therefore,

$$\begin{aligned} \frac{B}{Y_0} &= 2 \left(\frac{2b}{\lambda_g} \right) \left(\ln \frac{b}{4s} + 1 \right) + \frac{2\pi t b}{\lambda_g s} \\ &= \frac{4b}{\lambda_g} \left(\ln \frac{b}{4s} + 1 + \frac{\pi t}{2s} \right) \end{aligned}$$

This agrees exactly with Eq. (9-10), which was obtained by adding the thickness correction to the zero-thickness value. It should be remembered that this exact agreement assumes $s/b \ll 1$. However, more detailed calculations have indicated close agreement for $s/b \leq 0.25$, and fair agreement for s/b at least as large as 0.6.

D. DERIVATION

The derivation of Eqs. (9-2) and (9-3) is based on a conformal-mapping analysis by N. Davy⁹ of the double-semi-infinite-plate boundary shown in Fig. 9-7. He obtained the following formula for the capacitance per unit length between the two plates over the regions $BCDP$ and $Q'B'C'D'P'$ of the boundary:

$$C' = -\frac{\epsilon}{\pi} \ln [k \operatorname{sn}^2(u_2, k)] \quad (9-11)$$

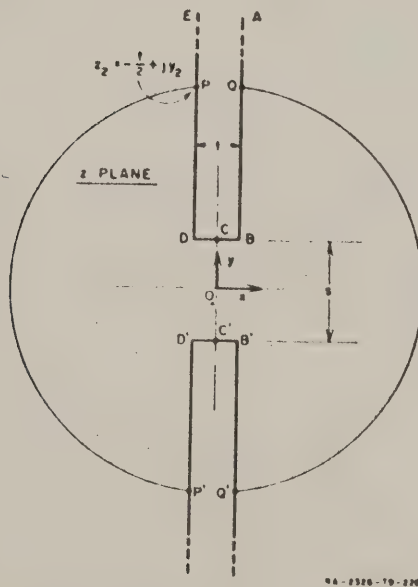


FIG. 9-7
SEMI-INFINITE-PLATE BOUNDARY IN z PLANE

where $k = \sqrt{1 - k'^2}$ is a real positive parameter between 0 and 1 that may be solved as a function of t/s from the following equation:

$$\frac{t}{s} = \frac{K(k') - 2E(k') + k'^2 K(k')}{2[2E(k) - k'^2 K(k)]} \quad (9-12)$$

The symbol u is a complex variable that is a function of $z = x + jy$, and $sn(u, k)$ is an elliptic function.^{9,10} The transformation relating z and u is

$$z = j \frac{s}{2} \left\{ \frac{u \left[k'^2 - \frac{2E(k)}{K(k)} \right] - 2 zn(u, k) - \frac{cn(u, k) dn(u, k)}{sn(u, k)}}{2E(k) - k'^2 K(k)} \right\} - \frac{t}{2} \quad (9-13)$$

where zn , cn , and dn also are elliptic functions.

At point P between D and E on the boundary, u is negative real, approaching zero as y_2 approaches infinity. The following limiting values are valid for $u \rightarrow 0$.

$$sn(u, k) \rightarrow u \quad (9-14)$$

$$cn(u, k) \rightarrow 1 \quad (9-15)$$

$$dn(u, k) \rightarrow 1 \quad (9-16)$$

$$zn(u, k) \rightarrow \left[1 - \frac{E(k)}{K(k)} \right] u \quad (9-17)$$

Substituting these in Eq. (9-13) we obtain in the limit $u \rightarrow 0$,

$$y_2 = \frac{s}{2[2E(k) - k'^2 K(k)] (-u_2)} \quad (9-18)$$

while Eq. (9-11) reduces to

$$C' = \frac{\epsilon}{\pi} \ln \left(\frac{1}{k u_2^2} \right) \quad (9-19)$$

Combining Eqs. (9-18) and (9-19), leads (in the limit $y_2 \rightarrow \infty$) to the following:

$$C' \left(\frac{t}{s}, \frac{y_2}{s} \right) = \frac{2\epsilon}{\pi} \ln \left[\frac{2y_2}{s} \cdot \frac{2E(k) - k'^2 K(k)}{\sqrt{k}} \right] \quad (9-20)$$

This may be simplified for $t/s \rightarrow 0$, since then $k \rightarrow 1$, $k' \rightarrow 0$, $E(k) \rightarrow 1$, and $k'^2 K(k) \rightarrow 0$. Thus

$$C' \left(0, \frac{y_2}{s} \right) = \frac{2}{\pi} \ln \frac{4y_2}{s} \quad (9-21)$$

Now we shall define the capacitance increment $\Delta C'(t/s)$ by

$$\Delta C'(t/s) = \lim_{y_2 \rightarrow \infty} \left[C' \left(\frac{t}{s}, \frac{y_2}{s} \right) - C' \left(0, \frac{y_2}{s} \right) \right] \quad (9-22)$$

Hence the formula for the capacitance increment is

$$\Delta C'(t/s) = \frac{2\epsilon}{\pi} \ln \frac{E(k) - (1/2)k'^2 K(k)}{\sqrt{k}} \quad (9-23)$$

REFERENCES

1. N. Marcuvitz, *Waveguide Handbook*, pp. 218-221 (McGraw-Hill Book Co., Inc., New York, N.Y., 1951).
2. *Op. cit.*, pp. 229-238.
3. *Op. cit.*, pp. 307-310.
4. *Op. cit.*, pp. 310-312.
5. J. R. Whinnery, H. W. Jamieson and T. E. Robbins, "Coaxial-Line Discontinuities," *Proc. IRE*, **32**, pp. 695-709 (1944).
6. N. Marcuvitz, *op. cit.*, pp. 248-255.
7. *Op. cit.*, pp. 404-406.
8. C. G. Montgomery, R. H. Dicke, and E. M. Purcell, *Principles of Microwave Circuits*, p. 172 (McGraw-Hill Book Co., Inc., New York, N.Y., 1948).
9. N. Davy, "The Field Between Equal Semi-Infinite Rectangular Electrodes or Magnetic Pole Pieces," *Phil. Mag.*, Ser. 7, Vol. 35, pp. 819-840 (December 1944).
10. F. Oberhettinger and W. Magnus, "Anwendung der Elliptischen Funktionen in Physik und Technik" (Springer-Verlag, Berlin, 1949).

CHAPTER 10

TECHNIQUES FOR COMPENSATING STRIP-LINE T-JUNCTIONS

A strip-line T junction of the type illustrated in Fig. 10-1(a) whose three arms have a characteristic admittance Y_1 and whose shunt arm has a characteristic admittance Y_2 can be represented at the terminal planes T_1 and T_2 by the circuit of Fig. 10-1(b). The positions of the reference planes are defined by the condition that if a short circuit is placed at one of them there will be no transmission of energy between the arms containing the other two planes.

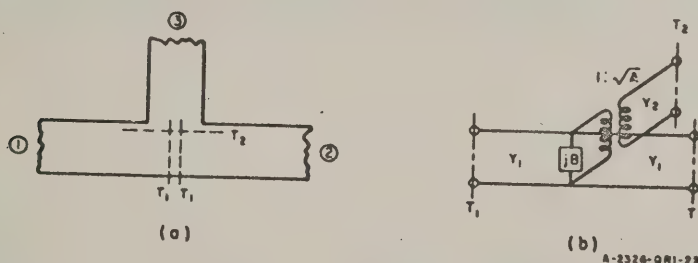


FIG. 10-1

EQUIVALENT CIRCUIT OF AN UNCOMPENSATED STRIP-LINE T-JUNCTION

Measurements made on these junctions during the course of a previous study contract¹ showed that $B/Y_1 \ll 1$ at all frequencies. Furthermore, it was found possible to reduce the value of B to a negligibly small value by either adding a small tab or making a small indentation (depending on the value of Y_1/Y_2) on the side of the through arm opposite from the shunt arm. The turns ratio, \sqrt{A} , of the transformer in the shunt arm was found to have a value near unity at low frequencies but to decrease to values much less than unity at higher frequencies.

An investigation has been made during the present contract of ways of reducing the frequency variation of \sqrt{A} . In Fig. 10-2 are illustrated four junction configurations whose performance has been measured. The indentation in the shunt arm of the T junction of Fig. 10-2(a), and the hole in the shunt arm of the T junction in Fig. 10-2(b), have the effect of adding a series inductance between the through arm and the

¹ Also see Chapter 11.

shunt arm. It was found that these modifications increased the frequency sensitivity of the turns ratio over that of unmodified junctions.

The button added to the shunt arm of the T-junction in Fig. 10-2(c) increases the effective shunt capacity at the junction of the shunt and through arms. It was found that the frequency sensitivity of the turns ratio in this junction was slightly less than that of an uncompensated junction but that the junction susceptance, B , was increased by a factor of 12 to 1 over that of an uncompensated T-junction.

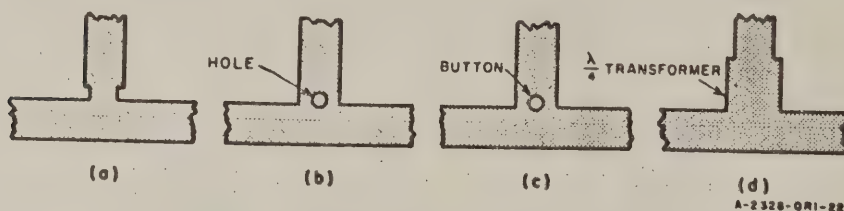


FIG. 10-2

COMPENSATED STRIP-LINE T-JUNCTIONS

Theoretically the quarter-wavelength transformer placed in series with the shunt arm in Fig. 10-2(d) increases the frequency at which the transformer turns ratio deviates appreciably from unity. However it also introduces a junction susceptance that is positive at low frequencies and negative at high frequencies. An approximate equivalent circuit of this junction is shown in Fig. 10-3.

The admittance Y_{1n} seen looking into Port 1 when an open circuit is placed at Port 2 is given by

$$Y_{1n} = G_{in} + jB_{in} = AY_n \frac{(Y_2 + jY_n \tan \theta)}{(Y_n + jY_2 \tan \theta)} + jB.$$

10-1

At the match frequency when $\theta = 90^\circ$ it is desired that $G_{in} = Y_2$. Hence, it is necessary that $Y_2 = \sqrt{A} Y_n$. Making these substitutions one finds that

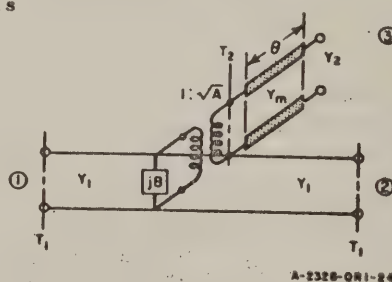


FIG. 10-3

EQUIVALENT CIRCUIT OF A STRIP-LINE T-JUNCTION COMPENSATED WITH A $\lambda/4$ TRANSFORMER

$$Y_{1a} = \frac{A(\cot^2 \theta + 1)Y_2}{(\cot^2 \theta + A)} + j \frac{\sqrt{A} \cot \theta (1 - A)}{\cot^2 \theta + A} Y_2 + jB$$

The real coefficient of Y_2 in the above expression $A(\cot^2 \theta + 1)/\cot^2 \theta + A = A'$ is the square of the equivalent transformer turns ratio.

In order to test the effectiveness of this type of compensation, a T-junction having $Y_1 = Y_2 = 0.02$ mho was modified by placing in the shunt arm a quarter-wavelength transformer. The value of A and shunt susceptance B for the uncompensated junction is shown in Fig. 10-4. The turns ratio A' was designed to be unity when $b/\lambda = 0.125$. The desired characteristic admittance Y_0 was computed to be 0.02235 mho. the effective length of the transformer was assumed to be the distance from the reference plane T_2 to the end of the transformer. The dimensions of the junction are listed in Table 10-1.

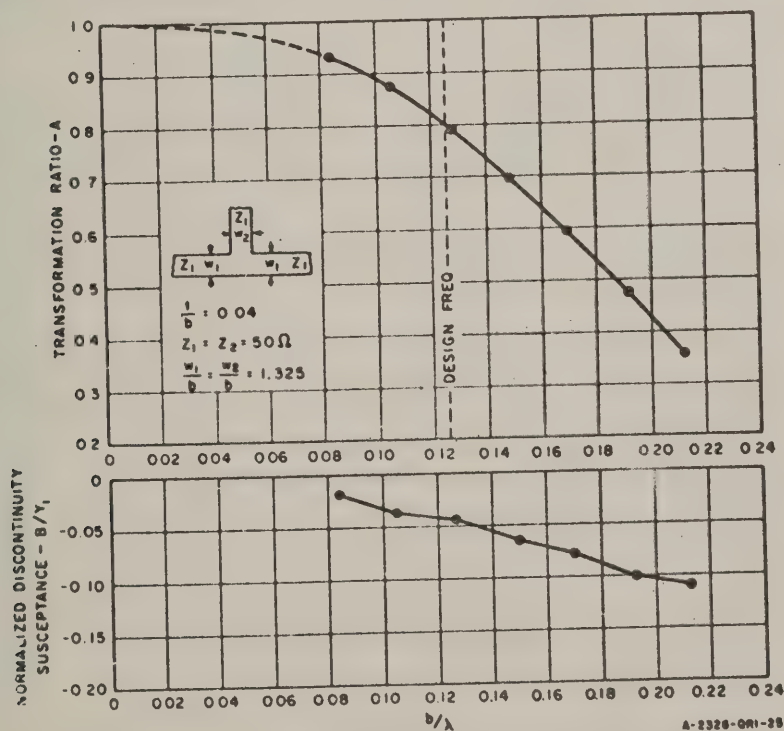


FIG. 10-4

MEASURED PERFORMANCE OF AN UNCOMPENSATED STRIP-LINE T-JUNCTION

TABLE 10-1
DIMENSIONS OF COMPENSATED STRIP-LINE T-JUNCTION
(Inches)

| | |
|---|--------|
| Strip thickness t | 0.020 |
| Plate spacing b | 0.500 |
| Width W of strip having $Y_1 = 0.02 \text{ mho}$ | 0.6625 |
| Width W' of strip having $Y_2 = \text{mhos}$ | 0.775 |
| Length of transformer measured from reference plane T_2 | 1.000 |

Both the measured and theoretical values of A' are plotted in Fig. 10-5 and it is seen that they differ by only about 0.05 for all but the highest values of b/λ . By comparing the measured value of A' of the compensated junction with the A of the uncompensated junction it can be seen that the quarter wavelength transformer almost doubles the frequency range over which the square of the transformer turns ratio deviates from unity by less than 5 percent.

The measured values of B'/Y_1 for the compensated junction are shown at the bottom of Fig. 10-5, compared with the theoretical values. Although the shapes of the two curves are quite similar, they differ considerably in magnitude. It can also be seen that the total excursion of B'/Y_1 for the compensated junction is approximately three times as great as that of B/Y_1 for the uncompensated junction.

It is believed that in most applications the high values of junction susceptance for the T-junctions of Fig. 10-2(c) and 10-2(d) make them less desirable as circuit elements than a T junction of the type similar to that shown in Fig. 10-1(a) in which B/Y_1 has been reduced to a very low value by means of a compensating tab as described above.¹ Chapter 11 describes measurements made on T-junctions of the type shown in Fig. 10-1 for various values of Y_1 and Y_2 .

REFERENCE

1. S. B. Cohn, P. M. Sherk, J. K. Shimizu, E. M. T. Jones, "Strip Transmission Lines and Components," SRI Project 1113, Contract DA-36-039 SC-63232, Stanford Research Institute, Menlo Park, California (February 1957).

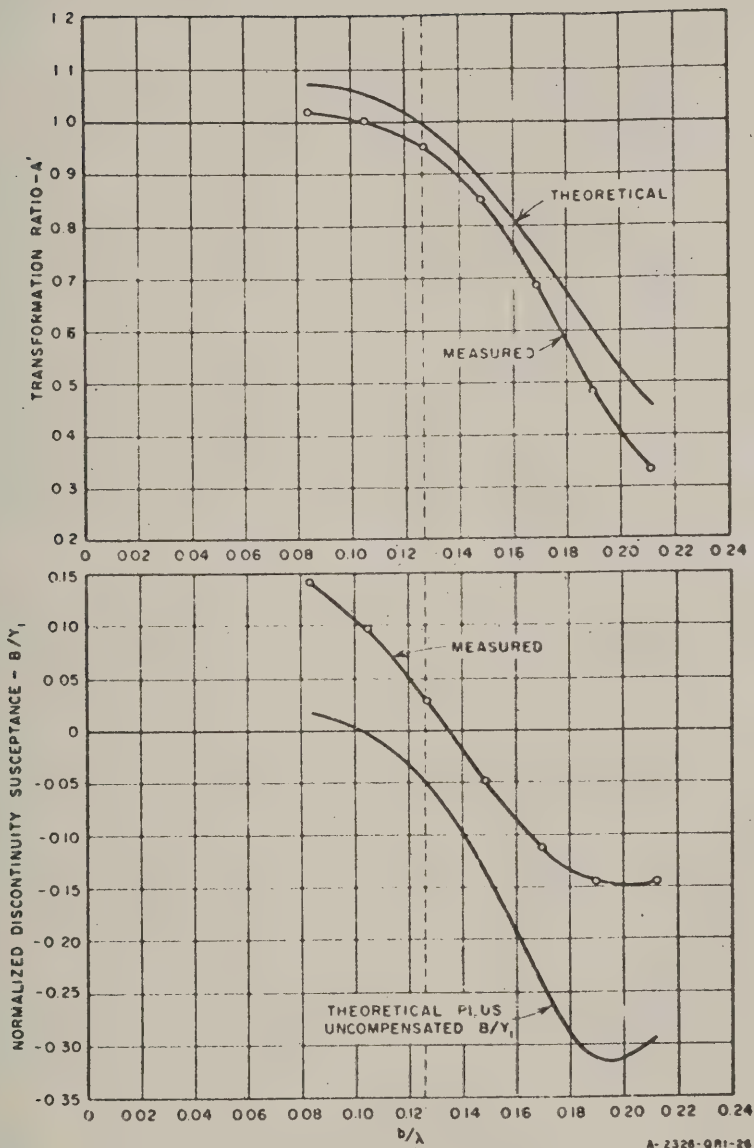


FIG. 10-5

MEASURED PERFORMANCE OF A STRIP-LINE T-JUNCTION COMPENSATED
WITH A $\lambda/4$ TRANSFORMER

CHAPTER 11

MEASURED EQUIVALENT CIRCUITS OF COMPENSATED AND UNCOMPENSATED STRIP-LINE T-JUNCTIONS

A. GENERAL

This chapter of the report describes the measured equivalent circuits of sixteen different types of strip-line T-junctions. A symmetrical T-junction of the type considered here is illustrated in Fig. 11-1(a) and is seen to consist of a series arm with a characteristic impedance Z_{01} , and a shunt arm with a characteristic impedance Z_{02} . At the terminal planes, P_1 and P_2 , the T-junction shown in Fig. 11-1(a) can be represented by the equivalent circuit of Fig. 11-1(b) proposed by J. Lamb¹ for a symmetrical transmission-line T-junction. Here the position of each of the reference planes P_1 and P_2 is defined as the transverse plane at which a short circuit would prevent power flow between the other two arms. To determine the positions of P_1 and P_2 experimentally, the calibrated short-circuiting elements should be placed $n\lambda/2$ away from P_1 and P_2 , where the integer n is large enough that the short-circuiting elements will not affect the discontinuity fields of the junction.

As can be seen, the equivalent circuit of Fig. 11-1(b) differs from that of a simple shunt connection of three transmission lines because of

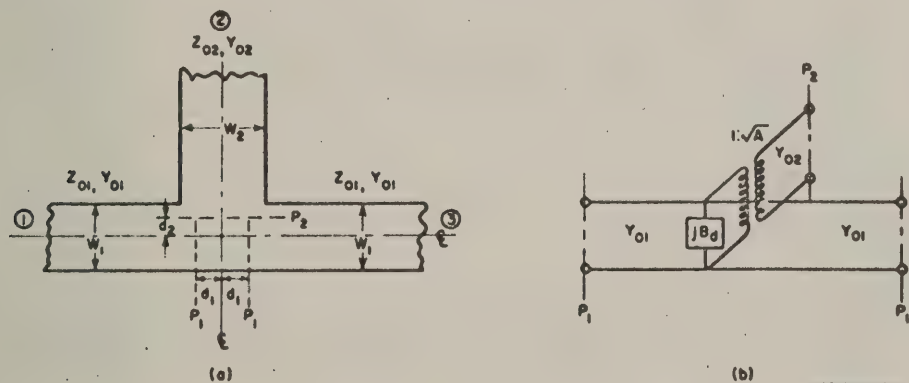


FIG. 11-1

EQUIVALENT CIRCUIT OF AN UNCOMPENSATED STRIP-LINE T-JUNCTION

the presence of the transformer with turns ratio A and of the normalized discontinuity susceptance B_d/Y_{01} . In order to fully compensate the T-junction it would be necessary to make A equal to unity and B_d/Y_{01} equal to zero over the usable frequency range of the strip line.

In Chapter 10, the results of measurements made on this type of T-junction were described and it was shown that one can compensate either the transformer turns ratio, A , so that it is unity, or the normalized discontinuity susceptance, B_d/Y_{01} , so that it is zero, but that it is virtually impossible to compensate both simultaneously. The value of A was made to be nearly unity by adding a one-quarter wavelength transformer in series with the shunt arm having a characteristic impedance Z_{02} as shown in Fig. 11-2(a).

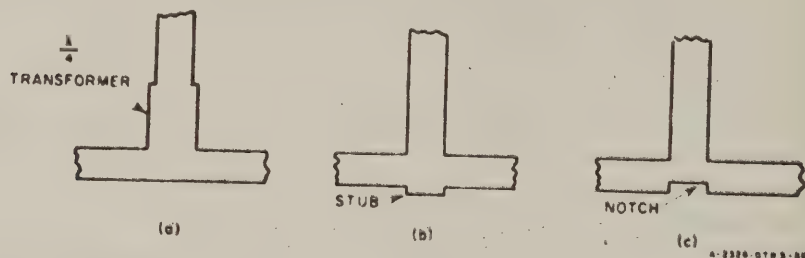


FIG. 11-2
COMPENSATED STRIP-LINE T-JUNCTIONS

Although it was possible to improve the transformer turns ratio by this method, the junction susceptance was increased, which made the junction more frequency-sensitive than before it was compensated. On the other hand, in the previous study contract,² measurements made on these junctions showed that it was possible to reduce the value of B_d to a negligibly small value by either adding a small tab or making a small indentation (depending on the value of Z_{01}/Z_{02}) on the side of the through arm opposite from the shunt arm, as shown in Fig. 11-2(b) and (c). In this case it was found that when B_d was compensated the transformer turns ratio A decreased to values slightly less than that of the uncompensated junction.

It is believed that in most applications the high values of junction susceptance for the T-junctions of Fig. 11-2(a) make them less desirable as circuit elements than a T-junction of the type similar to that shown

in Fig. 11-2(b) in which B_d/Y_{01} has been reduced to a very low value by means of a compensating stub or notch.

Described in this chapter are some measurements made on uncompensated T-junctions of the type shown in Fig. 11-1(a) for various values of Z_{01} and Z_{02} . A simple method is described for computing the size of compensating stub necessary to reduce the junction susceptance to a negligible value for those junctions in which B_d is negative.

B. EQUIVALENT CIRCUIT DATA

The equivalent-circuit parameters of sixteen uncompensated T-junctions were measured for values of Z_{01} of 35, 50, 70, and 100 ohms, and values of Z_{02} of 35, 50, 70, and 100 ohms. The dimensions of the junctions are listed in Table 11-1.

In Fig. 11-3 a plot of the normalized reference-plane positions d_1/b and d_2/b are shown versus the stub impedance Z_{02} . For each of the sixteen T-junctions, d_1 and d_2 were measured over the frequency band of 2 to 5 kMc, corresponding to a range of b/λ of 0.085 to 0.212. It was found that both d_1 and d_2 were almost independent of frequency for all sixteen T-junctions. The reference-plane positions shown in Fig. 11-3 are the values which were measured at 3 kMc or $b/\lambda = 0.127$; therefore these data may be used at any frequency up to at least 5 kMc, or $b/\lambda = 0.212$. A similar T-junction measurement reported in the previous study contract² has also shown that the reference-plane positions were fairly independent of frequency.

The transformer turns ratio, A , of each of the sixteen T-junctions is plotted versus b/λ in Fig. 11-4. Because of the numerous data accumulated, the data are shown divided into four families of curves each having a different value of Z_{01} .

As can be seen from these curves, measurements were made over the frequency range of 2 to 5 kMc or b/λ ranging from 0.085 to 0.212 for all T-junctions except those containing lines with Z_{01} or Z_{02} of 35 ohms. The data for these latter T-junctions are plotted from 2 to 4 kMc or b/λ

TABLE 11-1
DIMENSIONS OF UNCOMPENSATED
STRIP-LINE T-JUNCTION
(inches)

| | |
|---|-------|
| Strip thickness t | 0.020 |
| Plate spacing b | 0.500 |
| Width w_1 and w_2 for impedance of Z_{01} and Z_{02} having the following values: | |
| 35 ohms | 1.050 |
| 50 ohms | 0.663 |
| 70 ohms | 0.405 |
| 100 ohms | 0.210 |

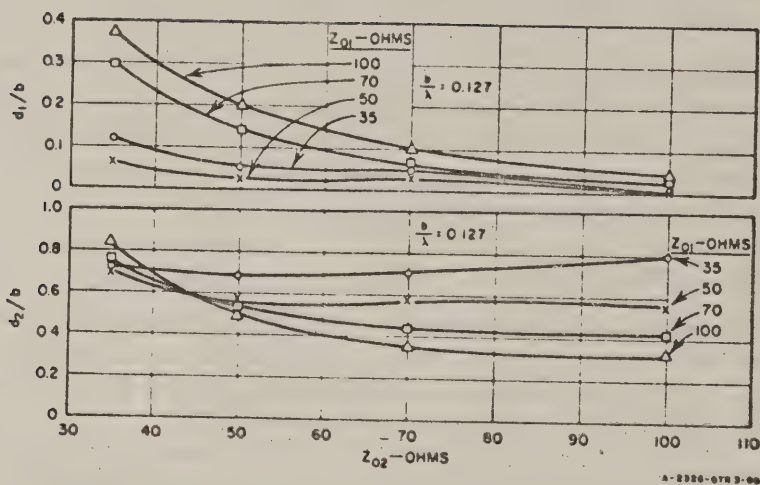
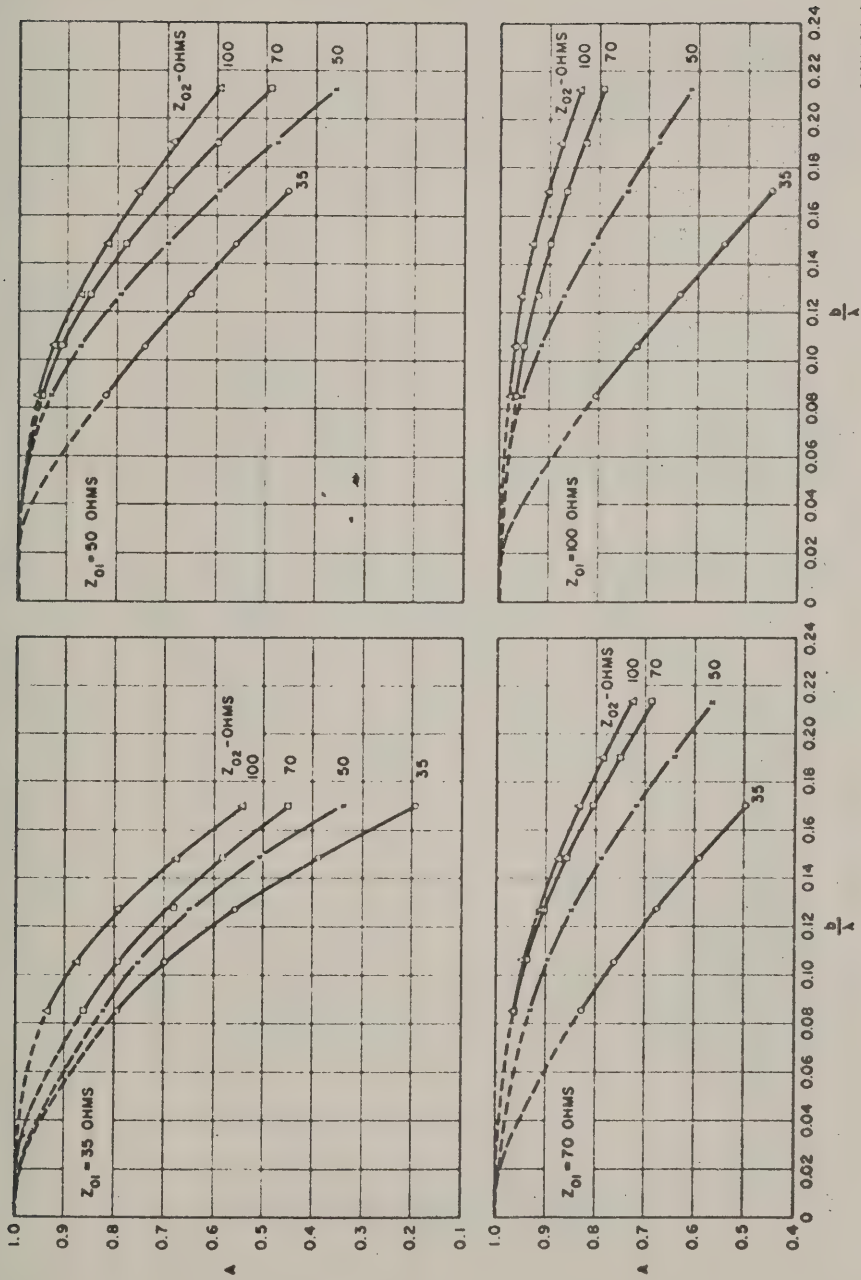


FIG. 11-3
REFERENCE-PLANE LOCATIONS VERSUS Z_{02}

ranging from 0.085 to 0.169. Data are not recorded for higher frequencies because the curves had perturbations in them that, it is believed, were due to the first higher mode of the 35-ohm lines whose cut-off frequency is 4610 Mc.²

In Fig. 11-5 values of the normalized junction susceptance B_d/Y_{01} of the sixteen T-junctions are shown plotted versus b/λ . These data are also shown divided into the same four families of curves. Inspection of these data show that when the characteristic impedance Z_{02} of the shunt arm is equal to or greater than the characteristic impedance Z_{01} of the series arm, the values of the normalized junction susceptance B_d/Y_{01} are negative. When Z_{02} is less than Z_{01} , the normalized junction susceptance is positive. Inspection of the data shows that in any uncompensated T-junction there is a value of Z_{02} slightly less than Z_{01} where B_d/Y_{01} is zero.

Although the data presented in Figs. 11-3 to 11-5 are for strip-line T-junctions with air-filled cross section and with the ratio of $t/b = 0.040$, these data may be applied to other cross sections. For instance, it is expected that these data should hold for any strip-thickness ratio, t/b ,



C-3326-0720-87

FIG. 11-4
MEASURED TRANSFORMER TURNS RATIO OF 16 UNCOMPENSATED STRIP-LINE T-JUNCTIONS

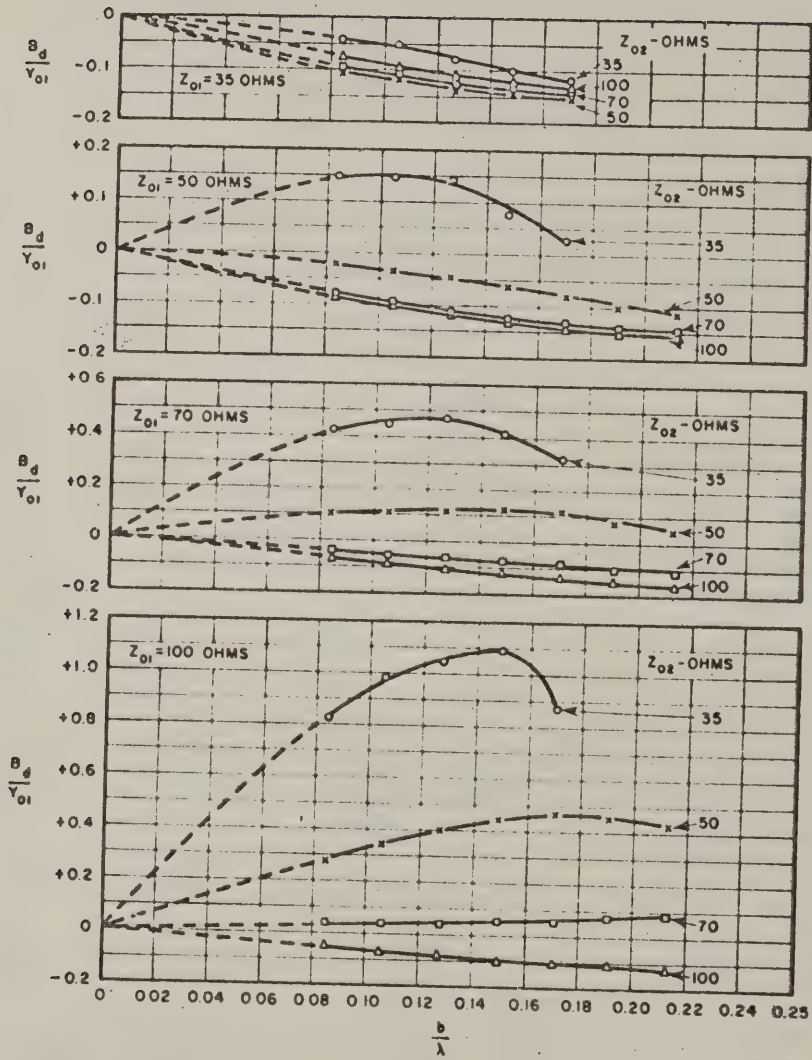


FIG. 11-5
MEASURED DISCONTINUITY SUSCEPTANCE OF 16 UNCOMPENSATED
STRIP-LINE T-JUNCTIONS

up to at least 0.125° if the same characteristic impedances are maintained. In the case of a dielectric-filled cross section ($\epsilon_r > 1$), the characteristic impedances Z_{01} and Z_{02} of Figs. 11-3 to 11-5 should be divided by the square root of the dielectric constant (that is, the strip width ratio w/b should be maintained the same). For cross sections where the strips are printed on thin dielectric sheets with large air spacings, no data have been taken, but probably good results may be obtained using the data shown in Figs. 11-3 to 11-5 by maintaining the same characteristic impedances.

C. COMPENSATION OF B_d

In the previous study contract,² it was shown that the junction susceptance B_d of the T-junction could be reduced to a negligible value by adding a short stub or introducing a small notch opposite the shunt arm. When the sign of B_d was positive a small notch was introduced, and when the sign of B_d was negative a short stub was added. The width of the notch or stub chosen was identical to the shunt strip width, w_2 , and the correct length of the notch or stub was determined experimentally for each T-junction. These data have shown that for a T-junction modified with a stub, the value of B_d remained compensated over a very wide frequency range, while a modified T-junction with a notch showed that the value of B_d was compensated over a limited frequency band.

In this chapter a simple technique is described for computing the length of stub necessary to compensate a negative junction susceptance. The validity of the techniques was verified by measurements made on two different junctions. No attempt was made to compensate for the T-junctions having positive B_d , since it has been previously shown that this type of compensation is narrow-band. One of the experimental T-junctions has $Z_{01} = Z_{02} = 35$ ohms, the other has $Z_{01} = Z_{02} = 100$ ohms. Each was compensated by adding a stub of 100 ohms characteristic impedance opposite the shunt arm. A high-impedance compensating stub was chosen since it behaves more like a lumped compensating susceptance than would a low-impedance stub.

The length of the compensating stub is chosen so that its positive susceptance will be equal and opposite to the negative susceptance B_d of the junction near the middle of the frequency band. The susceptance of

² In the previous contract,² equivalent circuit measurements made on similar T-junctions with $t/b = 0.040$ and $t/b = 0.125$ showed very close agreement.

the stub is assumed to be that of an open-circuited line having a length, l , equal to the stub length. The formula for computing l is

$$l = \frac{\lambda}{2\pi} \tan^{-1} \frac{-B_d}{0.01} \text{ inch} \quad (11-1)$$

Here λ is the free space wavelength given in inches, B_d is the value of susceptance given in Fig. 11-5, and 0.01 is the value of the admittance of a compensating stub having an impedance of 100 ohms.

The lengths of the compensating stubs of these two T-junctions possessing $Z_{01} = Z_{02} = 35$ ohms and $Z_{01} = Z_{02} = 100$ ohms were determined at a frequency of 3 kMc or $b/\lambda = 0.127$. From Fig. 11-5 one finds that in the junction having $Z_{01} = Z_{02} = 35$ ohms, B_d has a value of 0.0022 mho and that in the junction having $Z_{01} = Z_{02} = 100$ ohms, B_d has a value of 0.00085 mho. The length l of the stub was calculated to be 0.136 and 0.054 inch for the T-junctions with $Z_{01} = Z_{02} = 35$ ohms and $Z_{01} = Z_{02} = 100$ ohms, respectively.

The measured results for these compensated T-junctions are shown in Fig. 11-6 and 11-7 together with the curves of the uncompensated junctions. It is seen that in both T-junctions the junction susceptance has been reduced to a negligible value over the measured frequency range. Figures 11-6 and 11-7 also show that by compensating the T-junction for B_d , the transformer turns ratio A is decreased by about 0.05 over the measured frequency range. Measurements of the reference-plane positions for the compensated T-junctions have shown that these values agreed very closely with the uncompensated T-junction curves shown in Fig. 11-3.

REFERENCES

1. J. Lamb, "The Experimental Behavior of the Coaxial Line Stub," J. Inst. Elect. Engineers (London) 93, pp. 188-190 (May 1946).
2. S. B. Cohn, P. M. Sherk, J. K. Shimizu, E. M. T. Jones, "Strip Transmission Lines and Components," Final Report, SRI Project 1114, Contract DA-36-039 SC-63232, Stanford Research Institute, Menlo Park, California (February 1957).

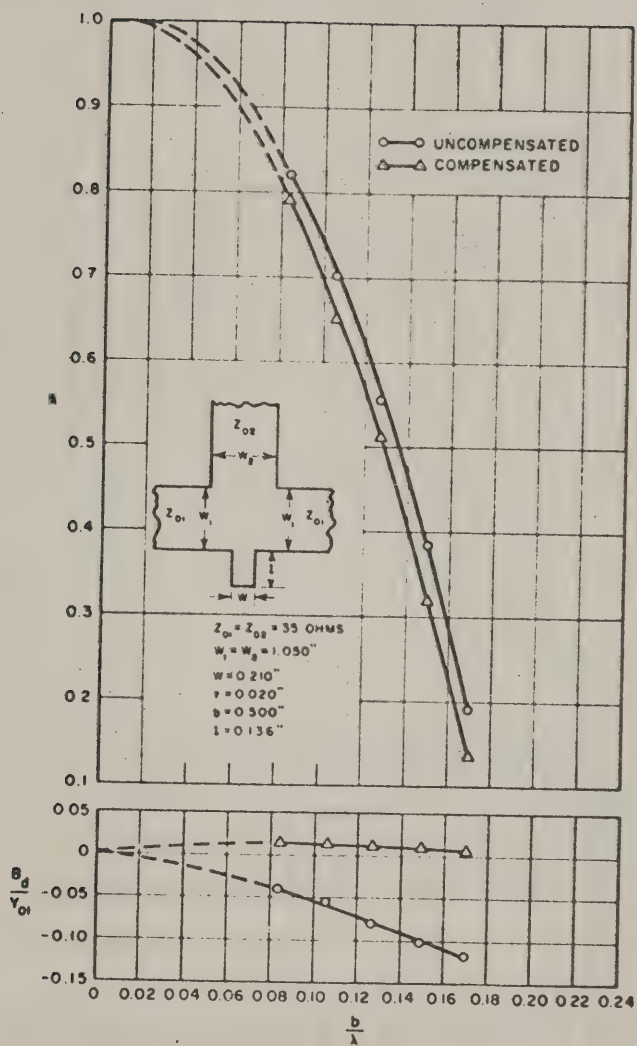


FIG. 11-6
MEASURED EQUIVALENT CIRCUIT OF A COMPENSATED STRIP-LINE
T-JUNCTION WITH $Z_{01} = Z_{02} = 35 \text{ ohms}$

CHAPTER 12

WIDE-STOP-BAND WAVEGUIDE FILTERS

A. GENERAL

During a previous SRI study program the experimental and theoretical performance of corrugated waveguide filters with longitudinal slots were described.¹ It was shown that these filters have wide, well-matched pass bands with low insertion loss and wide high-attenuation stop bands free of spurious responses. In addition, these filters are relatively easy to machine and assemble. The design procedure described was useful for stop-band bandwidths up to about 2:1.

Recently SRI has developed two filters of this type for the Hewlett Packard Co. that have well-matched, low-loss, pass-band bandwidths of about 1.55:1 and stop-band bandwidths of about 3:1. One of these filters is designed to be placed in series with the output of their Signal Generator 626A, which has a frequency range of 10,000 to 15,500 Mc. The other is designed to be placed in series with the output of their Signal Generator 628A, which has a frequency range of 15,000 to 21,000 Mc. The purpose of these filters is to suppress the second and third harmonic frequencies of these generators.

It is believed that the procedure used in designing these extraordinarily wide-stop band filters is of sufficient interest that it should be published. Therefore, with the permission of the Hewlett Packard Co., and with the consent of the Signal Corps Technical Officer, the design and measured performance of these filters are described in this chapter.

B. FILTER SPECIFICATIONS

Table 12-1 presents a list of the specifications for the two filters described in Section A.

TABLE 12-1
SPECIFICATIONS FOR THE TWO WAVEGUIDE FILTERS

| ITEM SPECIFIED | FILTER I | FILTER II |
|---|----------------|----------------|
| Pass band (kMc) | 10-15.5 | 15-21 |
| Stop band (kMc) | 20-47 | 30-63 |
| VSWR in pass band | <1.5 | <1.5 |
| Insertion loss in pass band (db) | <0.5 | <0.5 |
| Insertion loss in stop band (db) | 40 | 40 |
| Inner dimensions of terminating waveguide (in inches) | 0.750 by 0.375 | 0.510 by 0.255 |

C. PRACTICAL CONSIDERATIONS

1. SCALING

The two filters are sufficiently alike so that, with the use of the usual scaling procedure, one design can be obtained from the other. In actual practice an enlarged scale model of Filter I was designed and constructed, since this filter has the broader pass-band and stop-band bandwidths. This scale model was adjusted for optimum performance, and Filters I and II were then designed from measurements taken on the scale model.

2. PHYSICAL STRUCTURE

Photographs of the final model of Filter II are shown in Fig. 12-1. The filter was given the form illustrated in order to make its construction as simple as possible so that it can be economically mass produced. The filter consists of two pairs of identical parts, which can be relatively easily machined, and which can be assembled without brazing or soldering. Stepped transformers, rather than tapered sections, were used to match between the filter and the terminating waveguides to simplify machining. Furthermore, the longitudinal slots in the corrugated filter extend into the stepped transformers so that the filter and stepped transformers can be machined from a single piece of material. The gap between the top and bottom sections of the filter was made as large as possible, since the tolerance that must be held on this dimension increases with increasing gap height. Nevertheless, the sizes of the filter dimensions were definitely limited by the need to attenuate the higher-order modes as well as the dominant mode in the stop band.

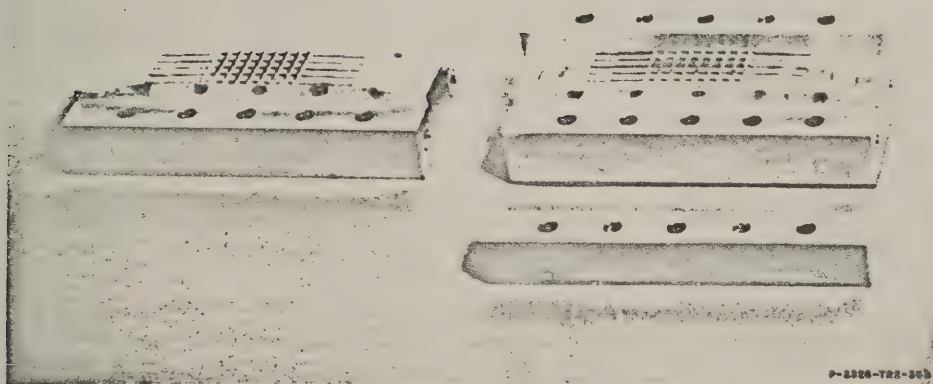
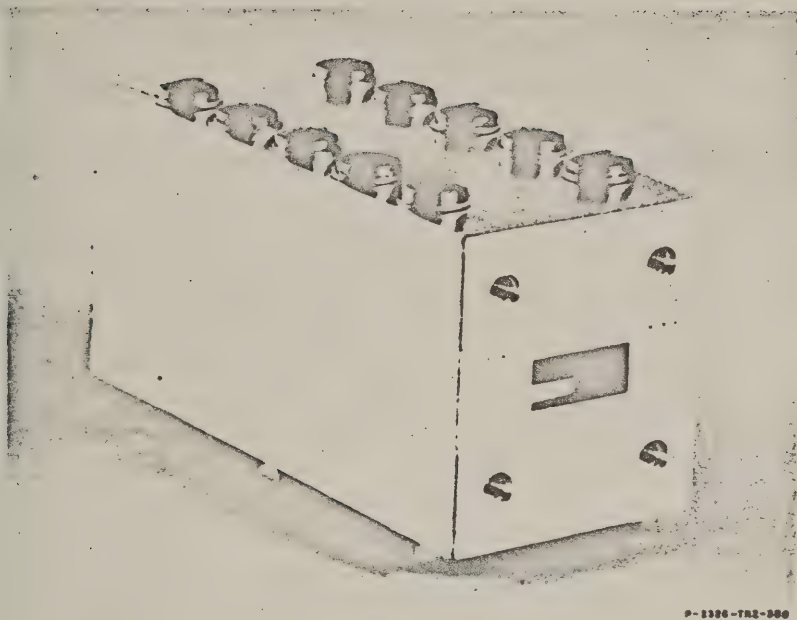


FIG. 12-1

PHOTOGRAPHS OF FILTER HAVING 15-21 kc PASS BAND AND 30-63 kc STOP BAND

3. CHOICE OF NUMBER OF LONGITUDINAL SLOTS

The waveguide modes which this filter attenuates can be analyzed as a composite of plane waves traveling in the waveguide at an angle which depends on the order of the mode. To a first approximation, the doubly periodic filter structure attenuates these component plane waves on the

basis of frequency only and independent of the direction in which they are propagated—provided that the center-to-center spacing of the bosses is a small fraction of a wavelength. It is necessary, therefore, that the filter structure be made sufficiently fine that it can attenuate the highest frequency in the stop band. This requirement places an upper limit on the length, a/n of a filter section [shown in profile in Fig. 12-2(a) and in cross section in Fig. 12-2(b)]. Here a is the width of the waveguide and n is an integer. In this case $n = 5$ is chosen, and this choice fixes the length, $(l + l')$ and, to a large extent, limits the dimensions b and b' .

4. LIMITATIONS ON WIDTH OF SLOTS

In previous designs, deep narrow slots were used.¹ However, in order to achieve the stop-band bandwidth described here, it is necessary to increase the width, l , of the slots and decrease their depth, $(b - b')/2$, and also to decrease the gap, b' . There are, however, limita-

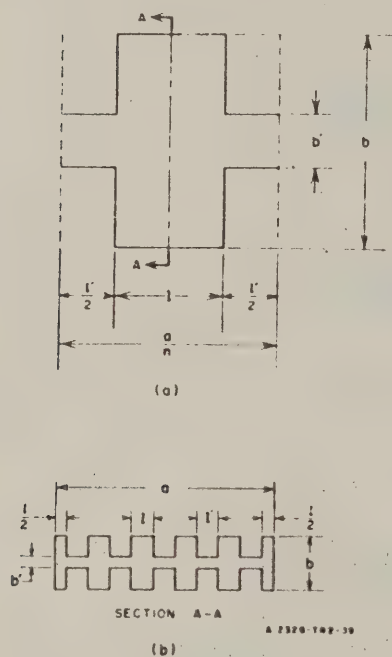


FIG. 12-2

A SINGLE FILTER SECTION OF THE CORRUGATED WAVEGUIDE FILTER

tions on this process. First, the dimension b' should not be too small, because of manufacturing tolerances mentioned earlier. Second, the slot depth, $(b - b')/2$, should not be too small nor should the slot width, l , be too wide, because a compensating reduction of the dimension b' is required. Under these conditions, the presence of the longitudinal slots aggravates the problem because the length of a full filter section is fixed by the value chosen for n ($n = 5$). The area of the bosses is thus seen to shrink rapidly as the slot width is increased.

D. ELECTRICAL DESIGN

The cut off frequencies, the points of infinite attenuation, and the optimum filter terminating impedance can all be determined from the image parameters of a filter section, when there are no longitudinal slots. The addition of longitudinal slots changes the filter parameters, so that after a preliminary design is worked out, compensating changes must be made in the filter dimensions.

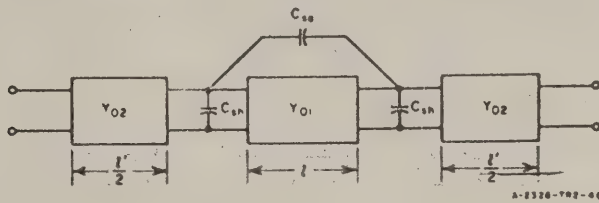


FIG. 12-3

EXACT EQUIVALENT NETWORK OF A CORRUGATED WAVEGUIDE
FILTER SECTION FOR THE DOMINANT MODE

It is to be noted that the equivalent circuit using the *T*-junction parameters as described in a previous report¹ is not easily applied in the design of a filter with slots which are wide compared to the gap b' , because the published data that give these parameters do not cover the cases of wide shallow slots.² On the other hand, accurate calculations of the essential parameters of a corrugated waveguide filter having wide slots have been made with the circuit of Fig. 12-3 as a basis. These have been published, complete with nomograms and supplementary graphs, in a "Theoretical and Experimental Study of a Waveguide Filter Structure," by S. B. Cohn.³ It is these supplementary graphs that are most useful in the initial design work for finding the dimensions of a filter section.

1. THEORY

From the equivalent circuit of the filter half-section, Fig. 12-4, one may easily derive the normalized filter image admittance

$$y_I = \frac{\cot \frac{\epsilon'}{2}}{\delta} \sqrt{\frac{\left(b_{oc} + \frac{\tan \frac{\theta'}{2}}{\delta}\right) \left(b_{sc} + \frac{\tan \frac{\theta'}{2}}{\delta}\right)}{\left(b_{sc} - \frac{\cot \frac{\theta'}{2}}{\delta}\right) \left(b_{oc} - \frac{\cot \frac{\theta'}{2}}{\delta}\right) (-1)}} \quad (12-1)$$

and the image phase shift

$$\Theta = 2 \tanh^{-1} \sqrt{\frac{\left(b_{oc} + \frac{\tan \frac{\theta'}{2}}{\delta}\right) \left(b_{sc} - \frac{\cot \frac{\theta'}{2}}{\delta}\right)}{\left(b_{sc} - \frac{\cot \frac{\theta'}{2}}{\delta}\right) \left(b_{oc} + \frac{\tan \frac{\theta'}{2}}{\delta}\right)}} \quad (12-2)$$

where $\delta = b'/b$, $\theta' = \beta l'$ is the electrical length of the low impedance portion of the filter, and b_{oc} and b_{sc} are the normalized open- and short-circuit susceptances of the high-impedance portion including the step discontinuity, as indicated in Fig. 12-4. The normalizing admittance is

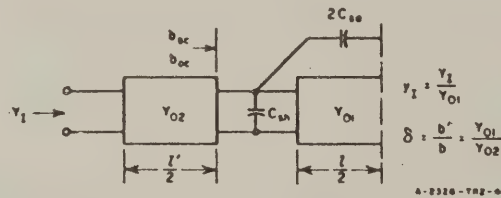
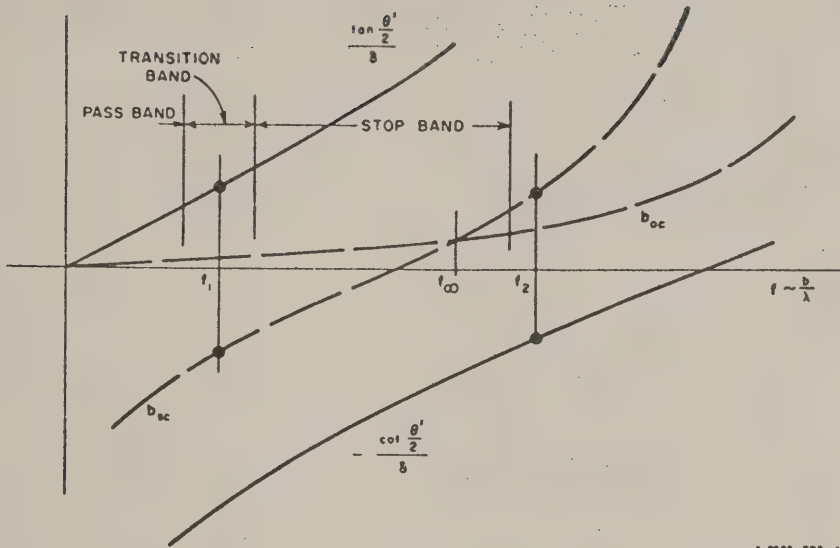


FIG. 12-4

EQUIVALENT NETWORK OF THE HALF-SECTION

that of a parallel-plane waveguide of height b . Graphs of b_{oc} and b_{sc} for several values of l/b and δ are given in Ref. 3. The analysis here is based on parallel-plane propagation, since it is from this viewpoint that the operation of the filter is best understood, and since this type of propagation is directly applicable to the design. Consequently one uses the free-space wavelength λ instead of λ_g .



A-2520-VMS-48

FIG. 12-5.

GRAPH OF QUANTITIES WHICH DETERMINE CRITICAL FREQUENCIES

Equations (12-1) and (12-2) are made more significant if one examines Fig. 12-5, which shows the quantities of these equations sketched versus relative frequency. It is seen that the lowest frequency at which y_1 is zero is f_1 , the cut-off frequency between the pass band and the stop band, and that f_1 is determined from

$$b_{sc} + \frac{\tan \frac{\theta'}{2}}{\delta} = 0 \quad (12-3)$$

The next significant frequency is a point of infinite attenuation, f_∞ , that occurs where

$$b_{sc} = b_{oc} \quad (12-4)$$

There one finds that β increases by 180 degrees abruptly. Finally, the cut-off frequency above the stop band, f_2 , is determined by

$$b_{oc} - \frac{\cot \frac{\theta'}{2}}{\delta} = 0 \quad (12-5)$$

It is now possible, using a given ratio, l/b , and the corresponding graphs of b_{oc} and b_{ec} , and using a given cut-off frequency, f_1 , to choose various values of f_∞ and then calculate f_2 for each f_∞ chosen. If desired, several designs can thus be obtained and the one with the most useful stop-band width and physical dimensions can be chosen, as was done in this case. The process is best illustrated with the following numerical example by which Filter I was designed.

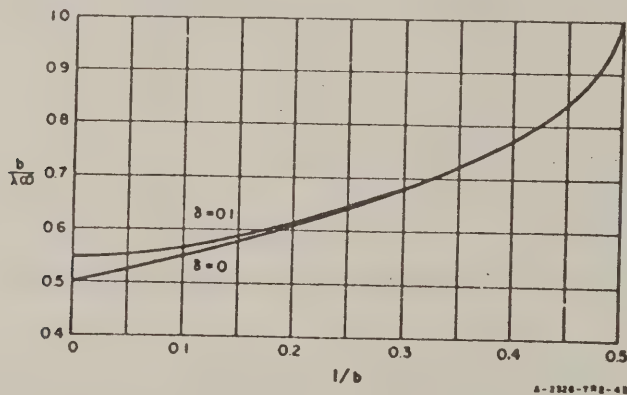


FIG. 12-6

GRAPH SHOWING RELATION OF FREQUENCY OF INFINITE ATTENUATION TO SLOT PROPORTIONS FOR FILTER WITH NO LONGITUDINAL SLOTS

2. DESIGN PROCEDURE FOR MIDDLE SECTIONS

A quasi-universal curve for f_∞ is shown in Fig. 12-6, and curves of b_{ec} and b_{oc} vs. b/λ , the frequency variable, for $l/b = 1/\pi$ and $\delta = 0.1$ are given in Fig. 12-7. First, $f_1 = 17.5$ kMc and $f_\infty = 45$ kMc are chosen. From Fig. 12-6 one obtains $b/\lambda_\infty = 0.698$ for $l/b = 1/\pi$. The values of b and l are then calculated. These are found to be $b = 0.183$ inch and $l = 0.0583$ inch. For five longitudinal slots in a waveguide 0.750 inch wide, a full filter section is $0.750/5 = 0.150$ inch long. Thus, $l + l' = 0.150$ inch and $l' = 0.0917$ inch. From this value of l' we find the cut-off electrical length of the low-impedance portion of the half

section, $\theta'_1/2 = 24.5$ degrees. The value of δ may now be obtained by solving Eq. (12-3) graphically. Thus, at cut-off frequency f_1 ,

$$b_{s.c} = -\frac{\tan 24.5^\circ}{\delta} = -\frac{0.456}{\delta} \quad (12-6)$$

Additional curves similar to the solid curve of Fig. 12-7 may be calculated for values of δ near $\delta = 0.1$ from the approximate formula

$$b'_{s.c} = b_{s.c} - \frac{2b}{\lambda} \ln \frac{\delta'}{\delta} \quad (12-7)$$

where the unprimed values are those already known. It is not necessary to compute many curves of $b'_{s.c}$, however. Instead, a judicious choice of δ' permits Eq. (12-3) to be solved by an iterative process at a single frequency—in this case f_1 . Here δ' was initially chosen as $\delta' = 0.13$.

New values of $b'_{s.c}$ at cut-off frequency f_1 are now computed from Eqs. (12-6) and (12-7), and the average of the two values is used to compute a second trial value of δ' by means of Eq. (12-6). In this case the process converged in three steps to $\delta' = 0.176$, from which we find $b' = 0.0322$ inch. The value of $b'_{s.c}$ at the end of the stop band, f_2 , is now calculated from Eq. (12-5)

$$b'_{s.c} = \frac{1}{0.176 \times 0.456} = 12.5.$$

To obtain f_2 , the curve of $b'_{s.c}$ for $\delta' = 0.176$ is plotted as shown in Fig. 12-7. First, the curve for $b_{s.c}$ is extrapolated, and a few points calculated for $b'_{s.c}$ from Eq. (12-7). From this new curve we find $b/\lambda_2 = 0.87$ at $b'_{s.c} = 12.5$, and f_2 is easily calculated from

$$\frac{f_2}{f_1} = \frac{b}{\lambda_2} \cdot \frac{\lambda_1}{b} \text{ to be } f_2 = 55 \text{ kMc,}$$

which is well above 47 kMc, the end of the stop band. The filter dimensions, before introducing longitudinal slots, are $b' = 0.0322$ inch, $l = 0.0917$ inch, $l = 0.0583$ inch, and $b = 0.1830$ inch. In this initial design the cut-off frequencies ($f_1 = 17.5$ kMc and $f_2 = 55$ kMc) provide

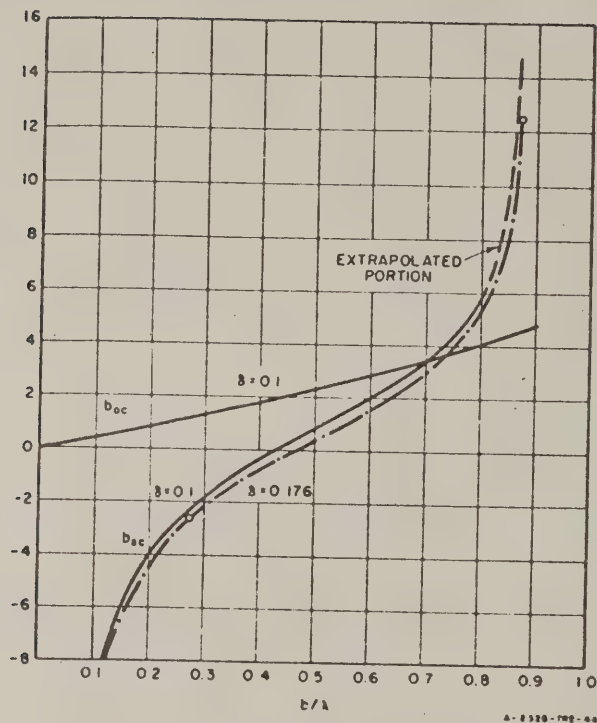


FIG. 12-7

GRAPH OF SUSCEPTANCES b_{sc} AND b_{oc} OF EQUIVALENT NETWORK OF FILTER I WITH NO LONGITUDINAL SLOTS

sufficient margin that seven filter sections give a calculated minimum insertion loss of 52 db at 20 kMc, and still greater insertion loss at 47 kMc, with resistive terminations.

In order to compensate for the effect of the longitudinal slots, the gap b' was reduced 35 percent from the above. This amount was estimated to be slightly more than sufficient, so that the gap of an experimental scale model of this filter described in Part E of this chapter could be easily adjusted by a milling operation, if needed.

3. DESIGN OF TRANSFORMING END SECTIONS

Impedance-transforming end sections (to keep the input VSWR low) were so designed for the filter that the slot width l , the dimension b , and

the capacitive gap b' are the same in the end sections as in the filter proper, thereby simplifying the filter construction

The design of such filter end sections is described in the book *Very High Frequency Techniques*.⁴ It is recommended there that the zero-frequency image admittance of the end sections be made equal to that of the middle sections of the filter, $y_I(0)$, and that the image phase constant of the end sections be 90 degrees at approximately $0.9 f_1$. The image admittance of the middle sections is thus transformed to an almost constant value throughout the major portion of the total pass band and the filter is well-matched when terminated in a conductance equal to $y_I(0)$.

Here, however, we have but one filter dimension to adjust in designing the end section and it is not possible to follow the above method exactly. Fortunately, a good match is required only in the specified pass band, 10-15.5 kMc, which is the upper portion of the total pass band. Figure 12-8 is a sketch of the variation with frequency of the image admittance, y_I , of the middle sections and y'_I of the end sections of the filter, normalized to the admittance, Y_b , of a parallel plate waveguide of height $b = 0.183$ inch.

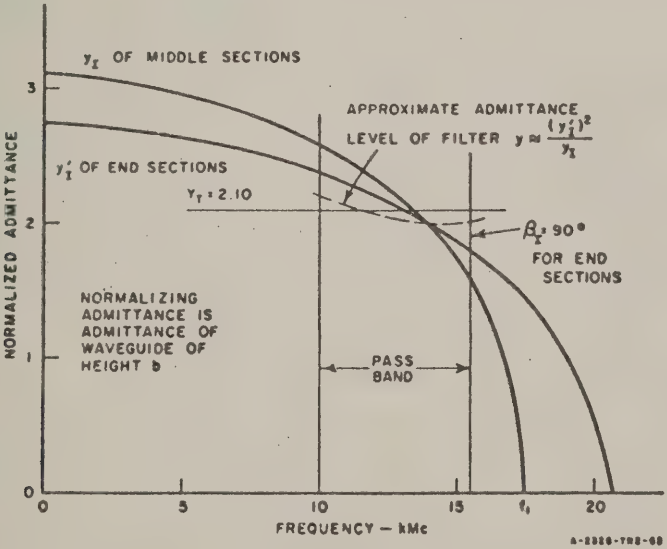


FIG. 12-8
SKETCH OF NORMALIZED IMAGE ADMITTANCE VS. FREQUENCY OF
MIDDLE AND END SECTIONS FOR FILTER I

Critical points are marked as well as the estimated optimum filter terminating admittance $Y_T = 2.10$. The height of the terminating waveguide, b_T , is determined from the mean admittance level, $b_T = b/Y_T = 0.183/2.10 = 0.0872$ inch. The effect of the longitudinal slots makes it necessary to decrease b_T from the value calculated here, as explained in a following section. Although the filter and input waveguide have low-frequency cut-offs which are not identical, the above approach to the impedance matching problem has given good results.

4. DESIGN OF STEPPED TRANSFORMERS

Finally, quarter-wavelength optimum stepped transformers⁵ were designed to match the filter terminating impedance to the rectangular waveguide. This is illustrated in Fig. 12-9 for Filter II, which is similar to Filter I in all respects except size and frequency band.

If each stepped transformer section has the same low-frequency cut-off, the transformation ratio Z_{in}/Z_{out} would be 4.30 for the initial design described above. However, since the first few transformer sections next to the filter are to be slotted, it can be seen that the decrease in the cut-off frequency of those steps tends to increase Z_{in}/Z_{out} . After taking this factor into account, as described below, Z_{in}/Z_{out} was increased to 4.78. (The value of 4.78 was not, however, used for the final filter design; this is explained in Sec. E, which describes adjustments of the design that evolved during testing.) The pass-band ratio for the transformer, on a guide-wavelength basis, was chosen as $p = 2.50$ in Cohn's notation;⁵ this allowed ample margin over the value of 2.17 for the specified pass band of the filter. Thus, the frequency limits are 9.7-16.0 kMc, and the center frequency is $f_0 = 12.6$ kMc. Maximum theoretical pass-band VSWR is 1.023 and five $\lambda_{go}/4$ steps are used.

5. EFFECT OF LONGITUDINAL SLOTS IN THE TRANSFORMERS AND TERMINATING WAVEGUIDE

It was assumed that the impedance Z_{og} of the longitudinally slotted guide is

$$Z_{og} = Z_0(\omega) / \sqrt{1 - (\lambda/\lambda_c)^2} \quad (12-8)$$

where $Z_0(\omega)$ is the impedance of the slotted waveguide at infinite frequency and λ_c is the cut-off wavelength of the slotted waveguide. Both $Z_0(\omega)$ and (λ/λ_c) are functions of the height of the steps, h_i , which is taken as the independent variable for the purpose of plotting curves of those quantities.

First $Z_0(\omega)$ is calculated for several values of $h < b$ by considering TEM propagation in the longitudinal direction. Since the line is uniform in the direction of propagation,

$$Z_0(\omega) = \frac{1}{vC_0} \quad (12-9)$$

where C_0 is the capacitance in farads per meter of the waveguide of width a meters, and v is the velocity of light in meters per second. The capacitance C_0 can be expressed as

$$C_0 = C_{pp} + C_d \quad (12-10)$$

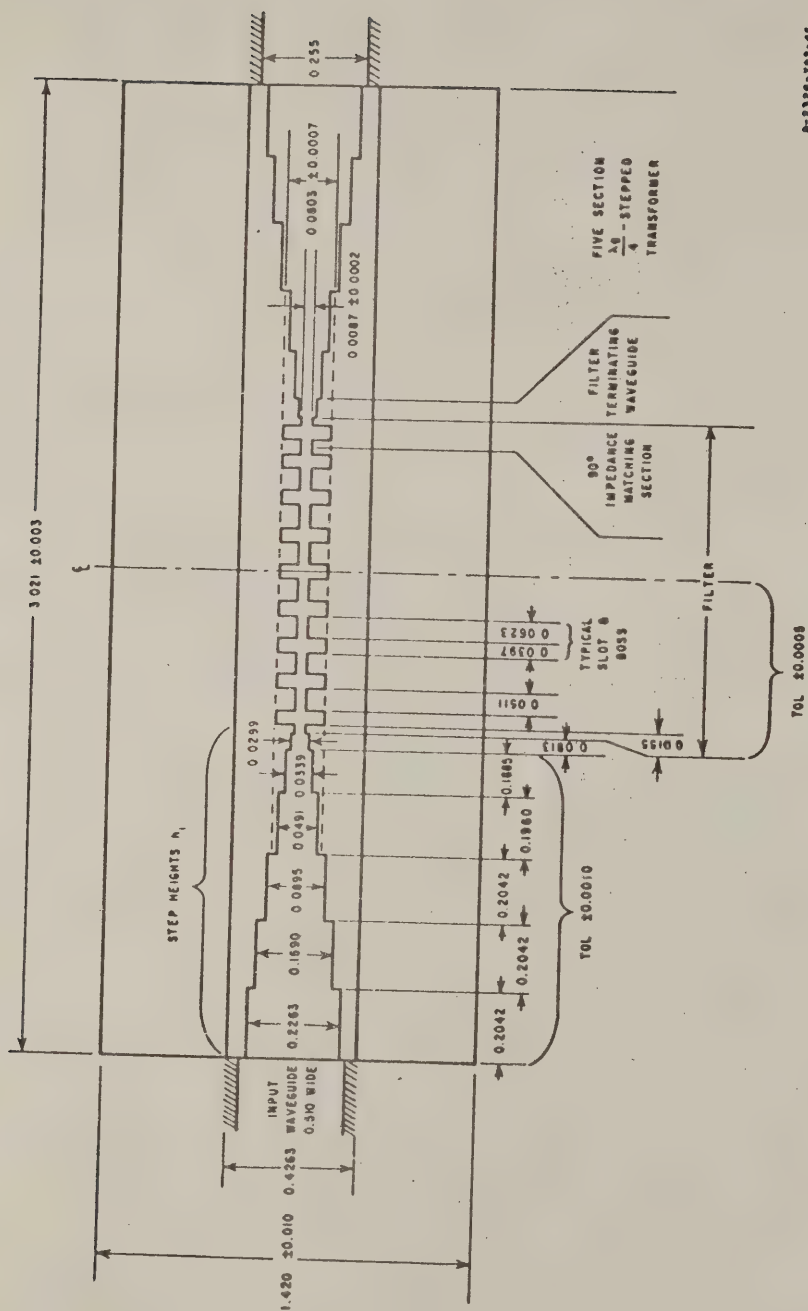
Here C_{pp} is the total parallel-plate capacitance of the longitudinal slots and ridges in the waveguide of width a and C_d is the total discontinuity capacitance of the $2n$ step discontinuities, which can be obtained from published curves.⁶

The cut-off wavelength, λ_c , of a rectangular waveguide with longitudinal slots is then calculated from the condition for transverse resonance for the values of h used above. For this calculation it is necessary to consider the change in the inductance as well as the change in the capacitance, since the transmission line is not uniform in this case. A low-frequency approach is entirely adequate, hence the capacitance per meter is C_0/a , where C_0 is given above, and the inductance per meter is

$$L_0 = \mu_0 \frac{(lb + l'b')}{l + l'} \quad (12-11)$$

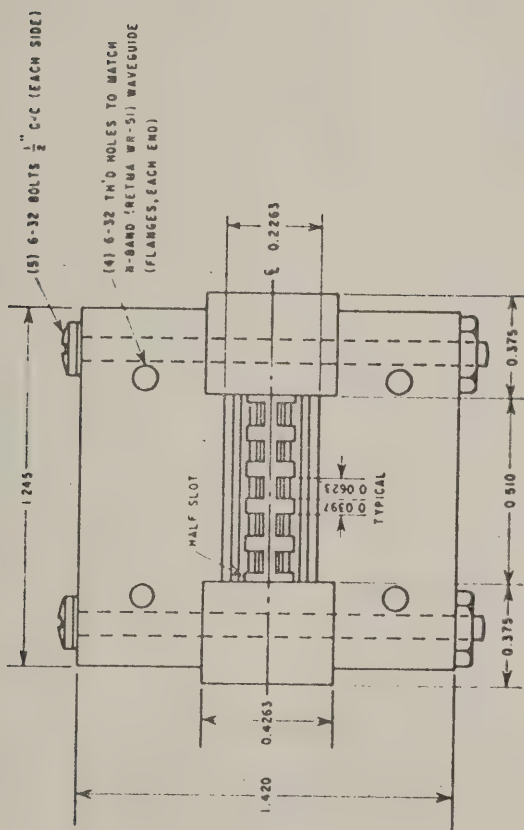
where μ_0 is the permeability of free space in henries per meter and l, l', b , and b' are given in meters. Here unit width is understood. A new phase velocity in the transverse direction is then calculated

$$v_p = 1/\sqrt{L_0 C_0/a} \quad (12-12)$$



8-2326-782-45

FIG. 12-9
SKETCH OF FILTER II GIVING DIMENSIONS



A-2326-TM2-48

FIG. 12-9 (Continued)
SKETCH OF FILTER II GIVING DIMENSIONS

The new cut-off wavelength is now

$$\lambda_c = 2a \left(\frac{v}{v_p} \right) \quad (12-13)$$

A graph of Z_{0g} vs. h is then made, using Eq. (12-8), and from this graph the step height, h_s , is obtained for each Z_{0g} of the stepped transformer, and also for the optimum filter terminating impedance, all as previously calculated. Also, new values of length, $\lambda_{gs}/4$, are calculated at the middle of the pass band for each slotted step from the new values of λ_c obtained above.

E. EXPERIMENTAL MODEL OF FILTER

1. DESCRIPTION

Because of a lack of signal sources giving full frequency coverage above 21 kMc, it was decided, as mentioned earlier, to build an enlarged scale model of Filter I in 1.872-inch-wide waveguide for operation at lower frequencies, and to test this experimental filter throughout its entire operating range. The experimental-filter frequency range is given in Table 12-2. After the experimental filter was adjusted as required, the specified filters were made by scaling the measured dimensions of the experimental filter. In order to permit the use of standard test equipment, two smooth waveguide tapers were constructed to match 1.872- by 0.872-inch standard waveguide to the 1.872- by 0.936-inch filter input waveguide. The experimental filter was made in three separate pieces--two stepped transformers and the filter proper.

TABLE 12-2
EXPERIMENTAL FILTER FREQUENCY RANGE

| PASS BAND | STOP BAND | INPUT AND OUTPUT WAVEGUIDES |
|---------------|----------------|-----------------------------|
| 4.0 - 6.2 kMc | 8.0 - 18.9 kMc | 1.872 × 0.936 inch I.D. |

2. ADJUSTMENT OF GAP FOR OPTIMUM PERFORMANCE IN PASS BAND

Initial tests on the scale model showed the cut-off frequency, f_1 , to be too close to the upper edge of the pass band. This is shown on Curve A of VSWR vs. frequency of Fig. 12-10(a), and Curve A of insertion-loss vs. frequency of Fig. 12-10(b). The important filter dimensions and

the filter performance for the initial test on the scale model are shown on Line A of Table 12-3. One can also see that the upper stop-band cut-off frequency, f_2 , is too low. It was decided to try first to obtain good performance in and around the pass band, and then extend the stop band. On this basis, the gap b' was judged to have been overcompensated. Consequently, the dimension b' was increased, yielding the results on Line B of Table 12-3 and Curves B of Fig. 12-10. It is seen that the pass-band VSWR is less than 1.4, and f_1 is well removed from the upper edge of the pass band.

Thus the design theory—which applies rigorously only to structures with transverse slots—has been shown experimentally to yield a good first approximation that can be easily improved by a minor adjustment of the gap dimension.

TABLE 12-3
STEPS IN THE DEVELOPMENT OF THE EXPERIMENTAL FILTER OF TABLE 12-2

| | FILTER DIMENSIONS (inches) | | | | CUT-OFF FREQUENCY (kMc) | | PASS BAND | | IMPEDANCE TRANSFORMATION RATIO OF TRANSFORMERS |
|----|-------------------------------|-------|--------|--------|----------------------------|-------|------------|-------------------|---|
| | b' | b | l | l' | f_1 | f_2 | VSWR | Insertion Loss | R |
| A) | 0.050 | 0.457 | 0.1456 | 0.2287 | 6.3 | ~15.4 | See Fig. 9 | < 0.9 | 4.78 |
| B) | 0.060 | 0.457 | 0.1456 | 0.2287 | 6.7 | ~15.4 | < 1.4 | not meas. | 4.78 |
| C) | 0.032 | 0.297 | 0.1456 | 0.2287 | 6.7 | ~20 | < 2.8 | < 1.4 | 4.78 |
| D) | 0.032 | 0.297 | 0.1456 | 0.2287 | 6.7 | ~21 | < 1.4 | < 0.45 | 8.11 |

3. ADJUSTMENT OF SLOT DEPTH TO EXTEND STOP BAND; CHANGE OF IMPEDANCE LEVEL

However, the data also show that the theory used breaks down as far as f_∞ and f_2 are concerned when longitudinal slots are added to the structure. It is believed that a TE_{11} or TM_{11} mode incident on the sections of the stepped transformer in which there are longitudinal slots can excite in these slots the horizontally polarized TE_{01} mode when slot height $b > \lambda/2$. In this case the TE_{01} slot mode can exist above about 13 kMc for the experimental filter as initially designed. The effect of the gap is analogous to that of longitudinal slots centered in the broad walls of a rectangular waveguide and is, therefore, negligible for this transmission mode. The periodicity caused by the transverse slots does form a filter structure but its first pass band falls in the desired stop band. This difficulty could probably be overcome by omitting the slots from the

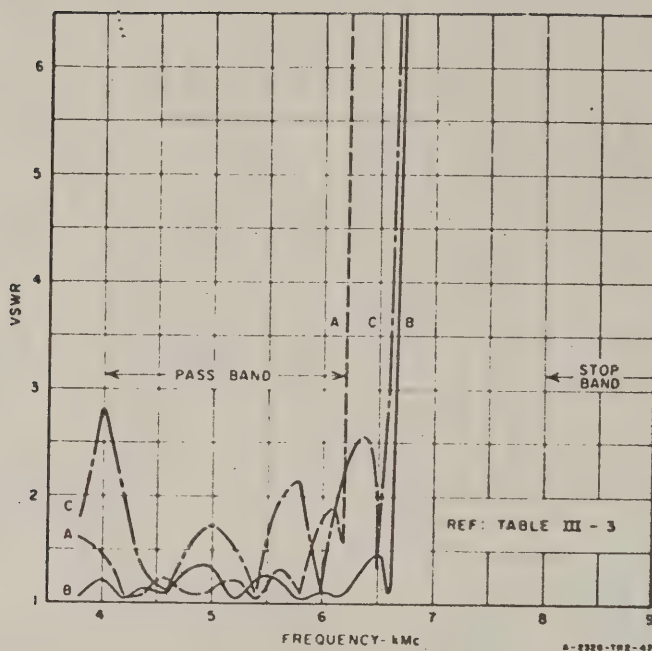


FIG. 12-10
MEASURED PERFORMANCE OF EXPERIMENTAL FILTER SHOWING
PROGRESSIVE DEVELOPMENT

region of the stepped transformers as was done in an earlier design,¹ thus preventing the TE_{11} and TM_{11} modes from being incident on the longitudinal slots in the filter. However, the structural complexity of the filter would be increased thereby, which would increase the manufacturing cost.

Appropriate steps indicated by the above discussion were then taken to extend the stop band. First the dimension b was reduced to 0.297 inch; the undesired slot-mode cut-off frequency was thus increased to 20 kMc. Then the dimension b' was reduced in order to maintain cut-off frequency f_1 constant. Here, again, the reduction in b' was made proportionally greater than the reduction in b so that the gap b' could be increased, if necessary, by a milling operation. As indicated on Line C of Table 12-3 and in Fig. 12-10(b), the cut-off frequency f_1 remained stationary and f_2 increased to approximately 20 kMc, while on the other hand, the pass-band

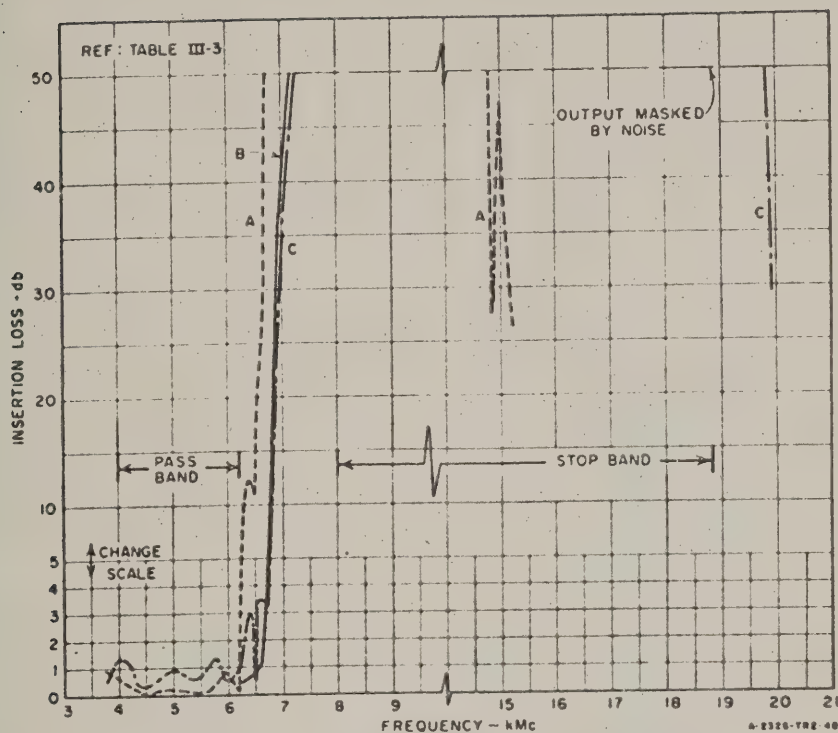


FIG. 12-10 (Continued)

MEASURED PERFORMANCE OF EXPERIMENTAL FILTER SHOWING PROGRESSIVE DEVELOPMENT

performance deteriorated. This deterioration of performance in the pass-band was expected, since the optimum filter terminating impedance was substantially reduced along with the reduction of dimensions b and b' , while the impedance transformers were not altered in any way. The next step was to redesign the transformers.

4. REDESIGN OF STEPPED TRANSFORMERS

Toward this end the following calculation, valid at low frequencies, was made. It was assumed that the change in the optimum filter terminating admittance, and hence the change in the transformation ratio, is proportional to $\sqrt{(C'/L')/(C/L)}$, where L and C are series inductance and shunt capacitance per section, respectively, and the prime stands for the new value of these quantities. It is not necessary, here, to know L and C

explicitly, but merely to recognize that, to a good approximation, C is inversely proportional to b' and L is directly proportional to b . We now have, using the values of b and b' on Lines B and C of Table 12-3,

$$\frac{Y'_T}{Y_T} = \sqrt{\frac{b_B b'_B}{b_C b'_C}} = \sqrt{\frac{0.457 \times 0.060}{0.297 \times 0.032}} = 1.698. \quad (12-14)$$

Here Y_T is the originally calculated filter terminating admittance for which the first stepped transformer was designed, and Y'_T is the new value. The new transformation ratio is $R = 1.698 \times 4.78 = 8.11$.

New values of impedance ratios were calculated for each step of the transformer which consisted, as before, of five $\lambda_g/4$ sections. It is to be noted that the complete filter assembly, as indicated in Fig. 12-9(a), ends on each side in the first $\lambda_g/4$ section of the transformer, not in the input waveguide.

5. ADJUSTMENT OF LENGTH OF FILTER-TERMINATING WAVEGUIDE SECTIONS

Instead of connecting the filter directly to the stepped transformers, a section of filter-terminating waveguide approximately equal in length to a transformer section was built integrally into the end of each stepped transformer. Under matched conditions these should have no effect on the filter performance, but if slight mismatches did exist in the transformers and in the filter, the length of these sections could be adjusted to reduce the VSWR peaks in the pass band. Accordingly, these filter-terminating sections were shortened progressively during testing until the VSWR in the upper half of the pass band was as low as could be achieved by this adjustment. The effect of this adjustment on the VSWR peak in the lower portion of the pass band was smaller, but was also beneficial. These results are shown in Fig. 12-11, and are summarized on Line D of Table 12-3.

The stepped transformers were tested separately by connecting them back to back after the above adjustment was made. The VSWR pattern (not shown) indicated that the transformer bandwidth is close to the design value, while the maximum VSWR is 1.15 for two transitions. A single transition would thus have a maximum VSWR of about 1.07. It is felt that this is not an unreasonable departure from the design value of 1.023, because the theory is strictly applicable to transformer sections all having the same cut-off frequency.

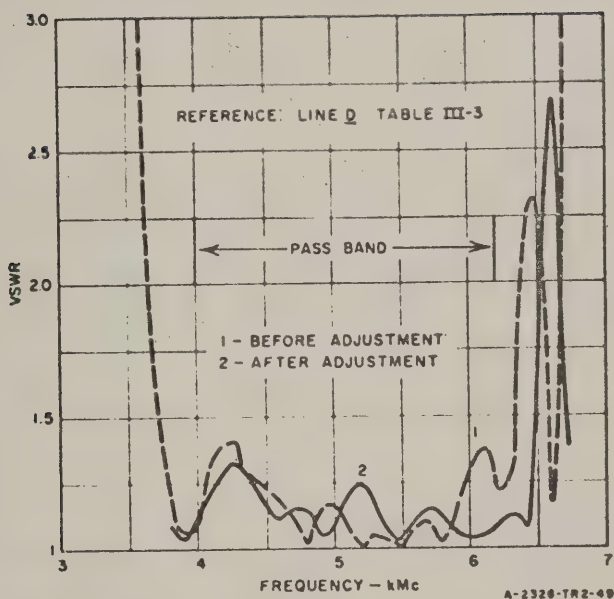


FIG. 12-11
MEASURED VSWR OF FINAL EXPERIMENTAL FILTER DESIGN
SHOWING IMPROVEMENT OBTAINED BY REDUCING
TERMINATING GUIDE LENGTHS BETWEEN FILTER
AND EACH TRANSFORMER

6. PERFORMANCE OF SCALE MODEL WITH HIGHER MODES INCIDENT

The solid line in Fig. 12-12 is the insertion loss for the filter when the filter and terminating waveguides are lined up in the normal fashion, while the vertical dashed lines ending in a circle indicate sharp responses (predominantly in the transition region) that occur only when higher modes are strongly excited. These higher modes were excited by rotating the filter slightly on its axis and by offsetting the filter transversely between the terminating waveguides until a maximum response was obtained. It is seen that the filter, which was designed to suppress these higher modes as well as the dominant mode, does so by more than the desired 40 db throughout the specified stop band.

F. FILTERS I AND II

Final models of Filter I for the 10-15.5 kMc band (stop band 20 to 47 kMc) and of Filter II for the 15-21 kMc band (stop band 30 to 63 kMc) were designed by measuring the experimental model directly and then using an appropriate scale factor. Because of lack of test equipment, these final models could be tested in only part of their operating range and these results are shown in Figs. 12-13 and 12-14.

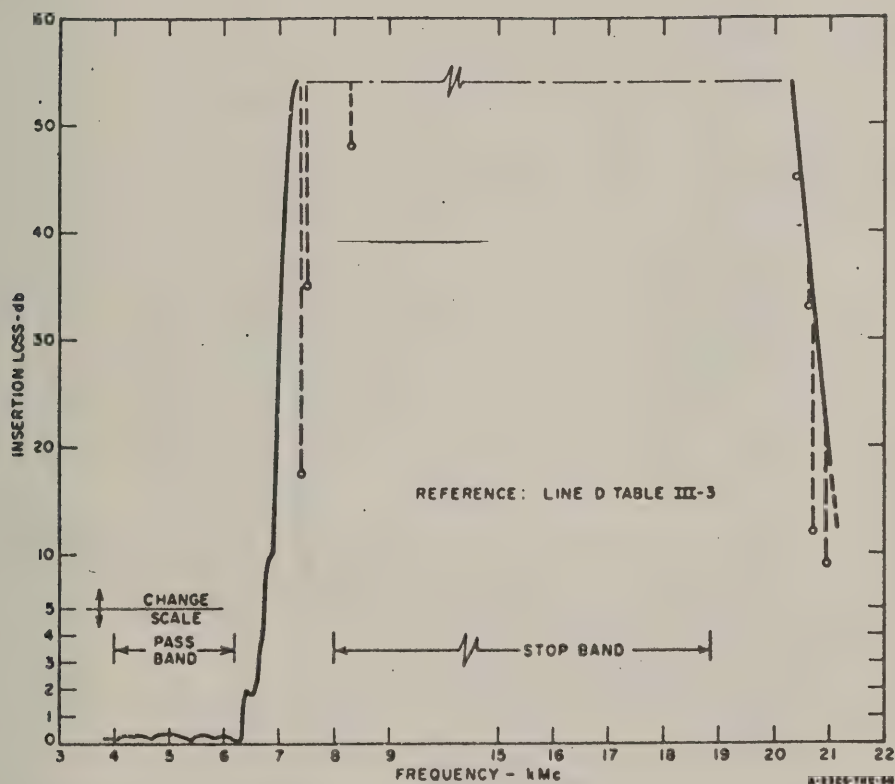


FIG. 12-12

MEASURED PERFORMANCE OF EXPERIMENTAL FILTER SHOWING EFFECT
OF ARTIFICIALLY GENERATED HIGHER MODES

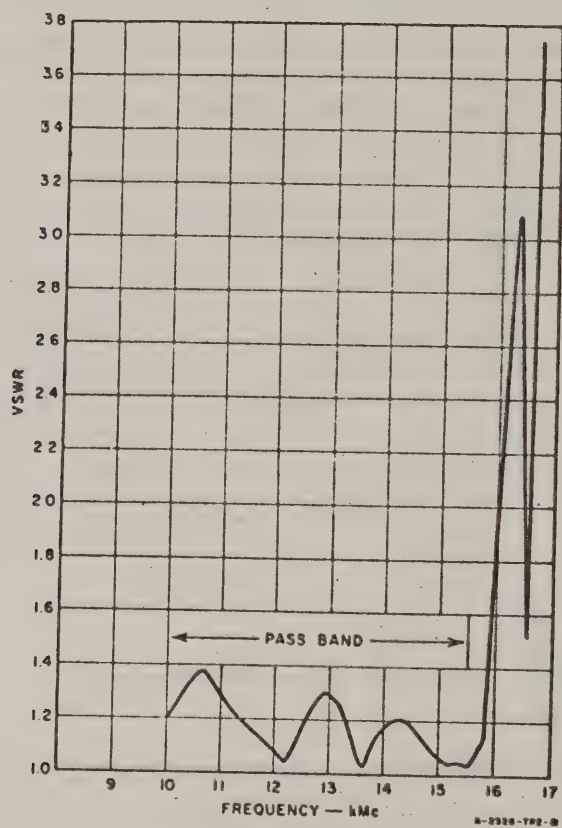


FIG. 12-13
MEASURED VSWR OF FILTER I

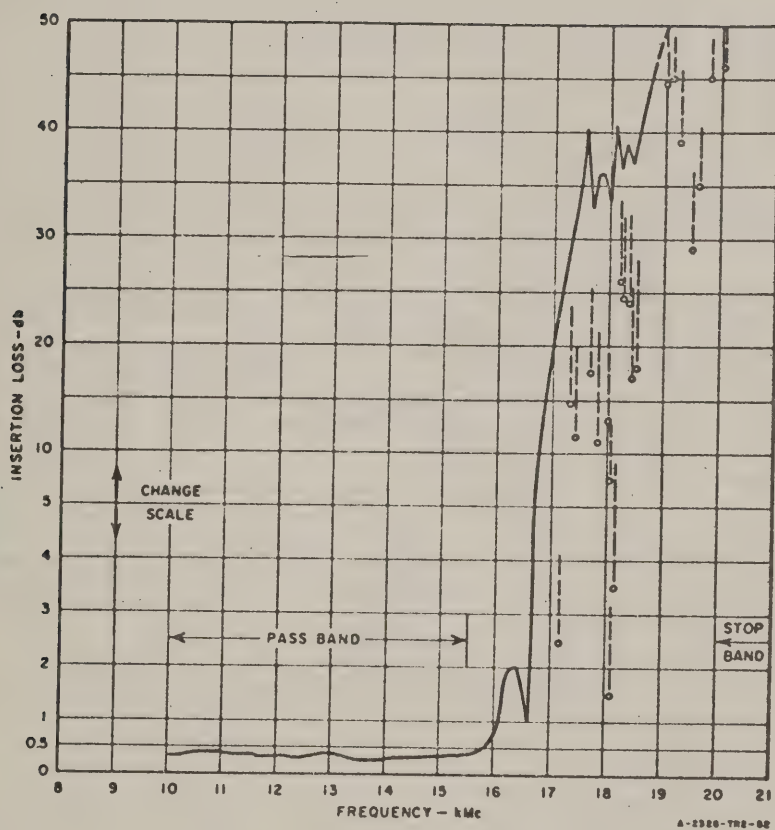


FIG. 12-13 (Continued)
 MEASURED PERFORMANCE OF FILTER I SHOWING EFFECT
 OF ARTIFICIALLY GENERATED HIGH MODES

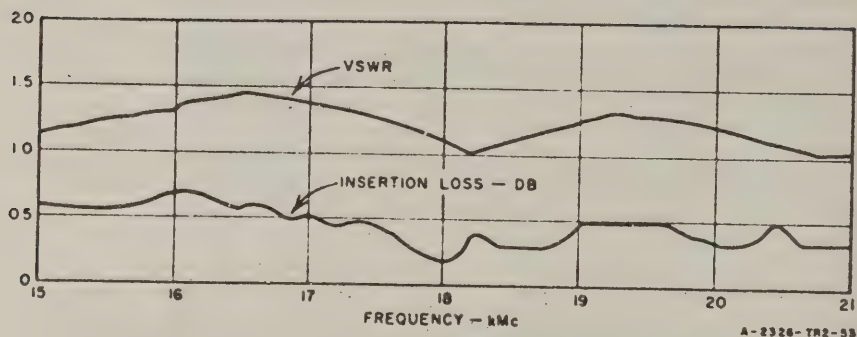


FIG. 12-14
MEASURED PERFORMANCE OF FILTER II

REFERENCES

1. S. B. Cohn, O. Heinz, B. M. Schiffman, E. M. T. Jones, J. K. Shimizu, and F. S. Coale, "Research on Design Criteria for Microwave Filters," Final Report, SRI Project 1331, Contract DA 36-039 SC-64625, Stanford Research Institute, Menlo Park, California (June 1957).
2. N. Marcuvitz, *Waveguide Handbook*, Vol. 10, Radiation Laboratory Series, Massachusetts Institute of Technology, pp. 336-350, (McGraw-Hill Book Company, Inc., New York, New York 1951).
3. S. B. Cohn, "A Theoretical and Experimental Study of a Waveguide Filter Structure" Technical Report No. 39, Cruft Laboratory, Harvard University, Cambridge, Massachusetts (April 25, 1948). This is partially covered in two Proc. IRE articles: Vol. 37, pp. 651-656, June 1949, and Vol. 38, pp. 799-803, July 1950.
4. Staff Radio Research Laboratory, Harvard University, *Very High-Frequency Techniques*, Vol. II, pp. 666-669, (McGraw-Hill Book Company, Inc., New York, New York, 1947).
5. S. B. Cohn, "Optimum Design of Stepped Transmission-Line Transformers," Proc. IRE 43, 4, Part 1, pp. 16-21, (April 1955).
6. J. R. Whinnery and H. W. Jamieson, "Equivalent Circuits for Discontinuities in Transmission Lines," Proc. IRE 32, pp. 98-114, (February 1944).

CHAPTER 13

EXTENSION OF TABLE FOR TCHEBYSCHIEFF AND MAXIMALLY FLAT LOW-PASS-FILTER ELEMENT VALUES

A. GENERAL

Louis Weinberg has published extensive tables of normalized element values for dissipationless Tchebyscheff and maximally flat filters for various termination ratios and amplitudes of Tchebyscheff pass-band ripple.^{1,2} For microwave applications, one is usually interested only in cases having termination ratios such that the reflection loss in the pass band is minimum, i.e., for the maximally flat filters there is no reflection loss at $\omega = 0$, and for the Tchebyscheff filters the reflection loss falls to zero at the minimum point of each ripple of pass-band attenuation. Weinberg's tables do not cover this minimum reflection case for Tchebyscheff designs having less than $\frac{1}{2}$ db pass-band attenuation ripple except for some cases where the number of reactive elements is odd. Since minimum reflection designs having less than $\frac{1}{2}$ db of ripple are of considerable interest for microwave filter design, element values were calculated for nondissipative minimum-reflection designs with 0.01, 0.1, and 0.2 db ripple corresponding to VSWR ripples of 1.10, 1.36, and 1.54, respectively. These element values were calculated by the method outlined in Fig. 2.2 of Ref. 3, and are presented in Table 13-1. Weinberg's element values for the 0.5, 1.0, 2.0, and 3.0 ripple cases are also included, by courtesy of Dr. Weinberg. His data for the minimum-loss, maximally flat case are presented in Table 13-2 for completeness.

B. USE OF THE TABLES

As illustrated in Figs. 13-1 and 13-2, the element values represent alternately *shunt* capacitance and *series* inductance. The load resistance next to Element 1 is always one ohm. If the circuit starts out with a shunt capacitance $C_1 = g_1$ next to the one-ohm load resistance, one circuit is obtained, while if the circuit is chosen to start out with a series inductance, $L_1 = g_1$, next to the one-ohm load, the *dual* circuit is obtained. This is illustrated in Figs. 13-1 and 13-2 for the case of $n = 4$. (Applying duality to the voltage generator and resistor r in Fig. 13-1 will result in a current generator with a conductance in parallel. However,

TABLE 13-1
ELEMENT VALUES FOR CHEBYSHEFF FILTERS

| VALS (ω) | F_1 | F_2 | F_3 | F_4 | F_5 | F_6 | F_7 | F_8 | F_9 | F_{10} | F_{11} | F_{12} |
|----------------------|--------|--------|--------|--------|--------|--------|--------|--------|--------|----------|----------|----------|
| 0.01 db ripple | | | | | | | | | | | | |
| 1 | 0.0960 | | | | | | | | | | | 1.0000 |
| 2 | 0.4498 | 0.4077 | | | | | | | | | | 0.9084 |
| 3 | 0.6291 | 0.5702 | 0.6291 | | | | | | | | | 1.0000 |
| 4 | 0.7120 | 1.2003 | 1.3232 | 0.6476 | | | | | | | | 0.9084 |
| 5 | 0.7513 | 1.3049 | 1.5713 | 1.3049 | 0.7583 | | | | | | | 1.0000 |
| 6 | 0.7813 | 1.3600 | 1.6986 | 1.5709 | 1.4970 | 0.7998 | | | | | | 0.9084 |
| 7 | 0.7969 | 1.3924 | 1.7401 | 1.6333 | 1.7401 | 1.3924 | 0.7969 | | | | | 1.0000 |
| 8 | 0.8072 | 1.4130 | 1.7624 | 1.6433 | 1.8029 | 1.4130 | 1.5254 | 0.7333 | | | | 0.9084 |
| 9 | 0.8144 | 1.4270 | 1.8043 | 1.7120 | 1.9057 | 1.7120 | 1.8044 | 1.4270 | 0.8144 | | | 1.0000 |
| 10 | 0.8196 | 1.4369 | 1.8192 | 1.7311 | 1.9362 | 1.7500 | 1.9055 | 1.6527 | 1.5817 | 0.7446 | | 0.9084 |
| 0.1 db ripple | | | | | | | | | | | | |
| 1 | 0.3052 | | | | | | | | | | | 1.0000 |
| 2 | 0.8430 | 0.6220 | | | | | | | | | | 0.7378 |
| 3 | 1.0312 | 1.1674 | 1.0312 | | | | | | | | | 1.0000 |
| 4 | 1.0880 | 1.3061 | 1.7703 | 0.8180 | | | | | | | | 0.7378 |
| 5 | 1.1468 | 1.3712 | 1.9750 | 1.3712 | 1.1468 | | | | | | | 1.0000 |
| 6 | 1.1681 | 1.4030 | 2.0562 | 1.5770 | 1.9029 | 0.8638 | | | | | | 0.7378 |
| 7 | 1.1811 | 1.4239 | 2.0968 | 1.7733 | 2.0968 | 1.4239 | 1.1811 | | | | | 1.0000 |
| 8 | 1.1897 | 1.4346 | 2.1199 | 1.9039 | 2.1699 | 1.5640 | 1.9444 | 0.8778 | | | | 0.7378 |
| 9 | 1.1956 | 1.4425 | 2.1345 | 1.9467 | 2.2053 | 1.6167 | 2.1345 | 1.4425 | 1.1956 | | | 1.0000 |
| 10 | 1.1999 | 1.4483 | 2.1444 | 1.9705 | 2.2253 | 1.6438 | 2.2046 | 1.5821 | 1.9628 | 0.8853 | | 0.7378 |
| 0.2 db ripple | | | | | | | | | | | | |
| 1 | 0.4342 | | | | | | | | | | | 1.0000 |
| 2 | 1.0378 | 0.6745 | | | | | | | | | | 0.6499 |
| 3 | 1.2275 | 1.1525 | 1.2275 | | | | | | | | | 1.0000 |
| 4 | 1.3928 | 1.2844 | 1.8761 | 0.8668 | | | | | | | | 0.6499 |
| 5 | 1.3794 | 1.3370 | 2.1600 | 1.3370 | 1.3194 | | | | | | | 1.0000 |
| 6 | 1.3598 | 1.3632 | 2.2394 | 1.4555 | 2.0974 | 0.8838 | | | | | | 0.6499 |
| 7 | 1.3722 | 1.3781 | 2.2754 | 1.5091 | 2.2754 | 1.3781 | 1.3722 | | | | | 1.0000 |
| 8 | 1.3694 | 1.3875 | 2.2963 | 1.5217 | 2.3413 | 1.4975 | 2.1349 | 0.8972 | | | | 0.6499 |
| 9 | 1.3600 | 1.3938 | 2.3093 | 1.5340 | 2.3728 | 1.5340 | 2.3093 | 1.3938 | 1.3600 | | | 1.0000 |
| 10 | 1.3503 | 1.3983 | 2.3181 | 1.5417 | 2.3994 | 1.5556 | 2.3720 | 1.5066 | 2.1514 | 0.9034 | | 0.6499 |
| 0.5 db ripple | | | | | | | | | | | | |
| 1 | 0.6986 | | | | | | | | | | | 1.0000 |
| 2 | 1.4029 | 0.7071 | | | | | | | | | | 0.50402 |
| 3 | 1.5963 | 1.0967 | 1.5963 | | | | | | | | | 1.0000 |
| 4 | 1.6703 | 1.1926 | 2.3661 | 0.8419 | | | | | | | | 0.50402 |
| 5 | 1.7058 | 1.2296 | 2.5498 | 1.2296 | 1.7058 | | | | | | | 1.0000 |
| 6 | 1.7254 | 1.2479 | 2.6064 | 1.3137 | 2.4758 | 0.8676 | | | | | | 0.50402 |
| 7 | 1.7372 | 1.2583 | 2.6381 | 1.3444 | 2.6381 | 1.2583 | 1.7372 | | | | | 1.0000 |
| 8 | 1.7451 | 1.2637 | 2.6564 | 1.3590 | 2.6964 | 1.3389 | 2.5093 | 0.8796 | | | | 0.50402 |
| 9 | 1.7504 | 1.2690 | 2.6678 | 1.3673 | 2.7239 | 1.3673 | 2.6678 | 1.2690 | 1.7504 | | | 1.0000 |
| 10 | 1.7543 | 1.2723 | 2.6754 | 1.3725 | 2.7392 | 1.3804 | 2.7231 | 1.3485 | 2.5239 | 0.8862 | | 0.50402 |
| 1.0 db ripple | | | | | | | | | | | | |
| 1 | 1.0377 | | | | | | | | | | | 1.0000 |
| 2 | 1.8219 | 0.6850 | | | | | | | | | | 0.37598 |
| 3 | 2.0236 | 0.9941 | 2.0236 | | | | | | | | | 1.0000 |
| 4 | 2.0991 | 1.0644 | 2.8111 | 0.7892 | | | | | | | | 0.37598 |
| 5 | 2.1349 | 1.0911 | 3.0009 | 1.0911 | 2.1349 | | | | | | | 1.0000 |
| 6 | 2.1546 | 1.1041 | 3.0634 | 1.1218 | 2.9367 | 0.8101 | | | | | | 0.37598 |
| 7 | 2.1644 | 1.1116 | 3.0934 | 1.1736 | 3.0934 | 1.1116 | 2.1644 | | | | | 1.0000 |
| 8 | 2.1744 | 1.1161 | 3.1107 | 1.1839 | 3.1488 | 1.1839 | 2.9685 | 0.8375 | | | | 0.37598 |
| 9 | 2.1797 | 1.1192 | 3.1215 | 1.1897 | 3.1747 | 1.1897 | 3.1215 | 1.1192 | 2.1797 | | | 1.0000 |
| 10 | 2.1836 | 1.1213 | 3.1286 | 1.1933 | 3.1890 | 1.1900 | 3.1738 | 1.1763 | 2.9824 | 0.8210 | | 0.37598 |
| 2.0 db ripple | | | | | | | | | | | | |
| 1 | 1.5296 | | | | | | | | | | | 1.0000 |
| 2 | 2.4881 | 0.6075 | | | | | | | | | | 0.24418 |
| 3 | 2.7107 | 0.8327 | 2.7107 | | | | | | | | | 1.0000 |
| 4 | 2.7925 | 0.8896 | 3.6963 | 0.6819 | | | | | | | | 0.24418 |
| 5 | 2.8319 | 0.8985 | 3.7427 | 0.8985 | 2.8319 | | | | | | | 1.0000 |
| 6 | 2.8521 | 0.9071 | 3.7667 | 0.9393 | 3.7151 | 0.6964 | | | | | | 0.24418 |
| 7 | 2.8655 | 0.9119 | 3.7780 | 0.9535 | 3.7780 | 0.9119 | 2.8655 | | | | | 1.0000 |
| 8 | 2.8733 | 0.9151 | 3.7848 | 0.9605 | 3.8335 | 0.9510 | 3.7477 | 0.7014 | | | | 0.24418 |
| 9 | 2.8790 | 0.9171 | 3.7956 | 0.9643 | 3.8598 | 0.9643 | 3.9056 | 0.9171 | 2.8790 | | | 1.0000 |
| 10 | 2.8831 | 0.9186 | 3.8128 | 0.9667 | 3.8743 | 0.9704 | 3.9589 | 0.9554 | 3.7619 | 0.7040 | | 0.24418 |
| 3.0 db ripple | | | | | | | | | | | | |
| 1 | 1.9653 | | | | | | | | | | | 1.0000 |
| 2 | 3.1033 | 0.5339 | | | | | | | | | | 0.17215 |
| 3 | 3.3487 | 0.7117 | 3.3487 | | | | | | | | | 1.0000 |
| 4 | 3.4389 | 0.7483 | 4.1671 | 0.5920 | | | | | | | | 0.17215 |
| 5 | 3.4817 | 0.7638 | 4.5381 | 0.7638 | 3.4817 | | | | | | | 1.0000 |
| 6 | 3.5045 | 0.7685 | 4.6061 | 0.7929 | 4.4641 | 0.6033 | | | | | | 0.17215 |
| 7 | 3.5182 | 0.7723 | 4.6386 | 0.8019 | 4.6386 | 0.7723 | 3.5182 | | | | | 1.0000 |
| 8 | 3.5277 | 0.7745 | 4.6575 | 0.8089 | 4.6990 | 0.8018 | 4.4990 | 0.6073 | | | | 0.17215 |
| 9 | 3.5340 | 0.7760 | 4.6692 | 0.8118 | 4.7272 | 0.8118 | 4.6692 | 0.7760 | 3.5340 | | | 1.0000 |
| 10 | 3.5384 | 0.7771 | 4.6768 | 0.8136 | 4.7425 | 0.8164 | 4.7260 | 0.8051 | 4.5142 | 0.6091 | | 0.17215 |

Thevenin's theorem may be applied to give the voltage generator and series resistor as shown in Fig. 13-2.) Both circuits will have the same response. The generator resistance, r or r' , is given in the column on the right in Table 13-1. Note that the value given in the table is either r or $1/r'$, depending on which of the two dual circuits is chosen, i.e., whether $g_1 = C_1$ or $g_1 = L'_1$, respectively. For the Tchebyscheff case the element values given will yield a design with an equal-ripple pass-band extending from $\omega = 0$ to $\omega = 1$. Above $\omega = 1$ the attenuation rises monotonically. In the maximally flat case the attenuation is zero at $\omega = 0$ and has a maximum number of derivatives equal to zero at that point also. For the element values in Table 13-2, the 3 db point occurs at $\omega = 1$.

Given the element values for a suitable low-pass prototype filter, the methods of Ref. 3 can be used for obtaining a microwave, band pass filter design with pass band ripple properties similar to those of the prototype. The element values given in Tables 13-1 and 13-2 correspond exactly to the g_i values defined in Fig. 2.2 of Ref. 3. The circuit form with unprimed termination resistance r and with capacitance $C_1 = g_1$ next to the $R = 1$ ohm termination is the proper one to use with the design equations of Ref. 3.

TABLE 13-2
ELEMENT VALUES FOR MAXIMALLY FLAT FILTERS

| VALUE OF n | R_1 | R_2 | R_3 | R_4 | R_5 | R_6 | g_7 | g_8 | g_9 | g_{10} |
|--------------|--------|--------|-------|--------|--------|--------|------------------------------|--------|--------|----------|
| 1 | 2.000 | | | | | | For this case $r = 1/r' = 1$ | | | |
| 2 | 1.414 | 1.414 | | | | | | | | |
| 3 | 1.000 | 2.000 | 1.000 | | | | | | | |
| 4 | 0.7654 | 1.848 | 1.848 | 0.7654 | | | | | | |
| 5 | 0.6180 | 1.618 | 2.000 | 1.618 | 0.6180 | | | | | |
| 6 | 0.5176 | 1.414 | 1.932 | 1.932 | 1.414 | 0.5176 | | | | |
| 7 | 0.4450 | 1.247 | 1.802 | 2.000 | 1.802 | 1.247 | 0.4450 | | | |
| 8 | 0.3902 | 1.111 | 1.663 | 1.962 | 1.962 | 1.663 | 1.111 | 0.3902 | | |
| 9 | 0.3473 | 1.000 | 1.532 | 1.879 | 2.000 | 1.879 | 1.532 | 1.000 | 0.3473 | |
| 10 | 0.3129 | 0.9080 | 1.414 | 1.782 | 1.975 | 1.975 | 1.782 | 1.414 | 0.9080 | 0.3129 |

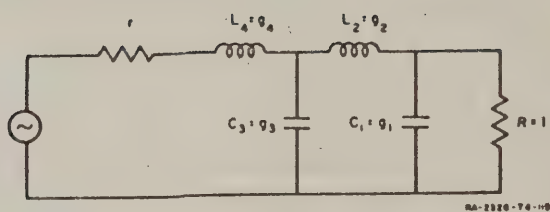


FIG. 13-1
A LOW-PASS FILTER HAVING $n = 4$ REACTIVE ELEMENTS

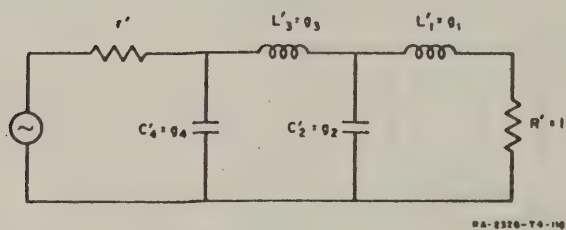


FIG. 13-2
A FILTER CIRCUIT WHICH CAN BE OBTAINED FROM THAT
IN FIG. 13-1 BY USE OF THE PRINCIPLE OF DUALITY

REFERENCES

1. L. Weinberg, "Network Design by Use of Modern Synthesis Techniques and Tables," Tech. Memo. 427, Hughes Aircraft Company, Research Laboratories, Culver City, California (April 1956); also *Proceedings of the National Electronics Conferences*, Vol. 12, (1956).
2. L. Weinberg, "Additional Tables for Design of Optimum Ladder Networks," Tech. Memo. 434, Hughes Aircraft Company, Research Laboratories, Culver City, California (31 August 1946).
3. S. B. Cohn, et al, "Research on Design Criteria for Microwave Filters," SRI Project 1331, Contract DA-36-039 SC-64625, Stanford Research Institute, Menlo Park, California (June 1957).

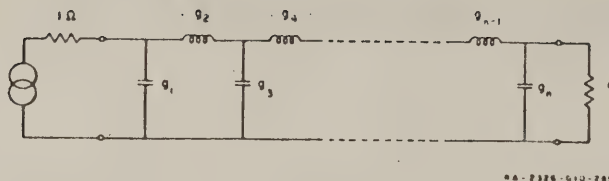
PHASE-SHIFT AND TIME-DELAY RESPONSE OF MICROWAVE NARROW-BAND FILTERS*

A. GENERAL

The phase shift response of a transmission circuit is an important consideration in the design of communication and radar systems. In order to avoid overshoot, ringing, and broadening of signal pulses, the phase shift vs frequency characteristic must be closely linear over the bandwidth of the signal spectrum.¹ Variation of the insertion loss or gain of the transmission system over this bandwidth will also introduce distortion, but usually nonlinearity of the phase-shift characteristic is far more serious in microwave systems.

The phase shift response of a frequency filter cannot be linear at all frequencies. In fact, with the more commonly used types of filters, there is considerable deviation from linearity even inside the pass band. However, if the signal bandwidth is very small compared to the width of the pass band, the deviation from linearity of the phase characteristic will be small over the width of the signal spectrum. It is only in cases where the signal occupies an appreciable part of the pass band that distortion due to phase curvature is important. For that reason, in microwave applications the phase characteristic is usually only of concern in narrow-band band-pass filters, whose bandwidths are not much wider than that of the signal spectrum. Consequently, this chapter is primarily concerned with the most commonly used microwave narrow-band filter, the multiple-coupled-resonator filter designed to have either a maximally flat or equal-ripple insertion-loss response.^{2,3,4} In addition, consideration is given to the maximally flat time-delay response,^{5,6} which may also be achieved in a multiple-coupled-resonator structure. The design data for all of these response functions are available in low-pass prototype-filter form^{2,3,4,6} as shown in Fig. 14-1. Thus, the phase-shift calculations given in this chapter may be applied to low-pass, high-pass, and band-rejection filters, as well as to band-pass filters. In fact, for simplicity the graphical data presented here are plotted against the frequency parameter of the low pass prototype, but are easily applied to narrow-band band-pass filters by means of formulas provided.

* This material has been published. See S. B. Cohn, "Phase-Shift and Time-Delay Response of Microwave Narrow-Band Filters," *The Microwave Journal* 3, pp. 47-51 (October 1960).



GA-2326-G10-785

FIG. 14-1
LOW-PASS PROTOTYPE FILTER

Although microwave signal spectra are usually narrow relative to their center frequencies, there are increasing applications utilizing pulse lengths of the order of a millimicrosecond where the relative width of the spectrum is large. For such cases, approximate synthesis procedures developed by Matthaei^{7,8,9} may be used in designing the necessary wide-band filters. It is not known at this time whether the prototype-low-pass-filter phase-shift data contained in this chapter may be applied to these wide-band filters, since they would be expected to deviate strongly from non-minimum-phase behavior.

It was once generally believed that multiple-resonator filter designs based on a nondissipative prototype having maximally flat insertion loss response are preferable to ones having equal-ripple response. It has been demonstrated, however, that the nondissipative equal-ripple prototype design (with ripples of about 0.01 to 0.1 db) is superior in a number of respects. For a given number of elements and given stop-band bandwidth it yields better selectivity and lower pass band dissipation loss.^{10,11} Furthermore, the coupling elements are more nearly uniform than with the maximally flat design so that structural errors between their relative sizes are likely to be smaller.

Thus, from standpoints of selectivity, dissipation loss, and practical design, the equal-ripple response is superior to the maximally flat insertion-loss response. However, it is still generally believed that the maximally flat insertion-loss filter provides a more linear phase characteristic than the equal-ripple filter, so that the former would be preferred where distortion might be a problem. In order to determine whether this is indeed true, a quantitative comparison of various five-element filters was made. The results show that in usual applications where the purpose of the filter is to provide isolation between channels,

and not to limit the bandwidth of the signal spectrum, the maximally flat insertion loss filter is actually likely to be inferior to the equal-ripple filter. In less usual applications, where the filter's function is to decrease the bandwidth of the signal spectrum, so that the phase characteristic near and beyond the 3-db points is important, both types of response would usually give poor results, with the equal-ripple response the inferior of the two.

It must be emphasized that the data and conclusions given in this chapter apply only to five-element filters. It is believed, however, that similar performance will result with other numbers of elements, although quantitative values will be different. Therefore, in applications requiring linear phase shift and numbers of elements other than five, it is definitely worthwhile to carry out calculations like those in this chapter to see which response function is most suitable. The formulas given in Sec. D will make such calculations straightforward.

The maximally flat time-delay filter offers a phase characteristic greatly superior to that of the equal-ripple and maximally flat insertion-loss filters, but has a number of disadvantages that preclude its use in most cases: (1) Its insertion-loss response (in decibels) vs frequency approximates a parabolic curve, so that its VSWR increases rapidly as f deviates from the center frequency, f_0 . Thus over most of its 3-db bandwidth the VSWR and reflection coefficient are high. As a result, reflection interactions with a slightly mismatched load or generator may seriously affect the otherwise good phase-shift response of this type of filter. (2) For a given selectivity, more elements are needed. In fact, no matter how many elements are used, this type of filter cannot provide greater selectivity than a parabolic insertion-loss-response curve. (3) The multiple resonator structure is highly unsymmetrical, with a very large variation in the coupling elements from one end to the other. This large variation increases the difficulty in the design, and makes values of the couplings more likely to be in error relative to each other. The only application for which the maximally flat time-delay filter may be preferable is one where the filter is intended to reduce the spectrum bandwidth without causing overshoot or ringing. The excellent linearity of the phase function even beyond the 3-db points makes this filter well suited for this purpose.

B. TIME-DELAY AND PHASE SHIFT RELATIONSHIP

The insertion loss in decibels of a filter operated between equal-resistance terminations is defined as follows in terms of the quantities shown in Fig. 14-2.

$$L = 20 \log_{10} \left[\frac{V_g}{2V_L} \right] \quad (14-1)$$

The insertion phase shift of the filter is defined as

$$\phi = \angle \left(\frac{V_g}{V_L} \right) = \tan^{-1} \frac{\text{Im}(V_g/V_L)}{\text{Re}(V_g/V_L)} \quad (14-2)$$

For ϕ in radians, the time delay (i.e., group delay) in seconds of a signal passing through the filter from source to load is

$$t_d = \frac{d\phi}{d\omega} \quad (14-3)$$

where ω is the angular frequency $2\pi f$ in radians per second.

If $d\phi/d\omega$ is not constant over the bandwidth of the signal spectrum (i.e., if ϕ vs ω is not linear), the time delay will vary over different portions of the spectrum, and distortion will result. Thus, a constant time delay over the spectrum width is necessary for distortionless transmission. In comparing different filters, the amount of deviation from constant time delay over the signal bandwidth provides a good indication of probable performance. Of course, insertion-loss variation over the



NA 3778-010-206

FIG. 14-2
CONNECTION OF FILTER TO ITS TERMINATIONS

bandwidth will also affect the fidelity of signal transmission, but in typical microwave applications this source of distortion is not likely to be serious.

The phase-shift and time-delay curves presented in this report were evaluated for the low pass prototype filter appropriate to each response type. The phase-shift function of the derived band-pass filter is obtained from these curves simply by transforming the frequency scale as shown in Fig. 14-3. Frequency transformation relations for a number of kinds of coupled-resonator circuits have been given.^{2,8} In the case of narrow bandwidth (less than a few percent), these all reduce to

$$\omega' = \frac{2\omega'_1(\omega - \omega_0)}{\omega_1 \omega_0} \quad (14-4)$$

where (see Fig. 14-3) ω' is radian frequency for the low-pass prototype filter, ω'_1 is a particular value of ω' , $\omega = 2\pi f$ is radian frequency for the band-pass filter, ω_0 is the center angular frequency of the band pass filter, and

$$w_1 = \frac{\omega_2 - \omega_1}{\omega_0} \quad (14-5)$$

is the relative bandwidth of the band-pass filter between angular frequencies ω_1 and ω_2 that correspond to ω'_1 .

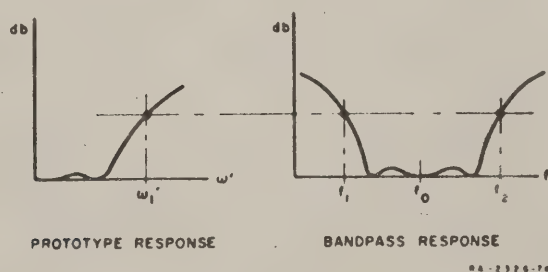


FIG. 14-3
CORRESPONDENCE BETWEEN FREQUENCY SCALES FOR
LOW-PASS-PROTOTYPE FILTER AND EQUIVALENT
BAND-PASS FILTER

Equation (14-3) may be rewritten as

$$t_d = \frac{d\phi}{d\omega'} \cdot \frac{d\omega'}{d\omega} \quad (14-6)$$

where $d\phi/d\omega'$ is the time delay of the prototype filter. Equations (14-4), (14-5), and (14-6) yield

$$t_d = \frac{\omega_1}{\pi(f_2 - f_1)} \cdot \frac{d\phi}{d\omega'} \quad (14-7)$$

This formula enables one to calculate the time delay of a narrow-band band-pass filter in terms of its bandwidth ($f_2 - f_1$), the corresponding radian frequency ω_1 , and the time delay of the prototype filter. With coupled-resonator filters whose bandwidth is more than about 2 percent and not more than about 10 percent, Eq. (14-6) should be used with a more precise relationship between ω' and ω than Eq. (14-4).¹⁵

The time-delay curves in this chapter are normalized with respect to the center-frequency time delay t_{d0} . Thus, if absolute time delay values are desired, one need merely multiply the normalized values by t_{d0} , which may be calculated at f_0 by Eq. (14-3), (14-6), or (14-7).

C. CALCULATED RESULTS

Phase-shift-versus-frequency curves are shown in Fig. 14-4 for dissipationless low-pass prototype filters having maximally flat insertion-loss response and equal-ripple response with ripple levels of 0.01 and 0.5 db. The location of each 3-db point is indicated. All of the curves exhibit nonlinearity. The 0.5-db-ripple phase-shift curve has a minor undulation superimposed. This curve is typical of those for equal-ripple filters having high ripple amplitude, and explains why equal-ripple filters have had a poor reputation as far as phase linearity is concerned. However, the curve for 0.01-db ripple is strikingly improved, and in fact appears more nearly linear than the curve for the maximally flat insertion-loss case.

Normalized time-delay curves are shown in Figs. 14-5 and 14-6. In Fig. 14-5, the frequency scale is normalized with respect to the 3-db point, while in Fig. 14-6 it is normalized with respect to the 60-db point.

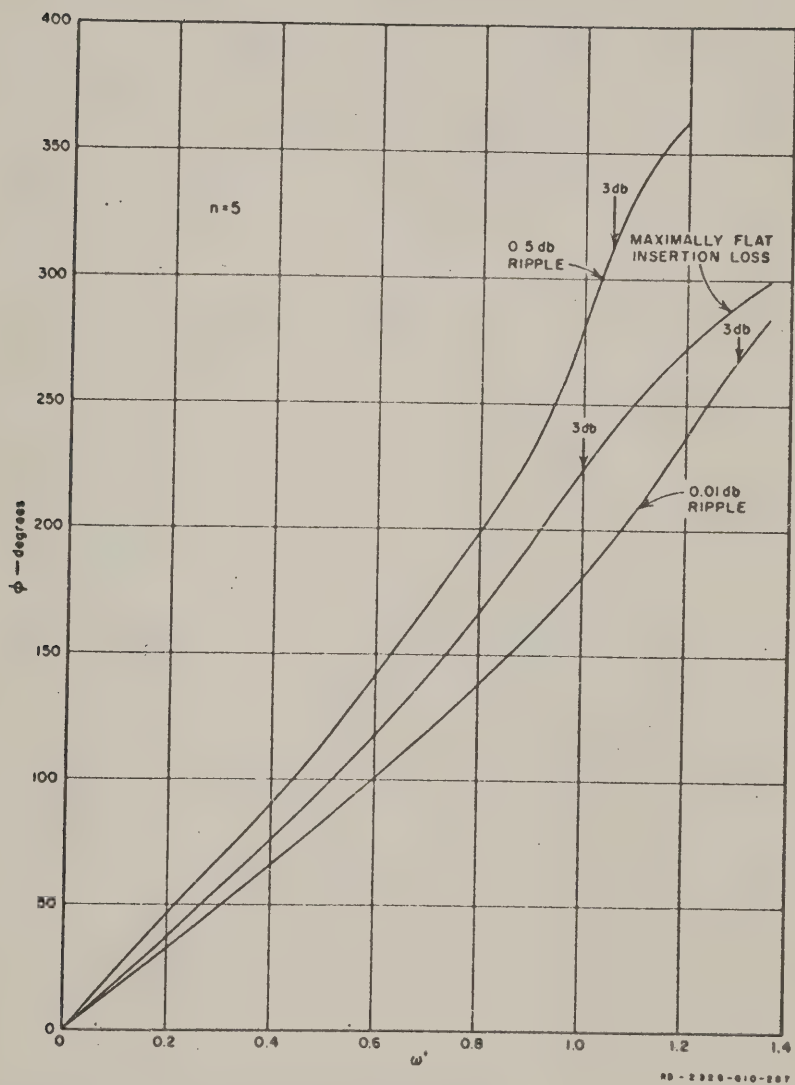


FIG. 14-4

INSERTION-PHASE-SHIFT RESPONSE OF FIVE-ELEMENT EQUAL-RIPPLE
AND MAXIMALLY FLAT INSERTION-LOSS PROTOTYPE FILTERS

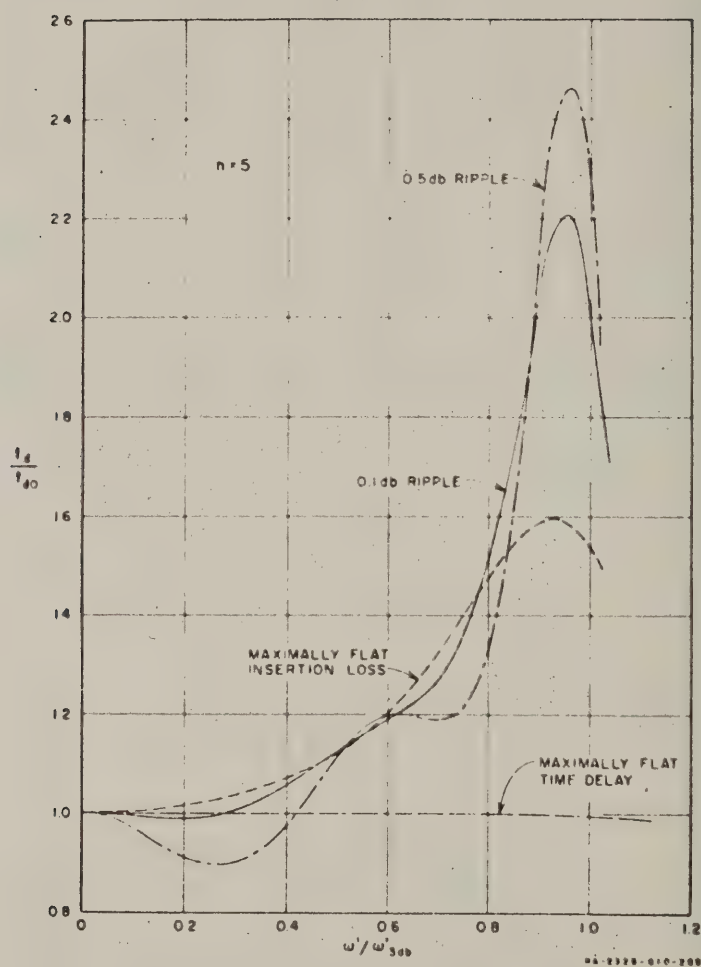


FIG. 14-5
 NORMALIZED TIME DELAY VERSUS ω/ω'_{3db} FOR
 VARIOUS PROTOTYPE FILTERS

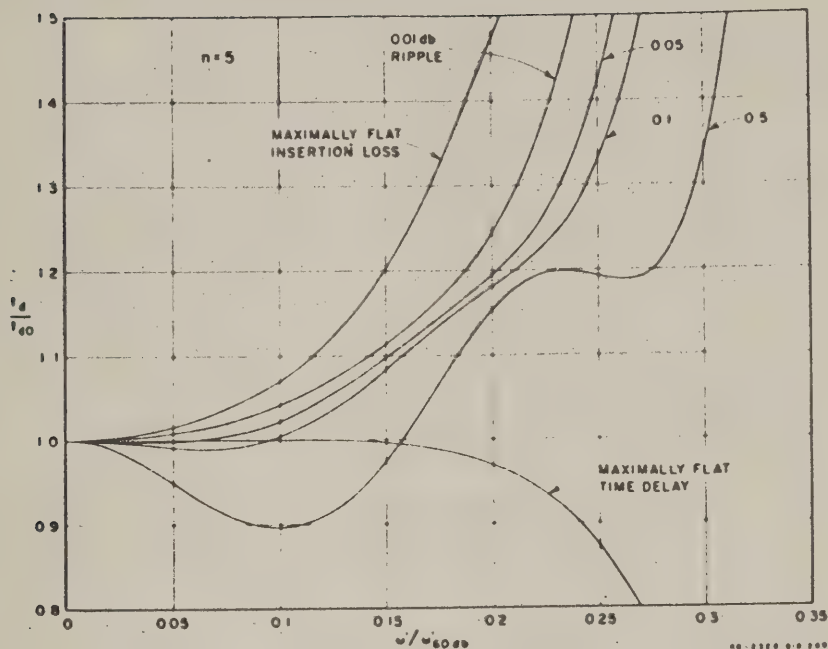


FIG. 14-6

NORMALIZED TIME DELAY VERSUS ω'/ω'_{60db} FOR VARIOUS PROTOTYPE FILTERS

Inspection of Fig. 14-5 shows that a high peak of time delay occurs just before the 3-db point. This peak is lowest for maximally flat insertion-loss response, and increases with ripple level in the equal-ripple cases. Thus, if important components of the signal spectrum extend out to or beyond the 3-db points, objectionable distortion is likely to occur in all cases, being least objectionable in the maximally flat insertion loss case.

In usual applications, however, the signal spectrum will already be confined to a specific bandwidth before entering the filter. By making the filter passband sufficiently wider than the signal bandwidth, the spectrum may be limited to a portion of the time-delay curve that is almost constant. Figure 14-5 shows the equal-ripple filter to be superior in this case, if the ripple amplitude is of the order of 0.1 db. As an example, the curve for 0.1-db ripple is constant within 1 percent for $\omega'/\omega'_{3db} \leq 0.31$, while the curve for maximally flat insertion loss meets that tolerance only for $\omega'/\omega'_{3db} \leq 0.16$.

The curves in Fig. 14-6 are even more interesting from a practical standpoint. In the usual application, the signal channel is to be isolated from one or more other channels spaced specified distances away in frequency. Thus, a normalization of the frequency scale such that the bandwidth at a given insertion-loss level in the stop band is the same for all curves provides a useful basis of comparison. In Fig. 14-6, the frequency normalization is with respect to the 60 db point. However, the normalization point may be easily altered. In all cases, except the maximally flat time delay case, the insertion-loss curves merge together and all increase at a 30-db per octave rate above about 50 db. Thus, the graph in Fig. 14-6 may be applied to other values of stop-band insertion loss above 50 db by dividing the numbers on the abscissa scale by $10^{(L_s - 60)/20}$ where L_s is the value of stop-band insertion loss, and $n = 5$ is the number of elements in the prototype filter circuit.

An interesting property revealed by Fig. 14-6 is that the initial upward curvature of the time-delay curve for maximally flat insertion loss changes gradually to downward curvature as the ripple level is increased. Close examination indicates that the initial curvature disappears for a ripple level of about 0.03 or 0.04 db. In addition to this effect on curvature, the equal-ripple case is also aided by its greater selectivity compared to the maximally flat case, permitting the former a wider pass band when the stop bandwidths are made the same. Comparisons of the curves show that for a ± 1 -percent tolerance on t_d , a 0.1-db ripple filter can be used out to $0.106 \omega'_{60\text{db}}$, while the maximally flat insertion-loss filter can be used only out to $0.049 \omega'_{60\text{db}}$. For a ± 10 -percent tolerance on t_d , a 0.5-db-ripple filter can be used out to $0.184 \omega'_{60\text{db}}$, while the maximally flat insertion-loss filter can be used only out to $0.116 \omega'_{60\text{db}}$. Thus, the improvement offered by equal-ripple filters with properly chosen ripple level is substantial.

Figures 14-5 and 14-6 show the maximally flat time-delay filter to have greatly superior time-delay characteristics to the other filters considered. However, its mismatch and design disadvantages discussed in Sec. A must be borne in mind in selecting the best filter for a given application. For example, at $\omega' = 0.1 \omega'_{60\text{db}} = 0.645 \omega'_{3\text{db}}$ the maximally flat time-delay filter has 1.25 db of insertion loss due to reflection, and a VSWR of 3.0. The other filters, except for the 0.5-db-ripple one, are well matched at these frequencies.

D. FORMULAS USED FOR PHASE SHIFT CALCULATIONS

The following formulas were used in computing the insertion-phase-shift and time-delay data of Figs. 14-4, 14-5, and 14-6. They are given in generalized form so that the reader may use them for other values of ripple amplitude and n .

The insertion voltage ratio of a nondissipative equal-ripple prototype filter may be determined in magnitude and phase from the following polynomial function:

$$P_n(p, x) = p^n + f_{n-1}(x)p^{n-1} + f_{n-2}(x)p^{n-2} + \dots \quad (14-8)$$

where $p = \sigma + j\omega'$, which is the complex radian-frequency variable, n is the degree of the polynomial, and x is a parameter related to the ripple level. For steady-state excitation at frequency $p = 0 + j\omega$, the insertion phase shift is given by

$$\phi = \tan^{-1} \left[\frac{\operatorname{Im} P_n(j\omega', x)}{\operatorname{Re} P_n(j\omega', x)} \right] \quad (14-9)$$

while the insertion voltage ratio is simply proportional to $|P_n(j\omega', x)|$. For n even, the polynomial $P_n(p, x)$ may be expressed in factored form by¹²

$$P_n(p, x) = \prod_{m=1}^{n/2} \left[p^2 + 2x \cos \frac{\pi(2m-1)}{2n} p + x^2 + \sin^2 \frac{\pi(2m-1)}{2n} \right] \quad (14-10)$$

and, for n odd and ≥ 3 by

$$P_n(p, x) = (p + x) \prod_{m=1}^{(n-1)/2} \left[p^2 + 2x \cos \frac{\pi m}{n} p + x^2 + \sin^2 \frac{\pi m}{n} \right] \quad (14-11)$$

The parameter x is given by¹²

$$x = \sinh \left[\frac{1}{n} \sinh^{-1} \left(\frac{1}{10^{L_n/10} - 1} \right)^{1/2} \right] \quad (14-12)$$

where L_n is the ripple level in decibels; i.e., the difference in decibels between the maximum and minimum insertion loss in the pass band of the prototype filter. The relative-insertion-voltage ratio, $|P_n(j\omega', x)|$, has equal-ripple behavior in the range $-1 \leq \omega' \leq 1$, and increases monotonically outside that range.

Multiplied-out forms of $P_n(p, x)$ are given by Matthaei¹² for $n = 2$ to 5, and his expression for $P_5(p, x)$ was used with Eq. (14-12) in computing the data in this report. Alternatively, the insertion phase shift is equal to the sum of the phase angles of all the individual factors in Eq. (14-10) or (14-11).

Each quadratic factor in Eqs. (14-10) and (14-11) can be reduced to a pair of binomial factors $(p - p_n)(p - p_n^*)$, in which p_n and p_n^* are a complex-conjugate pair of roots of the polynomial. For n even,

$$p_n = -x \cos \frac{\pi(2n-1)}{2n} + j \sqrt{x^2 + 1} \sin \frac{\pi(2n-1)}{2n} \quad (14-13)$$

and for n odd,

$$p_n = -x \cos \frac{\pi n}{n} + j \sqrt{x^2 + 1} \sin \frac{\pi n}{n} \quad (14-14)$$

These formulas give pairs of roots p_n and p_n^* for $n \geq 1$. In addition, the polynomial for n odd has a single root $p_0 = -x$. When plotted in the complex $p = \sigma + j\omega'$ plane, the roots of the polynomial all lie in the left half plane on an ellipse whose major axis coincides with the $j\omega'$ axis and whose minor axis coincides with the σ axis. The axial ratio of the ellipse varies with the ripple level, the ellipse becoming a circle as the ripple level goes to zero. In that limit, the insertion-loss response becomes maximally flat, with its 3-db point at $\omega' = x \rightarrow \infty$.

When the frequency scale for the maximally flat insertion-loss case is adjusted so that the 3-db point occurs at $\omega' = 1$, the formulas for the polynomial and its roots p_n , p_n^* are as follows: for n even,

$$P_n(x) = \prod_{n=1}^{n/2} \left[p^2 + \left(2 \cos \frac{\pi(2n-1)}{2n} \right) p + 1 \right] \quad (14-15)$$

$$p_n = -\cos \frac{\pi(2n-1)}{2n} + j \sin \frac{\pi(2n-1)}{2n}, \quad (14-16)$$

and for n odd,

$$P_n(x) = (p+1) \prod_{a=1}^{(n-1)/2} \left[p^2 + \left(2 \cos \frac{\pi a}{n} \right) p + 1 \right], \quad (14-17)$$

$$p_n = -\cos \frac{\pi n}{n} + j \sin \frac{\pi n}{n}, \quad n \geq 1 \quad (14-18)$$

$$p_0 = -1. \quad (14-19)$$

The phase-shift formulas for the maximally flat and equal ripple insertion-loss examples considered in this chapter were evaluated by means of an electronic computer. The time delay values were later obtained from the phase-shift values by numerical differentiation. The increment used, $\Delta\omega' = 0.05$ is fine enough to ensure very good accuracy except at the high peaks near the 3-db points, where a slight error may exist.

E. CONCLUSIONS

The investigation described in this chapter was restricted to narrow-band filters based on five-element, nondissipative, low-pass prototypes. However, the results for numbers of elements other than five are expected to be similar although with quantitative values changed.

For $n = 5$, if the bandwidth of the signal spectrum is less than half of the 3 db bandwidth of the filter, the equal ripple design with proper choice of ripple level offers superior phase-shift and time-delay characteristics compared to the maximally flat insertion loss design. When the spectrum is less than or equal to three-tenths of the 3-db bandwidth, best results are obtained with ripple levels of about 0.03 to 0.1 db.

In most cases, a microwave filter is intended to isolate the signal spectrum from adjacent channels. The stop-band bandwidth is then a specified quantity. On the basis of equal stop band bandwidth, equal ripple filters offer a strong advantage over maximally flat insertion-loss filters. As an example, for a +1-percent tolerance on time delay, an 0.1-db ripple

filter can transmit a signal spectrum bandwidth that is 18.4 percent of the 60-db stop-band bandwidth, while for the maximally flat insertion-loss filter this figure would be only 11.6 percent.

In some applications, a filter is used to reduce the width of the signal spectrum. This may be done either to remove undesired portions of the spectrum or to broaden the pulse width intentionally. Both the maximally flat insertion-loss and equal-ripple designs are likely to cause ringing and overshoot when used for this purpose. More suitable for such applications is the maximally flat time-delay filter. This has a very flat time-delay characteristic over the pass-band and well beyond the 3-db points. However, its disadvantages of pass-band mismatch, poor selectivity, and practical design difficulties limit its application to cases where an equal-ripple-insertion-loss design will not suffice.

REFERENCES

1. S. Goldman, *Frequency Analysis, Modulation, and Noise*, Chap. IV (McGraw-Hill Book Company, Inc., New York City, 1948).
2. S. B. Cohn *et al.*, "Research on Design Criteria for Microwave Filters," Final Report, SRI Project 1331, Contract DA 36-039 SC-64625, Stanford Research Institute, Menlo Park, California (June 1957).
3. S. B. Cohn, "Direct-Coupled Resonator Filters," *Proc. IRE* **43**, pp. 187-196 (February 1957).
4. S. B. Cohn, "Parallel-Coupled Transmission-Line-Resonator Filters," *IRE Trans. PGMT-6*, pp. 223-231 (April 1958).
5. L. Storch, "Synthesis of Constant-Time-Delay Ladder Networks Using Bessel Polynomials," *Proc. IRE* **42**, pp. 1666-1675 (November 1954).
6. L. Weinberg, "Additional Tables for Design of Optimum Ladder Networks, Part II," *Journal of the Franklin Institute* **264**, pp. 127-138 (August 1957).
7. See Chapter 20 of this report.
8. See Chapter 21 of this report.
9. G. L. Matthaei, "Band-Pass Microwave Filter Design—A New Method and Its Relation to Other Methods," 1960 IRE International Convention Record, Part 3, pp. 95-122.
10. S. B. Cohn, "Dissipation Loss in Multiple-Coupled-Resonator Filters," *Proc. IRE* **47**, pp. 1342-1348 (August 1959).
11. See Chapter 17 of this report.
12. G. L. Matthaei, "Synthesis of Tchebyscheff Impedance-Matching Networks, Filters, and Interstages," *IRE Trans. PGCT-3*, pp. 163-172 (September 1956).

CHAPTER 15

A GENERALIZED APPROACH FOR DIRECT-COUPLED FILTER DESIGN

A. GENERAL

In the Final Report¹ on an earlier, related project, Cohn presented an improved method for direct-coupled filter design and gave information for applying the method to the design of a variety of types of lumped-element and microwave filters. For convenience, we will review part of a lumped-element example for Ref. 1, and then derive from it a generalized statement for this viewpoint of design. Using this generalized statement, principles for the selection of approximate low-pass to bandpass transformations will be developed.

B. REVIEW OF AN EXAMPLE FROM REF. 1

One may design a lumped-element, band-pass filter directly from a low-pass prototype^{1,2,3} by use of the transformation

$$\omega' = \frac{\omega_1'}{\omega} \left(\frac{\omega}{\omega_0} - \frac{\omega_0}{\omega} \right) \quad (15-1)$$

In this equation, ω' is the frequency variable of the low-pass prototype, while ω is the corresponding variable for the band-pass filter. In Figs. 15-1(a) and 15-1(b), $\omega' = 0$ maps to ω_0 , ω_1' maps to ω_2 , and (considering negative values of ω') $-\omega_1'$ maps to ω_1 . The band-pass filter bandwidth is fixed by

$$\omega = \frac{\omega_2 - \omega_1}{\omega_0} \quad (15-2)$$

where

$$\omega_0 = \sqrt{\omega_2 \omega_1} \quad (15-3)$$

The attenuation characteristic of the bandpass filter may be calculated directly from the attenuation characteristic of the low-pass prototype

by use of Eqs. (15-1) to (15-3). The attenuation of the prototype at frequency ω' and the attenuation of the band-pass filter at frequency ω will be the same when ω' and ω are related by Eq. (15-1).

If ω' is the frequency variable of the circuit in Fig. 15-2(a)* and Fig. 15-1(a) at its response, then substituting the right side of Eq. (15-1) for ω' in the impedances and admittances of the circuit in Fig. 15-2(a) will result in the circuit in Fig. 15-2(b) with the response shown in Fig. 15-1(b). The circuit in Fig. 15-2(b) has both series and shunt resonators; in many applications, however, it is desirable to have all of the resonators of the same form. In Ref. 1 this result is achieved by using so-called impedance inverters, which are two-port networks having ± 90 degrees image phase shift and an inversion parameter, K . If an impedance Z_b is connected to one port of an impedance inverter, then the impedance Z_a seen at the other end is

$$Z_a = \frac{K^2}{Z_b} \quad (15-4)$$

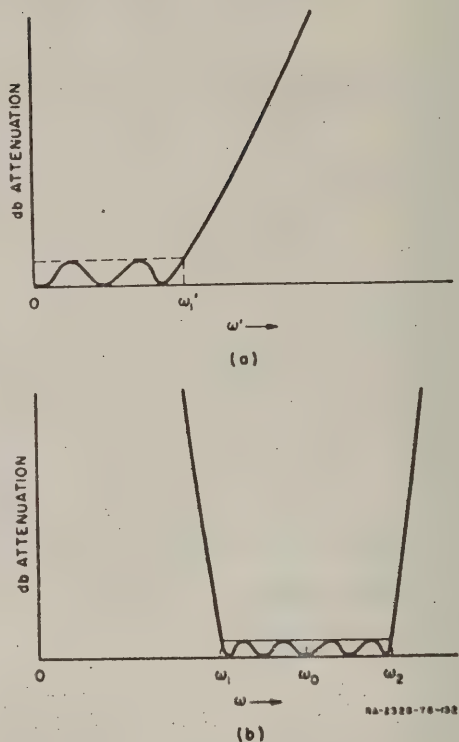
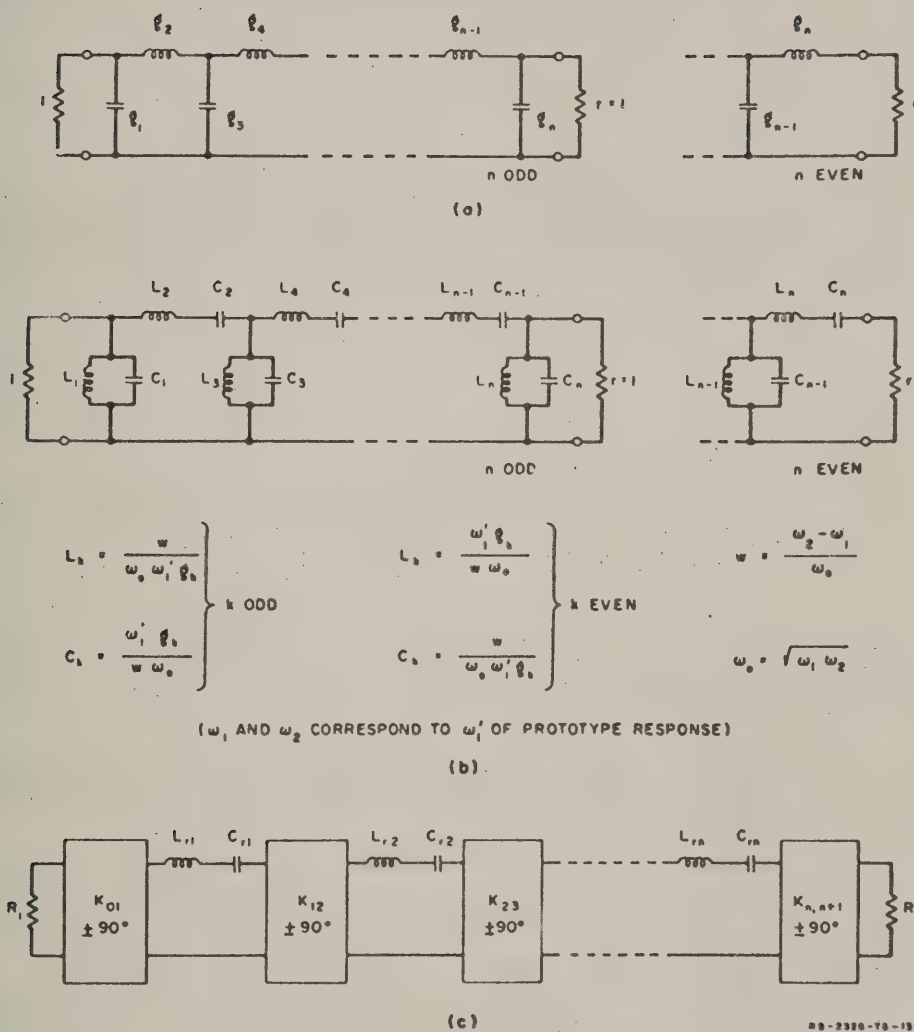


FIG. 15-1

A TCHEBYSCHIEFF LOW-PASS FILTER RESPONSE FOR THE CASE OF $n = 5$, AND THE RESULTING BAND-PASS FILTER RESPONSE WHICH WOULD BE OBTAINED BY A LOW-PASS TO BAND-PASS TRANSFORMATION

* Note that in Fig. 15-2(a) it is assumed that $r = 1$ for n odd. This will be true for lossless Tchebyscheff or maximally flat filters which have zero reflection at one or more pass-band frequencies. Element values for such filters can be obtained by the formulas in Fig. 2-2 of Ref. 1, or from the tables in Ref. 2 or Ref. 3. If the formulas in this discussion are to be used for a circuit where n is odd but $r \neq 1$, then r should be replaced by $1/r$ in the following equations for the inverter parameters.



28-2320-76-133

FIG. 15-2

TRANSFORMATIONS FROM A LOW-PASS PROTOTYPE TO A BAND-PASS FILTER
CONTAINING IMPEDANCE INVERTERS

By introducing impedance inverters, series resonators can be made to look electrically like shunt resonators, and the form of circuit in Fig. 15-2(c) becomes theoretically possible.

In the circuit of Fig. 15-2(c), for each resonator

$$\omega_0 = \frac{1}{\sqrt{L_{rk} C_{rk}}} \quad (15-5)$$

must be satisfied, but either L_{rk} or C_{rk} may be chosen arbitrarily. In Ref. 1, a derivation is given showing that the parameters of the inverters adjacent to the ends are related to the elements of the prototype filter in Fig. 15-2(a) by

$$K_{01} = \sqrt{\frac{\omega_0 w L_{r1} R_1}{\omega_1' g_1}} \quad (15-6)$$

and

$$K_{n,n+1} = \sqrt{\frac{\omega_0 w L_{rn} R_n r}{\omega_1' g_n}} \quad (15-7)$$

while all of the other inverter parameters are computed from the relation

$$K_{k,k+1} = \frac{\omega_0 w}{\omega_1'} \sqrt{\frac{L_{rk} L_{r(k+1)}}{g_k g_{k+1}}} \quad (15-8)$$

The impedance inverters can be approximated by a variety of different networks, but two which are particularly applicable for use in the circuit in Fig. 15-2(c) are shown in Fig. 15-3. Since these inverters are frequency-sensitive, they are accurate only for filters of narrow bandwidths. However, by altering the mapping function, accurate designs are obtained for fairly large bandwidths.¹ In a practical situation, the negative elements in the impedance inverters are absorbed into the adjacent positive elements of the same kind so as to eliminate all negative elements in the final circuit.*

* The negative elements at the ends, of course, cannot be absorbed into the resistive terminations. The end inverters can be handled as described in Section C, Part 5 in Ref. 1 or as in Chapter 16 of this report.

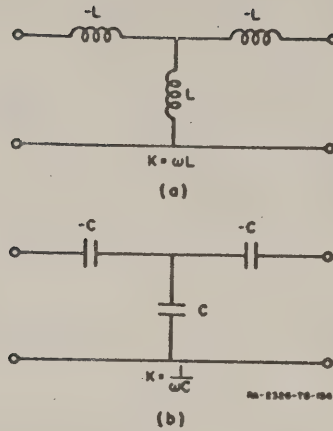


FIG. 15-3
TWO CIRCUITS SUITABLE FOR USE
AS IMPEDANCE INVERTERS

C. A GENERALIZED STATEMENT OF COHN'S DESIGN METHOD

1. DESIGN RELATIONS WITH MAPPING UNSPECIFIED

Cohn applies the method just described to a variety of different structures and introduces modified mappings that give good accuracy for filter designs running to around 20-percent bandwidth. For the purposes of Chapters 16 and 19 of this report, it will be helpful to use a generalized statement of his design method in which the resonator functions and the low-pass to bandpass transformation are left unspecified. Appropriate functions may be selected for the filter structure under consideration in any given case.

By Eq. (15-5) the reactance of the k th resonator in Fig. 15-2(c) can be expressed in the form

$$X_k(\omega) = \omega L_{rk} - \frac{1}{\omega C_{rk}} = \omega_0 L_{rk} \frac{\omega}{\omega_0} - \frac{\omega_0}{\omega} \quad (15-9)$$

It is seen that this reactance function is the same as the mapping function Eq. (15-1) except for the constant multiplier. This will also be true in the generalized case, i.e., the resonator and mapping functions used will

be the same except for their constant multipliers. Thus for the generalized circuit in Fig. 15-4 we may specify the resonator function for the k th resonator as

$$X_k(\omega) = a_k F(\omega), \quad (15-10)$$

while the low-pass to bandpass transformation will be

$$\omega' = \delta F(\omega) \quad (15-11)$$

where a_k and δ are constants. The bandwidth factor δ is related to ω'_1 , ω_1 , ω_0 , and ω_2 in Figs. 15-1(a), (b) by use of the relations

$$\omega'_1 = \delta F(\omega_2) = -\delta F(\omega_1) \quad (15-12)$$

$$\omega' = 0 = F(\omega_0) \quad (15-13)$$

In this generalized form, Eqs. (15-6) to (15-8) become

$$K_{01} = \sqrt{\frac{a_1 R_1}{\delta g_1}} \quad (15-14)$$

$$K_{n,n+1} = \sqrt{\frac{a_n R_n}{\delta g_n}} \quad (15-15)$$

and, for all the other inverters,

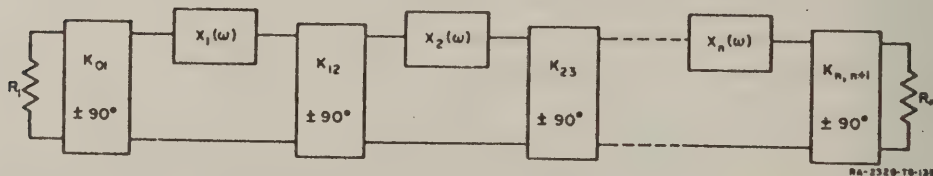


FIG. 15-4

A GENERALIZED, BAND-PASS FILTER CIRCUIT USING IMPEDANCE INVERTERS

$$K_{k, k+1} = \frac{1}{\delta} \sqrt{\frac{a_k a_{k+1}}{g_k g_{k+1}}} \quad (15-16)$$

where r and the g_k are from the low-pass prototype, Fig. 15-2(a). It is interesting to note that the coupling coefficient between resonators k and $k+1$ is

$$(\text{coupling coefficient}) = \frac{K_{k, k+1}}{u \sqrt{a_k a_{k+1}}} \frac{1}{u \delta \sqrt{g_k g_{k+1}}} \bigg|_{\omega_0} = \frac{\omega_0}{2} \frac{dF(\omega)}{d\omega} \bigg|_{\omega_0} \quad (15-17)$$

In the case of the lumped-element circuit of Fig. 15-2(c) and the mapping in Eq. (15-1), $a_k = \omega_0 L_{rk}$, $\delta = \omega'_1/\omega$, and $u = 1$.

Using the principle of duality, we may immediately write down the corresponding general relations for the circuit in Fig. 15-5. The shunt resonators in this circuit are coupled by two-port networks which, for convenience, will herein be called *admittance inverters*. The admittance inverter is simply the dual of the impedance inverter, i.e., an admittance inverter has ± 90 degrees image phase shift and an inversion parameter, J , associated with it. If an admittance Y_b is connected to one end of the inverter, the admittance Y_a seen at the other end is

$$Y_a = \frac{J^2}{Y_b} \quad (15-18)$$

By Eq. (15-4) it is seen that for a given inverter either the J or K definition may be used, and $J = 1/K$. However, it will be convenient to use the term *impedance inverter* for inverters appropriate for networks of the

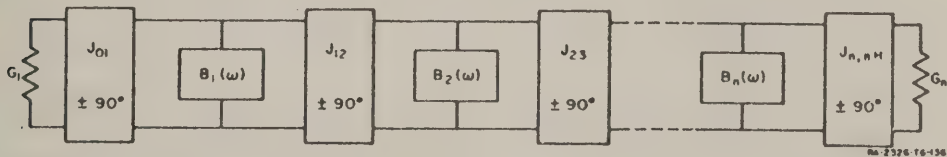


FIG. 15-5

A GENERALIZED, BAND-PASS FILTER CIRCUIT USING ADMITTANCE INVERTERS

form in Fig. 15-4, and admittance inverter for inverters appropriate for networks of the form in Fig. 15-5. Figure 15-6(a), (b) shows circuits suitable for use as admittance inverters which are analogous to the impedance inverters in Fig. 15-3(a), (b).

For the circuit of Fig. 15-5 the resonator and mapping functions are, respectively,

$$B_k(\omega) = b_k F(\omega) \quad (15-19)$$

and

$$\omega' = \delta F(\omega) \quad (15-20)$$

where b_k and δ are again constants, and Eqs. (15-12) and (15-13) apply as before. By duality

$$J_{01} = \sqrt{\frac{b_1 G_1}{\delta g_1}} \quad (15-21)$$

$$J_{n,n+1} = \sqrt{\frac{b_n G_n r}{\delta g_n}} \quad (15-22)$$

and, for all other inverters,

$$J_{k,k+1} = \frac{1}{\delta} \sqrt{\frac{b_k b_{k+1}}{g_k g_{k+1}}} \quad (15-23)$$

where r and the g_k are from the low-pass prototype, Fig. 15-2(a). For this case the coupling coefficient between resonators k and $k+1$ is

$$(\text{coupling coefficient}) = \frac{J_{k,k+1}}{uv \sqrt{b_k b_{k+1}}} = \frac{1}{u \delta \sqrt{g_k g_{k+1}}} \left| u = \frac{\omega_0}{2} \frac{dF(\omega)}{d\omega} \right|_{\omega_0} \quad (15-24)$$

2. SELECTION OF A MAPPING FUNCTION $F(\omega)$

As previously mentioned, the mapping function is determined in principle by the reactance or susceptance functions of the resonators

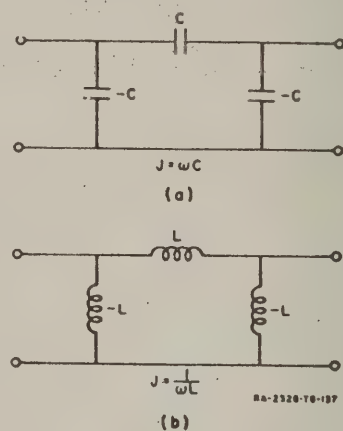


FIG. 15-6
TWO CIRCUITS SUITABLE FOR USE
AS ADMITTANCE INVERTERS

However, these functions may be unnecessarily complicated for designing filters of, say, 20-percent bandwidth or less, so that it often becomes desirable to replace them by an approximate function, which is accurate for an adequate range in the vicinity of ω_0 . Furthermore, the inverter parameters of the couplings generally vary with frequency, making it convenient to select an altered mapping function that helps to account for this effect. It is then convenient to regard the K - or J -parameters of Figs. 15-4 and 15-5 as independent of frequency, while the selectivity of the resonators and the frequency variation of the couplings are both accounted for by the choice of $F(\omega)$.

As indicated by Eqs. (15-10), (15-13), and (15-19), at the midband frequency, ω_0 , the resonator reactances in Fig. 15-4 will all be zero; on the other hand, the resonator susceptances in Fig. 15-5 will all be zero as a result of $F(\omega_0) = 0$. Frequencies for which $F(\omega) = \infty$ correspond to frequencies of infinite attenuation in these circuits. Thus, if $F(\omega)$ has a first-order pole at the frequency ω_a , then, for an n -resonator filter of the form in either Fig. 15-4 or 15-5, there will occur an n th-order pole of attenuation at the frequency ω_a . Because of this, an accurate mapping function $F(\omega)$ will be zero at ω_0 , and will be infinite at the frequencies proper for generating those frequencies of infinite attenuation required by inspection of the actual filter structure. For filters of narrow or moderate bandwidth, this should be used only as a guide for picking a simple $F(\omega)$ function which has the form of skewness that the actual transmission characteristic will have. However, for predicting the response of wideband filters designed by the methods of Chapters 19 and 20, it will be desirable to try to pick an $F(\omega)$ function that will generate all of the important poles of attenuation and important pass bands occurring in the transfer function of the actual network.

The filter structure in Chapter 16 presents a possible example for application of these principles. Although the discussion in that chapter is confined to the case of narrow or moderate bandwidth, it will be of interest to go through the reasoning one might use to arrive at an $F(\omega)$ function that would be appropriate if the methods of Chapter 19 were applied to the design of a wideband filter of this type.

The form of the filter is shown in Fig. 16-1(a): At zero frequency the reactance of each coupling capacitor is infinite, while the susceptance of each of the shunt transmission line resonators is also infinite, as a result of the short-circuit at one end of each resonator. For a filter with n shunt resonators, there will thus be a $(2n + 1)$ -order pole of attenuation at $\omega = 0$. To approximate this condition when the circuit of Fig. 16-1 is converted

to the representation in Fig. 15-5, it is desirable to use an $F(\omega)$ function which has a second-order pole at $\omega = 0$ (which implies a $2n$ -order pole of attenuation for $\omega = 0$ in the transfer function). The connection points for the shunt resonator lines in Fig. 16-1 will usually be different for the different resonators, but at certain higher frequencies the various $B_k(\omega)$ will again become infinite, though all $B_k(\omega)$ will not necessarily be simultaneously infinite. In a practical case, the closest poles of attenuation at frequencies $\omega > \omega_0$ will be grouped in the vicinity of $\omega = 3.5 \omega_0$. Their effect will be accounted for approximately if $F(\omega)$ has a first-order pole at $\omega = 3.5 \omega_0$, which will cause an n -resonator circuit of the form shown in Fig. 15-5 to have an n th order pole of attenuation at that frequency. Then the suggested $F(\omega)$ function is*

$$F(\omega) = \frac{-(\omega - \omega_0)}{\omega^2 (\omega - 3.5 \omega_0)} \quad (15-25)$$

where the $(\omega - \omega_0)$ factor in the numerator fixes the band center, the ω^2 factor in the denominator creates a second-order pole in $F(\omega)$ at $\omega = 0$, the $(\omega - 3.5 \omega_0)$ factor creates a first-order pole at $\omega = 3.5 \omega_0$, and the minus sign is introduced so that $F(\omega)$ will be negative for $\omega < \omega_0$, as is implied by Eq. (15-12).

It is desirable to have some expression for δ in Eq. (15-20) in terms of the pass-band edges ω_1 and ω_2 in Fig. 15-1(b). This would ordinarily be done by solving Eq. (15-12) for ω_1 and ω_2 in terms of ω_1' and ω_0 , and then obtaining an expression for δ in terms of ω_1' , $\omega_2 - \omega_1$, and ω_0 . However, using the $F(\omega)$ of Eq. (15-25) this involves finding the roots of third-degree polynomials. In such cases it is easiest to make a plot of

$$\frac{\omega'}{\delta} = F(\omega) \quad (15-26)$$

normalized so that $\omega_0 = 1$, and then find normalized values of ω_1 and ω_2 which will have the required ratio ω_2/ω_1 and which will satisfy Eq. (15-12).

* Using the representation in Fig. 15-4 or 15-5 where the inverters are regarded as frequency invariant, and the frequency sensitivities of both the resonators and couplings are accounted for by $F(\omega)$, the resonator function $F(\omega)$ need not be a physically realizable reactance function. Also, some simplification is obtained if the $F(\omega)$ function contains only the factors required to give a good approximation for positive values of ω , as is the case for Eq. (15-25).

For bandwidths up to at least 10 percent, and possibly greater, it will be convenient and usually sufficiently accurate to use a simpler $F(\omega)$ function:

$$F(\omega) = \frac{\omega - \omega_0}{\omega} \quad (15-27)$$

for the case in Fig. 16-1(a). As is true for Eq. (15-25), the slope of this function is greater for frequencies $\omega < \omega_0$ than for frequencies $\omega > \omega_0$. For this function, simultaneous solution of Eqs. (15-12) and (15-13) yields

$$\delta = \omega_1' \frac{(\omega_2 + \omega_1)}{\omega_2 - \omega_1} \quad (15-28)$$

and

$$\omega_0 = \frac{2\omega_2\omega_1}{\omega_2 + \omega_1} \quad (15-29)$$

3. DETERMINATION OF THE RESONATOR CONSTANTS a_k OR b_k

Having selected an appropriate function $F(\omega)$ and having determined the bandwidth factor δ for the mapping, it is still necessary to have a way of relating the resonator constants a_k or b_k in Eq. (15-10) or Eq. (15-19), respectively, to the parameters of the actual resonator. For filters of narrow or moderate bandwidth this is done most easily by relating the slope of the actual resonator function to the slope of $F(\omega)$ at frequency ω_0 . For the case of Fig. 15-4, let $dX^r(\omega)/d\omega$ be the slope of the reactance of the k th resonator as calculated from the circuit of the actual resonator rather than from the approximation function Eq. (15-10). Then a_k may be calculated from

$$a_k = \frac{\frac{dX^r(\omega)}{d\omega}}{\frac{dF(\omega)}{d\omega}} \bigg|_{\omega=\omega_0} \quad (15-30)$$

* This is the same mapping as is used for the capacitive-gap coupled filter discussed in Ref. 1

Analogously, the constants b_k for Eq. (15-19) and Fig. 15-5 may be calculated by the formula

$$b_k = \left. \frac{\frac{dB^r(\omega)}{d\omega}}{\frac{dF(\omega)}{d\omega}} \right|_{\omega=\omega_0} \quad (15-31)$$

Once again the superscript r in $dB^r(\omega)/d\omega$ is used to indicate that this is the slope of the resonator susceptance as calculated from the circuit of the actual resonator.

Experience shows that this method of matching derivatives at ω_0 will not be satisfactory in many cases of wideband design, and for such cases the procedure described in Chapters 19 and 20 is recommended.

REFERENCES

1. S. B. Cohn, et al, "Research on Design Criteria for Microwave Filters," Final Report, Chap. 2, SRI Project 1311, Contract DA 36-039 SC-64625, Stanford Research Institute, Menlo park, California (June 1957). Also, "Direct-Coupled-Resonator Filters," *Proc. IRE* 45, pp. 187-196 (February 1957).
2. L. Weinberg, "Network Design by Use of Modern Synthesis Techniques and Tables," Tech. Memo. 427, Hughes Aircraft Company, Research Laboratories, Culver City, California (April 1956). Also, *Proceedings of the National Electronics Conference* Vol. 12, (1956).
3. See Chapter 13 of this report.

CHAPTER 16

DESIGN OF BAND-PASS FILTERS WITH VERY WIDE STOP BANDS

A. GENERAL PROPERTIES OF THE RESONATORS AND FILTER CIRCUIT

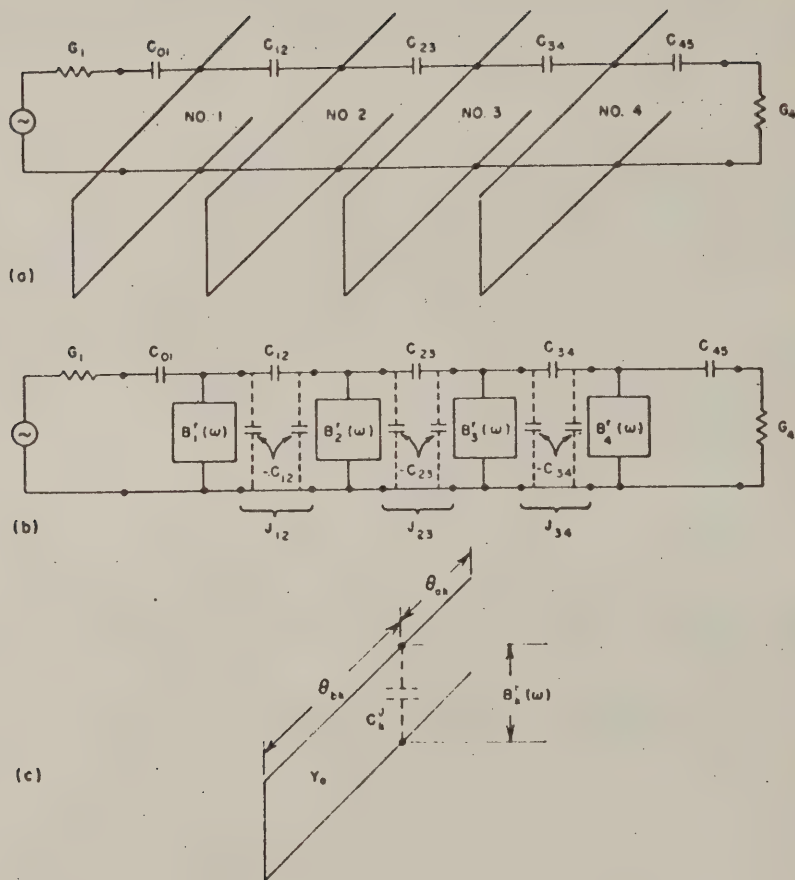
The form of filter under consideration is a cascade of capacitively coupled shunt resonators, as shown in Fig. 16-1(a). The resonators consist of transmission lines which are nominally one-quarter wavelength long at the mid-band frequency, ω_0 . As shown in Fig. 16-1(c), the resonator lines are short-circuited at one end, and the coupling connection point is a distance θ_{aa} from the open-circuited end, where the parameters θ_{aa} and θ_{bb} in the figure are electrical lengths measured at the mid-band frequency, ω_0 . Various capacitances associated with the couplings will contribute a shunt capacity across the coupling points of each resonator line, as is indicated by C_k^J in the figure. This capacitance must be treated as part of the resonator, and as a result

$$\theta_{aa} + \theta_{bb} < \frac{\pi}{2} \quad (16-1)$$

while if there were no C_k^J the sum of these two electrical lengths would be exactly $\pi/2$.

In order to see why the proposed filter structure should have very wide stop bands, let us set $C_k^J = 0$ so that the resonator electrical length will be exactly $\pi/2$ radians at frequency ω_0 . Then if θ_{aa} is zero in Fig. 16-1(c), so that the coupling point is at the open-circuit end of the resonator, the susceptance characteristic will have the shape of the heavy solid line in Fig. 16-2(a). If all of the resonators of the filter were connected in this manner the filter would have pass bands centered around the frequencies $\omega_0, 3\omega_0, 5\omega_0$, etc., and there would be infinite attenuation at the frequencies $\omega = 0, 2\omega_0, 4\omega_0$, etc., where $B_k'(\omega) = \infty$. Now if the connection points for the resonators are moved so that θ_{aa} is just slightly less than $\theta_{bb}/2$, then the resonator susceptance characteristic will look like the dashed lines in Fig. 16-2(a). Note that there will still be

* The superscript r is introduced here for reasons discussed in connection with Eqs. (15-30) and (15-31).



BB-2526-130

FIG. 16-1

WIDE-STOP-BAND FILTER

The basic form of the band-pass filter with wide stop bands is shown at (a). At (b) the filter is converted to the equivalent form in Fig. 15-5 using inverters as shown in Fig. 15-6(a). The circuit from which the resonator function $B'_k(\omega)$ is computed is shown at (c)

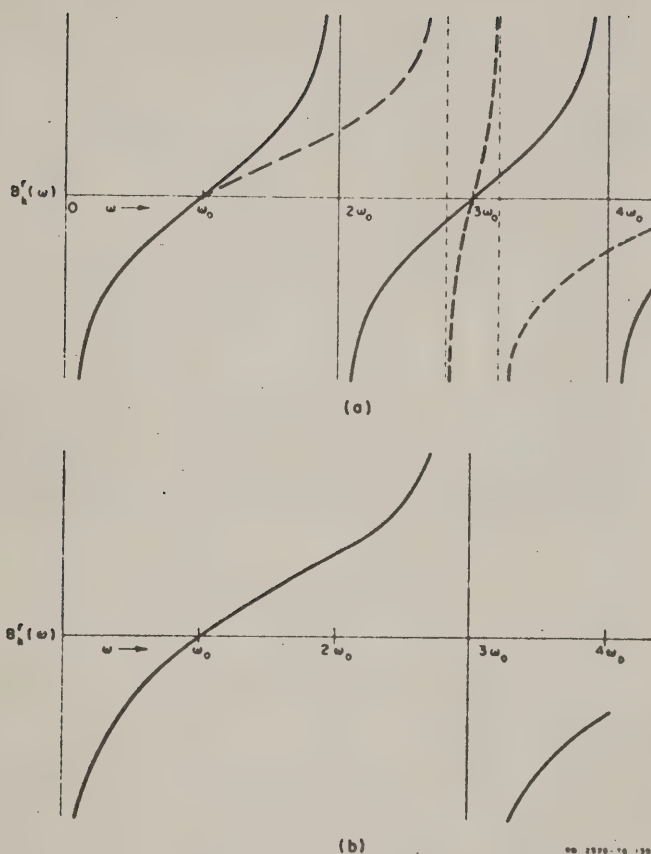


FIG. 16-2

RESONATOR SUSCEPTANCE CHARACTERISTICS FOR THE CIRCUIT
IN FIG. 16-1(c) WHEN $C_k^J = 0$

The case of $\theta_{ek} = 0$ is shown by the solid lines at (a), while the
case of $\theta_{ek} = \rho_{bk}/2$ is shown at (b)

pass bands centered at ω_0 , $3\omega_0$, $5\omega_0$, etc., but the frequencies of infinite attenuation adjacent to $3\omega_0$ will be moved in close to the $3\omega_0$ pass band; the lower frequency of infinite attenuation occurs when the short-circuited side of the line is $\lambda_0/2$ long [thus yielding $B_k'(\omega) = \infty$], and the higher frequency of infinite attenuation occurs when the open-circuited end of the line is $\lambda_0/4$ long [also yielding $B_k'(\omega) = \infty$]. If we set $\theta_{ek} = \theta_{bk}/2$, then the two poles of $B_k'(\omega)$ adjacent to $3\omega_0$ will merge with the zero at $3\omega_0$, leaving a net first-order pole at $3\omega_0$, as shown in Fig. 16-2(b). In

this manner the frequency $3\omega_0$ becomes an infinite attenuation point instead of a pass-band center, and the first higher-order pass band will be centered at $5\omega_0$.

If some of the resonators in the filter are offset so that $\theta_{ab} = \theta_{bb}/2$, they will remove the pass band at $3\omega_0$ as described above; if others of the resonators are offset so that $\theta_{ab} = \theta_{bb}/4$, they will create an infinite attenuation point at $5\omega_0$ and that pass band will also be eliminated. If desired, still other resonators may be offset by such an amount as to suppress the $7\omega_0$ pass band, etc. In this manner it should be possible to construct filters free of spurious pass bands up to frequencies that are very high compared with ω_0 .

The resonator capacitance C_k^J has the effect of altering the resonant frequency ω_0 somewhat, and it also alters the slope of the resonator susceptance characteristic. The total resonator susceptance is

$$B_k^r(\omega) = Y_0 \tan\left(\frac{\theta_{ab}\omega}{\omega_0}\right) - Y_0 \cot\left(\frac{\theta_{bb}\omega}{\omega_0}\right) + C_k^J\omega \quad (16-2)$$

where Y_0 is the line characteristic admittance. At ω_0 where resonance occurs, Eq. (16-2) yields

$$\frac{B_k^J}{Y_0} = \frac{C_k^J\omega_0}{Y_0} = \cot \theta_{bb} - \tan \theta_{ab} \quad (16-3)$$

In order to short out the pass bands at $3\omega_0$, $5\omega_0$, or $7\omega_0$, ..., it is required that $\theta_{ab} = \theta_{bb}/2$, or $\theta_{ab} = \theta_{bb}/4$, or $\theta_{ab} = \theta_{bb}/6$, and so on, respectively, as previously mentioned. Having related θ_{ab} and θ_{bb} , one may solve Eq. (16-3) for the total electrical length, $\theta_{ab} + \theta_{bb}$, required to give resonance in the presence of a given capacitive susceptance B_k^J . If l_k is the resonator length, then

$$\frac{l_k}{(\lambda_0/4)} = \frac{\theta_{ab} + \theta_{bb}}{\pi/2} \quad (16-4)$$

where λ_0 is the wavelength in the medium of propagation at the frequency ω_0 . Figure 16-3 shows a plot of $l_b/(\lambda_0/4)$ vs. B_K^J/Y_0 for resonators offset to suppress the pass band in the vicinity of $3\omega_0$, while Fig. 16-4 shows a similar plot for resonators offset to suppress the pass band in the vicinity of $5\omega_0$.

As discussed in Chapter 15 of this report, the function

$$F(\omega) = \frac{\omega - \omega_0}{\omega} \tag{16-5}$$

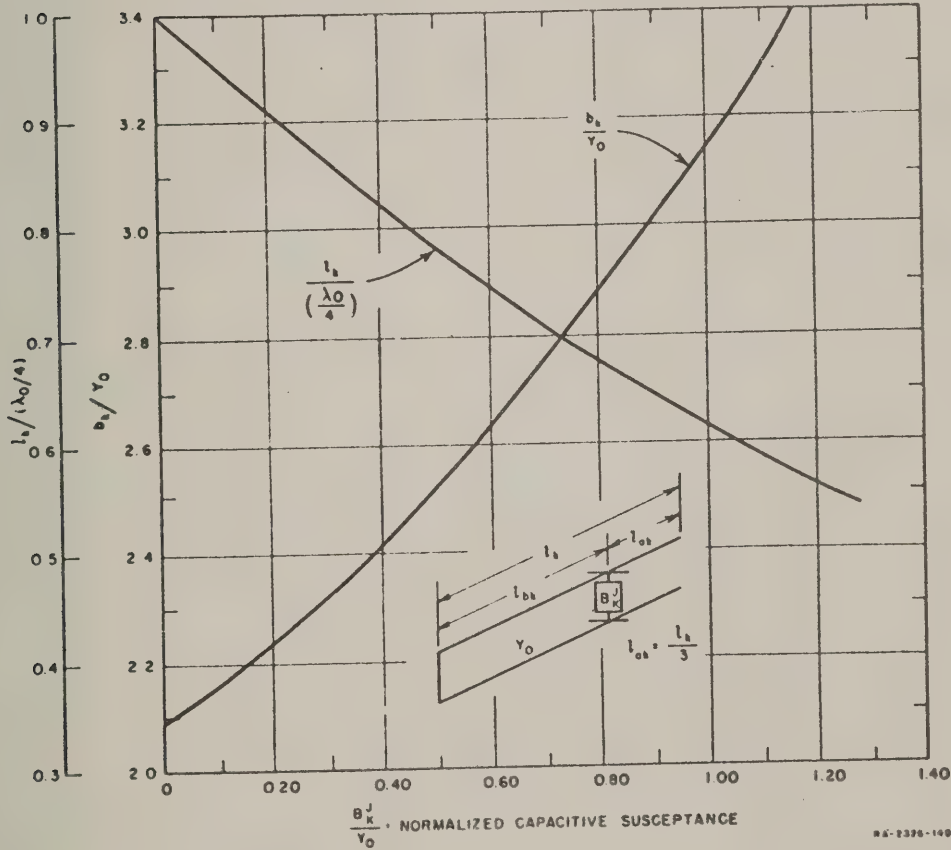


FIG. 16-3
CHART FOR DESIGN OF RESONATORS TO SUPPRESS THE SPURIOUS PASS BAND
IN THE VICINITY OF $3\omega_0$

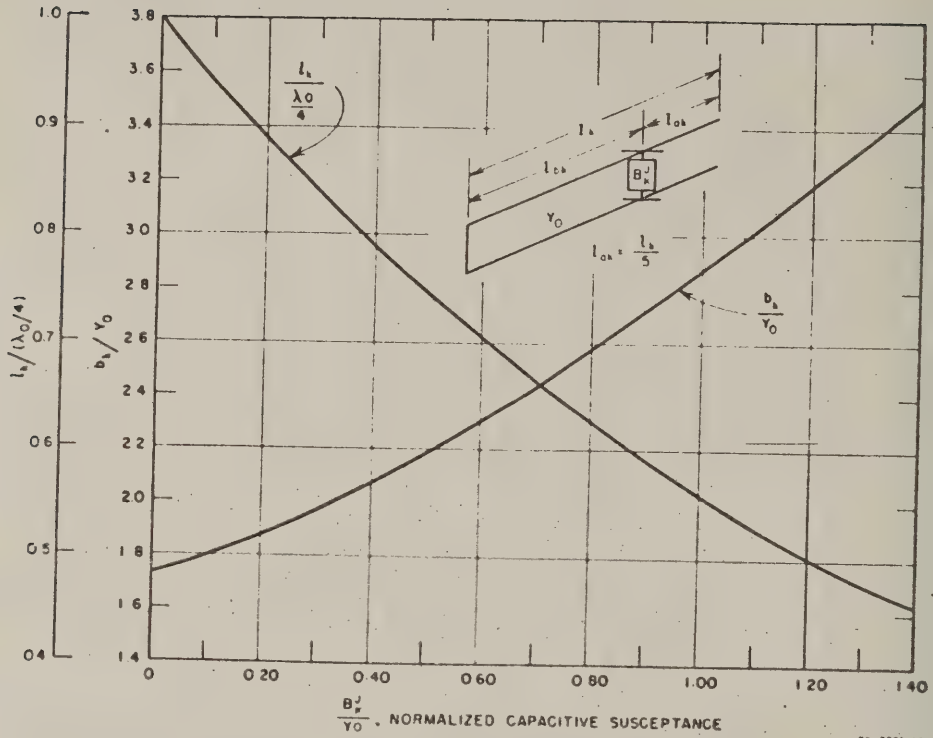


FIG. 16-4

CHART FOR DESIGN OF RESONATORS TO SUPPRESS THE SPURIOUS PASS BAND
IN THE VICINITY OF $5\omega_0$.

should be a reasonably good resonator and mapping function approximation for design of filters of the type in Fig. 16-1(a) if the bandwidth is of the order of 10 percent or less. Then using Eq. (15-31), the resonator constant, b_k , of Eq. (15-19) is found to be

$$\frac{b_k}{Y_0} = \frac{\theta_{ak}}{\cos^2 \theta_{ak}} + \frac{\theta_{bk}}{\sin^2 \theta_{bk}} + \frac{B_k^J}{Y_0} \quad (16-6)$$

after normalizing with respect to the characteristic admittance Y_0 . Figure 16-3 shows a plot of b_k/Y_0 vs. B_k^J/Y_0 for resonators offset to suppress the $3\omega_0$ resonance, while Fig. 16-4 shows a similar plot for resonators designed to suppress the $5\omega_0$ resonance.

B. PROPERTIES OF THE INTERIOR COUPLING

Let us now consider the design of all of the capacitive couplings except the end couplings. Using the approximate resonator and mapping function in Eq. (16-5), ω_0 and the bandwidth factor δ are given by Eqs. (15-28) and (15-29) where ω'_1 , ω_1 , and ω_2 are corresponding band edge points as shown in Figs. 15-1(a), (b) and discussed in Chapter 15. Then the inverter parameters, $J_{k,k+1}$, of the interior couplings are given by Eq. (15-23) where the g_k are obtained from the low-pass prototype¹ and the b_k are obtained by knowledge of the junction capacitive susceptance B_k^J and use of Eq. (16-6) or the plots in Fig. 16-3 or 16-4. However, before the b_k can be accurately evaluated, we must first determine how to evaluate the B_k^J .

The circuit in Fig. 16-1(b), (c) is of the form of that in Fig. 15-5 with the admittance inverters realized as shown in Fig. 15-6(a). Each interior coupling may be represented as shown in Fig. 16-5 where

$$C_{k,k+1} = \frac{J_{k,k+1}}{\omega_0} \quad (16-7)$$

is the series coupling capacitance and the C_l are the shunt capacitances of any series lengths of line between the shunt resonators and the coupling capacitance. The capacitors - $C_{k,k+1}$ shown with dotted lines are introduced to form the admittance inverter and, in turn, the positive shunt $C_{k,k+1}$ capacitors are added outside of the admittance inverter box in order to keep the total net shunt capacitance as it should be. These positive shunt

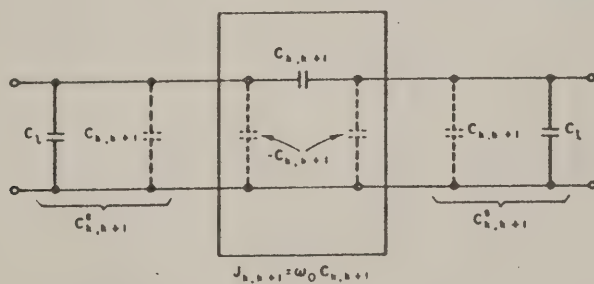


FIG. 16-5

DEFINITION OF PARAMETERS ASSOCIATED WITH THE
WIDE-STOP-BAND FILTER COUPLINGS

$C_{k,k+1}$ capacitances are essential in order to properly represent the influence of the capacitive couplings on the resonant frequency of the resonator. Thus the total shunt capacitance presented to each of the adjacent resonators by a coupling capacitor and its connecting lines is indicated by $C'_{k,k+1}$. Then the total shunt capacitance across the k th resonator as shown in Fig. 16-1(c) is

$$C_k^J = C'_{k-1,k} + C^* + C'_{k,k+1} \quad (16-8)$$

which offers a shunt susceptance

$$B_k^J = \omega_0 C_k^J \quad (16-9)$$

The Capacitor C^* is a junction capacitance which comes from the equivalent circuit for the transmission line junction itself. By Chapter 11 of this report it is seen that for strip transmission line, three-line T-junctions this shunt capacitance is often negative. This would probably also be true for a strip transmission line "plus junctions" such as would be required when constructing the filter in Fig. 16-1(a) in strip transmission line form.

C. PROPERTIES OF THE END COUPLINGS

The end couplings in Fig. 16-1(b) pose a special problem since they cannot be represented directly by impedance inverters. In the case of the interior couplings, the shunt capacitances $C_{k,k+1}$ shown in Fig. 16-5 are absorbed into the adjacent resonators where they take part in the resonator function. However, the end sections are connected to resistive terminations and the shunt capacitance on the termination side cannot be absorbed in this way.

Looking from Resonator 1 toward the left in Fig. 16-1(b), the admittance seen is

$$Y = \frac{1}{\frac{1}{jB_{01}} + \frac{1}{G_1}} = \frac{(B_{01}^2/G_1)}{1 + \left(\frac{B_{01}}{G_1}\right)^2} + \frac{jB_{01}}{1 + \left(\frac{B_{01}}{G_1}\right)^2} \quad (16-10)$$

Looking from Resonator 1 to the left in Fig. 15-5 we see the purely real admittance

$$Y' = \frac{J_{01}^2}{G_1} \quad (16-11)$$

Equating the real part of Eq. (16-10) to (16-11) and solving for B_{01} gives

$$B_{01} = \omega_0 C_{01} = \frac{J_{01}}{\sqrt{1 - \left(\frac{J_{01}}{G_1}\right)^2}} \quad (16-12)$$

The imaginary part of Eq. (16-10) is a capacitive susceptance which must be included as part of the resonator. For the input coupling we must therefore replace C_{01}^* by a new capacitance

$$C_{01}^* = C_1 + \frac{C_{01}}{1 + \left(\frac{B_{01}}{G_1}\right)^2} \quad (16-13)$$

where C_1 is the shunt capacitance of any length of line between Resonator 1 and the input coupling capacitor C_{01} , and the second term is the capacitance corresponding to the susceptive part of Eq. (16-10) where C_{01} is obtained by Eq. (16-12). Then analogously to Eq. (16-8), the total shunt capacitance across Resonator 1 is

$$C_1' = C_{01}^* + C^* + C_{12}^* \quad (16-14)$$

where C^* and C_{12}^* are as defined in the discussion of the interior couplings.

In like manner, for an n -resonator filter, the last coupling susceptance is

$$B_{n,n+1} = \omega_0 C_{n,n+1} = \frac{J_{n,n+1}}{\sqrt{1 - \left(\frac{J_{n,n+1}}{G_n}\right)^2}} \quad (16-15)$$

$$C_{n,n+1}^e = C_l + \frac{C_{n,n+1}}{1 + \left(\frac{k_{n,n+1}}{G_n} \right)^2} \quad (16-16)$$

and the capacitance across the n th resonator is

$$C_n^J = C_{n,n+1}^e + C_n^* + C_{n-1,n}^e \quad (16-17)$$

D. DESIGN USING BAR TRANSMISSION LINE CONSTRUCTION

The wide-stop-band filters under construction can be built using any of a variety of different types of construction. Figure 16-6 shows one possible kind of strip transmission line construction in which the center

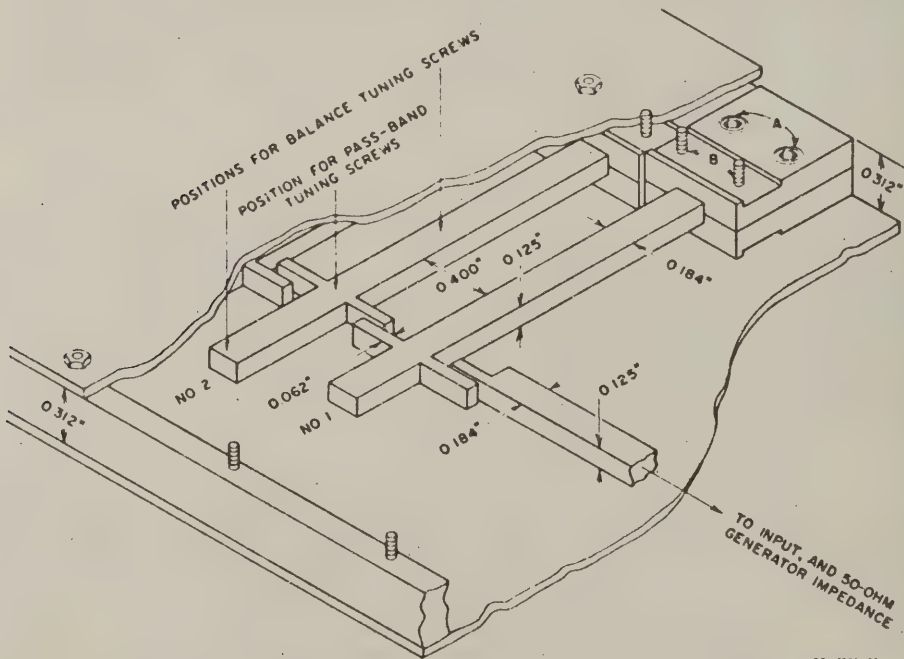


FIG. 16-6

A BAR TRANSMISSION LINE CONSTRUCTION FOR THE FILTER IN FIG. 16-1(a)

conductor is a rectangular metal bar. The coupling capacitors $C_{k,k+1}$ of Fig. 16-1(a) are realized by the capacitance between the coupling tabs which protrude at right angles to each resonator. For the case shown in the figure, the ground plane spacing is 0.312-inch; and the resonator, the input line, and the output line are all 0.184- by 0.125-inch bars, which gives them a characteristic impedance of 50 ohms when air dielectric is used. The resonator bars are supported and short-circuited at one end by metal supporting and clamping blocks. The recessed screws marked *A* are used to clamp the two halves of the shorting blocks together at the proper location on the resonator bar. After a pair of shorting blocks has been clamped to a resonator bar at the proper spot, the resonator is positioned and fastened to the lower ground plane by use of the screws marked *B*. After all of the resonators have been located on the lower ground plane, the upper ground plane is laid on and nuts are put on the screws marked *B* to press the upper ground to the shorting blocks. Note that the upper and lower sides of the shorting blocks have been recessed slightly to create high contact pressure at the inner edge of the shorting blocks. Design data have been prepared for this type of construction to simplify the work of applying the preceding theory.

By using approximations similar to those used for thick strips in Ref. 2, the series-coupling capacitance $C_{k,k+1}$ and shunt capacitance $C_{k,k+1}^*$ for various coupling tab spacings were estimated. These capacitances are plotted in Figs. 16-7(a) and 16-7(b). The ground plane spacing and the bar and coupling tab dimensions are to be taken as in Figs. 16-6 and 16-7(a). As is the case for *T*-junctions,³ there are definite reference planes in a "plus junction" at which short circuits will block all transmission. From measurements made on a two-resonator design, it is estimated that the proper points from which to measure the distances l_{ak} and l_{bk} in Fig. 16-3 and 16-4 are about 0.010-inch from the centerline of the coupling tabs, as indicated in Fig. 16-8. In calculating the shunt capacitances $C_{k,k+1}^*$ in Fig. 16-7(b) the reference plane for computing the tab line capacitance C_l was taken as the edge of the resonator bar. Measurements made on trial filter designs suggest that the plus-junction capacitance C^* should be about $-0.10 \mu\text{mf}$. Also, calculations and measurements indicate that the open-circuit end of each resonator bar should be shortened by about 0.055-inch to account for the fringing capacitance from the open-circuited end. The 0.010-inch reference plane displacement value, the value for C^* , and the 0.055-inch correction for resonator end fringing capacitance are all approximate values. However, if tuning screws are used, these values should be close enough.

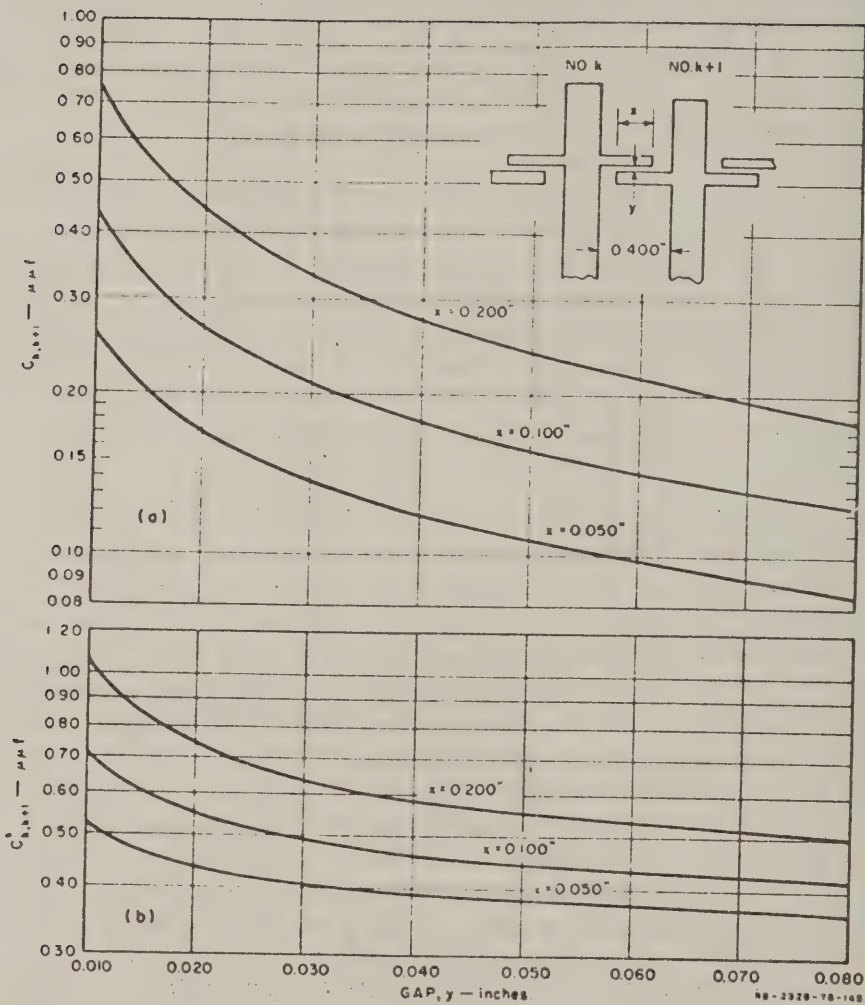


FIG. 16-7
CHARTS OF ESTIMATED VALUES OF THE CAPACITANCES ASSOCIATED WITH THE
COUPLINGS FOR THE CONSTRUCTION IN FIG. 16-6

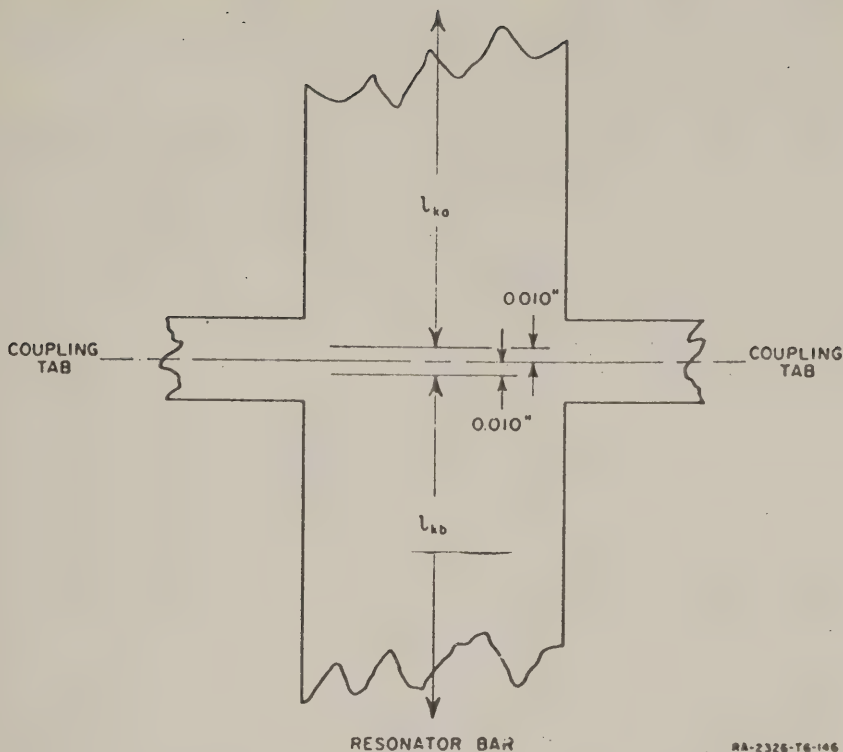


FIG. 16-8

DEFINITION OF THE JUNCTION REFERENCE PLANES
FOR THE CONSTRUCTION IN FIG. 16-6

The design process begins by calculating δ and ω_0 by Eqs. (15-28) and (15-29). Then using Eq. (15-27) in (15-20), the attenuation characteristic of the low-pass prototype can be related to the expected attenuation characteristic for the band-pass filter. With the aid of Eq. (15-20) of this report, and Fig. 2-2 of Ref. 4 or the attenuation charts in Ref. 5, one can quickly estimate how many resonators will be required to give a required rate of cut-off for a given type of transmission characteristic (i.e., maximally flat, Tchebyscheff, etc.).* Then the prototype element values [see Fig. 15-2(a)] may be obtained from the tables in Ref. 1 or 6.

Accurate design of a filter of this type requires some iteration in the calculations. This is because the values of the inverter parameters

*The frequency scale of the plots in Ref. 5 are normalized to the frequencies of the 3-db points while the Tchebyscheff prototype filters in Refs. 1 and 6 are normalized with respect to their equal-ripple band-edge points. This should be taken into account when using the charts in Ref. 5 with the prototypes from Refs. 1 or 6.

$J_{k,k+1}$ are influenced by the values of the resonator parameters b_k , which are in turn influenced by the capacitance C_k^J , which is influenced by the value of $J_{k,k+1}$. In the examples tried, the calculations converged with only a few iterations. Since the couplings in the middle of the filter have the smallest values of $C_{k,k+1}$ and the resonators thus have smaller C_k^J , the middle resonators are influenced least by their C_k^J . Because of this it is best to start with the middle couplings first. Equation (15-23) may be expressed in a form more convenient for iterative calculations, i.e.,

$$\frac{J_{k,k+1}}{Y_0} = d_{k,k+1} \sqrt{\frac{b_k}{Y_0} \frac{b_{k+1}}{Y_0}} \quad (16-18)$$

where

$$d_{k,k+1} = \frac{1}{\delta \sqrt{g_k g_{k+1}}} \quad (16-19)$$

The procedure is then to first compute $d_{k,k+1}$, estimate values for B_k^J/Y_0 and B_{k+1}^J/Y_0 for the resonators adjacent to the coupling in question. Then trial values for b_k and b_{k+1} are obtained from Fig. 16-3 or 16-4. Next $J_{k,k+1}/Y_0$ is obtained by Eq. (16-18), and by Eq. (16-7) and the fact that $Y_0 = 0.020$ (for the construction in Fig. 16-6), a trial coupling capacitance value $C_{k,k+1}$ is obtained. By Fig. 16-7(a) the trial coupling dimensions are obtained; using these coupling dimensions, trial values for C_k^J and C_{k+1}^J are obtained from Fig. 16-7(b). Next an improved value for $B_k^J = B_{k+1}^J$ is obtained by use of Eqs. (16-8) and (16-9). If this deviates appreciably from the original estimate for B_k^J , the calculation should be repeated. As these calculations are carried out for the adjacent couplings, the B_k^J may have to be revised slightly again since the coupling capacitance and, hence, the C_k^J vary from resonator to resonator. Fortunately, however, the effect of the B_k^J on the coupling capacitances $C_{k,k+1}$ should usually be relatively small so that the calculations converge to satisfactory values rapidly.

If the terminations are equal (as in Fig. 16-6), then $G_1 = G_n = Y_0$ and Eqs. (15-21) and (15-22) may be written in the form

* When starting calculations for the middle resonator (or resonators), let $B_k^J/Y_0 = B_{k+1}^J/Y_0$.

$$\frac{J_{01}}{Y_0} = e_{01} \sqrt{\frac{b_1}{Y_0}} \quad (16-20)$$

and

$$\frac{J_{n,n+1}}{Y_0} = e_{n,n+1} \sqrt{\frac{b_n}{Y_0}} \quad (16-21)$$

where

$$e_{01} = \frac{1}{\sqrt{\delta g_1}} \quad (16-22)$$

and

$$e_{n,n+1} = \sqrt{\frac{r}{\delta g_n}} \quad (16-23)$$

Using these equations and Eqs. (16-12) and (16-15) the calculations of B_1^J and B_n^J for the end resonators are much the same as for the other resonators. But in this case Fig. 16-7(b) cannot be used directly, since C_{01}^* and $C_{n,n+1}^*$ in Eqs. (16-14) and (16-17) are given by Eqs. (16-13) and (16-16). Figure 16-7(b) can be used, however, if we write Eqs. (16-14) and (16-17) in the forms

$$C_1^J = C_{01}^* - \frac{C_{01} \left(\frac{b_{01}}{G_1} \right)^2}{1 + \left(\frac{b_{01}}{G_1} \right)^2} + C^* + C_{12}^* \quad (16-24)$$

and

$$C_n^J = C_{n,n+1}^* - \frac{C_{n,n+1} \left(\frac{B_{n,n+1}}{G_1} \right)^2}{1 + \left(\frac{B_{n,n+1}}{G_n} \right)^2} + C^* + C_{n-1,n}^* \quad (16-25)$$

A first-order approximation for the negative terms should suffice.

Having established compatible values of $C_{k, k+1}$ and B_k' throughout the filter, the theoretical lengths of the resonators as compared with a quarter wavelength are obtained from Figs. 16-3 and 16-4, or Eq. (16-3). In computing the actual lengths of the bars, the end fringing capacitances and the junction reference planes should be taken into account as previously mentioned.

E. RESULTS OF SOME TRIAL DESIGNS

A two-resonator filter designed for a five-percent bandwidth centered at 1 kMc was built in the construction shown in Fig. 16-6. This filter was designed to stop the spurious response that would normally occur at S-band. Without tuning screws it had a very narrow pass band at 3.8 kMc because the open- and short-circuited sides of the resonators produced short-circuits at the coupling tabs at slightly different frequencies [this creates the situation discussed in connection with the dashed lines in Fig. 16-2(a)]. At the frequency of the spurious pass band which a given resonator is to suppress, there will be a point of high voltage at the open-circuited end of the resonator and one or more additional points of high voltage between the coupling-tab junction and the short-circuited end of the resonator. If pairs of tuning screws are placed through the cover plates at the open-circuited end of the resonator and also at one of the high-voltage points between the junction and the short circuit (see Fig. 16-6), it then becomes possible to tune for "balance" between the electrical lengths of the open- and short-circuited sides of the resonator in order to ensure suppression of the spurious pass band. It is also desirable to then add a third pair of screws through the cover plates above and below the junction of the resonator bar and the coupling tabs. These latter screws are used to tune the resonator accurately to the desired pass-band frequency after the "balance" screws have been adjusted to suppress the higher spurious pass band. By this technique, the pass band at 3.8 kMc of the two-resonator filter was eliminated and the filter had a stop band up to around 5 kMc where there was another pass band, as was expected for this filter.

The two-resonator filter was used to obtain estimates of the junction reference planes and capacitance C^* discussed in connection with Fig. 16-8, and also to obtain check information on the coupling capacitance computations. Next a four-resonator filter was constructed as shown in Fig. 16-9 and photographed in Fig. 16-10. This filter was designed to have a

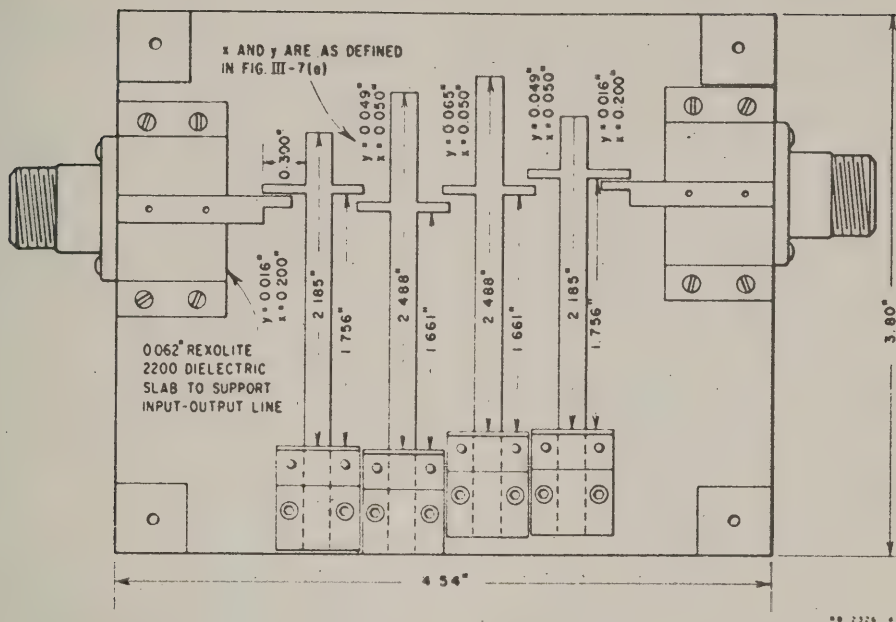


FIG. 16-9

BASIC DIMENSIONS OF A FOUR-RESONATOR, WIDE-STOP-BAND FILTER DESIGN

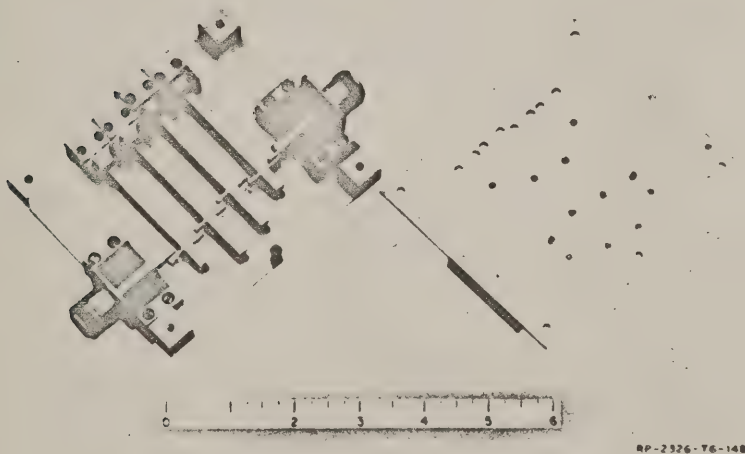


FIG. 16-10

PHOTOGRAPH OF THE FILTER WHOSE DIMENSIONS ARE GIVEN IN FIG. 16-9

0.5-db Tchebyscheff ripple with a bandwidth of 5 percent centered at 1100 Mc. The two center resonators were designed, using Fig. 16-3, to suppress the spurious pass band in the vicinity of $3\omega_0$, the two end resonators were designed with the aid of Fig. 16-4 to suppress the $5\omega_0$ spurious pass band. The resonators were synchronously tuned at the primary pass-band frequency by use of Dishal's tuning procedure.⁷

The measured pass-band response of the filter is shown in Fig. 16-11. The center frequency turned out to be a little low; however, this could be easily corrected by shortening the resonator bars by an amount computed

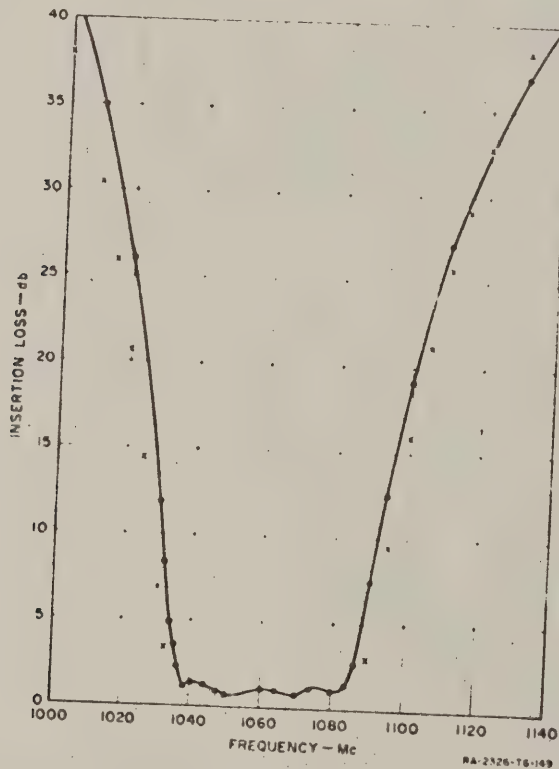


FIG. 16-11

THE MEASURED RESPONSE OF THE FILTER IN FIG. 16-10
IN THE VICINITY OF THE PASS BAND

The solid line is the measured response while the x's represent attenuation values mapped from the low-pass prototype with the low-pass to band-pass transformation

from the error in the band center frequency.* The crosses in Fig. 16-11 are points calculated from the attenuation characteristic of the lossless, low-pass prototype by use of the mapping defined by Eq. (15-20) and Eqs. (15-27) to (15-29) with ω_0 set to the measured band center. It is seen that the measured attenuation characteristic is close to the theoretical, though a little narrower. If desired, the bandwidth could be increased to exactly the desired amount by decreasing the gap spacing, y , of the resonators [see Fig. 16-7(a)]. The amount that the gaps should be altered can be estimated by inserting the measured band edge frequencies in Eq. (15-28) to obtain a measured value of δ . Then, knowing the measured δ one can estimate the required change in gap spacing to give the desired value of δ by use of Eqs. (16-18), (16-19), and (16-7), and Fig. 16-7(a).

Figure 16-12 shows the stop-band characteristics of this filter. It had been expected that this filter would have no spurious pass bands up to around 7 kMc; however, as the figure shows, the 5-kMc spurious pass band is present. This pass band was practically unaffected by the tuning screws on end resonators even if the screws were nearly touching the resonator bars (the end resonators were the ones which were to suppress this band). Probing the fields did not reveal higher order modes. Some study of this phenomenon indicates that with the large coupling capacitances on the input and output sides of the end resonators, their coupling tabs can become resonant in a manner similar to a half-wavelength, capacitively coupled resonator. Apparently because of this resonance, the pass-band suppression effect of the end resonators was destroyed.

The pass band in the vicinity of 5 kMc could very probably be removed by redesigning the input and output couplings so that the input and output lines are capacitively coupled directly to the side of the end resonator bars without the use of end coupling tabs. Also, this problem would probably have been avoided if the end resonators had been made to suppress the spurious pass band around $3\omega_0$ while the middle resonators were made to suppress the pass band around $5\omega_0$. Then the coupling tabs on the resonators which were to suppress the $5\omega_0$ band would have had relatively light coupling and probably would not have become resonant in the vicinity of $5\omega_0$ (note that the end couplings in Fig. 16-9 are much tighter than the other couplings).

* The estimated value for C^* given in the preceding discussion contains a correction from the value used in the design discussed above. Filters designed with this improved value for C^* should have a relatively higher mid-band frequency.

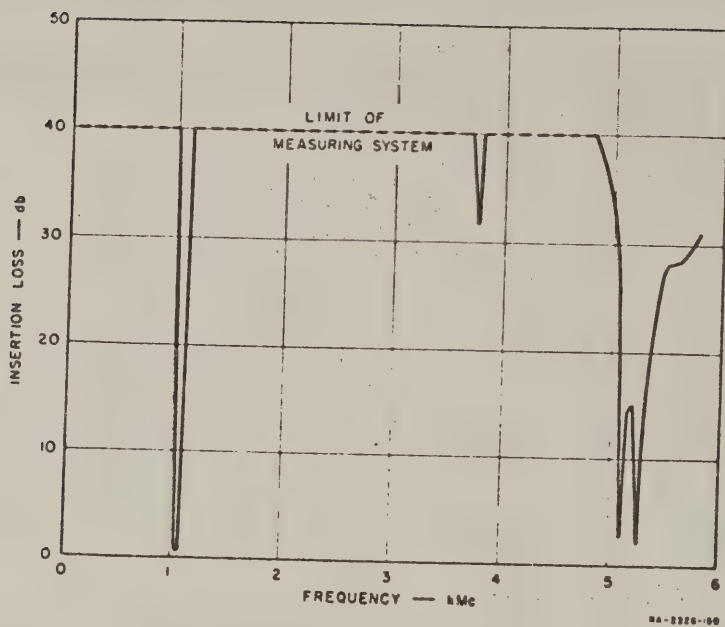


FIG. 16-12

THE STOP-BAND RESPONSE OF THE FILTER IN FIG. 16-10

Although balance tuning screws were included in the design of this filter, they were not expected to prove necessary because, if two of the resonators developed a very narrow spurious resonance, a pass band would not be likely to occur since the other pair of resonators would not have the same frequency for their spurious resonance. Preliminary tests revealed no $3\omega_0$ spurious band (as was expected from the above reasoning) and the balance tuning screws were not used. However, after all of the measurements were nearly completed, the dip in attenuation near 3.8 kMc was noticed. If time had been available to repeat the tuning procedure and the measurements, this dip could probably have been raised by adjusting the balance tuning screws on Resonators 2 and 3 (designed to suppress the $3\omega_0$ spurious pass band).

* Adjusting the balance tuning screws will alter the pass-band tuning, although the pass-band tuning screws will not affect the balance tuning (see Fig. 16-6). The balance screws should always be adjusted before the filter is tuned at the pass-band center frequency.

REFERENCES

1. See Chapter 13 of this report.
2. S. B. Cohn, et al, "Strip Transmission Lines and Components," Final Report, Chaps. 2 and 3, SRI Project 1114, Contract DA 36-039 SC-63232, Stanford Research Institute, Menlo Park, California (February 1957).
3. See Chapter 11 of this report.
4. S. B. Cohn, et al, "Research on Design Criteria for Microwave Filters," Final Report, Chap. 2, SRI Project 1331, Contract DA 36-039 SC-64625, Stanford Research Institute, Menlo Park, California (June 1957). Also, "Direct-Coupled-Resonator Filters," *Proc. IRE* 45, pp. 187-196 (February 1957).
5. *Reference Data for Radio Engineers*, 4th ed. pp. 193-189, International Telephone and Telegraph Corp., New York (1956).
6. L. Weinberg, "Network Design by Use of Modern Synthesis Techniques and Tables," Tech. Memo. 427, Hughes Aircraft Company, Research Laboratories, Culver City, California. (April 1956). Also, *Proceedings of the National Electronics Conference* Vol. 12, (1956).
7. M. Dishal, "Alignment and Adjustment of Synchronously Tuned Multiple-Resonator-Circuit Filters," *Proc. IRE* 39, pp. 1448-1455 (November 1951).

CHAPTER 17

A METHOD FOR DESIGNING WIDE-PASS-BAND, MICROWAVE FILTERS FROM LUMPED-ELEMENTS PROTOTYPES

A. GENERAL

In this chapter many of the concepts discussed in Chapter 15 will be used, but in a quite different way than they were for the narrow or moderate bandwidth theory utilized for the filter treated in Chapter 16. In that case the coupling element values were obtained from low-pass prototype element values along with bandpass resonator parameters evaluated at the mid-band frequency [see Eqs. (15-30) and (15-31)]. In the wide-pass-band design method about to be discussed, parameters of the wideband microwave filter will be fixed at a band-edge frequency as well as at the mid-band frequency. Also, the wideband method to be described will focus on the image parameters of the various sections of the prototype and band-pass filters rather than upon resonators and couplings.

B. A MODIFIED LOW-PASS PROTOTYPE AND ITS BANDPASS EQUIVALENT

Although the design point of view to be described can be adapted for designing filters whose individual sections are not symmetrical, the example to be considered will consist of symmetrical sections. Because of this it will be desirable to define the low-pass prototype as consisting of symmetrical sections also. By reasoning similar to that used by Cohn¹ in going from the circuit in Fig. 15-2(b) to that in Fig. 15-2(c), it is possible to convert the prototype circuit in Fig. 15-2(a) of this report to that in Fig. 17-1. The values of the inductances $L_{a,k}$ are arbitrary. The impedance inverters are considered to be ideal and are introduced only as an aid to mathematical reasoning.* The impedance-inverter parameters in Fig. 17-1 are related to the element values^{2,3} g_k and r of the circuit in Fig. 15-2(a) by

$$K_{01} = \sqrt{\frac{R_1 L_{a,1}}{g_1}} \quad (17-1)$$

* To this writer's knowledge it is impossible to build an impedance inverter that will operate down to DC.

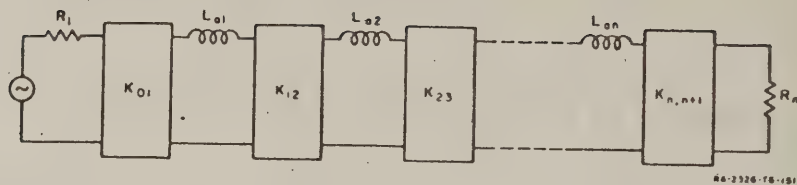


FIG. 17-1

THE LOW-PASS PROTOTYPE IN FIG. 15-2(a) MODIFIED
TO INCLUDE IMPEDANCE INVERTERS

$$K_{k,k+1} = \sqrt{\frac{L_{0k} L_{0k+1}}{g_k g_{k+1}}} \quad (17-2)$$

and

$$K_{n,n+1} = \sqrt{\frac{L_{0n} R_n r}{g_n}} \quad (17-3)$$

There will be situations where one would want to do this differently; however, for the purposes of the example to be considered it will be convenient to set

$$L_{0k} = \frac{R_1}{\omega'_1} = \frac{R_n}{\omega'_1} \quad (17-4)$$

and split each coil in half to give symmetrical sections as shown in Fig. 17-2. Then Eqs. (17-1) to (17-3) become

$$K_{01} = \frac{R_1}{\sqrt{g_1 \omega'_1}} \quad (17-5)$$

$$K_{k,k+1} = \frac{R_1}{\omega'_1 \sqrt{g_k g_{k+1}}} \quad (17-6)$$

Note that in Fig. 15-2(a) it is assumed that $r = 1$ for n odd. This will be true for lossless Tchebyscheff or maximally flat filters which have zero reflection at one or more pass-band frequencies. Element values for such filters can be obtained from Chapter 13. If the formulas in this discussion are to be used for a circuit where n is odd but $r \neq 1$, then r should be replaced by $1/r$ in the following equations for the inverter parameters.

and

$$K_{n,n+1} = R_1 \sqrt{\frac{r}{g_n \omega'_1}} \quad (17-7)^*$$

If the lossless prototype circuit in Fig. 15-2(a) is for a Tchebyscheff or maximally flat filter of the usual sort, where the pass band has one or more frequencies with perfect transmission, then the circuit in Fig. 17-2 will necessarily be symmetrical. For convenience, we shall assume that this is the case.

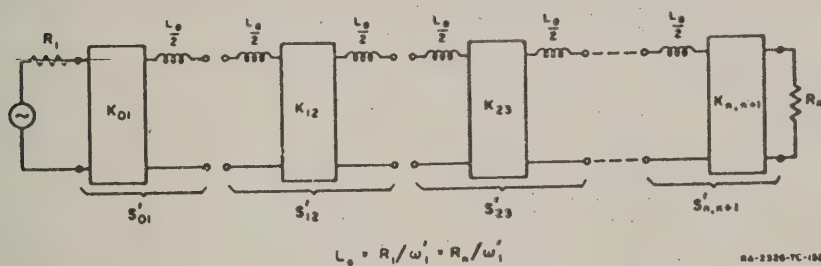


FIG. 17-2

THE LOW-PASS PROTOTYPE USED FOR THE WIDE-PASS-BAND FILTER
EXAMPLE DISCUSSED HEREIN

The image impedance of sections S'_{12} to $S'_{n-1,n}$ in Fig. 17-2 is given by

$$Z_{k,k+1}^i(\omega') = K_{k,k+1} \sqrt{1 - \left(\frac{\omega'}{\Omega_{k,k+1}} \right)^2} \quad (17-8)$$

where ω' is the frequency variable of the prototype and

$$\Omega_{k,k+1} = \frac{\omega'_1 2K_{k,k+1}}{R_1} \quad (17-9)$$

* See footnote on preceding page.

is the cut-off frequency of section $S'_{k,k+1}$. In like manner the image attenuation $\alpha_{k,k+1}$ and $\beta_{k,k+1}$ for section $S'_{k,k+1}$ are given by

$$\left. \begin{aligned} \alpha_{k,k+1} &= 0 \\ \beta_{k,k+1} &= \sin^{-1} \frac{\omega'}{\Omega_{k,k+1}} \pm \frac{\pi}{2} \\ \omega' &\leq \Omega_{k,k+1} \end{aligned} \right\} \quad (17-10)$$

when

and

$$\left. \begin{aligned} \alpha_{k,k+1} &= \cosh^{-1} \frac{\omega'}{\Omega_{k,k+1}} \\ \beta_{k,k+1} &= \frac{\pi}{2} \pm \frac{\pi}{2} \\ \omega' &\geq \Omega_{k,k+1} \end{aligned} \right\} \quad (17-11)$$

when

The $\pm \pi/2$ phase terms appear because the impedance inverters necessarily introduce $\pm \pi/2$ phase. For the purposes of this paper, either sign is chosen as may be appropriate with regard to a given microwave structure.

The end sections S'_{01} and $S'_{n,n+1}$ in Fig. 17-2 cannot be treated conveniently from the image point of view, but by joining them together as shown in Fig. 17-3 their basic properties can be determined on the insertion-loss basis. Since the transmission circuit in Fig. 17-3 is lossless and symmetrical, its attenuation may be determined from the mid-section impedance $r'_e + jx'_e$ by the relation⁴

$$\frac{P_{avail}}{P} = 1 + \left(\frac{x'_e}{r'_e} \right)^2 = 1 + \left(\frac{\omega' R_1^2}{\omega_1^2 2K_{01}^2} \right)^2 \quad (17-12)$$

$$= 1 + \left(\frac{\omega'}{\Omega_{01}} \right)^2 \quad (17-13)$$

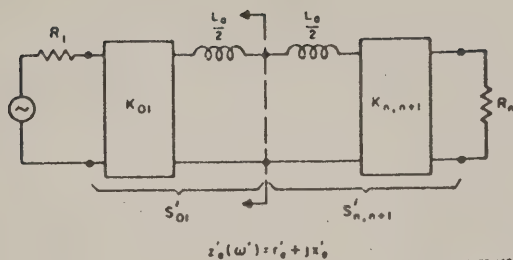


FIG. 17-3

ARRANGEMENT FOR FIXING THE PARAMETERS OF THE
PROTOTYPE END SECTIONS

where

$$\Omega_{01} = \Omega_{n,n+1} = \frac{\omega'_1 2K_{01}^2}{R_1^2} = \frac{\omega'_1 2K_{n,n+1}^2}{R_n^2} \quad (17-14)$$

is the 3-db-down frequency of the end sections as connected in Fig. 17-3.

It will usually be desirable to represent the bandpass form of the circuit in Fig. 17-2 with the aid of a frequency transformation

$$\omega' = \delta F(\omega) \quad (17-15)$$

such as was described in Chapter 15. Then the equivalent circuit takes the form shown in Fig. 17-4 where it is convenient to define X_n so that

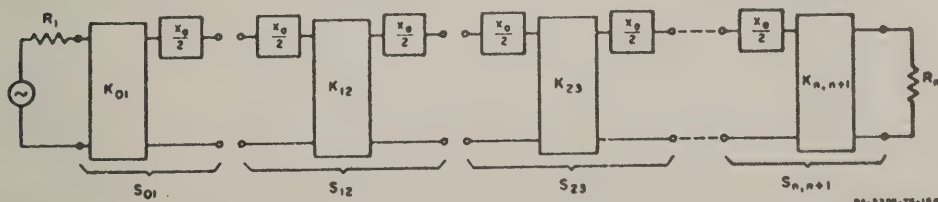


FIG. 17-4

A BAND-PASS FILTER MODEL DERIVED FROM THE PROTOTYPE IN FIG. 17-2

$$X_0 = L_0 \omega' = L_0 \delta F(\omega) = \frac{R_1 \delta F(\omega)}{\omega'_1} \quad (17-16)$$

With this definition for X_0 , the inverter parameters $K_{k,k+1}$ will be the same for both the low-pass prototype in Fig. 17-2 and its bandpass equivalent in Fig. 17-4.

The dual forms of the circuits in Figs. 17-1 to 17-4 should also be useful in some situations, and they may be obtained directly by applying duality to the results of this section.

C THE GENERAL BASIS FOR THIS WIDEBAND DESIGN PROCEDURE

Ordinarily when designing a wide-pass-band microwave filter on the image basis, the filter is constructed from a number of identical, symmetrical sections with some modified sections at the ends of the filter in order to improve the match between the filter image impedance and the terminations. This design approach usually gives reasonably good results if the design specifications are not too strict, but it is often very difficult to produce a nearly optimum design by such methods.

The prototype equivalent circuit in Fig. 17-2 (and its dual) is helpful for wideband microwave filter design in that it provides a guide for precision design of filters consisting of symmetrical sections. If the circuit in Fig. 17-2 is a maximally flat or Tchebyscheff prototype, the image cut-off frequencies $\Omega_{k,k+1}$ and the zero-frequency image impedances $Z_{k,k+1}^i(0')$ will be found to vary from section to section as is illustrated by examples in Table 17-1. Note that the image cut-off frequency of the individual sections often extends considerably beyond the cut-off frequency of the over-all filter, i.e., beyond $\omega'_1 = 1$. Also note that the zero-frequency image impedances are generally considerably smaller than the termination impedances $R_1 = R_2 = 1$, and that they vary from section to section. The basic wideband design approach is then to design the symmetrical sections of the bandpass filter so that the image properties of the sections will vary from one part of the filter to another in the same manner as the image properties vary from section to section in the prototype. In the case of the end sections of the microwave filter, they are connected together and designed using the prototype end sections connected as in Fig. 17-3 as a guide for design. A recommended procedure for quantitatively relating the microwave filter sections to those of the prototype will now be discussed.

Table 17-1

IMAGE PARAMETERS OF LOW-PASS MAXIMALLY FLAT AND TCHEBYSCHIEFF FILTERS OF FORM IN FIG. 17-2 WITH $n = 9$ REACTIVE ELEMENTS AND $R_1 = R_9 = 1$.

| (A) MAXIMALLY FLAT | | | |
|----------------------------------|-------------------|--------------------|---|
| $k, k+1$ | $\Omega_{k, k+1}$ | $Z_{k, k+1}^1(0')$ | Filter 3 db, point at $\omega_1 = 1$ |
| 0, 1 and 9, 10 | 5.759* | | |
| 1, 2 and 8, 9 | 3.394 | 1.697 | |
| 2, 3 and 7, 8 | 1.616 | 0.308 | |
| 3, 4 and 6, 7 | 1.179 | 0.590 | |
| 4, 5 and 5, 6 | 1.032 | 0.516 | |
| (B) TCHEBYSCHIEFF, 0.1-db RIPPLE | | | |
| $k, k+1$ | $\Omega_{k, k+1}$ | $Z_{k, k+1}^1(0')$ | Filter equal-ripple band, edge at $\omega_1 = 1$ |
| 0, 1 and 8, 10 | 1.673* | | |
| 1, 2 and 8, 9 | 1.523 | 0.762 | |
| 2, 3 and 7, 8 | 1.140 | 0.570 | |
| 3, 4 and 6, 7 | 1.077 | 0.539 | |
| 4, 5 and 5, 6 | 1.059 | 0.530 | |
| (C) TCHEBYSCHIEFF, 1.0-db RIPPLE | | | |
| $k, k+1$ | $\Omega_{k, k+1}$ | $Z_{k, k+1}^1(0')$ | Filter equal-ripple band, edge at $\omega_1 = 1$ |
| 0, 1 and 9, 10 | 0.918* | | |
| 1, 2 and 8, 9 | 1.281 | 0.641 | |
| 2, 3 and 7, 8 | 1.070 | 0.535 | |
| 3, 4 and 6, 7 | 1.038 | 0.519 | |
| 4, 5 and 5, 6 | 1.029 | 0.515 | |

* 3-db point for end sections connected as in Fig. 17-3. Other $\Omega_{k, k+1}$ for $k = 1$ to $n - 1$ are the image cut-off frequencies for the interior sections.

D. QUANTITATIVE RELATIONS BETWEEN PROTOTYPE AND MICROWAVE FILTER SECTIONS

1. THE MAPPING FUNCTION

The low-pass to bandpass mapping function should be selected using the principles discussed in Chapter 15. As far as is practical, all frequencies of infinite attenuation which are close to the primary pass band should be accounted for in the selection of the mapping function. If there is a secondary pass band close to the primary pass band, it is well to account for this also (see example in Section E). In the wideband

design procedure under consideration, the mapping function will not be used directly for calculation of circuit element values but, rather, for predicting the number of sections which will be required to give a given rate of attenuation, and for predicting the relation between the cut-off frequencies ω_1 and ω_2 and the "midband" frequency ω_0 [see Fig. 15-1(b)]. The design equations for the individual sections will consist of constraint equations established at the mid-band frequency ω_0 and either one of the band-edge frequencies ω_1 or ω_2 .

2. THE END SECTIONS

Let us suppose that it has been decided to establish the design constraints at the midband frequency ω_0 and the lower band edge frequency ω_1 . The frequencies correspond to $\omega' = 0$ and $-\omega'_1$, respectively, for the low-pass prototype in Figs. 17-2 and 17-3. At $\omega' = 0$ the mid-plane impedance in Fig. 17-3 is

$$z'_e(0) = \frac{K_{01}^2}{R_1} \quad (17-17)$$

while at $-\omega_1 = -1$ this impedance is

$$z'_e(-\omega'_1) = \frac{K_{01}^2}{R_1} - j \frac{\omega'_1 L_4}{2} = r'_e + jx'_e \quad (17-18)$$

By Eq. (17-12) we see that the attenuation of the circuit in Fig. 17-3 at $-\omega'_1$ is fixed if the ratio x'_{01}/r'_{01} is fixed. By Eqs. (17-4) and (17-18)

$$\left. \frac{x'_e}{r'_e} \right|_{\omega' = -\omega'_1} = \frac{-R_1^2}{2K_{01}^2} \quad (17-19)$$

The corresponding bandpass microwave circuit is shown in Fig. 17-5 with unprimed symbols. At the lower band-edge frequency ω_1 the identical sections S_{01} and $S_{n,n+1}$ are constrained to satisfy the condition

* ω_0 is the bandpass mapping of $\omega' = 0$ for the prototype. It is generally located to one side of the mid-point between ω_1 and ω_2 .

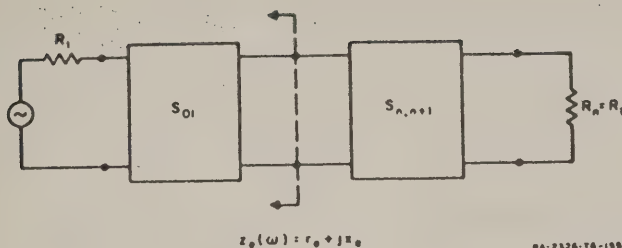


FIG. 17-5

ARRANGEMENT FOR DETERMINING THE PARAMETERS OF THE
MICROWAVE FILTER END SECTIONS

$$\left. \frac{x_e}{r_e} \right|_{\omega=\omega_1} = \left. \frac{x'_e}{r'_e} \right|_{\omega'=-\omega_1} = \frac{-R_1^2}{2K_{01}^2} \quad (17-20)$$

At the mid-band frequency ω_0 the bandpass end sections are constrained so that

$$z_e(\omega_0) = \text{purely real.} \quad (17-21)$$

The design of the microwave filter is conveniently carried out in normalized form, and it is desirable to apply an additional constraint on the normalized $z_e(\omega)$ impedance in Fig. 17-5 so that

$$z_e(\omega_0) = z'_e(0') = \frac{K_{01}^2}{R_1} \quad (17-22a)$$

where the primed quantities are for the prototype and the unprimed are for the microwave filter. For cases (such as in the example to follow where $Z_{01}^0 = R_1$ is specified) it will not be possible to satisfy Eq. (17-22a) along with Eqs. (17-20) and (17-21). In such cases Eq. (17-22a) is replaced by simply changing the impedance scale of all of the interior sections of the filter by the factor

$$s = (\text{Impedance scale factor}) = \frac{z_e(\omega_0)}{z'_e(0')} \quad (17-22b)$$

i.e., we take the end section impedance level $z_e(\omega_0)$ as it comes, and adjust the rest of the filter to correspond. This will change the image impedance levels of the interior sections, but the ratios of impedance levels between the different interior sections and the ratios of impedance levels between the interior sections and the end sections will remain the same.

3. THE INTERIOR SECTIONS

Figure 17-6 shows one of the lossless, symmetrical, interior sections having an image impedance $Z_{k,k+1}^I(\omega)$ and a pass-band image phase $\beta_{k,k+1}$. Since the section is lossless, the pass-band image attenuation is zero. At the band-edge frequency, ω_1 , the constraint is applied that

$$Z_{k,k+1}^I(\omega_1) = sZ_{k,k+1}^I(-\omega_1') \quad (17-23)$$

where $Z_{k,k+1}^I(\omega')$ is the prototype image impedance from Eq. (17-8), and s is the scale factor from Eq. (17-22b). Examination of the examples in Table 17-1 will show that if ω_1 is the lower equal-ripple band edge of a Tchebyscheff filter as in Fig. 15-1(b), or is the lower 3-db point of a maximally flat filter, then $Z_{k,k+1}^I(-\omega_1')$ for the corresponding prototype will always be real and positive. (Note in the examples in Table 17-1 that the image cut-offs of the interior sections always go beyond the cut-off frequency for the over-all filter.)

At the midband frequency, ω_0 , the constraint

$$Z_{k,k+1}^I(\omega_0) = sZ_{k,k+1}^I(0') = sK_{k,k+1} \quad (17-24)$$

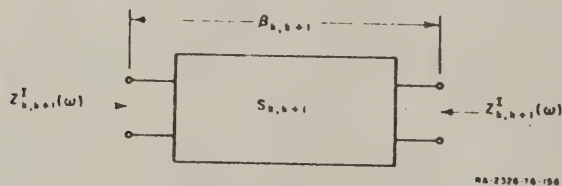


FIG. 17-6

A SYMMETRICAL, LOSSLESS, MICROWAVE FILTER SECTION $S_{k,k+1}$ WITH IMAGE PARAMETERS AS DISCUSSED IN THE TEXT

is applied and also the constraint

$$\beta_{k,k+1} \Big|_{\omega=\omega_0} = \left(\text{odd multiple of } \frac{\pi}{2} \right) \quad (17-25)$$

where $\beta_{k,k+1}$ is the image phase of interior section $S_{k,k+1}$. The last constraint equation follows from the fact that the interior sections of the prototype in Fig. 17-2 have $\pm \pi/2$ image phase shift at $\omega' = 0$ because of the inverters $K_{k,k+1}$. It should be possible to satisfy Eqs. (17-23) to (17-25) simultaneously.

E. A DESIGN EXAMPLE

As an example to test this procedure, the design method just described was applied to the filter structure shown in Fig. 17-7. The low-pass prototype [see Fig. 15-2(a)] had $n = 6$ reactive elements which when converted to the form in Fig. 17-2 give five internal sections plus the two end sections. The prototype filter had 0.1-db Tchebyscheff pass-band ripple which corresponds to the element values:

$$\begin{array}{ll} g_1 = 1.1681 & g_5 = 1.9029 \\ g_2 = 1.4039 & g_6 = 0.8618 \\ g_3 = 2.0562 & r = 0.7378 \\ g_4 = 1.5170 & \omega'_1 = 1.000 \end{array} \quad (17-26)$$

where the g_k and r are as indicated in Fig. 15-2(a), and ω'_1 is the equal-ripple band edge as indicated in Fig. 15-1(a).³

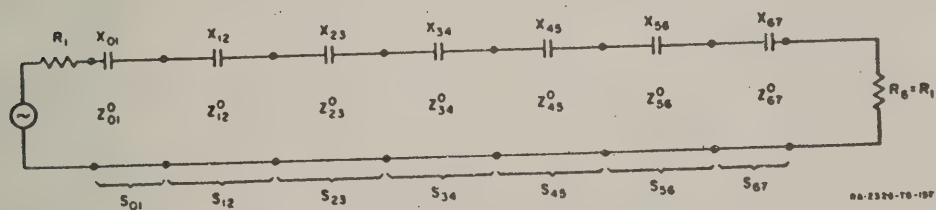


FIG. 17-7

A FILTER STRUCTURE SUITABLE FOR "HIGH-PASS" MICROWAVE FILTER APPLICATIONS

In order to predict the relation between ω_0 , ω_1 , and ω_2 , and to predict the rate of cut-off for the filter, a mapping function was selected using the principles discussed in Chapter 15. Note that the filter in Fig. 17-7 consists of sections of transmission line coupled by series capacitors. At low frequencies the attenuation can be accounted for by a single capacitor equivalent to the seven capacitors shown connected in series, since for very low frequencies the effect of the transmission lines will be negligible. Thus it is seen that this circuit will have a first-order pole of attenuation at $\omega = 0$. Wideband filters of the type shown in Fig. 17-7 are band-pass in nature, but are used mainly as high-pass filters since the attenuation in their upper stop band is very weak. Generally, the first spurious pass band will be centered around 2.5 times the center frequency of the first pass band if the first pass band has $\omega_2/\omega_1 = 2$. On this basis it was decided to try the mapping

$$\omega' = \delta F(\omega) = \delta \frac{(-1) \left(\frac{\omega}{\omega_0} - 1 \right) \left(\frac{\omega}{\omega_0} - 2.5 \right)}{\sqrt[6]{\frac{\omega}{\omega_0}}} \quad (17-27)$$

The $\{(\omega/\omega_0) - 1\}$ factor maps $\omega' = 0$ to the primary pass-band center at ω_0 , while the $\{(\omega/\omega_0) - 2.5\}$ factor accounts for the closely adjacent spurious pass band centered near $\omega = 2.5 \omega_0$. By Eq. (17-16) and the approximate band-pass model in Fig. 17-4 it is seen the $F(\omega)$ in Eq. (17-27) must have a one-sixth order pole at $\omega = 0$ if the over-all transfer function of the network with $n = 6$ reactances X_n is to have first-order pole of attenuation for $\omega = 0$. The (-1) multiplier was included so that $F(\omega)$ would satisfy Eq. (15-12).

Comparison of the computed results of trial designs with the theoretical attenuation predicted by mapping the attenuation characteristic of the low-pass prototype using Eq. (17-27) showed that the $F(\omega)$ in Eq. (17-27) has too steep a slope for $\omega \rightarrow 0$ even with its pole at the origin reduced to one-sixth order. It was decided that the excessive error might be the result of extra slope created by the numerator factors. For this reason the mapping

$$\omega' = \delta F(\omega) = \frac{\delta(-1) \cos\left(\frac{\pi}{2} \frac{\omega}{\omega_0}\right)}{\sqrt[6]{\frac{\omega}{\omega_0}}} \quad (17-28)$$

was tried, since the cosine function in the numerator would not contribute any slope to the function when ω becomes small, and since it also roughly accounts for the higher pass band. It was found that this mapping function will predict the rate of cut-off for the filter with good accuracy. For the general case where the prototype has n reactive elements Eq. (17-28) becomes

$$\omega' = \frac{\delta(-1) \cos\left(\frac{\pi}{2} \frac{\omega}{\omega_0}\right)}{\sqrt[n]{\frac{\omega}{\omega_0}}} \quad (17-29)$$

Using Eq. (15-12) we note that

$$F(\omega_2) = -F(\omega_1) \quad (17-30)$$

Because a bandwidth ratio in excess of $\omega_2/\omega_1 = 2$ was desired, a plot was made of $F(\omega)$ vs. ω/ω_0 from which values of ω_1 and ω_2 which satisfy Eq. (17-30) could be readily selected. From this plot, the values $\omega_1/\omega_0 = 0.656$ and $\omega_2/\omega_0 = 1.397$ were found to satisfy Eq. (17-30) and have about the desired ratio, i.e., $\omega_2/\omega_1 = 2.1$. Using Eq. (15-12) and the fact that $\omega_1^* = 1$ for the given prototype, the bandwidth factor δ was computed to be 1.810. In this manner the mapping function Eq. (17-28) was completely specified.

The prototype in Fig. 15-2(a) is converted to the form in Fig. 17-2 with the aid of Eqs. (17-5) to (17-7). Letting $R_1 = 1$ for the normalized design we obtain

$$\begin{aligned} K_{01} &= K_{67} = 0.9252 \\ K_{12} &= K_{56} = 0.7809 \\ K_{23} &= K_{45} = 0.5886 \\ K_{34} &= 0.5662 \end{aligned} \quad (17-31)$$

while $L_0 = 1$. For convenience R_1 in Fig. 17-7 is normalized to be the same as in the prototype in Fig. 17-2.

Figure 17-8 shows the left end section S_{01} for the filter in Fig. 17-7, which is identical with the right end section S_{67} . It is convenient to set the line characteristic impedance

$$Z_{01}^0 = R_1 \quad (17-32)$$

Also we can set

$$X_{01} = \gamma_{01} \frac{\omega_0}{\omega} \quad (17-33)$$

and

$$\theta_{01} = \phi_{01} \frac{\omega}{\omega_0} \quad (17-34)$$

where X_{01} and θ_{01} are, respectively, the coupling reactance and the electrical line length, while γ_{01} and ϕ_{01} are their values at ω_0 . Calculating the input impedance for the circuit in Fig. 17-8 and forming x_e/r_e , we find that Eq. (17-20) for this particular structure takes the form

$$\frac{-R_1^2}{2K_{01}^2} = \frac{\left(\gamma_{01} \frac{\omega_0}{\omega_1}\right) \left[1 - \frac{\gamma_{01}}{R_1} \left(\frac{\omega_0}{\omega_1}\right) \tan \phi_{01} \frac{\omega_1}{\omega_0} - \tan^2 \phi_{01} \frac{\omega_1}{\omega_0}\right]}{R_1 \left[1 + \tan^2 \left(\phi_{01} \frac{\omega_1}{\omega_0}\right)\right]} \quad (17-35)$$

Having specified Z_{01}^0 by Eq. (17-32), the constraint condition in Eq. (17-21) requires that

$$\begin{aligned} \gamma_{01} &= R_1 \left(\frac{1 - \tan^2 \phi_{01}}{\tan \phi_{01}} \right) = X_{01} \Big|_{\omega=\omega_0} \\ &= -2R_1 \cot(\pi - 2\phi_{01}). \end{aligned} \quad (17-36)$$

Having the values $\omega_1' = 1$, $R_1 = 1$, $K_{01} = 0.9252$, and $\omega_1/\omega_0 = 0.656$, the only unknowns in Eqs. (17-35) and (17-36) are γ_{01} and ϕ_{01} . Simultaneous

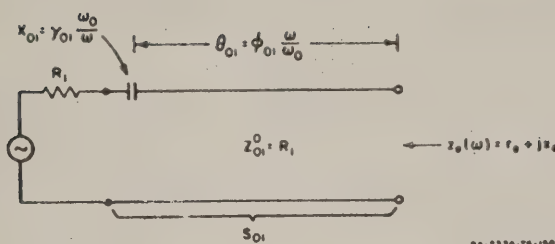


FIG. 17-8

DEFINITION OF PARAMETERS FOR THE END SECTIONS IN FIG. 17-7

solution with a computer gave $\gamma_{01} = -0.5216$ ohms and $\phi_{01} = 0.9129$ radian. The scale factor in Eq. (17-22b) is found to be in this case

$$s = \frac{R_1 \cot^2 \phi_{01}}{(K_{01})^2 / R_1} \quad (17-37)$$

which in this case turns out to be $s = 0.6974$.

For the interior sections (Fig. 17-9) the constraint Eq. (17-23) becomes for this case

$$Z_{k,k+1}^0 \sqrt{\left[-\cot \left(\phi_{k,k+1} \frac{\omega_1}{\omega_0} \right) \right] \left(\cot \left\{ \phi_{k,k+1} \frac{\omega_1}{\omega_0} + \left[\cot^{-1} \frac{\cot (\pi - 2\phi_{k,k+1})}{\omega_1 / \omega_0} \right] \right\} \right)} \quad (17-38)$$

$$= s Z_{k,k+1}^i (-\omega_1')$$

while the constraint Eq. (17-24) becomes

$$(Z_{k,k+1}^0) \cot \phi_{k,k+1} = s Z_{k,k+1}^i (0') \quad (17-39)$$

In this case the constraint Eq. (17-25) is satisfied by enforcing

* Graphical solution is not difficult. A plot of γ_{01} vs ϕ_{01} is made from Eq. (17-35). Then corresponding values of γ_{01} and ϕ_{01} are substituted in the right side of Eq. (17-34) to obtain a solution.

$$\gamma_{k,k+1} = X_{k,k+1} \Big|_{\omega=\omega_0} = Z_{k,k+1}^0 \left(\frac{1 - \tan^2 \phi_{k,k+1}}{\tan \phi_{k,k+1}} \right) \quad (17-40)$$

Dividing Eq. (17-38) by (17-39) gives

$$(\cot \phi_{k,k+1}) \sqrt{\left[-\cot \left(\phi_{k,k+1} \frac{\omega_1}{\omega_0} \right) \cot \left\{ \phi_{k,k+1} \frac{\omega_1}{\omega_0} + \cot^{-1} \left[\frac{\cot (\pi - 2 \phi_{k,k+1})}{\omega_1/\omega_0} \right] \right\} \right]} = \frac{Z_{k,k+1}^1(-\omega_1')}{Z_{k,k+1}^1(0')} \quad (17-41)$$

The right side of this equation is evaluated using Eqs. (17-8), (17-9), and (17-26) for the prototype filter. When $\omega_1/\omega_0 = 0.656$ is specified, the only remaining unknown in Eq. (17-41) is $\phi_{k,k+1}$. The required solutions may be obtained by plotting the left-hand side vs. $\phi_{k,k+1}$ for the given ω_1/ω_0 value. With the $\phi_{k,k+1}$ values obtained, the line characteristic impedances $Z_{k,k+1}^0$ may be obtained from Eq. (17-39), while the mid-band series capacitor reactance values $\gamma_{k,k+1}$ may be obtained from Eq. (17-40). The design parameters are summarized in Table 17-2.

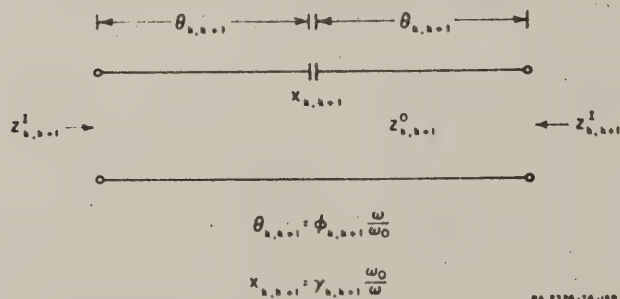


FIG. 17-9
DEFINITION OF PARAMETERS FOR THE INTERIOR SECTIONS IN FIG. 17-7

Table 17-2

DESIGN PARAMETERS FOR FILTERS IN FIG. 17-7 FOR SPECIFICATIONS:

$$\omega_1/\omega_0 = 0.656, \omega_2/\omega_0 = 1.397, \text{ AND } R_1 = R_6 = 1.$$

| $X_{k,k+1} \Big _{\omega/\omega_0} = \gamma_{k,k+1} \text{ ohms}$ | $B_{k,k+1} \Big _{\omega/\omega_0} = \phi_{k,k+1} \text{ radians}$ | $Z_{k,k+1}^0 \text{ ohms}$ |
|---|--|--------------------------------|
| $\gamma_{01} = \gamma_{67} = -0.5216$ | $\phi_{01} = \phi_{67} = 0.9129$ | $Z_{01}^0 = Z_{67}^0 = 1$ |
| $\gamma_{12} = \gamma_{56} = -0.3309$ | $\phi_{12} = \phi_{56} = 0.9030$ | $Z_{12}^0 = Z_{56}^0 = 0.6905$ |
| $\gamma_{23} = \gamma_{45} = -0.4798$ | $\phi_{23} = \phi_{45} = 0.9743$ | $Z_{23}^0 = Z_{45}^0 = 0.6045$ |
| $\gamma_{34} = -0.5061$ | $\phi_{34} = 0.9860$ | $Z_{34}^0 = 0.5964$ |

The response of this filter was calculated with a digital computer and is plotted in Figs. 17-10(a), (b). An exact mapping of the low-pass prototype would require that the response have 0.1 db Tchebyscheff ripple between $\omega_1/\omega_0 = 0.656$ and $\omega_2/\omega_0 = 1.397$, as was predicted with the mapping Eq. (17-28) with $\delta = 1.810$. As is seen from the pass-band characteristic in Fig. 17-10(a), the Tchebyscheff ripple characteristic is not perfect, but comes close to the desired shape. The lower 0.1-db point occurs at $\omega/\omega_0 = 0.660$, which is very close to the desired 0.656 value. The upper 0.1-db point occurs at 1.425, which exceeds the predicted cut-off by 0.028. This error is also not great, and is of little consequence since the desired, usable bandwidth is exceeded. And for this type of wideband filter only the lower attenuation band is of interest, as was previously mentioned. The solid lines in Fig. 17-10(b) show the calculated attenuation characteristic of this filter, while the dashed lines show the attenuation characteristic predicted by mapping the attenuation characteristic of the prototype filter using the mapping equation, Eq. (17-28). As the figure shows, the calculated response and the mapping of the prototype response agree almost exactly close to cut-off, and differ by only a db or so in the region of high attenuation.

Figure 17-11 shows a possible strip transmission line construction for the filter defined by Fig. 17-7 and Table 17-2. This structure consists of printed-circuit, copper foil center conductors etched on slabs of dielectric material with copper foil on the outer sides of the dielectric slabs to form the ground planes. The series capacitors in Fig. 17-7 are realized by gaps in the strip center conductors. However, in order to obtain the amount of series capacitance required for a wideband filter of this sort, it is desirable to use additional copper strips

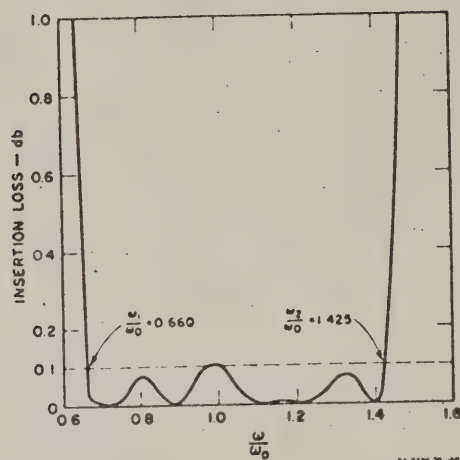


FIG. 17-10(a)

CALCULATED PASS-BAND RESPONSE FOR THE FILTER DEFINED BY FIG. 17-7 AND TABLE 17-2

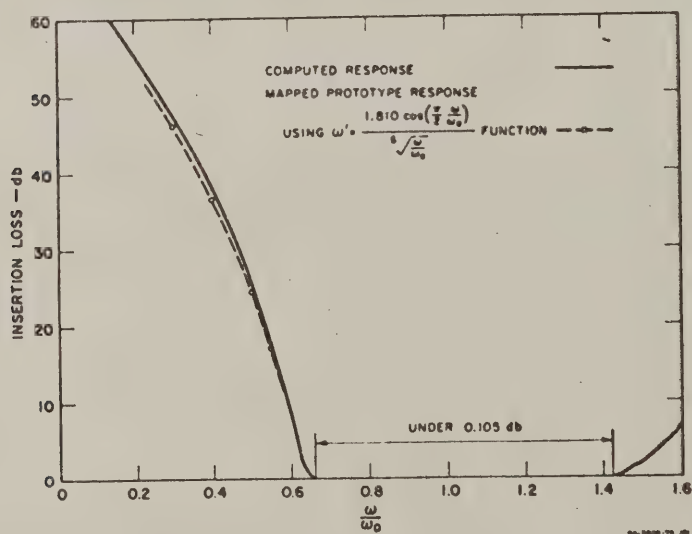


FIG. 17-10(b)

COMPUTED ATTENUATION CHARACTERISTIC FOR THE FILTER DEFINED BY FIG. 17-7 AND TABLE 17-2, AND THE RESPONSE PREDICTED BY MAPPING THE ATTENUATION OF THE LOW-PASS PROTOTYPE

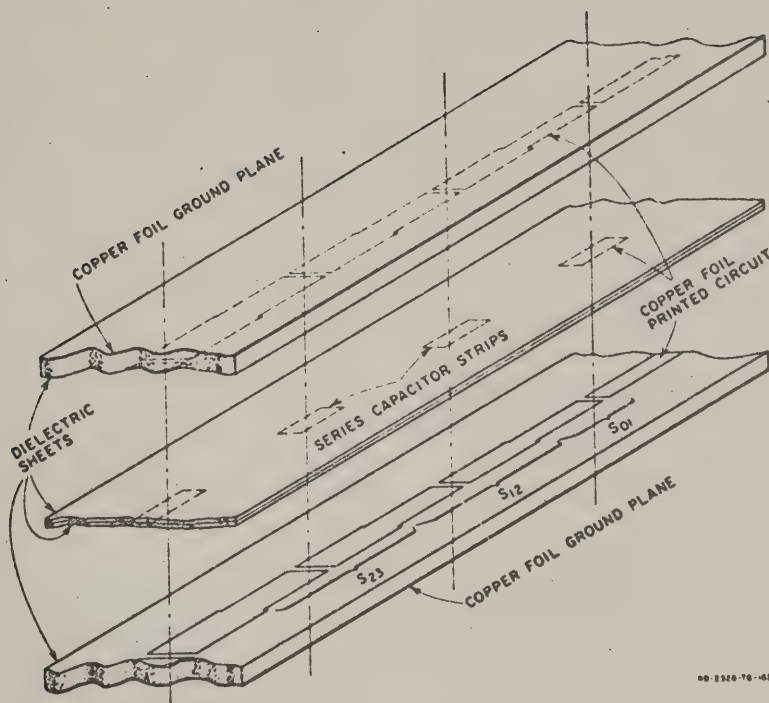


FIG. 17-11

EXPLODED VIEW OF A POSSIBLE PRINTED-CIRCUIT, STRIP-TRANSMISSION-LINE CONSTRUCTION FOR THE FILTER DEFINED BY FIG. 17-7 AND TABLE 17-2

which overlap adjacent sides of each gap so as to increase the series capacitance. In Fig. 17-11 the center conductor circuit is printed on both the upper and lower dielectric slabs so that the overlapping, capacitor strips (etched from copper foil on thin slabs of dielectric) may be placed between. Note that the overlap strips are narrower than the transmission line strips. This shields the overlap strips so that they will operate as series, open-circuited stubs connected at the gaps. In this manner the series capacitor strips increase the series capacitance directly at the gaps, but have negligible capacitance with respect to the ground planes.

F. DISCUSSION OF GENERAL APPLICATION OF THESE METHODS

The methods described for the preceding example may be adapted for use with a variety of different kinds of structures. The mapping function

used will depend on the type of structure. In some cases the prototype form in Fig. 17-2 will not be appropriate, but some other form such as the dual of that in Fig. 17-2 will. E. M. T. Jones and S. B. Cohn of this laboratory designed a low-pass filter by methods basically similar to those described here but with still another prototype.* Their prototype consisted of a circuit of the form in Fig. 15-2(a) broken up into symmetrical pi sections. The image characteristics of these pi sections were mapped by a tangent function mapping, and then the mapped image characteristics were approximated by pi sections formed from transmission lines. The computed response of the resulting filter design was quite good.

Perhaps it would be well to point out the nature of the approximations involved in the wideband design method of this report. The method will be exact for any symmetrical microwave filter structure (Fig. 17-6) whose image impedance and propagation characteristics duplicate those of the band-pass model in Fig. 17-4. The reactances X_n in Fig. 17-4 are mappings of the prototype reactances as indicated in Eq. (17-16), and the impedance-inverter parameters are independent of frequency. Even though microwave structures for which the model in Fig. 17-4 is appropriate can be made to have image characteristics very similar to those of the model, it will usually be impossible for all of the image properties to duplicate those of the model. For example, if one obtains a low-pass to bandpass mapping function $F(\omega)$ that gives the bandpass model (Fig. 17-4) an image impedance characteristic duplicating that of the microwave structure, the pass-band image phase will usually not duplicate that of the microwave structure. Thus, this design procedure will usually involve approximations; however, in the examples worked out so far, the errors due to these approximations are not great.

* Though the method for wideband, band-pass filter design described herein occurred to this writer independently, their low-pass filter design, which is similar in design philosophy, was carried out quite some time ago.

REFERENCES

1. S. B. Cohn, et al, "Research on Design Criteria for Microwave Filters," Final Report, Chap. 2, SRI Project 1331, Contract DA 36-039 SC-64625, Stanford Research Institute, Menlo Park, California (June 1957). Also, "Direct-Coupled-Resonator Filters," *Proc. IRE* 45, pp. 187-196 (February 1957).
2. L. Weinberg, "Network Design by Use of Modern Synthesis Techniques and Tables," Tech. Memo. 427, Hughes Aircraft Company, Research Laboratories, Culver City, California (April 1956). Also, *Proceedings of the National Electronics Conference* Vol. 12, (1956).
3. See Chapter 13 of this report.
4. E. M. T. Jones and S. B. Cohn, "Two Theorems for Dissipationless Symmetrical Networks," *Proc. IRE* 45, p. 1016 (July 1957).

CHAPTER 18

DESIGN OF WIDE-BAND (AND NARROW-BAND) BANDPASS MICROWAVE FILTERS USING STUBS OR PARALLEL-COUPLED LINES*

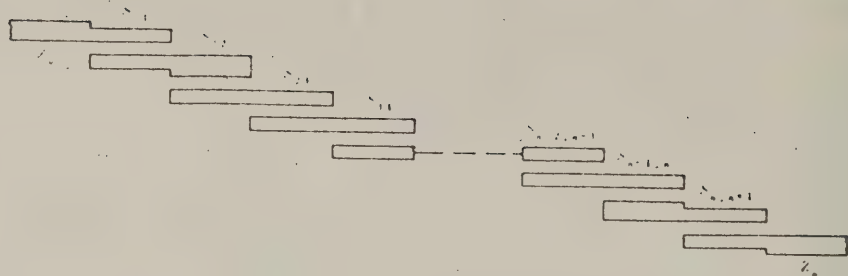
A. GENERAL

In Chapter 17 a general method for design of wide-band, microwave filters was presented and, as an example, applied to the case of filters consisting of lengths of transmission line coupled by series capacitors. The design method used mixes the image impedance and insertion-loss points of view; the individual sections of the filter are designed by equations derived from the image point of view, while the proper choice of the image parameters for the various sections of the filter is determined from a lumped-element prototype designed using the insertion-loss method. In this manner the simplicity of the image point of view is obtained along with the precision typical of insertion-loss design methods. The methods used are most accurate for band-pass filters with narrow pass bands, but still have good accuracy for band-edge ratios of two to one.

The types of bandpass filters to be treated in this report are shown in Figs. 18-1, 18-2, and 18-3. The filter in Fig. 18-1(a) is of the parallel-coupled type for which Cohn¹ has presented approximate design equations accurate for filters of narrow or moderate bandwidth; the filter form shown in Fig. 18-1(d) was previously treated by Jones² on an exact basis. It can be shown that exact design procedures based on Richard's transformation³ can be derived for all of these filters for either narrow or wide bandwidths. Examples of the use of these procedures will be found in the literature.^{2,4,7} However, the paper by Jones² which treats the form of filter in Fig. 18-1(d) is the only one of these references which deals specifically with any of the filters in Figs. 18-1(a) to 18-3 on an exact, insertion-loss design basis. A serious practical disadvantage of exact methods for designing these particular filter structures is that the synthesis of special transfer functions is required[†] at the outset of

* The material in this chapter has been published. See G. L. Matthaei, "Band-Pass Microwave Filter Design--A New Method and Its Relation to Other Methods," 1960 *IRE International Convention Record*, Part 3, pp 95-122. See also, G. L. Matthaei, "Design of Wide-Band (and Narrow-Band) Band-Pass Microwave Filters on the Insertion Loss Basis," *IRE Trans. PGMTT-8*, pp 580-593 (November 1960).

† Whether or not special transfer functions are required depends on the locations of the frequencies of infinite attenuation inherent to the desired filter structure. By choosing certain filter structures, the more common transfer functions can be used.^{6,7} Such structures, however, may not always be the most convenient to fabricate.

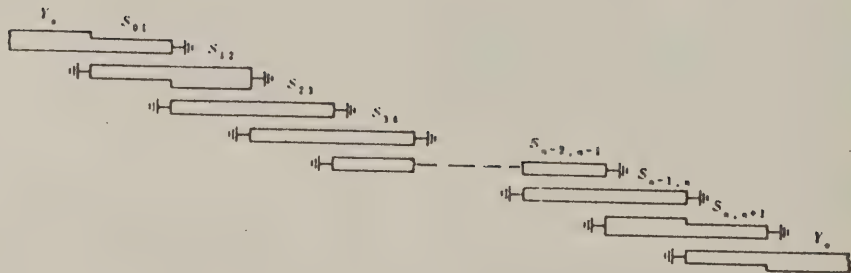


Each section $S_{k,k+1}$ is characterized by even and odd mode impedances $(Z_{ee})_{k,k+1}$ and $(Z_{oo})_{k,k+1}$ respectively. ^{8,13}

RB-2326-17-176

FIG. 18-1(a)

PARALLEL-COUPLED, STRIP-TRANSMISSION-LINE FILTER WITH OPEN-CIRCUITED SECTIONS
(Each section is one-quarter wavelength long where the reference wavelength is that at the midband frequency, ω_0 .)



Each section $S_{k,k+1}$ is characterized by even and odd mode admittances $(Y_{ee})_{k,k+1}$ and $(Y_{oo})_{k,k+1}$ respectively. ^{8,13}

RB-2326-17-177

FIG. 18-1(b)

PARALLEL-COUPLED, STRIP-TRANSMISSION-LINE FILTER WITH SHORT-CIRCUITED SECTIONS
(This filter is the dual of that in Fig. 18-1(a). Each section $S_{k,k+1}$ is one-quarter wavelength long where the reference wavelength is the propagation wavelength at the midband frequency, ω_0 .)

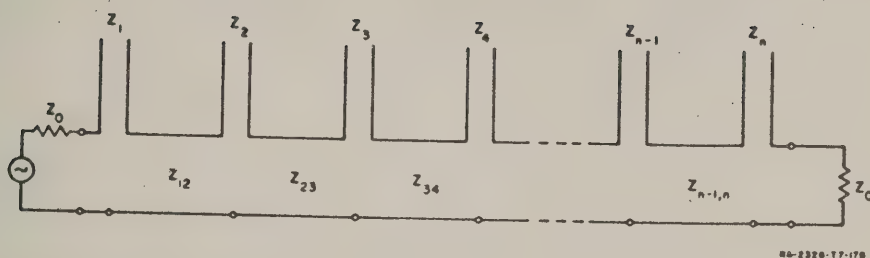


FIG. 18-1(c)

BANDPASS FILTER USING QUARTER-WAVELENGTH SERIES STUBS AND
QUARTER-WAVELENGTH CONNECTING LINES
(Filters of the form in Fig. 18-1(a) can always be converted to this form)

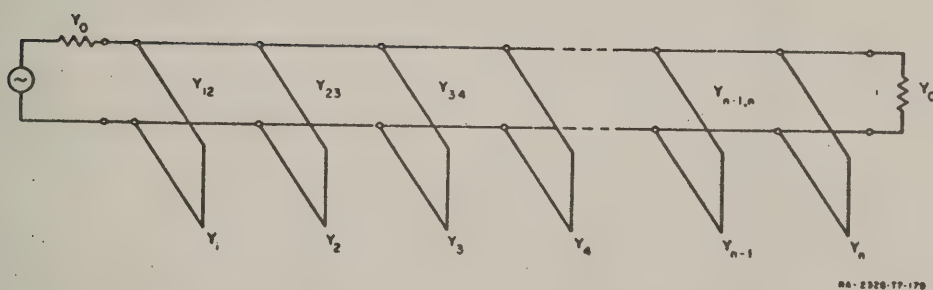
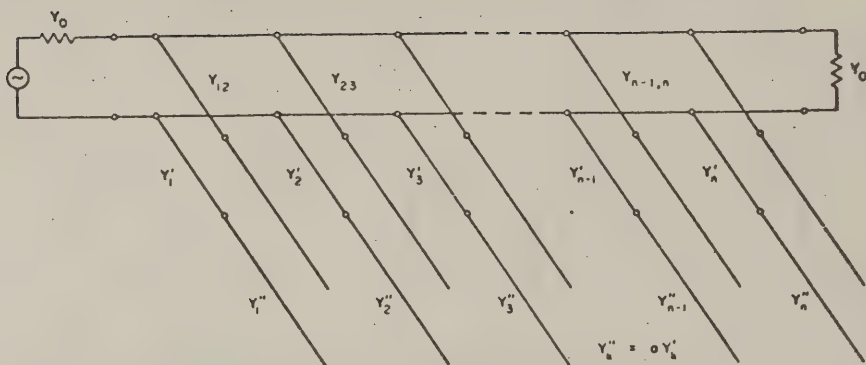


FIG. 18-1(d)

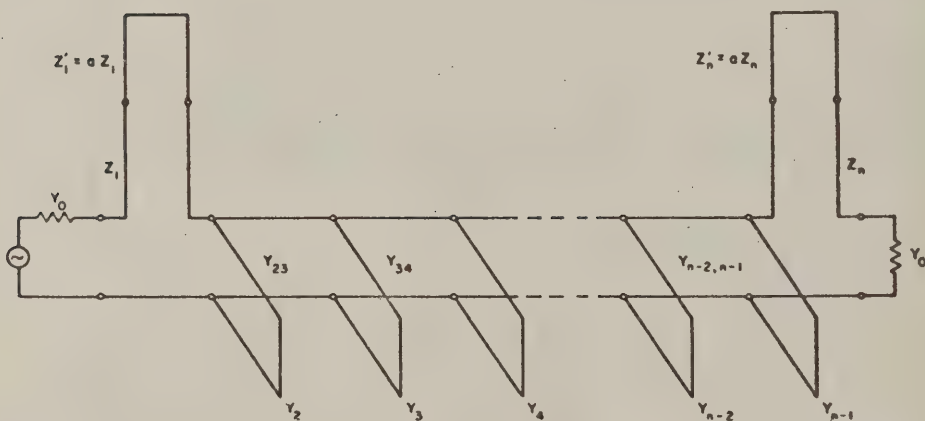
BANDPASS FILTER USING QUARTER-WAVELENGTH SHUNT STUBS AND
QUARTER-WAVELENGTH CONNECTING LINES
(This filter is the dual of that in Fig. 18-1(c). The reference wavelength
is the propagation wavelength at the midband frequency, ω_0 .)



NO. 2320-77-100

FIG. 18-2

BANDPASS FILTER WITH HALF-WAVELENGTH SHUNT STUBS AND
QUARTER-WAVELENGTH CONNECTING LINES
(The reference wavelength is the propagation wavelength
at the midband frequency, ω_0 .)



NO. 2320-77-101

FIG. 18-3

BANDPASS FILTER WITH QUARTER-WAVELENGTH SHUNT STUBS, QUARTER-WAVELENGTH
CONNECTING LINES, AND HALF-WAVELENGTH SERIES STUBS AT THE ENDS
(The reference wavelength is that at the midband frequency, ω_0 .)

the design process,² and, all in all, a great deal of computational labor is needed. Even though the design procedures described herein are computationally very simple and only approximate; the results, as the examples show, are satisfactory for most practical precision design problems.

In Part B, the use of the design equations and the results of design examples will be discussed. To make routine use of the design equations more convenient, their derivation will be treated separately in Part C. Some of the results of Chapter 17 will be briefly summarized during the following discussions to provide continuity.

B. PRACTICAL APPLICATION OF THE DESIGN EQUATIONS

1. EQUIVALENCE OF THE NETWORKS IN FIGS. 18-1(a) TO 18-1(d)

The filter in Fig. 18-1(b) is simply the dual of that in Fig. 18-1(a). It can be obtained directly from the circuit in Fig. 18-1(a) by replacing the open circuits by short circuits and by replacing each even- or odd-mode impedance $(Z_{oe})_{k,k+1}$ and $(Z_{oo})_{k,k+1}$ respectively, by corresponding *odd-* and *even mode* admittances

$$\begin{aligned}(Y_{oo})_{k,k+1} &= Y_0^2 (Z_{oe})_{k,k+1} \\ (Y_{oe})_{k,k+1} &= Y_0^2 (Z_{oo})_{k,k+1}\end{aligned}\tag{18-1}$$

where $Y_0 = 1/Z_0$ is the characteristic admittance of the input and output lines. By use of the equivalences shown in Fig. 18-4,^{*} it is seen that the circuit in Fig. 18-1(c) is exactly equivalent to that in Fig. 18-1(a), while the circuit in Fig. 18-1(d) is exactly equivalent to that in Fig. 18-1(b). Thus, any of these four circuits can be derived from any other, by use of duality and the equivalences in Fig. 18-4; when derived from one another in this manner, all will yield exactly the same transmission characteristic.

For simplicity, the design equations applicable for these four filter structures [Fig. 18-1(a) to 18-1(d)] will be expressed in the specific form for the structure in Fig. 18-1(a). Any of the other forms may then

* The correctness of these equivalences can be verified with the aid of the impedance and admittance matrices for parallel-coupled strips given by Jones⁸ or by using Richard's transformation to map the elements in Equivalent Circuits (5) and (6) of Table II of Ozaki and Ishii's work⁵ into the corresponding transmission line form.

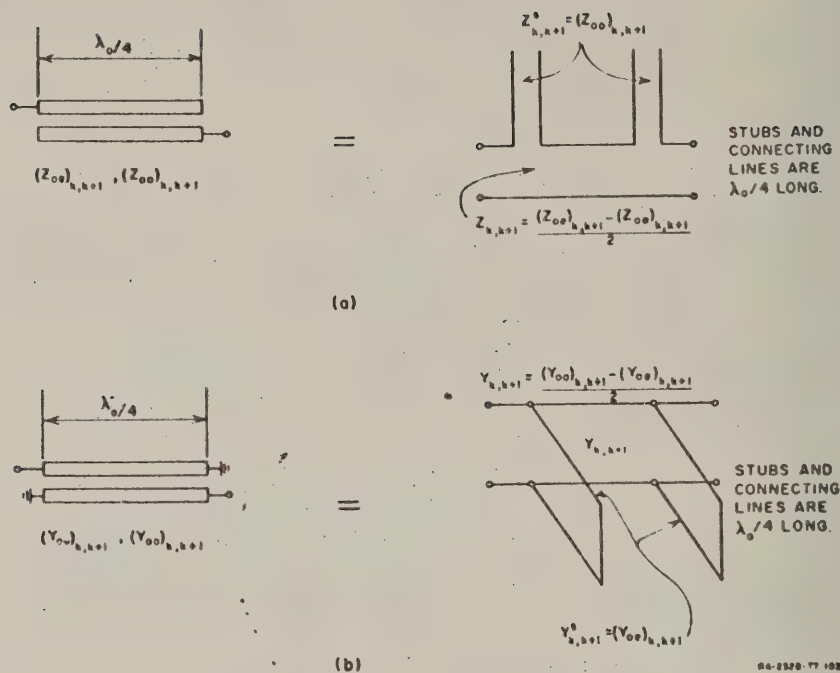


FIG. 18-4

EQUIVALENCE BETWEEN PARALLEL-COUPLED STRIP-LINE SECTIONS AND SECTIONS CONSISTING OF STUBS WITH CONNECTING LINES

be obtained by duality and Fig. 18-4. In converting from the form in Fig. 18-1(a) to, say, the form in Fig. 18-1(d), it should be noted that the characteristic admittance of the shunt stub at each end is determined solely by the end sections of the filter in Fig. 18-1(a); however, the characteristic admittance of each of the shunt stubs in the interior of the filter in Fig. 18-1(d) is determined by the corresponding two adjacent sections in Fig. 18-1(a) so that

$$Y_h = Y_{h-1,h}^* + Y_{h,h+1}^*$$

$$Y_0^2 [Z_{h-1,h}^* + Z_{h,h+1}^*] = Y_0^2 [(Z_{00})_{h-1,h} + (Z_{00})_{h,h+1}] \quad (18-2)$$

where $Y_0 = 1/Z_0$ is again the characteristic admittance of the input and output lines, and the $Y'_{k,k+1}$ and $Z'_{k,k+1}$ are defined in Fig. 18-4. It is helpful to note that in the case of Fig. 18-1(d), the characteristic admittances of the connecting lines are given by

$$Y_{k,k+1} = Y_0^2 \left[\frac{(Z_{oe})_{k,k+1} + (Z_{oo})_{k,k+1}}{2} \right] = Y_0^2 K_{k,k+1} \quad (18-3)$$

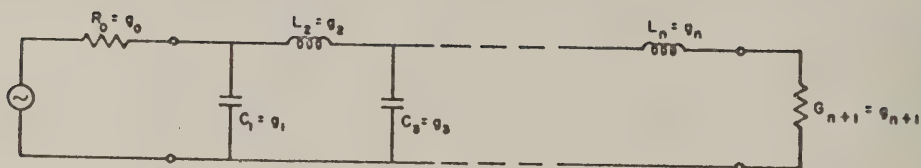
where the $K_{k,k+1}$ are impedance inverter parameters to be discussed later (they are defined numerically in Tables 18-1 and 18-2).

The filter structures in Figs. 18-2 and 18-3 are not equivalent to those in Figs. 18-1(a) to Fig. 18-1(d). However, they are closely related structures which can readily be treated using many of the same concepts and equations.

2. USE OF MAPPING FUNCTIONS, AND SELECTION OF APPROPRIATE LUMPED-ELEMENT PROTOTYPES

In the design procedure described herein, the band-pass microwave filter derives characteristic properties of its response from a lumped-element prototype filter having analogous low-pass filter response properties. Figure 18-5 shows a typical low-pass prototype and defines the prototype parameters $g_0, g_1, \dots, g_n, g_{n+1}$. The design equations in Tables 18-1 to 18-3 assume that the prototype filter is either symmetric or antimetric⁹—a condition satisfied by the common maximally flat or Tchebyscheff lossless filter designs (which have one or more frequencies at which zero reflection occurs). Weinberg¹⁰ and Chapter 13 of this report give tables of element values for such filters (Ref. 10 also includes tables for filters which are not symmetric or antimetric). The use of symmetric or antimetric prototypes along with equal terminations in the final microwave filter (as depicted in Figs. 18-1 to 18-3) is usually desirable, and so has been made implicit in the equations in Tables 18-1 to 18-3. However, these conditions are not necessary, and equations for other cases may be derived by the theory in Sec. C.

Figure 18-6 shows a typical, lossless, low pass-filter, maximally flat response along with the equation for this response. The frequency ω'_1 establishes the pass band edge while A_n is the db attenuation which is permissible within the pass band. The frequency ω'_0 is a frequency at which



A typical, low-pass prototype. The dual of this circuit would also be satisfactory.

$$g_k \Big|_{k=1 \text{ to } n} = \begin{cases} \text{The inductance of a series coil,} \\ \text{or the capacitance of a shunt capacitor.} \end{cases}$$

$$g_0 = \begin{cases} \text{The generator resistance } R_0 \text{ if } g_1 = C_1, \text{ but is} \\ \text{defined as the generator conductance } G_0 \text{ if } g_1 = L_1. \end{cases}$$

$$g_{n+1} = \begin{cases} \text{The load resistance } R_{n+1} \text{ if } g_n = C_n, \text{ but is} \\ \text{defined as the load conductance } G_{n+1} \text{ if } g_n = L_n. \end{cases}$$

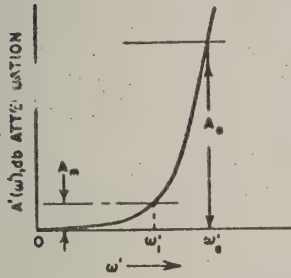
NOTE: An additional prototype parameter ω'_1 is defined in Figs. 18-6 and 18-7.

RA-2326-T7-103

FIG. 18-5

DEFINITION OF THE LOW-PASS PROTOTYPE PARAMETERS $g_0, g_1, \dots, g_n, g_{n+1}$
(The symmetry about the middle of the filter indicated in the equations of Tables 18-1 to 18-3 results from the use of symmetric or antimetric prototypes. The common maximally flat or Tchebyscheff prototypes, which have one or more frequencies where zero reflection occurs, always satisfy this symmetry or antimetry condition.)

Prototype Response

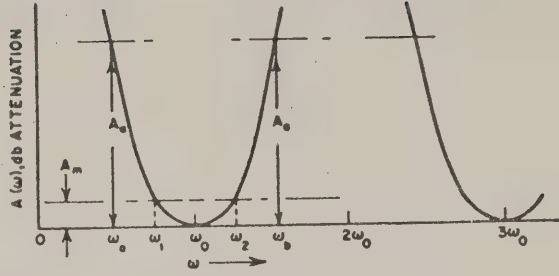


$$A'(\omega') = 10 \log_{10} \left[1 + \epsilon \left(\frac{\omega'}{\omega_1'} \right)^{2n} \right] \text{ db}$$

where

$$\epsilon = \text{antilog}_{10} \left(\frac{A_0}{10} \right) - 1$$

Band-Pass Filter Response



$$A(\omega) = A'(\omega') \text{ db}$$

where

$$\omega' = \mu_n F_n \left(\frac{\omega}{\omega_0} \right)$$

$$\mu_n = \frac{\omega_1'}{F_n \left(\frac{\omega_1}{\omega_0} \right)}$$

and

$$F_n \left(\frac{\omega}{\omega_0} \right)$$

is given in Eqs. (18-4a), (18-4b) or (18-5).

To determine n required for given values of ω_1/ω_0 , A_m , ω_0/ω_0' and A_0 , find smallest integer n value which satisfies

$$n \geq \frac{\log_{10} \left\{ \frac{\left[\text{antilog}_{10} \left(\frac{A_0}{10} \right) \right] - 1}{\epsilon} \right\}}{2 \log_{10} \left(\frac{\omega_0'}{\omega_1'} \right)}$$

where

$$\omega_0' = \mu_n F_n \left(\frac{\omega_0}{\omega_0} \right)$$

AD-2500 77-00

FIG. 18-6

EQUATIONS AND PARAMETERS FOR MAXIMALLY FLAT RESPONSE

TABLE 18-1
DESIGN EQUATIONS ESPECIALLY SUITED FOR
FILTERS OF THE FORM IN FIGS. 18-1(a) AND 18-1(b)

Use mapping Eq. (18-4a) or (18-4b) and Fig. 18-6 or 18-7 to select prototype having required value of n . Equations below are for filters in the form of Fig. 18-1(a). There are $n + 1$ parallel-coupled sections for an n -reactive-element prototype when using the design procedure below.

(a) Sections S_{01} and $S_{n, n+1}$

$$\frac{K_{01}}{Z_0} = \frac{1}{\sqrt{g_0 g_1} \omega'_1} = \frac{K_{n, n+1}}{Z_0} \quad , \quad \theta_1 = \frac{\pi \omega_1}{2 \omega_0}$$

$$Q = \cot \theta_1 \quad , \quad P = \sqrt{\frac{Q(Q^2 + 1)}{Q + \frac{1}{2(K_{01}/Z_0)^2}}}$$

$$s = Z_0 \left(\frac{P \sin \theta_1}{K_{01}/Z_0} \right)^2$$

$$(Z_{oe})_{01} = (Z_{oe})_{n, n+1} = Z_0 (1 + P \sin \theta_1)$$

$$(Z_{oo})_{01} = (Z_{oo})_{n, n+1} = Z_0 (1 - P \sin \theta_1)$$

(b) Sections S_{12} to $S_{n-1, n}$

$$\frac{K_{k, k+1}}{Z_0} = \frac{1}{\omega'_1 \sqrt{g_k g_{k+1}}} \quad , \quad N_{k, k+1} = \sqrt{\left(\frac{K_{k, k+1}}{Z_0} \right)^2 + \frac{\tan^2 \theta_1}{4}}$$

$$(Z_{oe})_{k, k+1} = (Z_{oe})_{n-k, n-k+1} = s \left(N_{k, k+1} + \frac{K_{k, k+1}}{Z_0} \right)$$

$$(Z_{oo})_{k, k+1} = (Z_{oo})_{n-k, n-k+1} = s \left(N_{k, k+1} - \frac{K_{k, k+1}}{Z_0} \right)$$

where θ_1 and s are defined as in (a) above and $k = 1, 2, \dots, n - 1$.

TABLE 18-2
DESIGN EQUATIONS FOR FILTERS ESPECIALLY SUITED FOR
REALIZATION IN THE FORM IN FIGS. 18-1(c) AND 18-1(d)

Use mapping Eq. (18-4a) or (18-4b) and Figs. 18-6 or 18-7 to select prototype. Equations below are for filters in the form of Fig. 18-1(a), but they are readily converted to the form in Fig. 18-1(c) or 18-1(d) by use of Fig. 18-4. Using these equations, sections S_{01} and $S_{n,n+1}$ are omitted, and there will be $n - 1$, parallel-coupled sections for an n -reactive-element prototype.

Sections S_{12} to $S_{n-1,n}$

$$\frac{K_{12}}{Z_0} = \frac{K_{n-1,n}}{Z_0} = \frac{\sqrt{2}g_0g_1}{\sqrt{g_1g_2}}$$

$$\left. \frac{K_{k,k+1}}{Z_0} \right|_{k=2 \text{ to } n-2} = \frac{K_{n-k,n-k+1}}{Z_0} = \frac{2g_0g_1}{\sqrt{g_kg_{k+1}}}$$

$$\theta_1 = \frac{\pi}{2} \frac{\omega_1}{\omega_0}, \quad N_{k,k+1} = \sqrt{\left(\frac{K_{k,k+1}}{Z_0} \right)^2 + \left(\omega_1' g_0 g_1 \tan \theta_1 \right)^2}$$

$$(Z_{oe})_{k,k+1} = (Z_{oe})_{n-k,n-k+1} = Z_0 \left(N_{k,k+1} + \frac{K_{k,k+1}}{Z_0} \right)$$

$$(Z_{oo})_{k,k+1} = (Z_{oo})_{n-k,n-k+1} = Z_0 \left(N_{k,k+1} - \frac{K_{k,k+1}}{Z_0} \right)$$

where $k = 1, 2, \dots, n - 1$.

TABLE 18-3
DESIGN EQUATIONS FOR FILTERS OF THE FORM IN FIG. 18-3

Use mapping Eq. (18-5) and Fig. 18-6 or 18-7 to select prototype

$$\omega_1 = \frac{R\omega_0}{2\omega_0}, \quad \omega_\infty = \frac{T\omega_0}{2\omega_0}$$

where ω_∞ is a frequency of infinite attenuation as indicated in example in Fig. 18-11. Referring to Fig. 18-3:

$$a = \cot^2 \theta_\infty, \quad Z_1 = Z_n = \frac{[\phi(\tan \theta_1)^2 - 1]\omega_1' g_0 g_1}{Y_0(a+1) \tan \theta_1}$$

$$Z_1' = Z_n' = aZ_1, \quad C_a = 2dg_2$$

where $d \leq 1$ is a constant (typically one-half or somewhat larger) which may be chosen to give a desired impedance level in the interior of the filter.

$$\frac{J_{23}}{Y_0} = \frac{J_{n-2, n-1}}{Y_0} = \frac{\sqrt{g_2 C_a}}{g_0 g_2 g_3} \quad \frac{J_{k, k+1}}{Y_0} \Big|_{k=3 \text{ to } n-3} = \frac{C_a}{g_0 g_k g_{k+1}}$$

$$M_{k, k+1} = \sqrt{\left(\frac{J_{k, k+1}}{Y_0}\right)^2 + \left(\frac{C_a \tan \theta_1}{2g_0}\right)^2}$$

$$Y_{k, k+1}^* \Big|_{k=2 \text{ to } n-2} = Y_{n-k, n-k+1}^* = Y_0 \left(M_{k, k+1} - \frac{J_{k, k+1}}{Y_0} \right)$$

Then for the shunt stubs:

$$Y_2 = Y_{n-1} = \frac{Y_0 \omega_1' (1-d) g_2}{g_0} \tan \theta_1 + Y_{23}^*$$

$$Y_k \Big|_{k=3 \text{ to } n-2} = Y_{n-k+1} = Y_{k-1, k}^* + Y_{k, k+1}^*$$

And for the connecting lines:

$$Y_{k, k+1} \Big|_{k=2 \text{ to } n-1} = Y_{n-k, n-k+1} = J_{k, k+1}$$

a stated attenuation, A_s db, is required. An analogous, maximally flat, band-pass response such as might be obtained by the filters in Figs 18-1(a) to 18-1(d) is also shown. Note that this response has arithmetic symmetry about ω_0 so that the essential parameters of the response may be specified simply as ω_1/ω_0 , A_s , A_0 , and ω_s/ω_0 . The response of the band-pass filter may be predicted directly from that of the low-pass filter by mapping the ω' frequency scale of the low-pass filter to the ω frequency scale of the band-pass filter, as indicated in the figure. For the circuits in Fig. 18-1(a) to 18-1(d) and the design equations in Table 18-1 and 18-2, the proper function $F_n(\omega/\omega_0)$ to use is

$$F_n\left(\frac{\omega}{\omega_0}\right) = \frac{-\cos\left(\frac{\pi}{2} \frac{\omega}{\omega_0}\right)}{\sqrt[n]{\left|\sin\left(\frac{\pi\omega}{2\omega_0}\right)\right|}} \quad (18-4a)$$

For narrow or moderate bandwidths the simpler function

$$F_n\left(\frac{\omega}{\omega_0}\right) = \left(\frac{\omega}{\omega_0} - 1\right) \quad (18-4b)$$

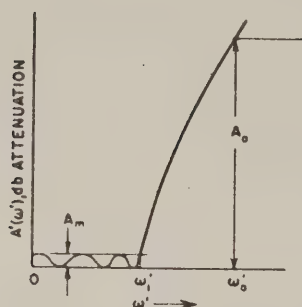
will also give good accuracy.¹ As will be shown, the accuracy of Eq. (18-4b) is fair even for wide bandwidths. For the circuit in Fig. 18-3 and the equations in Table 18-3, the proper function to use is

$$F_n\left(\frac{\omega}{\omega_0}\right) = \frac{-\cos\left(\frac{\pi\omega}{2\omega_0}\right)}{\sqrt[n]{\left|\sin\left(\frac{\pi\omega}{2\omega_0}\right)\right| \left[\sin\frac{\pi}{2} \left(\frac{\omega - \omega_\infty}{\omega_0}\right)\right]^2 \left[\sin\frac{\pi}{2} \left(\frac{\omega - 2\omega_0 + \omega_\infty}{\omega_0}\right)\right]^2}} \quad (18-5)$$

where ω_∞ is a frequency of infinite attenuation, to be specified. An accurate, general mapping for the circuit in Fig. 18-2 has not been determined.

Figure 18-7 shows corresponding curves and equations for the case of filters having Tchebyscheff responses. Since the choice of mappings is determined by the type of filter structure rather than by the type of response, the functions in Eqs. (18-4) and (18-5) apply as before.

Prototype Response



$$A'(\omega') = 10 \log_{10} \left\{ 1 + \epsilon^2 \cosh^2 \left[n \cosh^{-1} \left(\frac{\omega'}{\omega_1} \right) \right] \right\} \text{ db}$$

for

$$\omega' \geq \omega_1$$

$$A'(\omega') = 10 \log_{10} \left\{ 1 + \epsilon^2 \cosh^2 \left[n \cosh^{-1} \left(\frac{\omega'}{\omega_1} \right) \right] \right\} \text{ db}$$

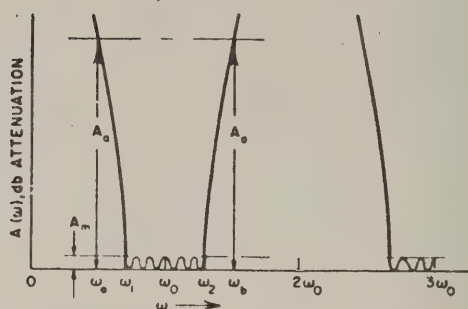
for

$$\omega' \leq \omega_1$$

where

$$\epsilon = \left\{ \left[\text{antilog}_{10} \left(\frac{A_m}{10} \right) - 1 \right] \right\}$$

Band-Pass Filter Response



$$A(\omega) = A'(\omega') \text{ db}$$

where

$$\omega' = \mu_n F_n \left(\frac{\omega}{\omega_0} \right)$$

$$\mu_n = \frac{\omega_1}{\omega_0}$$

$$F_n \left(\frac{\omega}{\omega_0} \right)$$

and

$$F_n \left(\frac{\omega}{\omega_0} \right)$$

is given in Eqs. (10-4a), (10-4b), or (10-5).

To determine n required for given values of ω_1/ω_0 , A_m , ω_0/ω_2 , and A_0 , find smallest integer n value which satisfies

$$n \geq \frac{\cosh^{-1} \sqrt{\frac{\text{antilog}_{10} \left(\frac{A_0}{10} \right) - 1}}{\cosh^{-1} \left(\frac{\omega_1}{\omega_0} \right)}}$$

where

$$\omega_1' = \mu_n F_n \left(\frac{\omega_1}{\omega_0} \right)$$

NO 2326 77-105

FIG. 18-7

EQUATIONS AND PARAMETERS FOR TCHEBYSCHOFF RESPONSE

For both the maximally flat and Tchebyscheff cases, the number of reactive elements required in the low-pass prototype, n , is fixed by the parameters ω_1/ω_0 , A_n , ω_s/ω_0 , and A_s . In Figs. 18-6 and 18-7 equations are given for solving for n in terms of these parameters. Since the $F_n(\omega_s/\omega_0)$ in Eqs. (18-4a) and (18-5) are also functions of n , one must estimate a value of n to use in these functions, solve for n to get an improved value, and then repeat the process. However, since the $F_n(\omega_s/\omega_0)$ are only weak functions of n , the process will converge very quickly. In the case of Eqs. (18-4a) and (18-4b) the latter equation may be easily used to obtain n accurately for narrow-band cases, and this equation will also give a fairly accurate value of n in wide band cases. In wide-band cases the value of n obtained using Eq. (18-4b) can be inserted in Eq. (18-4a), and the equation for n can then be used again to obtain a more accurate verification of the n value.

3. A DESIGN PROCEDURE ESPECIALLY SUITED TO FILTERS REALIZED IN THE FORMS IN FIGS. 18-1(a) AND 18-1(b)

Table 18-1 summarizes a design procedure which gives good impedance levels for filter structures such as those in Figs. 18-1(a) and 18-1(b). After an appropriate prototype is selected, as described above, the parameters g_0 , g_1 , ..., g_n , g_{n+1} , and ω'_1 from the low pass prototype are used along with the bandpass-filter lower-band-edge ratio, ω_1/ω_0 , to obtain the filter design in a straightforward manner as outlined.

Figures 18-8(a) to 18-8(c) show the results of some trial designs obtained using a Tchebyscheff prototype having 0.10-db pass-band ripple and $n = 6$ reactive elements. The curves show the response computed by a digital computer from the circuit element values. For Fig. 18-8(a), $\omega_1/\omega_0 = 0.975$ was used, which calls for a 5-percent bandwidth. As is seen from the figure, there is no noticeable deviation from the design objective, and points mapped from the low-pass prototype response by use of Eq. (18-4a) and also by Eq. (18-4b) are all in excellent agreement with the computed response. Figure 18-8(b) shows the computed response for a design obtained using $\omega_1/\omega_0 = 0.850$, which calls for a 30-percent bandwidth. In this case there is a very slight deviation from perfect Tchebyscheff character, inasmuch as two of the peaks of the pass-band ripples do not quite reach the 0.10-db level. In this case points mapped from the prototype response using Eq. (18-4a) are in practically perfect agreement with the filter response, while points mapped using Eq. (18-4b) show some noticeable error.

at the higher attenuation levels. Figure 18-8(c) shows the computed response for a design obtained using $\omega_1/\omega_0 = 0.650$, which calls for a band-edge ratio of $\omega_2/\omega_1 = 2.077$. In this case the deviation from a perfect response is more noticeable, the most important deviation being that the frequency ratio of the 0.10-db band-edge points is about $\omega_2/\omega_1 = 1.96$ instead of 2.077. All of the expected pass-band ripples are present, although in this case two of the ripple peaks are reduced to half size. Points mapped from the prototype response by use of Eq. (18-4a) appear to fall almost exactly where the response curve would have been if the slight shrinkage in the pass-band width had not occurred. Points mapped by use of Eq (18-4b) weave across the computed response some, but follow it surprisingly closely.

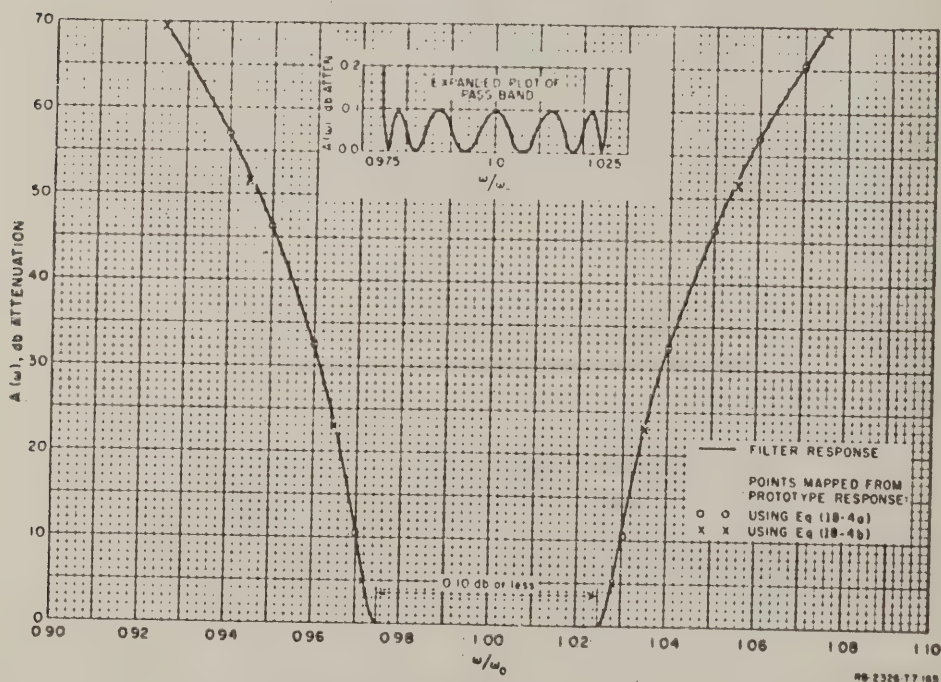


FIG. 18-8(a)

COMPUTED RESPONSE OF FILTERS DESIGNED AS IN TABLE 18-1
TO HAVE 5-PERCENT BANDWIDTH
(Design value for ω_1/ω_0 was 0.975. Prototype had 0.10 db
Tchebyscheff pass-band ripple with $n = 6$ reactive elements)

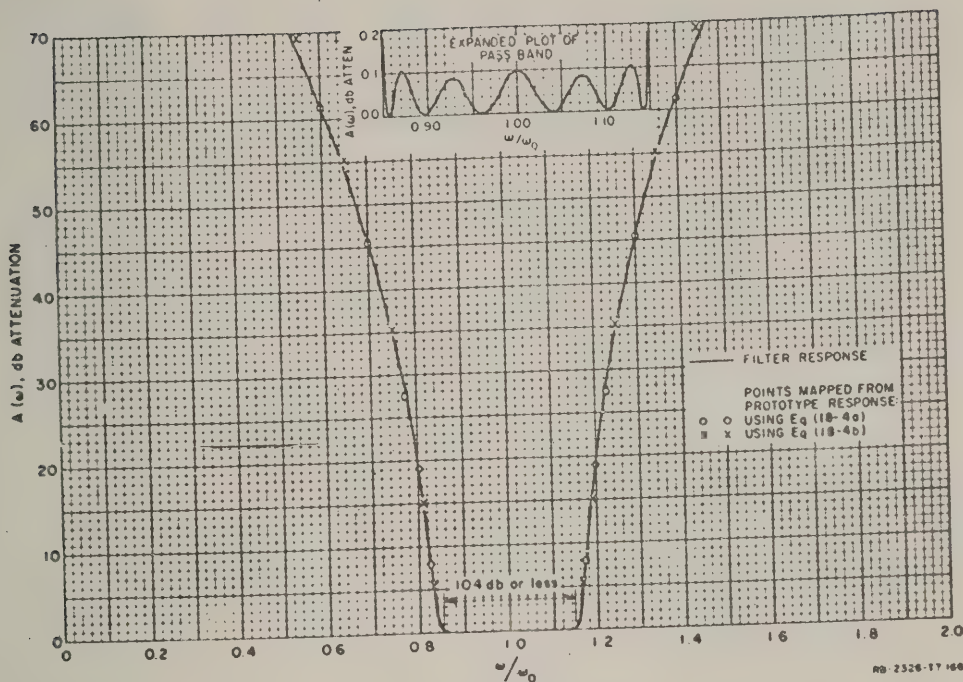


FIG. 18-8(b)

COMPUTED RESPONSE OF FILTERS DESIGNED AS IN TABLE 18-1
TO HAVE 30-PERCENT BANDWIDTH
(Design value of ω_1/ω_0 was 0.850.
Prototype same as for Fig. 18-8(a))

Table 18-4 gives the odd- and even-mode impedances for these filters realized in the form in Fig. 18-1(a). Using construction methods to be outlined later, all three of these designs should be quite practical. Filters designed by use of Table 18-1 and realized in the form in Fig. 18-1(a) or 18-1(b) are of special practical interest for applications where bandwidths of perhaps 50 percent or less are desired. Although the forms in Figs. 18-1(a) and 18-1(b) are also practical for larger bandwidths, filters designed by Table 18-2 and realized in the form in Fig. 18-1(d) will have reasonable element values for large bandwidth designs and become attractive because they require two less sections to achieve a given response.

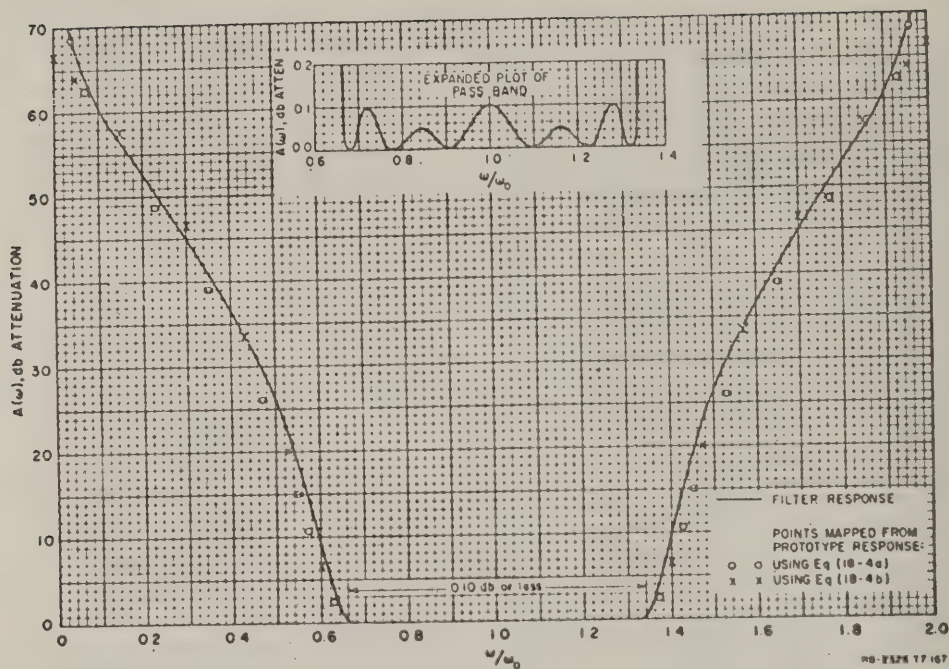


FIG. 18-8(c)

COMPUTED RESPONSE OF FILTERS DESIGNED AS IN TABLE 18-1
TO HAVE APPROXIMATELY 2 to 1 BANDWIDTH
(Design value for ω_1/ω_0 was 0.650, which calls for $\omega_2/\omega_1 = 2.077$.
Prototype same as for Fig. 18-8(a)

TABLE 18-4

SUMMARY OF EVEN-MODE AND ODD-MODE IMPEDANCE VALUES FOR THE FILTERS
OF FIGS. 18-8(a) TO 18-8(c) DESIGNED BY USE OF TABLE 18-1
AND REALIZED IN THE FORM IN FIG. 18-1(a)

| | FIG. 18-8(a) (5% Bandwidth) | FIG. 18-8(b) (30% Bandwidth) | FIG. 18-8(c) (2 to 1 Bandwidth) |
|---------------------------------|--------------------------------|---------------------------------|------------------------------------|
| $(Z_{oe})_{01} = (Z_{oe})_{67}$ | 1.251 | 1.540 | 1.716 |
| $(Z_{oe})_{12} = (Z_{oe})_{56}$ | 0.996 | 1.023 | 1.142 |
| $(Z_{oe})_{23} = (Z_{oe})_{45}$ | 0.981 | 0.937 | 0.954 |
| $(Z_{oe})_{34}$ | 0.980 | 0.927 | 0.933 |
| $(Z_{oo})_{01} = (Z_{oo})_{67}$ | 0.749 | 0.460 | 0.284 |
| $(Z_{oo})_{12} = (Z_{oo})_{56}$ | 0.881 | 0.491 | 0.208 |
| $(Z_{oo})_{23} = (Z_{oo})_{45}$ | 0.895 | 0.536 | 0.250 |
| $(Z_{oo})_{34}$ | 0.896 | 0.542 | 0.255 |

All values normalized so that $Z_0 = 1$.

A corresponding filter designed by Cohn's equations¹ was compared with the 5-percent-bandwidth filter described herein, in order to compare the two design methods. The designs were found to be basically similar, except that Cohn's equations yielded slightly different end sections and a 7-percent higher impedance level in the interior sections of the filter. For filters of about 10 percent bandwidth or less, either method should give good designs, but Cohn's design method has an advantage of being computationally even simpler than that described herein. For bandwidths greater than about 10 or 15 percent, the accuracy of Cohn's equations begins to deteriorate noticeably and the design equations described herein are recommended.

4. A DESIGN PROCEDURE ESPECIALLY SUITED TO FILTERS REALIZED IN THE FORMS IN FIGS. 18-1(c) AND 18-1(d)

In the design procedure of Table 18-1, the end sections S_{01} and $S_{n,n+1}$ are, in a sense, primarily impedance-transforming sections. Using that design procedure moderate impedance levels are maintained in the interior sections of filters realized in the forms in Figs. 18-1(a) or 18-1(b) regardless of the bandwidth of the filter, but this is achieved by not making full use of all of the natural modes of oscillation of which the circuit is capable. Using the design procedure in Table 18-2, the end sections S_{01} and $S_{n,n+1}$ are eliminated, and the remaining network makes full use of all possible natural modes. Table 18-2 is thus seen to call for $n - 1$ bandpass filter sections to realize a response mapped from an n -reactive element prototype, while the design method in Table 18-1 calls for $n + 1$ bandpass filter sections to achieve the same response. Designs obtained by Table 18-2 will usually yield impractical impedance levels for filters of the forms in Figs. 18-1(a) and 18-1(b), but the impedance levels are moderate for wide band filters of the forms in Figs. 18-1(c) and 18-1(d). The form in Fig. 18-1(d) which is quite practical for wide band designs, becomes less practical for narrow-band designs since the characteristic admittances of the shunt stubs then become quite large.

Figure 18-9 shows the response of a filter designed using Table 18-2 from a 0.10 db ripple, $n = 8$, Tchebyscheff prototype with $\omega_1/\omega_0 = 0.650$. Table 18-5 shows the element values for a realization as in Fig. 18-1(d). In this case the pass-band ripples are more uneven than in the previous examples; however, the bandwidth suffered less shrinkage than in the

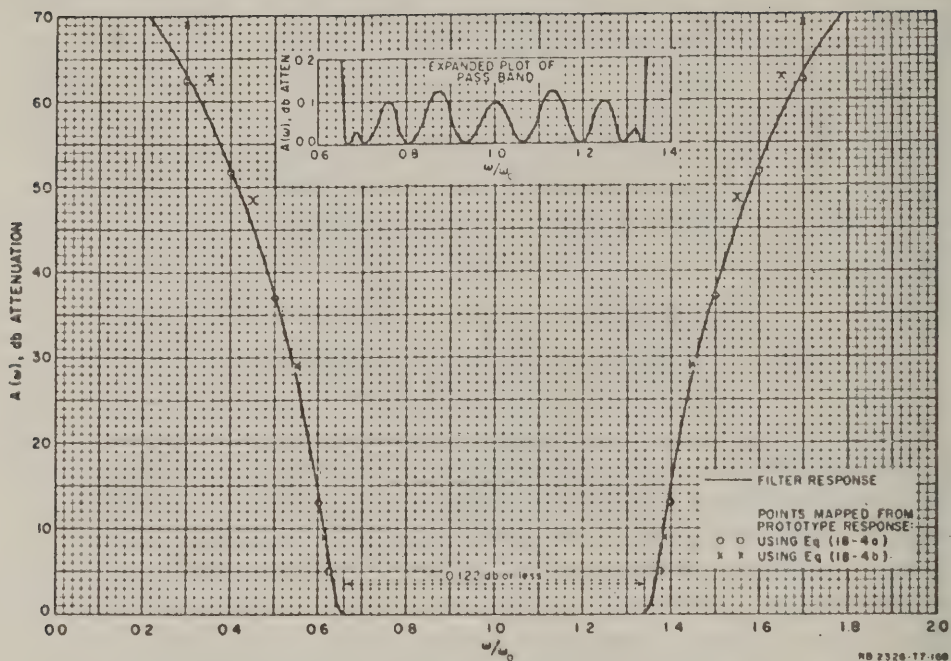


FIG. 18-9

COMPUTED RESPONSE OF A FILTER DESIGNED AS IN TABLE 18-2 TO HAVE APPROXIMATELY 2 TO 1 BANDWIDTH
(Design value for ω_1/ω_0 was 0.650. Prototype had 0.10 db Tchebyscheff pass-band ripple with $n = 8$ reactive elements.)

TABLE 18-5

ELEMENT VALUES FOR THE FILTER OF FIG. 18-9
REALIZED AS SHOWN IN FIG. 18-1(d)

(Filter designed using Table 18-2 from a 0.10 db ripple, $n = 8$, Tchebyscheff prototype using $\omega_1/\omega_0 = 0.650$.)

| | |
|---------------------------|---------------------------|
| $Y_1 = Y_8 = 1.042$ | $Y_3 = Y_6 = 2.049$ |
| $Y_{12} = Y_{78} = 1.288$ | $Y_{34} = Y_{56} = 1.292$ |
| $Y_2 = Y_7 = 2.050$ | $Y_4 = Y_5 = 2.087$ |
| $Y_{23} = Y_{67} = 1.564$ | $Y_{45} = 1.277$ |

All values normalized so $Y_0 = 1$.

previous 2-to-1 bandwidth design whose response was shown in Fig. 18-8(c). In both the case of Fig. 18-8(c) and the case of Fig. 18-9, the filter has seven sections; however, it should be noted that the latter response has a steeper cut-off, since it was designed from an $n = 8$ instead of an $n = 6$ prototype. It is thus seen that points mapped from the prototype response by use of Eq. (18-4a) are again quite accurate, but those using Eq. (18-4b) show appreciable error at high attenuation levels.

If filters in the form of Fig. 18-1(c) or 18-1(d) are desired, but with a somewhat different impedance level for their interior sections, this can be accomplished by using a modified form of the calculation procedure in Table 18-3 as is described in Sec. C-4.

5. DESIGN OF FILTERS IN THE FORM IN FIG. 18-2

Filters in the form shown in Fig. 18-2 can be readily designed by a modified use of Table 18-2. The design is carried out to first give a filter in the form in Fig. 18-1(d) with the desired passband characteristic and bandwidth. Then each shunt, quarter-wavelength, short-circuited stub of characteristic admittance Y_k is replaced as shown in Fig. 18-2 by a shunt, half-wavelength, open-circuited stub having an inner quarter-wavelength portion with a characteristic admittance

$$Y'_k = \frac{Y_k (a \tan^2 \theta_1 - 1)}{(a + 1) \tan^2 \theta_1} \quad (18-6)$$

and an outer quarter-wavelength portion with a characteristic admittance

$$Y''_k = a Y'_k \quad (18-7)$$

The parameter a is fixed by

$$a = \cot^2 \left(\frac{\pi \omega}{2 \omega_0} \right) \bigg|_{(\omega_\infty / \omega_0) < (\omega_1 / \omega_0)} \quad (18-8)$$

* The reference wavelength is that at the mid band frequency ω_0 .

where $\theta_1 = \pi\omega_1/2\omega_0$, and ω_∞ is a frequency at which the shunt lines present short circuits to the main line and cause infinite attenuation. The principle upon which the above substitution is made is that Eqs. (18-6) to (18-8) are constrained to yield half wavelength open-circuited stubs which have exactly the same susceptances at the band-edge frequency ω_1 as did the quarter-wavelength short-circuited stubs that they replace, while both kinds of stubs have zero admittance at ω_0 .

To test out this procedure a filter was designed as in Table 18-2 to give 30 percent bandwidth ($\omega_1/\omega_0 = 0.850$) using a 0.10-db Tchebyscheff prototype with $n = 8$. Then, choosing $\omega_\infty/\omega_0 = 0.500$, which gives $a = 1$, the quarter-wavelength stubs were replaced by half-wavelength stubs as described above, and the resulting computed response is shown in Fig. 18-10.

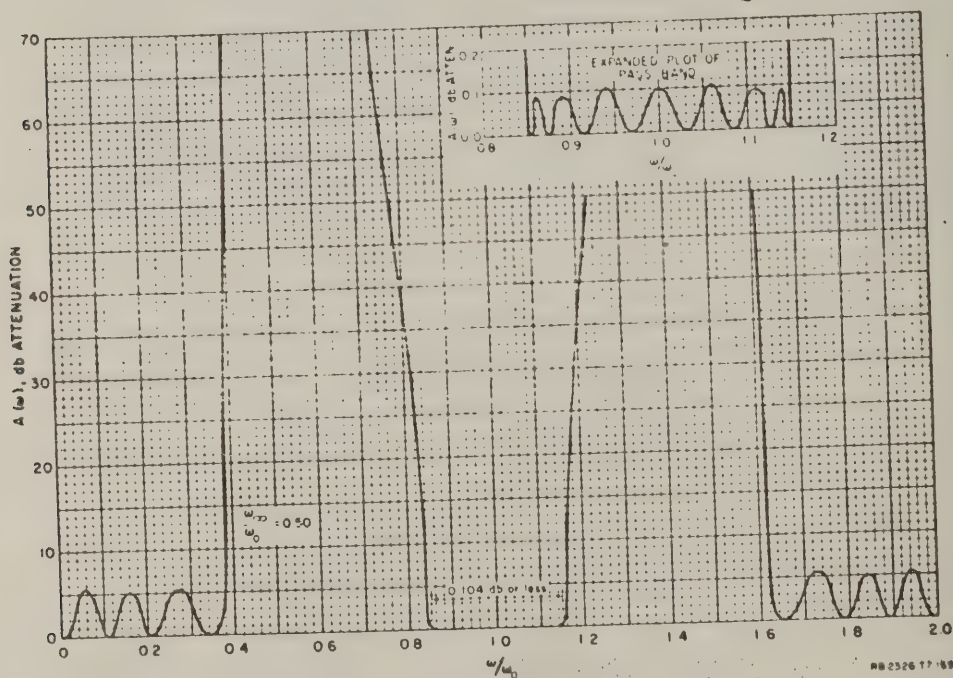


FIG. 18-10

COMPUTED RESPONSE OF A 30-PERCENT-BANDWIDTH BANDPASS FILTER
DESIGNED IN THE FORM IN FIG. 18-2
(Design value for $\omega_1/\omega_0 = 0.850$. Prototype had 0.10 db Tchebyscheff
ripple with $n = 8$ reactive elements.)

Note that the pass band is almost exactly as prescribed, and that there are low attenuation regions in the vicinity of $\omega = 0$ and $\omega = 2\omega_0$, which are to be expected. The element values for this filter are shown in Table Table 18-6.

TABLE 18-6
ELEMENT VALUES FOR THE FILTER OF FIG. 18-10
REALIZED AS SHOWN IN FIG. 18-2
(Filter designed from a 0.10 db ripple,
 $n = 8$, Tchebyscheff prototype using
 $\omega_1/\omega_0 = 0.850$ and $\omega_\infty/\omega_0 = 0.500$.
This, then, calls for $a = 1$ so
that $Y'_k = Y''_k$ throughout.)

| | |
|-----------------------------|-----------------------------|
| $Y'_1 = Y'_8 = 1.806$ | $Y'_3 = Y'_6 = 3.584$ |
| $Y'_{12} = Y'_{78} = 1.288$ | $Y'_{34} = Y'_{56} = 1.292$ |
| $Y'_2 = Y'_7 = 3.585$ | $Y'_4 = Y'_5 = 3.614$ |
| $Y'_{23} = Y'_{67} = 1.364$ | $Y'_{45} = 1.277$ |

All values normalized so that $Y_0 = 1$.

The 2-to-1-bandwidth filter design (Fig. 18-9 and Table 18-5) was also converted to this form using $\omega_\infty/\omega_0 = 0.500$, and its response was computed. The features of the pass band looked much the same as those in the expanded plot in Fig. 18-9, while the stop bands consisted of very sharp attenuation spikes surrounding $\omega/\omega_0 = 0.500$, in a manner similar to that in Fig. 18-10, except that the attenuation bands were much narrower.

Filters of the form in Fig. 18-2 should be particularly useful where the pass bands around $\omega = 0$ and $\omega = 2\omega_0$ are not objectionable, and where there is a relatively narrow band of signals to be rejected. By the proper choice of ω_∞ , the infinite attenuation point can be so placed as to give maximum effectiveness against the unwanted signals. Although using the same ω_∞ for all of the stubs should give the best passband response, it may be permissible to stagger the ω_∞ points of the stubs slightly to achieve broader regions of high attenuation. Filters of the form in Fig. 18-2 are practical for narrower bandwidths than are those in the form in Fig. 18-1(d) because of the larger susceptance slope of half-wavelength stubs for a given characteristic admittance. For example, in the case of Fig. 18-10, the shunt stubs for this filter as shown in

Fig. 18-2 have characteristic admittances $Y'_k = Y''_k$, which are 0.471 times the characteristic admittances of the shunt stubs of the analogous filter in the form in Fig. 18-1(d) from which it was designed. Thus narrower bandwidths can be achieved without having the characteristic admittances of the shunt stubs become excessive.

6. DESIGN OF FILTERS IN THE FORM IN FIG 18-3

For filters in the form of Fig 18-3 the mapping function in Eq. (18-5) should be used along with the equations in Table 18-3. In this case ω_∞ is the frequency of infinite attenuation created by the half-wavelength series stubs at the ends. The parameter d may be chosen to adjust the impedances of the interior of the filter to a convenient level.

This type of filter gives a cross between the type of response obtained using a filter as in Fig. 18-1(d), and that obtained by a filter as in Fig. 18-2. At first a design of the form in Fig. 18-1(d) was tried, but with the end stubs (only) replaced with shunt, half-wavelength, open-circuited stubs. This gave infinite attenuation at $\omega = 0$ and ω_∞ as expected, but yielded a point of very low attenuation (around 10 db) between these two frequencies (and between other corresponding frequencies). It was then found that by using an altered design procedure which yields series, half-wavelength, short-circuited stubs at the ends, the desired type of response could be obtained without excessive drop in attenuation between $\omega = 0$ and ω_∞ .

Figure 18-11 shows the computed response of a filter designed using Table 18-3 to give approximately 2 to 1 bandwidth. The prototype, again, had 0.10-db Tchebyscheff ripple, and $n = 8$. The remaining design parameters were $\omega_1/\omega_0 = 0.650$, $\omega_\infty/\omega_0 = 0.500$, and $d = 0.500$. In this case the pass-band ripples are not as well developed as in the previous examples. It has been found that the design theory used herein works best if all of the sections are of the same basic form since the end sections are different from the other sections in this case the larger deviation from a 0.10-db equal-ripple response is not surprising. (From a practical standpoint, this deviation may be good, since the ripples are small at the band edges where incidental dissipation will tend to increase the pass-band loss most.) Points mapped from the prototype response using Eq. (18-5) are seen to come fairly close to the computed response, although not as close as Eq. (18-4a) did where it was applicable. Both Eqs. (18-4a) and (18-5)

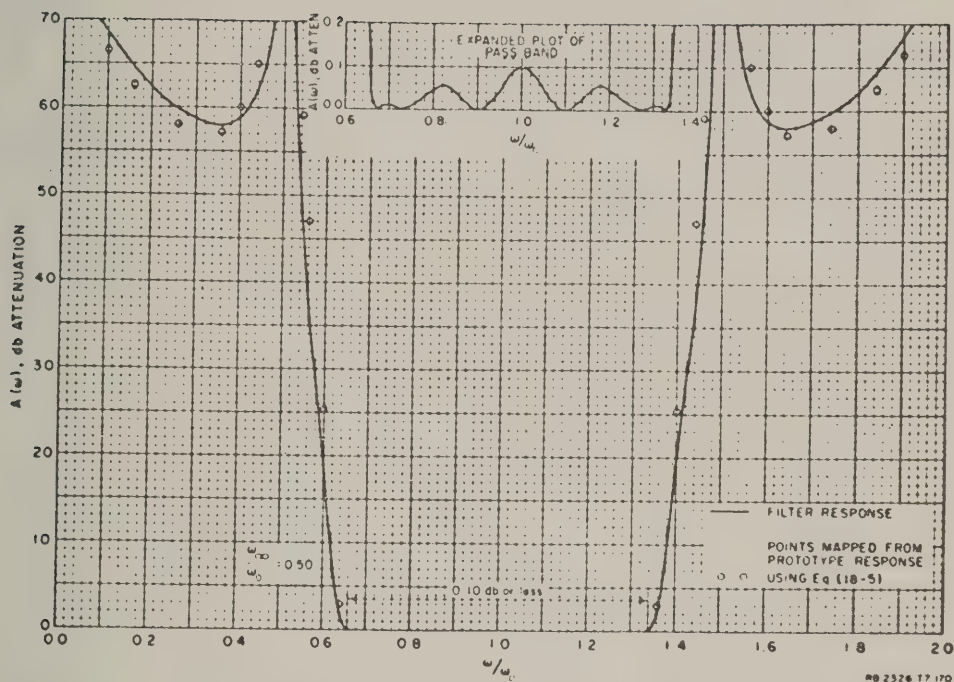


FIG. 18-11

COMPUTED RESPONSE OF A FILTER AS IN FIG. 18-3, WITH APPROXIMATELY 2 TO 1 BANDWIDTH
(Design value for ω_1/ω_0 was 0.650. Prototype had 0.10 db Tchebyscheff ripple with $n = 8$ reactive elements. Parameters d and ω_∞/ω_0 were both chosen as 0.500.)

were derived on the same basis and should probably yield similar accuracy. The larger deviations in this case are probably due at least in part to the fact that the passband response itself deviates more from the design objective. The element values for this filter design are given in Table 18-7.

TABLE 18-7
ELEMENT VALUES FOR THE FILTER OF FIG. 18-11
REALIZED AS SHOWN IN FIG. 18-3
(Filter designed using Table 18-3 from a 0.10-db ripple, $n = 8$, Tchebyscheff prototype using $\omega_1/\omega_0 = 0.650$ and $\omega_\infty/\omega_0 = 0.500$.)

| | |
|---------------------------|---------------------------|
| $Z_1 = Z_8 = 0.606$ | $Y_3 = Y_6 = 1.235$ |
| $Z'_1 = Z'_8 = 0.606$ | $Y_{34} = Y_{56} = 0.779$ |
| $Y_2 = Y_7 = 1.779$ | $Y_4 = Y_5 = 1.258$ |
| $Y_{23} = Y_{67} = 0.823$ | $Y_{45} = 0.770$ |

7. SUGGESTED WAYS FOR FABRICATING THE FILTERS UNDER CONSIDERATION

For bandwidths of perhaps around 20 percent or less, filters of the form in Fig. 18-1(a) are readily realized in printed-circuit form by use of Cohn's data for zero-thickness, parallel-coupled strips (see Refs. 13 and 1). Larger bandwidths are difficult using this construction because the gaps between the conductors must become extremely small. A suggested way for getting around this problem while still using printed circuit construction is shown in Fig. 18-12.¹⁵ Instead of just two slabs of dielectric, four slabs are used, two of which are relatively thin. Then alternate conductors are printed to form a double layer as shown in the cross-sectional view so that the adjacent conductor can be interleaved. This gives a relatively large odd-mode capacitance without the need for extremely close spacings. The cross-section of the conductors is no

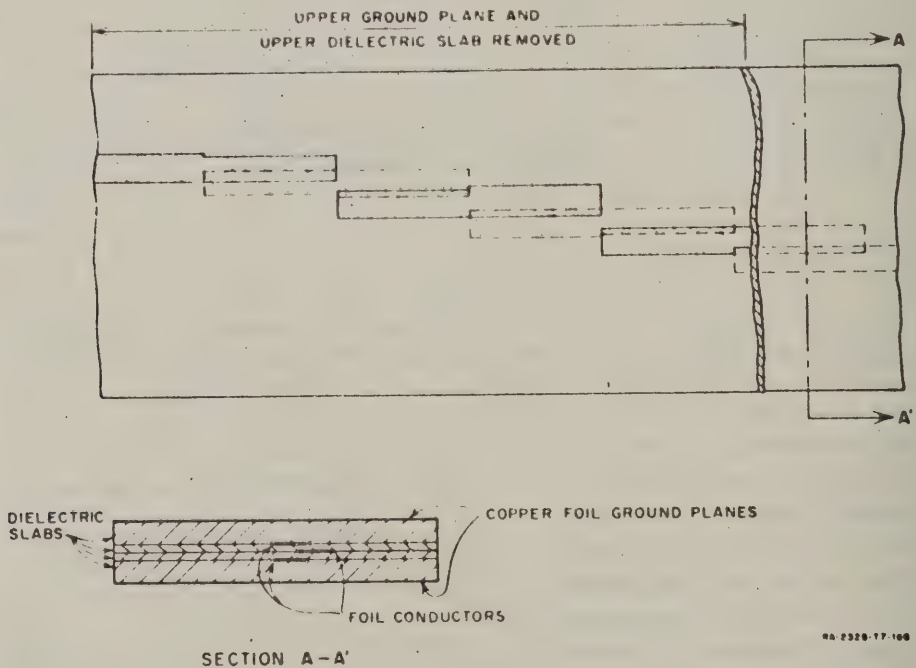


FIG. 18-12

POSSIBLE MEANS FOR FABRICATING WIDE-BAND FILTERS OF THE TYPE IN FIG. 18-1(a)
USING PRINTED CIRCUIT TECHNIQUES

(In order to achieve tight coupling with reasonably large conductor spacings, alternate conductor strips are made to be double so that conductor strips can be interleaved.)

longer balanced geometrically; however, by proper design, the even- and odd-mode impedances for both the single- and double-layer conductors can be made the same.¹⁵

Figure 18-13 shows a suggested way for realizing filters of the type in Fig. 18-1(b). In this case the conductors are rectangular bars supported mechanically by the short-circuits at their ends. This construction can be used for either narrow-or-wide-band filters and has the advantages that it does not require dielectric material (hence it has no dielectric loss), and that, with rounded corners on the conductors, it should have relatively high power-handling capability.

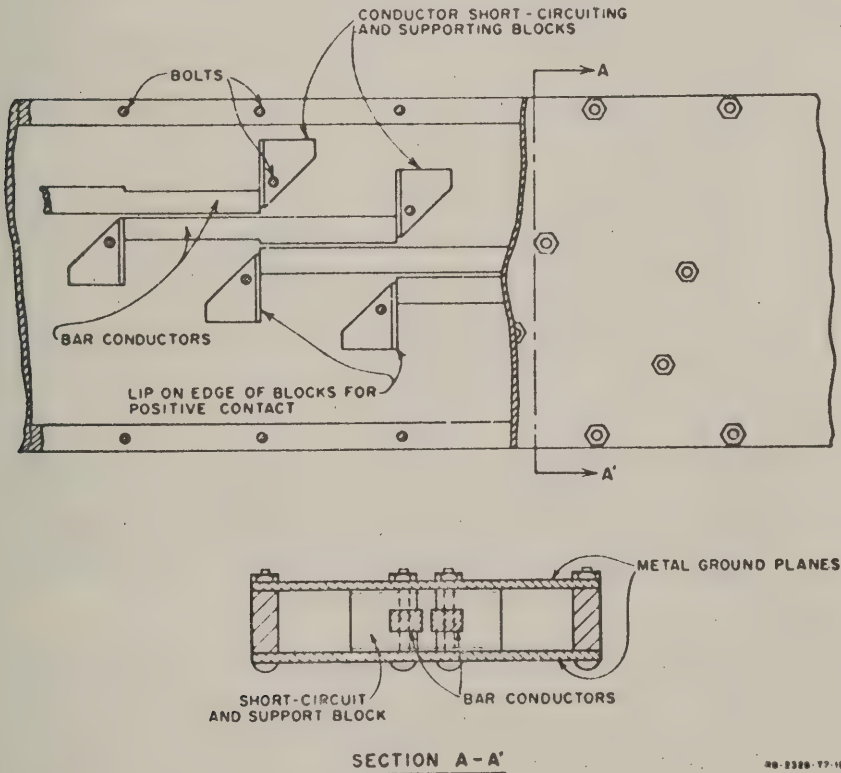


FIG. 18-13

POSSIBLE MEANS FOR FABRICATING WIDE-BAND FILTERS OF THE TYPE
IN FIG. 18-1(b) IN BAR-TRANSMISSION-LINE CONSTRUCTION
(The short-circuiting blocks support the bar conductors so that no
dielectric material is required.)

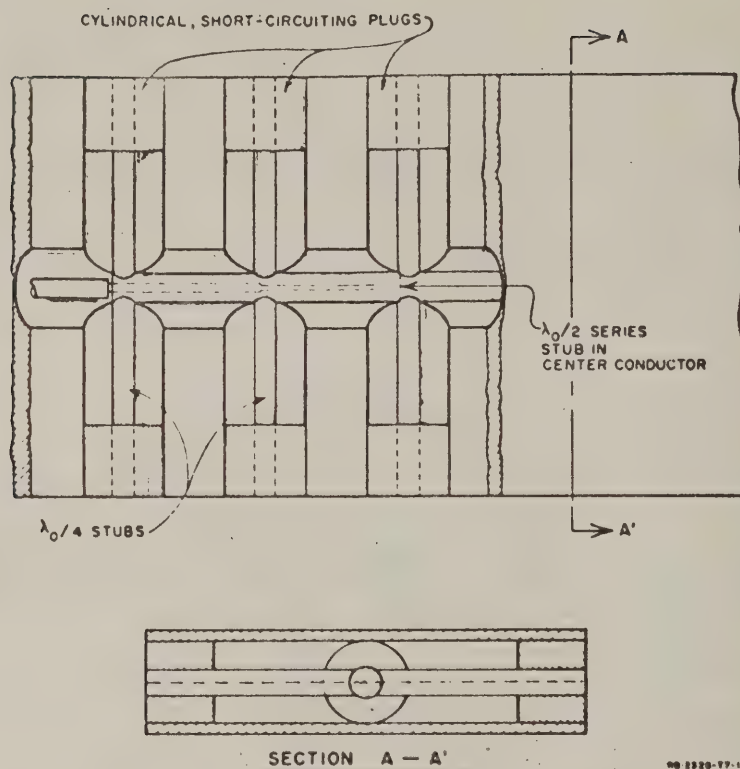


FIG. 18-14

POSSIBLE WAY FOR FABRICATING WIDE-BAND FILTERS OF THE TYPE IN FIG. 18-3
IN SPLIT-BLOCK CONSTRUCTION

(The shunt, quarter-wavelength, short-circuited stubs are realized in parallel pairs so that the characteristic admittance of each stub will be cut in half, and so that the structure will be self-supporting. The series, half-wavelength, short-circuited stubs are inside the center conductor.)

The filter type in Fig. 18-1(c) is not very attractive because of the difficulties involved in building series, open-circuited stubs. However, the types in Figs. 18-1(d), 18-2, and 18-3 can all be built readily in either printed-circuit construction,* or coaxial split-block construction, and probably also in waveguide. Figure 18-14 shows the filter type in Fig. 18-3 in split-block construction. The shunt, quarter-wavelength, short-circuited stubs are realized in parallel pairs, so that

* When using printed circuit construction, the data in Chapter 11 for correction of junction effects should be quite helpful.

their characteristic admittances will be cut in half, and so that the structure will be self-supporting. The series, half-wavelength, short-circuited stubs are inside the center conductor and may be supported by the short-circuit connection at their inner end.* By using a two-layer center conductor, a similar effect could be achieved in printed-circuit construction by locating the series stub between the two center-conductor layers. The dual of the circuit in Fig. 18-2 would have series, half-wavelength, short-circuited stubs, which would be quite practical when realized in waveguide. The circuit in Fig. 18-3 could probably be built in waveguide using series and shunt stubs protruding at right angles to the main waveguide.

C. THEORETICAL BASIS FOR THE FILTER EQUATIONS AND MAPPING FUNCTIONS

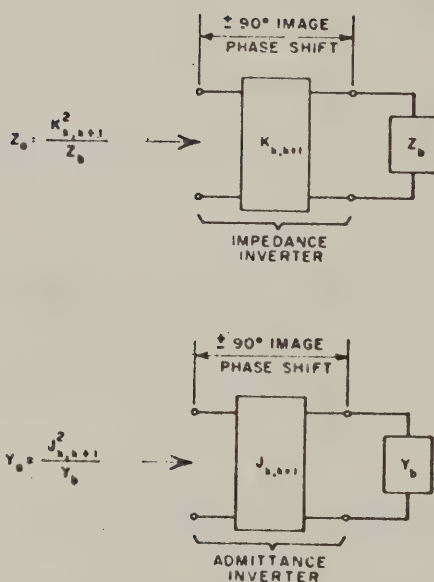
1. MODIFIED PROTOTYPES AS A BASIS FOR DESIGN

The first step in deriving the design equations used herein is to convert the low-pass prototype (Fig. 18-5) to a modified form that involves impedance inverters or admittance inverters. The concept of impedance inverters has previously been discussed in detail by Cohn;¹⁴ admittance inverters are simply the dual representations of impedance inverters, and are introduced only for convenience. Figure 18-15 summarizes the basic properties of these two types of inverters.

Using methods similar to those of Cohn,¹⁴ any circuit like that in Fig. 18-5 may be converted into either of the dual forms in Fig. 18-16. In form at (a), in the figure, which uses impedance inverters, all of the elements $R_0, L_{01}, L_{02}, \dots, L_{0n}, R_L$ may be chosen arbitrarily; the inverter parameters $K_{k,k+1}$ are then computed as indicated.

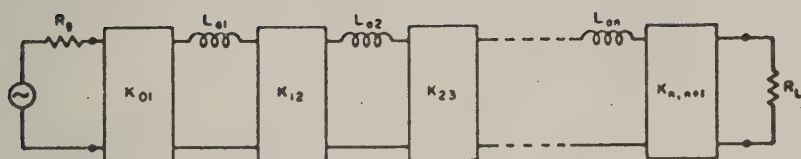
Analogous conditions hold for the dual circuit at (b) in Fig. 18-16. In the discussion to follow, the impedance (or admittance) inverters will be assumed to be idealized so that their electrical behavior is exactly as indicated in Fig. 18-15. They will be used merely as an aid to mathematical reasoning, and no direct attempt will be made to find a circuit which approximates their idealized performance. Instead, as indicated below, the approximations will be based upon the impedance inverters plus part of each adjacent element.

* In the example of Fig. 18-11 and Table 18-7 it would have been better to have used a larger value of d so that the admittances of the interior sections would be larger and hence the center conductor would be larger in diameter. This would facilitate the fabrication of the series stub.



DA 2328-171

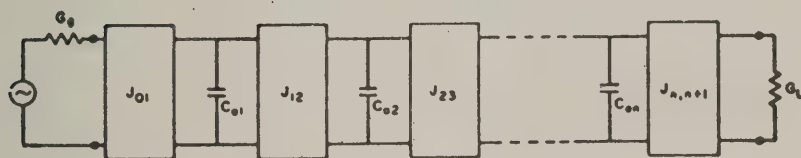
FIG. 18-15
DEFINITION OF IMPEDANCE INVERTERS
AND ADMITTANCE INVERTERS



$$K_{01} = \sqrt{\frac{R_0 L_{01}}{g_0 g_1}}, \quad K_{b,b+1} = \sqrt{\frac{L_{0b} L_{0(b+1)}}{g_b g_{b+1}}}, \quad K_{n,n+1} = \sqrt{\frac{L_{0n} R_L}{g_n g_{n+1}}}$$

$b = 1 \text{ to } n-1$

(a) MODIFIED PROTOTYPE USING IMPEDANCE INVERTERS



$$J_{01} = \sqrt{\frac{G_0 C_{01}}{g_0 g_1}}, \quad J_{b,b+1} = \sqrt{\frac{C_{0b} C_{0(b+1)}}{g_b g_{b+1}}}, \quad J_{n,n+1} = \sqrt{\frac{C_{0n} G_L}{g_n g_{n+1}}}$$

$b = 1 \text{ to } n-1$

(b) MODIFIED PROTOTYPE USING ADMITTANCE INVERTERS

RD 528-77-172

FIG. 18-16

LOW-PASS PROTOTYPES MODIFIED TO INCLUDE IMPEDANCE INVERTERS OR ADMITTANCE INVERTERS

(The $g_0, g_1, \dots, g_n, g_{n+1}$ are obtained from the original prototype as in Fig. 18-5, while the $R_0, L_{01}, \dots, L_{0n}$, and R_L or the $G_0, C_{01}, \dots, C_{0n}$, and G_L may be chosen as desired.)

2. PROCEDURE FOR DERIVING THE EQUATIONS IN TABLE 18-1

The design equations in Table 18-1 are based on the modified prototype shown at (a) in Fig. 18-16, while Fig. 18-17 shows the manner in which the element values are specified, and the manner in which the prototype is broken into sections. The image impedance, $Z'_{k,k+1}(\omega')$, and phase, $\beta_{k,k+1}$, (in the pass band) for each of the prototype interior sections (S'_{12} to $S'_{n-1,n}$) are readily shown to be

$$Z'_{k,k+1}(\omega') = K_{k,k+1} \sqrt{1 - \left(\frac{\omega' R_g}{\omega'_1 2K_{k,k+1}} \right)^2} \quad (18-9)$$

and

$$\beta_{k,k+1} \left| \omega' \leq \frac{2K_{k,k+1}\omega'_1}{R_g} \right. = \sin^{-1} \left(\frac{\omega' R_g}{\omega'_1 2K_{k,k+1}} \right) \pm \frac{\pi}{2} \quad (18-10)$$

where, as before, ω'_1 is the cut off frequency for the low-pass prototype. The choice of $\pm \pi/2$ in Eq. (18-10) depends on whether the inverter is taken to have ± 90 degrees phase shift. The work of Jones and Bolljahn shows⁶ that the image impedance and pass-band image phase for a parallel coupled section as shown at (a) in Fig. 18-4 are given by

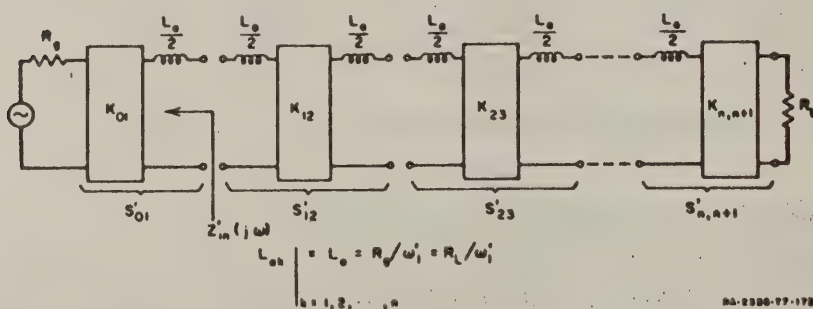


FIG. 18-17

MODIFIED PROTOTYPE FOR DERIVING THE DESIGN EQUATIONS IN TABLE 18-1

$$Z_I = \frac{\sqrt{(Z_{oe} - Z_{oo})^2 + (Z_{oe} + Z_{oo})^2 \cos^2 \theta}}{2 \sin \theta} \quad (18-11)$$

and

$$\beta = \cos^{-1} \left[\left(\frac{Z_{oe} + Z_{oo}}{Z_{oe} - Z_{oo}} \right) \cos \theta \right] \quad (18-12)$$

where $\theta = \pi\omega/2\omega_0$, and where Z_{oe} and Z_{oo} are the even- and odd-mode line impedances, respectively. The parameters of the parallel-coupled sections S_{12} to $S_{n-1,n}$ in Fig. 18-1(a) are related to the prototype sections S'_{12} to $S'_{n-1,n}$ of the prototype by forcing the following correspondences between the two structures:

- (1) The image phase of the parallel-coupled sections when $\omega = \omega_0$ must be the same as the image phase of the prototype sections when $\omega' = 0$.
- (2) The image impedances of the parallel-coupled sections when $\omega = \omega_0$ must be the same (within a scale factor s) as the image impedances of the corresponding prototype sections when $\omega' = 0$. (18-13)
- (3) The image impedance of the parallel-coupled sections when $\omega = \omega_1$ must be the same (within a scale factor s) as the image impedances of the corresponding prototype sections when $\omega' = \omega'_1$.

Correspondence (1) is fulfilled in this case by choosing the + sign in Eq. (18-10). Equating Eqs. (18-9) and (18-11) and evaluating each side at the appropriate frequencies indicated above, two equations are obtained from which the equations in part (b) of Table 18-1 may be derived (with the help of the information in Figs. 18-16 and 18-17) by solving for Z_{oe} and Z_{oo} .

The end sections, S_{01} and $S_{n,n+1}$, must be treated as a special case. Defining $Z_{i,n}(j\omega)$ as the impedance seen looking in the right end of the parallel-coupled section S_{01} in Fig. 18-1(a), with the left end connected to the input line of impedance Z_0 , the following correspondences are forced with respect to $Z'_{i,n}(j\omega')$ indicated in Fig. 18-17:

* Taking $R_g = R_L = Z_0$.

- (1) $\operatorname{Re} Z_{i,n}(j\omega_0) = \operatorname{Re} Z'_{i,n}(j\omega_1)$ for the parallel-coupled terminating circuit, just as $\operatorname{Re} Z'_{i,n}(j\omega) = \operatorname{Re} Z'_{i,n}(-j\omega'_1)$ for the terminating circuit of the prototype. (18-14)
- (2) $\operatorname{Im} Z_{i,n}(j\omega_1)/\operatorname{Re} Z_{i,n}(j\omega_1)$ must equal $X'/R' = \operatorname{Im} Z'_{i,n}(-j\omega'_1)/\operatorname{Re} Z'_{i,n}(-j\omega'_1)$ computed from the prototype.

Defining

$$P = \frac{(Z_{oe})_{01} - (Z_{oe})_{01}}{R_g 2 \sin \theta_1} \quad (18-15)$$

and

$$Q = \frac{(Z_{oe})_{01} + (Z_{oe})_{01}}{R_g 2 \tan \theta_1} \quad (18-16)$$

it can be shown that Correspondence (1) in Eqs. (18-14) will be obtained if

$$Q = \cot \theta_1 \quad (18-17)$$

is satisfied, where $\theta = \pi\omega_1/2\omega_0$. Further, Correspondence (2) requires that

$$Q^3 + Q(1 - P^2) + \frac{X'}{R'} P^2 = 0 \quad (18-18)$$

be satisfied. Substituting Eq. (18-17) in Eq. (18-18), and solving for $(Z_{oe})_{01}$ and $(Z_{oe})_{01}$ yields the results in Part (a) of Table 18-1. Even if $R_g = Z_0$, the above conditions will generally result in an impedance level for $Z_{i,n}(j\omega)$ of the band-pass filter which is different from that of $Z'_{i,n}(j\omega)$ for the prototype. The impedances of the interior sections must therefore be corrected by multiplying by the scale factor s indicated in Table 18-1.

3. PROCEDURE FOR DERIVING THE EQUATIONS IN TABLE 18-2

Figure 18-18 shows the manner in which the modified prototype at (a) in Fig. 18-16 is broken into sections and the elements specified for deriving the equations in Table 18-2. Note that in this case, the end impedance inverters, K_{01} and $K_{n,n+1}$, are both made equal to the terminating resistances $R_g = R_L$. For the end inductances, $L_{s1} = L_{sn} = R_g g_{0g}$; however,

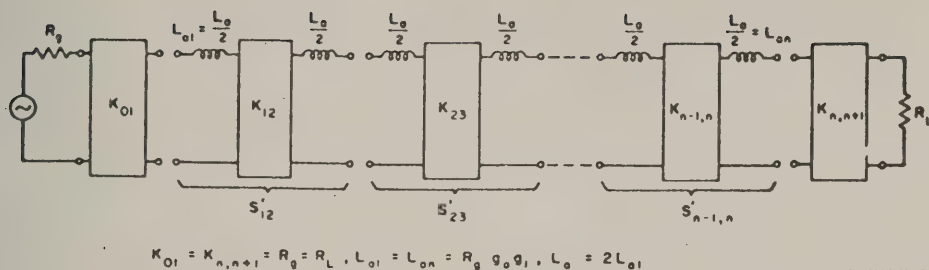


FIG. 18-18

MODIFIED PROTOTYPE FOR DERIVING THE EQUATIONS IN TABLE 18-2

$L_{02} = L_{03} = \dots = L_{0,n-1}$ are made equal to $2L_{01}$, so that the structure can be broken into symmetrical sections without need for end sections. Using the indicated values for the L_{0k} , the $K_{k,k+1}$ are obtained by use of Fig. 18-16. Then all of the sections are designed by use of Eqs. (18-9) to (18-12) and the correspondences given in (18-13).

4. PROCEDURE FOR DERIVING THE EQUATIONS IN TABLE 18-3

Figure 18-19 shows the modified prototype used for deriving the equations in Table 18-3. In this case most of the structure is in the form shown at (b) in Fig. 18-16. However, inverters J_{01} , J_{12} , $J_{n-1,n}$, and $J_{n,n+1}$ have been omitted. Here, L_1 and C_2 have the same values that they had in their original prototype form in Fig. 18-5. Capacitor C_2 is

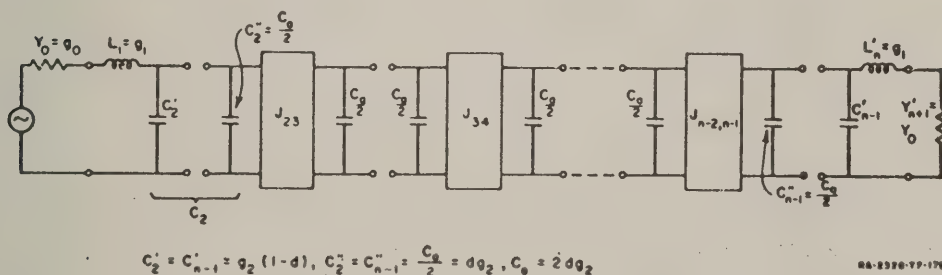


FIG. 18-19

MODIFIED PROTOTYPE FOR DERIVING THE EQUATIONS IN TABLE 18-3

(Parameter d may be used to adjust the impedance level in the center part of the filter. In the example of Fig. 18-13, d was chosen as one-half, to split $C_2 = C_2' + C_2''$ in half.)

split into two parts, C'_2 and C''_2 , and the parameter d is used to establish what fraction of C_2 becomes C''_2 . Then the capacitance values $C_{.3} = C_{.4} = \dots = C_{.n-2}$ are established so that all of the interior sections can be broken into symmetrical sections. The interior sections are then related to parallel-coupled sections as at (b) in Fig. 18-4 by dual procedures to those used for the interior sections for Tables 18-1 and 18-2. The parallel-coupled sections are then converted to stub form by the equivalence at (b) in Fig. 18-4. The end sections are designed by forcing the stubs to have reactances at $\omega = \omega_0$ and $\omega = \omega_1$ (on a normalized basis) which are the same as those of the corresponding prototype elements, L_1 and C'_2 , at $\omega' = 0$ and $\omega' = -\omega'_1$, respectively.

This same general viewpoint should be useful for designing filters in the form in Fig. 18-1(d) [also as in Fig. 18-1(c)] to give some desired impedance level in the interior part of the filter. To accomplish this, the prototype in Fig. 18-13 should be converted to its dual form analogous to that shown at (a) in Fig. 18-16. Then the capacitor C_1 is split, just as C_2 is split in Fig. 18-19. The resulting design equations are

$$C_a = 2dg_1, \quad \frac{J_{12}}{Y_0} = \frac{J_{n-1,n}}{Y_0} = \frac{g_0 \sqrt{g_1 C_a}}{\sqrt{g_1 g_2}}$$

$$\left. \frac{J_{k,k+1}}{Y_0} \right|_{k=2 \text{ to } n-2} = \frac{g_0 C_a}{\sqrt{g_k g_{k+1}}}, \quad M_{k,k+1} = \sqrt{\left(\frac{J_{k,k+1}}{Y_0} \right)^2 + \left(\frac{g_0 \omega'_1 C_a \tan \theta_1}{2} \right)^2},$$

$$Y_{k,k+1}^s \Big|_{k=1 \text{ to } n-1} = Y_0 \left(M_{k,k+1} - \frac{J_{k,k+1}}{Y_0} \right),$$

$$Y_1 = Y_n = g_0 Y_0 \omega'_1 (1-d) g_1 \tan \theta_1 + Y_{12}^s$$

$$Y_k \Big|_{k=2 \text{ to } n-1} = Y_{n-k+1} = Y_{k-1,k}^s + Y_{k,k+1}^s$$

$$Y_{k,k+1} \Big|_{k=1 \text{ to } n-1} = Y_{n-k, n-k+1} = J_{k,k+1}$$

Although this technique has been used successfully for achieving small adjustments in impedance level within a filter, the filter-response accuracy resulting when this technique is used to achieve large changes in impedance level has not been tested.

5. SELECTION OF MAPPING FUNCTIONS

Previous work of Cohn,¹ and also the plots presented herein, show that when the function in Eq. (18-4b) is used as indicated in Fig. 18-6 or 18-7 to map the response of a low-pass prototype, it will predict quite accurately the response of bandpass filters of the form in Fig. 18-1(a) having narrow or moderate bandwidth. Although the function in Eq. (18-4b) is very useful, it should not be expected to give high accuracy for wide-band cases because it is not periodic (which the filter response is), nor does it go to infinity for $\omega = 0, 2\omega_0, 4\omega_0$, etc., which is necessary in order to predict the infinite attenuation frequencies in the response of the bandpass filter structure. It might at first seem that the function

$$F_n\left(\frac{\omega}{\omega_0}\right) = -\cot\left(\frac{\pi\omega}{2\omega_0}\right) \quad (18-19)$$

would solve this problem nicely, since it is periodic as desired, it varies similarly to Eq. (18-4b) in the vicinity of ω_0 , and it has poles at the desired frequencies $\omega = 0, 2\omega_0, 4\omega_0$, etc. However, if the structures in Figs. 18-1 are analyzed, it will be seen that no matter what value of n is used, the poles of attenuation at $\omega = 0, 2\omega_0, 4\omega_0$, etc., are always first-order poles.* Meanwhile, an n -reactive-element prototype as in Fig. 18-5 (which will have an n th-order pole at $\omega' = \infty$) will map so as to give n th order poles at $\omega = 0, 2\omega_0$, etc., if the function in Eq. (18-18) is used. This important source of error is corrected in the case of Eq. (18-4a) by replacing $\cot(\pi\omega/2\omega_0)$ by $\cos(\pi\omega/2\omega_0)/|\sin(\pi\omega/2\omega_0)|$, and then taking the n th root of the denominator. In this manner the poles generated by the zeros of $|\sin(\pi\omega/2\omega_0)|$ become of $1/n$ order, which causes the n th-order pole at $\omega' = \infty$ for the prototype response to map into first-order poles of the bandpass filter response at the desired frequencies.

* For example, for the filter form in Fig. 18-1(d), as $\omega \rightarrow 0$ the effect of all of the shunt stubs can be reduced to that of a single, shunt, zero-impedance branch which would produce a first-order pole of attenuation at $\omega = 0$. (One way in which higher-order poles can be generated is to produce shunt, zero-impedance branches alternating with series branches having infinite impedance.)

In the case of the circuit in Fig. 18-3, the poles of attenuation at $\omega = 0, 2\omega_0, 4\omega_0$, etc., will again always be of first order regardless of the value of n used. However, the series stubs at each end produce second-order poles at the frequency ω_∞ and at other corresponding points in the periodic response.* Thus, the

$$\sqrt[n]{|\sin(\pi\omega/2\omega_0)|}$$

factor in the denominator of Eq. (18-5) assures that the n th-order poles at $\omega' = \infty$ in the prototype response will always map to first-order poles at $\omega = 0, 2\omega_0$, etc., for the band-pass filter response. In addition, the factor

$$\sqrt[n]{\left[\sin \frac{\pi}{2} \left(\frac{\omega - \omega_\infty}{\omega_0} \right) \right]^2 \left[\sin \frac{\pi}{2} \left(\frac{\omega - 2\omega_0 + \omega_\infty}{\omega_0} \right) \right]^2}$$

is introduced to cause the n th-order pole at infinity in the prototype response to map to second-order poles at ω_∞ (and other periodic points) for the band-pass filter response. In this manner, all of the proper poles of attenuation are introduced with their proper order.

These principles can also be applied to the structure in Fig. 18-2, but this structure presents some new difficulties. It can be seen that this structure will develop n th-order poles of attenuation at ω_∞ and corresponding periodic points, but the half-wavelength stubs also introduce additional natural modes of oscillation which create, in addition to the desired pass band, a low-pass pass band (and corresponding periodic pass bands) as shown in the response in Fig. 18-10. This additional low-pass pass band approaches ω_∞ quite closely, with the result that, although the pole at ω_∞ is of relatively high order, its effectiveness is weakened by the close proximity of this low-pass pass band. The function

$$F_n\left(\frac{\omega}{\omega_0}\right) = \tan\left(\frac{\pi\omega}{\omega_0}\right) \quad (18-20)$$

* This can be seen as follows: For $\omega = \omega_\infty$, each of the series stubs represents an infinite-impedance series branch. For this single frequency, the interior part of the filter can be replaced by an equivalent T -section with a finite shunt impedance. Thus, the structure can be reduced (for the frequency ω_∞) to two, series, infinite-impedance branches separated by a finite, shunt-impedance branch. This can be seen to result in a second-order pole of attenuation. (If the impedance of the equivalent shunt branch had been zero, the pole of attenuation would have been raised to third order.)

for the case of $\omega_\infty/\omega_0 = 0.50$ would map the prototype response to give a low-pass pass band, an n th-order pole at ω_∞ , and the desired pass band centered at ω_0 . However, it would not properly predict how close the low-pass pass band comes to ω_∞ , nor could it account for the oversize attenuation ripples which occur in this band (see Fig. 18-10). As a result, the function in Eq. (18-20) predicts an overly optimistic rate of cut-off at the edges of the pass band centered at ω_0 . It is probable that a useful approximation could be obtained by using a mapping function such as that in Eq. (18-20) with additional factors added which create zeros in $F_n(\omega/\omega_0)$, close to, but somewhat off of, the $j\omega$ axis (regarded from the complex-frequency point of view). Proper location of these zeros could then be used to extend the low-pass pass band upwards toward ω_∞ , which should give the proper effect.

REFERENCES

1. S. B. Cohn, et al, "Research on Design Criteria for Microwave Filters," Final Report, Chap. 4, SRI Project 1331, Contract DA 36-039 SC-64625, Stanford Research Institute, Menlo Park, California (June 1957). Also, S. B. Cohn, "Parallel-Coupled Transmission-Line Resonator Filters," *Trans. IRE Vol MTT-6*, pp. 223-231, (April 1958).
2. Final Report for SRI Project 1331 (see Reference 1 above), Chapter 3, also: Jones, E. M. T., "Synthesis of Wide-Band Microwave Filters to have Prescribed Insertion Loss," *IRE Convention Record*, 1956 National Convention, Part 5, pp. 119-128.
3. Richards, P. I., "Resistor-Transmission-Line Circuits," *Proc. IRE* 36, pp. 217-220, (February 1948).
4. Ozaki, H. and Ishii, J., "Synthesis of Transmission-Line Networks and the Design of UHF Filters," *IRE Trans. PGCT-2*, pp. 325-336 (December 1955).
5. Ozaki, H., and Ishii, J., "Synthesis of a Class of Strip-line Filters," *IRE Trans. PGCT-5*, pp. 104-109 (June 1958).
6. A. I. Grayzel, "A Synthesis Procedure for Transmission Line Networks," *IRE Trans. PGCT-5*, pp. 172-181 (September 1958).
7. N. B. Welsh and E. S. Kuh, "Synthesis of Resistor-Transmission-Line Networks," Report No. 74, ONR Contract N7-onr-29529, Electronics Research Laboratory, University of California, Berkeley, California (July 15, 1958).
8. Final Report for SRI Project 1331 (see Reference 1 above), Chapter 4. Also: E. M. T. Jones and J. T. Bolljahn, "Coupled-Strip-Transmission-Line Filters and Directional Couplers," *IRE Trans. PGMTT-4*, pp. 75-81 (April 1956).
9. E. A. Guillemin, *Synthesis of Passive Networks* p. 371 (John Wiley and Sons, New York, N.Y., 1957).
10. L. Weinberg, "Network Design by Use of Modern Synthesis Techniques and Tables," Tech. Memo. 427, Hughes Aircraft Company, Research Laboratories, Culver City, California (April 1956). Also, *Proceedings of the National Electronics Conference* Vol. 12, (1956).
11. See Chapter 13 of this report.
12. *Reference Data for Radio Engineers*, 4th ed. pp. 188-198 (International Telephone and Telegraph Corp., New York, N.Y.).
13. S. B. Cohn, et al, "Strip Transmission Lines and Components," Final Report, Chap. 3, SRI Project 1114, Contract DA 36-039 SC-63232, Stanford Research Institute, Menlo Park, California (February 1957). Also: S. B. Cohn, "Shielded Coupled-Strip Transmission Line," *IRE Trans. PGMTT-3* pp. 29-38, (October 1955).
14. Final Report for SRI Project 1331 (see Reference 1 above), Chap. 2. Also: S. B. Cohn, "Direct-Coupled-Resonator Filters," *Proc. IRE* 45, pp. 187-196 (February 1957).
15. Design data for coupled-lines as shown in Fig. 18-12 have been prepared. See Chapter 7 of this report.

CHAPTER 19

AN EXPERIMENTAL WIDE-BAND, BAND-PASS FILTER

A. GENERAL

The objectives of this trial filter design were

- (1) To provide an initial design for an S-band, band-pass filter to be used in a diplexer requested by the Signal Corps. [It was decided to use a form of construction such that an X-band version of the same filter (required for another diplexer also requested by the Signal Corps) could be designed by simply scaling the dimensions of the S-band model.]
- (2) To test the practical usefulness of the design methods discussed in Chapter 18. (In particular, it was desired to find out how much the discontinuities at the junctions between the stubs and the main transmission line would disrupt the idealized design and cause deviation from the desired response.)
- (3) To obtain some approximate equivalent circuit data for the double stub, plus junctions which are desirable for a stub filter of this type, and to find out if the junction effect can be compensated. (These data will facilitate the design of other filters of this class in the future.)

The over-all design approach for the diplexer will be discussed in Chapter 20. For the present it is enough to note that a filter is required having at least an octave bandwidth with a lower cut-off frequency of 2 Mc, a very rapid rate of attenuation rise below 2 Mc, and 0.5 db maximum attenuation in the pass band. The design methods described in Chapter 18 of this report should be very useful for such a design, and in particular, the type of filter in Figs. 18-3 and 18-11 of that chapter should be particularly desirable. That type of filter has infinite attenuation points at finite, stop-band frequencies by virtue of series, half wavelength (at the mid-band frequency) stubs at the ends of the filter. However, since it was desirable to be able to scale this design to X-band and the end stubs would be very difficult to fabricate in a scaled-down X-band version, it was decided to eliminate these end stubs. The form chosen for the filter consisted of a main transmission line with

short-circuited, quarter-wavelength (at the mid-band frequency) shunt stubs spaced at quarter-wavelength intervals along the line. This latter type of filter does not have as rapid a rate of cut-off (for a given number of circuit elements) as does the first-mentioned type, but it is simpler to fabricate, since it does not use series stubs at the ends.

B. COMPUTATION OF FILTER ELEMENT VALUES

The filter was designed from a lumped-element, Tchebyscheff low-pass prototype having $n = 10$ reactive elements and an 0.10-db pass-band ripple. The low-pass prototype element values were obtained from the tabulations in Chapter 13 of this report. The lower-band-edge frequency normalized with respect to the mid-band frequency, f_0 , was taken as $f_1/f_0 = 0.630$ which implies a normalized upper-band-edge frequency of $f_2/f_0 = 1.370$ (see Fig. 18-7) and gives a band-edge ratio of $f_2/f_1 = 2.175$. The filter element values were computed by use of the equations in Part C-4 of Chapter 18 with the admittance level parameter d set equal to one.*

An open-wire transmission-line representation of the resulting filter is shown in Fig. 19-1. Note that all of the shunt stubs (except the end stubs) have been replaced by double stubs in order to double the impedance level of the interior stubs. This was done because the filter was to be fabricated in strip-transmission-line form, and if single shunt stubs were used in the interior of the filter they would have to be very wide and might create large junction effects.

The element values for the circuit in Fig. 19-1 are shown in Table 19-1. For convenience $n = 10$ was chosen for the computation of the filter design because that is the largest value of n for which tabulated values of the low-pass prototype elements were available. However, in order to obtain the desired high rate of cut-off, $n = 13$ was required. Thus having computed the design as for an $n = 10$ Tchebyscheff filter, three additional sections identical to section S_{36} were then inserted at the middle of the filter.† The design obtained in this manner is not quite the same as would have been obtained if an analogous, Tchebyscheff, lumped-element, low-pass prototype with $n = 13$ had been used. However, the difference should be small.

* Using $d = 1$ gives the same results as would be obtained if the design were first computed in parallel-coupled form by use of Table 18-2 and then converted to stub filter form (see Chapt. 18).

† For a definition of "section" as used herein see Sec. B of Chapt. 18.

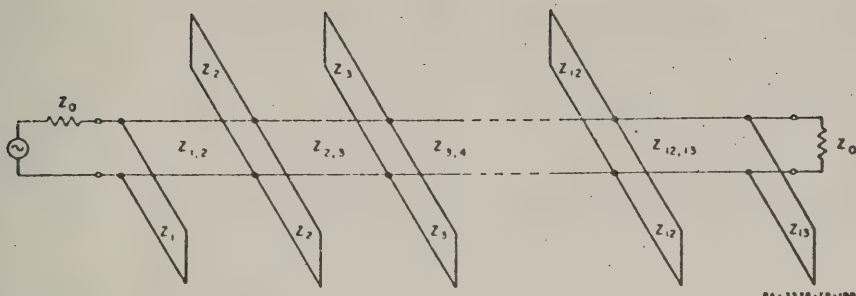


FIG. 19-1

OPEN-WIRE TRANSMISSION LINE REPRESENTATION OF THE WIDE-BAND
BAND-PASS FILTER UNDER DISCUSSION

TABLE 19-1

ELEMENT VALUES FOR A BAND-PASS FILTER OF THE FORM IN FIG. 19-1
HAVING $n = 13$, A BAND-EDGE RATIO OF $f_2/f_1 = 2.175$, AND
APPROXIMATELY 0.1 db TCHERYSCHIEFF PASS-BAND RIPPLE.

| | | | |
|------------------------------|------|-----------------------------|------|
| $Z_0 = 50$ | ohms | $Z_4 = Z_{10} = 52.4$ | ohms |
| $Z_1 = Z_{13} = 52.8$ | | $Z_{4,5} = Z_{9,10} = 39.6$ | |
| $Z_{1,2} = Z_{12,13} = 38.8$ | | $Z_5 = Z_9 = 52.1$ | |
| $Z_2 = Z_{12} = 53.7$ | | $Z_{5,6} = Z_{8,9} = 39.8$ | |
| $Z_{2,3} = Z_{11,12} = 36.7$ | | $Z_6 = Z_8 = 52.0$ | |
| $Z_3 = Z_{11} = 53.7$ | | $Z_{6,7} = Z_{7,8} = 39.8$ | |
| $Z_{3,4} = Z_{10,11} = 38.9$ | | $Z_7 = 52.0$ | |

These element values were computed as described in Sec. C-4 of Chapter 18, using a low-pass prototype with $n = 10$. The final design was augmented to become an $n = 13$ design by inserting in the middle of the filter three additional sections identical to Section $S_{5,6}$. For a definition of "section" as used herein see Sec. B of Chapt. 18.

C. JUNCTION EFFECT AND CHOICE OF PHYSICAL CONSTRUCTION

As was previously mentioned, one consideration in the choice of construction was that it should be possible to scale the filter design for use at X-band. Other considerations were that the filter should have very low loss (hence, dielectric support material was to be avoided), and that the construction should be chosen to minimize the junction effect at the stubs so that the actual performances would agree with the theoretical

Using strip-transmission-line or coaxial-line construction, the junction effects can be reduced by keeping the ground plane spacing or the outer shield, respectively, of relatively small size. However, in order to be able to scale the design to X-band, these dimensions cannot be reduced very much. Having established reasonable dimensions for the outer shield, the question remains as to whether strip-transmission-line or coaxial-line construction will have the least junction effect.

Previous work on this contract shows that the equivalent circuit for a strip-transmission-line T-junction is as shown at (b) in Fig. 19-2, where the terminal planes are defined at (a). Using strip transmission lines with center conductors much wider than they were thick, one of the most significant properties manifested in the equivalent circuit was that the transformer turns ratio \sqrt{A} decreased considerably at the higher frequencies. This effect is believed to result from the dimensions of the junction being a significant portion of a wavelength, hence operating like a transmission-line transformer. In the case of coaxial line of comparable size, this transformer ratio \sqrt{A} is found to be less frequency sensitive, which is to be expected since use of round center conductors reduces the maximum dimensions at the junction. However, Ref. 1 shows that the magnitude of the junction susceptance B_d is much larger than in the case of corresponding strip-line T-junctions. This is believed to be due to the fact that when forming a T-junction from coaxial line, part of the side wall of the outer conductors must be removed in order to form the junction. This reduces the

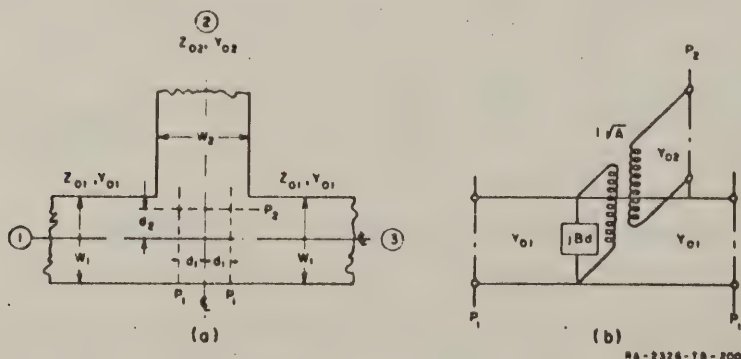


FIG. 19-2

EQUIVALENT CIRCUIT OF A STRIP-LINE T-JUNCTION

net capacitance per unit length of the lines in the vicinity of the junction, hence calls for a *negative* susceptance in the equivalent circuit in order to account for the reduction in capacitance in the vicinity of the junction.*

From these observations it was decided to use strip-transmission-line construction with *rectangular bar* center conductors. Making the center conductors rectangular reduces the junction dimensions (for given ground plane spacing and line impedances) as compared with a junction of strip lines with thin wide center conductors. Thus, the bar center conductors should result in less frequency sensitivity in \sqrt{A} . Also, using any strip-transmission-line configuration the outer conductor (i.e., the ground planes) are not disturbed in the region of the junction so that the junction susceptance should not be excessive.

The construction details of the filter design and the important dimensions are shown in Figs. 19-3 to 19-5, and a photograph of the interior of the completed filter is shown in Fig. 19-6. The center conductors and shorting blocks were made of brass while the ground planes are aluminum.

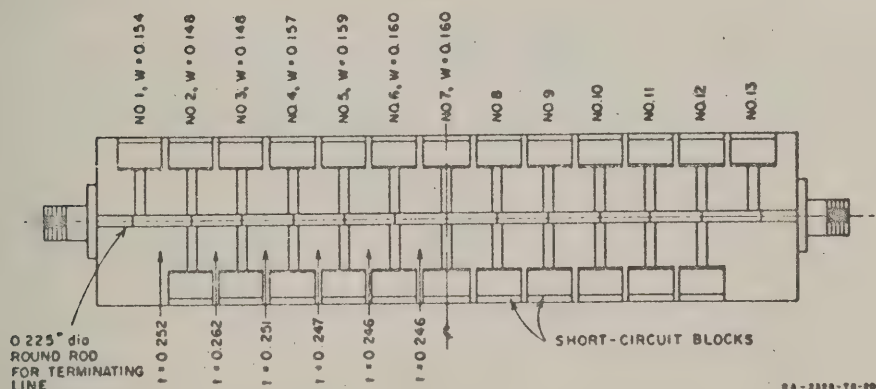
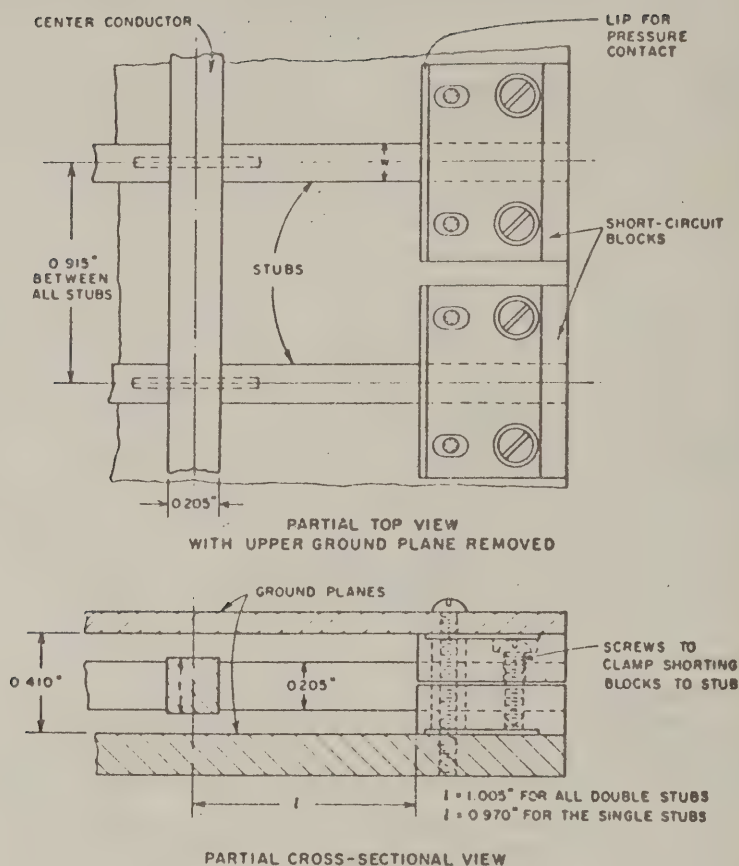


FIG. 19-3

LAYOUT OF STRIP TRANSMISSION LINE BAND-PASS FILTER WITH
UPPER GROUND PLANE REMOVED

* Reference 1 shows a positive sign for the junction susceptance of a coaxial line T-junction. It is believed that this sign is an error and should have been negative which is, of course, necessary in order to represent negative (i.e., subtracted) capacitance.



42-2510-10-000

FIG. 19-4
SOME CONSTRUCTION DETAILS OF THE BAND-PASS FILTER

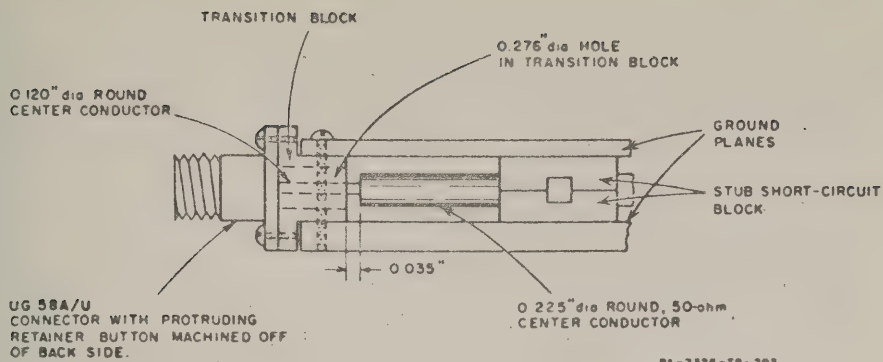


FIG. 19-5
DETAILS OF TRANSITION FROM FILTER TO TYPE-N CONNECTOR

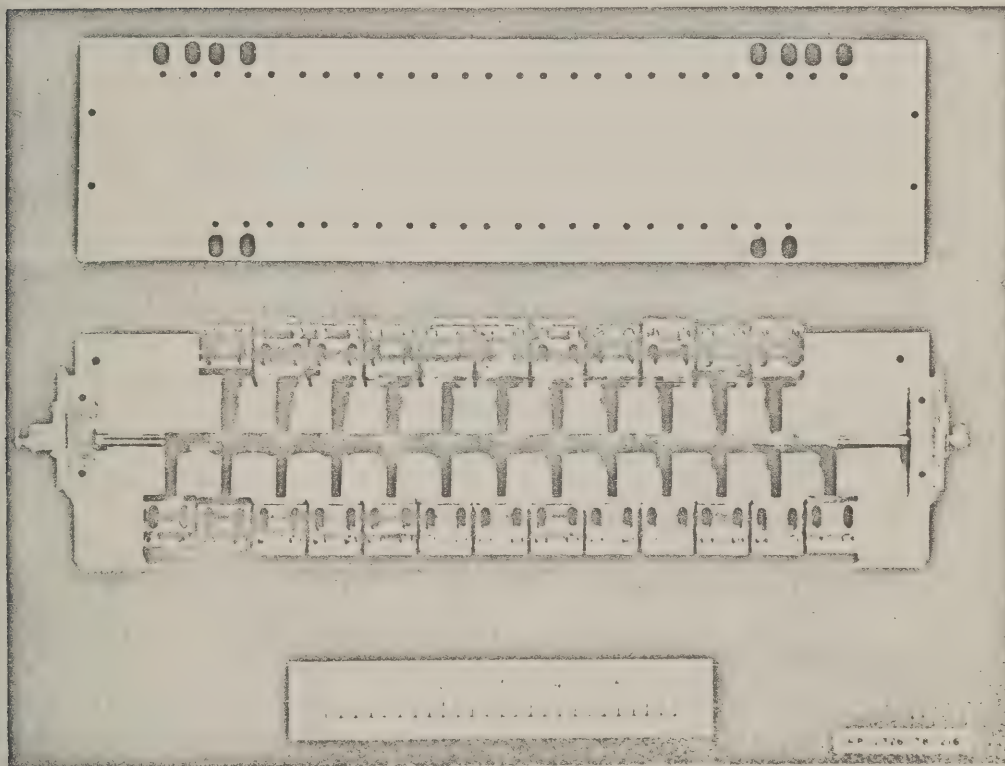


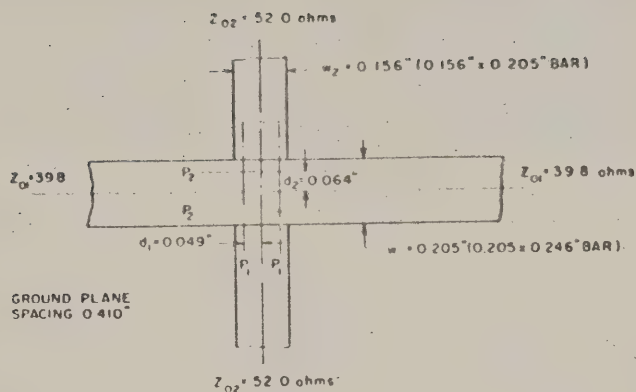
FIG. 19-6
PHOTOGRAPH OF WIDE-BAND BAND-PASS FILTER

Working back from the measured results discussed in Sec. D below an equivalent circuit for a typical plus junction of this filter was deduced and is shown in Fig. 19-7. Although the numerical values in this equivalent circuit are probably of only moderate accuracy, they should give a good picture of the nature of the junction effect in such plus junctions. As was hoped, the frequency sensitivity of the transformers in the equivalent circuit appeared to be slight. They probably had some effect, however, as is evidenced by the fact that the filter band-edge ratio is slightly larger than specified. (Previous data on T-junctions show that \sqrt{A} tends to decrease at higher frequencies, an effect which would tend to widen the pass band of a filter of this type.) No attempt was made to obtain numerical values for the parameters associated with the T-junctions for the single stubs at the ends of the filter. However, it should be noted that in the case of the T-junctions at the ends of the filter, either the junction susceptance is less or the position of the reference plane P_2 is different since the end single stubs were required to be 0.035 inch shorter than the double stubs in the rest of the filter (see dimensions for l in Fig. 19-4).

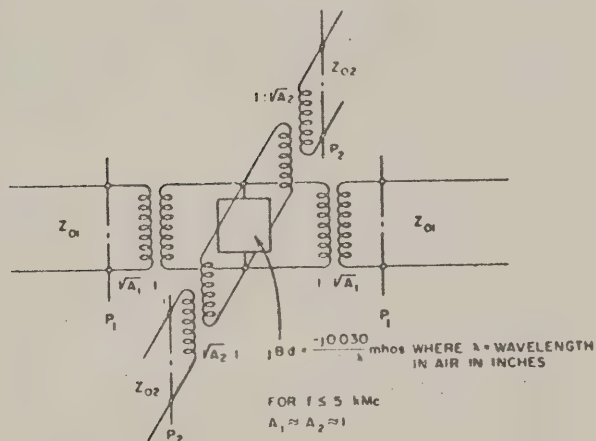
Once we have an equivalent circuit of the sort in Fig. 19-7 for the plus junctions, we compensate for the junction effect as follows. The effective electrical distance along the main conductor between sets of stubs is measured from the reference planes P_1 . Similarly, the lengths of the short-circuited stubs are measured from the reference planes P_2 , but the lengths of the stubs must be computed so as to bring about shunt resonance at the frequency f_0 with the susceptance jB_d shunted across their terminals. If \sqrt{A} deviates appreciably from one, this must, of course, also be accounted for in the design. However, in most cases it will be desirable to choose the filter construction so \sqrt{A} will be very nearly unity, since if it deviates much from unity it becomes frequency sensitive.

D EXPERIMENTAL RESULTS

The design center frequency for this filter was $f_0 = 3.225$ kMc which corresponds to 0.915 inch for one-quarter wavelength in air. Since no electrical data were available with regard to the type of junctions in this filter, the various stubs were spaced apart by 0.915 inch (measured between their centerlines) and all of the stubs were set to be 0.915 inch long (measured from the centerline of the center conductor to the short-circuit blocks). The resulting response had a bandwidth ratio of



(a)



(b)

44-7326-19-204

FIG. 19-7

ESTIMATED EQUIVALENT CIRCUIT FOR TYPICAL PLUS-JUNCTION
IN THE FILTER OF FIGS. 19-3 TO 19-6

$f_2/f_1 = 2.20$, which is reasonably close to the desired value of 2.175, the pass-band VSWR was reasonably good (there were VSWR ripples with very low minima and with maxima ranging from 1.5 to 2.05), but the center frequency was considerably higher than desired (i.e., it was $f_0 = 3.860$ instead of 3.225 kMc). The short-circuit blocks on the stubs were then readjusted to lengthen the stubs with the objective in mind of obtaining the optimum pass-band response regardless of what value f_0 might come out to have.*

After several trial adjustments of the stub lengths, the response in Fig. 19-8 was obtained using the stub lengths indicated in Fig. 19-4. This response has a band-edge ratio f_2/f_1 of 2.214 which exceeds the desired value by 0.039. The pass-band reflection-loss ripples have peaks that, for the most part, lie between 0.10 and 0.16 db, which is satisfactorily close to the 0.10-db objective. The minimum insertion loss is about 0.2 db (near the center of the pass band) while the insertion loss runs about 0.5 db near the edge of the pass-band. This higher insertion loss near the band edges is to be expected since dissipation loss always increases markedly near cut-off †. The lower stop band is seen to reach a level of 35 db at a frequency which is 92 percent of the cut-off frequency. The center frequency is $f_0 = 3.60$, which will have to be corrected in the final design of the filter for the previously mentioned diplexer.‡

Rough measurements were made on this filter up to 11 kMc. It was found to have a second pass band starting at about 9.1 kMc. If there were no junction effects, this second pass band would have been expected to occur at 9.44 kMc. Also, some narrow, spurious responses were noted at about 7 kMc where, according to idealized theory, the attenuation should be about the highest. Reasons for these spurious responses can, however, be readily deduced as follows, if the effects of imperfect tuning are considered.

* By adjusting the stub lengths for optimum pass band response the proper ratio between the lengths of the connecting lines and the lengths of the stubs was found. Then to change the center frequency the lengths of both the connecting lines and the stubs must be changed proportionally.

† The center conductors of this filter are brass. If these parts are silver plated, the dissipation loss of this filter should be reduced significantly since brass has about twice the skin resistance of silver.

‡ Besides a change in f_0 , the final design for the diplexer will include other modifications needed for connecting this filter in series with a low-pass filter (see Chapter 20).

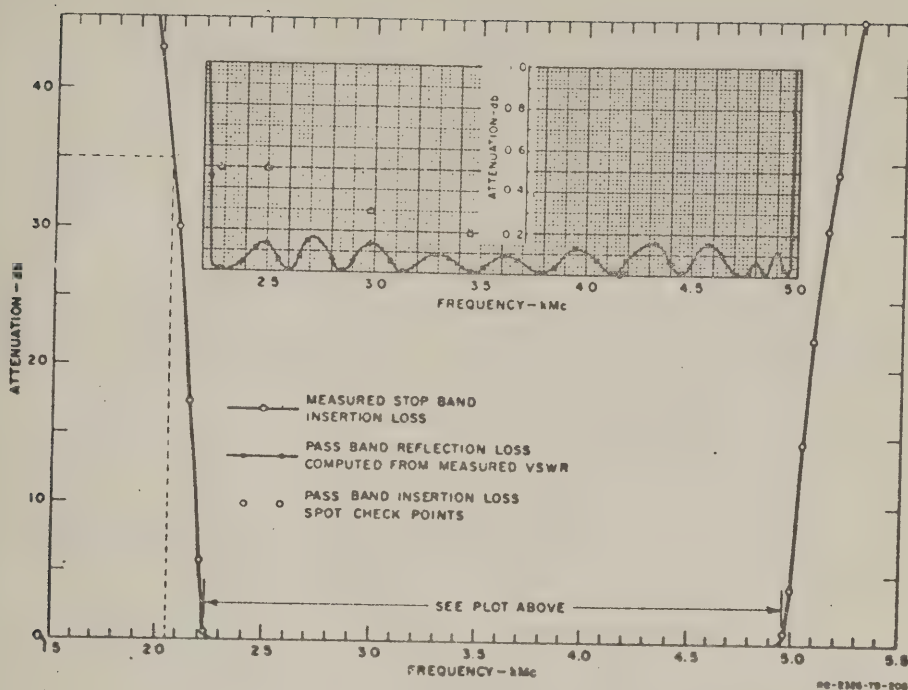


FIG. 19-8

MEASURED RESPONSE OF THE FILTER SHOWN IN FIG. 19-6

For the frequency $f = 2f_0$ the stubs and connecting lines are ideally exactly $\lambda_0/2$ long. For frequencies in that vicinity the circuit can then be represented by a transmission line periodically shunted by series-resonant circuits as indicated in Fig. 19-9. Since the connecting lines are all $\lambda_0/2$ long, they can, as a narrow-band approximation, be removed and all of the shunt circuits connected together in parallel. It is readily seen that if all of these shunt circuits resonate at the same frequency they can be replaced by a single shunt branch and no spurious responses are possible. However, if the shunt branches do not all resonate at the same frequency the network becomes a Foster-form reactance network. The net shunt susceptance will then oscillate between zero and infinity over the frequency range of the various resonances, and

spurious responses will result. It also appears that such effects could also come about in other ways. For example, if all of the shunt circuits resonated at the same frequency but the connecting lines varied in length with respect to each other, the varying influence of the connecting lines might tend to create an effect similar to that of the reactance function network described above. In addition it is seen that if two stubs are of different length from that of their connecting line, the connecting line could operate like a $\lambda/2$ resonator with shunt-coupling susceptance at its ends. This latter effect does not happen in a perfectly tuned circuit because the susceptance of the shunt stubs varies rapidly at the proper frequencies.

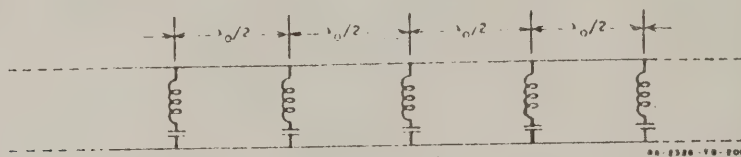


FIG. 19-9

EQUIVALENT CIRCUIT OF THE FILTERS IN FIG. 19-1 AT FREQUENCIES IN THE VICINITY OF $2f = 2f_0$ WHERE f_0 IS THE PASS-BAND CENTER

It should be noted that since parallel-coupled filters have stub filter equivalents, such spurious responses are to be expected also in parallel-coupled filters that are not perfectly tuned. Since perfect tuning throughout a filter is difficult to achieve, if stub or parallel-coupled filters are to be used for applications where narrow spurious responses in the vicinity of $2f_0$ would be objectionable, additional means should be provided to suppress such responses.

* This picture of the manner of operation is, of course, very approximate since it neglects the frequency-sensitive effects of the connecting lines as f deviates from f_0 .

REFERENCES

1. "Final Report on Development of Broadband Waveguide Components," Chapter 8, Sperry Report No. 5224-1336, Contract 36-039-SC-166, Sperry (March 1954).

MATHEMATICAL ANALYSIS OF DIPLEXER DESIGN

A. GENERAL

As has been mentioned in Chapter 19, the Signal Corps requested two diplexers, one of which was to send signals in the 1- to 2-kMc band out one channel and signals in the 2- to 4-kMc band out another channel.* The insertion loss was to be 0.5 db or less to as close to the 2-kMc crossover frequency as possible, and the cut-offs in the crossover region were to be very rapid. In this chapter the design method used for this diplexer will be described, and the results of a mathematical analysis of a simplified version of the diplexer design will be presented.

B. A VIEWPOINT FOR DIPLEXER DESIGN

A common approach for diplexer design in the past has been to use the image impedance design viewpoint and "fractional terminations."¹ At present, however, there are insertion loss design methods available which, in many cases, give precision filter designs much more easily than if image design methods were used. Consequently, it is desirable to investigate suitable means for diplexing filters which were designed individually on the insertion loss basis. The diplexer design method described herein is in many respects equivalent to the image theory fractional termination method, however, it makes no use of the image impedance point of view.

At (a) in Fig. 20-1 is shown a low-pass filter and a high-pass filter with dotted lines indicating wires for connecting these filters in series. If each of these filters were designed to operate normally with pure resistance terminations at both ends, their normal performance would be greatly disrupted by this connection. This disruption would be due to the fact that although each filter exhibits a nominally resistive input impedance in its individual pass band, each filter also exhibits large reactive impedances in its stop band. Thus if the filters shown at (a) in Fig. 20-1 have contiguous pass bands, the band-pass filter will

* A similar design was also desired for X-band.

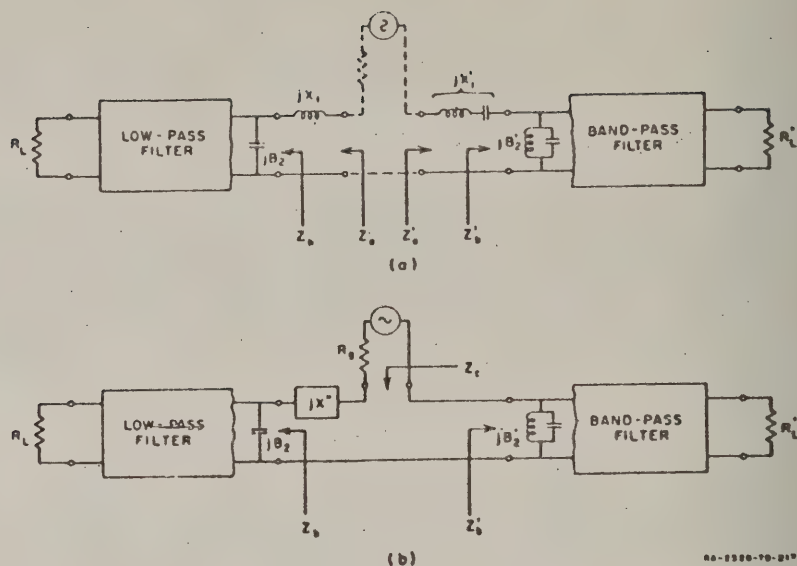


FIG. 20-1
FILTERS CONNECTED IN SERIES

introduce a large reactive component in the terminating impedance seen by the low-pass filter in the pass band of the low-pass filter, while the low-pass filter will introduce a large reactive component to the terminating impedance seen by the band-pass filter in the pass band of the band-pass filter.

The large stop-band reactive components of the input impedances Z_o and Z'_o of the filters at (a) in Fig. 20-1 are due largely to the series reactances X_1 and X'_1 shown. If these are removed, the remaining input impedances Z_o and Z'_o have the same real part characteristics but much smaller stop-band reactances. Thus, to form a diplexer, X_1 and X'_1 are removed and the remaining circuits are connected as shown at (b) in Fig. 20-1. Next an additional reactance jX'' is introduced to further adjust the imaginary part of Z_o in order to cause

$$Z_o = Z_o + Z'_o + jX'' \quad (20-1)$$

to approximate a pure resistance equal to R_0 as nearly as possible.* As can be deduced from the mathematical example about to be presented, in the pass band of the low-pass filter $Z'_0 + jX''_1$ represents under the conditions described above, a reactance about equivalent to X_1 in that band, so that the low-pass filter will operate very nearly in its normal fashion throughout its pass band. Likewise, in the pass band of the band-pass filter, $Z'_0 + jX'_1$ represents a reactance about equivalent to X'_1 in that band, so the band-pass filter will operate very nearly in its normal fashion throughout its pass band. However, the removal of the series branches X_1 and X'_1 may result in some reduction in stop band attenuation of one or both filters.†

The principles described above will be illustrated shortly in a numerical example. This same viewpoint may also be used for the design of parallel-connected diplexers by simply using the above viewpoint on the dual basis.

C. FILTER CIRCUITS FOR THE REQUIRED DIPLEXERS

It was decided to use in the diplexers for the Signal Corps a low-pass filter designed from a Tchebyscheff prototype with 0.10 db pass-band ripple and $n = 15$ reactive elements. Tabulated element values are not available for Tchebyscheff filters with this many elements, so that it was decided to use a corresponding design with $n = 9$ elements² and then repeat the two middle elements of the design a number of times in order to increase the number of elements to fifteen.⁵ This gives a design differing slightly from a true $n = 15$ Tchebyscheff design, but the difference will be small. Figure 20-2 shows the circuit for this filter and Table 20-1 gives element values for the resulting low-pass filter with the impedance level normalized so that $R_0 = R_L = 1$, and with the frequency scale normalized so that the equal ripple band-edge frequency is $\omega_1 = 1$.

It was decided to use band pass filters of the type discussed in Chapter 10 for the higher-frequency channel of the diplexers. However, in order to use the design viewpoint just discussed it will be necessary

* This assumes that the normal terminating impedance next to Z_0 and Z'_0 for the individual filters is R_0 . It also assumes that the frequency responses of the filters are scaled to intersect close to the 3 db points.

† The decrease in stop band attenuation resulting from the removal of X_1 and X'_1 is largely compensated for as a result of the input voltage reduction in the stop band of each filter due to the series loading of the other filter.

‡ The validity of this procedure can be seen more easily from the image design viewpoint. Working from that viewpoint it is common practice to use certain matching end sections with any number of identical interior sections.

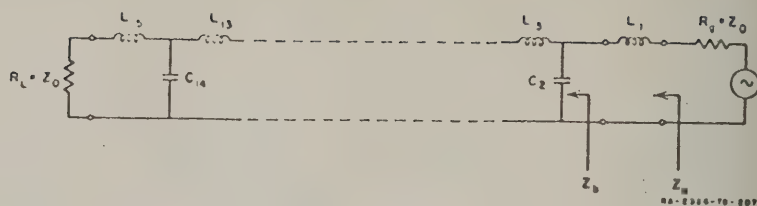


FIG. 20-2

LOW-PASS FILTER CIRCUIT FOR DIPLEXER

TABLE 20-1

NORMALIZING ELEMENT VALUES FOR
LOW-PASS FILTER IN FIG. 20-2*

These element values were obtained from an $n = 9$ reactive element, Tchebyscheff low-pass filter with 0.1 db ripple and with the equal-ripple band edge at $\omega_1 = 1$. The $n = 9$ filter was augmented to become an $n = 15$ reactive element design as described in the text.

| | |
|-------------------------|-------------------------|
| $R_s = R_L = Z_0 = 1$ | $L_5 = L_{11} = 2.2053$ |
| $L_1 = L_{15} = 1.1956$ | $C_6 = C_{10} = 1.6167$ |
| $C_2 = C_{14} = 1.4425$ | $L_7 = L_9 = 2.2053$ |
| $L_3 = L_{13} = 2.1345$ | $C_8 = 1.6167$ |
| $C_4 = C_{12} = 1.6167$ | |

for the filter to start out with a series stub instead of the shunt stub shown in Fig. 19-1.* The configuration shown in Fig. 20-3 is then a suitable one for this application. Using the design equations in Table 18-3, with $\alpha = \infty$ (which implies $Z'_1 = Z'_n = \infty$ in Fig. 18-3 of this report), $d = 1$, $\omega_1/\omega_0 = 0.630$ (which calls for $f_2/f_1 = 2.175$), along with an $n = 10$ reactive-element low-pass prototype with 0.10 db Tchebyscheff ripple, the transmission line impedances shown in Table 20-2 were obtained. As was done in the case of Table 19-1, the $n = 10$ design was augmented by additional sections in order to raise the value of n . In this case four additional sections were added to make $n = 14$ (since in the final design one stub will be removed).

* Although this series stub is to be removed in the diplexer filter (corresponding to removing X_1 in Fig. 20-1), it is necessary that the filter be designed as though this stub were to be present in order for the impedance relationships to come out properly.

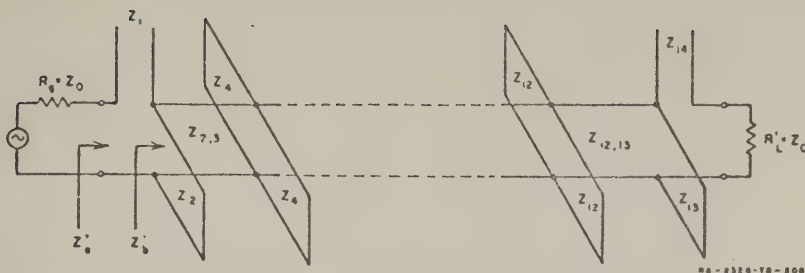


FIG. 20-3

BAND-PASS FILTER WITH SERIES STUBS AT THE ENDS

TABLE 20-2
LINE IMPEDANCES FOR THE BAND-PASS
FILTER IN FIG. 20-3

This $n = 14$ stub design was obtained by augmenting an $n = 10$ stub design as described in the text.

| | |
|------------------------------|-----------------------------------|
| $Z_0 = R_g = R'_L = 50$ ohms | $Z_{4,5} = Z_{10,11} = 39.6$ ohms |
| $Z_1 = Z_{14} = 91.3$ | $Z_7 = Z_{10} = 52.1$ |
| $Z_2 = Z_{13} = 34.9$ | $Z_{5,6} = Z_{9,10} = 39.8$ |
| $Z_{2,3} = Z_{12,13} = 47.3$ | $Z_6 = Z_9 = 52.0$ |
| $Z_3 = Z_{12} = 50.0$ | $Z_{6,7} = Z_{8,9} = 39.8$ |
| $Z_{3,4} = Z_{11,12} = 38.9$ | $Z_7 = Z_8 = 52.0$ |
| $Z_4 = Z_{11} = 52.4$ | $Z_{7,8} = 39.8$ |

As was discussed in Chapter 19 of this report, it is desirable to avoid series stubs in the final design of the band-pass filter for the diplexers since it is desired to be able to scale the S-band design to obtain an V-band design (a series stub would usually be built into the interior of the main center conductor). The series stub Z_1 in Fig. 20-3 provides a series reactance corresponding to X'_1 in Fig. 20-1; hence, this stub will be removed in the diplexing connection. If the line impedances in Tables 19-1 and 20-2 are compared, it will be found that for the lines in the interior of the filter, the impedances are identical except for the fact that for the case of Table 20-2 there is one additional section. However, at the ends of the filters the line impedances Z_1 to Z_3 are different, and, of course, Table 20-2 omits the connecting lines $Z_{1,2} = Z_{13,14}$ completely. The final design will be a composite of these

two designs. At the diplexer junction end of the filter the elements Z_2 , $Z_{2,3}$, and Z_3 from Table 20-2 will be used, while at the end of the filter away from the junction the end elements Z_1 , $Z_{1,2}$, Z_2 , $Z_{2,3}$, and Z_3 from Table 19-1 will be used. Thus the end of the filter next to the diplexer junction will be designed as though it were to incorporate a series stub, but that stub will be eliminated in the diplexer connection. Meanwhile, at the end of the filter away from the junction, the filter will be designed to use only shunt stubs. The remaining elements $Z_{3,4}$ to $Z_{11,12}$ of the filter will then be as indicated in Table 20-2. In this manner no series stubs will be required in the final design.

D. SIMPLIFIED FILTERS FOR USE IN MATHEMATICAL ANALYSIS OF DIPLEXER

In order to check the design approach outlined in Part B, it was decided to make a mathematical analysis of a simplified version of the diplexer. This version of the diplexer differs from the planned diplexer mainly in that fewer elements are used in the interior sections of the filters. The simplifications were introduced, of course, to reduce the amount of computation required.

The simplified version of the low pass filter is the same as the filter in Fig. 20-2 and Table 20-1, except that elements L_7 , C_8 , L_9 , and half of C_6 and C_{10} are removed. This leaves a design with $n = 11$ reactive elements. The response of this simplified filter was computed with a digital computer and is plotted in Fig. 20-4 with the frequency scale adjusted to put the 3 db point at 2 kMc. The 0.2 db ripple near cut off is apparently the result of adding additional elements to the original $n = 9$, 0.10 db ripple Chebyscheff design. Figure 20-5 shows the corresponding input impedance Z (see Fig. 20-2) normalized with respect to the terminating impedance Z_0 . As is expected, the imaginary part is relatively small in the pass band, but becomes large in the stop band.

A computer program suitable for computing the response of a symmetrical filter in the form of Fig. 20-3 with $n = 8$ stubs had been prepared previously. In order to utilize this program the simplified band-pass filter was taken as an $n = 8$ version of the $n = 14$ filter in Table 20-2. To accomplish this, stubs Z_5 to Z_{10} and their connecting lines, along with half of connecting lines $Z_{4,5}$ and $Z_{10,11}$ were removed. The computed response of this simplified filter is shown in Fig. 20-6 with its frequency

scale adjusted so that its lower 3 db point falls at 2 kMc. Figure 20-7 shows the computed input impedance Z'_0 (see Fig. 20-3) normalized to the termination impedance Z_0 .

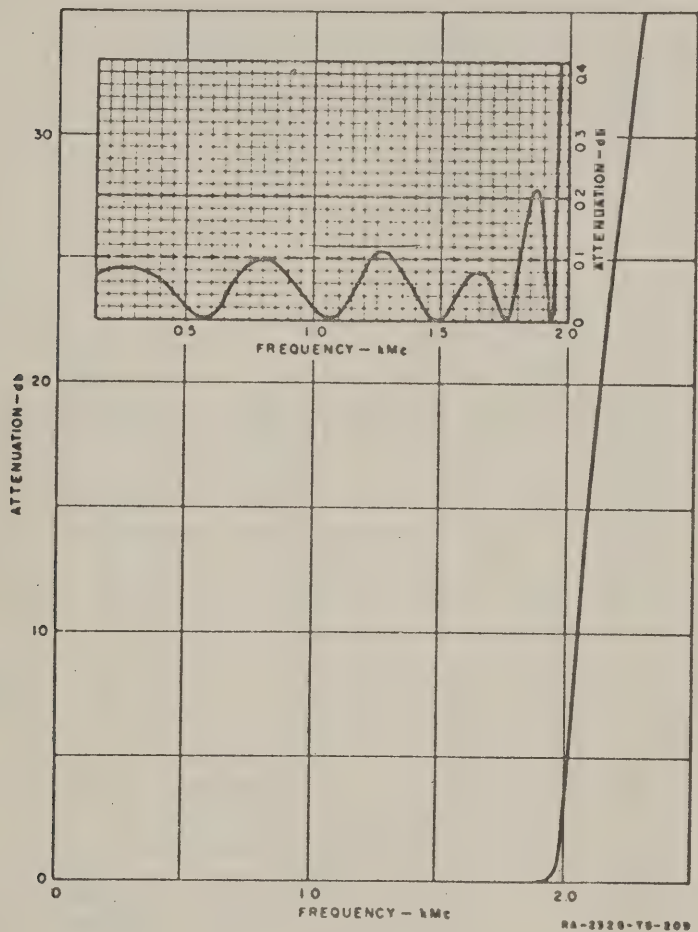


FIG. 20-4
 RESPONSE OF THE SIMPLIFIED VERSION OF THE FILTER IN FIG. 20-2
 AND TABLE 20-1

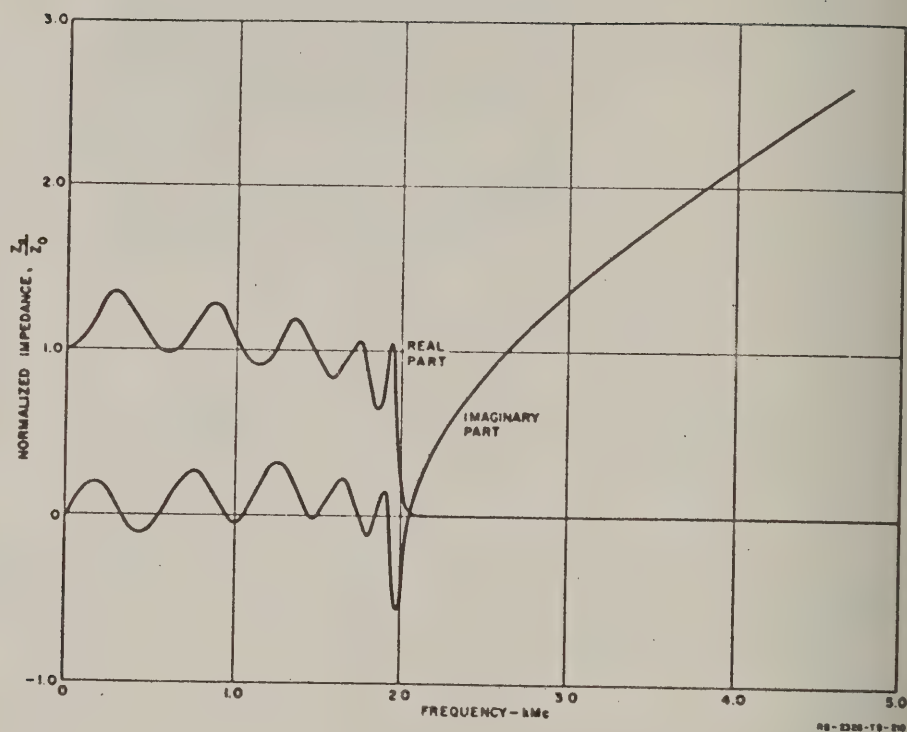


FIG. 20-5
 NORMALIZED INPUT IMPEDANCE Z_L/Z_0 OF THE SIMPLIFIED VERSION
 OF THE FILTER IN FIG. 20-2

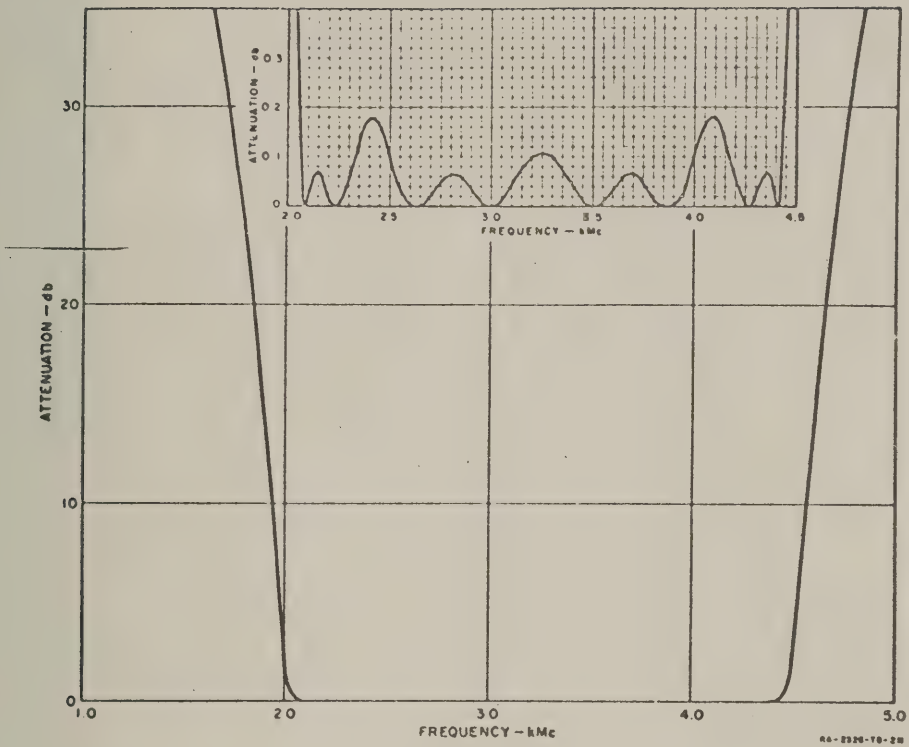


FIG. 20-6

RESPONSE OF THE SIMPLIFIED VERSION OF THE FILTER
IN FIG. 20-3 AND TABLE 20-2

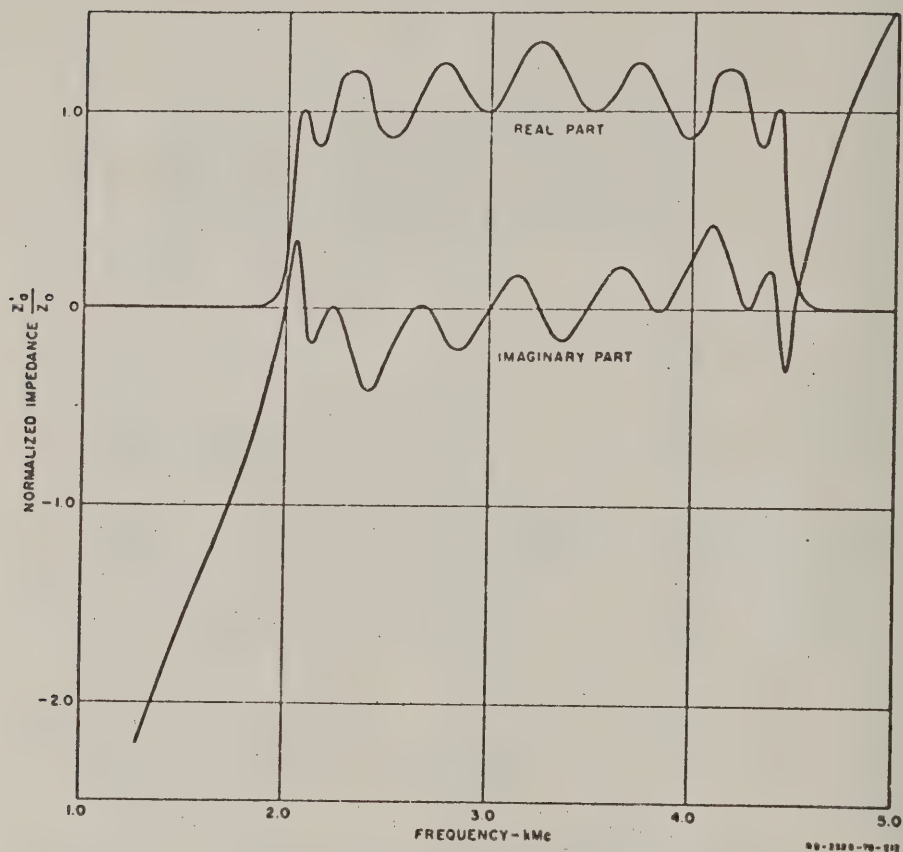


FIG. 20-7
 NORMALIZED INPUT IMPEDANCE Z'_0/Z_0 OF THE SIMPLIFIED VERSION
 OF THE FILTER IN FIG. 20-3

E. COMPUTED RESPONSE OF SIMPLIFIED DIPLEXER

In the proposed diplexer design L_1 is removed from the filter in Fig 20-2 and the series stub Z_1 is removed from the band-pass filter. Then the diplexer connection is as indicated in Fig. 20-8. Figure 20-9 shows normalized plots of $Re Z_b$ for the simplified low-pass filter and $Re Z_b$ for the simplified band-pass filter (see Fig. 20-8). The only place that the two curves overlap significantly is in the cross-over region where the sum of the two is indicated by a dotted line. Figure 20-10 shows plots of normalized values of $Im Z_b$ and $Im Z'_b$ and their sum. Note that these two reactive parts cancel each other out to some extent in the series connection, but the addition of another series reactance can improve the cancellation considerably. A type of reactance network which can give the desired effect is the series, antiresonant circuit indicated by jX'' in Fig. 20-8. The resonant frequency of this circuit would, of course, occur above the pass band of the band-pass filter. In the filter structure under consideration it is anticipated that this anti-resonant circuit will be realized by a short-circuited, radial line, hence, Fig. 20-11 shows the normalized reactance of a proposed radial line structure, and its effect when added to $(Im Z_b/Z_0 + Im Z'_b/Z_0)$. The reactance cancellation appears to be about optimum.

The main point of this diplexer analysis is to determine the optimum design of the diplexer junction so that the individual filters will not interfere with each other. A suitable index of how successful the design procedure has been is to compute the reflection loss for transmission into the terminals Z_c in Fig. 20-8. This loss also represents the ratio of the available power of the generator to the sum of the output powers out from both filters (assuming that the filters have no dissipation loss). This reflection loss was computed and is plotted in Fig. 20-12. It is noted that the loss is under 0.10 db over most of the band, but reaches a peak of 0.67 db at the cross-over frequency. If desired, the 0.67-db peak value could doubtless be brought down by moving the band edges of the filter together slightly.

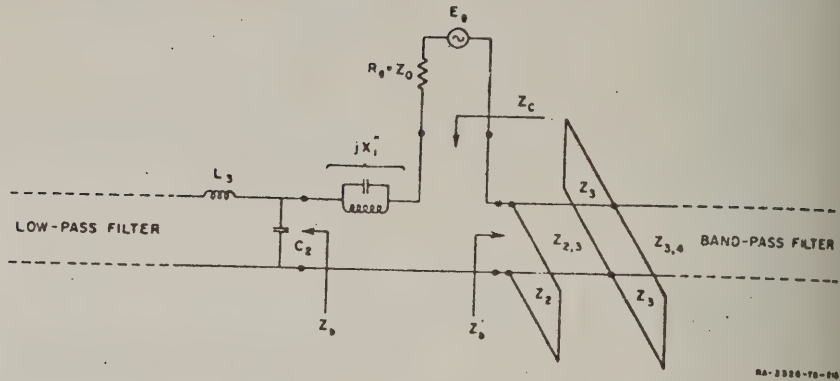


FIG. 20-8

MODIFICATION AND CONNECTION OF THE FILTERS IN FIGS. 20-2 AND 20-3 TO FORM A SERIES-CONNECTED DIPLEXER

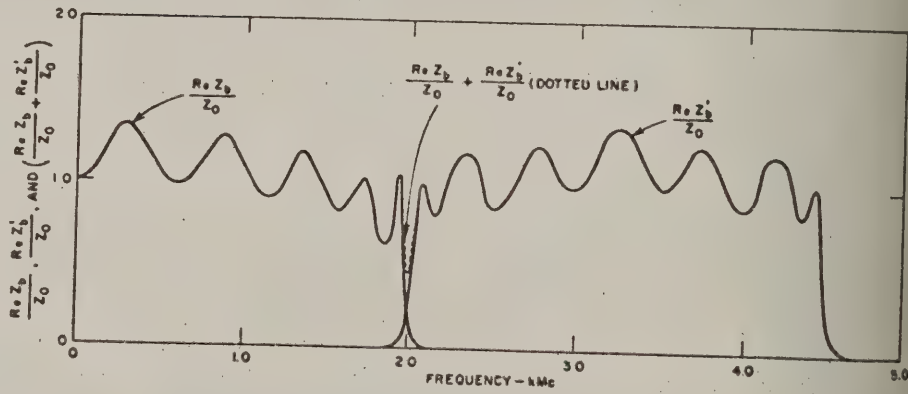


FIG. 20-9

THE NORMALIZED REAL PARTS OF THE IMPEDANCES Z_b AND Z'_b (AND THEIR SUM) FOR THE SIMPLIFIED VERSIONS OF THE FILTERS IN FIGS. 20-2 AND 20-3

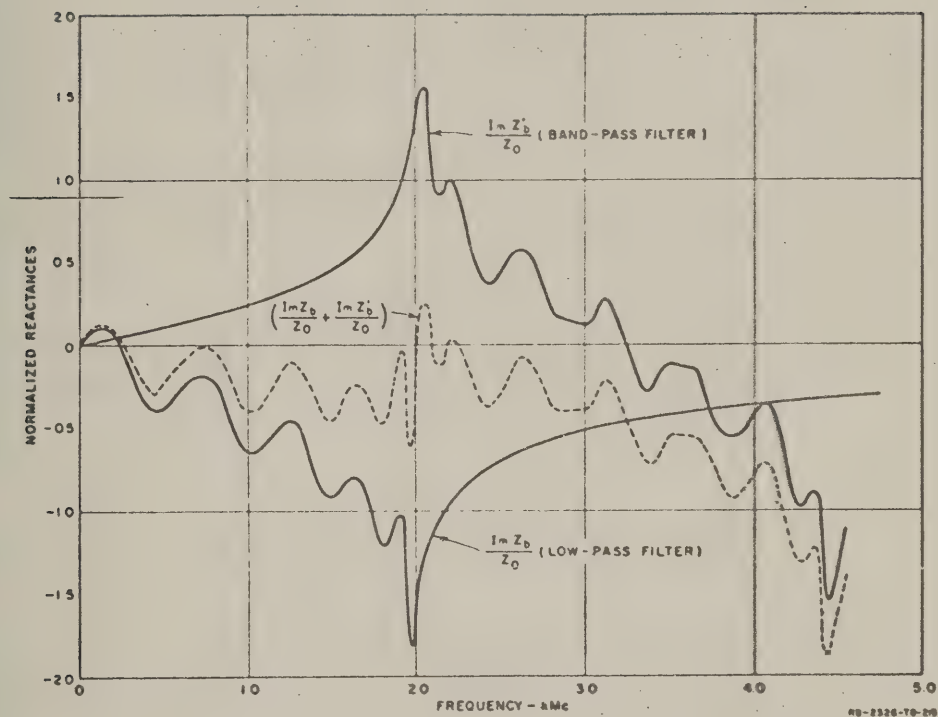


FIG. 20-10

THE NORMALIZED IMAGINARY PARTS OF THE IMPEDANCES Z_b AND Z_b'
(AND THEIR SUM) FOR THE SIMPLIFIED VERSIONS
OF THE FILTERS IN FIGS. 20-2 AND 20-3

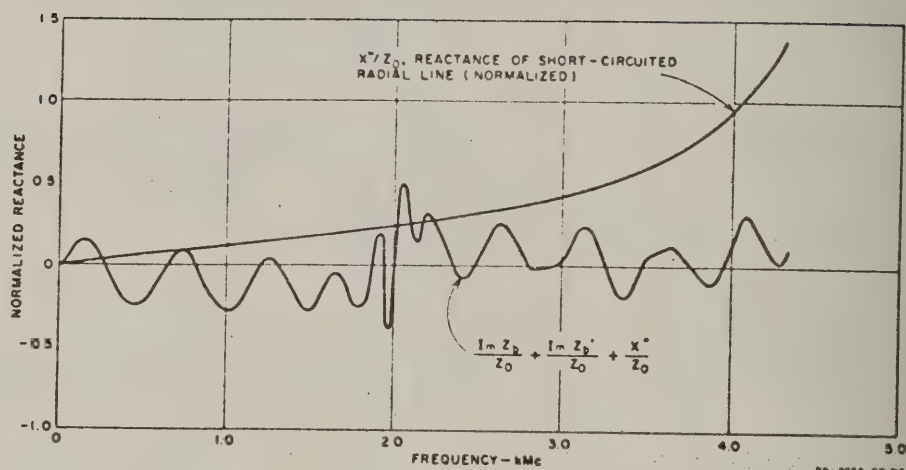


FIG. 20-11

THE NORMALIZED REACTANCE X''/Z_0 AND THE RESULTANT TOTAL NORMALIZED REACTANCE $Im Z_c/Z_0$ (SEE FIG. 20-8)

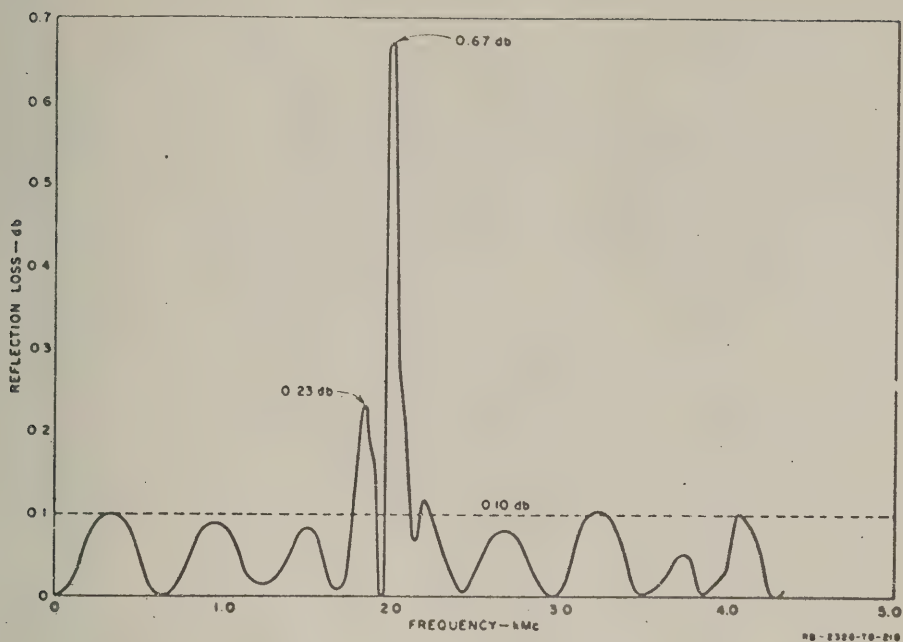
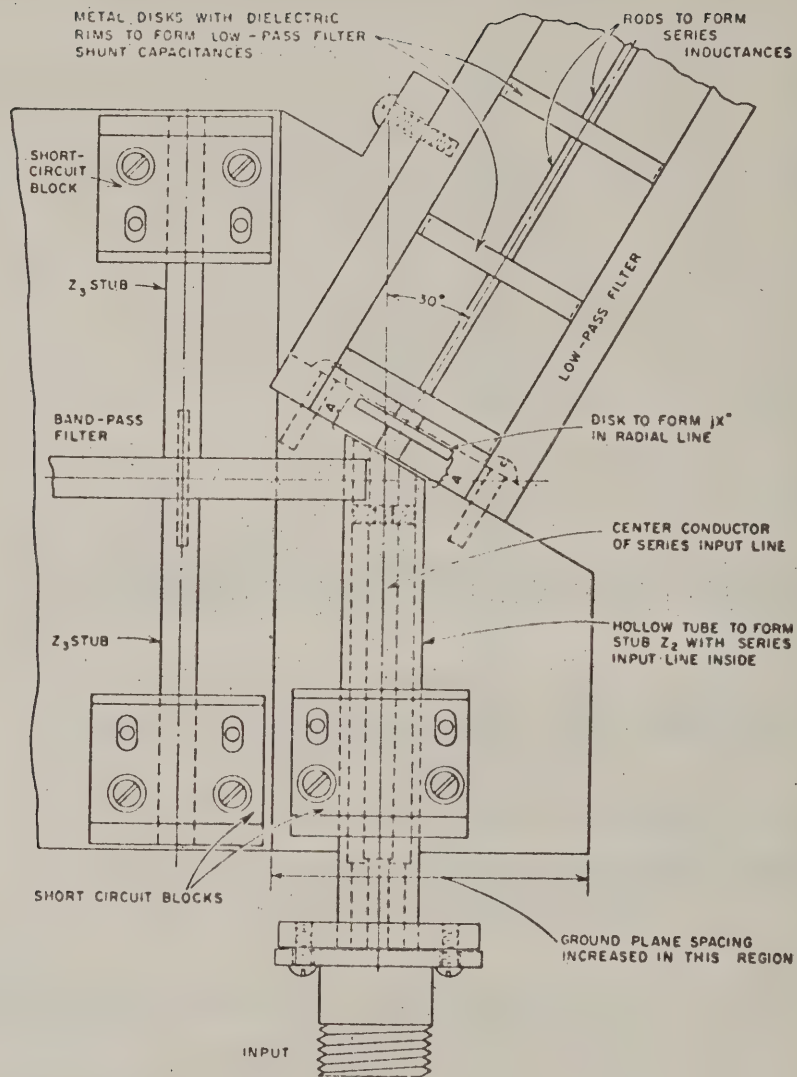


FIG. 20-12

THE POWER REFLECTION LOSS FOR TRANSMISSION INTO THE JUNCTION PORT
OF THE SIMPLIFIED DIPLEXER

F. PHYSICAL CONSTRUCTION OF THE SERIES-CONNECTED DIPLEXER

Probably most diplexers using filters having coaxial or strip transmission line construction utilize parallel connection. However, in this case it was desirable to use the type of filter discussed in Chapter 19 of this report as part of the diplexer, and that particular type of filter is not suitable for parallel connection since its shunt, short-circuited stubs would tend to short-circuit the low-pass filter. This difficulty of the parallel connection is bypassed by the novel series connection shown in Fig. 20-13 which was suggested by S. B. Cohn. In this partial drawing the band-pass filter is to extend to the left and is constructed in a manner similar to that shown in Fig. 20-6. The low-pass filter (extending upward in the figure) is of coaxial construction having metal disks with dielectric rims to realize the shunt capacitors and using connecting wires to realize the series inductances. The series connection



RB-2326-TB-219

FIG. 20-13

A PARTIAL VIEW OF A SERIES-CONNECTED DIPLEXER CONSTRUCTION.

is achieved by running the 50-ohm input line through the inside of stub Z_2 (see Fig. 20-8) with the center conductor being connected to the center conductor of the low-pass filter. It will be seen that the current on one conductor of the input line encounters the input impedance of both filters in series before arriving back in the input line on its other conductor. Thus, this connection is equivalent to that in Fig. 20-8.

The anti-resonant circuit jX'' in Fig. 20-8 is realized as shown in Fig. 20-13 as a short-circuited radial transmission line formed between the input shunt capacitive disk of the low-pass filter and a smaller additional disk shown in the figure. The spacing between the small disk and the adjacent opening of the input line is to be chosen to give nominally 50 ohms impedance from the input line up to the region of radial propagation indicated by the brackets marked A. This circumferential surface then represents the input port reference surface for the diplexer junction.

REFERENCES

1. E. A. Guillemin, *Communication Networks*, Vol. II, pp. 356-371 (John Wiley and Sons, New York City 1935).
 2. See Chapter 13 of this report.
-

CHAPTER 21

DESIGN OF A LOW-PASS FILTER FOR THE 1- TO 4-kMc DIPLEXER

A low-pass filter of fifteen reactive elements was made, based on the equivalent circuit and the normalized element and frequency values presented for the low-pass filter in Chapter 20 of this report.

A matched impedance level of fifty ohms and a 3-db-loss pass-band edge at 2.0 kMc were chosen in order for the prototype filter to be in conformance with the Signal Corps requirements for the low-pass filter section of the lower frequency diplexer. It was decided that the higher frequency diplexer would be directly scaled from the lower frequency one.

Construction of the filter is shown in the photograph, Fig. 21-1. It is seen to be constructed in coaxial line and to consist of dielectric-loaded disks, representing the shunt capacitances of the lumped-element prototype, and short sections of high impedance line, representing the series inductances of the lumped-element prototype.

The basis for treating transmission line sections as lumped elements has been given by Cohn¹ who shows that a very short length of line terminated in an impedance several times smaller than its characteristic impedance acts like a series inductance, L , of value

$$L = \frac{\ell Z_0}{v} \text{ henries} \quad (21-1)$$

where

ℓ is the short length of line

Z_0 is the characteristic impedance of the line

v is the velocity of propagation of energy in the line.

Similarly, a very short length of line terminated in an impedance several times larger than its characteristic impedance acts like a shunt capacitance, C , of value

$$C = \frac{\ell}{Z_0 v} \text{ farads.} \quad (21-2)$$

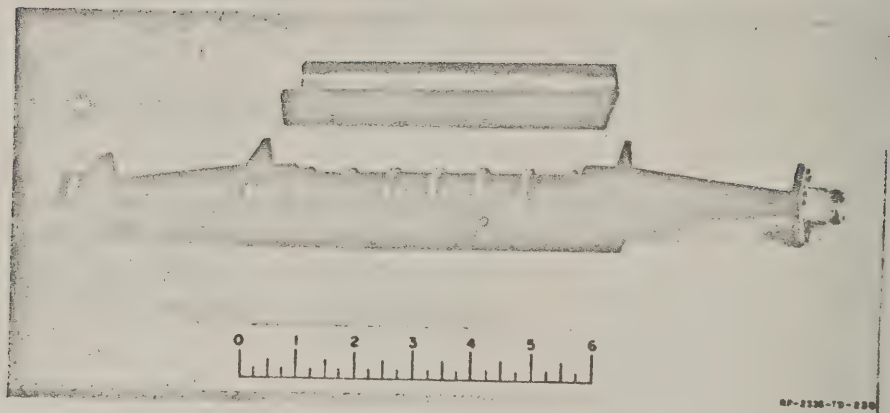


FIG. 21-1
LOW-PASS FILTER

those of the Type N coax in which measurements were to be made, requiring the use of a transition at each end of the filter. The transition used consisted of linear tapers in both inner and outer conductors, such that the 50-ohm impedance level was preserved at each point along the axis. It was about one-quarter wavelength long at the lowest frequency of interest.

The inductive end elements of the filter were given a small extra length, calculated to cancel the junction susceptance caused by the step to 50 ohms in the center conductor.

The final dimensions of the low-pass filter are shown in Fig. 21-2. Observe that the filter uses split-block construction, allowing direct observation of the fit of the center-conductor structure when it is installed. This feature shows clearly in the photograph, Fig. 21-1.

If other filters of this design are made, it is suggested that the Type N connector of Fig. 21-3 be used, because this connector design is superior to the one actually used on the engineering model of the low-pass filter. The connector design of Fig. 21-3 was the one used on the band-pass filter of the lower frequency diplexer.

A graph of the measured response of the low-pass filter is shown in Fig. 21-4. The measured reflection-loss response is quite close to the 0.1-db ripple, design value. The 0.2-db ripple at the edge of the pass band was anticipated in Chapter 20, and as was stated there, is apparently the result of adding additional elements to the nine-element, 0.1-db ripple, Tchebyscheff prototype design.

The first engineering model was found to have its band-edge about 6 percent too high in frequency. The cause of this discrepancy was that the lengths of the inductive elements were too great to have their inductances described accurately by Eq. (21-1). A more suitable representation for longer line lengths, also given by Cohn,¹ is based on a π network equivalent circuit, in which series reactance, X_s , of a length of line is related to line length by

$$X_s = Z_0 \sin \frac{\omega L}{v} \text{ ohms} \quad (21-3)$$

where ω is radian frequency. If X_s is interpreted as ωL , it becomes apparent that the inductance L must be a function of frequency, and thus no

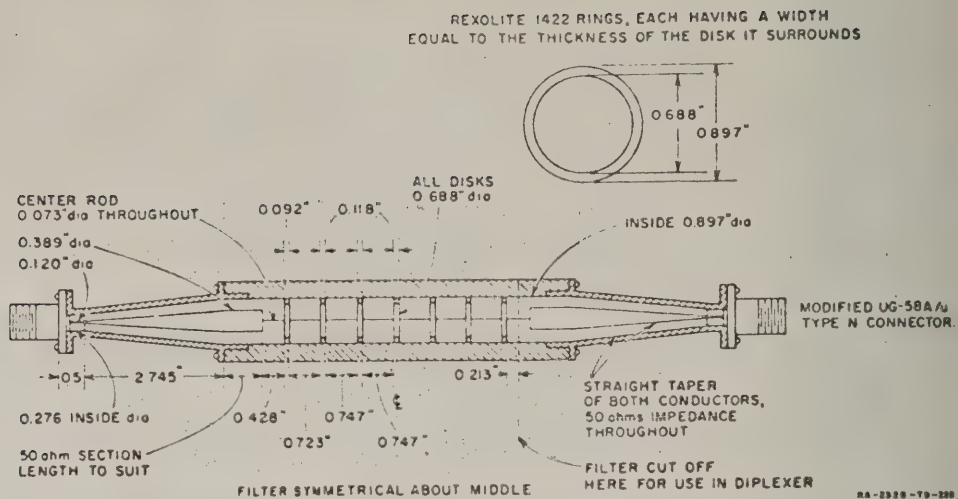


FIG. 21-2

DIMENSIONS OF THE FILTER IN FIG. 21-1
The low-pass filter in the diplexer shown in Fig. 22-6
is this same filter cut off as indicated above

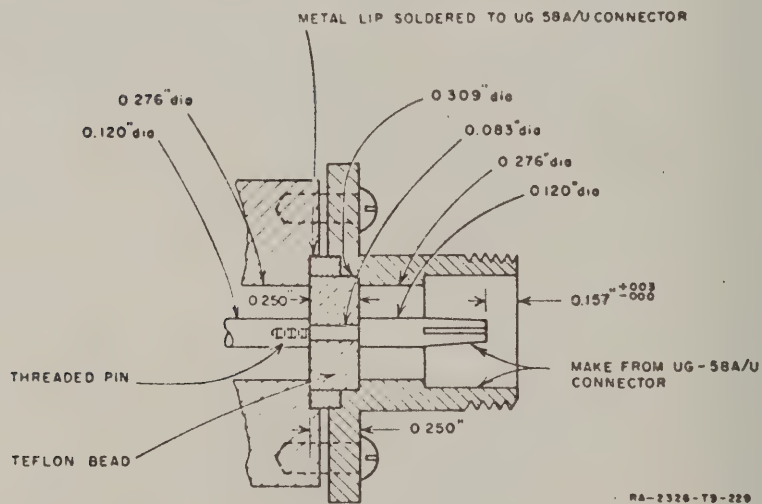


FIG. 21-3

MODIFIED TYPE-N CONNECTOR USED WITH THE FILTER IN FIGS. 21-1 AND 21-2

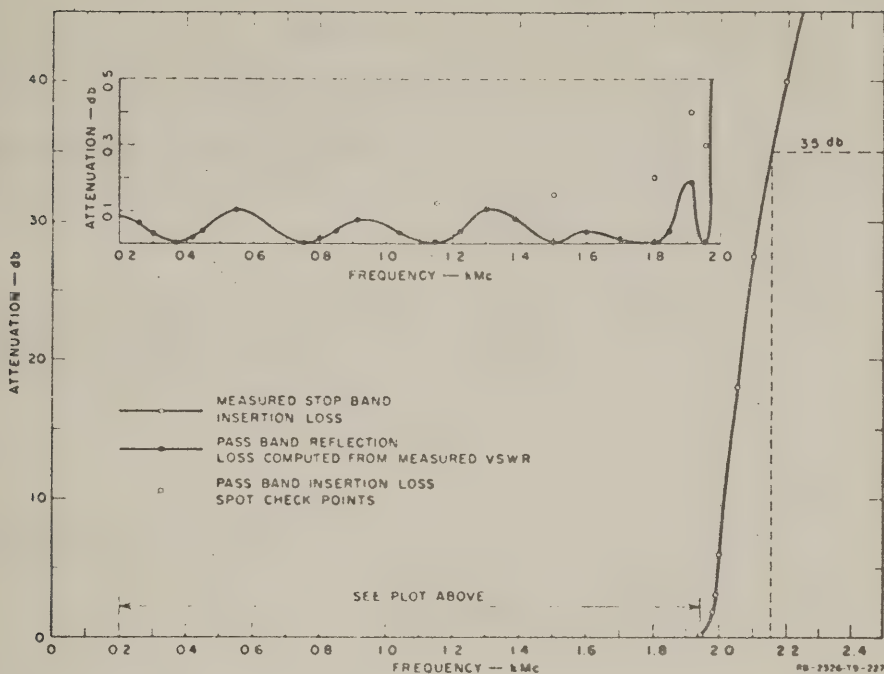


FIG. 21-4

MEASURED RESPONSE OF THE FILTER IN FIG. 21-1

longer equivalent to a lumped element. However, it is practical to let X_L be ωL at the band-edge frequency and then determine the lengths of line that will give the desired performance near the band-edge. Then, if line lengths are still relatively small, that is, less than about $1/6$ wavelength, the variation of inductance with frequency will be small, causing negligible performance deviations in the frequency range of usual interest.

When the lengths of the elements of the engineering model were corrected, the band-edge was properly located, as shown in the measured response curves in Fig. 21-4. The filter as shown in Fig. 21-1 was not tested to determine the extent of the high-attenuation stop band. However, after the filter had been modified to become part of the 1- to 4-kMc range diplexer discussed in Chapt. 22, the extent of its stop band was checked. It was found that there were some narrow spurious responses in the vicinity of 7.70 to 8.48 kMc; however, at frequencies below this region and

frequencies above this region on through X band, the attenuation was very high. Thus as the filter stands, the attenuation is good up to 3.85 times the cut-off frequency, and with some modification to suppress the spurious pass bands in the 7.70- to 8.48-kMc region the usable stop band might be extended considerably.

REFERENCES

1. S. B. Cohn, "Principles of Transmission-Line Filters," Chap. 26 of *Very High Frequency Techniques*, Vol. II, Sec. 26-4, p. 653 (McGraw-Hill Book Co., Inc., New York, N.Y., 1947).
2. S. B. Cohn, "Design of Transmission-Line Filters," Chap. 27 of *Very High Frequency Techniques*, Vol. II, p. 714 (McGraw-Hill Book Co., Inc., New York, N.Y., 1947).

CHAPTER 22

DIPLEXERS FOR THE 1- TO 4-kMc AND 4- TO 12.4-kMc RANGES AND THEIR MEASURED RESPONSES

A. GENERAL

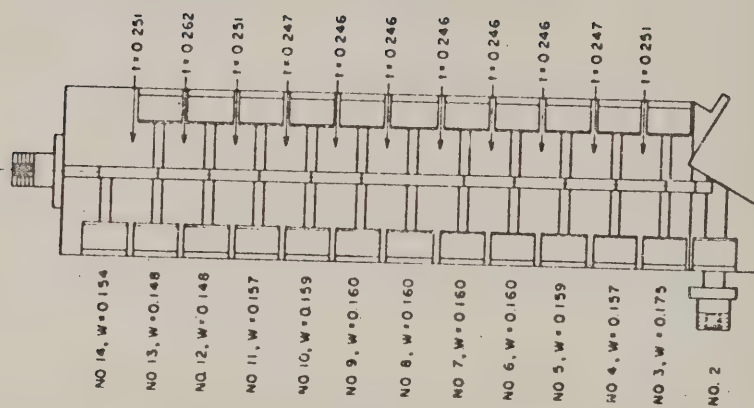
The Signal Corps requested two diplexers, one to operate in the 1- to 4-kMc range with the crossover at 2kMc, and another to operate in the 4- to 12.4-kMc range with the crossover at 8.2 kMc. It was desired to keep the loss in the pass-band at 0.5 db or less to as close to the crossover as possible; and the attenuation in the stop-band of the filters was to exceed 35 db, a level which was to be reached as rapidly as possible. It was also desired that the VSWR be 1.5 or less to as close to the crossover as possible.

Chapter 20 of this report describes a proposed design for these diplexers and presents a mathematical analysis of its performance. The basic design was chosen so that the diplexer for the 4- to 12.4-kMc band could be for the most part a scale model of the diplexer for the 1- to 4-kMc range. Diplexers for these two frequency ranges were fabricated, and details of their construction and their measured responses are included herein.

B. DIPLEXER FOR THE 1- TO 4-kMc RANGE

The mechanical details of the diplexer for the 1- to 4-kMc range are shown in Figs. 22-1 through 22-6. The higher-frequency channel of the diplexer is composed of a band-pass filter as shown in Figs. 22-1 through 22-3. The design of this filter is similar to that of the filter discussed in detail in Chapter 19 of this report. The lower frequency channel is composed of the low-pass filter shown in Figs. 21-1 and 21-2 of this report, cut off as indicated in Fig. 21-2. The two filters are connected in series using the connection shown in Fig. 22-4. Figure 22-6 shows a photograph of the completed diplexer with the cover plates removed.

Figure 22-7 shows the measured response for transmission through the lower frequency channel while Fig. 22-8 shows the corresponding response for transmission through the higher frequency channel. (In both cases 50-ohm terminating or source impedances were maintained at all three ports.)



FOR DETAILS OF
STUB NO. 2 AND
JUNCTION SEE
FIGS. 22-4, & 22-5.
(STUB NO. 1 IS
REMOVED. SEE
CHAPTER 20.)

NA-7580-78-2012

FIG. 22-1

BAND-PASS FILTER STRUCTURE FOR 1- TO 4-kMc DIPLEXER

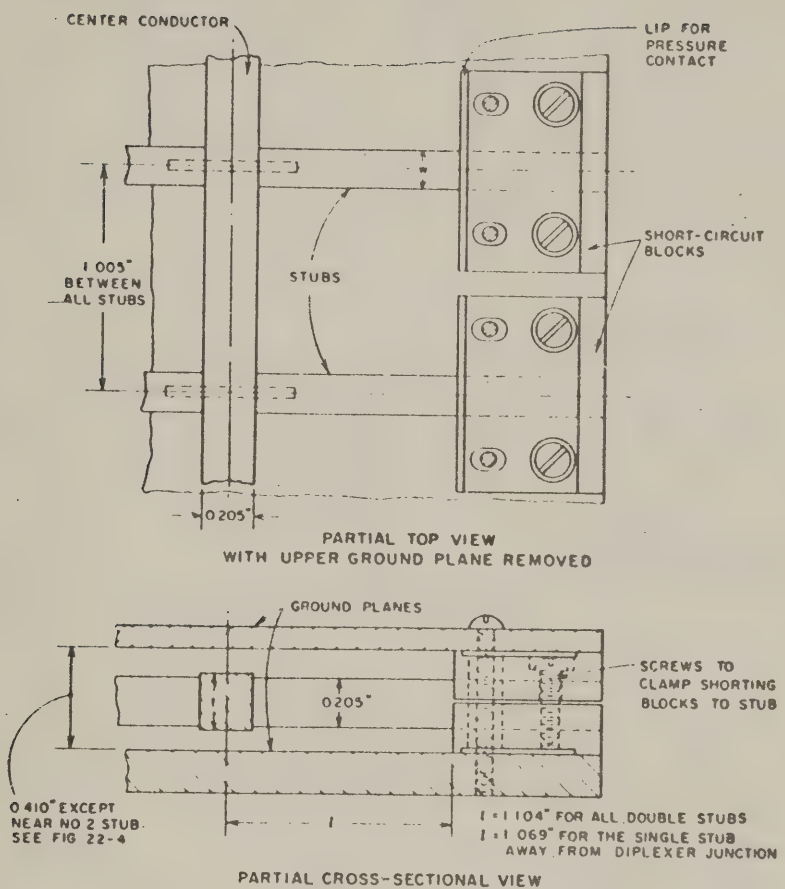
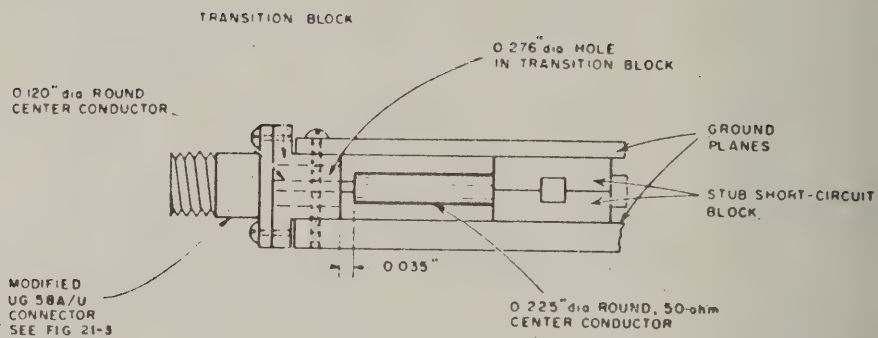
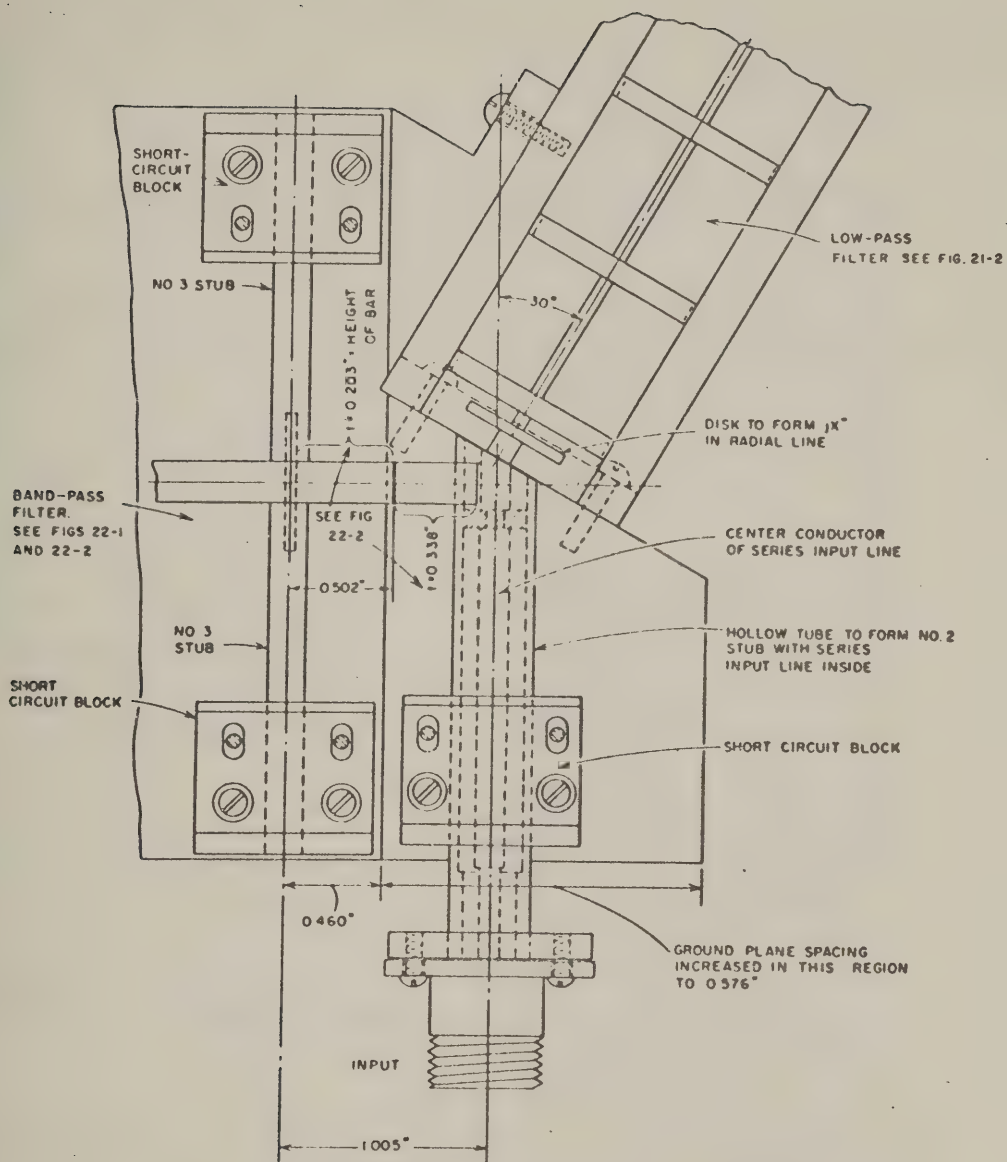


FIG. 22-2
BAND-PASS FILTER STRUCTURE FOR 1- TO 4-Mc DIPLEXER



RA-7526-TB-203R

FIG. 22-3
CONNECTOR MOUNT FOR BAND-PASS FILTER FOR 1- TO 4-kMc DIPLEXER



RD-5526-78-0100

FIG. 22-4

DETAILS OF DIPLEXER JUNCTION FOR 1- TO 4-kMc DIPLEXER

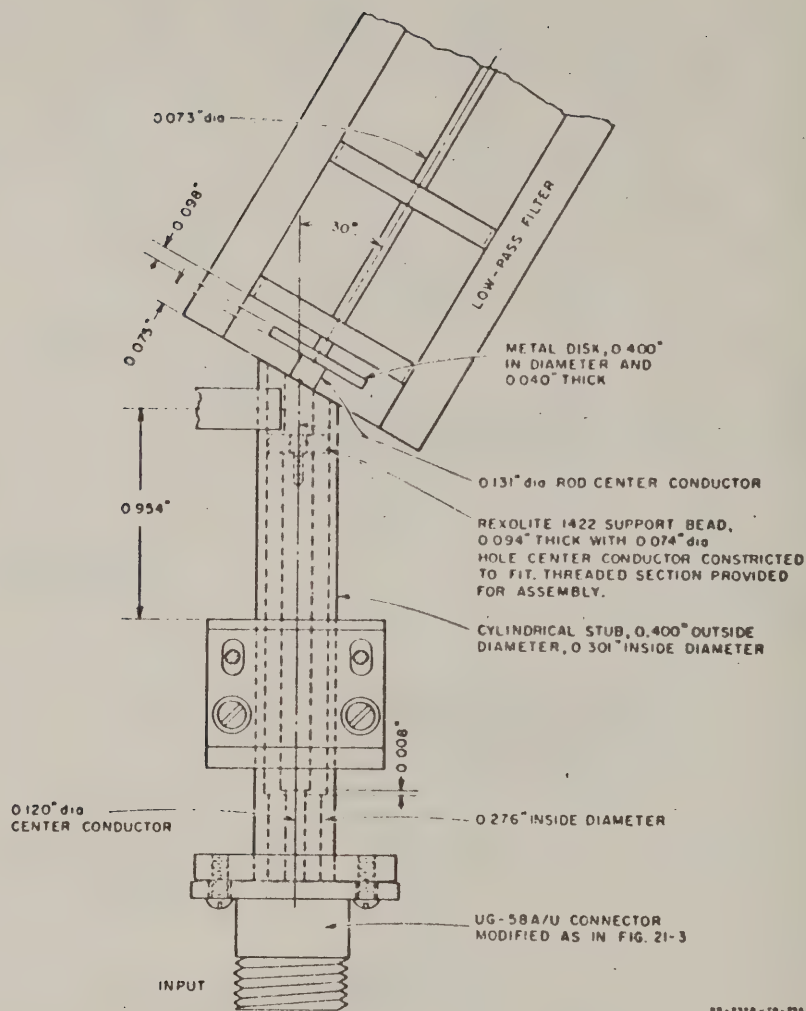


FIG. 22-5
FURTHER DETAILS OF DIPLEXER JUNCTION FOR 1- TO 4-kmc DIPLEXER

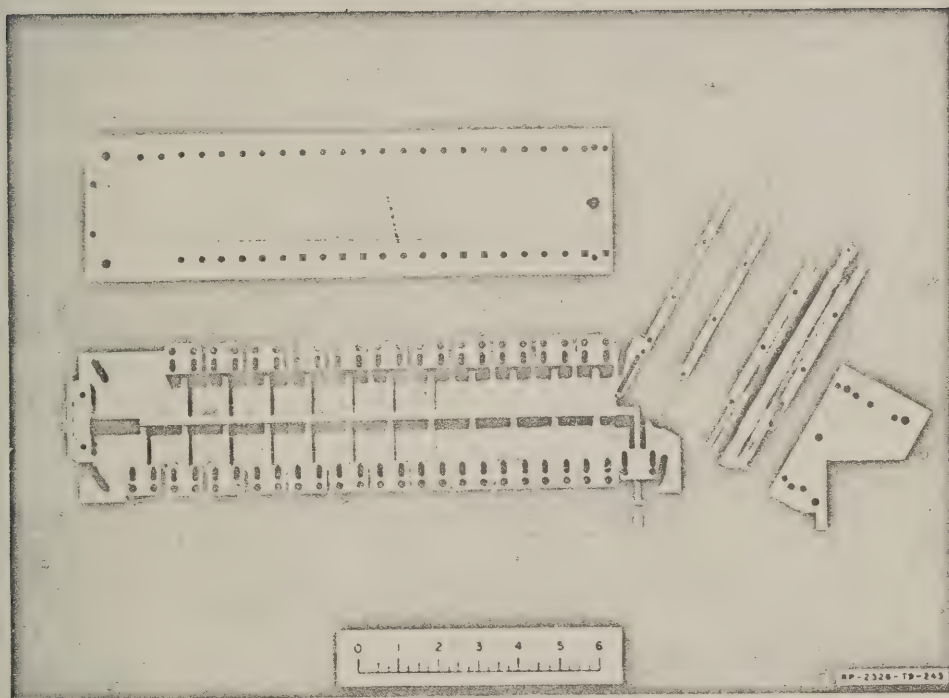


FIG. 22-6

PHOTOGRAPH OF THE 1- TO 4-Mc BAND DIPLEXER WITH THE COVER PLATES REMOVED

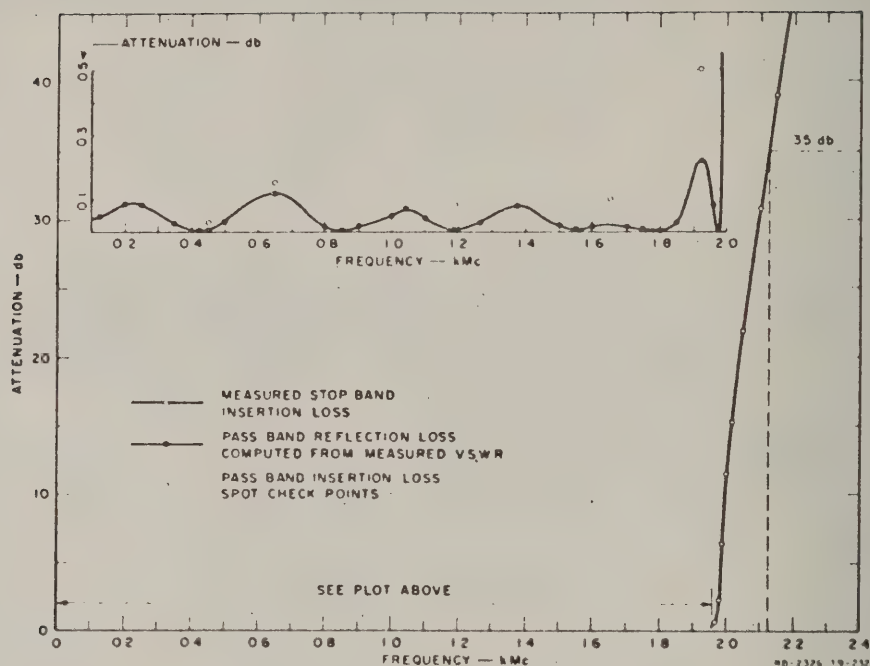


FIG. 22-7
MEASURED TRANSMISSION CHARACTERISTICS OF THE LOW-PASS CHANNEL
OF DIPLEXER IN FIG. 22-6

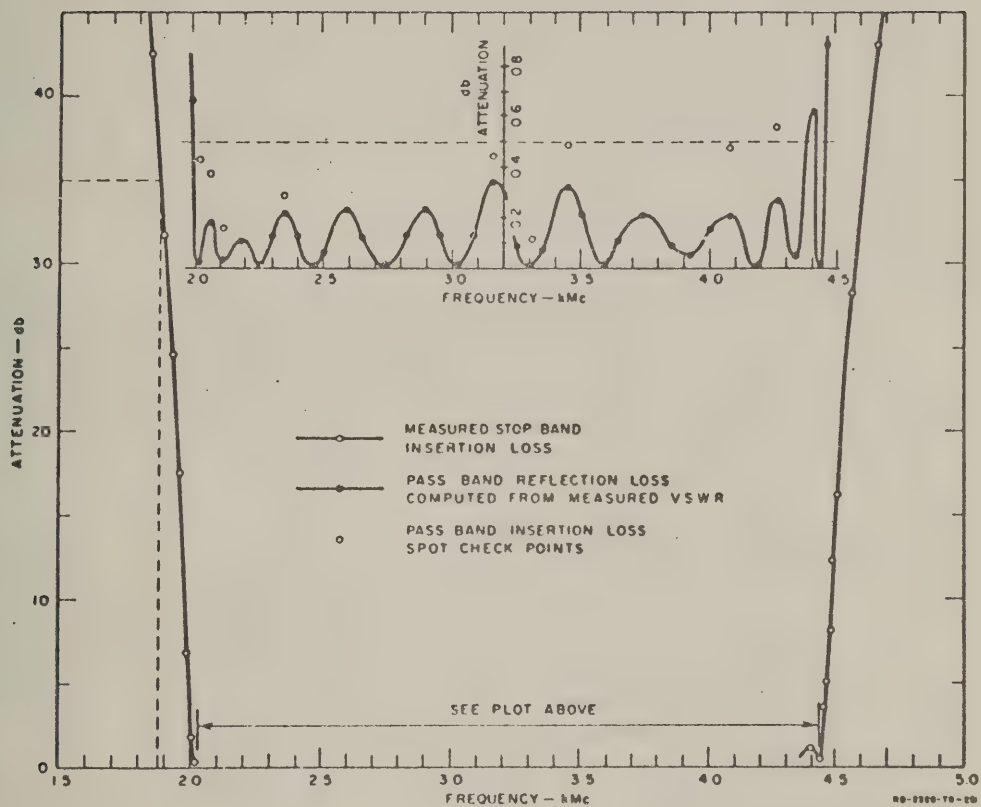


FIG. 22-8

MEASURED TRANSMISSION CHARACTERISTICS OF THE BAND-PASS CHANNEL
OF THE DIPLEXER IN FIG. 22-6

In order to detect the details of the pass band responses, extensive VSWR measurements were made in the pass bands and the reflection loss was then computed from the VSWR values. Insertion loss measurements were made at various spot check points in the pass bands so that the total loss (i.e., reflection loss plus dissipation loss) would also be evident. These measurements were made using tuned pads, the source and load circuits being tuned to a very low standing wave ratio with a slotted line prior to making each insertion loss measurement. The cut-off characteristics of the filters were also determined by insertion loss measurements. Figure 22-9 shows the cut-off characteristics of the two channels superimposed and also the VSWR measured at the junction port of the diplexer.

C. DIPLEXER FOR THE 4- TO 12.4-kMc RANGE

The mechanical details of this diplexer are shown in Figs. 22-10 through 22-19. In most respects it is a scaled down version of the diplexer for the 1- to 4-kMc range. However, since the filter structure becomes quite small when scaled down for use in the 4- to 12.4-kMc frequency range, it was necessary to design the special transitions shown in Figs. 22-17 and 22-18 in order to connect Type-N connectors to the miniaturized filter structures with a minimum of reflection. The Type-N connectors themselves were modified as in Fig. 22-19 to give low reflection on up through X-band, and to rigidly hold the center pin within the connector. The band-pass filter cover plate shown in Fig. 22-16 was machined from half-inch thick aluminum in order to provide flat surfaces for mounting the connector transition blocks and the low-pass filter; however, the center part of the cover plate was machined to 0.032-inch thickness to give flexibility, which helps to insure good contact at the short-circuiting strips along the edges of the band-pass filter. Photographs of the diplexer are shown in Figs. 22-20(a) and 22-20(b).

When the 4- to 12.4-kMc diplexer was first tested, its response appeared to be quite close to what was expected. However, at around 11 kMc there were some points where there was anomalous behavior. At these points the VSWR went up sharply to around 3.5, while the insertion loss went as high as 9 db. After some experimentation it was determined that this phenomena was due to a resonance of a ground plane mode within the band-pass filter structure. This mode was apparently excited by some dissymmetry of the center conductor structure with respect to the ground planes. It was found that this behavior could be largely eliminated by insertion of

small pieces of polyiron within the structure. This, however, also tended to introduce extra loss. Finally, some 0-80 screws were inserted between the stubs as is shown in Figs. 22-10 and 22-12 to prevent propagation of a ground plane mode. This stopped the anomalous behavior, but probably introduced some mistuning. After some adjustment of the lengths of the stubs in the band-pass filter, the responses shown in Figs. 22-21 through 22-23 were obtained. In all probability the VSWR at crossover (see Fig. 22-23) could be reduced to about that of the adjacent VSWR peaks if further adjustments were made with respect to the lengths of the stubs in the band-pass filter. As was done for the measurements on the lower frequency diplexer, the source and load impedances were tuned to nearly unity VSWR for each insertion loss measurement, except for some measurements where high attenuation was involved.

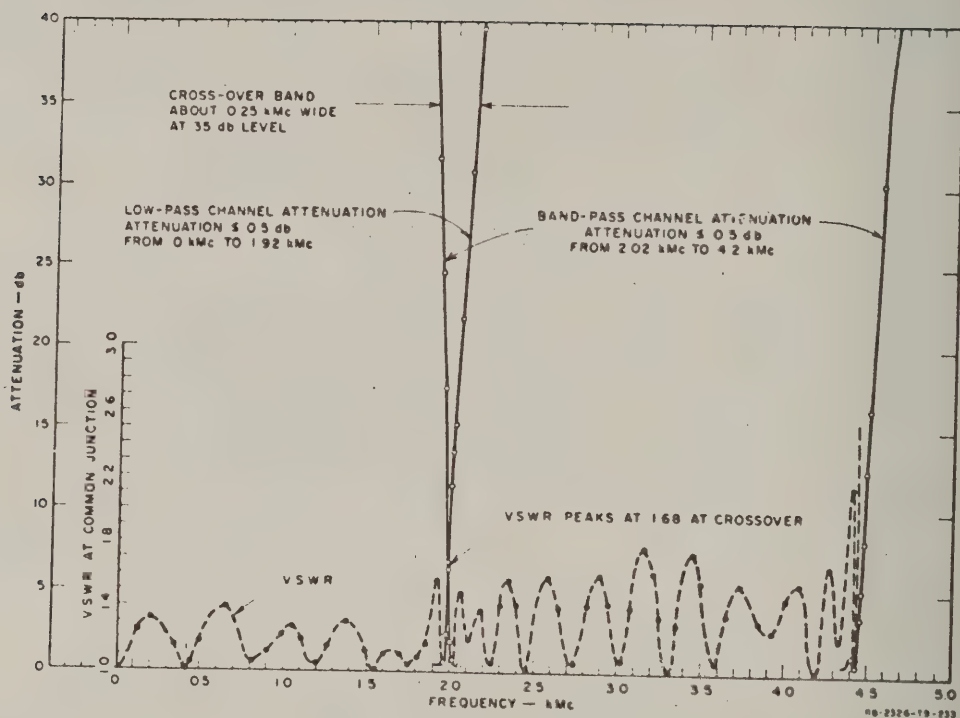


FIG. 22-9

VSWR AT JUNCTION PORT OF THE DIPLEXER IN FIG. 22-6, AND CUT-OFF CHARACTERISTICS OF THE LOW-PASS AND BAND-PASS CHANNELS SUPERIMPOSED

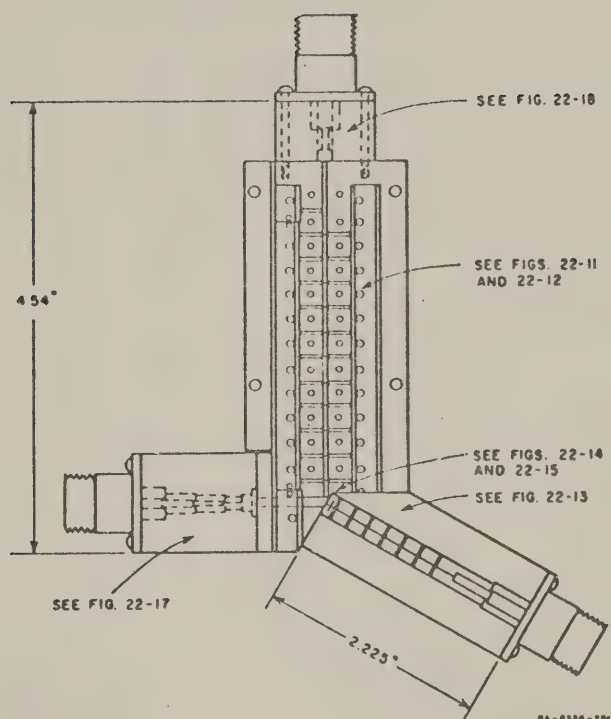


FIG. 22-10
DIPLEXER FOR THE 4- TO 12.4-kMc RANGE

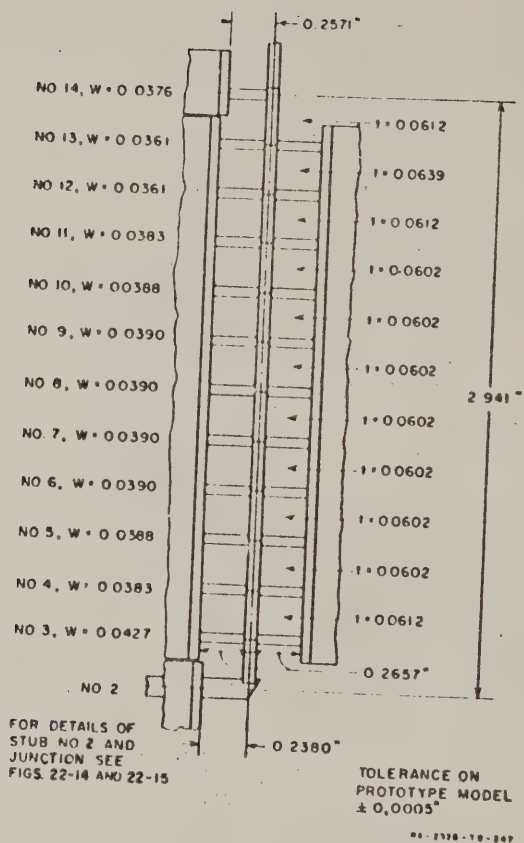
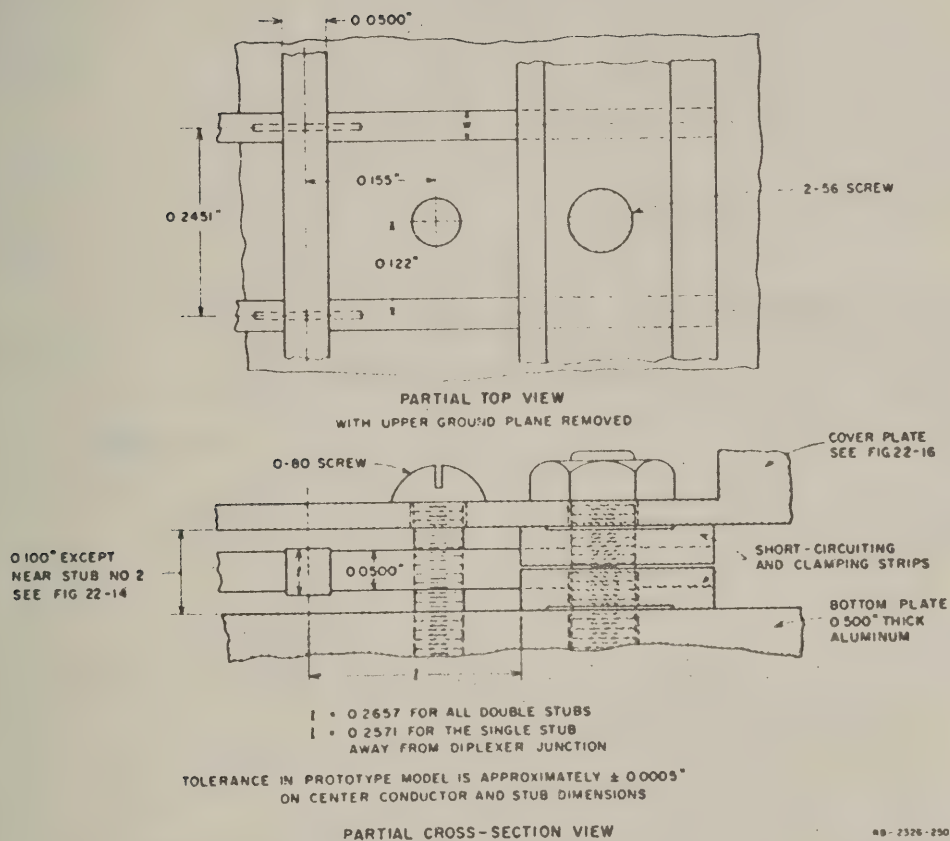
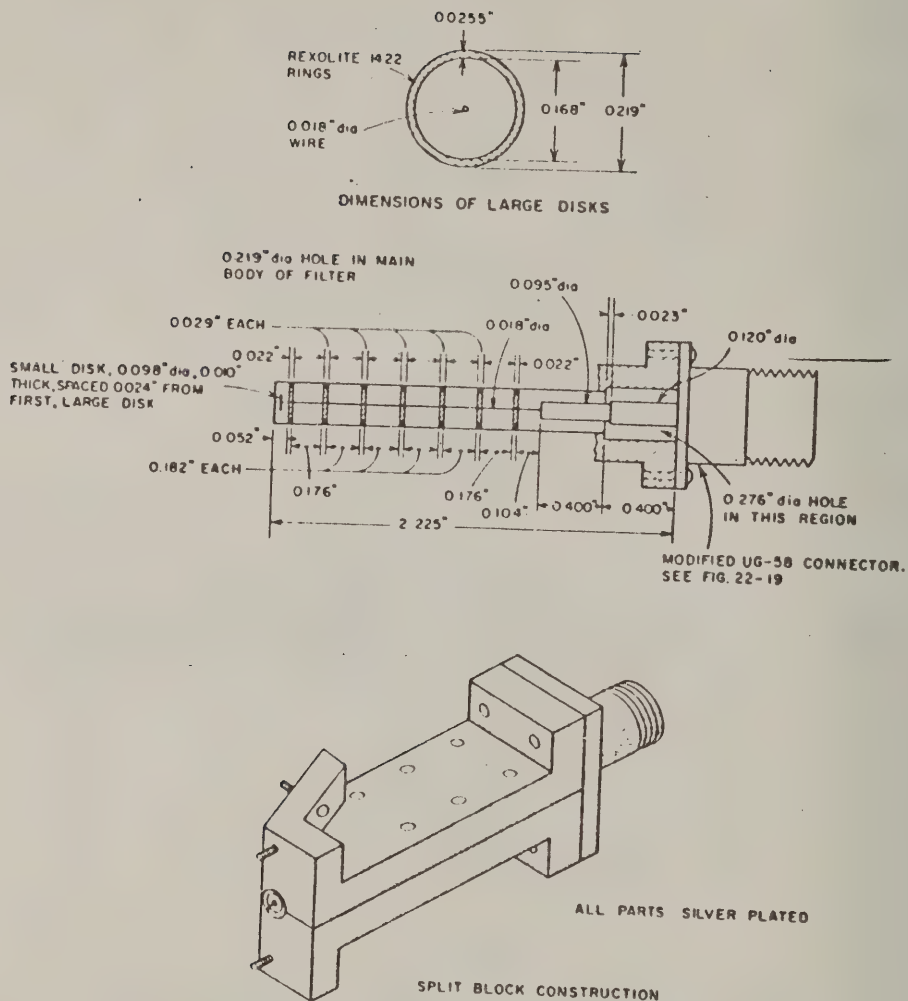


FIG. 22-11
BAND-PASS FILTER STRUCTURE FOR DIPLEXER
FOR THE 4- TO 12.4-kMc RANGE





90-2520-000

FIG. 22-13
LOW-PASS FILTER STRUCTURE FOR DIPLEXER FOR THE 4- TO 12.4-kMc RANGE

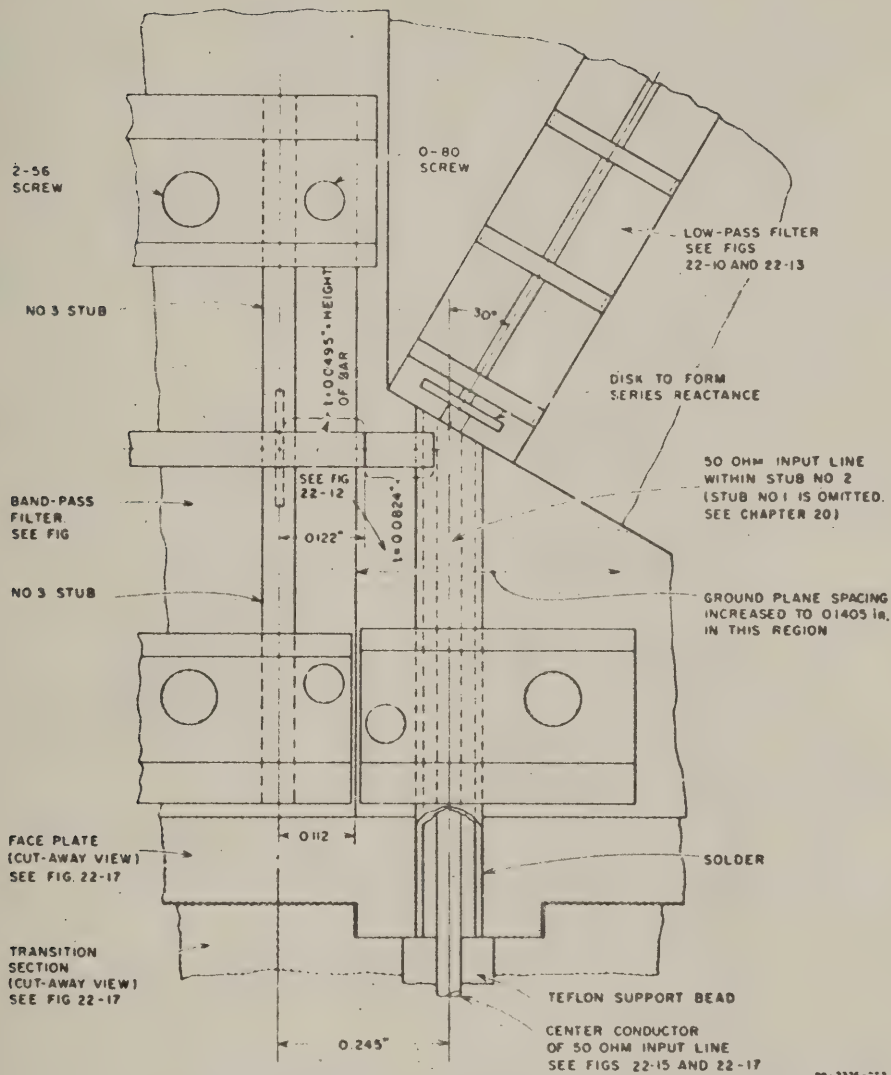
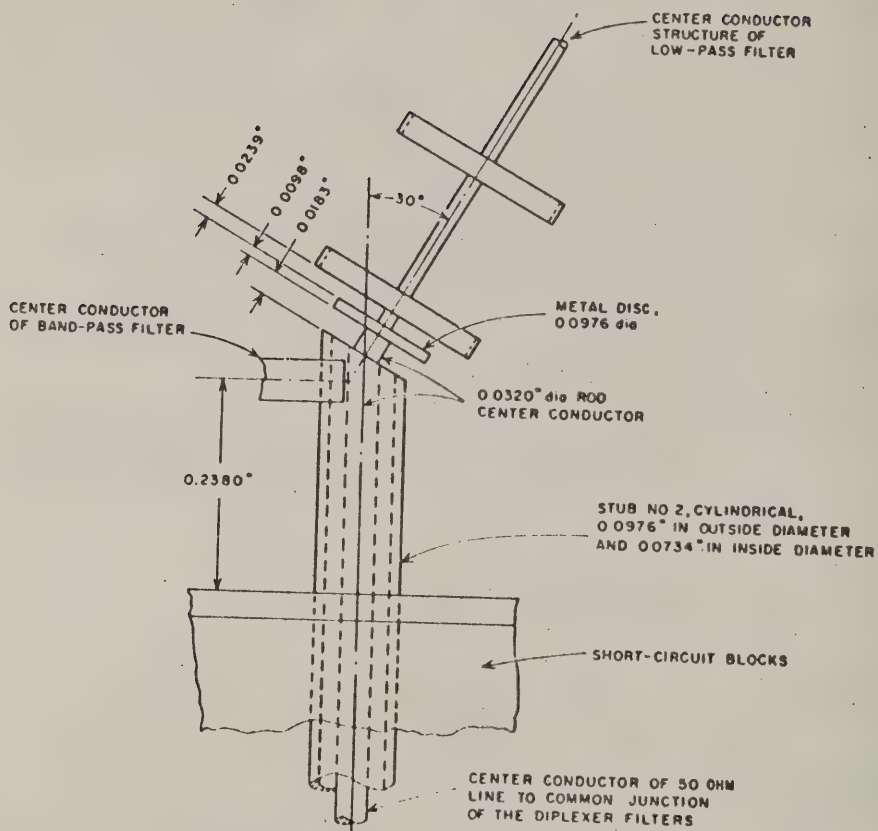


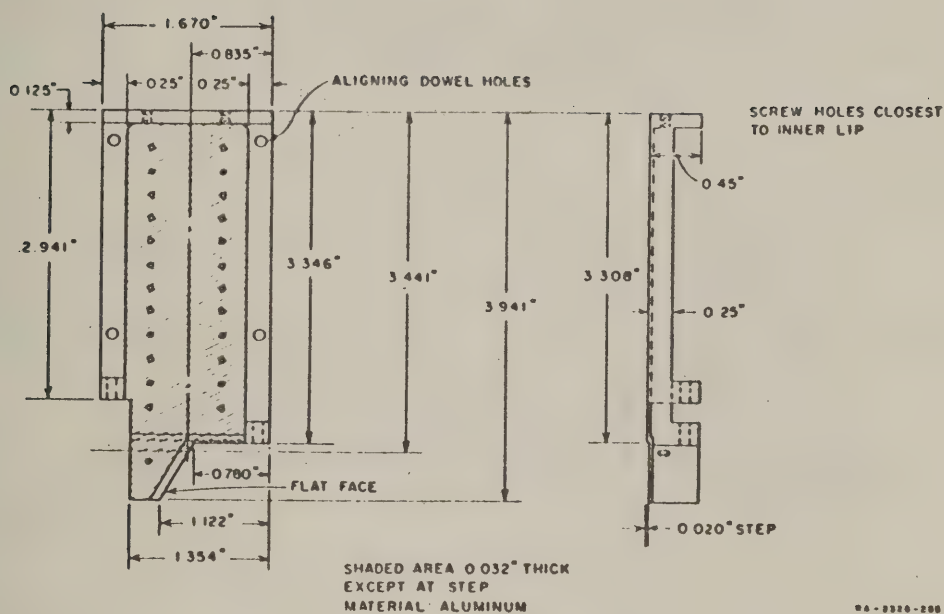
FIG. 22-14

DETAILS OF JUNCTION FOR DIPLEXER FOR THE 4- TO 12.4-kMc RANGE



49-2330-294

FIG. 22-15
 FURTHER DETAILS OF JUNCTION FOR DIPLEXER FOR THE 4- TO 12.4-kMc RANGE



96-3320-206

FIG. 22-16
COVER PLATE FOR BAND-PASS FILTER STRUCTURE FOR DIPLEXER
FOR THE 4- TO 12.4-kMc RANGE

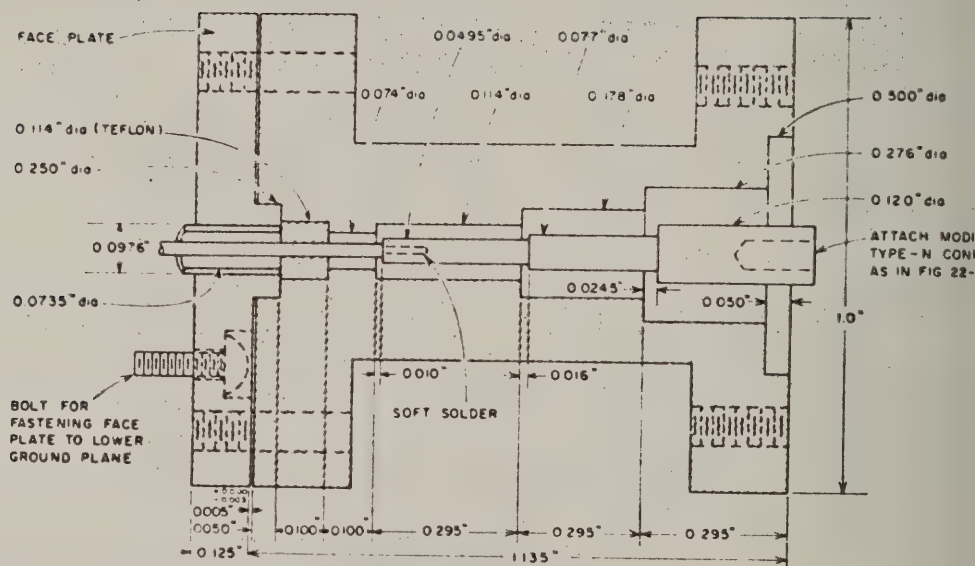


FIG. 22-17

TRANSITION FOR JUNCTION PORT FOR DIPLEXER FOR THE 4- TO 12.4-kMc RANGE

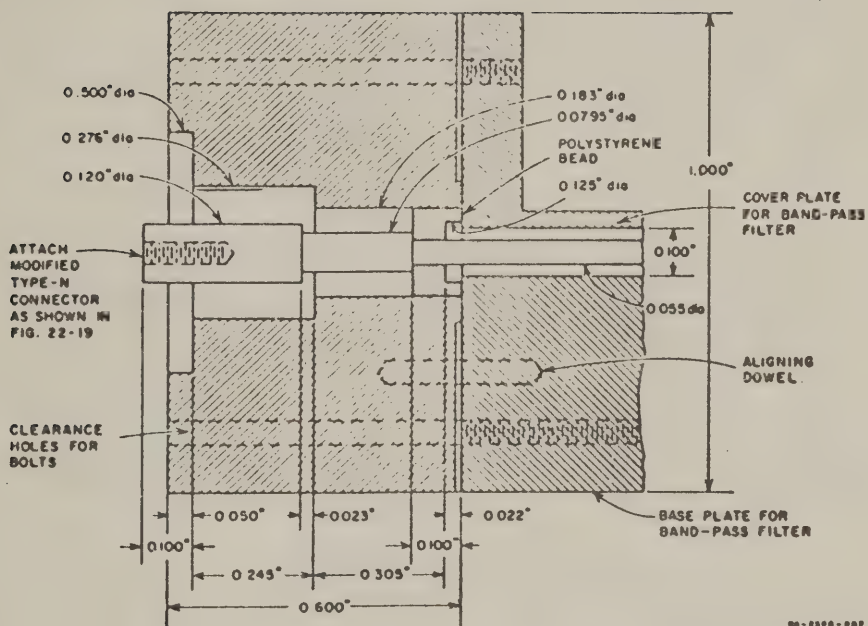


FIG. 22-18
TRANSITION FOR BAND-PASS FILTER PORT FOR DIPLEXER
FOR THE 4- TO 12.4-KMc RANGE

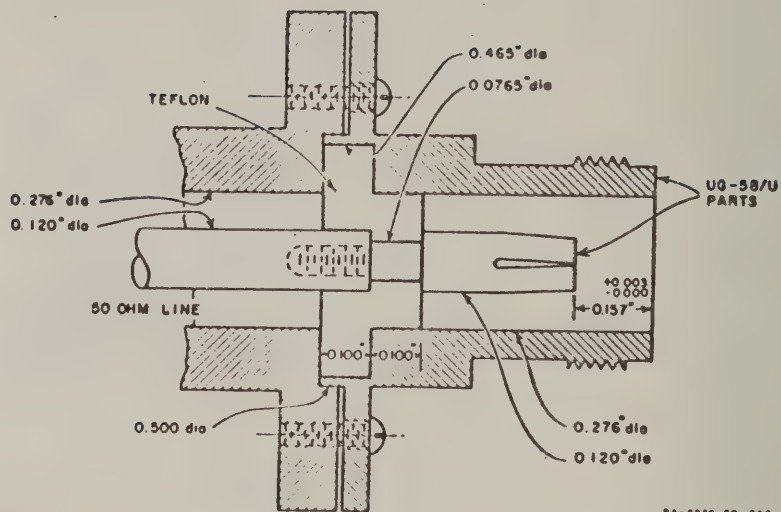
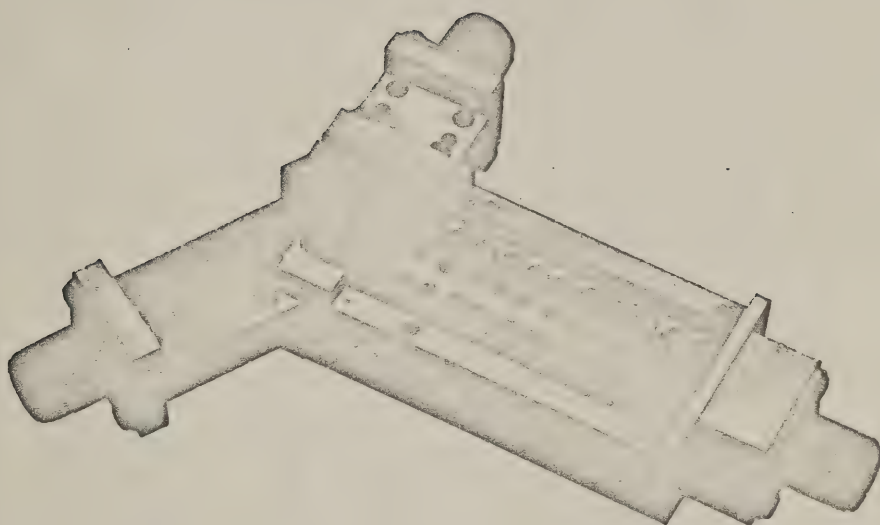


FIG. 22-19

MODIFIED TYPE-N CONNECTOR FOR DIPLEXER
FOR THE 4- TO 12.4-kMc RANGE



RP-2326-259

FIG. 22-20(a)
PHOTOGRAPH OF DIPLEXER FOR THE 4- TO 12.4-kMc RANGE

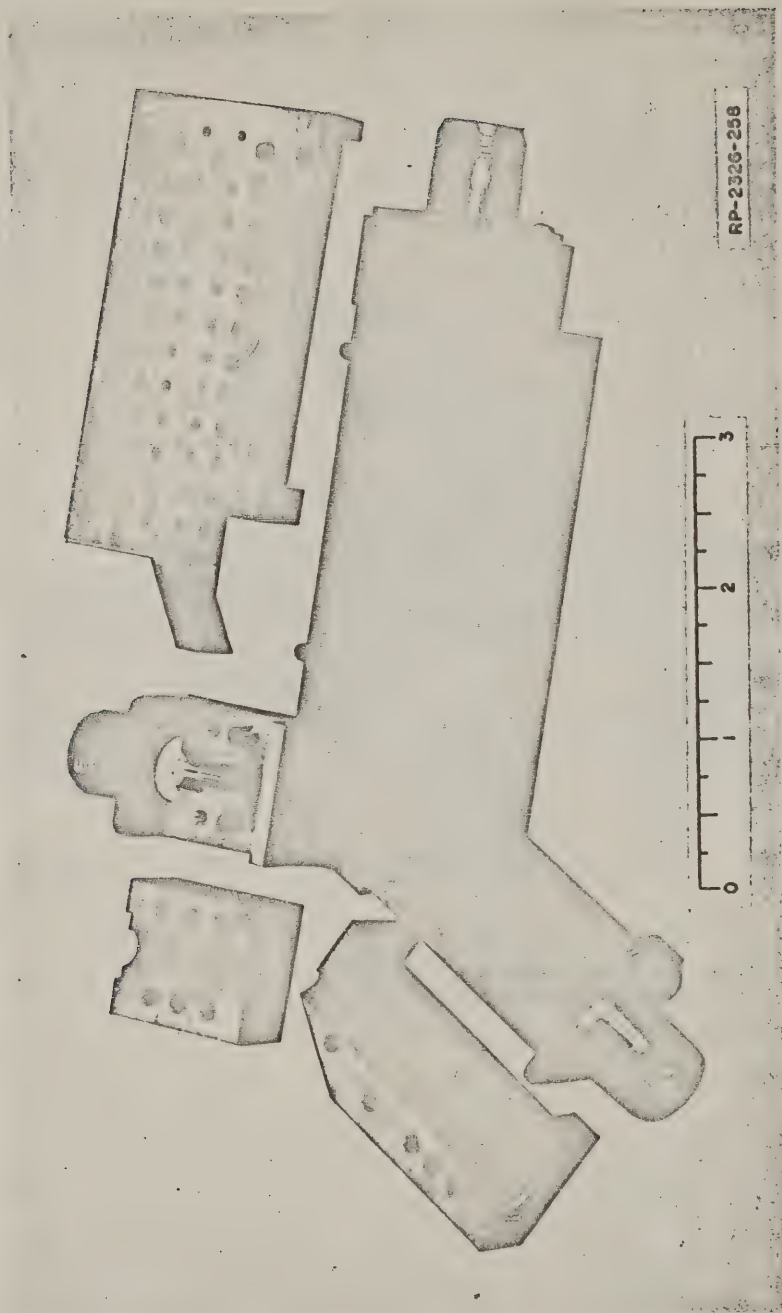


FIG. 22-20(b)
PHOTOGRAPH OF DIPLEXER IN FIG. 22-20(a) WITH COVER PLATES REMOVED

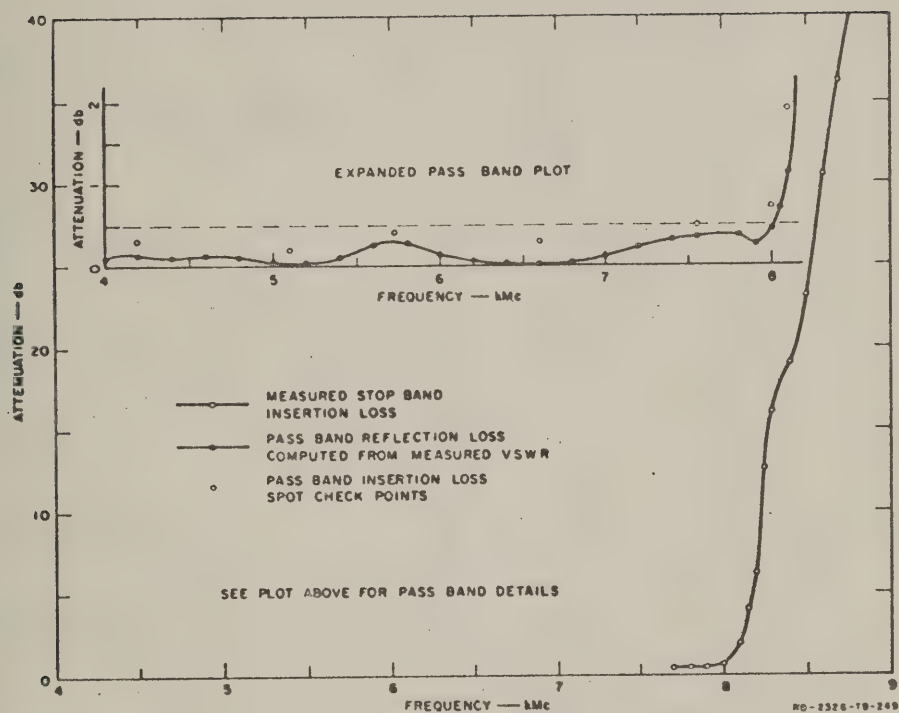


FIG. 22-21
MEASURED TRANSMISSION CHARACTERISTICS OF THE LOW-PASS CHANNEL
OF THE DIPLEXER IN FIGS. 22-20(a,b)

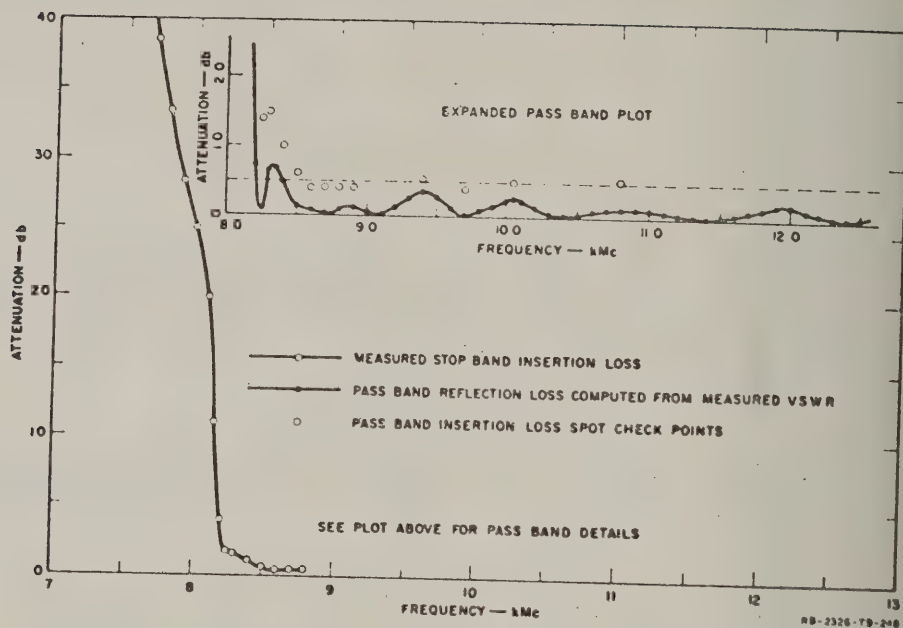


FIG. 22-22
MEASURED TRANSMISSION CHARACTERISTICS OF THE BAND-PASS CHANNEL
OF THE DIPLEXER IN FIGS. 22-20(a,b)

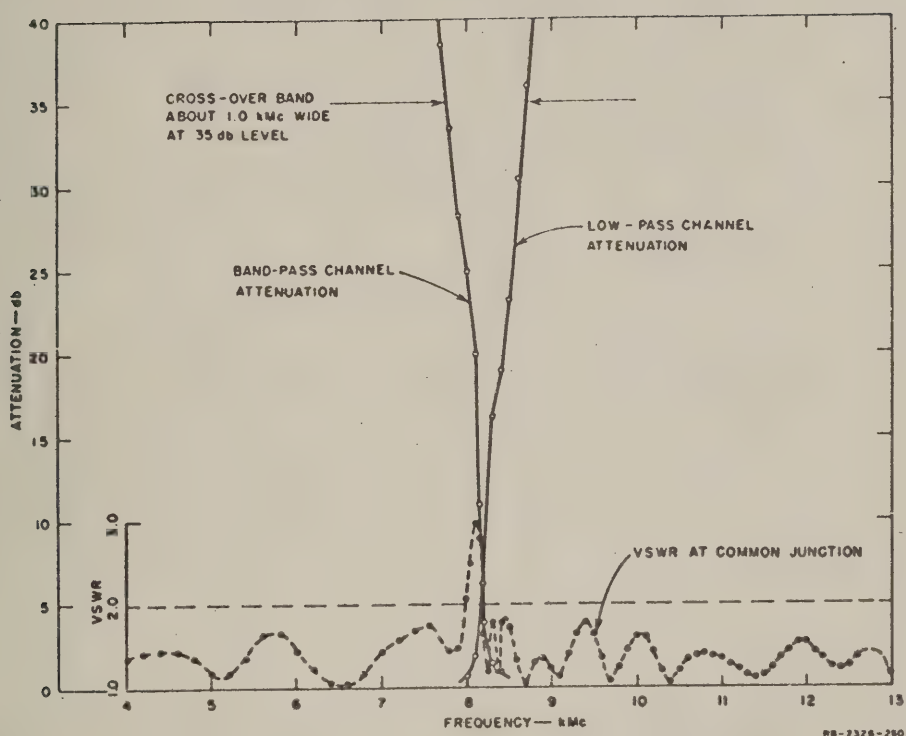


FIG. 22-23

VSWR AT JUNCTION PORT OF DIPLEXER IN FIGS. 22-20(a,b) AND LOW-PASS AND BAND-PASS CHANNEL CUT-OFF CHARACTERISTICS SUPERIMPOSED

DISSIPATION LOSS IN MULTIPLE-RESONATOR FILTERS*

A. GENERAL

In microwave filter design, the formulas and procedures usually assume nondissipative structures. The advantage of this assumption is a very great decrease in the mathematical labor of designing a given filter. Another advantage is that the designer has at his disposal a vastly larger variety of filter types, design methods, and design formulas, than if he restricted himself to design criteria taking dissipation into account. However, power dissipation is always present in a practical filter, and as a result the actual insertion-loss response function will deviate somewhat from the theoretical response of the ideal nondissipative structure. The deviation is most evident in the pass band where it usually appears as an increase in the minimum insertion loss, a rounding near the cut-off points, and a partial or complete obliteration of ripples. In the stop band the effect is usually very slight, except at infinite rejection points, which are reduced to finite insertion-loss levels. The loss is usually greater for band-pass than for low-pass filters and increases as the relative bandwidth is reduced.

Although microwave filters are usually designed as though dissipationless, the designer should in each case consider the effect of dissipation in order to determine whether his design will satisfy the intended application. This can be done in a standard manner when the image-parameter method is used, although an accurate computation would usually be difficult for a distributed-constant structure. Another method applicable to the calculation of the dissipation loss of coupled-resonator band-pass filters is presented in this report. This case is particularly important because arrangements of cascaded resonators are so widely used as filters, and because dissipation loss can become very large as bandwidth is decreased. The method of this report applies to all forms of construction, whether the resonators are waveguide cavities, resonant lengths of coaxial or strip line, lumped-element circuits, etc. The approximate approach used in computing center-frequency loss is equivalent to calculating the fields in lossless resonators coupled to yield a desired response function, and then calculating the power dissipated when these fields act upon the actual dissipative regions of the resonators. The formula obtained is simple and

* This material has been published. See S. B. Cohn, "Dissipation Loss in Multiple-Coupled-Resonator Filters," *Proc. IRE* 47, pp 1342-1348 (August 1959).

requires a knowledge only of the unloaded Q of the resonators the filter bandwidth, and the element values of the equivalent low-pass prototype from which the multiple-resonator filter was designed. The formula applies only to the center of the pass band, and assumes that the reflection loss is small, and that the dissipation loss does not exceed n db for very good accuracy or $2n$ db for fair accuracy where n is the number of resonators in the filter. However it is shown with examples how all of these conditions may be removed to obtain the actual insertion loss at all frequencies through computations on the low-pass prototype circuit.

Although the method used here is to assume first a nondissipative filter and then to compute the effect of finite Q elements, this is not the only possible approach to the design problem. Narrow-bandwidth coupled-resonator filters can be synthesized to have any physically realizable response function in the presence of dissipation. Dishal gives data that may be used for the design of such filters to yield maximally flat, equal-ripple, and maximally linear-phase response functions when resonators of finite unloaded Q are used.^{1,2} It turns out that for more than two resonators the filter must be constructed unsymmetrically in order to obtain these exact response functions and that for any given number of resonators an infinite number of sets of design parameters will yield the same response function. Taub and Bogner³ have shown for three resonators and Fubini and Guillemin⁴ for any number of resonators that if the requirement of minimum pass-band loss is added to the filter specification a single design will then be uniquely determined in the case of exact maximally flat or equal-ripple response. By means of Taub and Bogner's graphs the design parameters may be obtained quite readily for three resonator maximally flat filters but for the three resonator equal-ripple case and for all cases with more than three resonators a laborious computational procedure is necessary.

The works of Taub and Bogner and of Fubini and Guillemin on minimum-loss designs apply in detail only to the synthesis of filters having exact maximally flat or equal-ripple response for which it is necessary that the filter structure be unsymmetrical (except for $n = 1$ or 2). This dissymmetry produces mismatch loss at band center which is needed to overcome the rounding effect of dissipation loss. The rounding results from the greater dissipation loss toward the edges of the pass band than at the center,

but by introducing mismatch loss properly, the response may be flattened and the exact maximally flat or equal-ripple function achieved. However, it is clear that if this center-frequency mismatch is eliminated, the insertion loss will be reduced. Therefore the minimum-loss design for exact maximally flat or equal-ripple response does not give the least center-frequency insertion loss that can be achieved with the same unloaded Q , number of resonators, and bandwidth.

It should be realized that for most microwave applications a reduced insertion loss would be preferred to an idealized response shape. An important practical problem, therefore, is to find design parameters yielding the true minimum possible center-frequency loss and to determine the value of this loss and the shape of the response curve. This problem is studied in this report with the aid of the simple formula for center-frequency loss. This formula permits the various factors to be quickly evaluated and designs to be found yielding very close to the true minimum-possible loss.

B. COMPUTATION METHODS

An earlier report⁵ and published papers^{6,7} give convenient design formulas by which multiple-resonator band-pass filters may be designed to have the response function (transformed in frequency) of a low-pass prototype filter. The basic parameters entering into the design are the desired bandwidth of the multiple-resonator filter and the element values g_i of the low-pass prototype.⁸ For convenience, formulas for the element values of nondissipative maximally flat and equal-ripple low-pass prototype filters are included in the above-mentioned references.⁶ The use of these element values will yield good approximations to maximally flat and equal-ripple response in the multiple-resonator filter, if the resonator unloaded Q 's are sufficiently high. Usually, however, there will be sufficient dissipation loss to alter noticeably both the center-frequency loss and the shape of the response curve. Methods of calculating these effects will now be presented.

* In all cases the use of these formulas results in symmetrical coupled-resonator structures, although the low-pass prototype is unsymmetrical for equal-ripple response with n even. That is, although $g_1 \neq g_n$ and $-1 \neq 1$ in the latter case, the coupled-resonator filter derived from the prototype is symmetrical and has equal terminating impedances. Therefore, the insertion loss for the coupled-resonator filter is not strictly equal to the insertion loss of the prototype, but is equal to the difference in decibels between the maximum power available from the generator and the power delivered through the filter to the load.

1. CENTER-FREQUENCY LOSS

The following formulas, derived in Section E, give the insertion loss due to dissipation at the center of the pass band of a multiple-resonator filter:

$$L_0 = 4.343 \frac{\omega_1'}{w} \sum_{i=1}^n \frac{g_i}{Q_{u,i}} \text{ decibels} \quad (23-1)$$

where, as shown in Fig. 23-1, ω_1' is a point on the low-pass-prototype frequency scale corresponding to frequencies f_1 and f_2 on the band-pass frequency scale, w is the relative bandwidth $(f_2 - f_1)/f_0$ where f_0 is the center frequency, g_i (with $i = 1$ to n) are the respective element values of the prototype filter in farads and henries as shown in Fig. 23-2, $Q_{u,i}$ are the respective unloaded Q 's of the resonators, and n is the number of resonators in the filter. As is made clear in the derivation, this formula has very good accuracy for L_0 up to about n db, and fairly good accuracy up to about $2n$ db. In order for Eq. (23-1) to be valid, the filter must be well-enough matched at f_0 so that mismatch loss will be small. When this is not the case, the insertion loss will usually lie between the value given by Eq. (23-1) and that value plus the mismatch

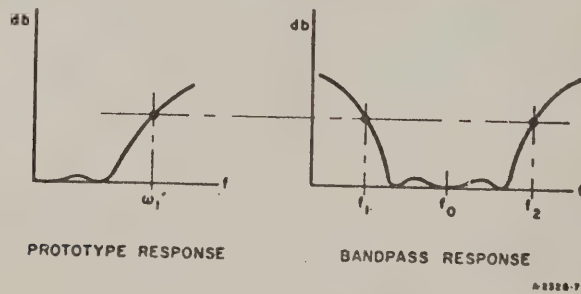


FIG. 23-1

CORRESPONDENCE BETWEEN LOW-PASS PROTOTYPE RESPONSE
AND EQUIVALENT BAND-PASS RESPONSE

loss of the nondissipative filter, which is given by $10 \log_{10} [(1+r)^2/4r]$ where r ohms and 1 ohm are the terminating resistances shown in Fig. 23-2.

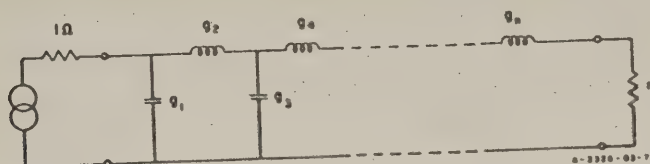


FIG. 23-2

NONDISSIPATIVE LOW-PASS PROTOTYPE FILTER

2. EXACT CALCULATION USING LOW-PASS PROTOTYPE

The approximations involved in Eq. (23-1) may be avoided if exact network calculations are made on an equivalent circuit of the multiple-resonator filter. The low-pass-prototype filter circuit of Fig. 23-3 is the most convenient for this purpose. The series resistances and shunt conductances are determined from the respective resonator unloaded Q 's by the following formulas, which are derived in Sec. E:

$$R'_i = \frac{\omega'_i g_i}{\omega Q_{u,i}} \text{ for } n \text{ even} \quad (23-2)$$

$$G'_i = \frac{\omega'_i g_i}{\omega Q_{u,i}} \text{ for } n \text{ odd.} \quad (23-3)$$

The capacitances and inductances, g_i , are related to the resonator and coupling parameters of the multiple-resonator filter by the same formulas used for the nondissipative case.^{5,6,7}

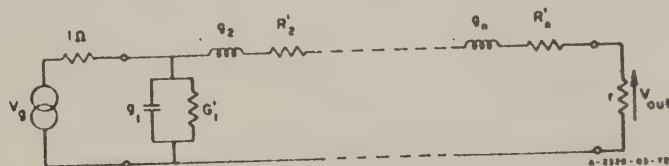


FIG. 23-3

DISSIPATIVE LOW-PASS PROTOTYPE FILTER

With the dissipative prototype filter of Fig. 23-3 thus fully determined, the frequency response on the ω' scale can be obtained exactly by direct calculation and then the frequency response of the multiple-resonator band-pass filter may be found by means of the frequency transformation between ω' for the low-pass filter and f for the band-pass filter. For bandwidths up to a few percent the following simple transformation gives good results

$$\frac{|f - f_0|}{f_0} = \frac{\omega}{2} = \frac{\omega'}{\omega'_1} \quad (23-4)$$

More precise transformation formulas are available for certain lumped-constant waveguide and strip-line configurations, and should be used for bandwidths of more than a few percent.⁵⁶

At the center frequency f_0 , corresponding to $\omega' = 0$, the computation is particularly simple, since the circuit is purely resistive and all quantities are real. At other frequencies the impedances and admittances are complex numbers, and the voltages and currents must be treated as complex also. In either case the most convenient procedure is to assume $V_{out} = 1$ volt and then to compute the voltages and currents back through the filter until V_g is determined. Then, since the power available from the generator is $(V_g/2)^2$ and the output power is V_{out}^2/r , the insertion loss of the coupled-resonator filter* is related to V_g/V_{out} by

$$L = 20 \log_{10} \left| \frac{V_g}{V_{out}} \right| = 10 \log_{10} \frac{4}{r} \text{ decibels} \quad (23-5)$$

This procedure gives directly the combined effect of mismatch and dissipation loss, and is valid at all frequencies—in the pass band, the transition band, and the stop band.

C. MINIMUM LOSS FOR SYMMETRICAL DESIGNS

1. APPROXIMATE MINIMUM-LOSS DESIGN

The design parameters of multiple-resonator filters having very nearly minimum-possible center-frequency loss irrespective of response-curve shape may be arrived at easily in the case of given values of unloaded Q and

* See preceding footnote.

stop-band bandwidth. The results are subject to the assumptions that the loss is small (not more than about n db) and that the insertion-loss ratio at the edges of the stop band is accurately given by the highest-power term in the insertion-loss polynomial. When the first assumption is met, Eq. (23-1) is accurate, and when the second is met, the stop-band insertion loss is given by the following formula derived in Section E:

$$L_s = 20 \log_{10} (\omega'_s)^n g_1 g_2 g_3 \dots g_n + C \quad (23-6)$$

where the subscript s indicates values at the stop-band limits, and C is a constant dependent upon the load resistance r , as discussed in Section E. Thus, if ω_s , Q_s , n , and r are assumed fixed and the element values g_i are allowed to vary, L_s will remain constant if

$$(\omega'_s)^n g_1 g_2 \dots g_n = \text{constant} \quad (23-7)$$

and L_s will be minimum if

$$\omega'_s (g_1 + g_2 + \dots g_n) = \text{minimum}. \quad (23-8)$$

Differentiating Eqs (23-7) and (23-8) we obtain

$$\frac{\delta \omega'_s g_1}{\omega'_s g_1} + \frac{\delta \omega'_s g_2}{\omega'_s g_2} + \dots + \frac{\delta \omega'_s g_n}{\omega'_s g_n} = 0$$

and

$$\delta \omega'_s g_1 + \delta \omega'_s g_2 + \dots + \delta \omega'_s g_n = 0.$$

These two equations can hold in general only if the quantities $\omega'_s g_i$ are all equal. Thus, subject to the approximations, minimum dissipation loss at f_0 is obtained when the elements in the prototype filter are equal:

$$g_1 = g_2 = g_3 = \dots = g_n. \quad (23-9)$$

* Equation (23-6) holds in the case of maximally flat response if $L_s \geq 20$ db, while in the other cases considered in this report experience has shown Eq. (23-6) to be within 1.5 db at 60 db for $n = 5$, and much closer for n smaller.

It is further necessary that r be close to unity; that is, that the terminating resistances be almost equal. If this were not the case, excessive mismatch loss would occur. It is likely that the true minimum-possible loss will be achieved in a given case by a set of g_i values that are somewhat unequal and by an r value slightly different from unity, but the center-frequency insertion loss of a symmetrical filter designed with $r = 1$ and $g_1 = g_2 = \dots = g_n$ will certainly be extremely close to the true minimum-possible loss, in cases where both Eqs. (23-1) and (23-6) are valid.

2. EXACT MINIMUM-LOSS DESIGN FOR SYMMETRICAL FILTER WITH $n = 3$

B. M. Schiffman of Stanford Research Institute has previously derived exact design formulas for three-resonator symmetrical filters yielding minimum-possible loss when the unloaded Q and stop-band bandwidth are specified.⁹ Figure 23-4 shows a comparison between the center-frequency

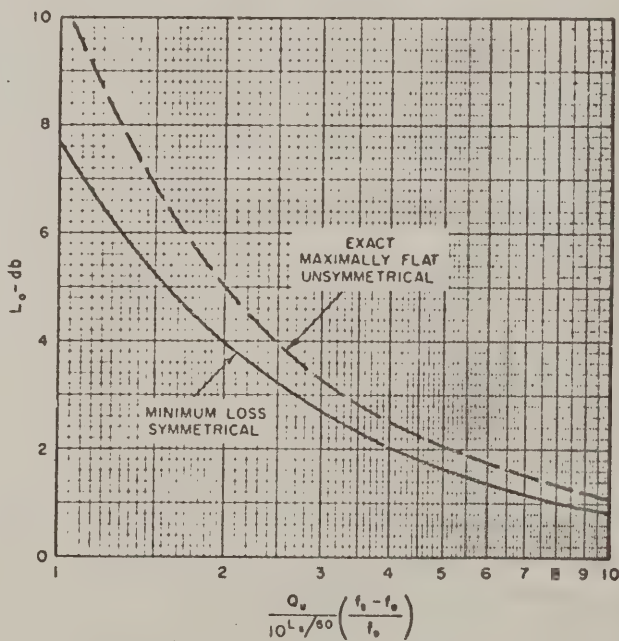


FIG. 23-4

COMPARISON OF MID-BAND INSERTION LOSS OF EXACT MAXIMALLY FLAT DESIGN OF TAUB AND BOGNER AND MINIMUM-LOSS DESIGN OF SCHIFFMAN

insertion loss of Schiffman's symmetrical filter and that of Taub and Bogner's³ maximally flat unsymmetrical filter. It is seen that to obtain the flat response of the latter filter, a designer must accept a higher loss as well as the inconvenience of the unsymmetrical construction.

Upon converting Schiffman's formulas into the notation of this report, it was found that the elements of his low-pass prototype approach equality as L_0 approaches zero. This agrees with the approximate analysis above. As an example of the effect of a high value of L_0 on the accuracy of the approximate analysis, the exact minimum-loss design having $L_0 = 3$ db has elements g_i in the ratio 1.0.775:1. An equal element filter with the same unloaded Q and stop-band bandwidth has $L_0 = 3.23$ db, about 8 percent higher. This discrepancy vanishes very rapidly as L_0 is reduced.

D. COMPARATIVE PERFORMANCE OF DIFFERENT DESIGNS

1. PASS-BAND RESPONSE

Exact calculations were made of the pass-band insertion-loss response of various coupled resonator filters having $n = 3$ and $n = 5$. A comparison of three response curves for three-resonator filters is shown in Fig. 23-5: The same Q_u and same 60-db bandwidth, $w_{3\text{dB}}$, are assumed for each case; that is, all curves if extended would intersect at the 60-db points. One of the curves is for the minimum-loss maximally flat case of Taub and Bogner.³ A second curve is labeled *pseudo maximally flat*, since it is the curve for a filter designed from a nondissipative maximally flat prototype. The third curve is for the minimum-loss symmetrical design of Schiffman.⁹

A number of interesting facts are evident from Fig. 23-5: (1) although the exact maximally flat case has minimum loss compared to all other possible maximally flat filters having the same n , Q_u , and $w_{3\text{dB}}$, it has higher center-frequency loss than the other two curves in the figure; (2) the rounding effect of dissipation is clearly evident in the other curves; and (3) as predicted above the minimum-loss symmetrical design has the least loss of the three curves at f_0 . This case also has the least loss throughout the pass band, and offers the greatest 3-db bandwidth. It may also be regarded as a pseudo-equal-ripple case, since the nondissipative low-pass prototype of the minimum-loss symmetrical filter has an equal-ripple response with ripple level of about 0.2 db. Note that dissipation has removed all but a suggestion of these ripples.

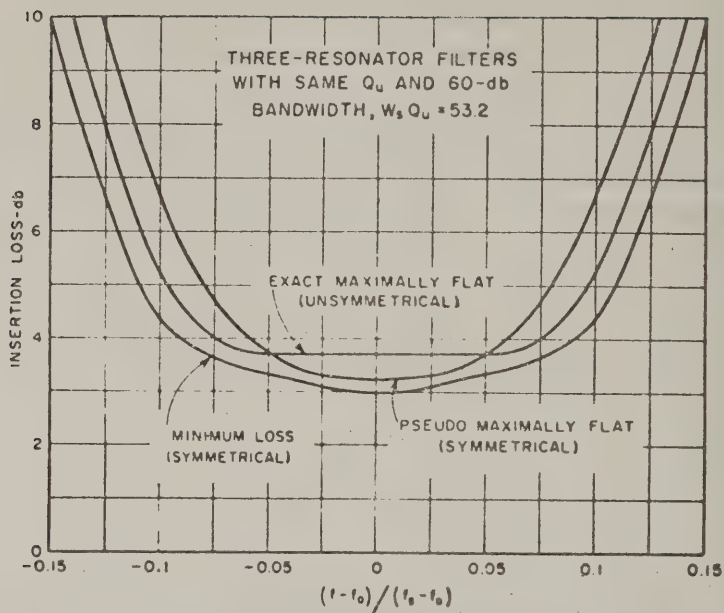


FIG. 23-5

PASS-BAND INSERTION-LOSS CURVES FOR THREE DIFFERENT THREE-RESONATOR FILTER DESIGNS

Figure 23-6 shows a similar set of response curves for various five-resonator filters. The same Q_u and same 60-db bandwidth are assumed throughout, as before. The results are qualitatively the same as for the three-resonator filters: (1) the minimum-loss exact maximally flat curve has higher midband loss than the other curves, which are again rounded by dissipation; (2) the equal-element curve offers the least loss at center frequency, although the 0.1 db pseudo-equal-ripple curve is almost as good; (3) the equal-element and pseudo-equal-ripple curves have less loss everywhere in the pass band than the exact maximally flat case; (4) all ripples are obliterated.

It is thus clear that the minimum-loss, exact maximally flat design does not give the least possible loss when restrictions on response-curve shape are removed. If the maximally flat response is definitely needed in a given application, it should be used. In most microwave applications, however, the rounded response curves of the other cases would be satisfactory.

and therefore would be favored because of their lower loss and better match in the pass band. Further advantages of these other cases are their ease of design from simple available formulas and their symmetrical physical structures. The rounding to be expected depends upon the amount of dissipation loss occurring in the filter. For example, if L_0 were 1.0 db, the response curves would conform much more closely to the curves for the lossless prototypes.

Fubini and Guillemin have shown that exact equal-ripple filters have considerably higher pass-band loss than a maximally flat filter of the same number of resonators, unloaded Q , and three-db bandwidth.⁴ This is true even for ripple levels as small as 0.001 db, and the loss increases very rapidly as the ripple level is increased. The reason for this behavior may be deduced from the curves of Figs. 23-5, and 23-6, where the ripples in the equal-element and pseudo equal-ripple curves have been removed by dissipation. Evidently, it is inherently difficult for a filter to produce ripples in the presense of dissipation, and to accomplish this a large

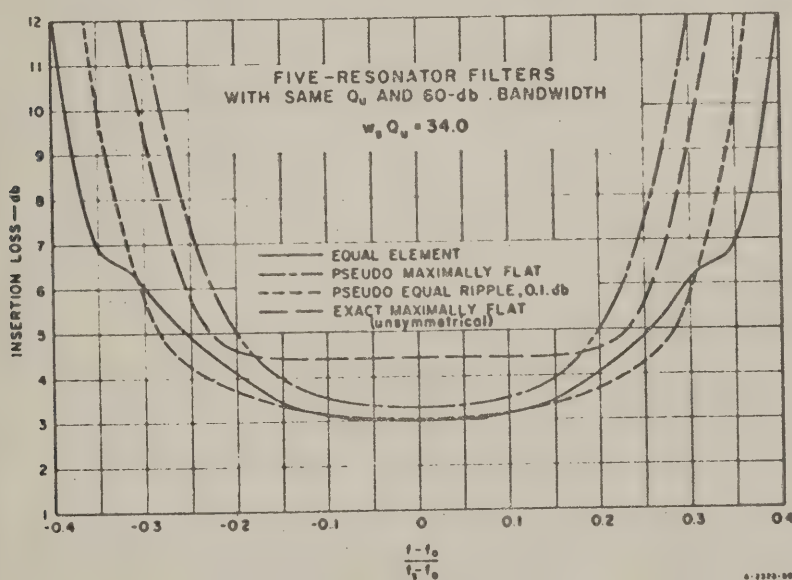


FIG. 23-6
PASS-BAND INSERTION-LOSS CURVES FOR FOUR DIFFERENT
FIVE-RESONATOR FILTER DESIGNS

amount of reflection loss must be introduced thus yielding a high pass-band insertion loss. This conclusion does not apply however, to the pseudo-equal-ripple case where the ripples of the nondissipative prototype are allowed to diminish or disappear in the presence of dissipation. In fact, Figs. 23-5 and 23-6 show that the pseudo-equal-ripple designs are superior to the pseudo maximally flat designs as far as both minimum loss and pass-band shape are considered.

2. CENTER-FREQUENCY LOSS

The approximate formula for center-frequency loss Eq. (23-1), has been checked against the exact insertion-loss curves of Figs. 23-5, and 23-6. In the case of three resonators Eq. (23-1) gives errors of only ± 0.09 and -0.07 db, respectively, for the minimum-loss (symmetrical) and pseudo maximally flat cases. Equation (23-1) should not be applied to the exact maximally flat case because of the mismatch in that design at f_0 . In the case of five resonators Eq. (23-1) gives errors of ± 0.02 , 0.00 , and ± 0.01 db respectively for the equal-element pseudo-equal-ripple, and pseudo-maximally-flat cases.

Equation (23-1) has been used to compare the center-frequency loss of filters with various response functions and the results are plotted in Fig. 23-7 versus the number of resonators. As a basis of comparison, the product of unloaded Q and relative bandwidth between 60-db points in the stop band is assumed to be equal to 100 in all cases. Since w and Q_u appear as a product in Eq. (23-1) the data will apply to any pair of values, such as 0.01 and 10 000 for example, having the product 100. Or if wQ_u differs from 100 L_0 in Fig. 23-6 should be scaled inversely proportional to wQ_u . The selection of stop-band bandwidth as the reference bandwidth instead of pass-band bandwidth is reasonable when isolation between channels is the most important consideration. In such cases, the number of resonators should be made large enough so that the pass band will equal or exceed the desired signal bandwidth.

The following cases are considered in Fig. 23-7: (1) equal-element prototype (2) pseudo-maximally flat and (3) pseudo-equal-ripple. In the latter category three different ripple levels are assumed for the nondissipative prototype—0.01 db (shown as a dash-dot curve), 0.1 db (plotted as triangular points), and 0.5 db (plotted as circular points). The latter two cases are shown only for n odd, since for n even they have

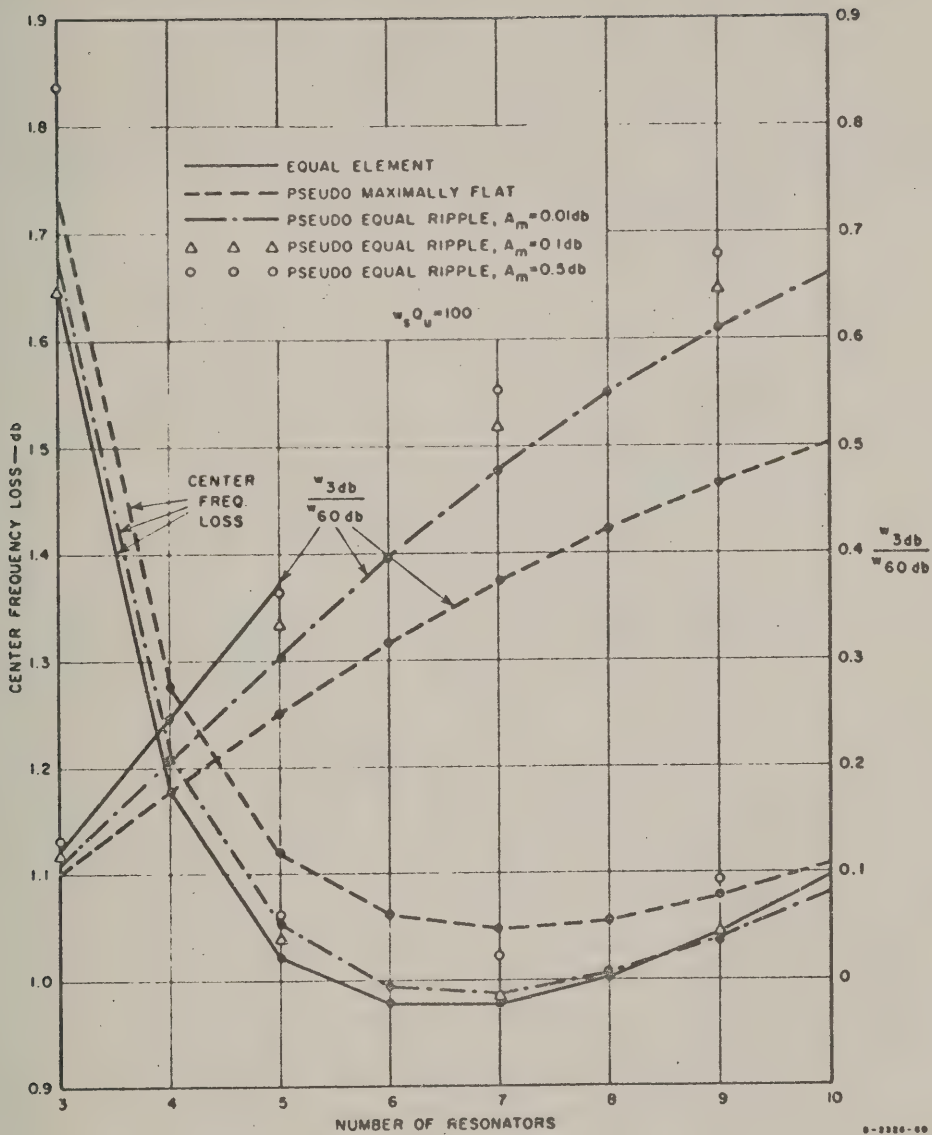


FIG. 23-7

CENTER-FREQUENCY DISSIPATION LOSS AND RELATIVE BANDWIDTH FOR VARIOUS SYMMETRICAL MULTIPLE-RESONATOR FILTERS

substantial mismatch loss at f_0 . Also plotted in Fig. 23-7 is the ratio of pass-band to stop-band bandwidth, w_{3db}/w_{60db} . These bandwidths were computed assuming no dissipation. Dissipation will reduce w_{3db} moderately, while hardly affecting w_{60db} .

A number of important facts may be deduced from Fig. 23-7: (1) the spread in loss among the different designs for a given value of n is only about 10 percent, a surprisingly small range; (2) the bandwidth ratio w_{3db}/w_{60db} increases with n , the slope being greatest for small n , and (3) the center-frequency loss drops sharply with n , reaching a minimum at $n = 6$ or 7 , and then rises slowly. This last observation is readily explained by the fact that the rapid increase in 3-db bandwidth with n reduces the loss more rapidly than the number of resonators added in cascade increases it.

The equal element curve in Fig. 23-7 is of special interest, since it was shown to approximate the minimum possible loss case, within a certain range of validity. This curve lies below the others for n up to 8, but not beyond. This behavior is reasonable, since the assumption expressed by Eq. (23-6) breaks down for $n > 5$.

The bandwidth data are also worth inspecting. For example, a ratio of bandwidths of 0.37 can be obtained by means of either five resonators with an equal element design or by seven resonators with a pseudo-maximally flat design. In either case the midband loss would be about the same.

If a stop band bandwidth other than the 60 db bandwidth were used as a reference, the general appearance of Fig. 23-7 would not change. However, quantitative differences in center-frequency loss and bandwidth ratio could be considerable. Also, the broad minimum in the loss curves would be likely to shift to another value of n .

E. DERIVATION OF FORMULAS

1. LOW-PASS EQUIVALENT OF DISSIPATIVE BAND PASS FILTER

The low-pass filter of Fig. 23-3 will now be justified as the equivalent of a band-pass filter having dissipative resonators. It has been shown previously that a band-pass filter consisting of coupled nondissipative resonators can be made equivalent in a narrow-bandwidth approximation to the lumped-constant band-pass filter of Fig. 23-8(a). The latter filter is equivalent to the low-pass prototype filter of Fig. 23-8(b),

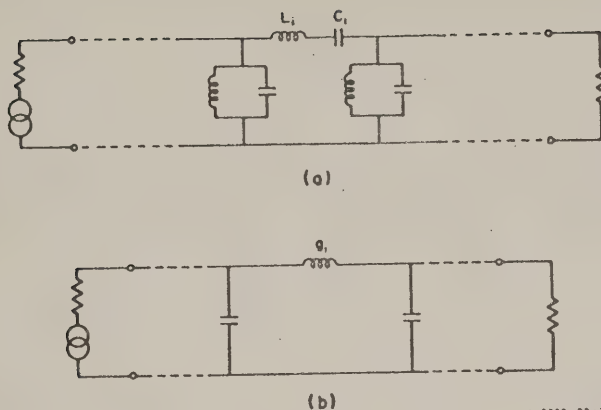


FIG. 23-8

NONDISSIPATIVE LUMPED-CONSTANT BAND-PASS FILTER (a),
AND EQUIVALENT LOW-PASS PROTOTYPE FILTER (b)

with the frequency transformation indicated in Fig. 23-1. The equivalence of Figs. 23-8(a) and 23-8(b), requires that the series reactances or shunt susceptances of corresponding arms be equal at corresponding frequencies. For example, for series arms

$$\omega' g_i = \omega L_i = \frac{1}{\omega C_i} \quad (23-10)$$

This relationship between reactances and susceptances causes equal voltages and currents to appear at all corresponding points in the two filters, and hence results in the insertion losses of the filters being the same. When the resonators have finite unloaded Q 's, one must introduce resistances and conductances into the lumped-constant band-pass circuit as indicated in Fig. 23-9(a). Then, to achieve equal dissipation loss in corresponding elements, the same resistances and conductances must be placed in the low-pass circuit of Fig. 23-9(b). Thus, for corresponding series arms

$$R_i' = R_i \quad (23-11)$$

Therefore

$$\frac{\omega' g_i}{R'_i} = \frac{1}{R_i} \left(\omega L_i - \frac{1}{\omega C_i} \right) = Q_{u,i} \left(1 - \frac{\omega_0^2}{\omega^2} \right) \quad (23-12)$$

where $Q_{u,i} = \omega L_i / R_i$ and $\omega_0^2 = 1/L_i C_i$. Now, assuming narrow bandwidth, we have

$$1 - \frac{\omega_0^2}{\omega^2} \approx \frac{\omega^2 - \omega_0^2}{\omega^2} \approx 2 \frac{\omega - \omega_0}{\omega_0}$$

If we let $\omega' = \omega_1$ and $\omega = \omega_2$ be corresponding frequencies,

$$1 - \frac{\omega_0^2}{\omega^2} \approx w, \quad (23-13)$$

where w is the relative bandwidth $(f_2 - f_1)/f_0$, as previously defined. Then combining Eqs. (23-12) and (23-13) we obtain

$$R'_i = \frac{\omega_1' g_i}{w Q_{u,i}} \quad (23-14)$$

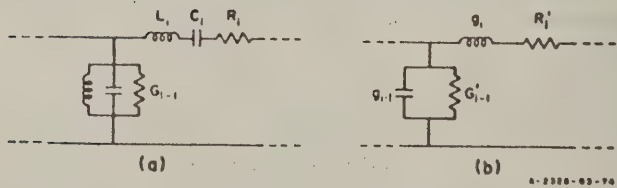


FIG. 23-9

DISSIPATIVE LUMPED-CONSTANT BAND-PASS FILTER (a),
AND EQUIVALENT LOW-PASS PROTOTYPE FILTER (b)

In a similar manner we obtain the relation for the shunt conductance G'_i :

$$G'_i = \frac{\omega'_1 g_i}{w Q_{u,i}} \quad (23-15)$$

The two identical formulas Eqs. (23-14) and (23-15), provide the desired relationship between the unloaded Q 's of the resonators in the band-pass filter and the equivalent resistances and conductances in the low-pass prototype.

2. CENTER-FREQUENCY LOSS FORMULA

Equation (23-1) can be obtained very simply from the low pass circuit of Fig. 23-3, since calculations at zero frequency only are involved. Let the load resistance, r be one ohm for convenience. It will be assumed that the resistances and conductances are small compared to unity, so that they affect the match at $\omega' = 0$ only slightly. Then the resistance looking to the right or left will be approximately one ohm anywhere in the filter. Thus in the vicinity of the i th arm, if we assume a shunt voltage of one volt, the series current will be one ampere. Then by Eqs. (23-14) and (23-15) the power dissipated in the i th arm will be

$$P_{d,i} = \frac{\omega'_1 g_i}{w Q_{u,i}} \text{ watts.} \quad (23-16)$$

The input and output powers at the i th arm are

$$P_{i,n} \approx 1 + \frac{1}{2} P_{d,i} \text{ watts}$$

$$P_{o,i} \approx 1 - \frac{1}{2} P_{d,i} \text{ watts}$$

and therefore the loss in the i th arm may be expressed in decibels as follows.

$$L_{o,i} = 10 \log_{10} \left(\frac{1 + \frac{1}{2} P_{d,i}}{1 - \frac{1}{2} P_{d,i}} \right) \approx 4.343 P_{d,i} \text{ decibels} \quad (23-17)$$

for $P_{d_i} < 0.5$. The total loss at $\omega' = 0$, or $f = f_0$, is

$$L_o \approx \sum_{i=1}^n L_{oi} = \frac{4.343\omega_1'}{\omega} \sum_{i=1}^n \frac{g_i}{Q_{ui}} \text{ decibels.} \quad (23-18)$$

The approximation in Eq. (23-17) holds within 2 percent for L_{oi} as large as 2 db. Calculations for numerous specific cases have shown that the other important approximation—that the resistance level anywhere in the filter is not affected by dissipation loss—causes very little error for L_o up to n db and only moderate error up to $2n$ db. This is true because the errors in the various terms of the summation in Eq. (23-18) tend to cancel each other.

3. STOP-BAND LOSS FORMULA

The insertion loss of the low-pass filter of Fig. 23-2 may be expressed rigorously in terms of a polynomial in ω' , as follows:

$$L = 10 \log_{10} (a_n \omega'^{2n} + a_{n-1} \omega'^{2n-2} + \dots + a_1 \omega'^2 + a_0) \text{ decibels} \quad (23-19)$$

where the constants a_i are related to the element values and terminating resistances in Fig. (23-2). In the stop band, only the higher powers of ω' are important and for ω' sufficiently large,

$$L_s \approx 10 \log_{10} (a_n \omega_s'^{2n}) \text{ decibels} \quad (23-20)$$

where the subscript s denotes a point in the stop band.

Assume that the element g_n adjacent to r is a series element. Then the ratio of voltage across r to that across g_{n-1} is

$$\frac{r}{r + j\omega_s' g_n} \approx \frac{r}{j\omega_s' g_n}$$

The admittance Y to the right of the g_{n-1} element is very much smaller than the susceptance $j\omega_s' g_{n-1}$, and hence the ratio of the voltages across g_{n-1} and g_{n-2} is

$$\frac{\frac{1}{Y + j \omega'_s g_{n-1}}}{j \omega'_s g_{n-2} + \frac{1}{Y + j \omega'_s g_{n-1}}} \approx \frac{1}{(j \omega'_s g_{n-1}) (j \omega'_s g_{n-2})}$$

If we assume the first element g_1 to be a shunt element, the ratio of input voltage to generator voltage will be

$$\frac{V_{in}}{V_g} = \frac{1}{j \omega'_s g_1}$$

Now, multiplying together all the voltage ratios in the filter

$$\left| \frac{V_{out}}{V_g} \right| = \frac{r}{\omega'_s g_1 g_2 g_3 \dots g_n} \quad (23-21)$$

The output power is

$$P_{out} = \frac{|V_{out}|^2}{r} = \frac{r |V_g|^2}{(\omega'_s g_1 g_2 \dots g_n)^2} \quad (23-22)$$

and the available power is

$$P_s = \left| \frac{V_g}{2} \right|^2 \quad (23-23)$$

Therefore, the stop-band power loss in decibels is

$$L_s = 20 \log_{10} (\omega'_s g_1 g_2 \dots g_n) - 10 \log_{10} (4r) \text{ decibels} \quad (23-24)$$

This equation assumes the terminating resistance, r , to be connected to a series element in the filter. If it were connected to a shunt element, the equation would be

$$L_s = 20 \log_{10} (\omega'_s g_1 g_2 \dots g_n) - 10 \log_{10} \left(\frac{4}{r} \right) \text{ db} \quad (23-25)$$

These formulas would be unchanged if the element g_1 next to the one-ohm generator resistor were a series element instead of a shunt element. It is also evident that reversing the direction of power flow would not alter these formulas.

REFERENCES

1. M. Dishal, "Design of Dissipative Band-pass Filters Producing Desired Exact Amplitude-Frequency Characteristics," *Proc. IRE* **37**, pp. 1050-1069 (September 1949).
2. *Reference Data for Radio Engineers*, 4th ed., pp. 188-204 (International Tel. and Tel. Corp., New York, New York, 1956). (See list of other references in footnote, p. 199.)
3. J. J. Taub and B. F. Dozier, "Design of Three-Resonator Band-Pass Filters Having Minimum Insertion Loss," *Proc. IRE* **45**, pp. 681-686 (May 1957).
4. E. G. Fubini and E. A. Guillemin, "Minimum Insertion Loss Filters," 1958 IRE Convention Record, Part 2, pp. 11-17.
5. S. B. Cohn, O. Heinz, R. M. Schiffman, F. M. T. Jones, J. K. Shimizu, and F. S. Coale, "Research on Design Criteria for Microwave Filters," Final Report, SRI Project 1331, Contract DA 36-039 SC-64625, Stanford Research Institute, Menlo Park, California (June 1957).
6. S. B. Cohn, "Direct-Coupled-Resonator Filters," *Proc. IRE* **45**, pp. 187-196 (February 1957).
7. S. B. Cohn, "Parallel-Coupled Transmission-Line-Resonator Filters," *IRE Trans. PMT-6*, pp. 223-231 (April 1958).
8. See Chapter 13 of this report.
9. S. B. Cohn, J. F. Cline, R. M. Schiffman, P. M. Sherk, "Design Data for Antenna-Multicoupler Systems," Scientific Report 1, SRI Project 2183, Contract AF 19(604)-2247, Stanford Research Institute, Menlo Park, California (August 1957).

DESIGN CRITERIA FOR HIGH-POWER FILTERS

A. GENERAL

In the microwave range, equipments often interfere with each other even when operating at different frequencies. This interchannel interference can arise from the generation and radiation of large amounts of RF energy outside of the operating bandwidth of a transmitter, or it can be the result of inadequate RF selectivity in a receiver. For example, magnetrons are known to produce strong harmonics, and are also likely to emit spurious "moding" energy at frequencies that are not harmonically related to the fundamental frequency (see Fig. 24-1). Some of these unwanted components may be at a level only 20 db below the fundamental, and hence are capable of causing serious interference to receivers in other systems. Fortunately, interchannel interference can be eliminated through the use of RF filters. High-power filters may be used between a generator and an antenna to prevent the radiation of signals outside the operating bandwidth, and low-power filters may be used at the input of a receiver to prevent the entrance of strong signals of undesired frequency. A discussion of filters in the high-power class will now be presented. Low-power filters represent less of a problem, and considerable design information for them may be found elsewhere in this report, in the final report of an earlier Stanford Research Institute program,¹ as well as in various other references.²

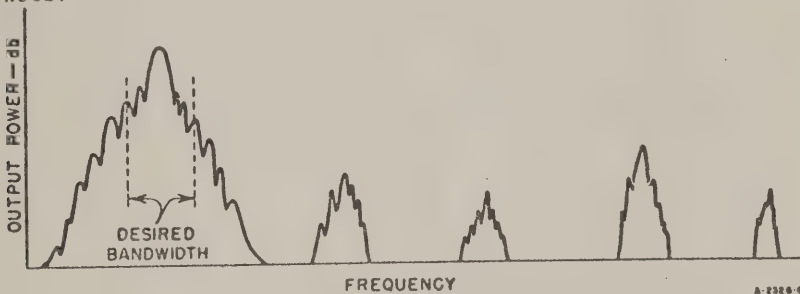


FIG. 24-1

TYPICAL OUTPUT SPECTRUM OF A MAGNETRON

All energy outside the desired bandwidth is unnecessary and contributes to interference

* This material has been published. See S. B. Cohn, "Design Considerations for High-Power Microwave Filters," *IRE Trans PGTT-7*, pp. 149-153 (January 1959).

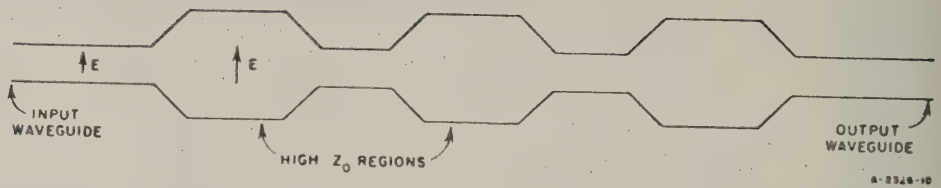


FIG. 24-2

E-PLANE VIEW OF HIGH-POWER FILTER STRUCTURE PROPOSED BY J. H. VOGELMAN

In the design of filters intended for high-power applications, one must prevent electric field strengths approaching the breakdown point. Sharp edges in high-field-strength regions must therefore be avoided, and resonant build up of the field must be limited to a safe value. One approach to the high-power filter problem has been made by J. H. Vogelmann,³ who has proposed the waveguide structure shown in Fig. 24-2. Vogelmann has shown how to compute the pass-band and spurious responses of this filter, and has verified experimentally its frequency response and high-power capability. A second approach has been used at Wheeler Laboratories in which resonant irises and resonant posts were quarter-wave coupled in a waveguide to synthesize an n -derived band-pass filter. Breakdown was avoided by evacuating the filter, which greatly increased the breakdown field strength. A third approach is to use the multiple-cavity type of band pass filter, in which inductive windows or posts are used for coupling the waveguide resonators. The power-handling capacity of this configuration has been studied recently at Stanford Research Institute, and it is shown in this chapter that this filter can have as large a power rating as desired, up to the full rating of the termination waveguide.

B. POWER HANDLING FORMULAS FOR MULTIPLE RESONATOR FILTERS

A multiple-resonator band-pass filter can be designed^{1,4,5} to have the response function of a lumped-constant low pass prototype filter, where, through an appropriate transformation, zero frequency for the latter corresponds to the center of the pass band for the former (see Fig. 24-3). Thus with the proper choice of coupling-element values and cavity lengths, the waveguide filter and prototype filter of Fig. 24-4 are equivalent. In this figure, $g_1, g_2, \dots, g_1, \dots, g_n$ are element values of the prototype filter (in farads for i odd and henries for i even);⁶ b_T is the height of the terminating guides, $b_1, b_2, \dots, b_1, \dots, b_n$ are cavity heights,

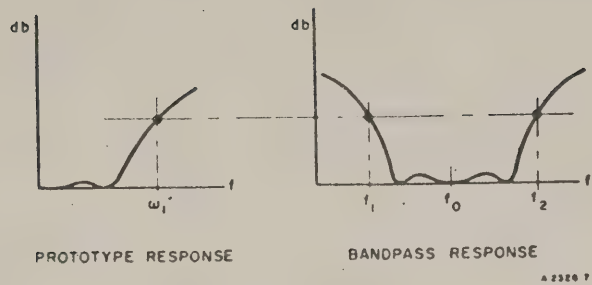


FIG. 24-3

CORRESPONDENCE BETWEEN LOW-PASS PROTOTYPE
RESPONSE AND EQUIVALENT BAND-PASS RESPONSE

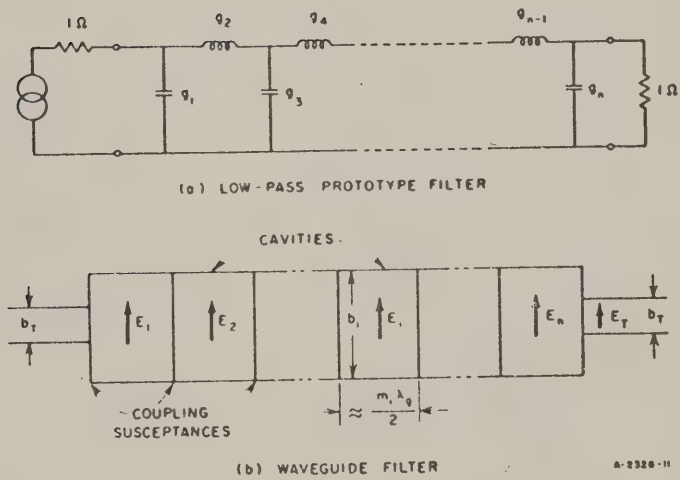


FIG. 24-4

LOW-PASS PROTOTYPE FILTER AND EQUIVALENT
WAVEGUIDE-CAVITY FILTER

$m_1, m_2, \dots, m_i, \dots, m_n$ are integers equal to the cavity lengths in half guide wavelengths, E_T is the maximum electric field strength in the matched output waveguide, and $E_1, E_2, \dots, E_i, \dots, E_n$ are the maximum electric field strengths in the cavities. In terms of these quantities, the cavity field strengths at the center of the pass band are given by the following formula, which is derived in Section E:

$$E_i = E_T \frac{\lambda_0}{\lambda_{g0}} \sqrt{\frac{2g_i \omega'_1 b_T}{m_i \pi w b_i}} \quad (24-1)$$

where $w = (f_2 - f_1)/f_0$, and where $\omega'_1 = 2\pi f'_1$ for the prototype filter and f_1 and f_2 for the band-pass filter are corresponding points of equal insertion loss (see Fig. 24-3). Note that ω'_1, f_1 , and f_2 may be taken as desired either at the

edges of the pass band, or at any insertion-loss level in the stop band. In this formula it is assumed that the waveguide width and guide wavelength are the same throughout.

It is desirable in a high-power multiple-cavity filter to have equal electric field strengths in the cavities, since this condition maximizes the power-handling capacity for a given degree of selectivity. Examination of Eq (24-1) shows that for cavities of equal size, the condition for equal electric field strength at the pass-band center is that g_1, g_2, \dots, g_n all be the same. The response function of the prototype low-pass filter for this special case is shown in Fig. 24-5 for various numbers of elements and with

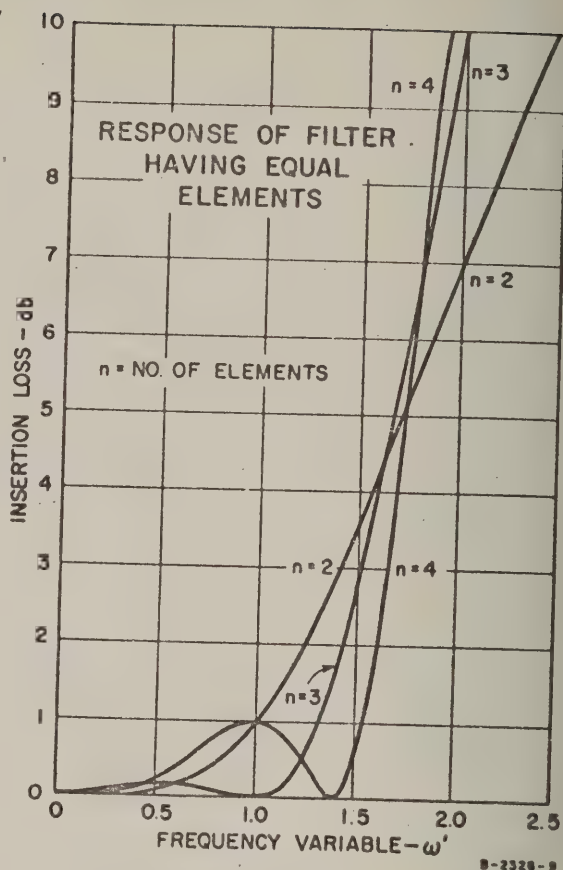


FIG. 24-5
INSERTION-LOSS-VERSUS-FREQUENCY RESPONSE
OF MULTIPLE-CAVITY FILTER WITH $g_i = 1$.

all values of g_i set equal to unity.^{*7} It is seen that only the central portion of the pass band of the equivalent band-pass filter can be used if the insertion loss (due to reflection) is to be low.

Figure 24-6 shows how the electric field strengths vary with frequency for the case of $g_i = 1$ in the prototype filter. These curves were computed from the prototype filter, recognizing that the voltages across the capacitances and the currents through the inductances are proportional to the field strengths in the respective cavities. It is seen in Fig. 24-6 that the field strengths are equal only at $\omega' = 0$, that is, at the center of the pass band of the equivalent bandpass filter. The power rating at any frequency with respect to the power capacity at band center is equal to the square of the reciprocal of the largest relative electric field strength at that frequency. Thus, for example, in the case of a four-cavity filter having $g_i = 1$, the power capacity at $\omega' = 0.4$ is 80 percent of that at $\omega' = 0$, and at $\omega' = 1$ it is 50 percent.

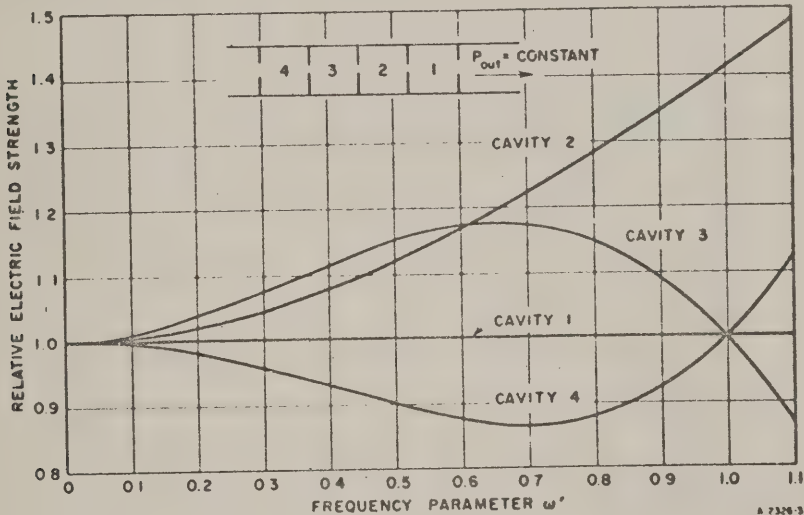


FIG. 24-6
EFFECT OF FREQUENCY ON ELECTRIC FIELD STRENGTHS
IN MULTIPLE-CAVITY FILTER WITH $g_i = 1$

* The general formula for the response function of an equal-element low-pass filter has been given by A. W. Lawson and R. M. Fano.

The power-handling capacity of the filter is defined best as a percentage of the power rating of the terminating waveguide. Thus, if the filter and terminating waveguide are under equal air pressure, the relative power capacity is as follows:

$$\text{Relative power capacity} = \left(\frac{E_T}{E_i} \right)^2 \cdot 100\% \quad (24-2)$$

where E_i is the largest of the cavity field-strength values in the filter at the frequency in question. Hence,

$$\text{Relative power capacity} = \frac{a_i \pi w b_i}{2g_i \omega'_1 b_T} \left(\frac{\lambda_{g0}}{\lambda_0} \right)^2 \cdot 100\% \quad (24-3)$$

The subscript i to be used in Eq. (24-3) is the number between 1 and n that minimizes this expression for a given n -resonator filter.

Examination of Eq. (24-1) shows that the cavity field strengths may be made equal even with unequal g_i values, if a_i and b_i are also made variable in the filter. Thus the superior maximally flat or equal-ripple response functions may be utilized without impairing the power rating of the filter, if the different cavities are properly proportioned. The larger cavities, of course, will have an increased number of undesired resonances, but the smaller cavities will tend to suppress these in the over-all response.

C. CALCULATED EXAMPLES

A few examples will now be given of the relative power capacity of typical filters. As a first example, assuming $g_i = 1$, $\omega'_1 = 1$, $w = 0.2$, $\lambda_0/\lambda_{g0} = 0.8$, $a_i = 2$, and $b_i = b_T$, Eq. (24-3) shows that at the center of the pass band the filter can be rated at 99 percent of the power rating of the terminating waveguide. As a second example, assume that 40-db of insertion loss is required at the edges of a 20 percent frequency band. For a four-cavity filter and $g_i = 1$, calculation shows that $\omega'_1 = 3.89$ at the 40-db point of the prototype filter, and therefore $\omega'_1 = 3.89$ and $w = 0.2$ are corresponding values. Now if we assume $\lambda_0/\lambda_{g0} = 0.8$, $a_i = 2$, and $b_i = 2b_T$, then the power rating at band center is 50.5 percent of the power capacity of the terminating waveguide.

As a comparison to the last example, consider the power rating of a four-cavity filter whose g_i values are designed to yield a maximally flat response,⁶ with the 40-db points still at the edges of a 20-percent frequency band. (The necessary data can be found in Chapter 13 and Fig. 18-6.) The g_i are $g_1 = g_4 = 0.765$, $g_2 = g_3 = 1.848$, and the 40-db point occurs at $\omega'_1 = 3.16$. In this case, the largest field strength occurs in the middle cavities, and, assuming the same values of λ_0/λ_{g0} , m , w , and b_i/b_T as in the last example, the filter rating at band center is equal to 33.5 percent of the power rating of the terminating waveguide. This should be compared with 50.5 percent in the preceding example.

Another interesting question is how the power rating of a multiple-resonator filter changes with the number of resonators when the stop-band bandwidth is held constant. The pass-band bandwidth will increase with the number of resonators, approaching the stop-band bandwidth in the limit, and it is therefore clear that the power rating will also increase. A calculation has been carried out for the case of equal elements and the parameters of the second example with the following results:

The advantage of using a large number of resonators is clearly evident. However, considerations of size, adjustment difficulty, and dissipation loss will place a limit of, perhaps, six to ten resonators in a practical filter.

| NUMBER OF RESONATORS | ω'_1 AT 40-db POINT | RELATIVE POWER CAPACITY (percent) |
|-------------------------|-------------------------------|--------------------------------------|
| 1 | 200 | 1.0 |
| 2 | 14.16 | 13.9 |
| 3 | 5.86 | 33.5 |
| 4 | 3.89 | 50.5 |
| 5 | 3.10 | 63.3 |
| 6 | 2.70 | 72.7 |
| 100 | 2.00 | 98.1 |

D. SYSTEM CONSIDERATIONS FOR HIGH-POWER FILTERS

It is evident from the preceding discussion that high-power filters are likely to have numerous undesired spurious responses. Figure 24-7 shows how several filters in cascade may be used to eliminate spurious responses out to very high frequencies. The filter of smallest bandwidth, Filter 1, must have larger cavities than the others in order to carry the required power. As a result it will almost inevitably have a number of spurious responses in the range of interest. These spurious responses can be suppressed by one or more filters of greater bandwidth and more widely spaced spurious responses, as shown in the figure.

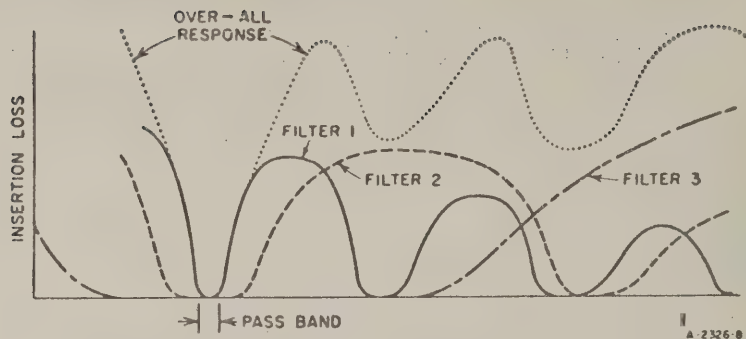


FIG. 24-7

CONNECTION OF FILTERS IN CASCADE TO ELIMINATE SPURIOUS RESPONSES

The high-power band-pass filter considered above provides stop-band insertion loss through reflection of the incident energy. In some instances this reflection may have an adverse effect on the power source, and the energy should be dissipated rather than reflected. As shown by the examples in Fig. 24-8 this may be done by means of a broad-band ferrite isolator, or by a circuit of hybrid junctions and a pair of identical band-pass filters so arranged as to divert the energy reflected from the filters into an auxiliary resistive load. Equivalent performance can be

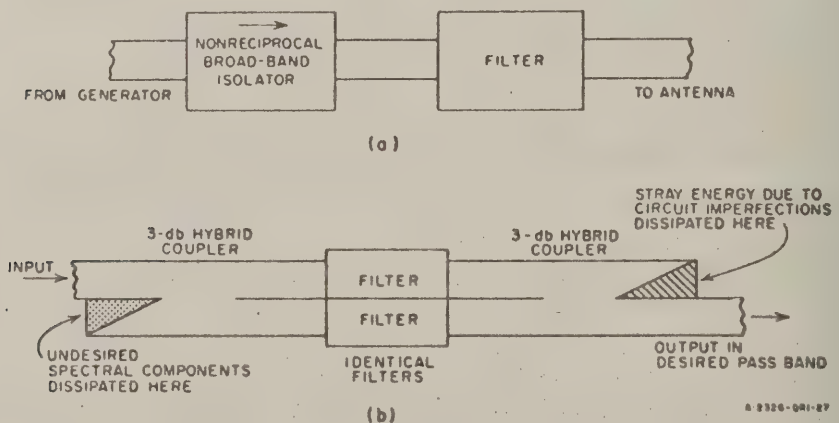


FIG. 24-8

SUGGESTED MEANS FOR DISSIPATING ENERGY REFLECTED FROM FILTER

Network in (a) utilizes a broadband nonreciprocal isolator; network in (b) utilizes a pair of identical filters and hybrid junctions

achieved by *directional filters*, which have the combined properties of directional couplers and of filters.^{1,8} Directional filters would be particularly useful for removing discrete spurious frequencies and dissipating their energy into a load.

It is believed that wide-bandwidth filters can also be achieved by leaky-wall structures like that of Fig. 24-9. Near the desired operating frequency the holes would be waveguides below cut-off, and very little energy would leak through them. Above the cut-off frequency of the holes, the energy would pass through the holes and be absorbed in the surrounding lossy material. By having a sufficient number of holes on all four walls of the waveguide, it should be possible to obtain a stop band free of spurious responses in any waveguide mode up to a very high frequency.

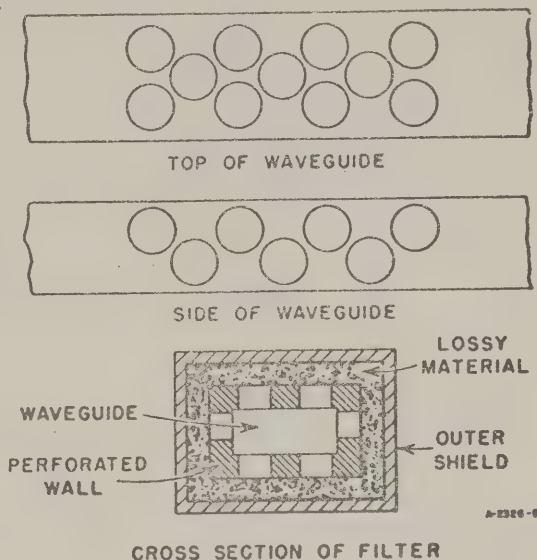


FIG. 24-9

LEAKY-WAVEGUIDE TECHNIQUES FOR DISSIPATING UNWANTED ENERGY ABOVE THE DESIRED SIGNAL FREQUENCY

E. DERIVATION OF FIELD-STRENGTH FORMULA FOR MULTIPLE-RESONATOR FILTER

The following derivation is based on an analysis of multiple-resonator filters carried out under a previous contract, and discussed in detail in Refs. 1 and 4. In that analysis, the low-pass prototype filter of Fig. 24-4(a) was related to the waveguide filter of Fig. 24-4(b) by means of the intermediary transmission-line circuit of Fig. 24-10. The equivalence of Fig. 24-10 to the waveguide filter is a direct one, with the lines of characteristic impedance Z_0 and electrical length 180 degrees representing the cavity resonators at resonance, and the lines of characteristic impedance $K_{i,i+1}$ and electrical length 90 degrees representing the coupling susceptances at the proper reference planes. It is shown in Refs. 1 and 4 that the latter length is independent of frequency to the

first order, and therefore the lines of characteristic impedance $K_{i,i+1}$ act as impedance inverting transformers over a wide band of frequencies. The equivalence of Fig. 24-10 to the low-pass prototype filter depends upon the change in frequency variable shown in Fig. 24-3.

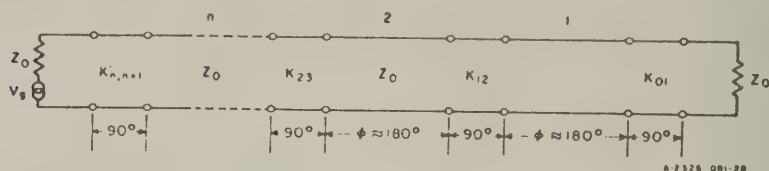


FIG. 24-10

EQUIVALENT CIRCUIT OF A MULTIPLE-RESONATOR FILTER

For convenience in the analysis, the cavities and terminating lines are assumed to have equal characteristic impedances Z_0 , and the cavity electrical lengths at resonance are assumed to be 180 degrees. At a later point in the analysis these quantities will be generalized. Also, for convenience the various elements are numbered from the load end of the filter.

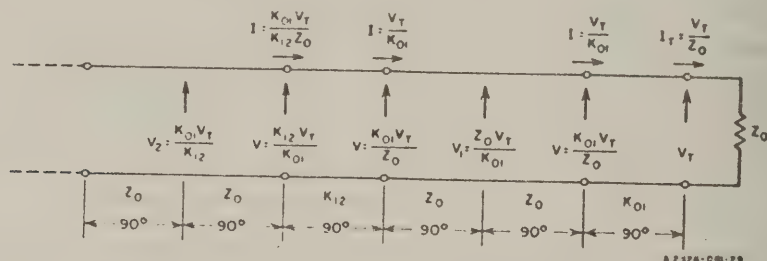


FIG. 24-11

VOLTAGE AND CURRENT MAGNITUDES IN THE EQUIVALENT MULTIPLE-RESONATOR FILTER

Figure 24-11 shows how the voltages and currents in the filter may be computed at the center frequency in terms of the voltage, V_T , across the load resistance. The phases of the various quantities are unimportant in this problem, and therefore only magnitudes of the voltages and currents are shown. The following simple relations between these magnitudes were used in the computation: for a 90-degree line of characteristic impedance Z_0 ,

$$V_{i_n} = Z_c I_{out} \quad \text{and} \quad I_{i_n} = \frac{V_{out}}{Z_c} \quad ; \quad (24-4)$$

and for a 180-degree line

$$V_{i_n} = V_{out} \quad \text{and} \quad I_{i_n} = I_{out} \quad (24-5)$$

Starting at the load end and proceeding back through the filter, one can verify the expressions in Fig. 24-11, and show that the voltages at the centers of the resonators are of the following form:

$$\begin{aligned} V_1 &= \frac{Z_0 V_T}{K_{01}} & V_2 &= \frac{K_{01} V_T}{K_{12}} \\ V_3 &= \frac{Z_0 K_{12} V_T}{K_{01} K_{23}} & V_4 &= \frac{K_{01} K_{23} V_T}{K_{12} K_{34}} \quad \text{etc.} \end{aligned} \quad (24-6)$$

In a waveguide filter the characteristic impedances $K_{i,i+1}$ are less than Z_0 and it is easily verified that the voltages V_i correspond to the maximum voltages in the various cavities.

In Refs. 1 and 4, the characteristic impedances $K_{i,i+1}$ are shown to be related to the element values g_i of the prototype filter by

$$\frac{K_{i,i+1}}{Z_0} = \frac{L}{\sqrt{g_i g_{i+1}}} \quad , \quad i = 1 \text{ to } n-1 \quad (24-7)$$

and

$$\frac{K_{01}}{Z_0} = \sqrt{\frac{L}{g_1}} \quad (24-8)$$

The formula for $K_{n,n+1}$ is not as simple in general, but in the usual case of a symmetrical waveguide filter $K_{n,n+1} = K_{01}$. (If an unsymmetrical waveguide filter is of interest, Ref. 1 or Ref. 4 should be consulted for the correct expression for $K_{n,n+1}$.) Subject to the assumption of half-wavelength cavities of height and width equal to that of the terminating waveguide, the parameter L is given by

$$L = \frac{\pi w}{2\omega'_1} \left(\frac{\lambda_{g0}}{\lambda_0} \right)^2 \quad (24-9)$$

where w is the relative bandwidth $(f_2 - f_1)/f_0$, and f_0 , f_1 , f_2 , and ω'_1 are defined in Fig. 24-3. λ_{g0} and λ_0 are the guide wavelength and free-space wavelength at the center frequency. (A more accurate form of Eq. (24-9) is given in Refs. 1 and 4, but Eq. (24-9) is sufficiently accurate for power-capacity calculations.) At this point the limitation on cavity length and height may be removed. A study of the original derivation of Eq. (24-9) shows that

$$L_i = \frac{m_i \pi w b_i}{2\omega'_1 b_T} \left(\frac{\lambda_{g0}}{\lambda_0} \right)^2 \quad (24-10)$$

where m_i is the length of the i th cavity in half guide wavelengths, b_i is the height of the cavity, and b_T is the height of the terminating waveguide. Combination of the above formulas results in

$$V_i = V_T \sqrt{\frac{g_i b_i}{L b_T}} = V_T \frac{\lambda_0}{\lambda_{g0}} \sqrt{\frac{2\omega'_1 g_i b_i}{m_i \pi w b_T}}, \quad i = 1 \text{ to } n \quad (24-11)$$

The voltages are related to the field strengths by

$$V_i = E_i b_i \quad \text{and} \quad V_T = E_T b_T \quad (24-12)$$

and hence

$$E_i = E_T \frac{\lambda_0}{\lambda_{g0}} \sqrt{\frac{2\omega'_1 b_T}{m_i \pi w b_i}} \quad (24-13)$$

where E_T is the maximum electric field strength in the output waveguide, and E_i is the maximum electric field strength in the i th cavity.

Equation (24-13) assumes that the cavity widths and terminating-waveguide widths are all equal. If this restriction is removed, one can show that Eq. (24-13) becomes

$$E_i = E_T \left[\frac{2g_i \omega'_1 a_T b_T}{\pi w a_i b_i} \right]^{1/2} \left[1 - \left(\frac{\lambda}{2a_T} \right)^2 \right]^{1/4} \left[1 - \left(\frac{\lambda}{2a_i} \right)^2 \right]^{1/4} \quad (24-14)$$

where a_i is the width of the i th cavity and a_T the width of the terminating waveguide.

REFERENCES

1. S. B. Cohn, O. Heinz, B. M. Schiffman, E. M. T. Jones, J. K. Shimizu, and F. S. Coale, "Research on Design Criteria for Microwave Filters," SRI Project 1331, Contract DA 36-039 SC-64625, Stanford Research Institute, Menlo Park, California (June 1957).
2. Ibid., Bibliography on pp. 227-231.
3. J. H. Vogelmann, "High Power Microwave Filters," RADC-711-57-148, Rome Air Development Center, Griffiss Air Force Base, New York (October 1957), ASTIA Document No. AD-131248.
4. S. B. Cohn, "Direct-Coupled-Resonator Filters," *Proc. IRE* 45, pp. 187-196 (February 1957).
5. See Chapter 15 of this report.
6. See Chapter 13 of this report for tables of element values.
7. G. L. Ragan, "Microwave Transmission Circuits," MIT Rad. Lab. Series Vol. 9, Chapter 10 by A. W. Lawson and B. M. Fano, p. 681 (McGraw-Hill Book Company, Inc., New York City, New York, 1948).
8. S. B. Cohn and F. S. Coale, "Directional Channel-Separation Filters," *Proc. IRE* 44, pp. 1018-1024 (August 1956).
9. S. B. Cohn, P. M. Sherk, J. K. Shimizu, E. M. T. Jones, "Strip Transmission Lines and Components," SRI Project 1114, Contract DA-36-039 SC-63232, Stanford Research Institute, Menlo Park, California (February 1957).

PERTURBATION ANALYSIS OF THE RESONANT FREQUENCY AND Q
OF CAVITIES LOADED WITH SMALL FERRITE SAMPLES

A. GENERAL

One of the tasks of this contract, assigned by the technical officer, was to investigate the properties of low-power microwave filters, which can be used as receiver pre-selectors, and which can be tuned by nonmechanical means over wide frequency bands. Chapters 25 and 26 describe three initial approaches to this problem utilizing ferrites. Later chapters describe techniques developed during the latter part of this contract which appear to be more practical.

During the initial part of this investigation a perturbation analysis was made of the resonant frequency and unloaded Q of cavities containing small amounts of ferrite material. The perturbation analysis is extremely accurate for cavities containing infinitesimal amounts of ferrite and can be used to obtain semi-quantitative results for ferrites occupying as much as 10 to 20 percent of the cavity volume. The amount of tuning that can be expected of a cavity containing this much ferrite is of the order of 10 percent.

A technique for connecting several directional filters that contain small amounts of ferrite and that tune over adjacent narrow frequency bands, to form a directional filter that tunes over a frequency band which is the sum of the tuning bands of the individual filters is illustrated in Fig. 25-1. The n biasing magnetic fields H_1, H_2, \dots , and H_n which are used to change the resonant frequencies of cavities can be applied either in the direction shown or else parallel to the electric field in the cavities. When it is desired to receive signals in the tuning range of a particular directional filter, its biasing field is set so that the directional filter is resonant at the desired frequency. In order to prevent other signals from passing through the other filters, each is biased so that its ferrite is at ferromagnetic resonance at the center of the tuning range of its directional filter.

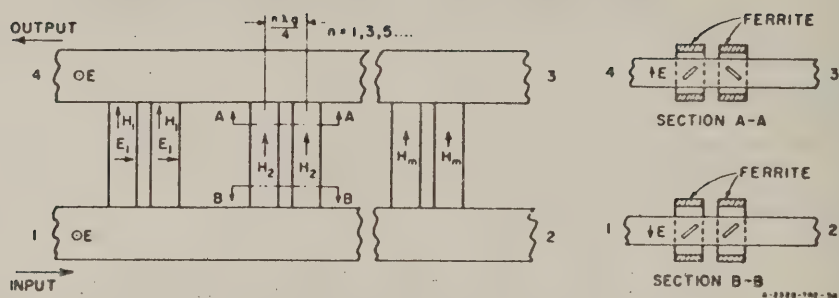


FIG. 25-1

A WIDE-BAND MAGNETICALLY TUNABLE FILTER COMPOSED OF CASCADED DIRECTIONAL FILTERS

B. VARIATION OF THE RESONANCE FREQUENCY OF A CAVITY BY MEANS OF FERRITES

In most discussions of the magnetic tuning of resonant cavities by means of ferrites, the perturbation theory of Bethe and Schwinger¹ is usually invoked. In the application of this theory, or for that matter of any available theory, there are several contributions to the total magnetic field acting on the magnetic electrons in the ferrite that are usually neglected. It is the purpose of this section to rederive the results of the Bethe-Schwinger perturbation theory, that are germane to the present problem, for the sake of easy reference; to point out the magnetic field contributions that are often neglected; and to include the effects of the Lorentz local field in some typical examples.

1. THE PERTURBATION FORMULAE

We start with the Maxwell equations (we shall use rationalized mks units throughout)

$$\nabla \times \tilde{\mathbf{E}} = -\frac{\partial \tilde{\mathbf{B}}}{\partial t}, \quad \nabla \times \tilde{\mathbf{H}} = \frac{\partial \tilde{\mathbf{D}}}{\partial t}, \quad (25-1)$$

and consider for the present a non-lossy medium. We define resonance in the case of sinusoidal time dependence as obtaining when

$$\tilde{\mathbf{E}} = \mathbf{E} \cos \omega t, \quad \tilde{\mathbf{H}} = \mathbf{H} \sin \omega t, \quad (25-2)$$

with \mathbf{E} and \mathbf{H} real. In the case of an exponential time dependence, $e^{+j\omega t}$, we define resonance to obtain when \mathbf{E} is purely real and \mathbf{H} is purely imaginary:

$$\mathbf{H} = +j\mathbf{H}', \quad \mathbf{B} = +j\mathbf{B}', \quad (25-3)$$

with \mathbf{H}' and \mathbf{B}' real.

In the sinusoidal and exponential time dependence cases, Eqs. (25-1) become respectively

$$\nabla \times \mathbf{E} = -\omega \mathbf{B}, \quad \nabla \times \mathbf{H} = -\omega \mathbf{D}, \quad (25-4a)$$

and

$$\nabla \times \mathbf{E} = -\omega \mathbf{B}', \quad \nabla \times \mathbf{H}' = -\omega \mathbf{D}, \quad (25-4b)$$

where all quantities are real. Since Eqs. (25-4a) and (25-4b) have the same form we shall not carry through both cases separately. We shall proceed from Eqs. (25-4a) and note that in the case of exponential time dependence it is really \mathbf{H}' and \mathbf{B}' that should appear in the formulas.

Let \mathbf{E} , \mathbf{D} , \mathbf{B} , and \mathbf{H} be the unperturbed resonance fields within the cavity of volume V . These quantities satisfy Eqs. (25-4a). For slightly perturbed fields we write

$$\nabla \times (\mathbf{E} + \delta \mathbf{E}) = -(\omega + \delta \omega) (\mathbf{B} + \delta \mathbf{B}),$$

$$\nabla \times (\mathbf{H} + \delta \mathbf{H}) = -(\omega + \delta \omega) (\mathbf{D} + \delta \mathbf{D}).$$

From these relations we get to first order

$$\begin{aligned}\nabla \times \delta \mathbf{E} &= -\omega \delta \mathbf{B} - \delta \omega \mathbf{B} \\ \nabla \times \delta \mathbf{H} &= -\omega \delta \mathbf{D} - \delta \omega \mathbf{D}.\end{aligned}\quad (25-5)$$

Multiplying the first of these equations by \mathbf{H} , the second by \mathbf{E} , adding the resulting expressions, and then integrating over the volume V , we get

$$\begin{aligned}& \delta \omega \int_V [\mathbf{E} \cdot \mathbf{D} + \mathbf{H} \cdot \mathbf{B}] d\tau + \omega \int_V [\mathbf{E} \cdot \delta \mathbf{D} + \mathbf{H} \cdot \delta \mathbf{B}] d\tau \\ &= - \int_V [\mathbf{H} \cdot \nabla \times \delta \mathbf{E} + \mathbf{E} \cdot \nabla \times \delta \mathbf{H}] d\tau \\ &= - \int_V [\nabla \cdot (\delta \mathbf{E} \times \mathbf{H}) + \nabla \cdot (\delta \mathbf{H} \times \mathbf{E}) - \delta \mathbf{E} \cdot \nabla \times \mathbf{H} - \delta \mathbf{H} \cdot \nabla \times \mathbf{E}] d\tau.\end{aligned}$$

Using Eqs. (25-4a) and transposing the last two terms on the right-hand side of the last equation, we obtain

$$\begin{aligned}& \delta \omega \int_V [\mathbf{E} \cdot \mathbf{D} + \mathbf{H} \cdot \mathbf{B}] d\tau + \omega \int_V [\delta (\mathbf{E} \cdot \mathbf{D}) + \delta (\mathbf{H} \cdot \mathbf{B})] d\tau \\ &= - \int_S [\delta \mathbf{E} \times \mathbf{H} + \delta \mathbf{H} \times \mathbf{E}] \cdot \mathbf{n} d\sigma \\ &= 0\end{aligned}\quad (25-6)$$

in the case of perfectly conducting cavity walls. Thus we get the formula

$$\frac{\delta \omega}{\omega} = - \frac{\int_V [\delta (\mathbf{E} \cdot \mathbf{D}) + \delta (\mathbf{H} \cdot \mathbf{B})] d\tau}{\int_V [\mathbf{E} \cdot \mathbf{D} + \mathbf{H} \cdot \mathbf{B}] d\tau}.\quad (25-7)$$

When the perturbation is due to the insertion of a magnetic or dielectric specimen in the cavity, losses are introduced into the system by the specimen. There is then a reduction in the unloaded Q , Q_0 , of the cavity as well as a shift in the resonance frequency. This may be represented (provided we use an exponential time dependence) as

$$\omega = \omega_1 + j\omega_2, \quad \omega_1 = 2\pi f.\quad (25-8)$$

It may be shown that, for accuracy to the order of $1/Q_0^2$,

$$\omega = \omega_1, \quad Q_0 = \omega_1/2\omega_2. \quad (25-9)$$

That this is a correct representation for free oscillations (the total energy, W , in a freely oscillating circuit varies as $W = W_0 e^{-\omega t/Q}$) may be seen by examining the field

$$\tilde{E} = E e^{j\omega t}$$

Then we have from Eqs. (25-8) and (25-9)

$$\tilde{E} = E e^{-(\omega/2Q_0)t} e^{j\omega t}$$

Now

$$\omega_2 = \omega_1/2Q_0$$

so that

$$\frac{\delta\omega_2}{\omega_1} = \frac{\delta\omega_1}{\omega_1} \cdot \frac{1}{2Q_0} + \delta\left(\frac{1}{2Q_0}\right) \quad (25-10)$$

Thus

$$\frac{\delta\omega}{\omega} = \frac{\delta\omega_1}{\omega_1} \left(1 + j \frac{1}{2Q_0}\right) - j \frac{\delta Q_0}{2Q_0^2} \quad (25-11)$$

In many cases in practice the first imaginary term in Eq. (25-11) is much smaller than the second, and we have

$$\frac{\delta\omega}{\omega} \approx \frac{\delta f}{f} - j \frac{\delta Q_0}{2Q_0^2} \quad (25-12)$$

2. FIELDS IN A FERRITE

In a ferrite that is magnetized in the z -direction, the internal B and H magnetic fields with harmonic time dependence are related by the well-known relations,

$$\begin{aligned} B_x &= \mu_0 (\mu_1 H_x - j\kappa H_y) , \\ B_y &= \mu_0 (j\kappa H_x + \mu_1 H_y) , \end{aligned} \quad (25-13)$$

$$B_z = \mu_0 \mu_{\parallel} H_z .$$

The general procedure, but not the details, for deriving these equations is outlined in Section C. A further word is in order with respect to the third of these equations. From the discussion in Section C just mentioned, it is noted that, even in the absence of an applied steady magnetic field, there is an effective local static field that is the resultant of the anisotropy and internal magnetic fields. In the case of an unmagnetized polycrystalline specimen, the orientation of the chosen z -axis and the direction of the local field at any point is completely random. Now the presence of the local field results in a ferromagnetic resonance phenomenon such that within a frequency range which is contained between 100 and 10,000 Mc the relative initial permeability of many ferrites is less than unity. Therefore we write $B_z = \mu_0 \mu_{\parallel} H_z$ and remark that μ_{\parallel} will be less than unity for small values of the applied field.

The coefficients μ_1 and κ in Eqs. (25-13) will be complex because of damping,

$$\mu_1 = \mu_1' - j\mu_1'' , \quad \kappa = \kappa' - j\kappa'' . \quad (25-14)$$

It should be noted that the magnetic field that appears in Eqs. (25-13) should be the total local field that acts on the magnetic electrons. However, as further noted in Section C it is not practicable to calculate the anisotropy field. Furthermore, it can be shown that the field ascribable to quantum mechanical exchange forces may fortunately be neglected at microwave frequencies. Thus for the local magnetic field, H^{loc} , we shall take

$$H^{loc} = H^* - n \cdot M + \frac{1}{3} M \quad (25-15)$$

Here H^* is the applied magnetic field in the absence of the ferrite specimen, and M is the magnetization per unit volume of the specimen. n is the

demagnetizing tensor expressed in dyadic form:

$$\bar{\bar{N}} = \mathbf{e}_x \mathbf{e}_x N_x + \mathbf{e}_y \mathbf{e}_y N_y + \mathbf{e}_z \mathbf{e}_z N_z \quad (25-16)$$

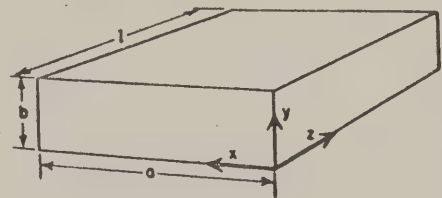
where \mathbf{e}_x is the unit vector and N_x is the demagnetizing factor in the x -direction, etc. $(1/3)M$ is the Lorentz field in a cubic crystal (most ferrites have cubic symmetry).

3. ILLUSTRATIVE EXAMPLES

We shall illustrate the use of the preceding analysis by calculating the effects of some ferrite samples in a rectangular waveguide cavity. The cavity shown in Fig. 25-2 will be supposed to operate in the TE_{10n} mode. The unperturbed field components are [we write them for an exponential time dependence and use Eq. (25-3)]

$$E_x = E_z = H_y = 0,$$

$$E_y = E_0 \sin \frac{\pi x}{a} \sin \frac{\pi z}{c},$$



A-2326-TR2-55

FIG. 25-2

RECTANGULAR CAVITY COORDINATE SYSTEM

$$H'_x = \sqrt{\frac{\epsilon_0}{\mu_0}} E_0 \frac{a}{(a^2 + c^2)^{1/2}} \sin \frac{\pi x}{a} \cos \frac{\pi z}{c}, \quad (25-17)$$

$$H'_z = -\sqrt{\frac{\epsilon_0}{\mu_0}} E_0 \frac{c}{(a^2 + c^2)^{1/2}} \cos \frac{\pi x}{a} \sin \frac{\pi z}{c},$$

where a is the width of the cavity in the x -direction, c is equal to $1/2 \lambda_g$, i.e., half the resonance wavelength in the cavity (the length of the cavity in the z -direction is $l = nc$). The height of the waveguide in the y -direction is b . The corresponding free-space wavelength is

$$\lambda = \frac{2ac}{\sqrt{a^2 + c^2}} \quad (25-18)$$

a. SMALL SPHERICAL SAMPLE

We shall consider first the case when a small spherical ferrite specimen is placed in the part of the cavity where the electric field is zero, for example, where $x = a/2$, $y = b/2$, $z = 0$. A steady magnetic field is assumed in the z -direction.

The demagnetizing factors for a sphere are

$$N_x = N_y = N_z = \frac{1}{3}. \quad (25-19)$$

Thus the demagnetizing and Lorentz fields cancel in a sphere. The only non-vanishing component of the magnetic field in the spherical specimen is H_z and therein

$$\mathbf{H} \cdot \mathbf{B} = \mu_1 \mu_0 H_z^2. \quad (25-20)$$

Assuming for the sake of simplicity that the sphere of ferrite material is small enough so that we may consider the field to be constant over the volume ΔV of the sphere, we get from Eqs. (25-7), (25-12), (25-17), (25-18), and (25-20) the result

$$\frac{\delta f}{f} - j \frac{\delta Q_0}{2Q_0} = -(\mu_1 - 1) \frac{\Delta V}{V} \frac{\lambda^2}{2b} \quad (25-21)$$

where V is the volume of the cavity. Thus, noting Eq. (25-14), we have

$$\mu_1' - 1 = - \frac{\delta f}{f} \frac{V}{\Delta V} \frac{2c}{\lambda^2}, \quad (25-22)$$

$$\mu_1'' = - \frac{\delta Q_0}{2Q_0^2} \frac{V}{\Delta V} \frac{2c}{\lambda^2}. \quad (25-23)$$

The relations of Eqs. (25-22) and (25-23) have been written in the form that is appropriate when one wishes to determine μ_1' and μ_1'' from measurements of the changes in resonance frequency and Q_0 . A spherical sample is most convenient for this purpose because of the simplicity of the expressions. The latter is due to the cancelling of the demagnetizing and Lorentz fields.

For the purpose of tuning a cavity magnetically, one is interested in the variation $\delta f/f$ as the steady magnetic field, H_0 , is varied. This variation is thus dependent upon the variation of μ'_1 as a function of H_0 .

b. THIN RECTANGULAR SLABS. I

We shall consider here the case where thin slabs of ferrite material of length $l = nc$, width b , and thickness t are placed in the cavity adjacent to the faces $x = 0$ and $x = a$. The static magnetic field will here again be assumed to be in the z -direction.

The demagnetizing factors for a thin plane specimen with the orientation stated above are²:

$$N_x = 1; \quad N_y = N_z = 0. \quad (25-24)$$

From Eq. (25-15) we find that the local magnetic field is

$$H_x^{loc} = H_x^a - \frac{2}{3} M_x,$$

$$H_y^{loc} = \frac{1}{3} M_y, \quad (25-25)$$

$$H_z^{loc} = H_z^a + \frac{1}{3} M_z.$$

For obtaining the values of the components of M that occur in Eqs. (25-25), we have first of all the Polder relations between the components of B and of H as given by Eqs. (25-13). We also have the further relation

$$B = \mu_0 (H + M). \quad (25-26)$$

² The demagnetizing factors in the y - and z -directions are very small when the thickness t is very small compared with the dimensions c and l . Instead of introducing the concept of demagnetizing factors in this case, one may use simply the continuity of the tangential component of the H field and of the normal component of the B field at the surface of the plane specimen, with results identical to those obtained below using the demagnetizing factors of Eq. (25-24).

Thus we find that, in general,

$$\begin{aligned}M_x &= (\mu_1 - 1)H_x - j\kappa H_y \\M_y &= j\kappa H_x + (\mu_1 - 1)H_y \\M_z &= (\mu_{11} - 1)H_z\end{aligned}\quad (25-27)$$

For the components of \mathbf{H} in Eqs. (25-27), it is logical to take the components of the internal field \mathbf{H}^i , where

$$\mathbf{H}^i = \mathbf{H}^e - \mathbf{n} \cdot \mathbf{M} \quad (25-28)$$

From Eqs. (25-27) and (25-28) we find for the present case:

$$M_x = \frac{\mu_1 - 1}{\mu_1} H_x^e, \quad M_y = \frac{j\kappa}{\mu_1} H_x^e, \quad M_z = (\mu_{11} - 1)H_z^e \quad (25-29)$$

Thus from Eqs. (25-25), (25-26), and (25-29), we have in the ferrite

$$\begin{aligned}B_x &= \mu_0 \left(\frac{4\mu_1 - 1}{3\mu_1} \right) H_x^e \\B_y &= \mu_0 \frac{4}{3} \frac{j\kappa}{\mu_1} H_x^e \\B_z &= \mu_0 \left(\frac{4\mu_{11} - 1}{3} \right) H_z^e\end{aligned}\quad (25-30)$$

Let the permittivity of the ferrite be ϵ ($\epsilon = \epsilon_r \epsilon_0$, where ϵ_r = dielectric constant). The electric field is tangential to the surfaces of the ferrite slabs (it is assumed that the ferrite material does not change appreciably the field distribution in the cavity) and must be continuous there. We assume that the thickness of the slabs is small enough so that the field has the same form in the ferrite medium as the unperturbed field. We now use Eqs. (25-17) and (25-30) to calculate the integrals of Eq. (25-7). We obtain

$$\begin{aligned}
\frac{\delta\omega}{\omega} = & \frac{t}{a} \frac{a^2}{a^2 + c^2} \left\{ \frac{5\mu_1^2 + 2 - 7\mu_1 + 4\kappa^2}{9\mu_1^2} \right\} \left\{ 1 - \frac{\sin \frac{2\pi t}{a}}{\frac{2\pi t}{a}} \right\} \\
& + \frac{4}{3} \frac{t}{a} (1 - \mu_H) \frac{c^2}{a^2 + c^2} \left\{ 1 + \frac{\sin \frac{2\pi t}{a}}{\frac{2\pi t}{a}} \right\} \\
& - \frac{t}{a} (\epsilon_r - 1) \left\{ 1 - \frac{\sin \frac{2\pi t}{a}}{\frac{2\pi t}{a}} \right\}
\end{aligned} \quad (25-31)$$

For very thin samples (i.e., for $2\pi t/a \ll 1$) and with small applied static magnetic fields, the second term in Eq. (25-31) predominates in the case of many ferrites. In this case we get from Eq. (25-31)

$$\frac{\delta f}{f} \approx \frac{8}{3} \frac{t}{a} (1 - \mu_H') \frac{c^2}{a^2 + c^2} \quad (25-32)$$

$$\frac{\delta Q_0}{Q_0} \approx - \frac{16}{3} Q_0 \frac{t}{a} \mu_H'' \frac{c^2}{a^2 + c^2}$$

c. THIN RECTANGULAR SLABS, II

Let us consider next the case when the applied static magnetic field is in the positive y -direction. In place of Eq. (25-13) we now have

$$\begin{aligned}
B_x &= \mu_0 (\mu_1 H_x + j\kappa H_y) \\
B_y &= \mu_0 \mu_H H_y \\
B_z &= \mu_0 (-j\kappa H_x + \mu_1 H_z)
\end{aligned} \quad (25-33)$$

and in place of Eq (25-27)

$$\begin{aligned} M_x &= (\mu_1 - 1)H_x + j\kappa H_z, \\ M_y &= (\mu_1 - 1)H_y, \\ M_z &= -j\kappa H_x + (\mu_1 - 1)H_z. \end{aligned} \quad (25-34)$$

From Eqs. (25-28) and (25-34) we get

$$\begin{aligned} M_x &= \frac{\mu_1 - 1}{\mu_1} H_x^0 + \frac{j\kappa}{\mu_1} H_z^0, \quad M_y = (\mu_1 - 1)H_y^0, \\ M_z &= \frac{-j\kappa}{\mu_1} H_x^0 + \left(\frac{\mu_1^2 - \kappa^2}{\mu_1} - 1 \right) H_z^0. \end{aligned} \quad (25-35)$$

Finally, by combining Eqs. (25-25), (25-35), and (25-26), we obtain for the particular case when H_y^0 is zero, as in Eq. (25-17),

$$\begin{aligned} B_x &= \mu_0 \left\{ \frac{4\mu_1 - 1}{3\mu_1} H_x^0 + \frac{1}{3} \frac{j\kappa}{\mu_1} H_z^0 \right\}, \\ B_y &= 0, \\ B_z &= \mu_0 \left\{ -\frac{4}{3} \frac{j\kappa}{\mu_1} H_x^0 + \left(\frac{4}{3} \frac{\mu_1^2 - \kappa^2}{\mu_1} - \frac{1}{3} \right) H_z^0 \right\} \end{aligned} \quad (25-36)$$

We shall let

$$\frac{\mu_1^2 - \kappa^2}{\mu_1} = \mu_e \quad (25-37)$$

μ_e is the effective relative permeability in the case of an infinite medium in which there propagates a plane wave in a direction that is perpendicular to the direction of the applied static magnetic field. Evaluating the integrals in Eq. (25-7), we find

$$\begin{aligned}
\frac{\delta\omega}{\omega} = & \frac{t}{a} \frac{a^2}{a^2 + c^2} \left\{ \frac{5\mu_1^2 + 2 - 7\mu_1 + 4\kappa^2}{9\mu_1^2} \right\} \left\{ 1 - \frac{\sin \frac{2\pi t}{a}}{\frac{2\pi t}{a}} \right\} \\
& - \frac{t}{a} \frac{c^2}{a^2 + c^2} \cdot \frac{1}{9} \left\{ 4 \left(\mu_e^2 + \frac{\kappa^2}{2\mu_1^2} \right) + 7\mu_e - 11 \right\} \left\{ 1 + \frac{\sin \frac{2\pi t}{a}}{\frac{2\pi t}{a}} \right\} \\
& - \frac{t}{a} (\epsilon_r - 1) \left\{ 1 - \frac{\sin \frac{2\pi t}{a}}{\frac{2\pi t}{a}} \right\} \quad (25-38)
\end{aligned}$$

For very thin slabs this becomes

$$\frac{\delta\omega}{\omega} \approx - \frac{2t}{a} \frac{c^2}{a^2 + c^2} \frac{1}{9} \left\{ 4 \left(\mu_e^2 + \frac{\kappa^2}{2\mu_1^2} \right) + 7\mu_e - 11 \right\} \quad (25-39)$$

$\delta f/f$ is obtained by taking the real part of Eq. (25-39).

C. DISCUSSION OF THE ACCURACY OF THE ASSUMED MATHEMATICAL MODEL OF THE FERRITE

The equation of motion for the magnetization M at a point in a ferrite specimen has the form

$$\frac{dM}{dt} = -|\gamma|\mu_0 M \times [H^* - N \cdot M + H_{ani.} + H_w] + \frac{\alpha}{M} \left[M \times \frac{dM}{dt} \right] \quad (25-40)$$

Here γ is the gyromagnetic ratio, $|\gamma| = g|e|/2m$; H^* is the value of the applied field, external to the specimen (assumed to be of a shape for which demagnetizing factors can be defined). In general, H^* has a static part and a time dependent part. N is the demagnetizing tensor expressed in dyadic form. $H_{ani.}$ and H_w are effective fields that take into account respectively the ferromagnetic anisotropy and the so-called Weiss molecular field that is responsible for ferro- and ferri-magnetism. The last term in Eq. (25-40) takes into account damping (α is a phenomenological damping constant). It results in the fact that all the permeability coefficients

are complex. The Lorentz field, $(1/3)M$ in the case of cubic symmetry does not appear in the equation of motion because it obviously has no effect for most ferrites (that have cubic symmetry) since $M \times M$ vanishes.

The anisotropy field is the property of a single crystal. It is the field that describes the effect of the observed magnetic anisotropy. This anisotropy arises because the electron spins experience the symmetry properties of the crystal through the quantum mechanical medium of spin-orbit interaction, the orbital wave functions having the symmetry of the crystal. In the case of the polycrystalline material used in practice, the net effect of the anisotropy field can be obtained only by averaging over all the randomly oriented crystals. A calculation of this type has not as yet been done; we shall neglect, therefore, anisotropy except for noting that, because of associated ferromagnetic resonance phenomena, it causes the relative permeability to be less than unity in the absence of an applied static magnetic field, over a large frequency range. Since the anisotropy field may be of the order of a few hundred gauss, its neglect should be remembered when using results similar to those of the preceding section for small values of the applied static field.

The Weiss molecular field, ascribable to quantum mechanical exchange forces, is proportional to $\nabla^2 M$ for cubic crystals. It can be shown that the effect of this field is negligible at microwave frequencies.

If one assumes a harmonic time dependence for the time dependent quantities in Eq. (25-40) and keeps only first order quantities, one obtains the time varying components of the magnetization in terms of the components of the magnetic intensity. Combining these relations with $B = \mu_0 (H + M)$, one obtains the well-known relations of the Polder permeability tensor as given in Eq. (25-13).

It must be remembered, however, that so far the Lorentz field has not been taken into account, because it drops out of Eq. (25-40). If one has a finite magnetic specimen in a magnetic field and considers the force acting at a point in the specimen, one gets the following picture. In addition to the externally applied field, H^e , one has, for one thing, the field due to the surface charges on the surface of the specimen. This is the demagnetizing field $-N \cdot M$. Further forces at the point in question arise from all the other dipole moments in the specimen. These may be taken into account in the following way. A (fictitious) sphere is cut out of the specimen around the point in question. The field of the dipoles in

the remaining part of the specimen is equal to the field of the surface charge distribution on the surface of the resulting cavity. This is the Lorentz field. The field of the magnetic dipoles within the sphere vanishes when either these dipoles are oriented randomly or, as is the case of most ferrites, if the magnetic environment of the given point has cubic symmetry.

Thus we see that, in addition to the fields considered in connection with Eq. (25-40), the Lorentz field must be taken into account in computing the change in resonance frequency of a cavity that contains a ferrite specimen.

D. DISCUSSION OF RESULTS

The theoretical derivation of the magnetic tuning of rectangular resonant cavities containing slabs of ferrite is similar to that of Jones, Cacheris, and Morrison,² but differs in three respects: first, the present analysis includes the effect of the Lorentz field; second, the unloaded Q of the cavity is computed; and third, the fields within the ferrite are determined through the concept of demagnetizing factors rather than by directly matching boundary conditions at the ferrite-air interface. The utility of the demagnetizing factors is illustrated in the discussion of the magnetic tuning effect of a small spherical ferrite sample.

Examination of the measured values of the permeability components^{2,3} reveals that the operating region of low magnetic field will be the most suitable for the purpose of tuning cavities when one takes into account the possible losses and the values of the required static magnetic field. Because μ_z increases with applied field, it may be seen that if the biasing field is oriented in the z -direction, increasing the biasing field will decrease the resonant frequency. On the other hand, if the control field is oriented along the Y -axis, increasing the magnetic field will increase the resonant frequency.

REFERENCES

1. H. A. Bethe and J. Schwinger, NDRC Rep. D1-117, Cornell University, Ithaca, New York (March 1943).
2. G. R. Jones, J. C. Cacheris and C. A. Morrison, "Magnetic Tuning of Resonant Cavities and Wide-Band Frequency Modulation of Klystrons," Proc IRE, Vol. 44, No. 10, pp. 1431-1438, (October 1956).
3. R. C. LeGraw and E. G. Spencer, "Tensor Permeabilities of Ferrites Below Magnetic Saturation," IRE Convention Record, Part 5, pp. 66-74, (1956).

TWO FERRITE-LOADED FILTER STRUCTURES

In Chapter 25, a perturbation analysis was presented of the tuning characteristics of cavities loaded with small pieces of ferrite. It was shown that tuning ranges of about 10 percent could be obtained in this manner. A technique was proposed for connecting several directional filters that contain small amounts of ferrite and that tune over adjacent narrow frequency bands, to form a composite directional filter that tunes over a frequency band that is the sum of the tuning bands of the individual filters.

In this chapter two other techniques are described for utilizing ferrites to tune over a wide frequency range. The quantitative performance of one of these filters is determined by utilizing the results of some microwave measurements while the performance of the other filter is determined by means of a perturbation analysis.

A. FERRITE-LOADED CAVITIES WITH MULTIPLE RESONANCES

1. DESCRIPTION OF SYSTEM

The basic element in the first of these tunable filters is a ferrite-loaded transmission-line cavity that is several half-wavelengths long. The tuning range of such a cavity can be made to cover a broad continuous band if sufficient phase shift is obtainable so that the electrical length of the cavity can be changed by 180 electrical degrees as the ferrite magnetization is varied. Thus referring to Fig. 26-1, which shows the natural resonant frequencies of the cavity when the ferrite is in the unmagnetized condition, it is seen that the cavity may be made to resonate at any frequency within the band of frequencies from f_1 to f_2 .

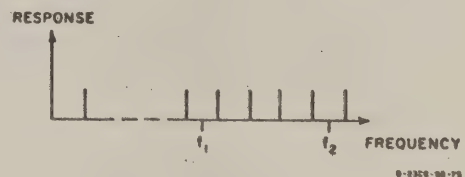


FIG. 26-1

MULTIPLE RESPONSES OF A
TRANSMISSION-LINE RESONATOR

where 180-degree phase shift is obtainable, by shifting the nearest resonant response to the desired frequency.

2. EXPERIMENTAL MEASUREMENTS ON FERRITE PHASE SHIFTER

A single cavity resonant in several different modes will have undesirable spurious responses and a stop band rejection insufficient for many applications. These spurious responses may be eliminated and the stop band rejection increased by cascading several ferrite loaded filters of different lengths. The way in which the spurious responses are eliminated is illustrated in Fig. 26-2, for the case of three cascaded filters, which shows that for the particular setting of the phase shifters in each cavity the composite filter transmits signals only at the desired frequency f_0 .

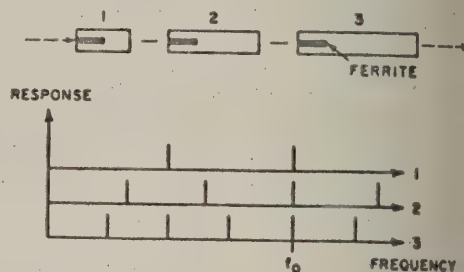


FIG. 26-2

CASCADE OF FILTER RESONATORS SHOWING METHOD OF ELIMINATING UNWANTED MODAL RESPONSES

At the time this investigation was started there were no easily accessible data on the frequency behavior of ferrite phase shifters. Therefore a series of measurements were performed on a very promising type of reciprocal waveguide phase shifter recently described by Reggia and Spencer¹ to determine its operating bandwidth. This phase shifter has low attenuation and produces large phase changes as the applied field is varied from zero to the order of a hundred oersteds. The phase shifter consists of a rectangular waveguide operating in the dominant TE_{10} mode with an axial ferrite rod lying along its centerline. The applied magnetic field is directed along the axis of the ferrite.

The phase shifter measured utilized a length of standard, rectangular X-band waveguide having inside cross-sectional dimensions of 0.9 by 0.4 inch. The ferrite used was a cylinder of Ferramic R-1 0.250 inch in diameter and 4.00 inches long. Reflections from the ends of the rod were small because each end of the rod was tapered over a length of 0.71 inch. The change in phase shift, $\Delta\phi$, and the change in the dissipation loss (insertion loss minus reflection loss) with applied field were measured

in the bridge circuit shown in Fig. 26-3. Measurements were made at a number of discrete frequencies between 8.2 and 10.6 kMc and the DC magnetizing field was varied from 0 to 77 oersteds. The results of these measurements are shown in Fig. 26-4.

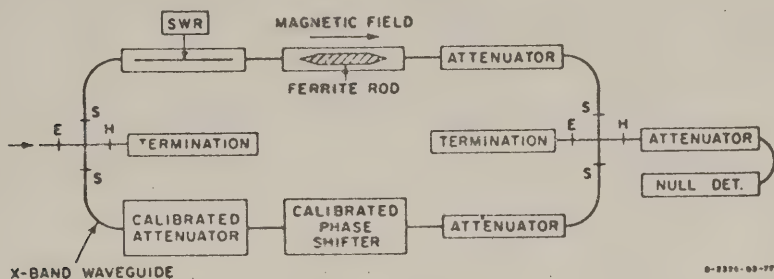


FIG. 26-3
SCHEMATIC DIAGRAM OF PHASE COMPARISON CIRCUIT

To make full use of these data in filter design, it is necessary to know not only the differential phase shift $\Delta\phi$ for various applied magnetic fields, but also the insertion phase shift $\Delta\phi_0$, for zero applied field.

Figure 26-5 gives values of insertion phase shift per unit length vs. frequency for the phase shifter. An uncertainty of 360m degrees— $m = 0, 1, 2$ —is inherent in the phase shift measurements from which this curve was calculated but this indeterminacy was removed, as explained later. Although all phase shift measurements were made using a ferrite rod tapered on both ends, the measured phase shift was in each case converted to phase shift per unit length by considering that the tapered rod and a uniform rod of the same diameter but different fixed length are approximately equivalent at all frequencies considered. The length of uniform rod equivalent to the tapered rod was calculated for one frequency ($f = 9.1$ kMc) with the aid of Fig. 13 of the paper by Reggia and Spencer¹ (which gives guide wavelength λ_{gr} vs. rod diameter), and the following formula for insertion phase shift in degrees, for a ferrite rod of effective length l_r ,

$$\Delta\phi_0 = 360 l_r \left(\frac{1}{\lambda_{gr}} - \frac{1}{\lambda_g} \right) \quad (26-1)$$

Thus by substituting in Eq. (26-1) $\lambda_g = 4.75$ cm ($f = 9.1$ kMc), $\lambda_{gr} = 2.7$ cm (from the Fig. 13 mentioned above) and $\Delta\phi_0 = 450$ degrees (measured value)

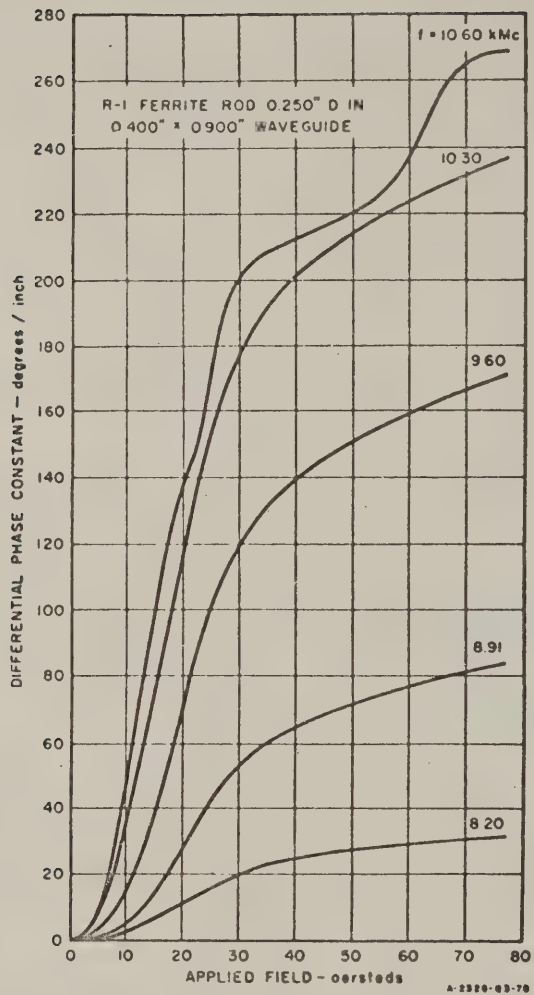


FIG. 26-4(a)

DIFFERENTIAL PHASE CONSTANT VS. APPLIED MAGNETIC FIELD

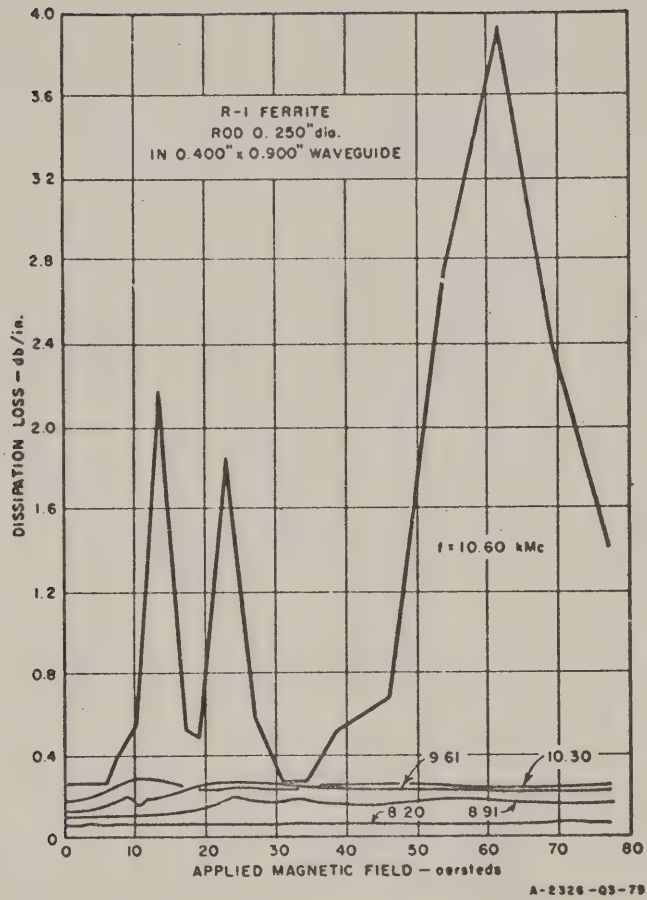


FIG. 26-4(b)
DISSIPATION LOSS VS. APPLIED MAGNETIC FIELD

we find $l_f = 7.82$ cm, or 3.08 inches. This value of l_f is not unreasonable, because the actual ferrite length is 4 inches, hence the indeterminacy of 360m degrees is removed, with $m = 0$. As a second check, a calculation of l_f at 8.2 kMc was made by comparing, at this frequency,, the insertion phase shifts of two tapered ferrite rods differing in length by 2 inches. In this case we measured a phase difference of 226 degrees (again accurate only to within +360m degrees, but we now assume $m = 0$). The measured differential phase shift is $\Delta\phi_0 = 352$ degrees at 8.2 kMc, whence $l_f = 3.11$ inches, which value is in close agreement with that previously calculated. It appears certain, therefore, that $m = 0$ in both of the above cases, and that Fig. 26-5 is correct as shown.

In these graphs only the rising magnetic field characteristics are given; it is to be noted, however, that there is a pronounced hysteresis effect. This can be seen in the curve of Fig. 26-6 which gives differential

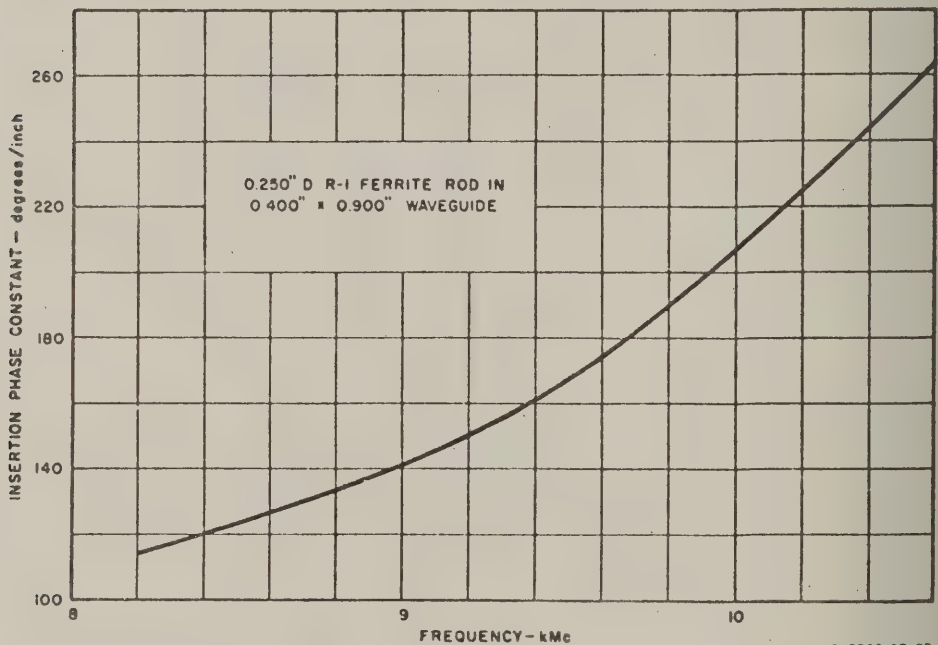


FIG. 26-5

INSERTION PHASE SHIFT VS. FREQUENCY FOR ZERO APPLIED MAGNETIC FIELD

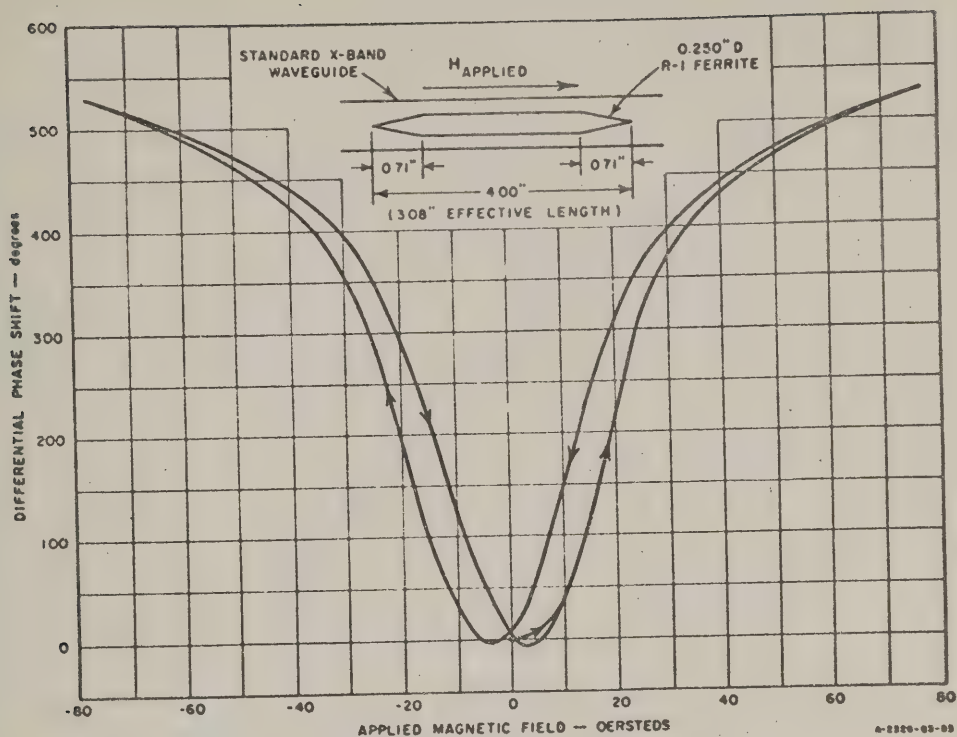


FIG. 26-6
PHASE SHIFT HYSTERESIS LOOP AT 9.6 kMc

phase shift for both increasing and decreasing DC fields, and for reversed field.

3. UTILIZATION OF DATA

The unloaded Q , Q_0 of a magnetically tunable resonator which is several half wavelengths long and partially filled with a well-matched ferrite rod can be obtained from the measured performance of ferrite phase shifters with the aid of the following formula:

$$Q_0 = \frac{\omega}{2} \frac{l_r \frac{d\beta_r}{d\omega} + l_a \frac{d\beta_a}{d\omega}}{\alpha_r l_r + \alpha_a l_a} \quad (26-2)$$

Here

$l_f + l_a$ = over-all cavity length

l_f = effective length of the ferrite rod

$\alpha_f l_f$ = dissipation loss (nepers) of the ferrite-loaded section of the cavity

αl_a = dissipation loss (nepers) of the air-filled section of the cavity

ω = radian frequency

$$\beta_f = \frac{2\pi}{\lambda_{gf}}$$

λ_{gf} = guide wavelength in ferrite-loaded section of the cavity

$$\beta = \frac{2\pi}{\lambda_g}$$

λ_g = guide wavelength in the air-filled section of cavity

$\frac{d\beta_f}{d\omega}$ = reciprocal of the group velocity in the ferrite-loaded section of the cavity

$\frac{d\beta}{d\omega}$ = reciprocal of group velocity in the air-filled section of the cavity.

The quantity $(d\beta_f/d\omega)$ can most easily be obtained from a graph of ω versus β_f . Such a graph for various values of applied magnetic field* is shown in Fig. 26-7. Also, for convenience, a frequency scale is included, and β_f is given in both radians per centimeter and degrees per centimeter. β_f was determined for various values of applied magnetic field by adding the insertion phase constant for zero applied magnetic field, the differential phase constant for varying applied field and β of the air-filled waveguide. The effect of slight mismatches was neglected in the calculations of the various phase constants of Fig 26-4 and the ω vs. β_f curves of Fig. 26-7 and this simplification appears to be justified by the smooth curves which result from these calculations.

The unloaded Q was calculated for a ferrite-loaded resonator at several pairs of values of ω and applied field by means of Eq. (26-2) and the data of Fig. 26-4 and Fig. 26-7, and these values are shown in Fig. 26-7

* The term applied magnetic field is understood here to mean the value of the field in the solenoid before the ferrite is inserted.

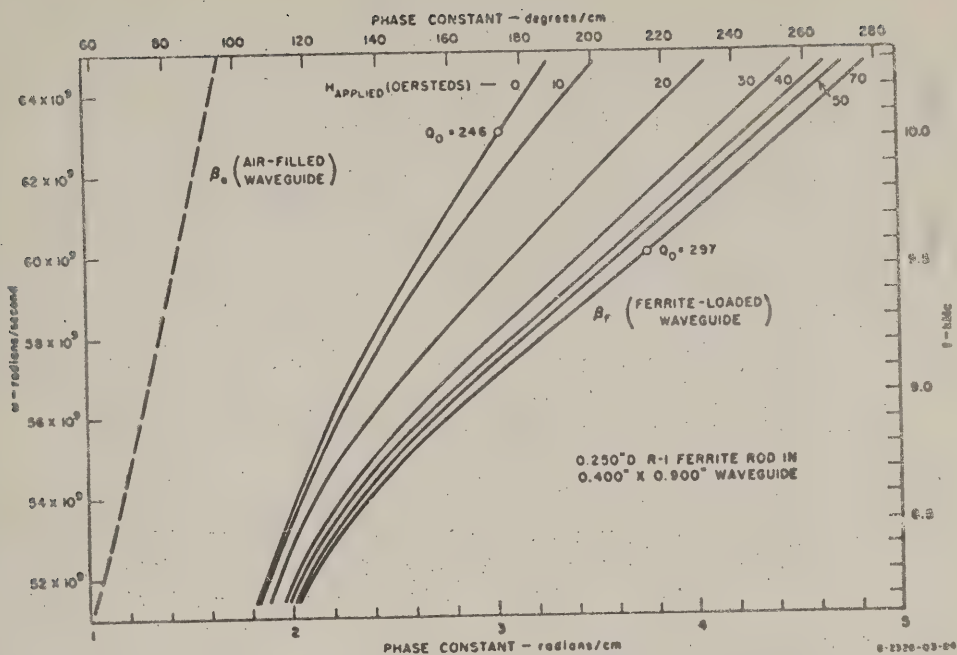


FIG. 26-7

ω - β_f CURVES FOR 1/4-INCH FERRITE ROD IN STANDARD X-BAND WAVEGUIDE

at their respective operating points. The values of Q_0 shown can be increased by adding a length of air-filled waveguide l_a . The tuning range of such a composite cavity can then be calculated, for any longitudinal mode, from Fig. 26-7 by means of the formula

$$\beta_f l_f + \beta l_a = n\pi \quad (26-3)$$

provided the two portions of the cavity are matched to each other.

Thus, from Fig. 26-4(a), one can easily determine that the (effective) length of the ferrite must be at least $(180/30) = 6.0$ inches in order to obtain 180 degrees phase shift at 8.20 kMc with an applied field of 70 oersteds. A ferrite-loaded cavity 6.0 inches long ($l_f = 15.24$ cm) will be tunable from 8.20 kMc to 10.30 kMc with a field of 70 oersteds or less before losses become excessive. In this case, Eq. (26-3) reduces to $\beta_f l_f = n\pi$, and ($n = 9$, $\beta_f = 1.85$ radians per centimeters) is the solution

that falls in the 0-70 oersted range at 8.2 kMc on Fig. 26-7. The field is about 12 oersteds for resonance at this frequency and Q_0 is calculated to be 264. As the field is reduced to zero, the cavity would tune in the $n = 9$ mode to about 8.3 kMc. To tune to a higher frequency it would be necessary to use the $n = 10$ mode corresponding to $\beta_f = 2.06$. Inspection of Fig. 26-7 shows that this mode would tune from about 8.25 to 8.65 kMc. Still higher frequencies are obtained by further increasing n . For filter cavities in which sections of air-filled waveguide have been added to obtain higher Q_0 and to form a composite filter for the purpose of suppressing unwanted modes as indicated in Fig 26-1, the loci of the points of resonance may be obtained by plotting on Fig 26-7 solutions of Eq. (26-3). There will be one locus (line segment) for each cavity and each value of n , and this plot may be used to determine suitable values of l_f and l_a and, finally, to serve as a tuning diagram. Other factors that also affect the tuning range, but which were not considered in the above argument, are the shape of the ferrite and the impedance match between the air-filled and ferrite-loaded portions of the cavity.

The experimental data and the analyses given herein indicate the performance that can be obtained from a ferrite-loaded waveguide phase shifter used as a resonator. It is seen that in order to obtain resonators having high Q it is necessary that the cavity length be greater than the length of the ferrite rod, and hence these filters would be rather bulky.

B. FERRITE TUNABLE FILTERS OPERATING NEAR FERROMAGNETIC RESONANCE

1. THEORY OF PROPOSED FILTER

The second scheme investigated here for constructing a magnetically tunable filter with a wide tuning range makes use of the dispersive properties of ferrites near ferromagnetic resonance. The actual device considered is shown in Fig. 26-8. It consists of two waveguide hybrid T's and two dispersive ferrite phase shifters, each of which is biased by means of an external magnetic field to have a slightly different ferromagnetic resonant frequency. Ideally the device operates in the following manner. Input power is equally divided by the first hybrid-T between the two arms containing the phase shifters. At frequencies either well above or well below the ferromagnetic resonance frequency, the waves passing through each phase shifter will suffer approximately the same amount of phase shift and hence they will combine in phase in the output hybrid-T and emerge

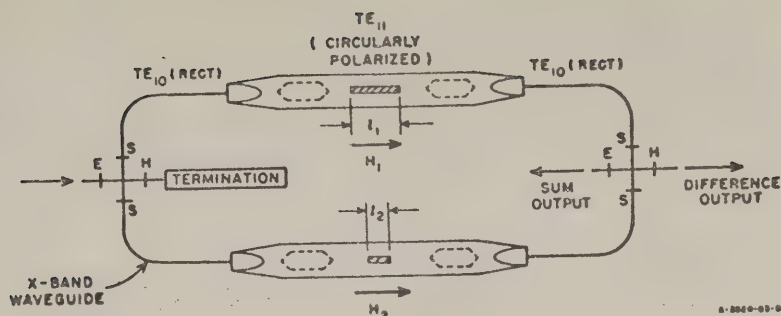


FIG. 26-8

SCHEMATIC DIAGRAM FOR FERROMAGNETIC RESONANCE BAND-SEPARATION FILTER

from the sum terminal. At frequencies near the ferromagnetic resonance frequency, where the phase delay of the phase shifters changes rapidly with frequency, the waves passing through the ferrite phase shifters will suffer unequal amounts of phase shift. At the frequency where the phase difference between the waves is 180 degrees, all the energy will emerge from the difference terminal in the output hybrid-T. Hence it is seen that at the difference terminal of the output hybrid-T the device will act as a band-pass filter while at the sum terminal it will have the characteristics of a band-rejection filter. The center frequency of these filter responses is changed by varying the biasing fields.

In an actual device the unavoidable dissipation loss in the ferrite will modify these ideal characteristics. In order to determine how serious the losses are, a theoretical study was made of a particular ferrite phase shifter. The phase shifter chosen for investigation consists of a circular waveguide that propagates a circularly polarized TE_{11} mode and which has a slim axial ferrite rod oriented along its center line. The ferrite rod is assumed to be reflectionless and ideal quarter-wave plates are assumed to exist at each end of the phase shifter to convert the circularly polarized wave into a linearly polarized wave.

2. THEORETICAL INVESTIGATION OF A FERRITE PHASE SHIFTER

The phase shift and attenuation functions of the slim ferrite rod in circular waveguide were derived by Dr. Carson Flammer. His initial assumptions, and results are summarized below.

A plane wave is first assumed to be traveling in an infinite ferrite medium magnetized in the z-direction, which is the direction of propagation. The equation of motion in a ferrite body in MKS units is

$$\frac{d\mathbf{M}}{dt} = \gamma\mu_0 (\mathbf{M} \times \mathbf{H}_e) - \frac{\mathbf{M} - \frac{|\mathbf{M}|}{|\mathbf{H}_e|} \mathbf{H}_e}{\tau} \quad (26-4)$$

where \mathbf{M} is the magnetization per unit volume, μ_0 is the permeability of free space, γ is the gyromagnetic ratio defined by $\gamma = ge/2m$ (radians/second) per (weber/meter²), \mathbf{H}_e is the effective magnetic field, and τ is the relaxation time of the ferrite material defined by $\tau = 2/(\gamma_0 |\Delta H|)$. Here $\gamma_0 = \gamma\mu_0$, and ΔH is the line breadth at half value of a curve of the imaginary part of the permeability μ'' (to be defined later) vs. the DC field inside the ferrite H_0^i . In Eq. (26-4) the first term on the right is that which accounts for precession of the elementary magnetic particles and the second term is the Bloch-Bloembergen damping term. Using Maxwell's equations and Eq. (26-4) the complex components of Polder's tensor $\mu_{\pm} = \mu_1' - j\mu_1''$ and $\kappa = \kappa' - j\kappa''$ were derived, and from these were obtained the effective permeabilities of circularly polarized waves, $\mu_{\pm} = \mu_1 \pm \kappa$, for the two senses of polarization. Thus for the real part of μ_{\pm} we have

$$\mu_{\pm}' = \mu_1' \pm \kappa' = 1 + \frac{\omega_M (\omega_0 \mp \omega) + \frac{1}{\tau^2}}{(\omega_0 \mp \omega)^2 + \frac{1}{\tau^2}} \quad (26-5)$$

and for the imaginary part

$$\mu_{\pm}'' = \mu_1'' \pm \kappa'' = \frac{\frac{\omega_M \omega}{\omega_0} \pm \frac{1}{\tau}}{(\omega_0 \mp \omega)^2 + \frac{1}{\tau^2}} \quad (26-6)$$

In Eqs. (26-5) and (26-6) the plus and minus signs are used respectively for field vectors rotating with and against the direction of precession of the magnetization, also $\omega = 2\pi f$ is angular frequency, $\omega_0 = |\gamma|\mu_0 H_0^i$ is the ferromagnetic resonance frequency of the ferrite material and ω_M is defined by $\omega_M = \gamma\mu_0 M_0$. Here M_0 is the DC magnetization in webers/mtr².

For the case of a finite circular rod whose length-to-diameter ratio is very large, the magnetic susceptibilities $\chi_z^{eff} = \chi_z^{eff'} - j\chi_z^{eff''}$ for circularly polarized waves were then derived: their real and imaginary parts are, respectively,

$$\chi_z^{eff'} = \frac{\omega_M(\omega_{res} + \omega) + \frac{\omega_M\omega_{res}}{(\omega_0\tau)^2}}{(\omega_{res} + \omega)^2 + \left(\frac{\omega_{res}}{\omega_0\tau}\right)^2} \quad (26-7)$$

$$\approx \frac{\omega_M(\omega_{res} + \omega)}{(\omega_{res} + \omega)^2 + \left(\frac{\omega_{res}}{\omega_0\tau}\right)^2} \quad (26-8)$$

and

$$\chi_z^{eff''} = \frac{\frac{\omega_M\omega}{\omega_0\tau}}{(\omega_{res} + \omega)^2 + \left(\frac{\omega_{res}}{\omega_0\tau}\right)^2} \quad (26-9)$$

In Eqs. (26-7), (26-8), and (26-9) ω_{res} is given for long thin cylinders by

$$\omega_{res} \approx \omega_0 + \frac{1}{2}\omega_M \quad (26-10)$$

The effective electric susceptibility for the long thin rod in the direction of orientation, z , is

$$\chi_{ez}^{eff} = \epsilon - 1 \quad (26-11)$$

and in the transverse directions (x and y)

$$\chi_{et}^{eff} = 2 \frac{\epsilon - 1}{\epsilon + 1} \quad (26-12)$$

Here ϵ is the relative dielectric constant of the ferrite. Finally, from the foregoing by means of perturbation theory, the propagation constants

for the circularly polarized TE_{11} mode in circular waveguide loaded with a slim, centrally located, ferrite rod are obtained

$$\beta_z = \beta_g + C \frac{s'}{s} \left(\beta_g X_z^{eff'} + \frac{k^2}{\beta_g} 2 \frac{\epsilon - 1}{\epsilon + 1} \right)$$

$$\alpha_z = C \frac{s'}{s} \beta_g X_z^{eff''} \quad (26-13)$$

In Eq. (26-13) β_g is the phase velocity in the unperturbed guide, k is the free-space phase velocity, s' and s are respectively the cross-sectional areas of the ferrite rod and waveguide, and $C = 1.0474$ for circular waveguide. Similar results were obtained by Lax;² however, it is to be noted that his formulas have two apparent errors, one a sign error and the other an incorrect value for the constant C .

3. CALCULATION OF RESPONSE BASED ON FOREGOING THEORY

In order to obtain numerical results it was necessary to assume a definite size of ferrite rods etc. The line width of the ferrite material is assumed to be $\Delta H = 30.8$ oersteds and the magnetic field is assumed to be of such magnitude in the two phase-shifters that ω_c/ω_0 has the values 0.700 and 0.635 which values and those chosen for l_1 and l_2 (approximately $2/3$ guide wavelength) yield theoretically the $\beta_z l$ and $\alpha_z l$ curves of Figs. 26-9 and 26-10. Here ω_c is the waveguide cut-off frequency. The dielectric constant of the ferrite is taken as 13.

With a voltage of $1/\sqrt{2}$ volts in each arm at the input to the phase-shifters the two outputs voltages are the complex sum and difference

$$S = \frac{1}{2} \left[e^{-(\alpha_z + j\beta_z)_1 l_1} + e^{-(\alpha_z + j\beta_z)_2 l_2} \right]$$

and

$$D = \frac{1}{2} \left[e^{-(\alpha_z + j\beta_z)_1 l_1} - e^{-(\alpha_z + j\beta_z)_2 l_2} \right] \quad (26-14)$$

Here the subscripts 1 and 2 apply respectively to $\omega_c/\omega_0 = 0.700$ and $\omega_c/\omega_0 = 0.635$. The insertion losses for the two outputs, are $-20 \log_{10} |S|$ and $-20 \log_{10} |D|$ decibels

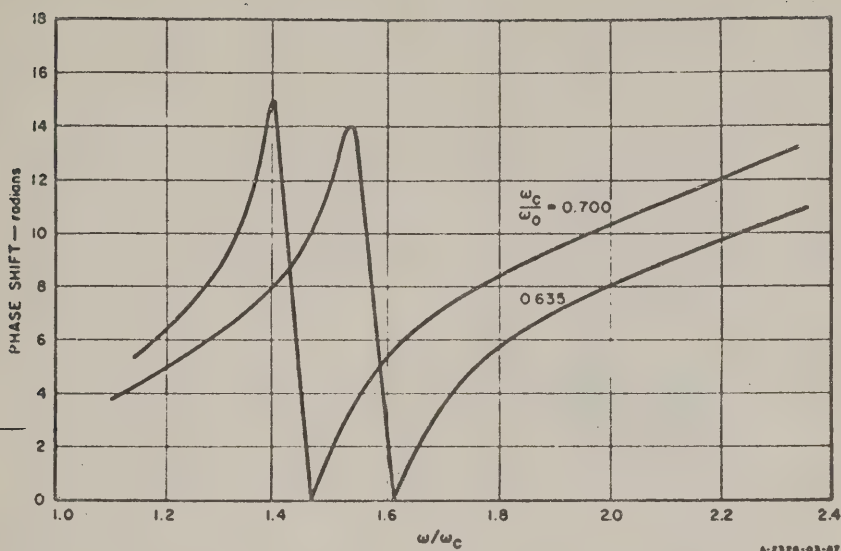


FIG. 26-9

THEORETICAL PHASE SHIFT VS. NORMALIZED FREQUENCY CURVES
FOR TWO FERROMAGNETIC RESONANCE FERRITE PHASE SHIFTERS

The calculated values of insertion loss are plotted against the normalized frequency variable ω/ω_c in Fig. 26-11. As can be seen the theoretical response does not appear to have useful characteristics for a resonance line width ΔH of 30.8 oersteds, which is about the smallest value that can be obtained with sintered garnets. If it were possible to construct a device of this type using single-crystal ferrites or garnets with resonance linewidths an order of magnitude smaller, it seems that more useful filter responses could be obtained. However this possibility seems remote at the present time.

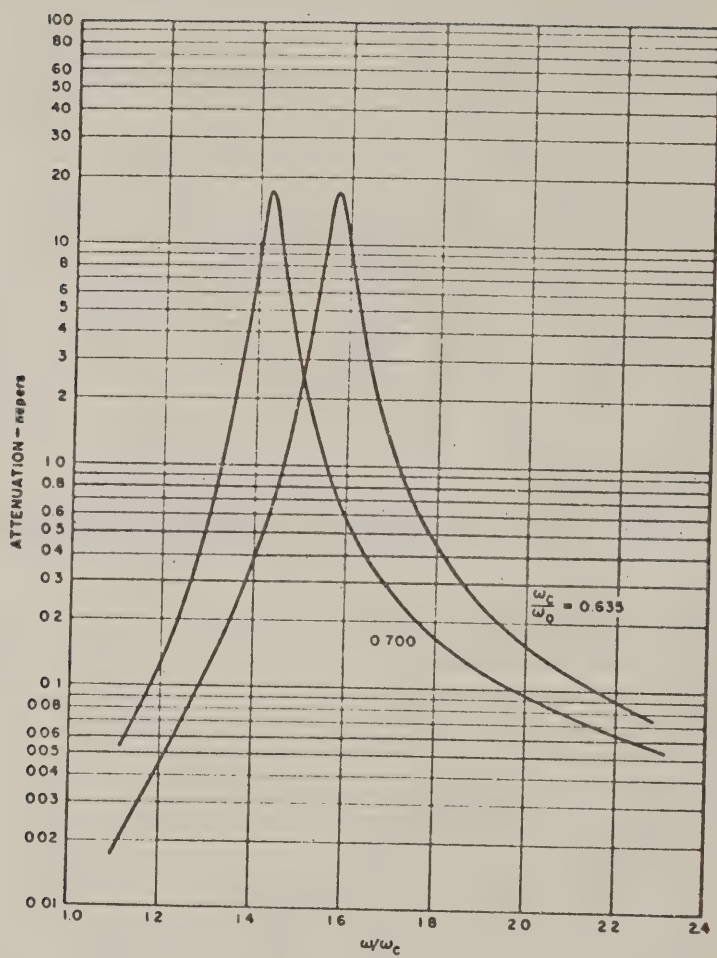


FIG. 26-10
THEORETICAL ATTENUATION VS. NORMALIZED FREQUENCY CURVES
FOR TWO FERROMAGNETIC RESONANCE FERRITE PHASE SHIFTERS

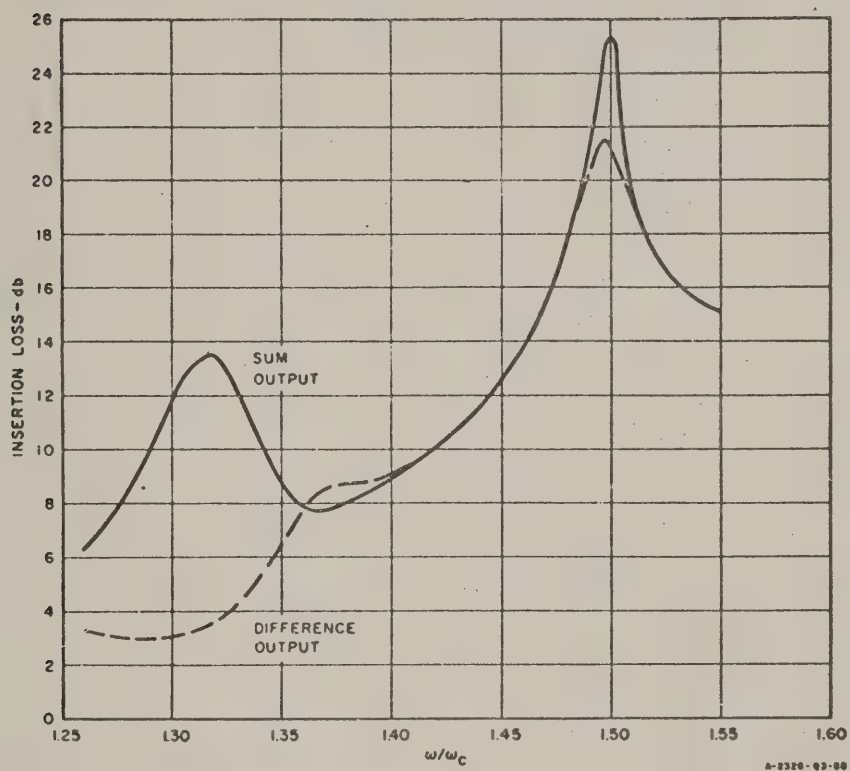


FIG. 26-11

THEORETICAL INSERTION LOSS VS. NORMALIZED FREQUENCY OF BAND-SEPARATION FILTER

REFERENCES

1. F. Beggia and E. G. Spencer, "a New Technique in Ferrite Phase Shifting for Beam Scanning of Microwave Antennas," *Proc. IRE* 45 11, pp. 1510-1517 (November 1957).
2. R. Lax, "Frequency and Loss Characteristics of Microwave Ferrite Devices," *Proc. IRE* 44 10 pp. 1368-1386 (October 1956).

TUNING OF RESONATORS BY DIODE BARRIER CAPACITANCE

A. GENERAL

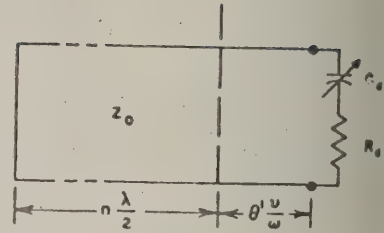
Recent advances in solid-state technology have resulted in the production of junction diodes that may be used as electronically variable capacitors at UHF.^{1,2} In the reverse bias condition, these diodes have a UHF equivalent circuit consisting of a capacitance in series with a resistance. As the reverse bias is varied, the series capacitance varies while the resistance remains practically constant. Experiments on a welded-contact, gold-bonded, germanium diode reported by Kotzebue³ indicate, however, that although the series resistance is practically independent of bias, in at least some cases the value of the series resistance decreases with frequency for a given fixed bias. As a result, the measurements,³ which were made in the range from 500 to 3500 Mc, imply a nearly constant diode Q vs. frequency characteristic for a fixed bias. These measurements are particularly interesting because it is generally assumed that the Q of a diode at very high frequencies will decrease inversely with frequency.^{1,2} In fact, Ref. 2 contains theoretical and experimental data which show very high Q 's at frequencies of a few kilocycles for diodes that have poor Q 's at UHF frequencies. Thus, if the constant Q vs. frequency characteristic reported in Ref. 3 is a characteristic exhibited more or less by all variable-capacitance diodes, it is a high-frequency effect that will not, in general, extend to very low frequencies.

Ratios of maximum to minimum capacitance of the order of 2.5 appear to be readily attainable. The maximum capacitance ranges from about 1 to 25 $\mu\mu\text{f}$ (most being in the 1 to 4 $\mu\mu\text{f}$ range) for different diode designs. So far the Q 's obtainable at UHF frequencies with such diodes are marginal for tunable-filter applications. Reference 1 cites an example of a diffused silicon junction diode which has a Q of 100 at 1000 Mc with a reverse bias of 7 volts (condition for minimum capacitance). At zero volts bias, the capacitance is greater by a factor 2.5, which yields a Q of $100/2.5 = 40$ at 1000 Mc since the series resistance remains constant. This is a very high-quality variable-capacitance diode at the present time, but as work

on such diodes progresses, no doubt at least somewhat higher Q 's will be attainable in the future. It is interesting to note that Ref. 2 predicts the possibility of Q 's of "several hundred" at 100 Mc, and shows curves for diodes which have Q 's ranging in the thousands at frequencies around 30 kc.

The objective of the analysis to follow is to show how electronically tunable UHF resonators can be designed using back-biased diodes such as those discussed above. One of the major objectives is to find circuitry which, for given diode characteristics, will provide as high a Q as possible across any given required tuning range. If a variable-capacitance diode is resonated directly with an inductance the tuning range will be maximum. However, by use of other resonator circuits it is possible to enhance the Q of the circuit at the price of reduced tuning range.

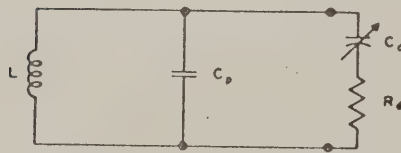
The resonator circuits to be treated herein are shown in Figs. 27-1 to 27-3. Biasing circuits have been omitted for simplicity. As will be shown, the circuit in Fig. 27-3 appears to be the most promising for most



RA-2326-T6-1099

FIG. 27-1

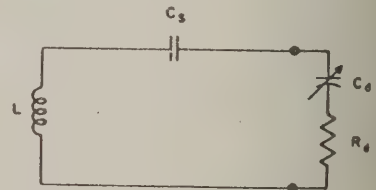
A TRANSMISSION LINE RESONATOR
TUNED BY THE BARRIER CAPACITANCE
OF A BACK-BIASED DIODE



RA-2326-T6-110

FIG. 27-2

A RESONATOR WITH DIODE-CAPACITANCE
TUNING AND AN EXTRA CAPACITANCE
 C_p TO ENHANCE THE Q OF THE DIODE



RA-2326-T6-120

FIG. 27-3

A RESONATOR WITH DIODE-CAPACITANCE
TUNING AND AN EXTRA CAPACITANCE C_s
TO ENHANCE THE Q OF THE DIODE

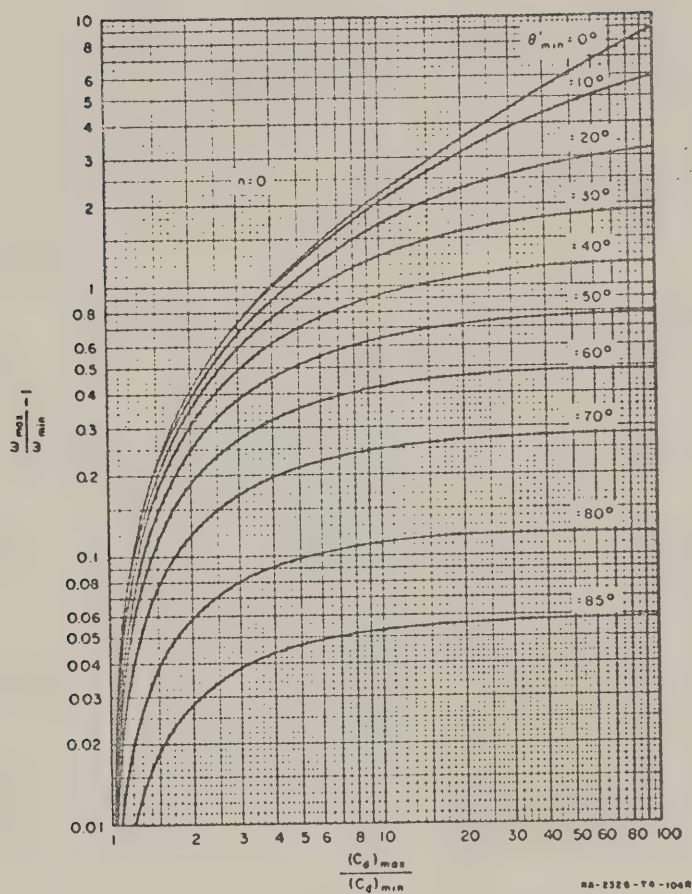


FIG. 27-4
 DESIGN-PARAMETER CHART FOR THE CIRCUIT IN FIG. 27-1
 FOR THE CASE WHERE $n = 0$

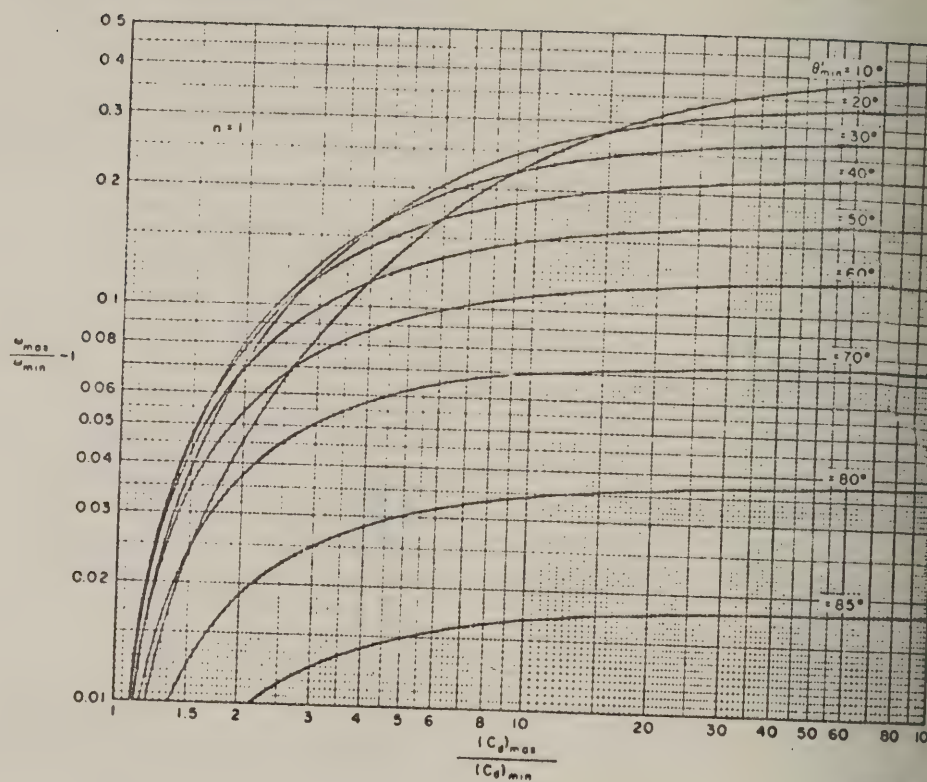


FIG. 27-5
 DESIGN PARAMETER CHART FOR THE CIRCUIT IN FIG. 27-1,
 FOR THE CASE WHERE $n = 1$

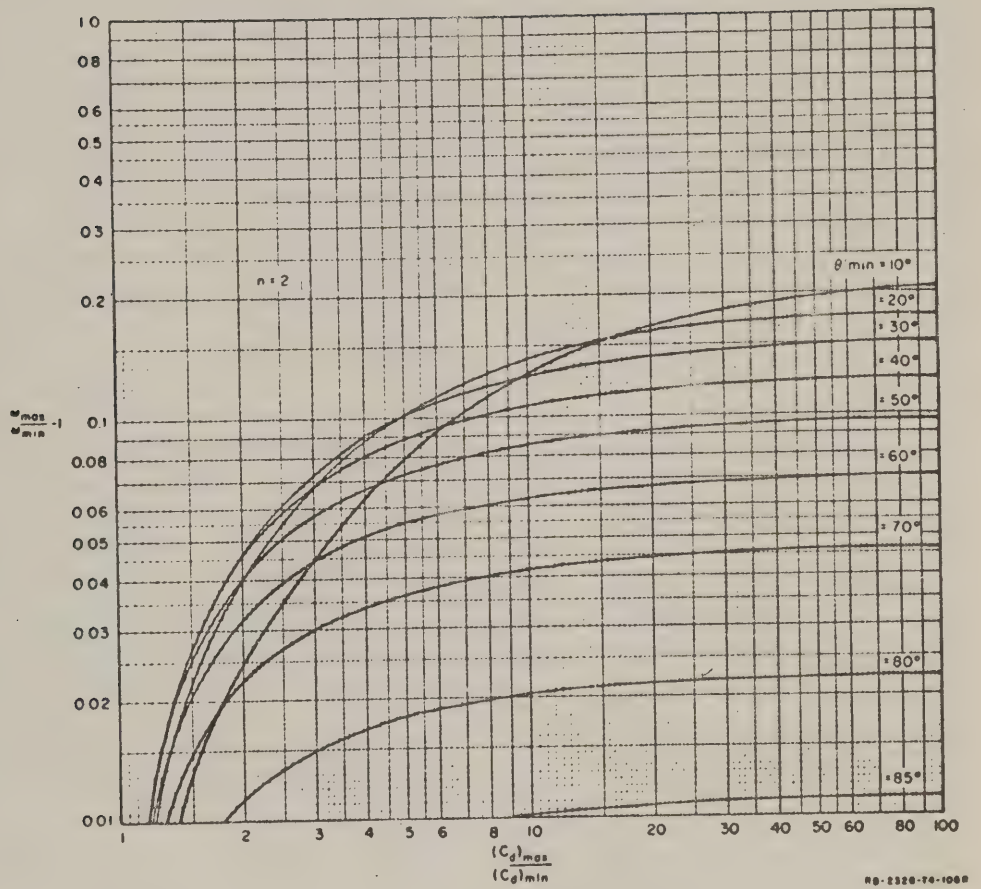


FIG. 27-6
 DESIGN PARAMETER CHART FOR THE CIRCUIT IN FIG. 27-1,
 FOR THE CASE WHERE $n = 2$

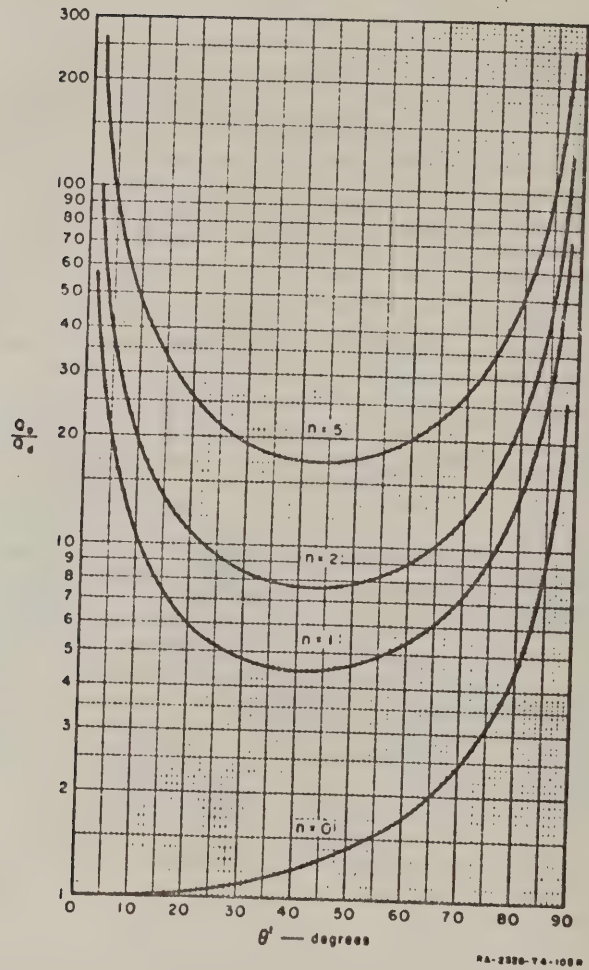


FIG. 27-7
 CHART FOR DETERMINING Q_0 , THE Q OF THE OVER-ALL CIRCUIT
 IN FIG. 27-1 IN TERMS OF Q_d , THE Q OF THE DIODE

Then for the given diode capacitance ratio $(C_d)_{\max}/(C_d)_{\min}$ one may determine an optimum value of θ'_{\min} for the selected value of n by use of the appropriate chart (Fig. 27-4, 27-5, or 27-6). Having θ'_{\min} , Z_0 is found from

$$Z_0 = \frac{1}{\omega_{\min} (C_d)_{\max} \tan \theta'_{\min}} \quad (27-6)$$

Next, with the aid of Eq. (27-4) or Fig. 27-7 the resonator Q can be obtained. The most critical case is at the frequency ω_{\min} where $Q_d = (Q_d)_{\min}$. Using $\theta' = \theta'_{\min}$ as the abscissa of Fig. 27-7, the ordinate becomes $Q_0/(Q_d)_{\min}$. It will be found that $Q_0/(Q_d)_{\min}$ will be larger if a value of n greater than zero can be used. However, using a larger value of n may limit the tuning range too much in some cases.

3. CORRECTION FOR TRANSMISSION-LINE LOSSES

In some cases it might be desirable to include the loss effects of the transmission line in the calculations in order to be sure that the net Q of the circuit will be as high as is required. The losses of the transmission line can be included in the calculations quite easily by replacing the transmission line having losses by a lossless transmission line in series with a resistor that accounts for the transmission line losses. The loss resistor can be lumped with the diode circuit and a new effective Q calculated for the diode circuit. Then the chart, Fig. 27-7, which assumes that the transmission line is lossless, may be used as before.

To calculate the equivalent loss resistor for the transmission line we note that for a short-circuited line

$$\begin{aligned} Z_{i_n} &= Z_0 \tanh (\alpha l + j \beta l) \\ &= Z_0 \frac{\tanh (\alpha l + j \tan \beta l)}{1 + j (\tanh \alpha l) \tan \beta l} \end{aligned} \quad (27-7)$$

where α is the attenuation constant in nepers per unit length, β is the phase constant in radians per unit length, and l is again the length of the line. If a $l \ll 1$, which would normally be the case, then

appreciably. If a capacitor C_p having a Q value Q_p is inserted in parallel with C_d , then the resulting Q of the circuit will be

$$Q_0 = \frac{\omega C_{\text{total}}}{G_{\text{total}}} = \frac{\omega C_d + \omega C_p}{\frac{\omega C_d}{Q_d} + \frac{\omega C_p}{Q_p}} \quad (27-12)$$

$$Q_0 = Q_d \left(\frac{C_d + C_p}{C_d + \frac{Q_d}{Q_p} C_p} \right)$$

From this equation it is seen that if $Q_p > Q_d$, the resulting Q of the diode with the shunt capacitor will exceed Q_d . In this case

$$C_{\text{max}} = (C_d)_{\text{max}} + C_p \quad (27-13)$$

while

$$\frac{C_{\text{max}}}{C_{\text{min}}} = \frac{(C_d)_{\text{max}} + C_p}{(C_d)_{\text{min}} + C_p} \quad (27-14)$$

where C_{max} and C_{min} are the maximum and minimum values of the total capacitance presented by the diode and C_p in parallel. Recalling that the resonant frequency of the circuit in Fig. 27-2 is given by

$$\omega = \frac{1}{\sqrt{LC}} \quad (27-15)$$

and that

$$\omega = \omega_{\text{max}} \text{ occurs when } C = C_{\text{max}} \quad (27-16)$$

while

$$\omega = \omega_{\text{min}} \text{ occurs when } C = C_{\text{min}} \quad (27-17)$$

we obtain

$$\frac{C_{\text{max}}}{C_{\text{min}}} = \left(\frac{\omega_{\text{max}}}{\omega_{\text{min}}} \right)^2 \quad (27-18)$$

Combining Eqs. (27-14) and (27-18) yields

$$\frac{(C_d)_{\min}}{C_p} = \frac{\left(\frac{\omega_{\max}}{\omega_{\min}}\right)^2 - 1}{\frac{(C_d)_{\max}}{(C_d)_{\min}} - \left(\frac{\omega_{\max}}{\omega_{\min}}\right)^2} \quad (27-19)$$

For convenience in carrying out designs for tunable resonators, $(C_d)_{\min}$ vs. $(\omega_{\max}/\omega_{\min}) - 1$ is plotted in Fig. 27-8 for various values of $(C_d)_{\max}/(C_d)_{\min}$. With the aid of this graph one can quickly determine which value of C_p in Fig. 27-2 will give a given required tuning range $\omega_{\max}/\omega_{\min}$ for given values of $(C_d)_{\max}$ and $(C_d)_{\min}$, provided that $(C_d)_{\max}/(C_d)_{\min}$ is large enough. In general, $\omega_{\max}/\omega_{\min}$ should not be specified any larger than necessary because if C_p is a low-loss capacitor the smaller the tuning range the larger Q will be across the tuning band.

Let us suppose that the Q 's of C_p and L are large enough that they may be neglected in comparison with the diode Q . Then Eq. (27-12) reduces to

$$Q_0 = Q_d \left(1 + \frac{C_p}{C_d}\right) \quad (27-20)$$

By Eq. (27-16) and Fig. 27-2 we see that the minimum values of Q_d and Q_0 occur at ω_{\min} , so that

$$\left. \frac{(Q_0)_{\min}}{(Q_d)_{\min}} \right|_{\omega=\omega_{\min}} = \left[1 + \frac{C_p}{(C_d)_{\max}} \right] \quad (27-21)$$

Similarly, the maximum values of Q_d and Q_0 occur at ω_{\max} , so that

$$\left. \frac{(Q_0)_{\max}}{(Q_d)_{\max}} \right|_{\omega=\omega_{\max}} = \left[1 + \frac{C_p}{(C_d)_{\min}} \right] \quad (27-22)$$

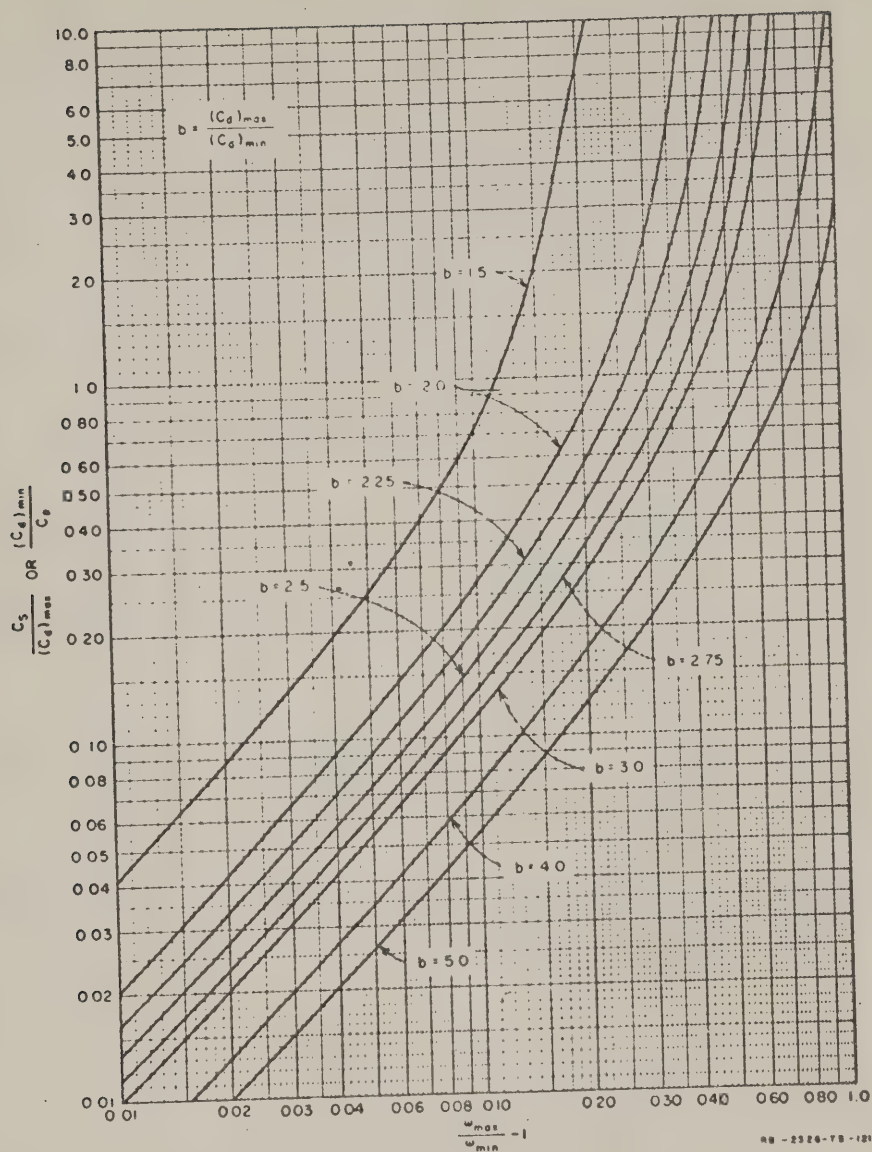


FIG. 27-8
DESIGN-PARAMETER CHART FOR THE CIRCUITS IN FIGS. 27-2 AND 27-3

Using Eqs. (27-19) and (27-22), values of $(Q_0)_{\dots}/(Q_d)_{\dots}$ vs $(\omega_{\dots}/\omega_{\text{in}}) - 1$ where computed for various values of $b = (C_d)_{\dots}/(C_d)_{\text{in}}$, and these data are plotted in Fig. 27-9. Using Eqs. (27-19) and (27-21), similar data for $(Q_0)_{\text{in}}/(Q_d)_{\text{in}}$ were computed, and they are plotted in Fig. 27-10. It should be noticed that for this case where the diode Q is to be enhanced by using a capacitance C_p in parallel with the diode,

$$\frac{(Q_0)_{\text{in}}}{(Q_d)_{\text{in}}} < \frac{(Q_0)_{\dots}}{(Q_d)_{\dots}} \quad (27-23)$$

That is, the resonator Q is enhanced most at ω_{\dots} where the diode Q is highest. As we shall see, if a series capacitance C_s is used for enhancing the diode Q instead of C_p , then the above situation is reversed so that the greatest enhancement of the circuit Q occurs at ω_{in} where it needs enhancing most.

D. USE OF SERIES CAPACITANCE FOR ENHANCING THE DIODE Q

Let us now consider the circuit in Fig. 27-3 where the Q of the diode circuit is enhanced by introducing a capacitance C_s in series with the diode. In this case

$$Q_0 = Q_d \left(\frac{C_s + C_d}{C_s + \frac{Q_d}{Q_s} C_d} \right) \quad (27-24)$$

where Q_s is the Q of the series capacitor. Also, in a manner analogous to the discussion in Part C,

$$C_{\dots} = \frac{(C_d)_{\dots} C_s}{C_s + (C_d)_{\dots}} \quad (27-25)$$

and

$$\frac{C_{\dots}}{C_{\text{in}}} = \frac{(C_d)_{\dots}}{(C_d)_{\text{in}}} \left[\frac{C_s + (C_d)_{\text{in}}}{C_s + (C_d)_{\dots}} \right] \quad (27-26)$$

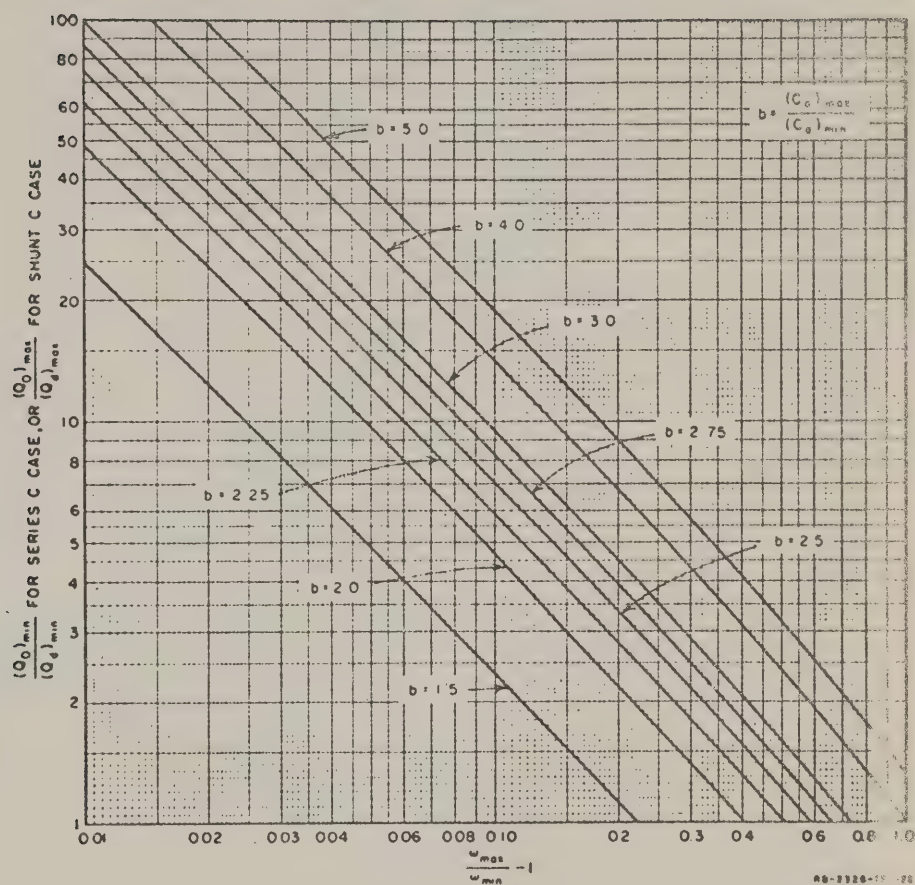


FIG. 27-9

CHART FOR DETERMINING C_0 , THE OVER-ALL Q OF THE CIRCUITS
IN FIGS. 27-2 AND 27-3, IN TERMS OF Q_d , THE DIODE Q

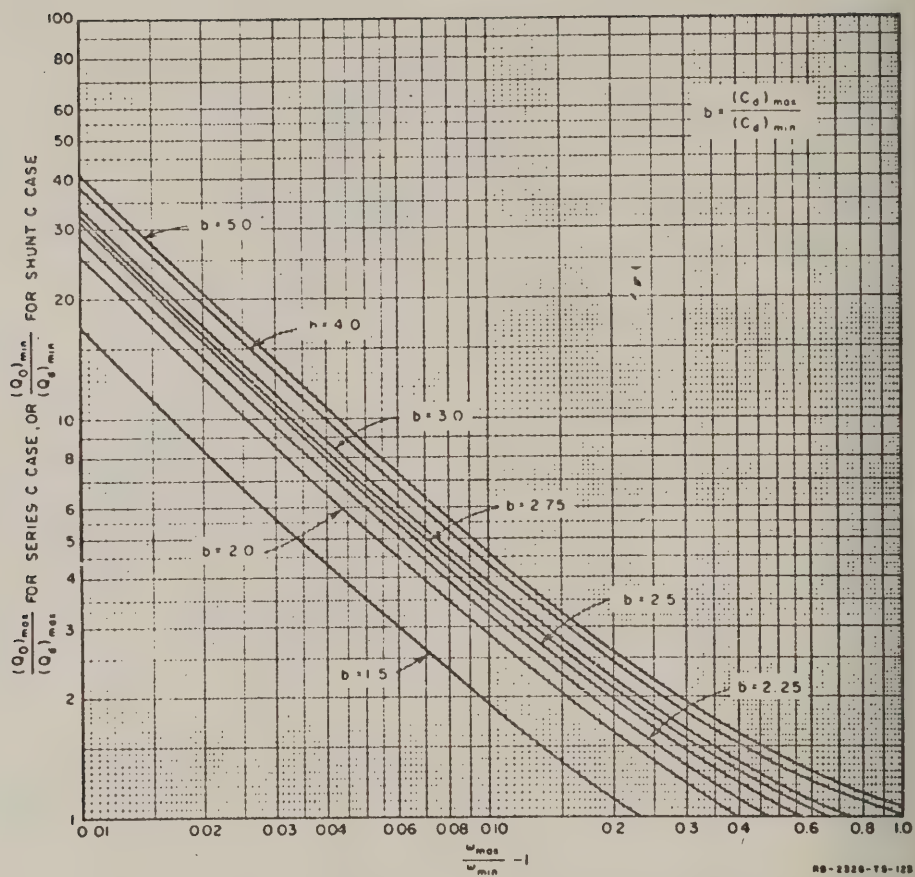


FIG. 27-10

CHART FOR DETERMINING Q_0 , THE OVER-ALL Q IN THE CIRCUITS OF FIGS. 27-2 AND 27-3, IN TERMS OF Q_d , THE DIODE Q

Combining Eqs. (27-18) and (27-26) yields

$$\frac{C_s}{(C_d)_{\max}} = \frac{\left(\frac{\omega_{\max}}{\omega_{\min}}\right)^2 - 1}{\frac{(C_d)_{\max}}{(C_d)_{\min}} - \left(\frac{\omega_{\max}}{\omega_{\min}}\right)^2} \quad (27-27)$$

Note that the right side of Eq. (27-27) is identical with the right side of Eq. (27-19), hence

$$\frac{C_s}{(C_d)_{\max}} \bigg|_{\text{const. of } C_s} = \frac{(C_d)_{\min}}{C_p} \bigg|_{\text{const. of } C_p} \quad (27-28)$$

and Fig. 27-8 also serves as a plot of $C_s/(C_d)_{\max}$ vs. $(\omega_{\max}/\omega_{\min})-1$ for various $b = (C_d)_{\max}/(C_d)_{\min}$.

If $Q_s \gg Q_d$, then Eq. (27-24) may be reduced to

$$Q_c = C_d \left(1 + \frac{C_d}{C_s} \right) \quad (27-29)$$

Analogously to Eqs. (27-21) and (27-22) where C_p is used, for this case where C_s is used,

$$\frac{(Q_0)_{\min}}{(Q_d)_{\min}} \bigg|_{\omega=\omega_{\min}} = \left[1 + \frac{(C_d)_{\max}}{C_s} \right] \quad (27-30)$$

and

$$\frac{(Q_0)_{\max}}{(Q_d)_{\max}} \bigg|_{\omega=\omega_{\max}} = \left[1 + \frac{(C_d)_{\min}}{C_s} \right] \quad (27-31)$$

As can be seen from Eqs. (27-28), (27-30), and (27-31), one may use Figs. 27-9 and 27-10 in the series capacitance case as plots of $(Q_0)_{\min}/(Q_d)_{\min}$ and $(Q_0)_{\max}/(Q_d)_{\max}$ vs. $(\omega_{\max}/\omega_{\min})-1$ for various

$b = (C_d)_{\dots} / (C_d)_{\dots}$. It should be noted that when series capacitance is used for enhancing the diode Q

$$\frac{(Q_0)_{\dots}}{(Q_d)_{\dots}} > \frac{(Q_0)_{\dots}}{(Q_d)_{\dots}} \quad (27-32)$$

which is advantageous since the circuit Q is boosted the most at the frequency ω_{\dots} where the diode Q is least.

E. SOME NUMERICAL EXAMPLES

Using diode data taken from Ref. 1, let us consider the case of a diode which has $(C_d)_{\dots} = 10 \mu\text{f}$, $(C_d)_{\dots} = 25 \mu\text{f}$, and $(Q_d)_{\dots} = 40$ while $(Q_d)_{\dots} = 100$ at 1000 Mc. Let us assume that the desired tuning range is from 1000 to 1100 Mc so that $(\omega_{\dots}/\omega_{\dots})-1 = 0.1$. Then, $(Q_d)_{\dots}$ will occur at 1100 Mc instead of 1000 Mc, so that its value would probably differ slightly from 100 at 1100 Mc; however, for simplicity we shall neglect this small difference. We shall assume that the only significant losses are in the diode for the following examples.

For the circuit of Fig. 27-1 with $n = 0$,

from Fig. 27-4 for

$$(\omega_{\dots}/\omega_{\dots})-1 = 0.1, \text{ and } (C_d)_{\dots}/(C_d)_{\dots} = 2.5$$

we find that

$$\theta'_{\dots} = 75^\circ.$$

From Fig. 27-7, with

$$\theta' = \theta'_{\dots} = 75^\circ, \text{ and } n = 0$$

we find that

$$(Q_0)/(Q_d)_{\dots} = 3.1.$$

This gives a Q_0 at ω_{\dots} of

$$(3.1)(40) = 124.$$

By Eq. (27-5),

$$\theta' = 1.1 (75) = 82.50^\circ \text{ at } \omega_{\dots}$$

By Fig. 27-7,

$$(Q_0)/(Q_d)_{\max} = 6, Q_0 = 6 (100) = 600 \text{ at } \omega_{\max}.$$

By Eq. (27-6), we find that

$$Z_0 = 4.28 \text{ ohms.}$$

In this case, it would be desirable to have a diode with a smaller $(C_d)_{\min}$ and $(C_d)_{\max}$ so that Z_0 could be larger.

For the circuit in Fig. 27-1 with $n = 1$

we find, from Fig. 27-5, that

$$\theta'_{\min} = 20^\circ$$

and, from Fig. 27-7, that

$$Q_0/(Q_d)_{\min} = 6.$$

Thus,

$$Q_0 = 6 (40) = 240 \text{ at } \omega_{\min}.$$

By Eq. (27-5),

$$\theta' = 40^\circ \text{ at } \omega_{\max}$$

so that, by Fig. 27-7,

$$Q_0/(Q_d)_{\max} = 4.4 \text{ and } Q_0 = 4.4 (100) = 440.$$

In this case, Eq. (27-6) gives

$$Z_0 = 43.8 \text{ ohms,}$$

which is a convenient value. Thus, for this case,

$$(C_d)_{\max} = 25 \mu\text{f}$$

is a good level of capacitance.

For the circuit in Fig. 27-1 with $n = 2$ or greater

we find that using the diode under consideration, the circuit cannot be used. In order to obtain the required tuning range,

$$(C_d)_{\max}/(C_d)_{\min} = 5$$

would be required.

For the circuit of Fig. 27-2,

we find from Fig. 27-8 that

$$(C_d)_{min}/C_p = 0.164$$

so that

$$C_p = 10/0.164 = 61 \mu\text{mf}$$

in order to give the desired tuning range. Now,

$$C_{max} = 25 + 61 = 86 \mu\text{mf}$$

so that

$$L = 1/(\omega_{min}^2 C_{max}) = 2.95 \times 10^{-10} \text{ henry.}$$

In this case, the values of C_p and L would be easier to realize if $(C_d)_{min}$ and $(C_d)_{max}$ were reduced in value. By Fig. 27-10,

$$(Q_0)_{min}/(Q_d)_{min} = 3.45,$$

so that

$$Q_0 = 3.45 (40) = 138 \text{ at } \omega_{min}.$$

By Fig. 27-9,

$$(Q_0)_{max}/(Q_d)_{max} = 7.1$$

so that

$$Q_0 = 100 (7.1) = 710 \text{ at } \omega_{max}.$$

For the circuit in Fig. 27-3

we obtain, in an analogous manner,

$$C_s = 4.1 \mu\text{mf}, \quad L = 7.27 \times 10^{-9} \text{ henry,}$$

$$Q_0 = 284 \text{ at } \omega_{min} \text{ and } Q_0 = 347 \text{ at } \omega_{max}.$$

In this case the given values of $(C_d)_{min}$ and $(C_d)_{max}$ give convenient values for C_s and L , as will be illustrated in Part F.

The Q values from the preceding examples are listed in Table 27-1. From these values it is evident that the circuit of Fig. 27-3 gives the best Q at ω_{min} while the circuit in Fig. 27-1 with $n = 1$ comes a fairly close

second. The circuit in Fig. 27-3 has the additional advantages of being realizable in a form which is far more compact than the circuit in Fig. 27-1, and the circuit of Fig. 27-3 has no resonances below the primary resonance, while the circuit in Fig. 27-1 with $n = 1$ does. However, the circuit in Fig. 27-1 with $n = 0$ or $n = 1$ should be a convenient one for testing diodes to determine their capacitance and Q values.

TABLE 27-1
COMPARISON OF RESONATOR Q 's OBTAINED WITH
THE CIRCUITS OF FIGS. 27-1 TO 27-3
Example. $(C_d)_{\max}/(C_d)_{\min} = 2.5$, $(Q_d)_{\min} = 40$, $(Q_d)_{\max} = 100$,
for frequency range 1000 to 1100 Mc

| TYPE OF RESONATOR | $(Q_0)_{\omega=\omega_{\min}}$ | $(Q_0)_{\omega=\omega_{\max}}$ |
|--------------------|--------------------------------|--------------------------------|
| Fig. 27-1, $n = 0$ | 124 | 600 |
| Fig. 27-1, $n = 1$ | 240 | 440 |
| Fig. 27-2 | 138 | 710 |
| Fig. 27-3 | 284 | 347 |

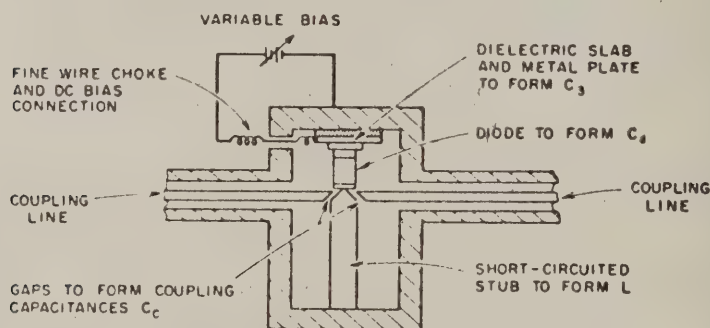
It is of interest to note how selective a filter would be if constructed with resonators such as those in the preceding examples. Let us consider the example for the circuit in Fig. 27-3 where the unloaded Q of the resonator averages about 300 as the tuning is varied across the band from 1000 to 1100 Mc. If the resonator has equal couplings at its input and output, and if these couplings are adjusted to give a 1-db mid-band insertion loss, then the 3-db bandwidth of the response will be about 31 Mc while the 100 Mc tuning range is only 3.2 times this much. Using the three-resonator filter data in Fig. 23-4, it is seen that for a minimum-loss, three-resonator filter designed to have a 3-db loss at midband, the bandwidth at the 20-db points will be 38.7 Mc if the unloaded Q 's of the resonators is 300. In this case the 100-Mc tuning range is 2.58 times as great as the bandwidth between 20-db points.

From these examples it is seen that the resonator Q 's attainable with present diodes at frequencies around 1000 Mc are not high enough to permit electronic tuning so as to separate a given signal completely from other strong signals whose frequencies are close to that of the desired signal. However, for situations where the incoming signals have reasonably constant average amplitude and are not too closely spaced in frequency, a filter such as that in the example above could determine the frequency of the incoming signal much more accurately than the tuning bandwidth to 20-db

bandwidth ratio suggests. This is possible if the electronic tuning is calibrated and synchronized with a recording device so that the signal frequency can be determined as the tuning frequency for which the output of the filter is maximum. Along with the conclusions in Sec. G of this chapter, a suggested method for obtaining broadband operation by use of paralleled, diode-tuned filters is briefly discussed.

F. PHYSICAL REALIZATION OF A RESONATOR USING C_s

Since the resonator circuit in Fig. 27-3 appears to be the most practical for use in UHF electronically tunable filters, let us see how such a resonator might be built. From Part E, $C_s = 4.1 \mu\text{f}$ while $L = 7.27 \times 10^{-9}$ henry. This value of C_s could be realized by a small slab of low loss dielectric material between metal plates. A circular slab of dielectric with a diameter of 0.370 inch and a thickness of 0.015 inch would be adequate if the relative dielectric constant were 2.5. Figure 27-11(a) shows a possible resonator design with C_s realized in such a manner. To realize L , we wish to use a short-circuited stub which is less than an eighth of a wavelength long. Since in air $\lambda = 11.8$ inch at 1 kMc, a one-inch stub should be about right. For a short-circuited stub less than an eighth of a wavelength long,



RA-2326-TS-124

FIG. 27-11(a)

A POSSIBLE FORM FOR A UHF, DIODE-TUNED RESONATOR
USING SEMI-LUMPED ELEMENTS AND A SERIES CAPACITOR C_s
TO ENHANCE THE DIODE Q

$$l = \frac{Z_0 l}{v} \quad (27-33)$$

where v is the velocity of propagation, Z_0 is the characteristic impedance of the stub, and l is the length of the stub. If l is measured in inches

$$Z_0 = \frac{L(1.18)10^{10}}{l} \quad (27-34)$$

For $l = 1$ inch and $L = 7.27 \times 10^{-9}$ henries we obtain $Z_0 = 85.7$, which is a very practical value for an air-dielectric line. Figure 27-11(a) shows a capacitively coupled resonator of the proposed design, while Fig. 27-11(b) shows its equivalent circuit. Note that the capacitor C_c acts as a DC blocking capacitor as well as to enhance the diode Q . The diode bias is applied by a fine wire choke connection to the diode side of C_c and to ground. It should be readily possible to build multiple-resonator, tunable, filters by cascading resonators of this type.

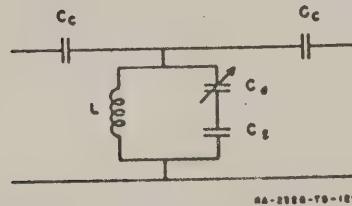


FIG. 27-11(b)
AN EQUIVALENT CIRCUIT FOR THE
RESONATOR IN FIG. 27-11(a)

G. CONCLUSIONS

The results of the investigation of electronic tuning of resonators with diode capacitors shows that this method of electronic tuning should be feasible for some applications, particularly at frequencies of 100 Mc or less for which the diode Q 's apparently are higher. For applications involving frequencies around 1000 Mc or above, the Q 's of diodes presently available are rather low, but probably good enough for some situations. In most cases, to build filters having sufficiently high resonator Q 's, additional high- Q elements must be added, which in turn will reduce the tuning range. In order to construct filters with such resonators so as to cover a wide tuning range it might be possible to use a group of parallel filters such that each filter would cover a portion of the required tuning range. This might be done in a practical way by adjusting the tuning voltages so that the resonators of all but one multi-resonator filter are so badly misaligned that little signal can come through in the unwanted frequency bands. However, the filter which covers the desired frequency would be electronically tuned so that it would pass that frequency.

REFERENCES

1. A. Uhlir, Jr., "The Potential of Semiconductor Diodes in High-Frequency Communications," *Proc. IRE* 46, pp. 1099-1115 (June 1958).
2. C. J. Spector, "Electronically Variable Capacitors," Transistor Engineering Services, Bell Telephone Laboratories, Task 7, 12th report on Signal Corp Contract DA 36-039 SC-64618 (14 April 1958).
3. K. L. Kotzebue, "A Semiconductor-Diode Parametric Amplifier at Microwave Frequencies," Technical Report 49 (Project 210), Stanford Electronics Laboratory, Stanford California, Contract Nonr 225 (24), NR 373 360 (4 November 1958).

MAGNETICALLY TUNABLE MICROWAVE FILTERS USING SINGLE-CRYSTAL YTTRIUM-IRON-GARNET RESONATORS

A. INTRODUCTION

With the increased use of continuously tunable microwave receivers, there has been a demand for a non-mechanically tuned, narrow-band filter which is tunable over a broad band of frequencies in the microwave frequency range. Previous attempts to solve this problem have included the use of cavities containing ferroelectrics, "varicaps" or voltage-tuned back-biased diodes, and ferrites (See Chapters 25 and 26 and Refs. 1-6). In general, tuning ranges of only a few percent are possible using these techniques while at the same time maintaining a high unloaded resonator (Q_0).

High losses are the main difficulty with the techniques listed above. These losses are greatly reduced by the use of the ferrimagnetic material, yttrium-iron-garnet (YIG). Single crystals of this material are now available commercially; they show extremely low losses when used as the resonant element in a bandpass (or band-reject) filter. The Q_0 of this material considered as a resonator is typically between 2,000 and 4,000 at X-band frequencies, and it therefore compares favorably with transmission-line and hollow-cavity resonators.

This new approach to the problem of non-mechanical tuning makes use of the equivalence between a resonant circuit, such as an inductively coupled cavity or lumped element series-resonant circuit, and an inductively coupled magnetic resonator, biased with a DC magnetic field. This equivalent circuit was first worked out analytically by Bloembergen and Pound⁷ and was first applied by DeGrasse⁸ to the design of an S-band filter limiter using a single-crystal YIG resonator.

The tunability feature results from the fact that the resonant frequency is nearly a linear function of the applied DC magnetic biasing field. This feature allows a very broad tuning range, limited mainly by the bandwidth of the microwave coupling structure employed.

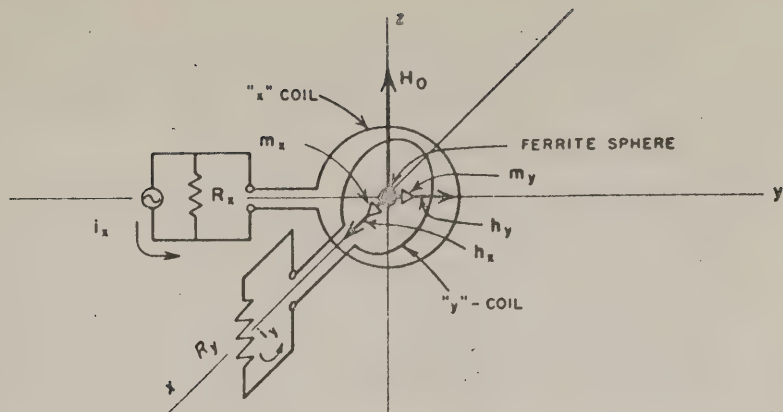
The first part of this chapter consists of a mathematical analysis of the equivalent circuit of a ferrimagnetic resonator coupled to external loads by means of loops, transmission lines, and waveguides. Analytical formulas for the external Q , Q_e , of the ferrimagnetic resonator are given for loop, transmission line and TE_{10} -mode waveguide coupling circuits. An expression is obtained which relates the unloaded Q of the ferrite resonator to the properties of the ferrite (i.e., saturation magnetization, damping time, and gyromagnetic ratio).

The second part of this chapter consists of descriptions of, and performance data taken on, two types of magnetically tunable filters operating in the X-band region and above. These are (1) a single resonator filter which has a tuning range from 1.0 kMc to 11.2 kMc, and (2) a two-resonator filter whose tuning range extends from 8.2 kMc to 14.0 kMc.

B. BASIC PRINCIPLE OF OPERATION

The basic idea of the magnetic resonance filter is illustrated in Fig. 28-1. Shown here are two coils which have their axes at right angles to each other, with a small ferrite sample at the intersection of the axes of the coils. When the sample is not magnetized, no power is transferred between the coils because the loop axes are perpendicular to each other and there is no interaction with the ferrite. When a DC field, H_0 , is applied along the z-axis, and an RF driving current, $i_e e^{j\omega t}$, is applied to the terminals of the x-coil, the magnetic moments of the electrons in the ferrite precess around the z-axis thus producing an RF magnetic moment along the y-axis and inducing a voltage in the y-circuit. The precession angle is largest, and thus the induced voltage in the y-coil is maximum at ferromagnetic resonance given by $\omega_0 = \mu_0 \gamma H_0$ for a spherical ferrite; where γ is the gyromagnetic ratio and is very close to 1.759×10^{11} for electrons in most ferrites. The drop-off in response away from resonance is determined by the degree of coupling of the external loads R_x and R_y and the internal losses in the ferrite. It is shown in Sec. C that the equivalent circuit of this device is a resonant circuit, inductively coupled to the output lines or loads. This circuit is also a gyrator; the phase shift in one direction through the circuit differs from the phase shift in the other direction by 180 degrees.

* These quantities are defined in Sec. B.



RA-2526-TB-109RR

FIG. 28-1
MAGNETIC RESONANCE FILTER

One requirement on the resonator in a low-insertion-loss narrow-band-pass filter is that the internal or unloaded Q , Q_u , be high. Although it is necessary to specify the application in more detail in order to specify what exactly is meant by "high Q_u ," it may be stated in general that Q_u 's of several hundred or higher are useful for filter design. Unloaded Q 's of this order are obtained at microwave frequencies with single-crystal yttrium-iron-garnet material.

The second requirement to obtain low insertion loss in a narrow-band, band-pass filter is that the external Q , Q_e , of the resonators be considerably lower than the unloaded Q , Q_u . It was not apparent from previous work by DeGrasse⁸ that sufficiently low Q_e could be obtained over a wide tuning range. It is shown in the experimental and theoretical studies reported below that sufficient coupling can actually be obtained without the use of the narrow-band impedance matching employed by DeGrasse.⁸

Two other characteristics of single crystal ferrimagnetic resonators must be considered in designing a magnetically tunable filter, namely (1) magnetocrystalline anisotropy and (2) the higher-order magnetostatic modes. The effects of these properties on filter characteristics and design are discussed below.

C. ANALYSIS AND MEASUREMENT OF COUPLING CHARACTERISTICS AND EQUIVALENT CIRCUITS OF FERRITE RESONATORS IN LUMPED-ELEMENT CIRCUITS, TRANSMISSION-LINES, AND WAVEGUIDES

1. BASIC RELATIONS

The analysis given below is unrestricted except that (1) the ferrite resonator is assumed to be small enough that the RF field is substantially uniform throughout the volume of the sample, (2) higher-order magnetostatic modes are not excited and (3) anisotropy is neglected. In this case, with the DC magnetic field H_0 , applied along the z-axis the RF magnetizations in the x and y directions are given by the following relations:

$$m_x = \chi'_{xx} h_{0x} + \chi'_{xy} h_{0y} \quad (a)$$

$$m_y = \chi'_{yx} h_{0x} + \chi'_{yy} h_{0y} \quad (b) \quad (28-1)$$

where

- m_x = x-component of RF magnetization within ferrite
- m_y = y-component of RF magnetization within ferrite
- h_{0x} = x-component of applied RF field
- h_{0y} = y-component of applied RF field
- χ'_{xx} = χ'_{yy} = x - x (y - y) component of effective tensor susceptibility
- χ'_{xy} = $-\chi'_{yx}$ = x - y (y - x) component of effective tensor susceptibility.

The effective tensor susceptibility of the ferrite sample depends on the shape of the sample. Analytical formulas for the effective susceptibility which include the loss in the ferrite have been developed by Flammer⁹ and are given below. These expressions were derived using the Bloch-Bloembergen¹⁰ formulation of the equations of motion of magnetization, including the effect of the shape-dependent demagnetizing factors N_x , N_y , and N_z for a general ellipsoidal sample.¹¹ These formulas for the effective tensor susceptibility are,

* MKS units are used throughout this section.

$$X_{zz}'' = \frac{\omega_a \left[\omega_0 + (N_y - N_z) \omega_a + \frac{j \omega / \tau}{\omega_0 - N_z \omega_a} \right] + \frac{\omega_a}{(\omega_0 - N_z \omega_a)^2} [\omega_0 + (N_y - N_z) \omega_a] \cdot \frac{1}{\tau^2}}{\left\{ \left[\omega_0 + (N_y - N_z) \omega_a + \frac{j \omega / \tau}{\omega_0 - N_z \omega_a} \right] \left[\omega_0 + (N_z - N_y) \omega_a + \frac{j \omega / \tau}{\omega_0 - N_z \omega_a} \right] - \omega^2 + \right.} \\ \left. \frac{1}{(\omega_0 - N_z \omega_a)^2 \tau^2} \cdot [\omega_0 + (N_z - N_y) \omega_a] [\omega_0 + (N_y - N_z) \omega_a] \right\}} \quad (a)$$

$$X_{yy}'' = \frac{\omega_a \left[\omega_0 + (N_z - N_x) \omega_a + \frac{j \omega / \tau}{(\omega_0 - N_z \omega_a)^2} \right] + \frac{\omega_a}{(\omega_0 - N_z \omega_a)^2} [\omega_0 + (N_z - N_x) \omega_a] \frac{1}{\tau^2}}{\left\{ \left[\omega_0 + (N_z - N_x) \omega_a + \frac{j \omega / \tau}{\omega_0 - N_z \omega_a} \right] \left[\omega_0 + (N_y - N_z) \omega_a + j \frac{\omega / \tau}{\omega_0 - N_z \omega_a} \right] - \omega^2 + \right.} \\ \left. \frac{1}{(\omega_0 - N_z \omega_a)^2 \tau^2} [\omega_0 + (N_z - N_x) \omega_a] [\omega_0 + (N_y - N_z) \omega_a] \right\}} \quad (b)$$

$$X_{zy}'' = -X_{yz}'' = \frac{-j \omega_a \omega}{\left\{ \left[\omega_0 + (N_z - N_x) \omega_a + j \frac{\omega / \tau}{\omega_0 - N_z \omega_a} \right] \left[\omega_0 + (N_y - N_z) \omega_a + j \frac{\omega / \tau}{\omega_0 - N_z \omega_a} \right] - \omega^2 \right.} \\ \left. + \frac{1}{(\omega_0 - N_z \omega_a)^2 \tau^2} [\omega_0 + (N_z - N_x) \omega_a] [\omega_0 + (N_y - N_z) \omega_a] \right\}} \quad (c)$$

(28-2)

in which

$$\omega_a = \mu_0 \gamma M_0 = \gamma_0 M_0$$

$$\omega_0 = \mu_0 \gamma H_0 = \gamma_0 H_0$$

$$\gamma = \text{gyromagnetic ratio} = g(e/2m)$$

N_x, N_y, N_z = effective demagnetizing factors in x, y, and z directions

τ = Bloch-Bloembergen phenomenological relaxation time

- g = Landé "g" factor ≈ 2.00 for electrons in most ferrites
 e/m = ratio of charge, e , to mass, m , of electron
 $= 1.759 \times 10^{11}$ coulombs/kg
 M_0 = saturation magnetization in amperes/meter
 μ_0 = intrinsic permeability of free space
 $= 1.256 \times 10^{-6}$ henries per meter.

In the case of a spherical geometry, $N_x = N_y = N_z = 1/3$, and Eq. (28-2) becomes, after some algebraic reduction and elimination of terms of order $1/\tau^2$ or smaller,

$$-X_{xx}^e = X_{yy}^e = \frac{\omega_0 \omega_m}{\omega_0^2 - \omega^2 + \frac{2j\omega}{\tau} \left(1 + \frac{\omega_m/3}{\omega_0 - \omega_m/3} \right)} \quad (a)$$

$$X_{xy}^e = -X_{yx}^e = \frac{-j\omega_m \omega}{\omega_0^2 - \omega^2 + \frac{2j\omega}{\tau} \left(1 + \frac{\omega_m/3}{\omega_0 - \omega_m/3} \right)} \quad (b)$$

(28-3)

2. DEVELOPMENT OF EQUIVALENT CIRCUIT REPRESENTATIONS

The complete equivalent circuit of the ferrimagnetic resonator located at the intersection of the two loops has previously been worked out in detail^{1,2} and is shown in Fig. 28-2. It consists of a resonant circuit which is coupled inductively to the signal current source i_s with source impedance R_s and to the load impedance R_y . In addition to the series-resonant circuit there is a non-reciprocal phase shifter which produces, with the coil arrangement shown in Fig. 28-1, an additional negative, 90-degree phase shift in the output voltage across R_y . With the signal generator connected to the y terminals, an additional positive 90-degree phase shift is produced across R_x . The analytical development of the circuit representation of the ferrimagnetic resonator has been carried out for the following cases:

- (1) Ferrimagnetic resonator located at the intersection of the axes of the two orthogonal loops shown in Fig. 28-1.

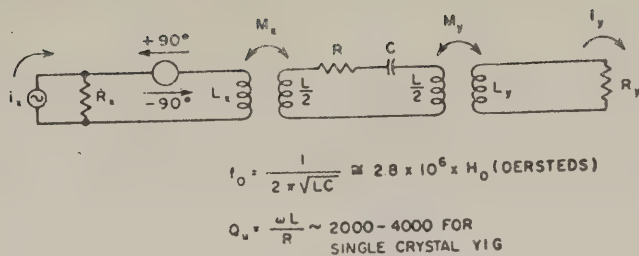


FIG. 28-2
EQUIVALENT CIRCUIT OF MAGNETIC RESONANCE FILTER

- (2) Resonator located at a position of the "detuned short" along a two-wire TEM-mode transmission line, shown in Fig. 28-3(b),
- (3) Same as (2) in a strip-center-conductor line
- (4) Resonator located at a position of the detuned short at the center of a TE_{10} -mode waveguide.

In each case the complete equivalent circuit of the ferrimagnetic resonator coupled to the external circuit is expressed in terms of the unloaded Q , Q_u , of the resonator and the coupled or external Q , Q_e .¹³ The unloaded Q , Q_u , of the ferrimagnetic resonator, is a property of the ferrimagnetic material and is independent of the external circuit coupling.* An analytical expression for Q_u derived from the equivalent circuit is given by,

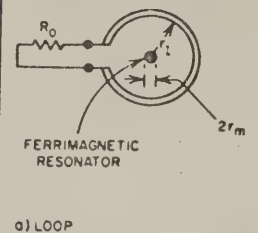
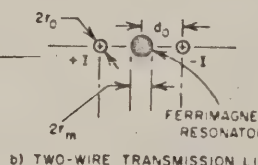
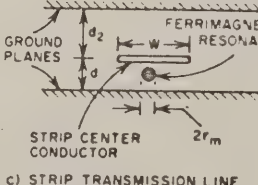
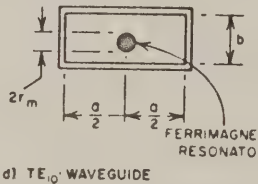
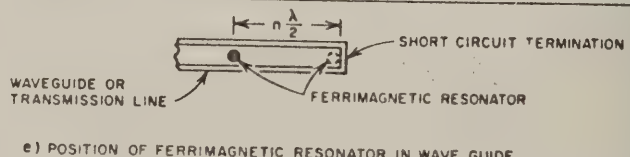
$$Q_u = (\omega_0 - N_s \omega_s) \tau / 2$$

$$= \frac{H_0 - N_s M_0}{\Delta H^i}$$
(28-4)

where ΔH^i is the line width given by

$$\Delta H^i = 2/\gamma_0 \tau$$

* This is true for the unperturbed resonator located at a sufficiently great distance away from the conducting boundaries of the waveguide. For close wall-to-resonator spacings the resistive losses due to "image" currents in the waveguide walls and also the detuning effects of these images would play an important part in determining the resonance characteristics.

| STRUCTURE | Q_e |
|--|---|
|  <p>a) LOOP</p> | $Q_e = \frac{4r_0^2 R_0}{\mu_0 V_m \omega_m} \left[1 + \left(\frac{\omega L_1}{R_0} \right)^2 \right]$ <p>V_m = VOLUME OF FERRIMAGNETIC RESONATOR</p> <p>$\omega_m = \gamma_0 M_0 = \gamma (\mu_0 M_0)$</p> <p>$L_1$ = SELF-INDUCTANCE OF LOOP</p> |
|  <p>b) TWO-WIRE TRANSMISSION LINE</p> | $Q_e = \frac{120 (\pi d_0)^2 \cosh^{-1} \frac{d_0}{r_0}}{\mu_0 \omega_m V_m}$ |
|  <p>c) STRIP TRANSMISSION LINE</p> | <p>NOTE. THIS FORMULA IS BASED ON INFINITE PARALLEL PLANE APPROXIMATION — SEE TEXT FOR CORRECTIONS</p> $Q_e = \frac{120 \pi w \frac{d_1}{d_2} (d_1 + d_2)}{\mu_0 \omega_m V_m}$ |
|  <p>d) TE₁₀ WAVEGUIDE</p> | $Q_e = \frac{60 \pi ab}{\mu_0 \omega_m V_m \left[1 - \left(\frac{f_c}{f} \right)^2 \right]^{\frac{1}{2}}}$ $= \frac{60 \pi ab}{\mu_0 \omega_m V_m} \pi \left(\frac{\lambda_g}{\lambda} \right)$ <p>f_c = CUTOFF FREQUENCY OF GUIDE, f = FREQUENCY</p> <p>λ_g = GUIDE WAVELENGTH; λ = FREE-SPACE WAVELENGTH</p> |
|  <p>e) POSITION OF FERRIMAGNETIC RESONATOR IN WAVE GUIDE</p> | |

8-2328-338

FIG. 28-3
EXTERNAL Q OF FERRIMAGNETIC RESONATOR IN VARIOUS WAVEGUIDE GEOMETRIES

Low values of unloaded Q are predicted for low resonant frequencies. In particular Eq. (28-4) predicts that Q_u will reach zero at a value of DC field and RF frequency given by $\omega_0 = N_s \omega_m$. For a spherical YIG resonator this low-frequency "cut-off" frequency occurs at $f_0 = \omega_m/3 \times 2\pi = 1670$ Mc. Measurements were made of Q_u in the frequency range of this cut-off which support this theory.¹⁴

Eq. (28-4) predicts that Q_u depends on $N_s \omega_m$. A long-rod geometry, for instance, with the DC magnetic field along the axis of the rod, so that $N_s = 0$, should yield a maximum value of Q_u . This effect, i.e., the effect of the shape on Q_u , has not yet to our knowledge been measured. Finally Eq. (28-4) shows that, for a constant relaxation time τ , Q_u is higher in the case of a lower-saturation magnetization material. For frequencies below about 2000 Mc, a low- M_0 , narrow-line-width material is desirable. This is discussed in Section G.

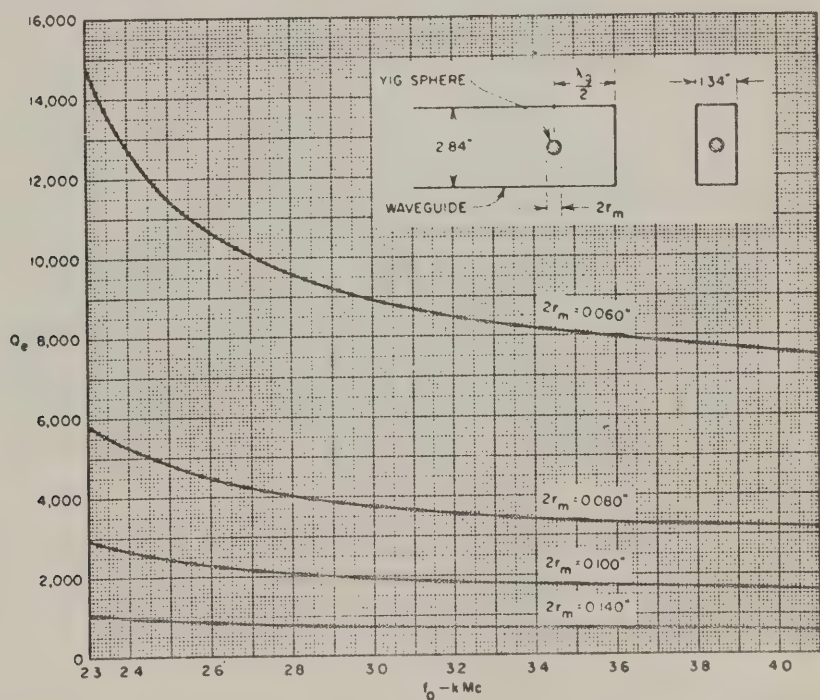


FIG. 28-4

Q_u OF SPHERICAL YIG RESONATOR IN S-BAND RECTANGULAR WAVEGUIDE

The external or coupled Q , Q_e , depends upon the volume of the ferromagnetic resonator, V_m , its saturation magnetization, M_0 , and the type and geometry of the coupling structure. Formulas for Q_e have been calculated for the four cases listed above and the resulting formulas are tabulated in Fig. 28-3. These formulas may be applied to the calculation of the Q_e of the uniform precessional mode for any ellipsoidal shaped magnetic resonator including rods, disks, etc.

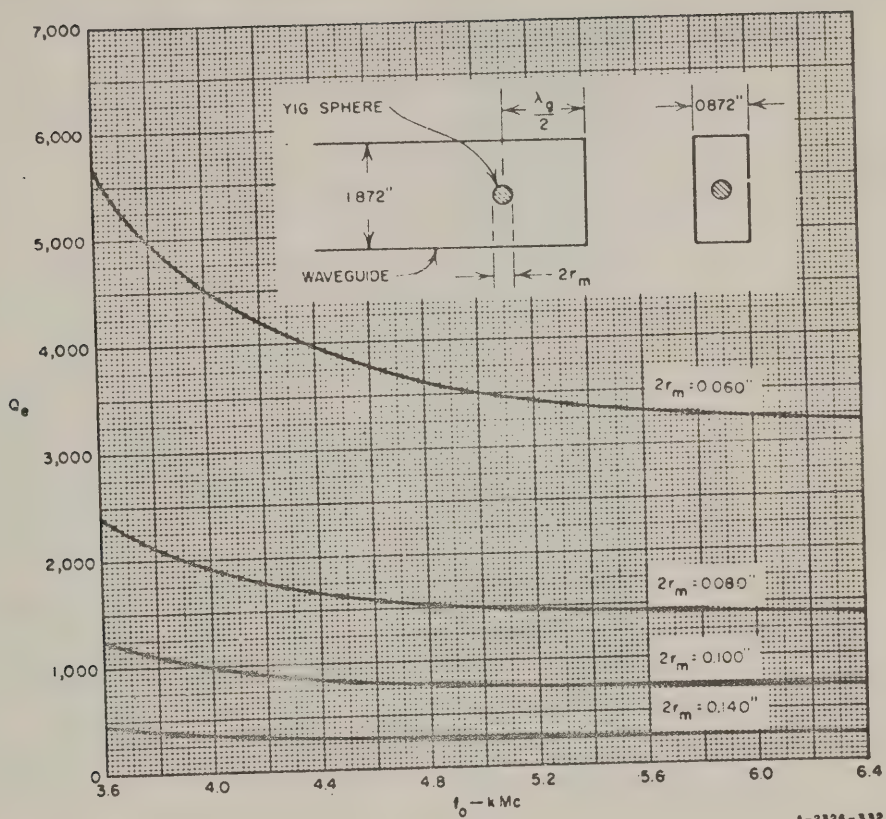
The external Q , Q_e , was calculated from the formula in Fig. 28-3 for YIG spheres mounted in standard-height TE_{10} -mode rectangular waveguide. The calculations were made for standard size S, G, and X-band guides with various YIG sphere diameters from 0.060 inch to 0.140 inch. The results of these calculations are shown in Figs. 28-4 through 28-6. These curves can be used for TE_{10} -mode rectangular guides of other than standard height by applying the following simple transformation:

$$Q_e \text{ of working waveguide} = Q_e \text{ of standard-height guide} \times \frac{\text{working guide height}}{\text{standard guide height}}$$

Thus a YIG spheroid in a one-quarter height TE_{10} -mode rectangular guide will have a Q_e equal to one-fourth that of a YIG spheroid in a standard-height guide. Similarly since Q_e is inversely proportional to the volume of the sphere, the Q_e of a 0.100-inch diameter sphere will be one-eighth that of a 0.050-inch diameter.

Since Q_e depends only on volume of the magnetic material, the calculated values shown in Figs. 28-4 through 28-6 as well as the formulas given in Fig. 28-3 can all be used for ellipsoidal resonator shapes other than spheres. In the case of the formulas in Fig. 28-3, the product abc of the semi-axes of the ellipsoid replaces r^3 in the denominator of each formula for Q_e . On the calculated curves, Figs. 28-4 through 28-6, an equivalent sphere diameter D_e^* is used where, $D_e^* = 2(abc)^{1/3}$.

The formulas for Q_e given in Fig. 28-3 were derived using two different methods. The first method, which employs the reciprocity theorem, is valid for lumped parameter coupling devices such as loops, and for TEM-mode transmission lines where the characteristic impedance is defined uniquely. The equation for Q_e of the magnetic resonator in the TE_{10} -mode rectangular waveguide shown in Fig. 28-3(d) was derived using a more general coupling



A-2326-332

FIG. 28-5
 Q_e OF SPHERICAL YIG RESONATOR IN G-BAND RECTANGULAR WAVEGUIDE

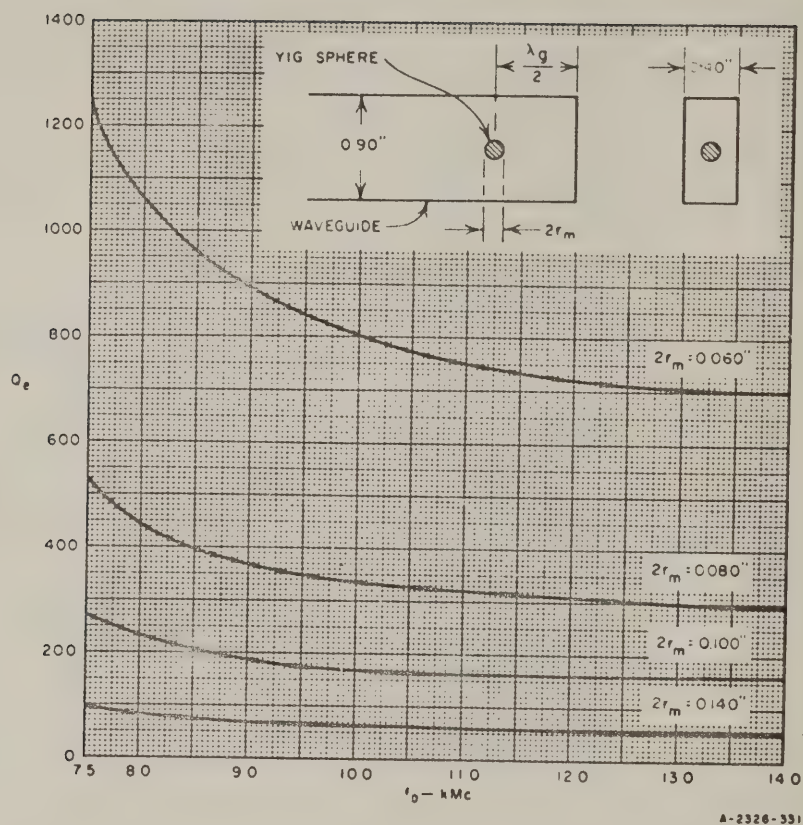


FIG. 28-6
 Q_e OF SPHERICAL YIG RESONATOR IN X-BAND RECTANGULAR WAVEGUIDE

formula which has been discussed by Slater.¹⁵ In this derivation, i.e., for the waveguide case a *linearly polarized* magnetic moment was assumed. The RF magnetic moment of a magnetic resonator is in general *elliptically polarized*. Therefore both components of RF magnetic moment can interact with an elliptically polarized waveguide field. The formula for Q_e given above is therefore valid only for the case where the magnetic sample is located in the linearly polarized field at the center of the guide.^{16*}

3. MEASUREMENT OF EQUIVALENT CIRCUIT QUANTITIES, Q_e AND Q_u

Measurements have been made of the Q_e of single-crystal YIG resonators in strip transmission lines and TE_{10} -mode rectangular waveguide and the results of these measurements are shown in Figs. 28-7 and 28-8. Figure 28-7 shows measurements made on spherical, single-crystal, YIG resonators of various diameters mounted on a wafer of polyfoam in a section of one-quarter height, standard-width, X-band waveguide. The waveguide was short-circuited and the YIG sphere was mounted one-half wavelength away from the short-circuit. The measurements were made in this configuration at 10.0 kMc using the impedance method described by Ginzton.¹⁷ The solid curve represents the theoretical formula for Q_e . Close agreement between the experimental and the theoretical values is evident. When resonator diameters greater than about 0.070 inch were used, the accuracy of the measurement was diminished by the relatively higher degree of coupling between the external circuit and the higher-order magnetostatic modes. The effect of the higher-order modes on filter performance is discussed in Section E.

In these waveguide measurements it was found that the presence of an appreciable amount of dielectric material in the region of the YIG sample sphere caused a variation of the measured values of Q_e and also of Q_u . It was found that these effects were eliminated when the spheres were mounted in a wafer of polyfoam.

Figure 28-8 shows measurements of Q_e of resonators in a strip-transmission-line coupling circuit. The strip-transmission-line configuration, shown in Fig. 28-8, has a 0.500-inch-wide, 0.020-inch-thick center conductor which is spaced 0.135 inch away from the outer conductor on both sides of the center conductor. The inside width of the outer conductor is 1.00 inch. The measurements of Q_e were made at a resonant frequency,

* Recently while this paper was being revised, the author became aware of a more general scattering formula which is applicable in the case where the ellipsoidal sample is at an arbitrary position in the guide. This formula is given in Ref. 18.

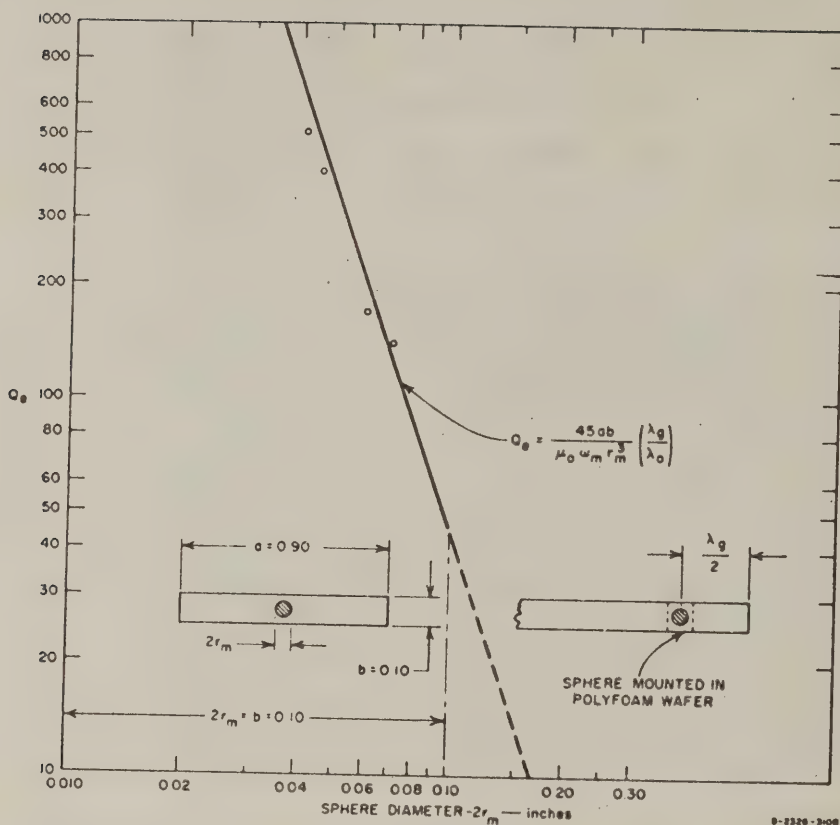


FIG. 28-7
THEORETICAL AND EXPERIMENTAL Q_e OF YIG RESONATORS
IN REDUCED (ONE-QUARTER) HEIGHT, STANDARD WIDTH
X-BAND WAVEGUIDE AT 10,000 Mc

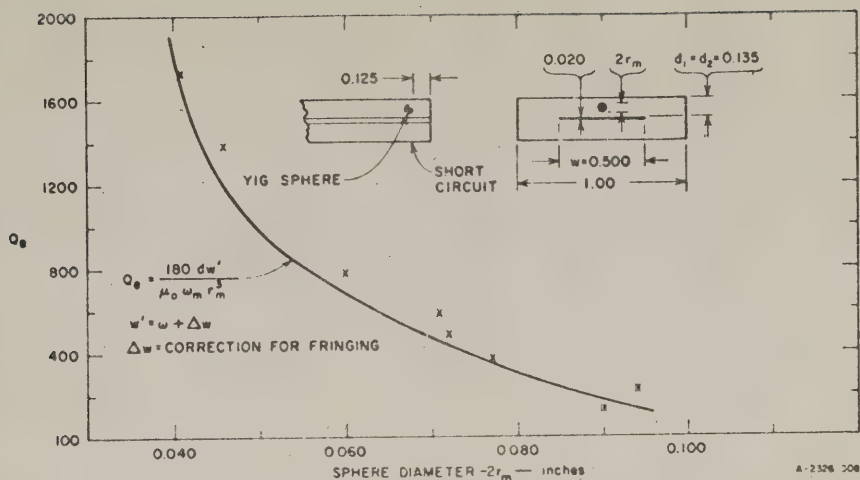


FIG. 28-8
THEORETICAL AND EXPERIMENTAL VALUES OF Q_e OF YIG RESONATOR
USING STRIP-TRANSMISSION-LINE

$f_0 = 3000$ Mc. The YIG resonator was mounted close to the short-circuited end of the strip transmission line. This is the position occupied by the resonator in a magnetically tunable filter where a broad tuning range is desired, since this position near the short-circuit remains a position of nearly maximum magnetic field as the frequency is varied. The minimum distance between the sphere and the short-circuited end is prescribed by the maximum allowable response to the higher-order magnetostatic modes. With the resonator touching the short-circuit, appreciable coupling to higher-order modes results. It was determined experimentally, in the case shown in Fig. 28-8 with 0.125-inch spacing between the resonator and the end wall, that the coupling to higher-order modes was very loose, i.e., $Q_e > 15,000$ for the most strongly coupled higher-order mode. The coupling to the uniform precession mode resonance at 3000 Mc was not measurably decreased by this spacing.

The theoretical values for Q_e of the strip transmission line are shown in Fig. 28-8 as the solid-line curve. This curve was calculated using the formula given in Fig. 28-3(c), which is very accurate for the cases where $w \gg d_1$ and d_2 , but which is not quite so accurate in this case where $w = 0.500$ inch and $d_1 = d_2 = 0.135$ inch. An empirical

correction was applied to improve the accuracy of this formula, by replacing w in Fig. 28-3(c) by a slightly larger value, w' , which takes into account the fringing of the field at the edge of the strip center conductor. This corrected width, w' , was obtained as follows: the characteristic impedance Z'_0 of the actual configuration shown in Fig. 28-8 was obtained from an accurate formula¹⁸ which includes the effect of the finite thickness of the center conductor and the fringing of the field at the two edges. This value of characteristic impedance Z'_0 was then used to compute an effective strip width, w' , based on the parallel-plane formula, i.e.,

$$w' = \frac{\eta_0}{Z'_0} \frac{d_1 d_2}{d_1 + d_2} \quad (28-5)$$

again using the actual conductor spacings d_1 and d_2 .

The agreement between the measured and theoretical values of Q_s was quite good, as is shown in Fig. 28-8. The measured values of Q_s begin to deviate appreciably from the calculated values only for the largest values of YIG sphere diameter, around 0.090 inch. For these largest sphere diameters the measured value of Q_s is also sensitive to the exact location of the sphere with respect to the conducting walls. This shows that the boundary conditions imposed on the motion of the magnetization by the conducting surfaces of the strip transmission line have an appreciable effect on the coupling.

The strip transmission line offers some advantages over the waveguide from the standpoint of flexibility of design. Examination of the formula in Fig. 28-3(c) for the Q_s of a strip transmission line shows that it is possible to adjust both the characteristic impedance of the line and Q_s independently by means of adjustments of the strip center conductor width, w , and ground plane spacings, d_1 and d_2 .

Figure 28-9 shows the measured values of the unloaded Q , Q_u , of a highly polished 0.064-inch-diameter YIG sphere as a function of frequency in the frequency range between 1.8 kMc and 12.6 kMc. The strip-transmission-line device shown in Fig. 28-8 was utilized, using the impedance method¹⁷ to obtain the data between 1.8 kMc and 4.8 kMc. The measured Q_u 's between 8.2 kMc and 12.4 kMc were obtained from the transmission-loss and bandwidth measurements made on the single-resonator tunable filter described in Section E. The equations for obtaining Q_u from bandwidth and insertion loss data have been given by Ginzton.¹⁷

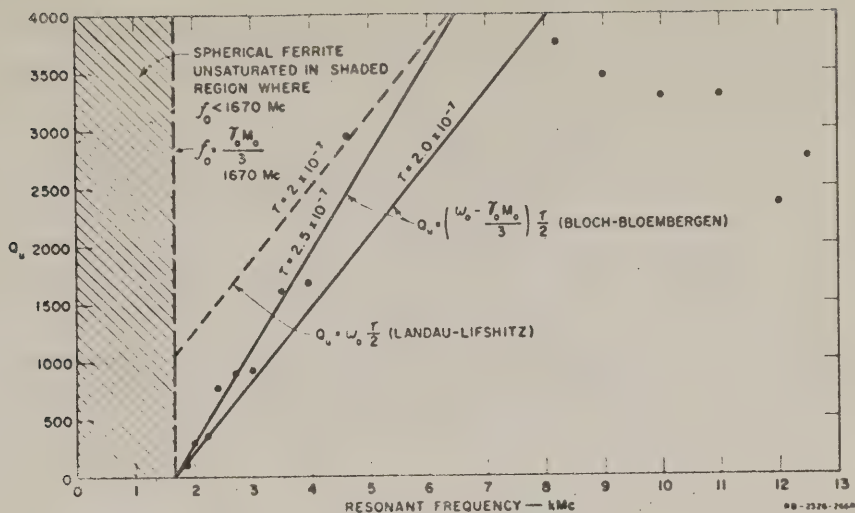


FIG. 28-9
MEASURED UNLOADED Q OF 0.064-INCH-DIAMETER YIG RESONATOR

The 1.8-4.8 kMc data lie along a nearly straight line in this frequency range. This straight line is described quite closely by Eq. (28-4) with $\tau = 2.5 \times 10^{-7}$. Equation (28-4) was derived using the Bloch-Bloembergen formulation of the equations of motion of magnetization.¹⁹ Also shown in Fig. 28-9 is a plot of Q_u vs frequency derived from the Landau-Lifshitz¹⁹ equations of motion of the magnetization with a constant relaxation time, $\tau = 2.0 \times 10^{-7}$. The corresponding equation for Q_u is,

$$Q_u = \omega_0 \tau / 2 \quad (28-6)$$

In the low-frequency region between 1.8 kMc and 4.8 kMc, the measured data follow more closely the straight-line curve based on the Bloch-Bloembergen equations of motion. A more detailed analysis is necessary to explain the frequency variation of Q_u at higher frequencies.

Q_u is critically dependent upon the surface polish of the YIG sample. In this case the rough YIG sphere was first ground from a raw YIG crystal by a tumbling process similar to that described by Carter, Edwards, and Reingold.²⁰ This particular sphere was then polished* utilizing a slightl

* Recently a more satisfactory polishing procedure was developed which utilized a motor-driven polishing head and 1-micron diamond polishing compound. This procedure will be reported at a later date.

different tumbling process described by Bond.²¹ The successive grades of abrasive grinding paper and powder used were as follows:

Silicon carbide, No. 360, No. 600

Emery polishing paper, No. 2/0 and 4/0.

Linde fine abrasive No. B-5125.

D. DC MAGNETIC FIELD REQUIRED FOR RESONANCE

The analytical treatment of the general case of resonance in a ferrite or garnet including magnetocrystalline anisotropy is quite complicated. For the special case, where the DC field is applied along one of the principal axes of the ellipsoid and also in one of the planes of crystal symmetry, the effect of anisotropy on the resonant frequency can be represented by "anisotropy" demagnetizing factors V_x^* and V_y^* in addition to the usual shape-dependent demagnetizing factors N_x , N_y , and N_z given in Eq. (28-2). The new resonant frequency ω_r , which results when these anisotropy demagnetizing factors are included in the equation of motion is,

$$\omega_r = \gamma_0 \{ [H_0 + (N_y + V_y^* - V_x)V_0] [H_0 + (N_x + V_x^* - V_y)V_0] \}^{1/2} \quad (28-7)$$

The anisotropy demagnetizing factors V_x^* and V_y^* have been given by Bickford²² for cubic crystals (into which class yttrium-iron-garnet falls) for the following two cases:

- (1) DC magnetic field in a (100) crystal plane,²³
- (2) DC magnetic field in a (110) crystal plane.

In Case (1) they are, considering only first-order anisotropy,

$$\mu_0 V_x^* = (2K_1/M_0^2) \cos 4\theta \quad (a)$$

$$\mu_0 V_y^* = \left(\frac{3}{2} + \frac{1}{2} \cos 4\theta \right) K_1/M_0^2 \quad (b) \quad (28-8)$$

* Definitions of the principal directions and planes in crystals are given in any standard textbook in solid-state physics or crystallography, such as Ref. 23. The Miller indices specifying either the three principal directions or planes of a cubic crystal are given by three sets of numbers, either brackets [] or parentheses () surrounding them indicating a principal direction or the principal plane perpendicular to that principal direction, respectively. For instance, [010] is one of the three equivalent directions in a cubic lattice while (010) is the plane perpendicular to this direction.

where θ , shown in Fig. 28-10(a) is the angle between the magnetization and a [100] crystal direction, and K_1 is the first-order anisotropy constant.²³

In Case (2) the effective demagnetization factors due to anisotropy are given by,

$$\mu_0 N_x^e = (2 - \sin^2 \theta - 3 \sin^2 2\theta) K_1 / M_0^2 \quad (a) \quad (28-9)$$

$$\mu_0 N_y^e = 2(1 - 2 \sin^2 \theta - 3/8 \sin^2 2\theta) K_1 / M_0^2 \quad (b)$$

where θ shown in Fig. 28-10(b) is the angle between the magnetization M_0 and a [100] crystal direction. The constant K_1/M_0 , has been measured for yttrium-iron-garnet by Dillon,²⁴ and was found to be -43 oersteds at room temperature.

A particular case which is very useful to us is the case of resonance with the DC magnetic field along the direction of the easy axis of magnetization. In the case of a cubic crystal structure with a negative K_1 , the easy axis is the [111] axis. Along this axis the resonant field for a spherical sample is given by,²⁵

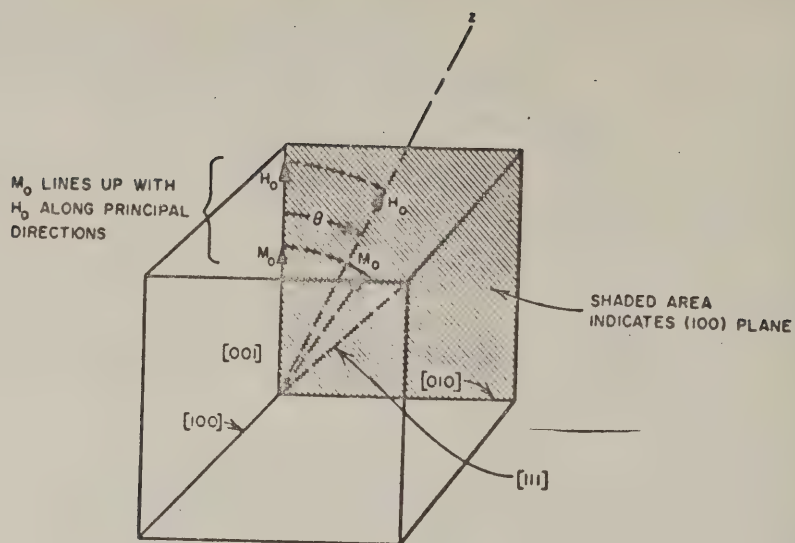
$$\frac{\omega_r}{\gamma_0} = H_0 + \frac{4}{3} \left| \frac{K_1}{M_0} \right| \quad (28-10)$$

and is independent of the rotation of the crystal around this axis. This case has been calculated for yttrium-iron-garnet at room temperature (300°K) where $K_1/M = -43$ oersteds and is shown in Fig. 28-11. The other two principal directions are also included in Fig. 28-11, i.e., the [100] axis and the [110] axis. Along these three principal axes only, the magnetization M_0 is lined up with the applied DC field, H_0 . The corresponding formulas for resonance are,

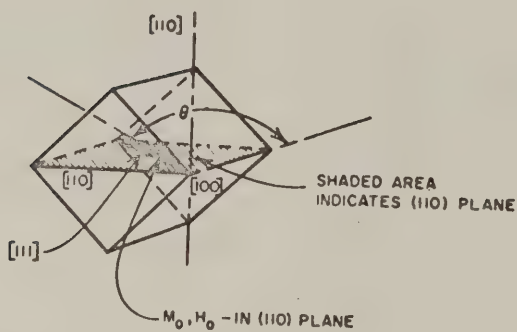
[100] axis

$$\frac{\omega_r}{\gamma_0} = H_0 - 2 \left| \frac{K_1}{M_0} \right| \quad (28-11)$$

* Occasionally, as when quoting results directly from a reference, the original units will be used. In specifying the DC magnetic field required for resonance (Fig. 28-11) gaussian units are used since specifications on magnets are almost universally given this way.



(a) M_0 AND H_0 IN (100) PLANE



(b) M_0 AND H_0 IN (110) PLANE

A-2326-329

FIG. 28-10
NOMENCLATURE OF DIRECTIONS AND PLANES IN CUBIC CRYSTAL

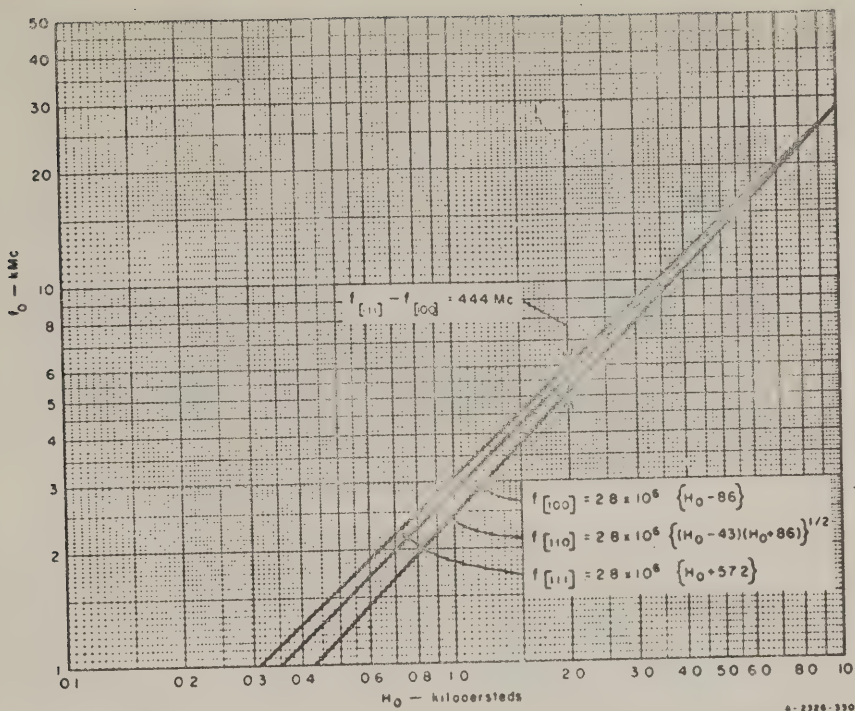


FIG. 28-11

RESONANT FREQUENCY OF YIG SPHERE VS APPLIED dc FIELD
WITH FIELD ALONG PRINCIPAL AXES

[110] axis

$$\frac{\omega_0}{\gamma_0} = \left(H_0 - \left| \frac{K_1}{M_0} \right| \right) \left(H_0 + 2 \left| \frac{K_1}{M_0} \right| \right)^{1/2} \quad (28-12)$$

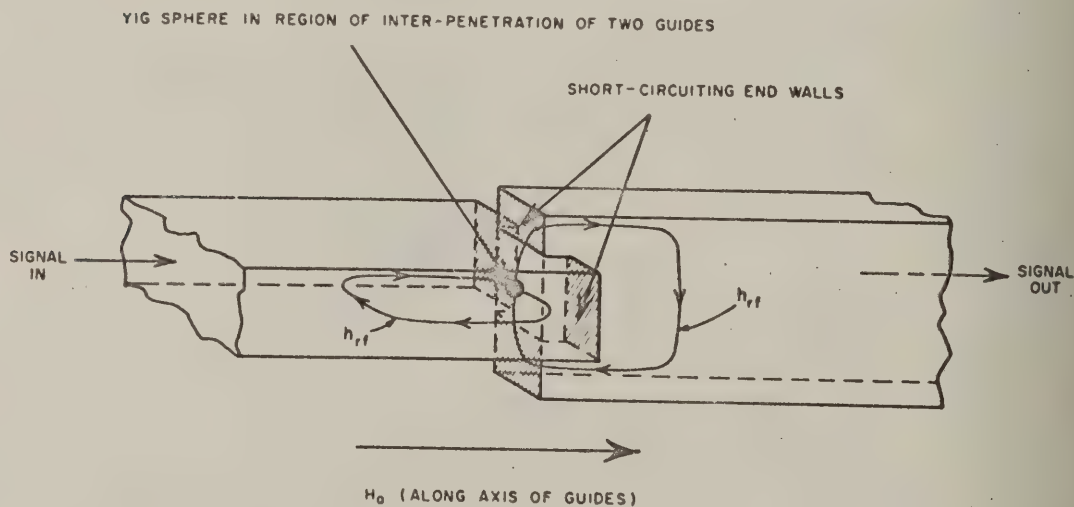
The variation of the resonant frequency as the orientation of the DC magnetic field along a sphere is changed from the "easy" [111] to the "hard" [100] direction, is 444 Mc. Thus, in the case of multi-resonator filters utilizing these garnet resonators the crystals axes must be accurately aligned with respect to the DC field.

The variation of the resonant frequency with temperature is caused by the variation of the anisotropy with temperature. This variation is considerable, especially at lower temperatures where the anisotropy constant, K_1 , is much larger than at room temperatures. This variation of the resonant frequency due to temperature changes can be calculated using Eqs. (28-8), (28-9), and (28-7).

It will be noted from Eq. (28-7) and Fig. 28-11 that there is a crystal orientation for which the effect of the anisotropy demagnetizing factors on the resonant frequency is cancelled to a considerable degree in the case where $N_x^a = -N_y^a$. In this orientation, the resonant frequency ω_r will be nearly constant as the temperature is varied. The residual variation of resonant frequency will depend on the ratio, $N_x^a M_0/H_0$, of the demagnetizing field to the biasing field. This ratio is quite small in the case of YIG at microwave frequencies. One angle θ exists in the (100) plane for which the above condition exists, i.e., $N_x^a = -N_y^a$. Referring to Artman's²³ Fig. 4 it is seen that this condition is met when $\theta \approx 21^\circ$. This angle could also be found by setting $N_x^a = -N_y^a$ in Eq. (28-9).

E. DEVELOPMENT OF SINGLE-RESONATOR TUNABLE FILTER

A single-resonator tunable filter using waveguide coupling was constructed which is tunable over the X-band frequency range from 7.00 kMc to 11.00 kMc. The waveguide coupling arrangement, shown in Fig. 28-12 is analogous to the crossed loops in Fig. 28-1. The single-crystal YIG sphere is mounted on a styrofoam support in the open iris region which is common



A-2326-334

FIG. 28-12
COUPLING PRINCIPLE OF SINGLE RESONATOR WAVEGUIDE FILTER

to the input and output waveguides. The depth of this region of interpenetration, as well as the guide height and resonator size, can be varied to control the coupling, Q_u , between the guides and the resonator. The bias field is applied along the common axis of the guides.

Figures 28-13 and 28-14 show the construction of the experimental single-resonator filter employing standard-width X-band waveguide. The half-height ($b = 0.200$ -inch) coupling sections used in this experimental filter are followed by E-plane circular bends (mean radius = 0.300-inch). These E-plane bends permit the use of a "c" type electromagnet for biasing along the axis of transmission of the guides. Immediately following the E-plane bends are 2.20-inch-long straight tapers joining the half-height sections to the full-height X-band input and output guides. The interpenetration of the two guides was accomplished by milling out 0.035-inch-deep slots in the face of the opposite section, as shown in Figs. 28-13 and 28-14.

The measured responses of this single-resonator filter when it was tuned to resonate successively at 8.20, 9.00, 10.00, and 11.00 kMc are shown in Fig. 28-15. Table 28-1 shows the insertion losses at these frequencies and also at 7.00 kMc. The 3-db bandwidths, and the peak response of the strongest subsidiary mode, are also shown in Table 28-1. Table 28-1 includes the values of Q_u which were calculated from the insertion loss and bandwidth data using equations given by Ginzton.¹⁷

A prominent feature of this single-resonator-filter response is the presence of a large number of subsidiary responses. These responses are due to higher-order magnetostatic resonances within the ferrimagnetic sample. These resonances, which were first analyzed by Walker²⁶ are due to the non-uniform motion of the magnetization within the ferrimagnetic sample and the resulting dipolar interactions between the magnetic moments. It was shown by Walker²⁶ that

these resonances are characterized by the fact that they are (1) independent of the size of the sample, i.e., that they depend upon the shape only, and (2) that they occur only at frequencies given by,

$$\omega_0 + \gamma_0 \frac{M_0}{2} \geq \omega \geq \omega_0$$

TABLE 28-1
PERFORMANCE OF SINGLE-RESONATOR FILTER

| $f(\text{kMc})$ | INSERTION LOSS AT RESONANCE (db) | 3-db BANDWIDTH (Mc) | Q_u | STRONGEST MAGNETOSTATIC MODE RESPONSE (db Below Transmission at Main Resonance) |
|-----------------|----------------------------------|---------------------|-------|---|
| 7.00 | 2.0 | Not measured | -- | -17 |
| 8.20 | 1.5 | 14 | 3600 | -18 |
| 9.00 | 1.2 | 20 | 3400 | -23 |
| 10.00 | 1.3 | 25 | 3200 | -17 |
| 11.00 | 1.1 | 28 | 3200 | |

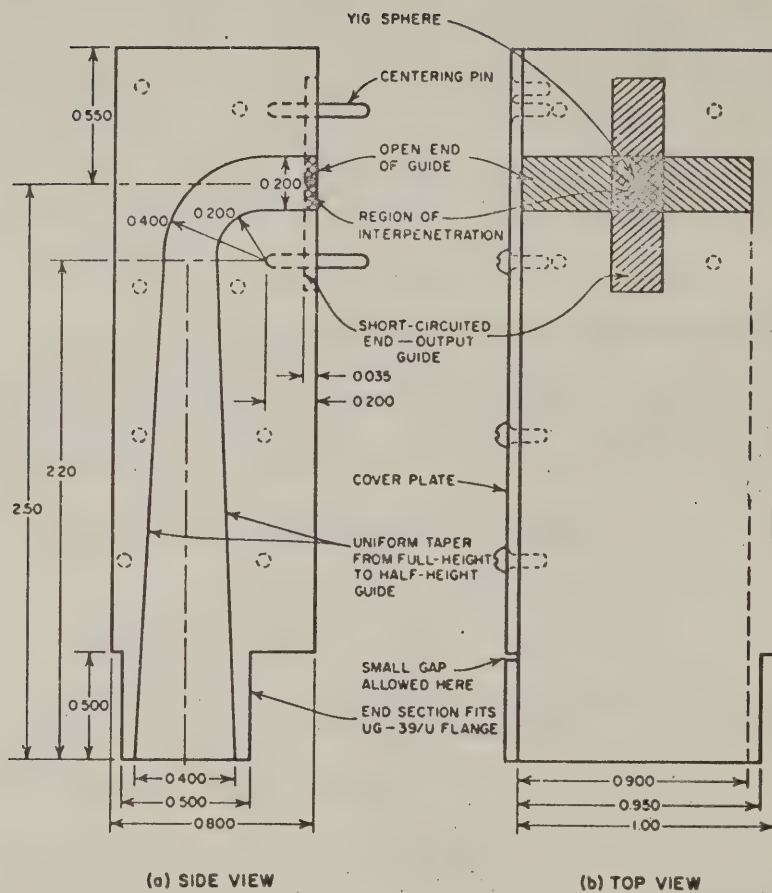


FIG. 28-13
CONSTRUCTION OF HALF-SECTION OF SINGLE-RESONATOR FILTER

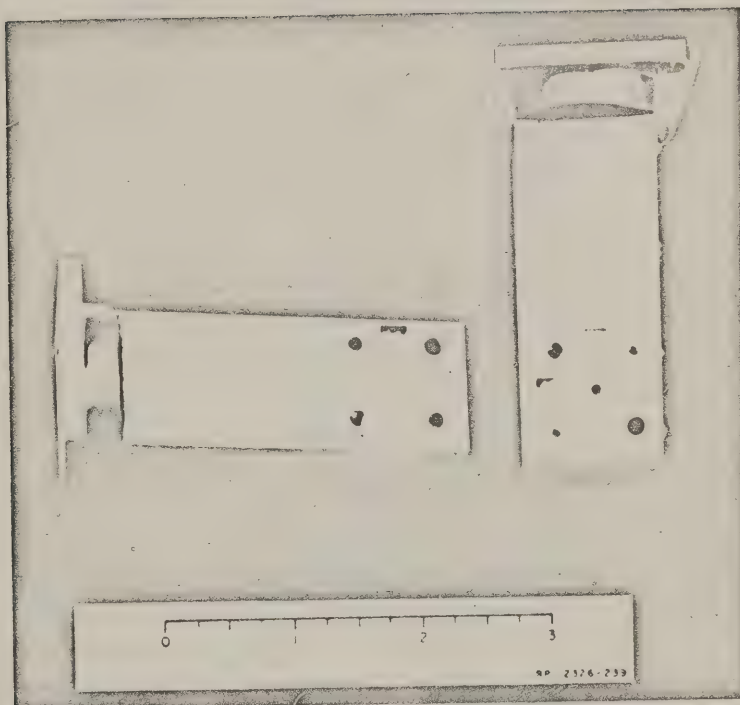


FIG. 28-14
PHOTOGRAPH OF SINGLE-RESONATOR FILTER

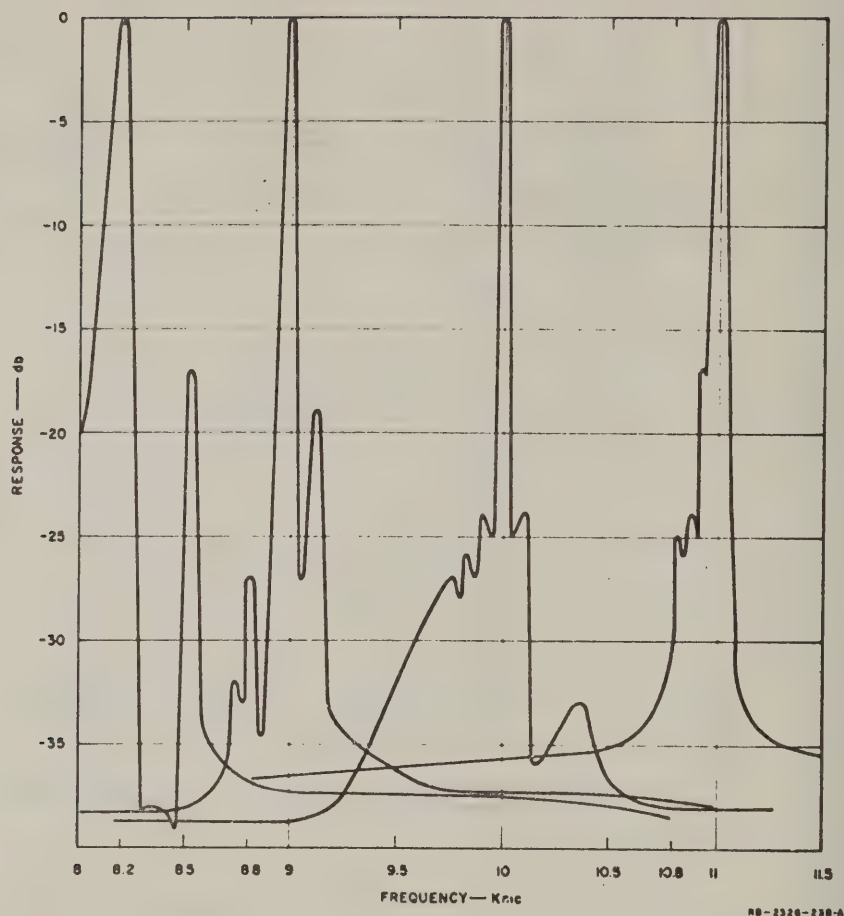


FIG. 28-15
SINGLE RESONATOR FILTER RESPONSE CURVES

$$\omega_0 = \gamma_0 H_0 .$$

Thus the resonant frequencies of these non-uniform resonances occur within a spectrum which is $\gamma_0 H_0 / 2$ cycles wide. For yttrium-iron-garnet in which the saturation magnetization, M_0 , is approximately 1395×10^2 amperes/meter, the width of this frequency band is 2450 Mc. Coupling to these resonances occurs when the RF coupling field is non-uniform over the dimensions of the sample. The maximum allowable response to higher-order modes thus dictates the largest-size ferrimagnetic resonator that can be used in a specific coupling circuit. From a practical standpoint, this restriction limits the diameter of the spherical resonator used in the present X-band single-resonator filter to less than around 0.100 inch.

The spurious responses due to the higher-order magnetostatic modes are greatly reduced by the use of two or more ferrimagnetic resonators which are coupled together directly by means of their external RF fields. This is described in detail in Section F.

A characteristic feature of this single-resonator filter using TE₁₀-mode waveguide is the increase of the 3-db bandwidth and the decrease of the insertion loss as the center frequency is raised. This increase in bandwidth, as well as the decrease in insertion loss, is due to the decrease of the external Q , Q_e , of the waveguide coupling circuit, as the frequency is increased (see Fig. 28-6). This variation of the bandwidth over the tuning range can be minimized by the use of a constant characteristic-impedance coupling circuit, such as the TEM-mode strip-transmission line shown in Fig. 28-2.

Another important aspect of the behavior of a YIG resonator is the saturation which occurs at high power levels. This effect is explained in terms of the nonlinear coupling between the uniform precession and the short wavelength spin waves, and has been investigated and explained by Suhl.^{27,28} Figure 28-16 shows the power-limiting behavior of the single-resonator filter when it was tuned to resonate at 9375 Mc. The signal input in this test experiment was a rectangular RF pulse one microsecond in duration with a pulse repetition frequency of one hundred pulses per second. Figure 28-16 shows the saturation (i.e., limiting) of the output level at about 15 watts peak input power. The power was then raised to about 2 kilowatts peak input power, at which point the resonant frequency

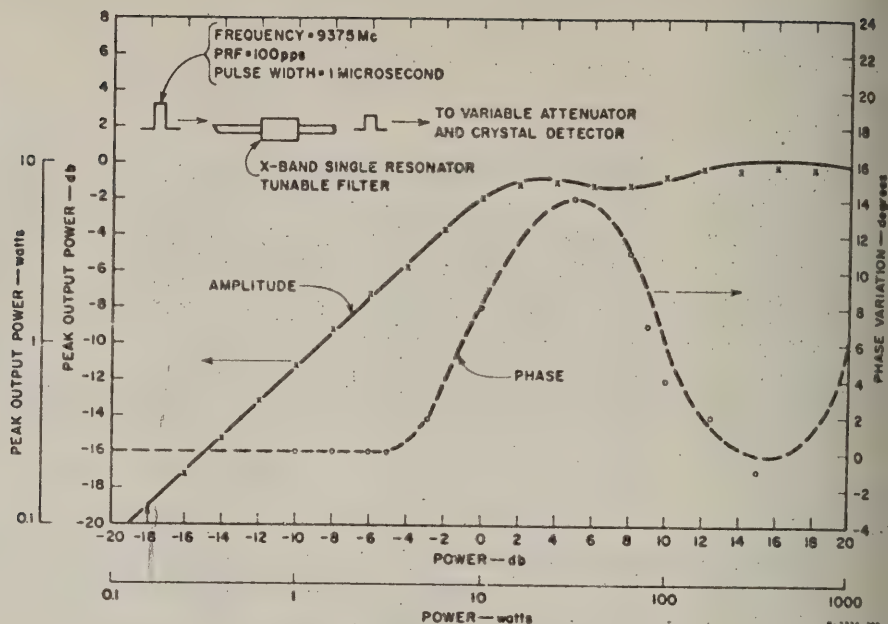


FIG. 28-16

AMPLITUDE AND PHASE OF OUTPUT OF X-BAND SINGLE RESONATOR FILTER VS INPUT POWER

of the filter began to drift, presumably because of the heating of the ferrite and the resulting change in the anisotropy demagnetizing factor.

According to an analysis by Siegman²⁹ of the limiting action in this type of device, the phase of the RF output should remain constant above the limiting threshold. Figure 28-16 shows a measured RF phase variation of only 14 degrees. Since the output pulse also showed an appreciable "spike" leakage at the leading edge of the pulse, this 14-degree variation of phase is not regarded as significant.

F. DEVELOPMENT OF A TWO-RESONATOR FILTER

Figure 28-17 shows the application of two YIG spheres to form a two resonator filter. Coupling between the two resonators is provided by the long-slot iris in a 0.010-inch-thick conducting wall separating the input and output waveguides.* The use of the long vertical coupling slot

* The use of polarized-slot coupling was suggested by Dr. E. M. T. Jones of Stanford Research Institute.

permits the vertical components of RF magnetic moment to be coupled through their external RF fields, and prevents the horizontal magnetic fields of the waveguides and the horizontal RF magnetic moments from being coupled together appreciably.

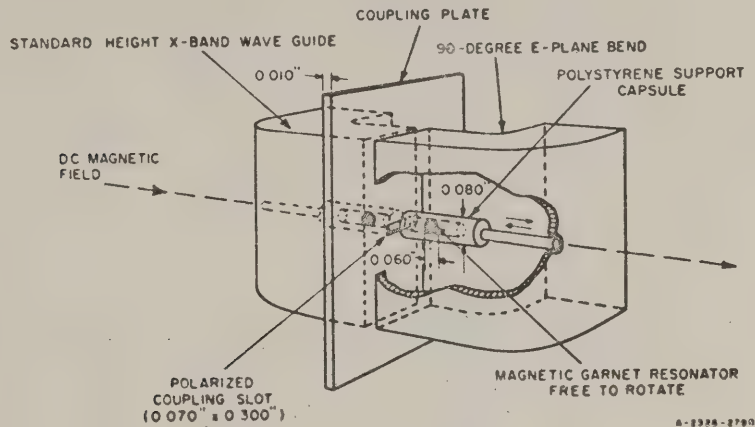


FIG. 28-17
TWO-RESONATOR FILTER

Synchronous tuning of the two resonators is achieved by mounting the YIG spheres in dielectric capsules so that they are free to turn in any direction. Application of a DC biasing magnetic field results in a torque which causes one of the "easy axes" of magnetization to align itself along the DC magnetic field. Thus, the detuning which would be caused by different alignment of the two resonators is eliminated.

Figure 28-18 shows the disassembled two-resonator filter with the coupling iris and the garnet spheres in 0.080-inch-diameter polystyrene capsules in view. The capsules are mounted on polystyrene rods which are adjusted to vary the spacing of the spheres. Two 90-degree E-plane bends are utilized to make it possible to use a "c"-type electromagnet.

In this experimental model, the input and output guides are standard height X-band guides. Here, as in the case of the single-resonator filter, the guide height or the sphere diameter can be varied to secure the desired filter response. The two garnet spheres used in this experimental model were 0.064 inch and 0.060 inch in diameter.

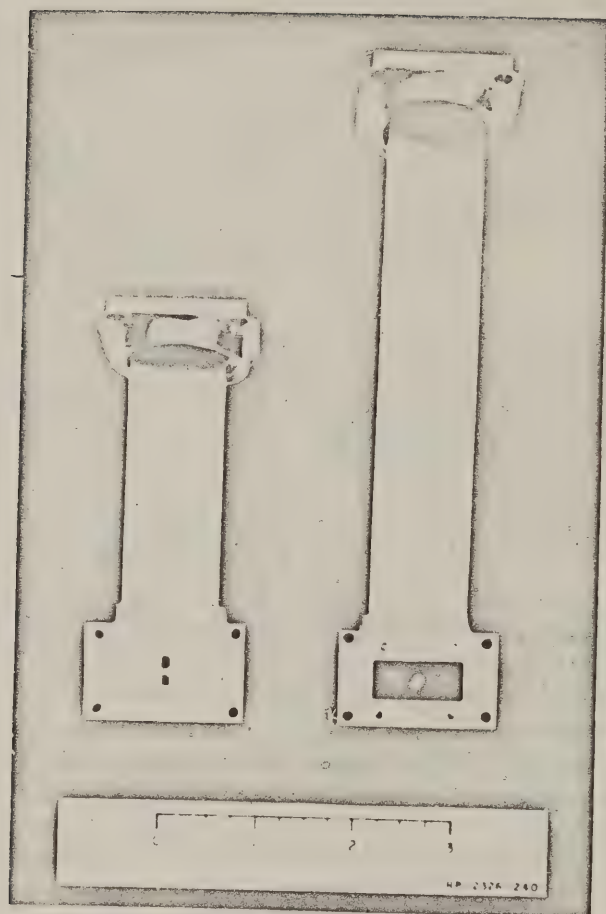
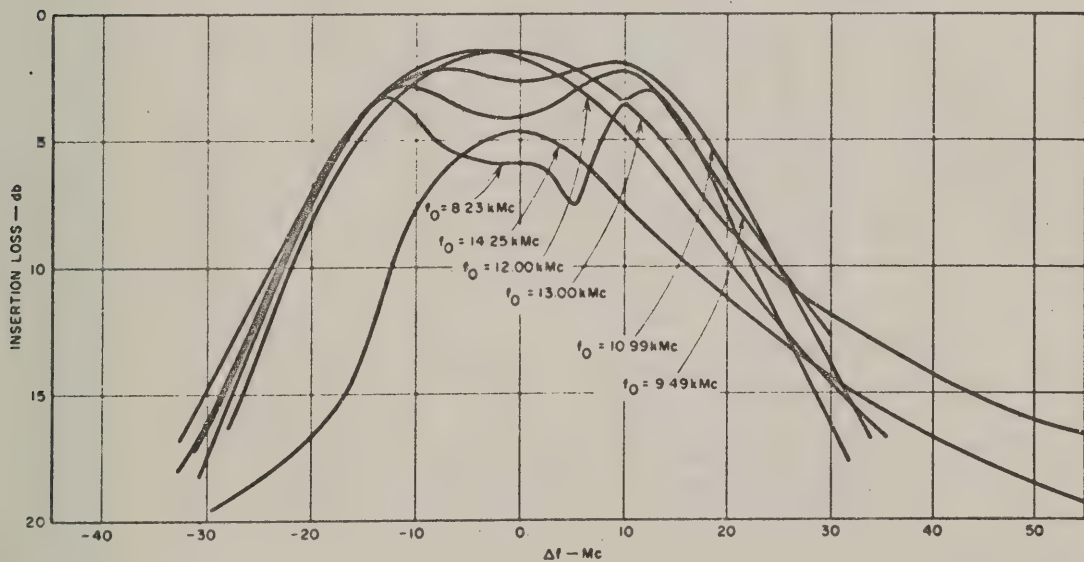


FIG. 28-18
DISASSEMBLED TWO-RESONATOR FILTER

Figure 28-19 shows the measured responses of the two-resonator filter tuned to 8.23 kMc, 9.49 kMc, 10.99 kMc, 12.00 kMc, 13.00 kMc, and 14.25 kMc. The initial adjustment of the filter was made at 9.49 kMc by varying the coupling slot dimensions and the spacing of the resonators to give the slightly overcoupled response with greater than 35 db insertion loss at frequencies far removed from the 9.49-kMc center frequency. This last requirement, i.e., on rejection loss at frequencies far removed from resonance, limits the maximum width of the coupling slot, since the coupling between the guides in the absence of the garnet resonators is proportional to the width of this slot. The isolation obtained in this way can be calculated.^{30,31} The slot dimensions used in this filter are 0.070 inch by 0.300 inch and were determined experimentally to give greater than 35 db off-channel rejection. The spacing between the centers of the YIG spheres was 0.164 inch. It was found that almost any desired degree of overcoupling could be obtained by closer spacing of the YIG resonators. The 3-db and 10-db bandwidths were nearly constant as the center frequency is varied and were about 32 Mc and 56 Mc, respectively.



RD-2326-337

FIG. 28-19
MEASURED RESPONSES OF TWO-RESONATOR FILTER

The trends observed in Fig. 28-19 are (1) a decrease of the degree of overcoupling with increasing frequency, (2) an approximately constant bandwidth throughout the tuning range, and (3) a decrease of insertion loss with increasing frequency. These trends are attributed to the same effect that caused the increase in bandwidth of the single-resonator filter, i.e., the increase, with increasing frequency, of the coupling between the resonators and the waveguides.

The maximum tuning range of this experimental two-resonator filter appears to be limited by the leakage at 15.5 kMc through the coupling slot. This is shown in Fig. 28-20, which is a plot over a broad band of the response of the filter tuned to 12.00 kMc. This leakage occurs when the slot becomes resonant, i.e., one-half wavelength long, at 15 kMc; the slot couples power between the two guides since it is not exactly parallel to the electric field of the waveguide. Evidently this slot response might be reduced by more accurate construction—this slot was cut by hand. Also a shorter, wider slot might give nearly the same response and insertion loss, while the half-wave slot resonance would be moved to a higher frequency.

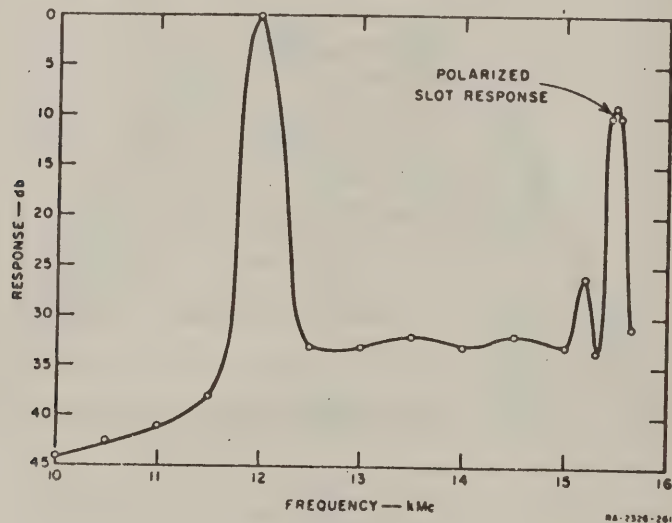


FIG. 28-20
RESPONSE OF TWO-RESONATOR FILTER TUNED TO 12 kMc
SHOWING POLARIZED SLOT LEAKAGE AT 15 kMc

Figure 28-21 shows the response of the two-resonator filter down to -30 db below the peak response, with the center frequency at 11.00 kMc. Unlike the results obtained on the single-resonator filter, no spurious responses are evident here. This greater rejection of the higher-order modes is explained by the fact that the RF fields of the higher-order modes decrease very rapidly with distance away from the spheres, much more rapidly than do the RF fields of the uniform mode. The higher-order modes of the two resonators are therefore coupled together very weakly through their external RF fields and the insertion loss of these modes is therefore very high compared to that of the uniform mode. This property of the two-resonator filter, i.e., the absence of spurious responses, is an important advantage of this type of filter over the single-resonator version.

G. POSSIBLE FUTURE DEVELOPMENTS

Several tunable filter devices are apparently feasible that involve extensions of basic concepts which have been evolved during this program. Also, there are problems not yet entirely solved, e.g., magnetostatic mode responses, which will receive additional attention.

Another type of magnetically tunable filter which appears to be feasible using YIG resonator elements is the band rejection filter. Figure 28-22 shows one possible design using YIG resonators spaced one quarter wavelength away from each other in waveguide, mounted at the center of the guide in the linearly polarized RF magnetic field at that point. Figure 28-22(c) also shows the equivalent lumped-element circuit of this device which consists of alternate series- and parallel-connected parallel resonant circuits.

Strip and coaxial transmission line coupling circuits appear to be feasible and have been employed by DeGrasse⁸ in the construction of an S-band filter-limiter and by Kotzebue³² in a tunable single-resonator filter. Objectives in future work on this subject should be to extend the state of the art of the application of these TEM-mode coupling structures.

Figure 28-23 shows a two-resonator filter structure which uses a strip-transmission-line coupling section. In this filter the biasing field is applied at right angles to the direction of transmission with the result that a U-bend is not required in order to use a "c"-type, biasing magnet. The use of broadband input transformer section enables

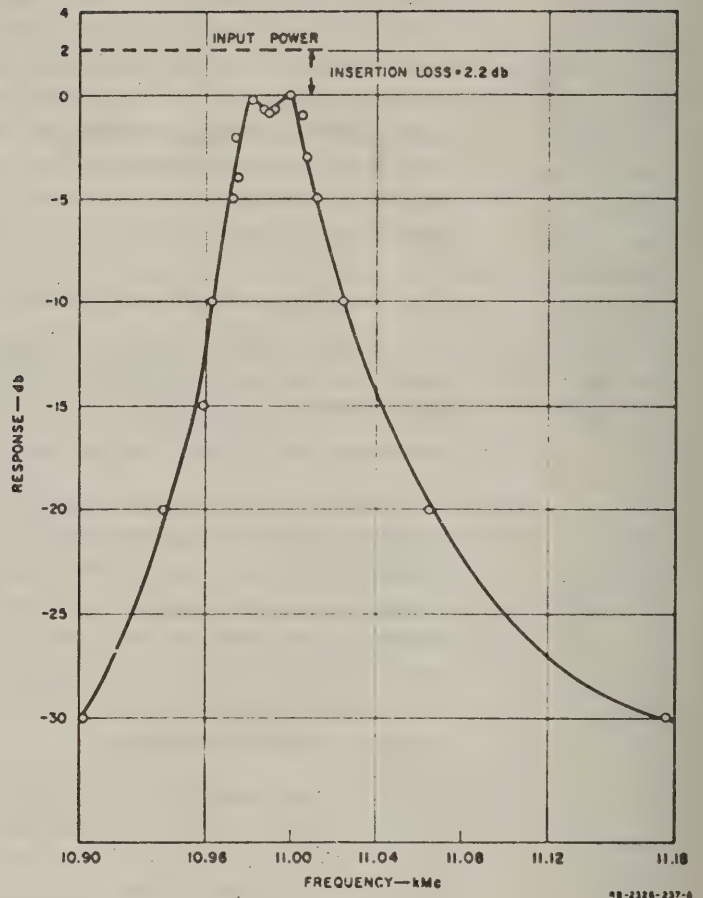


FIG. 28-21
MEASURED RESPONSE OF TWO-RESONATOR FILTER TUNED TO 11 kMc

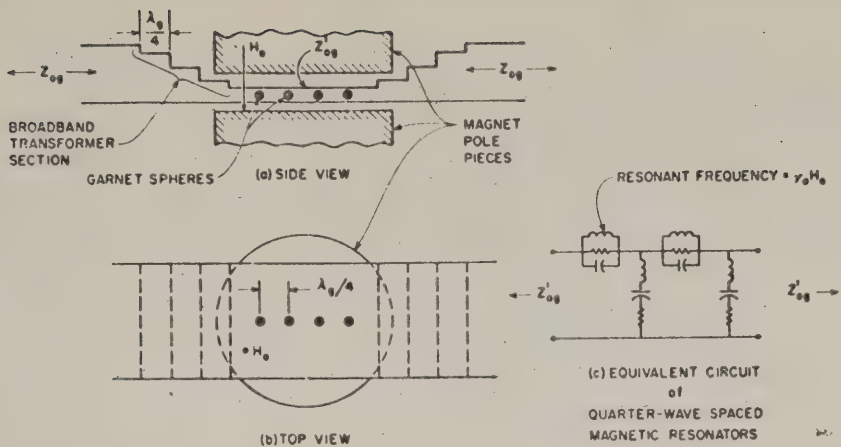


FIG. 28-22

TUNABLE BAND-REJECTION FILTER USING QUARTER-WAVE-SPACED YIG RESONATORS

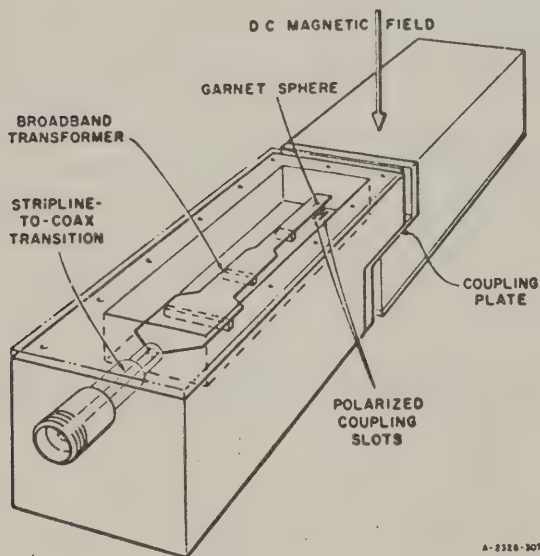


FIG. 28-23

STRIP-TRANSMISSION-LINE-COUPLED TWO-RESONATOR FILTER

the designer to achieve a narrow strip center in the coupling region and therefore to obtain tighter coupling to the YIG resonator. The coupling between the two resonators is obtained by means of the longitudinal slots shown here, which respond to the component of RF magnetic moment which is polarized along the length of the slots.

Very little effort was given, on this contract to the systematic measurement of the properties, i.e., unloaded Q and resonant frequency of the magnetic resonator as a function of DC magnetic field and crystal orientation. These properties should be measured on spheres of different diameters and disks to determine the influence, if any exists, of size and demagnetizing factors.

More effort should be devoted to the development of practical methods for obtaining coupling between resonators in multi-resonator filters. Experiments showed that, using proximity coupling between two with extremely closely spaced resonators, the two resonators did not have the same resonant frequency. This effect was ascribed to the fact that each resonator has a DC magnetic moment that affects the DC magnetic field in the vicinity of the other resonator. Thus, a difference in the sizes, and therefore the magnetic moments, of the two spheres can cause them to be subjected to different DC magnetic fields. Methods other than proximity coupling should therefore be investigated for the purpose of obtaining tight intra-resonator couplings. Possible methods might include the use of quarter-wavelength coupling sections of transmission line, and also short ($< \lambda/4$) coupling line sections with series capacitance, between the resonators.

The extension of these tunable filter devices to frequencies lower than S-band appears to be possible, by the use of a low-magnetization narrow-line-width garnet such as gallium-substituted yttrium-iron-garnet.³³ Work along these lines will be possible when some crystals of this material of usable purity and size become available.

REFERENCES

1. W. J. Gemulla, R. D. Hall, "Ferroelectrics at Microwave Frequencies," *"Microwave Journal*, Vol. 3, No. 2 (February 1960).
2. See Chapter 27 of this report.
3. A. Uhlir, Jr., "The Potential of Semiconductor Diodes in High-Frequency Communications," *Proc. IRE* 46, pp. 1099-1115 (June 1958).
4. G. R. Jones, J. C. Cacheris and C. A. Morrison, "Magnetic Tuning of Resonant Cavities and Wideband Frequency Modulation of Klystrons," *Proc. IRE* 44, pp. 1431-1438 (October 1956).
5. C. E. Ray, "Ferrite-Tuned Resonant Cavities," *Proc. IRE* 44, pp. 1446-1449 (October 1956).
6. C. E. Nelson, "Ferrite-Tunable Microwave Cavities and the Introduction of a New Reflectionless Tunable Microwave Filter," *Proc. IRE* 44, pp. 1449-1455 (October 1956).
7. N. Bloembergen and R. V. Pound, "Radiation Damping in Magnetic Resonance Experiments," *Phys. Rev.* 95, 1, pp. 8-12 (1 July 1954).
8. R. W. DeGrasse, "Low-Loss Gyromagnetic Coupling Through Single Crystal Garnets," *J. Appl. Phys.* Supplement to Vol. 30, No. 4, pp. 1555-1565 (April 1959).
9. Carson Flammer, "Resonance Phenomena in Ferrites," unpublished memorandum, Stanford Research Institute, Menlo Park, California (1956). Stanford Research Institute plans to publish this memorandum in the near future.
10. N. Bloembergen, "Magnetic Resonance in Ferrites," *Proc. IRE* 44, pp. 1259-1269 (October 1956). It has been pointed out by Flammer that Eq. (5) in this reference contains an error. The ω_0/τ should be deleted.
11. C. Kittel, "On the Theory of Ferromagnetic Resonance Absorption," *Phys. Rev.* 73, 2, pp. 155-161 (15 January, 1948).
12. P. S. Carter, Jr. and G. L. Matthaei, "Design Criteria for Microwave Filters and Coupling Structures," Tech. Report 8, SRI Project 2326, Contract DA 36-039 SC-74862, Stanford Research Institute, Menlo Park, California (September 1959).
13. Montgomery, Dicke, and Purcell, *Principles of Microwave Circuits*, Rad. Lab. Series No. 8, pp. 228-239 (McGraw-Hill Book Company, Inc., New York City, 1948).
14. P. S. Carter, Jr. and C. Flammer, "Unloaded Q of Single Crystal Garnet Resonator as a Function of Frequency," Letter to the Editor, *Trans. IRE*, Vol. MTT-8, No. 5, pp. 570-571 (September 1960).
15. J. C. Slater, *Microwave Electronics*, Chapter 7, p. 150 (D. Van Nostrand, Inc., New York, City, 1950).
16. H. J. Shaw and L. K. Anderson, "Interaction of Microwaves With Matter," Tech. Status Rpt. No. 9, Contract AF 49(638)-415, Microwave Laboratory, Stanford University, Stanford, California (1 May-31 July 1960).
17. E. L. Ginzton, *Microwave Measurements*, Chapt. 9, pp. 403-417 (McGraw-Hill Book Co., Inc., New York, N. Y., 1957).
18. S. B. Cohn, "Problems in Strip Transmission Lines," Transactions of the IRE Professional Group on Microwave Theory and Techniques, Vol. MTT3, pp. 119-126 (March 1955).
19. N. Bloembergen, "Magnetic Resonance in Ferrites," *Proc. IRE* 44, pp. 1259-1269 (October 1956).
20. J. L. Carter, E. B. Edwards, and I. Beingold, "Ferrite Sphere Grinding Technique," *Rev. Sci. Instr.*, Vol. 30, pp. 946-947; October 1959.
21. W. L. Bond, "Making Crystal Spheres," *Rev. Sci. Instr.* 22, 344 (1951).
22. L. R. Bickford, "Ferromagnetic Resonance Absorption in Magnetite Single Crystals," *Phys. Rev.* 78, 4 pp. 449-457 (15 May, 1950).

REFERENCES

23. C. Kittel, *Introduction to Solid State Physics*, Chap. 1 (John Wiley and Sons, Inc., New York, N. Y., 1953).
24. J. F. Dillon, Jr., *Phys. Rev.* **105**, 759 (1957).
25. J. O. Artman, "Microwave Resonance Relations in Anisotropic Single Crystal Ferrites," *Proc. IRE*, Vol. 44, No. 10 (October 1956).
26. L. R. Walker, "Magnetostatic Modes in Ferromagnetic Resonance," *Phys. Rev.* **105**, No. 2 (15 January, 1957).
27. H. Suhl, "The Non-Linear Behavior of Ferrites at High Signal Levels," *Proc. IRE*, Vol. 44, No. 10, pp. 1270-1284 (October 1956).
28. H. Suhl, *J. Phys. Chem. Solids* **1**, 207 (1957).
29. A. E. Siegman, "Phase-Distortionless Limiting by a Parametric Method," *Proc. IRE*, Vol. 47, No. 3 (March 1959).
30. H. A. Bethe, "Lumped Constants for Small Irises," Radiation Laboratory Report 43-22, Massachusetts Institute of Technology (March 24, 1943).
31. S. B. Cohn, "Microwave Coupling by Large Apertures," *Proc. IRE* **40**, pp. 696-699 (June 1952).
32. K. L. Kotzebue, "Broadband Electronically-Tuned Microwave Filters," 1960 IRE WESCON Convention Record, Part 1, Antennas, Microwave Theory and Techniques, Los Angeles, California (August 23-26, 1960).
33. E. G. Spencer and R. C. LeGraw, "Line Width Narrowing in Gallium Substitutes Yttrium Iron Garnet," *Bulletin of the American Physical Society, Series II*, Vol. 5, No. 1, Part I, p. 58 (27 January 1960).

DESIGN THEORY OF UP-CONVERTERS FOR USE AS ELECTRONICALLY TUNABLE FILTERS

A. GENERAL

1. DESCRIPTION OF THE PROPOSED DEVICES

Previous work on another contract dealt with the application of filter theory to the design of wideband parametric amplifiers and up-converters.^{1,2,3} This present discussion applies a similar theoretical approach to a different but closely related problem. The objective will be to obtain an electronically controlled *wide tuning range* using up-converters having a wide-band input-impedance-matching filter, a narrow-band output-impedance-matching filter, and a voltage-tunable pump oscillator such as a backward-wave oscillator.

Defining f as the input frequency, f' as the sideband output frequency, and f^p as the pump frequency, for a lower-sideband up-converter the output is at the lower sideband frequency

$$f' = f^p - f \quad (29-1)$$

For an upper-sideband up-converter, the output is at the upper sideband frequency

$$f' = f^p + f \quad (29-2)$$

For either type of up-converter, tuning action can be achieved if a narrow-band filter is used at the output so that only frequencies equal or very nearly equal to a specific frequency, f'_0 , can be passed. If the pump frequency f^p is varied then the input frequency which will be accepted by the amplifier will be given by

$$f = f^p - f'_0 \quad (29-3)$$

for the case of lower-sideband up-converters and

$$f = f'_0 - f^p \quad (29-4)$$

for the case of upper-sideband up-converters. In both cases the amplifiers will yield gain. The lower-sideband type introduces some negative resistance amplification in addition to the up-converter amplification, however, and will therefore generally give more gain. For gain to be achieved, the variable-capacitance diode must see proper terminations at both frequencies, f and f'_0 . Since f'_0 is a fixed frequency, it should be relatively easy to maintain proper termination at that frequency. The input frequency, f , varies, however, and the tuning range of the amplifier will be determined largely by the range of f for which proper terminating conditions can be maintained.

2. FACTORS PERMITTING LARGE TUNING RANGE

For convenience let us first consider the case of an upper-sideband up-converter with a fixed pump frequency. We analyze a wideband, upper-sideband up-converter using a fixed pump frequency f^p , with an input-impedance-matching filter whose pass band is centered at f_0 and an output-impedance-matching filter whose pass band is centered at f'_0 . In order to obtain maximum operating bandwidth it is necessary that the condition

$$\frac{w}{w'} = \frac{f'_0}{f_0} \quad (29-5)$$

be satisfied, where w is the fractional bandwidth $\Delta f/f_0$ of the input filter and w' is the fractional bandwidth $\Delta f'/f'_0$ of the output filter.^{1,2} Equation (29-5) says, in effect, that the input and output bands, Δf and $\Delta f'$, respectively, must be equal. From the theory of wideband up-converters,^{2,3} it is seen that if, for example, Δf were made larger than $\Delta f'$, then the output filter bandwidth $\Delta f'$ would have to be shrunk to be smaller than it could be if Δf and $\Delta f'$ were made to be equal. Since the smaller bandwidth will be the one that limits the over-all transmission the operating bandwidth necessarily becomes smaller if Δf and $\Delta f'$ are made unequal. Thus it is seen that for the usual case where the pump frequency is fixed, wide-band impedance matching must be accomplished

both at the signal input and also at the upper-sideband output band, and best results are obtained if the bandwidth for impedance match is equal for both of these bands

For the tunable up-converters considered herein, a quite different situation exists. In this case narrow rather than wide bandwidth is desired. A wide-band impedance match is desired at the input channel, however, so that the input acceptance band can be moved about by varying the pump frequency. Under these conditions we may expand the input bandwidth Δf and be quite happy with the required shrinkage of the sideband output bandwidth $\Delta f'$. With such an amplifier the bandwidth $\Delta f'$ of the upper-sideband filter will be the operating bandwidth of the amplifier while Δf will become the tuning range. If there were no practical considerations, such as the effects of losses and the need for practical impedance levels, the tuning range Δf could be made to approach infinity while the output bandwidth $\Delta f'$ would approach zero; practical considerations, however, do limit the obtainable tuning range. Nevertheless, it is clear that the tuning range obtainable with such a device is considerably greater than the bandwidth obtainable in an up-converter using a fixed pump frequency. As is seen from Ref. 2 or Ref. 3, bandwidths of the order of 16 percent appear to be feasible for upper-sideband up-converters having fixed pump frequencies. The tuning range which is feasible for up-converters with varying pump frequencies is thus likely to be several times this value.

An additional problem, not yet mentioned, arises in this case of an up-converter with varying pump frequency. Additional impedance matching for the pump input channel must be provided in order to pump the diode satisfactorily at frequencies throughout the required pump frequency range. It can be shown that it will generally be impossible to obtain a good match between the pump signal oscillator and the small resistance in the diode while tuning across the required pump frequency band. However, it is possible to design impedance-matching filters which will give a nearly uniform, minimum reflection level throughout the required band. Then it is merely necessary to have a pump oscillator with sufficient available power to compensate for the reflection loss.

The discussion above has been phrased in terms of upper-sideband up-converters. The same principles, however, apply to lower-sideband up-converters. The main difference between the two devices is that the

lower-sideband type tends to reflect a negative resistance through the coupling action of the varying capacitance. This negative resistance has the advantage that it contributes to the gain of the amplifier, but it also has the disadvantage that it could lead to oscillation if the amplifier were improperly terminated. Calculations indicate that good results should be obtainable by keeping the negative resistance small, so that stability will not be a problem.

B. DEFINITION OF DIODE PARAMETERS

The specification of the diode parameters will be the same as that used previously,^{1,2,3} but will be summarized here for easy reference. Following Rowe,⁵ the diode capacitance properties are defined in terms of C_0 and C_1 which are coefficients in the time series

$$C(t) = C_0 + 2C_1 \cos(2\pi f_p t + \phi_1) + \dots \quad (29-6)$$

where $C(t)$ is the time variation of the pumped diode. If the diode is to be resonated in shunt it is convenient to describe its operation in terms of the short-circuit admittances^{1,3}

$$\begin{aligned} B_{11} &= 2\pi f C_0, & B_{12} &= 2\pi f C_1 \\ B_{21} &= 2\pi f' C_1, & B_{22} &= 2\pi f' C_0 \end{aligned} \quad (29-7)$$

where B_{11} and B_{12} are seen to be the susceptance of C_0 and C_1 , respectively, at the signal frequency, and B_{22} and B_{21} are the corresponding susceptances evaluated at the sideband frequency defined by Eq. (29-1) for lower-sideband operation and Eq. (29-2) for upper sideband operation. In the discussion to follow, subscript zeros, such as

$$(B_{11})_0, (B_{12})_0, (B_{21})_0, (B_{22})_0$$

will be used to indicate parameters evaluated at the signal input midband frequency, f_0 , or at the sideband output midband frequency, f'_0 , whichever is appropriate for the given parameter.

Although the diode loss acts like a resistor in series with C_0 , in the shunt-diode case the diode loss is most easily accounted for approximately by an equivalent shunt conductance

$$G_d = \frac{2\pi f_0 C_0}{Q_d} = \frac{(B_{11})_0}{Q_d} \quad (29-8)$$

seen by input signal components and an equivalent shunt conductance

$$G'_d = \frac{2\pi f'_0 C_0}{Q'_d} = \frac{(B_{22})_0}{Q'_d} = G_d \left(\frac{f'_0}{f_0} \right)^2 \quad (29-9)$$

seen by the sideband components. Q_d is the operating Q of the diode at frequency f_0 , and Q'_d is the operating Q at f'_0 . Since the diode loss resistance is effectively in series with the capacitance

$$Q'_d = Q_d \frac{f_0}{f'_0} \quad (29-10)$$

Analogously, if the diode is to be resonated in series it is convenient to define its operation in terms of the open-circuit impedances^{1,3}

$$X_{11} = \frac{1}{2\pi f C_0^*}, \quad X_{12} = \frac{1}{2\pi f' C_1^*} \quad (29-11)$$

$$X_{21} = \frac{1}{2\pi f C_1^*}, \quad X_{22} = \frac{1}{2\pi f' C_0^*}$$

where

$$C_0^* = C_0(1 - a^2), \quad C_1^* = \frac{C_0(1 - a^2)}{a} = \frac{C_0^*}{a} \quad (29-12)$$

and

$$a = \frac{C_1}{C_0} \quad (29-13)$$

In this case the effects of losses are represented by series resistors

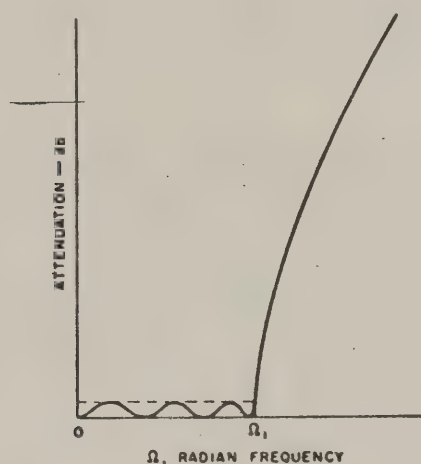
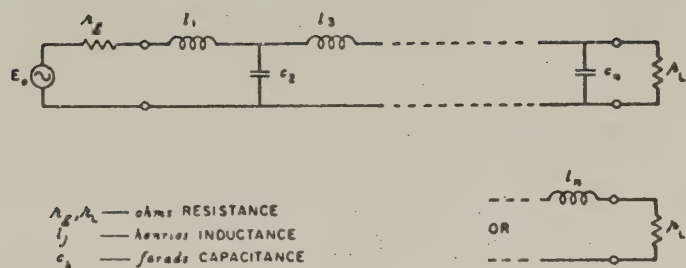
$$R_s = R'_s = \frac{1}{Q_d 2\pi f_0 C_0^*} = \frac{(X_{11})_0}{Q_d} = \frac{(X_{22})_0}{Q'_d} \quad (29-14)$$

which are the same at both the signal and sideband frequencies. Equations (29-11) to (29-13) are obtained from the short-circuit admittance equations by matrix inversion,^{1,3} and they assume that higher-order harmonic and sideband components of the mixing process are short-circuited. However, the work of Leenov⁶ suggests that if the unwanted components were open-circuited instead of short-circuited, the change in these parameters would not be large. The effect of certain reactive terminations on these unwanted components may be larger, and this possibility is now being investigated on another project at SRI.

C. DEFINITION OF FILTER PARAMETERS

In order to reduce the number of degrees of freedom involved in the amplifier design, the design of the various band-pass filters required will be based on the use of lumped-element, low-pass prototypes. When these low-pass prototypes have been specified, the only parameters which remain to be specified in the corresponding band-pass filters are their center frequencies, their impedance levels, and their fractional bandwidths. Their center frequencies, of course, will be determined by the desired operating bands. The impedance level of the input and pump channel filters will be determined from considerations of their desired bandwidths and the impedance matching properties which are required.

Figure 29-1 shows a typical low-pass prototype and a typical Tchebyscheff response for such a filter. Tables of normalized element values for Tchebyscheff and maximally flat low-pass filters of this kind are presently available.^{7,8,9} Figure 29-2 shows the corresponding band-pass filter obtained by the standard low-pass to band-pass transformation given in Eq. (a) in the figure. In Figs. 29-1 and 29-2 note that Ω is the low-pass radian frequency variable; Ω_1 is the low-pass radian cutoff frequency; f is the cyclic frequency variable of the band-pass filter; f_0 , f_1 , and f_2 are, respectively, the band-pass filter center frequency, the lower band-edge frequency, and the upper band-edge frequency; and w is the fractional bandwidth of the band-pass filter. The impedance level of the band-pass filter is determined by the choice of the load resistor R_L , and Eqs. (e) and (f) in Fig. 29-2 relate the element values in the band-pass filter to w , R_L , and f_0 , along with the element values and cutoff frequency Ω_1 of the low-pass prototype.

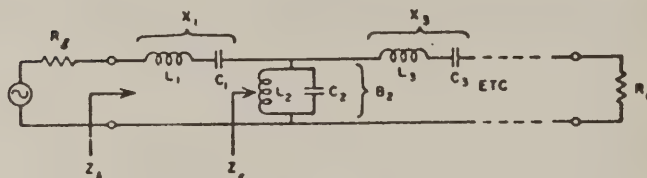
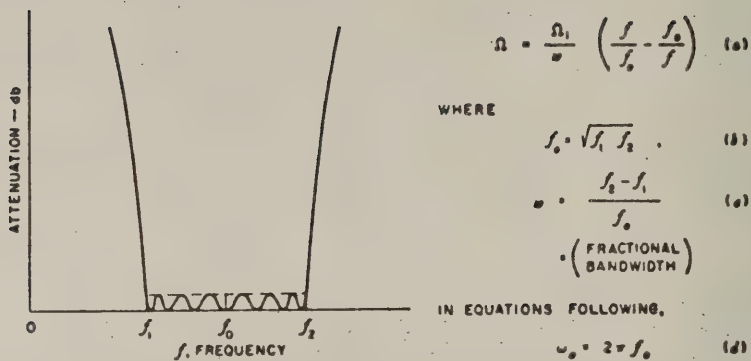


A-1000-5-0

FIG. 29-1

LOW-PASS PROTOTYPE FILTER AND A TYPICAL TCHEBYSCHIEFF RESPONSE

In an actual microwave device it will usually be necessary to use resonators which are a combination of semi-lumped and transmission-line elements rather than lumped-element resonators such as are shown in Fig. 29-2. For this reason it is convenient to use the equivalent representation shown in Fig. 29-3. In this case the actual nature of the resonators is left unspecified, but it is assumed that in the vicinity of f_0 they exhibit resonance characteristics similar to those of the resonators in Fig. 29-2. Then for frequencies near f_0 the resonator reactances X_j , or susceptances B_j , are approximated by resonator functions of the standard form indicated in Eqs. (a) and (d) in Fig. 29-3. The properties of each resonator are no longer defined in terms of an L and a C , but in terms of a center frequency f_0 and a slope parameter α or b .



R_L IS CHOSEN TO GIVE DESIRED IMPEDANCE LEVEL, AND $R_g = R_L (a_0/a_L)$

FOR SERIES BRANCHES

$$L_j = \left(\frac{R_L}{\omega \omega_0} \right) \left(\frac{\Omega_1}{A_L} \right), \quad C_j = \left(\frac{\omega}{\omega_0 R_L} \right) \left(\frac{A_L}{\Omega_1} \right) \quad (e)$$

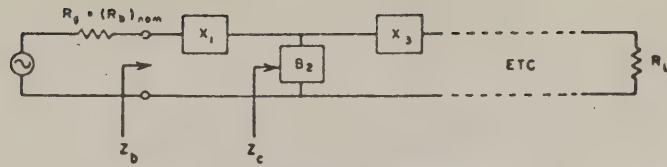
FOR SHUNT BRANCHES

$$C_b = \left(\frac{1}{\omega \omega_0 R_L} \right) \left(\frac{\Omega_1}{A_L} \right), \quad L_b = \left(\frac{\omega R_L}{\omega_0} \right) \left(\frac{1}{\Omega_1 A_L} \right) \quad (f)$$

8-20000-000

FIG. 29-2

SUMMARY OF RELATIONS FOR DESIGN OF LUMPED-ELEMENT BAND-PASS FILTERS FROM LOW-PASS PROTOTYPES



FOR SERIES BRANCHES, f NEAR f_0

$$x_j \approx \left(\frac{f}{f_0} - \frac{f_0}{f} \right) x_j \quad (a)$$

WHERE

$$x_j \text{ (SLOPE PARAMETER)} = \frac{\omega_0}{2} \left. \frac{dx_j}{d\omega} \right|_{\omega=\omega_0} = \frac{R_{B0}}{\omega} \left(\frac{\Omega_1 L_j}{A_L} \right) \quad (b)$$

AND

$$R_{B0} = Z_b \Big|_{f=f_0} \quad (c)$$

FOR SHUNT BRANCHES, f NEAR f_0

$$b_k \approx \left(\frac{f}{f_0} - \frac{f_0}{f} \right) b_k \quad (d)$$

WHERE

$$b_k \text{ (SLOPE PARAMETER)} = \frac{\omega_0}{2} \left. \frac{db_k}{d\omega} \right|_{\omega=\omega_0} = \frac{1}{\omega R_{B0}} (\lambda_k \Omega_1 c_k) \quad (e)$$

A-2590-550

FIG. 29-3

GENERAL DESCRIPTION OF BAND-PASS FILTERS IN TERMS OF RESONATOR SLOPE PARAMETERS

(Ω_1 , L_j , c_k and λ_k are defined in Fig. 29-1)

For series resonators the slope parameter x_j is related to the resonator reactance slope at frequency f_0 and also to the prototype parameters as indicated in Eq. (b) of Fig. 29-3. The parameter R_{B0} in Eq. (b) of the figure is defined by Eq. (c) along with the circuit drawing. For the configuration shown $R_{B0} = R_L$; however, in some forms of microwave filters an impedance level transformation takes place, so that it is desirable to introduce the parameter R_{B0} as indicated in Eq. (c) and the figure. It will be noted that the slope parameters x_j for series resonators have the dimensions of reactance, and it will be found that for a lumped-element circuit such as that in Fig. 29-2 the slope parameter for a series resonator is given by

$$x_j = 2\pi f_0 L_j = \frac{1}{2\pi f_0 C_j'} \quad (29-15)$$

where f_0 is the resonant frequency. For the general case of semi-lumped or distributed resonators, however, the slope parameter α , is most conveniently defined in terms of the derivative of the resonator reactance as in Eq. (b) in Fig. 29-3. For the case of shunt resonators and their slope parameters b_k , entirely analogous statements apply in terms of susceptance instead of reactance.

D. AN UP-CONVERTER MODEL FOR PURPOSES OF ANALYSIS AND DISCUSSION

The up-converter model discussed in this section incorporates some features which have been used at SRI quite successfully on a degenerate parametric amplifier, and it is believed that they could also be used to advantage in electronically tunable up-converters in certain frequency ranges. However, the design equations and charts in the following section should be applicable for any of a variety of coaxial, stripline, or waveguide types of up-converter structures. In this model the diode will be resonated in series for reasons summarized in Sec. K, although the design data to follow can be applied also for designs where the diode is resonated in shunt.

Figure 29-4 shows the model up-converter circuit. This circuit uses a three-resonator wideband input filter, a three-resonator moderately wideband pump circuit filter, and a narrow-band, single-resonator output filter. The diode plus the length of high-impedance transmission line introduces multiple resonances, one of which provides the resonance for the No. 1 resonator of the input filter, and another of which provides the resonance for the No. 1 resonator of the pump filter. Note that the diode representation includes C_0^d , C_1^d , and R_d in series along with L_d , the diode internal inductance. Since the number of resonators for the signal-input and pump filters may vary under different circumstances, it is convenient for both the input and pump filters to define the resonator formed by the diode circuit as the No. 1 resonator, even though the generator is actually at the other end. Under these conditions R_d becomes the generator internal impedance instead of R_g , but the power transmission properties are unaffected since the filter circuit obeys the reciprocity theorem.

The performance of the circuit in Fig. 29-4 can best be understood by considering its operation at the various frequencies of interest.

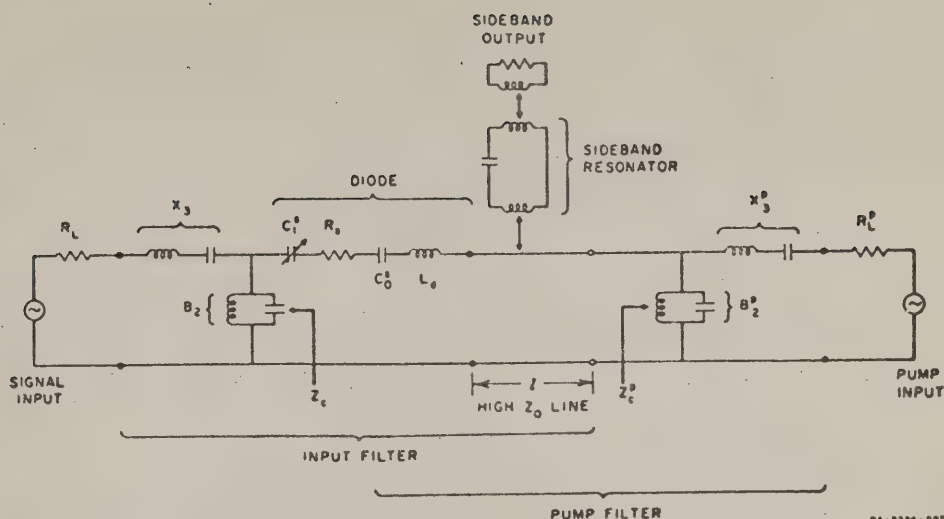


FIG. 29-4

A POSSIBLE CIRCUIT FOR AN UP-CONVERTER FOR ELECTRONICALLY TUNABLE FILTER APPLICATIONS

Figure 29-5 shows the equivalent circuit of the input filter circuit at frequency f and the output circuit at the sideband frequency f' , with a box labeled $X_{12}X_{21}$ to represent the coupling effect of C_1^i between energy components at frequencies f and f' . The operation of this box is different for lower-sideband up-converters than for upper-sideband up-converters,^{1,2,3} and its operation will be summarized in Secs. E and G. Since the pump filter center frequency, f_0^p , is much higher than the center frequency, f_0 , of the input filter, the susceptance B_2^p of the No. 2 resonator of the pump filter in Fig. 29-4 will be very large so that the high-impedance line is effectively short-circuited. At frequency f_0 , the high-impedance line is less than $\lambda/8$ long and acts much like a lumped inductance which brings the diode to series resonance at that frequency. Since C_0^i , L_0 , R_s , the impedance of the short-circuited line, and the impedance reflected through C_1^i (Z_2 in Fig. 29-5) are effectively in series, the diode and high- Z_0 line together may be represented as shown in Fig. 29-5 by R_s , Z_2 , and the series resonator X_1 .

At the pump-channel band-center frequency, f_0^p , the impedance Z_c in Fig. 29-4 will be reactive and nearly zero, and the diode plus the high- Z_0

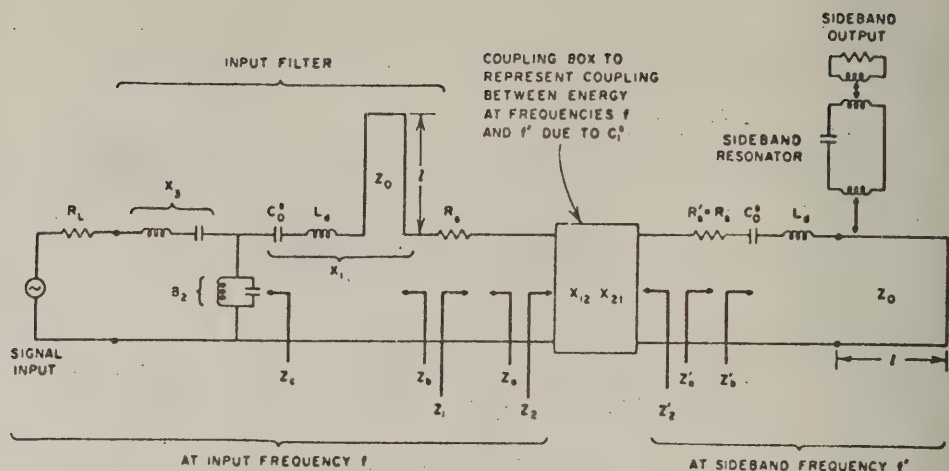


FIG. 29-5

A CIRCUIT WHICH IS APPROXIMATELY EQUIVALENT TO THAT IN FIG. 29-4 FOR ENERGY COMPONENTS AT THE INPUT FREQUENCY f OR THE SIDEBAND FREQUENCY f'

line will again exhibit resonance. The impedance seen looking into the high- Z_0 line from the right in Fig. 29-4 is given by

$$Z = \frac{(R_s + jX_d) + jZ_0 \tan \theta}{1 + \frac{j(R_s + jX_d) \tan \theta}{Z_0}} \quad (29-16a)$$

where $R_s + jX_d$ is the total impedance developed across the diode along with the input filter reactance Z_c in Fig. 29-4 at the pump frequency, f^p . Choosing Z_0 to be large as compared to R_s (a condition which is easy to fulfill since R_s might typically be around 4 ohms), to a good approximation Eq. (29-16a) becomes

$$Z = R_s' + jX_1' = \frac{R_s}{\left(1 - \frac{X_d}{Z_0} \tan \theta\right)} + \frac{j(Z_0 \tan \theta + X_d)}{\left(1 - \frac{X_d}{Z_0} \tan \theta\right)} \quad (29-16b)$$

In most cases the pump band center f_0^p will be above the self-resonant frequency of the diode; therefore, at f_0^p the reactance X_d will usually be inductive, and θ will be somewhat less than π . Under these conditions the quantity in the denominators of Eq. (29-16b) will be somewhat greater than one (since $\tan \theta$ is negative), and will be slowly varying since X_d/Z_0 will be increasing with frequency, while $\tan \theta$ will be decreasing in magnitude as the frequency increases.

Since θ will be roughly of the order of π , in some cases the denominators of the terms in Eq. (29-16b) will be very nearly one. Assuming for the moment that this is the case and that Z_c for the input filter in Fig. 29-4 is negligible at f_0^p , then Eq. (29-16b) is equivalent to the impedance of R_s , C_0^s , L_d , and the short-circuited, high- Z_0 line all connected in series as shown in Fig. 29-7(a). If the denominator in Eq. (29-16b) cannot be neglected, the magnitude of $R_d^p + jX_1^p$ will be affected as indicated by the equation, but the general nature of the performance will be qualitatively the same.

It is thus seen that for frequencies in the vicinity of f_0 and f_0^p ; C_0^s , L_d and the high- Z_0 line operate at least qualitatively in a manner similar to the series-resonant circuit shown in Fig. 29-7(a), which has the reactance characteristics shown in Fig. 29-7(b). The reactance slope in the vicinity of f_0 will be important in the design of the signal input

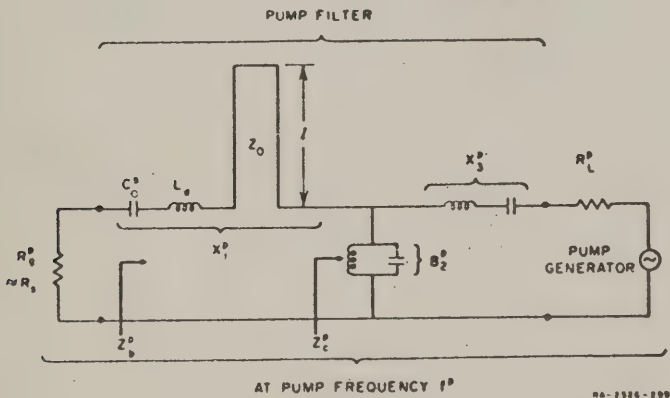


FIG. 29-6
A CIRCUIT APPROXIMATELY EQUIVALENT TO THAT IN FIG. 29-4
FOR ENERGY AT THE PUMP FREQUENCY f^p

filter, while the reactance slope in the vicinity of f_0^p will be important in the design of the pump input filter. At the sideband frequency f_0^s , the diode and high- Z_0 line in Fig 29-4 will see reactive impedances Z_c and Z_p^s of small magnitude, but the diode and line will not be resonant. However, the presence of the lightly-coupled sideband resonator in Fig 29-4 will introduce a narrow resonance at either the lower or upper sideband frequencies indicated in Fig. 29-7(b). It is desirable that this sideband output resonator be coupled as lightly as possible, consistent with low transmission loss, so that it will cause a minimum increase in the reactance slope in the vicinity of f_0^p . Since the up-converter would probably be followed by a fixed-tuned, superheterodyne receiver, an additional high- Q filter following the sideband output filter would be desirable to ensure high attenuation at the image frequency of the superheterodyne receiver.

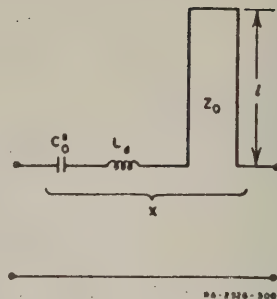


FIG. 29-7(a)
APPROXIMATE EQUIVALENT
CIRCUIT FOR THE DIODE
RESONATOR

Figure 29-8 shows portions of a possible strip transmission line amplifier of the type under consideration. The diode used is in a computer

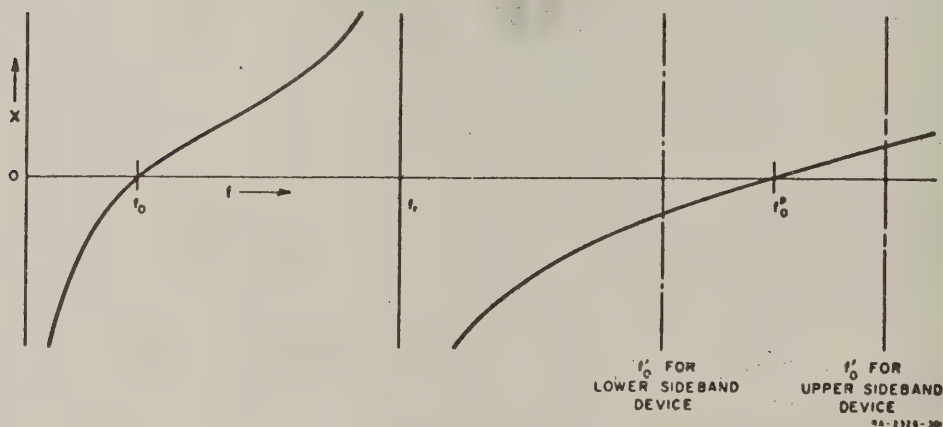


FIG. 29-7(b)
REACTANCE PROPERTIES OF THE RESONATOR IN FIG. 29-7(a)

diode package having a glass envelope and wire leads. (The Hughes 1N896 diodes are examples of varactor diodes packaged in this manner.) The wire diode leads then serve as the high- Z_0 line for resonating the diode. Resonators No. 2 and 3 for the signal input filter are realized as two semi-lumped shunt resonators separated by a quarter-wavelength (at frequency f_0) of line. The quarter-wavelength line eliminates the need to construct resonator No. 3 as a series resonator. The signal input filter would be of wide bandwidth and it could be designed using the theory in

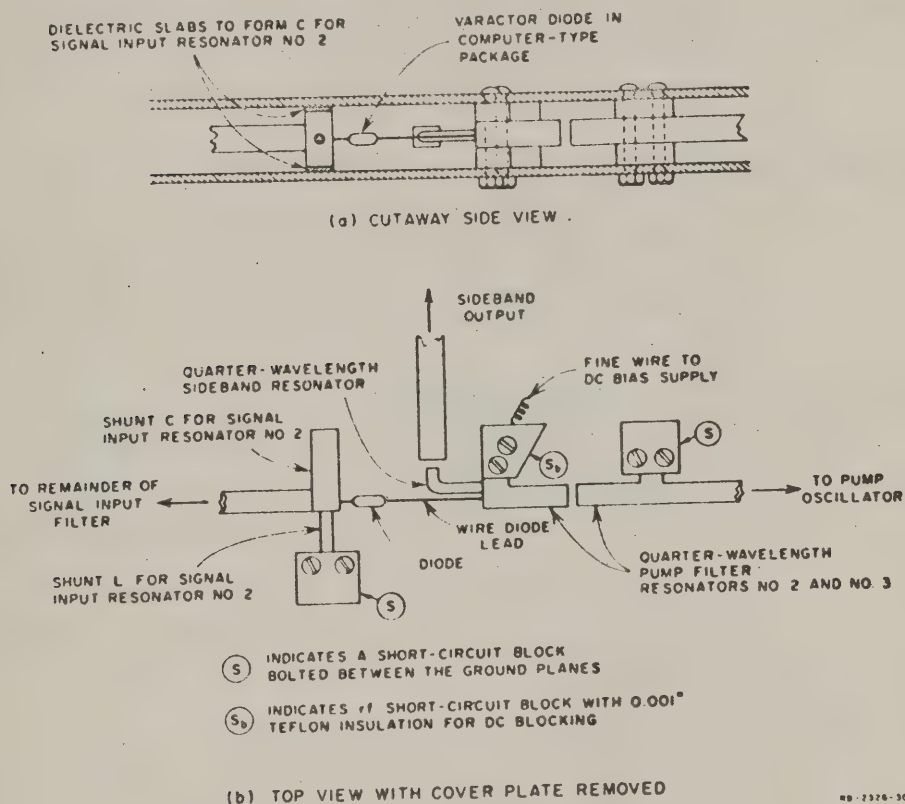


FIG. 29-8

A POSSIBLE STRIP-TRANSMISSION-LINE EMBODIMENT OF THE CIRCUIT IN FIG. 29-4
 The input, pump, and sideband filters are realized in practical microwave filter structures which will appear from the diode resonator circuit to be equivalent to those in Fig. 29-4 for the frequencies of interest

Secs. E or G along with techniques for design of wideband filters which have been previously treated.^{10,11}

The pump frequency must be able to shift an amount equal to the bandwidth of the signal input filter, but since the pump frequency band is centered considerably higher than that of the signal input band, the pump filter fractional bandwidth will be relatively small. Pump filter resonators No. 2 and No. 3 are realized as quarter-wavelength, direct-coupled, two-port resonators, since this construction is convenient for narrow or moderate bandwidths, and will not have any spurious pass bands until about three times the frequency of the first pass band.¹² Each resonator bar is series-capacitance-coupled at one end and shunt-inductance-coupled at the other. Looking to the right from the high- Z_0 wire in the diode circuit, the impedance of the structure appears much like Z'_c seen looking to the right from the high- Z_0 line in Fig. 29-4 for frequencies in the vicinity of f_0 .

The sideband output resonator shown in Fig. 29-8 is one-quarter wavelength long; it is inductively coupled to the diode and high- Z_0 wire circuit, but series-capacitance-coupled to the sideband output line.

The circuit shown in Fig. 29-8 appears to be a possible realization of an electronically tunable up-converter having input frequencies centered around 1000 Mc. However, other configurations are also possible.

E. DETERMINATION OF SIGNAL-INPUT AND SIDEBAND-OUTPUT CIRCUIT PARAMETERS FOR UPPER-SIDEBAND UP-CONVERTERS

When power is taken out at the upper sideband while the other components of the mixing process are suppressed, then the $X_{12}X_{21}$ coupling box in Fig. 29-5 operates like an impedance inverter so that^{1,3}

$$Z_2 = \frac{X_{12}X_{21}}{Z'_c} \quad (29-17)$$

and

$$Z'_2 = \frac{X_{12}X_{21}}{Z_c} \quad (29-18)$$

where, as indicated in Fig. 29-5, the unprimed impedances are evaluated at the signal input frequency, f , while the primed impedances are evaluated at the sideband frequency, f' . By the Manley-Rowe equations,^{4,5} the power P_2 entering the left side of $X_{12}X_{21}$ is related to the power P'_2 entering the right side of $X_{12}X_{21}$ by

$$\frac{P'_2}{P_2} = -\frac{f'}{f}, \quad (29-19)$$

where the minus sign indicates that if power flows into the left side, power will flow out of the right side

Let us define $(R_b)_{nom}$ as the nominal value of the signal input filter impedance Z_b in Fig. 29-5. The impedance $(R_b)_{nom}$ is purely real and is equal to the resistive terminating impedance which would give best transmission through the filter. In terms of Fig. 29-3,

$$(R_b)_{nom} = R_b = \frac{\nu_s}{\nu_L} R_{b0} \quad (29-20)$$

where ν_s and ν_L are from the lumped-element prototype. For purposes of computing the nominal gain of the amplifier, the signal input filter will be replaced by a Thevenin equivalent generator having an internal impedance equal to $(R_b)_{nom}$. At the sideband output frequency f'_0 , the impedance Z'_b in Fig. 29-5 will be purely real and will be defined as

$$R'_{b0} = Z'_b|_{f'=f'_0} \quad (29-21)$$

Using Eqs. (29-17) to (29-19) and the above definitions for $(R_b)_{nom}$ and R'_{b0} it can easily be shown that the nominal power gain for input signals in the vicinity of f_0 is

$$\frac{P'_{out}}{P_{avail}} = \frac{f'_0}{f_0} \frac{4(R_b)_{nom}R'_{b0}(X_{12}X_{21})_0}{\{(R_b)_{nom} + R_s\}(R'_{b0} + R'_s) + (X_{12}X_{21})_0^2} \quad (29-22)$$

where $R_s = R'_s$ is the diode loss resistance, P_{avail} is the available power of the input frequency f_0 , and P'_{out} is the nominal output power at the

sideband frequency f'_0 . The gain will vary somewhat across the tuning range due to variations in Z_b , $X_{12}X_{21}$, and f'/f , but Eq. (29-22) gives what will herein be referred to as the nominal gain of an upper-sideband up-converter.

In the design of an amplifier, the input and pump channel filters serve primarily as wideband impedance matching networks. Thus the first step in the design process is to design the diode resonator circuit and then determine the slope parameters α_1 , and α'_1 at frequencies f_0 and f'_0 , respectively, by use of the derivative form of Eq. (b) in Fig. 29-3. By Eq. (b) of Fig. 29-3, for a desired fractional bandwidth w of the input circuit, R_{b0} must be

$$R_{b0} = \alpha_1 w \left(\frac{\omega_L}{\Omega_1 \omega_1} \right) \quad (29-23)$$

and then $(R_b)_{\dots}$ is given by Eq. (29-20). The slope parameters α_j and ω_j for the other resonators of the input filter may then be computed from the lumped-element prototype filter parameters, R_{b0} , and w by use of Eqs. (b) and (c) in Fig. 29-3.

Knowing $(R_b)_{\dots}$ and f'_0/f_0 , and having values for $(X_{11})_0$, $R_s = R'_s$, and $a = C_1/C_0$ for the diode, the maximum gain will be obtained if R'_{b0} matches Z'_2 in Fig. 29-5, which requires that

$$R'_{b0} = R'_s + \frac{(X_{12}X_{21})_0}{(R_b)_{\dots} + R_s} \quad (29-24)$$

be satisfied. This can be expressed as

$$R'_{b0} = R'_s \left[1 + \frac{1}{\omega^2(T+1)} \right] \quad (29-25)$$

where

$$T = \frac{(R_b)_{\dots}}{R_s} = \frac{(R_b)_{\dots} Q_d}{(X_{11})_0} \quad (29-26)$$

and

$$v = \frac{1}{aO_d} \sqrt{\frac{f'_0}{f_0}} \quad (29-27)$$

Inserting Eq. (29-25) in (29-22) yields, after some manipulation,

$$\frac{\frac{P'_{out}}{P_{avail}}}{\frac{f'_0}{f_0}} = \frac{T}{(T+1)[v^2(T+1)+1]} \quad (29-28)$$

If this analysis is carried out on the dual basis for the case of the diode resonated in shunt we find the dual expressions

$$G_{b0} = b_1 w \left(\frac{r_L}{\Omega_1 l_1} \right) \quad (29-29)$$

$$(G_b)_{\dots} = G_b = \frac{r_s}{r_L} G_{b0} \quad (29-30)$$

$$G'_{b0} = G'_d \left[1 + \frac{1}{v^2(T+1)} \right] \quad (29-31)$$

$$T = \frac{(G_b)_{\dots}}{G_d} = \frac{(G_b)_{\dots} Q_d}{(B_{11})_0} \quad (29-32)$$

and Eqs. (29-27) and (29-28) apply as before. The parameter G'_d in Eq. (29-31) is again the equivalent shunt diode loss conductance given by Eq. (29-9). In order to facilitate design calculations a plot of $(P'_{out}/P_{avail})/(f'_0/f_0)$ vs v is shown in Fig. 29-9 for various values of T . The reference form for the band-pass filters is the dual of that in Fig. 29-3; the slope parameters and terminations for this dual filter may be conveniently specified directly in terms of the low-pass prototype in Fig. 29-1.

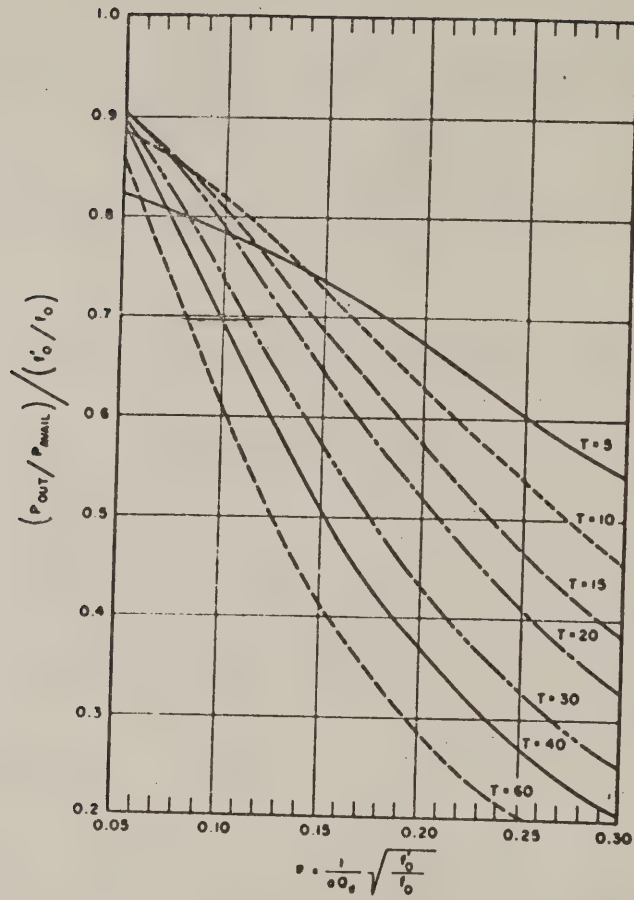


FIG. 29-9

CHART FOR DETERMINING THE GAIN OF UPPER-SIDEBAND UP-CONVERTERS

[$T = (R_b)_{\text{nom}}/R_s$ for the case of a diode resonated in series, and $T = (G_b)_{\text{nom}}/G_d$ for the case of a diode resonated in shunt. As is discussed in Sec. J., this chart does not apply accurately for the shunt resonance case if the diode has significant series inductive reactance.]

F. PUMP CIRCUIT IMPEDANCE MATCHING FILTER

In order that the pump channel have a nearly uniform reflection loss across the pump frequency band, it is necessary to design an impedance-matching filter as shown in Fig. 29-6. In this case the resistance R_6^p next to the No. 1 resonator is given by R_p in Eq. (29-16b). The No. 1 resonator, having a reactance X_1^p [given by Eq. (29-16b) for the case of Figs. 29-4, 29-6, and 29-8] is characterized by the slope parameter α_1^p computed at frequency f_0^p in Fig. 29-7(b) using the derivative form of Eq. (b) in Fig. 29-3. (Recall that in this case the resonance of the No. 1 resonator is created by the second series resonance of the diode circuit, as discussed in Sec. D.) The fractional bandwidth w_p of the pump filter is

$$w_p = w \frac{f_0}{f_0^p} \quad (29-33)$$

where w is again the desired fractional bandwidth of the input circuit. By Eq. (b) in Fig. 29-3

$$\left(\frac{\Omega_1 \ell_1}{\nu_L} \right)_p = \frac{\alpha_1^p w_p}{R_{60}^p} \quad (29-34)$$

where the subscript p on $(\Omega_1 \ell_1 / \nu_L)_p$ is introduced to indicate that these parameters refer to the low-pass prototype for design of the pump filter. Since, in accord with Figs. 29-1 and 29-3,

$$\frac{R_{60}^p}{R_s^p} = \left(\frac{\nu_L}{\nu_s} \right)_p \quad (29-35)$$

we may write Eq. (29-34) as

$$\left(\frac{\Omega_1 \ell_1}{\nu_s} \right)_p = \frac{\alpha_1^p w_p}{R_s^p} \quad (29-36)$$

where for the case of Figs. 29-4, 29-6, and 29-8, R_s^p is given by Eq. (29-16b). The problem now focuses on finding a low-pass prototype having $(\Omega_1 \ell_1 / \nu_s)_p$ as given by Eq. (29-36), with a desired amplitude of

Tchebyscheff pass-band attenuation ripple and with a minimum amount of reflection loss in the pass band. We are stuck with the prototype impedance $j\Omega_1 + \nu_g$, and the other elements of the prototype filter are introduced to optimize the impedance across the band $\Omega = 0$ to $\Omega = \Omega_1$.

Certain aspects of impedance matching problems of this type were treated by Bode.¹³ Fano treated the general limitations on lossless impedance matching, and also the design of certain Tchebyscheff impedance matching networks.¹⁴ Lallosa and Carlin^{15,16} and others have made various contributions to the theory of lossless and dissipative matching networks. This writer has extended Fano's work to permit practical design of lossless impedance matching networks for a wider class of loads.¹⁷ We will now briefly outline a procedure for determining the element values of the optimum low-pass prototype for the pump filter using the methods of Ref. 17.*

The Tchebyscheff filter reflection coefficient $\rho(p)$ between ν_g and the impedance seen looking into l_1 in Fig. 29-1 is defined as

$$\rho(p) = \frac{P_n(p, e)}{P_n(p, d)} \quad (29-37)$$

where, in Ref. 17, p is the complex frequency variable $p = \sigma + j\omega$, and $P_n(p, d)$ and $P_n(p, e)$ are polynomials in p tabulated in Appendix I of Ref. 17. (In Ref. 17, e and d above are replaced by x and y , respectively.) The degree of polynomials $P_n(p, d)$ and $P_n(p, e)$ is n , and this is also the number of reactive elements in the lumped-element prototype. These polynomials give a $|\rho(j\omega)|$ characteristic having an equal-ripple amplitude variation for frequencies between $p = j\omega = 0$ and $p = j\omega = j\omega_1 = j1$, where ω and ω_1 of Ref. 17 correspond to Ω and Ω_1 herein. The amplitude of the Tchebyscheff ripple of attenuation vs ω in the pass band is controlled by the parameter d in Eq. (29-37). Parameter d is given by

$$d = \sinh \left(\frac{\sinh^{-1} \sqrt{\frac{1}{H-1}}}{n} \right) \quad (29-38)$$

where

$$H = \text{antilog}_{10} \frac{(\text{db Tchebyscheff ripple})}{10} \quad (29-39)$$

Table 29-1 shows values of d for 0.2, 0.5, and 1.0 db Tchebyscheff ripple using $n = 2$ to 6.

* Since the above material was written this writer has re-surveyed some of the literature on impedance-matching network design and has noted that the works of Green¹⁸ and Barton¹⁹ contain very useful material for this application. This matter is discussed further in Chapter 30.

TABLE 29-1
LOW-PASS PROTOTYPE PARAMETER d FOR VARIOUS AMOUNTS OF
db TCHEBYSCHIEFF PASS-BAND RIPPLE AND
 n (Number of Reactive Elements)

| n | 0.2 db RIPPLE | 0.5 db RIPPLE | 1.0 db RIPPLE |
|-----|---------------|---------------|---------------|
| 2 | $d = 1.3620$ | $d = 1.0081$ | $d = 0.7762$ |
| 3 | 0.8148 | 0.6265 | 0.4942 |
| 4 | 0.5875 | 0.4582 | 0.3646 |
| 5 | 0.4615 | 0.3623 | 0.2895 |
| 6 | 0.3807 | 0.3000 | 0.2403 |

With d found, the parameter e in Eq. (29-37) is then found by¹⁷

$$e = d - 2 \left(\frac{\lambda_g}{\Omega_1 \ell_1} \right) \sin \frac{\pi}{2n} \quad (29-40)$$

Knowing d and e , $P_n(p, d)$ and $P_n(p, e)$ are completely defined as indicated in Appendix I of Ref. 17. [In the notation of Ref. 17, they are $P_n(p, x)$ and $P_n(p, y)$, respectively.] The normalized input impedance seen looking from λ_g into ℓ_1 in Fig. 29-1 is then¹⁷

$$Z(p) = \frac{P_n(p, d) + P_n(p, e)}{P_n(p, d) - P_n(p, e)} \quad (29-41)$$

where $Z(p)$ is normalized to make $\lambda_g = 1$. The element values of the prototype filter are then obtained by making a continued-fraction expansion of $Z(p)$.^{17,20*}

Taking $\lambda_g = 1$ and the equal-ripple band edge as $\Omega_1 = 1$, (in the notation of Ref. 17 this is $R_1 = 1$ and $\omega_1 = 1$), the above procedure will give the optimum low-pass prototype for the desired Tchebyscheff ripple and value of n . The amount of reflection loss can be reduced some by increasing n , but as n becomes larger the improvement in performance per unit increase in n becomes smaller and smaller. It can be shown that the maximum value of the reflection coefficient in the pass band is given by

$$|\rho|_{\max} = \frac{U_n(e)}{U_n(d)} \quad (29-42)$$

* Or preferably, by the methods described in Chapter 30 of this report.

where $U_n(d)$ and $U_n(e)$ are tabulated in Table IV of Ref. 17 and are plotted in Fig. 29-10 herein. Figure 5 of Ref. 17 shows another plot of these functions which is usable for larger values of d and e . The pump channel band-pass filter designed from this low-pass prototype will have the same maximum reflection loss in the pass band, the corresponding power transmitted to the diode being

$$A = \frac{P_{\text{transmitted}}}{(P_{\text{avail}})^p} = 1 - |\rho|_{\text{max}}^2 \quad (29-43)$$

times the available power $(P_{\text{avail}})^p$ of the pump signal generator. It will be found that the larger the slope parameter α_1^p and the larger the fractional

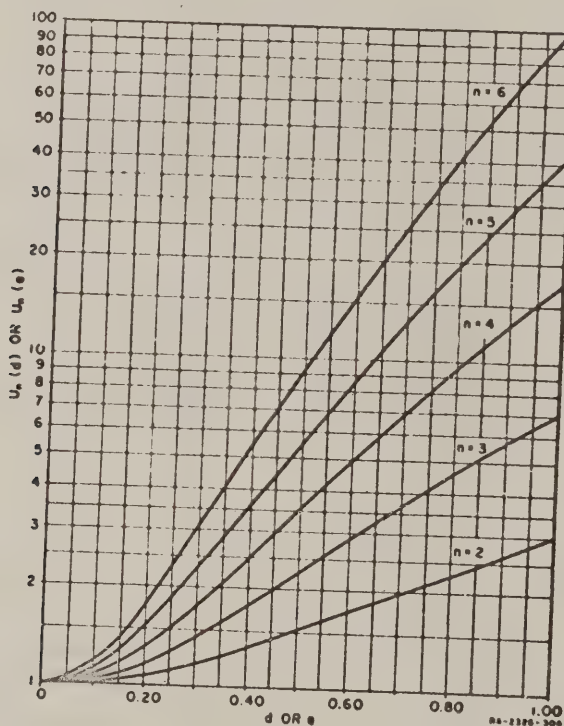


FIG. 29-10
CHART FOR USE IN DETERMINING THE REFLECTION LOSS
REQUIRED IN THE PUMP CIRCUIT WHEN USING AN OPTIMUM
TCHEBYSCHIEFF IMPEDANCE MATCHING FILTER

bandwidth ω_p , the smaller A must be and the more available power will be required. Of course, besides reflection loss the filter will also have a small amount of dissipation loss.

G. DETERMINATION OF SIGNAL INPUT AND SIDEBAND OUTPUT CIRCUIT PARAMETERS FOR LOWER-SIDEBAND UP-CONVERTERS

If power is taken out at the lower sideband instead of at the upper sideband, Eqs. (29-17), (29-18), and (29-19) become, respectively,

$$Z_2 = -\frac{X_{12}X_{21}}{(Z'_0)^*} \quad (29-44)$$

$$Z'_2 = -\frac{X_{12}X_{21}}{(Z_0)^*} \quad (29-45)$$

and

$$\frac{P'_2}{P_2} = \frac{f'}{f} \quad (29-46)$$

where the asterisk indicates the complex conjugate. Because of the negative sign in Eq. (29-44), this type of operation gives gain at the input frequency, f , due to negative input resistance. As is implied by Eq. (29-46), the power P'_2 (at the lower sideband frequency, f') going out the right side of $X_{12}X_{21}$ in Fig. 29-5 is larger than the power P_2 at frequency f going out the left side by the factor f'/f . Thus whatever gain is achieved at the input frequency is increased at the $X_{12}X_{21}$ box by the factor f'/f for power taken out at the sideband frequency f' .

In this case Eqs. (29-20), and (29-21) apply as before, but Eq. (29-22) becomes

$$\frac{P'_{out}}{P_{avail}} = \left(\frac{f'_0}{f_0}\right) \frac{4(R_b)_{nom} R'_{b0} (X_{12}X_{21})_0}{\{[(R_b)_{nom} + R_s](R'_{b0} + R'_s) - (X_{12}X_{21})_0\}^2} \quad (29-47)$$

which gives the nominal gain of the amplifier. The value of R_{b0} for the input filter is determined by Eq. (29-23) as before, but R'_{b0} cannot be

determined by impedance matching to maximize the gain as was done to obtain Eq. (29-24), since the maximum possible gain is now infinite (yielding oscillation). In this case we define a stability parameter

$$D = \frac{(R_b)_{nom} + R_s}{|Z_2|_{f=f_0}} = \frac{(R_b)_{nom} + R_s}{\left[\frac{(X_{12}X_{21})_0}{R'_{b0} + R_s} \right]} \quad (29-48)$$

which is seen to be the ratio of the nominal positive resistance of Z_s in Fig. 29-5 to the magnitude of the negative resistance Z_2 seen looking in the opposite direction. Parameter D fixes the nominal value of the negative resistance gain of the amplifier, and for stability, D must be greater than one. By Eq. (29-48)

$$R'_{b0} = \frac{D(X_{12}X_{21})_0}{(R_{b0} + R_s)} - R_s \quad (29-49)$$

$$= R_s \left[\frac{D}{v^2(T+1)} - 1 \right] \quad (29-50)$$

where T and v have the same meaning as in Eqs. (29-26) and (29-27), respectively. Substituting Eq. (29-50) in (29-47) gives

$$\frac{\frac{P'_{out}}{P_{avail}}}{\frac{f'_0}{f_0}} = \frac{4 \left[D - \left(v^2 T + \frac{D}{T+1} \right) \right]}{(D-1)^2} \quad (29-51)$$

The ratio $(P'_{out}/P_{avail})/(f'_0/f_0)$ is plotted vs v in Fig. 29-11(a), (b), (c) for $D = 2, 3, 4$ and various T values. These charts may also be used for the dual case where the diode is resonated in shunt by defining T as in Eq. (29-32). For the dual shunt-diode case Eq. (29-50) becomes the dual equation

$$G'_{b0} = G_d \left[\frac{D}{v^2(T+1)} - 1 \right] \quad (29-52)$$

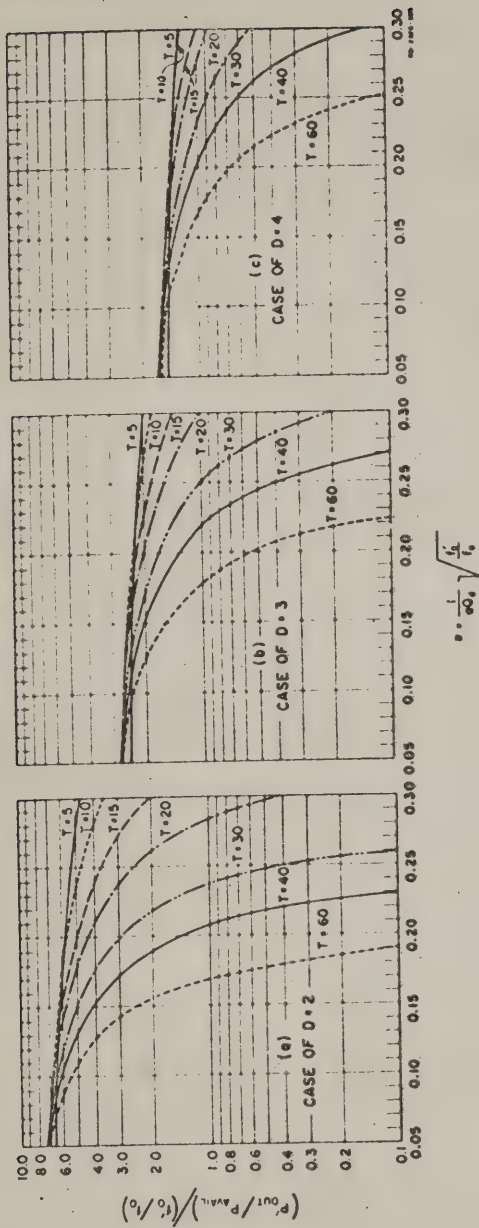


FIG. 29-11

CHARTS FOR DETERMINING THE GAIN OF LOWER-SIDEBAND UP-CONVERTERS
 $[T = (R_b)_{nom}/R_s$ for the case of a diode resonated in series, and $T = (G_b)_{nom}/G_d$ for the case of a diode resonated in shunt. Parameter D is the ratio of the magnitude of positive resistance to negative resistance seen at the diode (or for the shunt case positive conductance to negative conductance). As is discussed in Sec. J., these charts do not apply accurately for the shunt resonance case if the diode has significant series inductive reactance.]

II. ESTIMATED PERFORMANCE OF SOME DESIGN EXAMPLES

Let us estimate the performance of some up-converters having an input band center of $f_0 = 1$ kMc. The construction in Fig. 29-4 and 29-8 will be assumed using a Hughes 1N896 diode which has the computer-type package shown in Fig. 29-8. The lead wires on the diode will serve as the high- Z_0 line. The wires are 0.020 inch in diameter, and if a 0.500-inch ground-plane spacing is used they will have an impedance of 207 ohms. The diode will be assumed to have a C_0 value of $1.2 \mu\mu\text{f}$ (corresponding to a zero bias capacitance of about $2.3 \mu\mu\text{f}$). The series inductance L_d of the diode itself will be taken as 4×10^{-9} henries, and the operating Q will be taken as $Q_d = 35$ at $f_0 = 1$ kMc (from the manufacturer's data this appears to correspond to a cutoff frequency of around 70 kMc for this type of abrupt junction diode). The $a = C_1/C_0$ parameter of the diode will be taken to be 0.25.

In terms of the approximate equivalent circuit in Fig. 29-7(a), for the diode resonator

$$X(f) = \frac{-1}{2\pi f C_0'} + 2\pi f L_d + Z_0 \tan\left(\frac{\pi f}{2f_r}\right) \quad (29-53)$$

where f_r is the frequency shown in Fig. 29-7(b) for which the high Z_0 line is $\lambda/4$ long. Setting $f = f_0 = 10^9$, $C_0' = C_0(1 - a^2) = 1.17 \times 10^{-12} \text{ fd}$, $L_d = 4 \times 10^{-9} \text{ h}$, and $Z_0 = 207$ we find that $f_r = 3.21$ kMc is required which in turn calls for the $Z_0 = 207$ ohm line to be $l = 0.922$ inch long. The slope parameter α_1 at frequency f_0 is obtained from

$$\alpha_1 = \frac{\omega_0}{2} \frac{dX}{d\omega} \bigg|_{\omega = 2\pi f_0 = \omega_0}$$

$$= \frac{1}{2} \left[\frac{1}{2\pi f_0 C_0'} + 2\pi f_0 L_d + \left(\frac{\pi f_0}{2f_r} \right) \frac{Z_0}{\cos^2\left(\frac{\pi f_0}{2f_r}\right)} \right] \quad (29-54)$$

which gives $\alpha_1 = 145$ ohms. Solution of Eq. (29-53) shows that f_0^p in Fig. 29-7(b) will occur at about $f_0^p = 5.45$ kMc, and by calculations similar to Eq. (29-54) the slope parameter there is about $\alpha_1^p = 430$ ohms.*

Let us first consider an upper-sideband up-converter having an input tuning band-edge ratio of one-half octave (i.e., for the input filter, $f_2/f_1 = \sqrt{2}$ where f_1 and f_2 are defined in Fig. 29-2). This calls for $w = 0.348$. The input filter will be assumed to have $n = 3$ resonators and 1 db Tchebyscheff ripple. From tables^{7,8,9} of low-pass prototype filter elements we find that $(\Omega_1 \ell_1 / \gamma_g) = 2.024$ and $\gamma_g = \gamma_L$ for this case. Then by Eqs. (29-20) and (29-23) we obtain $(R_b)_{nom} = R_{b0} = 25$ ohms. Since $R_s = (X_{11})_0 / Q_d = 3.86$ ohms $T = (R_b)_{nom} / R_s = 6.5$. In this upper-sideband case $f'_0 = f_0^p + f_0 = 5.45 + 1 = 6.45$ kMc which gives by Eq. (29-27), $v = 0.291$. By use of T and v in Fig. 29-9 along with the fact that $f'_0/f_0 = 6.45$ we obtain $P'_{out}/P_{avail} = 3.48$ or a nominal gain of 5.3 db. By Eq. (29-25) it is found that the sideband resonator should be adjusted to couple a resistance of $R'_{b0} = 9.95$ ohms into the diode circuit at the upper-sideband frequency $f'_0 = 6.45$ kMc.

Using $\alpha_1^p = 430$ ohms, $w_p = wf_0/f_0^p = 0.0638$, and $R_g^p = R_s = 3.86$ ohms in Eq. (29-36) we get $(\Omega_1 \ell_1 / \gamma_g)_p = 7.1$ for the pump-filter low-pass prototype. A Tchebyscheff ripple of 0.5 db using an $n = 3$ resonator pump filter will be specified which by Table 29-1 calls for $d = 0.6265$. Then by Eq. (29-40), $e = 0.4855$. By Fig. 29-10, $U_3(0.6265) = 3.05$ and $U_3(0.4855) = 2.18$. By Eq. (29-42), $|\rho|_{max} = 0.715$. By Eq. (29-43), a minimum power of $A(P_{avail})^p = 0.49 (P_{avail})^p$ will be delivered to the diode where $(P_{avail})^p$ is the available pump power. Assuming that the diode is to be pumped with a peak-to-peak voltage of 6 volts, it is estimated that the diode will absorb about 30 mw of pump power when $f^p = f_0^p = 5.45$ kMc. Thus the required available pump power will be about $(P_{avail})^p = 30/A = 30/0.49 = 61$ mw, neglecting dissipation loss in the pump input filter. A 1 db dissipation loss would raise this figure to about 77 mw required available power.

Let us now make analogous calculations as described in Sec. G using the same diode and diode circuit having $f_0 = 1$ kMc, $f_0^p = 5.45$ kMc,

* In computing R_g^p and α_1^p the denominator in Eq. (29-16b) was neglected and the representation in Fig. 29-7(a) was used. This should cause little error in the performance estimates about to be computed since, as has been mentioned in Sec. D, the denominator of Eq. (29-16b) will be varying quite slowly. It can therefore be regarded as constant within the frequency range of interest. As a constant it would decrease the size of both R_g^p and α_1^p proportionally (about 25 percent in this case), but would cancel out in the computation given by Eq. (29-36).

$\alpha_1 = 145$ ohms, $\alpha_1^p = 430$ ohms, etc., as before. Again $\omega = 0.348$ will be used (half-octave input tuning range). In this case the output will be taken at the lower-sideband frequency: $f'_0 = f_0^p - f_0 = 5.45 - 1 = 4.45$ kMc. Since this gives negative resistance operation which increases the sensitivity to input impedance variations, the $n = 3$ resonator input filter will be assumed to have its Tchebyscheff ripple reduced to 0.25 db which calls for $(\Omega_1 \ell_1 / \lambda_g) = 1.3034$.³

The calculations as outlined in Sec. G call for $(R_b)_{nom} = R_{b0} = 38.7$ ohms, $R'_{b0} = 8.0$ ohms (when $D = 2$). Assuming a stability parameter of $D = 2$, the nominal power gain would be 13.4 db, 8.1 db greater than for corresponding upper-sideband design. The pump power required should be the same in both cases.

Similar calculations for a one-octave-tuning-range lower-sideband up-converter were made, again assuming the same diode circuit and the same f_0 , f_0^p , $f'_0 = 4.45$ kMc values. A value of 0.25 db Tchebyscheff ripple was assumed for the $n = 3$ resonator input filter. Since stability might be more of a problem using an octave input bandwidth, $D = 3$ was used. In this case $(R_b)_{nom} = 78.8$, $R'_{b0} = 5.45$, the nominal gain is 8.8 db, $A = 0.273$ and the required available pump power is about $(P_{avail})^p = 30/0.273 = 110$ mw, neglecting pump filter dissipation loss and assuming that the diode needs 30 mw of absorbed pump power. If the pump filter has 1 db dissipation loss, the required available power would be about 138 mw.

With respect to these performance estimates, it is well to note the factors that have been neglected. The calculated gain values neglect the dissipation loss of the input filter and the sideband output resonator. Also, it should be recalled that the gain given is the nominal gain; there will be some variation of gain across the band due to variations with frequency in the signal input impedance, Z_b , and the coupling, $X_{12}X_{21}$, and also due to variation in the up-conversion ratio, f'_0/f . In converting Fig. 29-4 to the form in Fig. 29-5 it was assumed that impedance $Z_c^p = 0$ at $f = f_0$, where Z_c^p would actually be a small reactance at $f = f_0$. This would affect the resonance characteristic somewhat. A similar assumption was made in obtaining the equivalent pump circuit in Fig. 29-6. Correction for these reactances would probably have a minor effect on the preceding performance estimates.

The calculations neglect the increase in the slope parameters α_1 and α_1^p due to the introduction of the sideband output resonator. If this

resonator is kept as loosely coupled as possible (consistent with low dissipation loss through the resonator) the increase in reactance slope due to the presence of this resonator will probably not be large. Of course, for a given required tuning range, any increase in α_1 will in turn result in somewhat less gain; while any increase in α_1' will in turn result in a larger pump reflection loss and a correspondingly larger required available pump power.

The calculation of $(R_b)_{\text{min}}$ for the signal input filter for a given lumped element prototype, a given slope parameter α_1 , and a given desired fractional bandwidth w , assumes that the diode resonator has a reactance characteristic as indicated by Eq. (a) in Fig. 29-3. The actual effective reactance of the diode resonator looks more like that shown in Fig. 29-7(b). The presence of the pole of reactance at frequency f_r will tend to narrow the actual bandwidth of the input filter. This effect would probably not be very large for a half-octave bandwidth input filter, but it might be quite appreciable in the case of an octave bandwidth filter. The net result is that a larger $(R_b)_{\text{min}}$ value will be required (which will result in a smaller R_{b0}' and somewhat less gain) in order to obtain the desired bandwidth, and the shape of the reactance characteristic will have to be considered in the design of the wideband input filter. In particular, the performance of the input filter will probably be best if its other resonators are designed to have similar resonance characteristics in the input frequency range of interest.

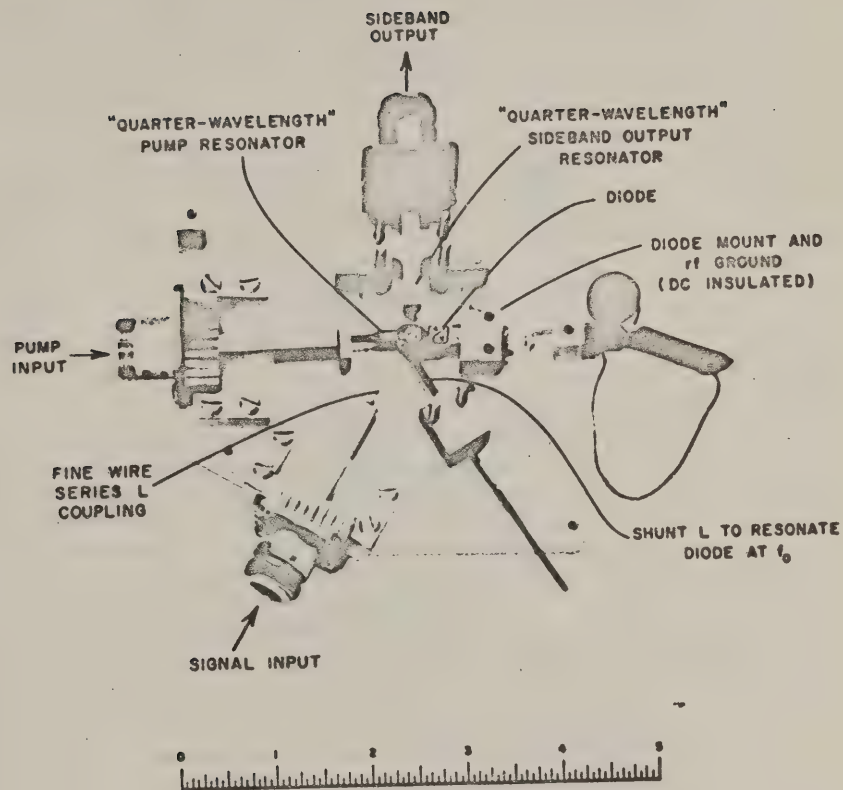
I. RESULTS OF A PRELIMINARY ELECTRONIC TUNING EXPERIMENT WITH AN UP-CONVERTING FILTER CIRCUIT

1. DESCRIPTION OF THE DEVICE AND ITS PERFORMANCE

Figure 29-12(a) shows a strip-transmission-line up-converter for electronically tunable filter applications which was fabricated in the SRI Electromagnetics Laboratory some time ago. It was designed and constructed for a trial experiment before most of the theory in Secs. B to H was worked out and, as will be evident from the analysis to follow, the performance of this device in no way represents the optimum performance that can be achieved with electronically tunable up-converters. However, quite a few things were learned from this experiment, and it appears desirable to share the experience gained.

Figure 29-12(a) shows the device with its cover plate removed, and Fig. 29-12(b) shows its equivalent circuit. The diode is resonated in parallel at the input band center, $f_0 = 1.2$ kMc, by use of a short-circuited stub. The signal input coupling is controlled by a series-inductance coupling made from high-impedance line (fine wire). The pump circuit uses a single resonator filter formed by a nominally one-quarter-wavelength resonator with series-capacitance coupling to the diode, and shunt-capacitance coupling to the pump input line.¹² The device is an upper-sideband up-converter, and the upper sideband output also consists of a single resonator filter. This sideband filter is also of the quarter-wavelength-resonator type, using series-capacitance coupling to the diode but with shunt-inductance coupling to the output line.

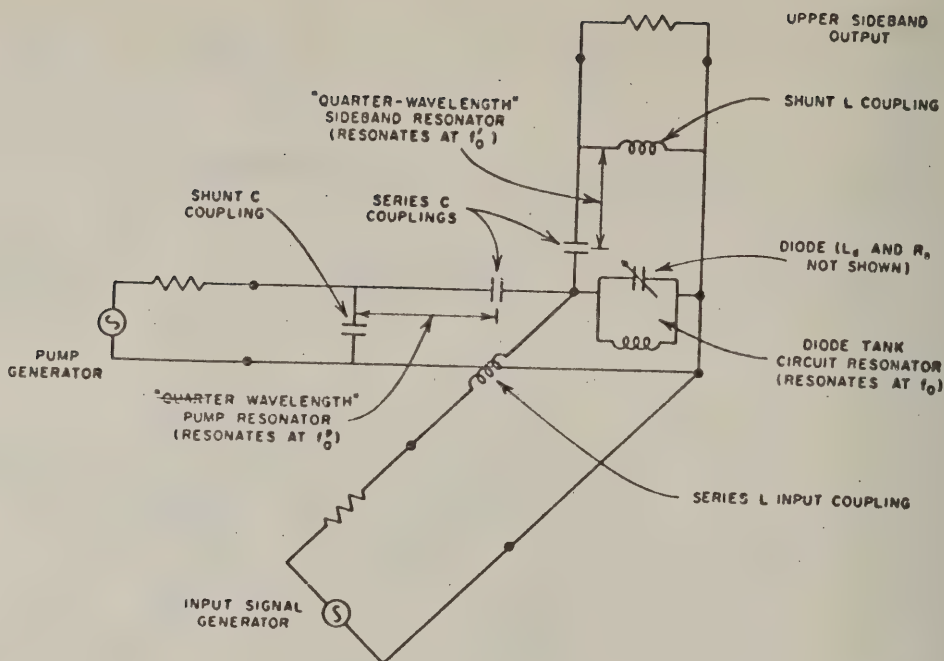
The device used an input band-center frequency of $f_0 = 1.2$ kMc, an output frequency of $f'_0 = 5.05$ kMc, and a pump-band-center frequency of $f_0^p = 3.85$ kMc. In testing this device it was found that the pump circuit resonator and the series-inductance input coupling did not adequately reject the sideband frequency f'_0 , making it necessary to add low-pass filters in the pump and input circuits. The diode used was an early Motorola Microwave Associates diode which had a cutoff frequency (for bias near reverse breakdown) of 36 kMc. As the analysis will show, one cannot



RP-2326-341

FIG. 29-12(a)

PHOTOGRAPH OF A STRIP-TRANSMISSION-LINE STRUCTURE (WITH COVER PLATE REMOVED)
USED FOR ELECTRONICALLY TUNABLE, UPPER-SIDEBAND UP-CONVERTER EXPERIMENTS



98-1326-1-2

FIG. 29-12(b)
EQUIVALENT CIRCUIT FOR THE STRUCTURE IN FIG. 29-12(a)

expect much gain in an upper-sideband device such as this when using a diode with such a low cutoff frequency. The main objective of the experiment was to demonstrate the electronic tuning properties of the device.

Figure 29-13 shows a plot of the gain vs. input frequency as the amplifier is tuned. For each input frequency the pump frequency was adjusted to give an upper-sideband output frequency of $f_0' = 5.05$ kMc, while the pump power level was adjusted always to maintain 0.5 microampere or less of diode current with 3.5 volts back bias. The 3-db down tuning bandwidth turned out to be 14.6 percent, which is considerably less than was at first anticipated. However, the analysis to follow shows that the performance is about what should be expected if one considers the deleterious effect of the diode's internal inductance.

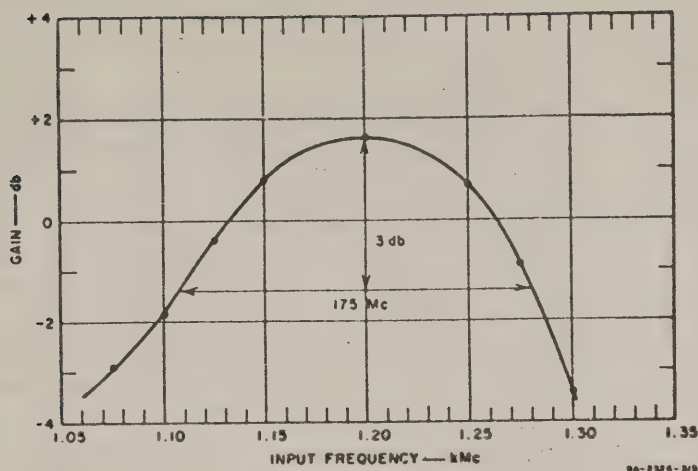


FIG. 29-13

ELECTRONIC TUNING PROPERTIES OF THE CIRCUIT IN FIG. 29-12(a)

For each input frequency the pump frequency was adjusted to give a 5.05 kMc upper-sideband output frequency, and the pump power was adjusted to give about 0.5 microampere diode current. As is discussed in Sec. I., the tuning range of this device was severely limited by the diode series inductance which made the diode self-resonant at a frequency quite close to the input tuning band

Table 29-2 shows the results of an experiment performed with this device. In this case the bias and pump power were adjusted at each tuning frequency in order to maximize the gain. The main effect of this was to vary the tuning of the diode tank circuit so that the amplifier was made to operate over a much wider tuning range. At certain frequencies it is seen that the gain is relatively high. This was found to occur when the lower sideband signal found resistive termination so that the amplifier had some negative resistance gain. The variable-bias operation illustrated by Table 29-2 is interesting inasmuch as it shows additional means for extending the tuning range. However, varying the bias introduces additional complications, since the bias voltage must track the pump frequency. Also since varying the bias affects the pump circuit, maintaining a uniform diode pump voltage swing becomes more difficult.

TABLE 29-2

UP-CONVERTING FILTER, OPERATION WITH VARIABLE BIAS

Operating Conditions:

Output set at 5.050 kMc for all tests by adjusting pump frequency so sum of signal and pump frequencies equals 5.050 kMc. For each signal frequency the diode bias and pump power level were peaked to give maximum gain (except where noted).

| INPUT FREQUENCY (kMc) | DIODE BIAS (volts) | GAIN (db) |
|--------------------------|-----------------------|--------------------------------------|
| 0.650 | 0.39 <i>forward</i> | - 2.4 |
| 0.700 | 0.34 <i>forward</i> | + 1.6 |
| 0.750 | 0.22 <i>forward</i> | +14.4 (must involve lower side band) |
| 0.750 | 0 (bias not peaked) | + 3.4 |
| 0.800 | 0.06 <i>forward</i> | + 6.6 (must involve lower side band) |
| 0.800 | 0 (bias not peaked) | + 6.1 (must involve lower side band) |
| 0.900 | 0.27 <i>reverse</i> | + 1.3 |
| 1.000 | 0.85 <i>reverse</i> | + 2.2 |
| 1.100 | 1.65 <i>reverse</i> | + 1.6 |
| 1.200 | 3.55 <i>reverse</i> | + 1.6 |
| 1.250 | 4.2 <i>reverse</i> | + 0.8 |
| 1.300 | 5.6 <i>reverse</i> | - 1.25 |

2. THEORETICAL PERFORMANCE ASSUMING DIODE INDUCTANCE IS ZERO

The diode used had a zero bias capacitance of $3.8 \mu\mu\text{f}$ and a capacitance near reverse breakdown of $1.4 \mu\mu\text{f}$ according to the manufacturer's specifications. The cutoff frequency, f_c , for the diode biased near reverse breakdown was rated as 36 kMc. This implies a diode series resistance of $R_s = 1/(2\pi f_c C_{\text{breakdown}}) = 3.16 \text{ ohms}$. The manufacturer indicates that the diode inductance is about $L_d = 3 \times 10^{-9}$ henries for this diode; however, let us ignore this inductance for the moment and compute the performance which would result if this inductance were zero. We will assume that $a = C_1/C_0 = 0.25$ and we estimate that under operating conditions $C_0 = 2.3 \mu\mu\text{f}$.

The diode tank circuit has, besides the capacitance C_0 , additional capacitance C_e contributed by the pump and output circuit couplings and by stray capacitance to the ground planes. It is estimated that C_e is $1 \mu\mu\text{f}$ or more; herein it will be assumed to be $1 \mu\mu\text{f}$.

Analogously to Eq. (29-15), if $C_0 + C_c$ is tuned out with a lumped inductance, the slope parameter of the input resonator at frequency f_0 will be $b_1 = 2\pi f_0(C_0 + C_c) = 0.0248$ mho. The input coupling to the device was designed to have $(G_b)_{nom} = G_{b0} = 0.00426$ mho. For a single-resonator filter with the fractional bandwidth referred to the 3-db points, $(\Omega_1 \ell_1 / \nu_L) = 2$. Thus, the fractional tuning bandwidth would be about $\omega = (G_b)_{nom} / b_1 (\Omega_1 \ell_1 / \nu_L) = 0.344$, provided that $L_d = 0$. It will be shown later that the measured fractional tuning range was shrunk to 0.146 largely because L_d was not zero.

Assuming $L_d = 0$, $(B_{11})_0 = 2\pi f_0 C_0 = 0.0173$ and $G_d = R_s (B_{11})_0^2 = 3.16(0.0173)^2 = 0.000946$. This gives $Q_d = (B_{11})_0 / G_d = 18.3$. Then $T = (G_b)_{nom} / G_d = 0.00426 / 0.000946 = 4.5$ and $\nu = (1/aG_d) \sqrt{f'_0/f_0} = [1/(0.25)(18.3)] \sqrt{5.05/1.2} = 0.448$. By Eq. (29-28), $P'_{out}/P_{avail} = 1.63$ or 2.12 db, a value that compares reasonably well with the midband gain in Fig. 29-13.

3. THEORETICAL PERFORMANCE INCLUDING EFFECTS OF L_d

Now let us recompute the performance of this device using the same f_0 , f'_0 , C_0 , $a = C_1/C_2$, R_s , C_c , and $(G_b)_{nom}$, but including $L_d = 3 \times 10^{-9}$, the approximate value of the diode series inductance as suggested by the diode manufacturer. In this case the total susceptance of the input resonator (diode tank resonator) will be

$$jB_1 = jB_{11}^* + j\omega C_c - j \frac{1}{\omega L_p} \quad (29-55)$$

where B_{11}^* is given by Eqs. (29-63) and (29-64). For the desired parallel resonance at $f = f_0$, L_p is chosen so that

$$\frac{1}{\omega_0 L_p} = (B_{11}^*)_0 + \omega_0 C_c \quad (29-56)$$

which makes $B_1|_{\omega=\omega_0} = 0$. The slope parameter of the input resonator is

$$b_1 = \left. \frac{\omega_0}{2} \frac{dB_1}{d\omega} \right|_{\omega=\omega_0}$$

$$= \frac{1}{2} \left[\frac{-\gamma' \omega_0 C_0^*}{(\gamma\gamma' - a^2)} + \frac{2(\gamma')^2 \omega_0 C_0^* \left(\frac{\omega_0}{\omega_r} \right)}{(\gamma\gamma' - a^2)^2} + \omega_0 C_p + \frac{1}{\omega_0 L_p} \right] \quad (29-57)$$

where the quantities γ , γ' and ω_r are as discussed in Sec. J. In this case $f_r = 1/2\pi\sqrt{C_0^* L_d}$ is 1.99 kMc, so $\omega_0/\omega_r = f_0/f_r = 1.2/1.99 = 0.603$ and $\omega_0'/\omega_r = f_0'/f_r = 5.05/1.99 = 2.54$. This gives $\gamma = -0.636$, and $\gamma' = 5.45$. Using $a = 0.25$, $C_0^* = C_0(1 - a^2) = 2.3(10^{-12})[1 - (0.25)^2] = 2.15 \times 10^{-12} \text{ fd}$, $L_d = 3 \times 10^{-9} \text{ h}$, and also $C_c = 1 \times 10^{-12}$ as before, by Eqs. (29-56), (29-57) and (29-63) we obtain the slope parameter $b_1 = 0.0484$. Then the estimated fractional tuning bandwidth would be $\omega = [(G_0)_{\text{out}}/b_1](\Omega_1 t_1/\chi_{L_1}) = (0.00426/0.0484)(2) = 0.176$. By Sec. J we obtain $(G_0') = 0.00203$, $(G_0'') = 0.0005$, and by Eq. (29-63) and the dual of Eq. (29-24) we obtain $G_{b_0}' = 0.00136$. By the dual of Eq. (29-22) the nominal gain (in this case the mid-tuning range gain) is $P_{\text{out}}'/P_{\text{avail}} = 1.825$ or 2.61 db.

Considering that the values used for the various parameters in these calculations are not known very accurately, the calculations are in rather good agreement with the measured results. The calculated tuning bandwidth of 17.6 percent would easily shrink to the measured tuning bandwidth of 14.6 percent by use of a somewhat larger value for L_d . The computed mid-band gain of 2.61 db does not include the losses in the input and output coupling networks; when some allowance is made for such dissipation loss, the computed gain appears to agree rather well with the measured midband gain of 1.6 db in Fig. 29-13.

It should be noted that the computed tuning range shrank from $\omega = 0.344$, when L_d was taken to be zero, to $\omega = 0.176$ when $L_d = 3 \times 10^{-9} \text{ h}$. The reason for this shrinkage in tuning range is that the presence of L_d makes the diode self-resonant at a frequency $f_r = 1.99 \text{ kMc}$, which is only 0.79 kMc above the tank resonant frequency f_0 . The susceptance B_1 of the diode resonator then looks something like the reactance characteristic in Fig. 29-7(b). The susceptance of B_1 is zero at f_0 , but goes to infinity at f_r . The closer f_r is to f_0 , the larger the slope parameter b_1 evaluated at f_0 will be and the smaller the tuning range. If, for example, this

device had been designed to operate with $f_0 = 0.8$ kMc instead of 1.2 kMc, the fractional tuning range would doubtless have been improved considerably, since then f_0 and f_r would be more widely separated. Of course, the tuning range could also have been increased by increasing the coupling to the signal input line to increase G_{s0} , while decreasing the coupling to the sideband resonator correspondingly to preserve the impedance match. This, however, would have reduced the gain which was already low as a result of diode loss.

• J. THE ADMITTANCE PARAMETERS OF A VARIABLE-CAPACITANCE DIODE HAVING APPRECIABLE SERIES INDUCTANCE

The open-circuit impedance equations of a variable-capacitance diode in a lower-sideband up-converter can be expressed (neglecting losses) as^{1,3}

$$\begin{bmatrix} j(-X_{11}) & j(-X_{12}) \\ jX_{21} & jX_{22} \end{bmatrix} \begin{bmatrix} I_1 \\ I_2^* \end{bmatrix} = \begin{bmatrix} V_1 \\ V_2^* \end{bmatrix} \quad (29-58)$$

where the $X_{j,k}$ are given by Eqs. (29-11) and (29-12). V_1 and I_1 are, respectively, the voltage across the diode and current through the diode at the signal frequency f , while V_2 and I_2 are the corresponding quantities at the lower sideband frequency f' . If the diode has series inductance, Eq. (29-58) becomes

$$\begin{bmatrix} j(-X_{11} + X_L) & j(-X_{12}) \\ jX_{21} & j(X_{22} - X_L') \end{bmatrix} \begin{bmatrix} I_1 \\ I_2^* \end{bmatrix} = \begin{bmatrix} V_1 \\ V_2^* \end{bmatrix} \quad (29-59)$$

where

$$X_L = 2\pi f L_d \quad , \quad (29-60)$$

$$X_L' = 2\pi f' L_d \quad , \quad (29-61)$$

and L_d is the diode internal series inductance. Note that since L_d has no frequency conversion properties, it does not affect the mutual-reactance terms in Eq. (29-58). By matrix inversion and some manipulation, Eq. (29-59) becomes

$$\begin{bmatrix} jB_{11}^* & jB_{12}^* \\ -jB_{21}^* & -jB_{22}^* \end{bmatrix} \begin{bmatrix} V_1 \\ V_2^* \end{bmatrix} = \begin{bmatrix} I_1 \\ I_2^* \end{bmatrix} \quad (29-62)$$

where the B'_{jk} are the equivalent short-circuit admittances

$$\left. \begin{aligned} B'_{11} &= \frac{-\gamma' \omega C'_0}{\gamma\gamma' - a^2} \\ B'_{22} &= \frac{-\gamma \omega' C'_0}{\gamma\gamma' - a^2} \\ B'_{12} &= \frac{a \omega C'_0}{\gamma\gamma' - a^2} \\ B'_{21} &= \frac{a \omega' C'_0}{\gamma\gamma' - a^2} \end{aligned} \right\} \quad (29-63)$$

where

$$\left. \begin{aligned} \gamma &= \left(\frac{\omega}{\omega_r}\right)^2 - 1 \\ \gamma' &= \left(\frac{\omega'}{\omega_r}\right)^2 - 1 \\ \omega_r &= \frac{1}{\sqrt{L_d C'_0}} \end{aligned} \right\} \quad (29-64)$$

$\omega = 2\pi f$, $\omega' = 2\pi f'$, $a = C_1/C'_0$, and C'_0 is as defined in Eq. (29-12).

For the case of an upper-sideband up-converter, Eq. (29-59) becomes

$$\begin{bmatrix} j(-X_{11} + X_L) & j(X_{12}) \\ j(X_{21}) & j(-X_{22} + X'_L) \end{bmatrix} \begin{bmatrix} I_1 \\ I_2 \end{bmatrix} = \begin{bmatrix} V_1 \\ V_2 \end{bmatrix} \quad (29-65)$$

where in this case V_2 and I_2 are the corresponding voltage and current at the upper-sideband frequency, f' . Matrix inversion of Eq. (29-65) gives

$$\begin{bmatrix} jB_{11}^* & jB_{12}^* \\ jB_{21}^* & jB_{22}^* \end{bmatrix} \begin{bmatrix} V_1 \\ V_2 \end{bmatrix} = \begin{bmatrix} I_1 \\ I_2 \end{bmatrix} \quad (29-66)$$

where the B_{jk}^* are again as defined by Eqs. (29-63) and (29-64).

If the diode has an equivalent series loss resistance, R_s , the corresponding effective parallel conductances are

$$(G_d') = \frac{R_s}{R_s^2 + (X_L - X_{11})_0^2} = \frac{R_s}{R_s^2 + \left(\frac{\gamma}{\omega_0 C_0}\right)^2} \quad (29-67)$$

at frequency f_0 , and

$$(G_d')' = \frac{R_s}{R_s^2 + (X_L' - X_{22})_0^2} = \frac{R_s}{R_s^2 + \left(\frac{\gamma'}{\omega'_0 C_0}\right)^2} \quad (29-68)$$

at frequency f'_0 .

In cases where the diode inductance has appreciable reactance, Eqs. (29-63), (29-67), and (29-68) should be used in place of Eqs. (29-7), (29-8), and (29-9). Equations (29-22), (29-24), (29-47), (29-48), and (29-49) can be applied to cases where the diode is resonated in shunt by simply replacing all of the impedance quantities in these series resonance equations by their corresponding dual (i.e., admittance) quantities for the parallel-resonance case. Then the admittance parameters defined by Eqs. (29-63), (29-67), and (29-68) may be inserted. However, it would not be accurate to use Eqs. (29-63), (29-67), and (29-68) with Eqs. (29-25), (29-28), (29-31), (29-51), and (29-52), or with Figs. 9, and 11(a), (b), (c) because these later equations and charts have assumed that $(B_{12}B_{21})_0 = \alpha^2(B_{11})_0^2(f'_0/f_0)$ and $G_d' = G_d(f'_0/f_0)^2$. These two relations are valid if $L_d = 0$, but they are not valid if Eqs. (29-63), (29-67), and (29-68) apply with $L_d \neq 0$.

K. CONCLUSIONS

1. THEORY OF UP-CONVERTERS AS ELECTRONICALLY TUNABLE FILTERS

Consideration of the preceding theory and calculations leads to the following conclusions:

- (1) Up-converters used as electronically tunable filters should be capable of very sizeable tuning ranges. Although the examples involve approximations, they indicate that tuning ranges of the order of one-half octave to perhaps one octave are possible.
- (2) Since the sideband output frequency is far removed from the input band, there are no problems with image responses. All possible spurious responses can be removed by a properly designed input filter.
- (3) The lower sideband type of up-converter will give significantly more gain than the upper sideband type, even if the nominal input filter resistance is several times as large as the negative resistance presented by the diode. With the input filter resistance several times the negative resistance of the diode, there need be little difficulty with stability. An isolator used at the input should make such an amplifier very stable, and the isolator would in most cases make the power emission from the input port negligible.
- (4) Although gain and noise figure are presumed to be only secondary considerations in the design of the proposed tunable up-converters, such devices do give sufficient gain to raise a weak signal out of the noise level, and it appears that their noise figure ought to be superior to that of superheterodyne receivers. For these reasons it is expected that a system using an electronically tunable up-converter at its input should have a better noise figure than a corresponding system with a superheterodyne receiver at its input.
- (5) It appears that presently available voltage-tunable oscillators should be adequate in many cases for providing the required pump power. Use of voltage-tunable oscillators should permit quite large tuning rates.
- (6) Since the up-converter would usually be followed by a fixed-tuned, superheterodyne receiver, the signal

acceptance bandwidth at any up-converter input tuning frequency would be very narrow--the bandwidth being determined by the IF bandwidth of the superheterodyne receiver. Thus tuning systems of the proposed type can be made to have very high resolution and sensitivity

2. INSIGHTS OBTAINED FROM THE ELECTRONIC TUNING EXPERIMENT

The trial device described in Sec. I performed very much as predicted by the theory. The experiments pointed up a number of practical matters which it would be well to keep in mind when designing more advanced devices of this type. They are:

- (1) If the diode is resonated in shunt, one should be sure that the self-resonant frequency of the diode is far removed from either the input or pump band center frequencies. If the diode self-resonant frequency is at all close to the input frequency band, the tuning range will be severely limited. If the diode self-resonant frequency is close to the pump frequency band, the pump impedance-matching problem will be much more severe.
- (2) Diode series resonant circuits of the form in Fig. 29-8 provide one means for getting around the problem of diode self resonance since the diode inductance is simply used as part of the required series inductance. This configuration is attractive also because it will be found that for a given impedance level in the associated filters, a diode with a smaller capacitance can be used. This will permit the use of diodes having higher Q 's (since high- Q diodes have relatively small capacitance). Another advantage of the series-resonance diode mount in Fig. 29-8 over the shunt-resonance mount in Fig. 29-12(a) is that stray capacitance is easier to control.
- (3) As far as is possible, it is desirable to use inductive coupling for resonators direct coupled to the diode circuit. This is illustrated in Fig. 29-8 where the sideband output resonator and the No. 2 resonator of the pump circuit are inductively coupled to the diode circuit. Using inductive coupling, the inductive reactance of these couplings merely contributes to the inductive reactance needed to resonate the diode at f_0 . Using capacitive couplings as was done in the device in Fig. 29-12(a) increases the total capacitance associated with the diode circuit, and increases the resonator slope parameter considerably at f_0 .

3. ADMITTANCE PARAMETERS OF A DIODE HAVING APPRECIABLE SERIES INDUCTANCE

The formulas derived for the admittance parameters of a diode having appreciable series inductance show that this inductance will often be an extremely important factor to consider in the design of an amplifier. It is seen that the diode admittances will change very rapidly at frequencies near the diode self-resonant frequency.

REFERENCES

1. C. W. Barnes, G. L. Matthaei, and R. C. Honey, "Application of New Techniques to Low Noise Reception," Quarterly Progress Report 7, SRI Project 2550, Contract AF 33(616)-5803, Stanford Research Institute, Menlo Park, California (March 1960). See Sec. III.
2. C. W. Barnes, G. L. Matthaei, and R. C. Honey, "Application of New Techniques to Low Noise Reception," Quarterly Progress Report 8, SRI Project 2550, Contract AF 33(616)-5803, Stanford Research Institute, Menlo Park, California (March 1960). See Sec. III.
3. G. L. Matthaei, "A Study of the Optimum Design of Wideband Parametric Amplifiers and Up-Converters," scheduled for publication in the January, 1961 issue of the *IRE Transactions of the Professional Group on Microwave Theory and Techniques*.
4. J. M. Manley and H. E. Rowe, "Some General Properties of Nonlinear Elements—Part 1. General Energy Relations," *Proc. IRE* 44, pp. 904-913 (July 1956).
5. H. E. Rowe, "Some General Properties of Nonlinear Elements. II. Small Signal Theory," *Proc. IRE* 46, pp. 850-860 (May 1958).
6. D. Leenov, "Gain and Noise Figure of a Variable-Capacitance Up-Converter," *Bell Syst. Tech. J.* 37, pp. 989-1008 (July 1958).
7. L. Weinberg, "Network Design by Use of Modern Synthesis Techniques and Tables," Tech. Memo. 427, Hughes Aircraft Company, Research Laboratories, Culver City, California (April 1956). Also, *Proc. of NEC* 12 (1956).
8. L. Weinberg, "Additional Tables for Design of Optimum Ladder Networks," Tech. Memo 434, Hughes Aircraft Company, Research Laboratories, Culver City, California (31 August 1956).
9. See Chapter 13 of this report.
10. See Chapter 18 of this report.
11. G. L. Matthaei, "Band-Pass Microwave Filter Design—A New Method and Its Relation to Other Methods," 1960 *IRE International Convention Record*, Part 3, pp. 95-122.
12. G. L. Matthaei, "Direct-Coupled, Band-Pass Filters with $\lambda_0/4$ Resonators," 1958 *IRE National Convention Record*, Part 1, pp. 98-111.
13. H. W. Bode, *Network Analysis and Feedback Amplifier Design*, pp. 363-368 (D. Van Nostrand Co., Inc., New York, 1945).
14. R. M. Fano, "Theoretical Limitations on the Broadband Matching of Arbitrary Impedances," *J. Franklin Inst.*, Vol. 249, pp. 57-83 and 139-154 (January and February 1950).
15. R. LaBosa and H. J. Carlin, "A General Theory of Wideband Matching with Dissipative 4-Poles," *J. Math. and Phys.*, Vol. 33, pp. 331-345 (January 1955).
16. H. J. Carlin, "Synthesis Techniques for Gain-Bandwidth Optimization in Passive Transducers," *Proc. IPE*, 48, pp. 1705-1714 (October 1960).
17. G. L. Matthaei, "Synthesis of Tchebyscheff Impedance-Matching Networks, Filters, and Interstages," *IRE Trans. PXCT-3* pp. 162-172 (September 1956).
18. E. Green, *Amplitude-Frequency Characteristics of Ladder Networks*, pp. 62-78 Marconi's Wireless Telegraph Co., Ltd., Chelmsford, Essex, England, 1954.
19. B. F. Barton, "Design of Efficient Coupling Networks," Technical Report 44, Contract DA 36-039-SC 63203, Electronic Defense Group, University of Michigan, Ann Arbor, Michigan (March 1955).
20. G. L. Matthaei, "Some Techniques for Network Synthesis," *Proc. IRE* 42, pp. 1126-1137 (July 1954).

LUMPED-ELEMENT PROTOTYPES FOR IMPEDANCE-MATCHING NETWORKS

A. GENERAL

Bode¹ has presented the theoretical restrictions applying to the design of lossless, wideband, impedance-matching networks for loads that may be represented by a single resistor and a single reactive element or resonator. Fano² has presented the theoretical restrictions applying to the design of lossless, wideband, impedance-matching networks for arbitrary loads. His results show that there is a gain-bandwidth limitation that applies to the impedance matching of any load containing reactive elements. Thus, if it is desired to match a generator with a resistive internal impedance to a load that consists of both resistive and reactive elements, a perfect match will be possible only at discrete frequencies. If an impedance match is desired across a finite frequency band, some mismatch must be tolerated; in general, the wider the bandwidth required, the higher must be the reflection loss in the operating band. Thus, it is seen that wideband impedance-matching networks must also be filters, since optimum transmission in the desired band of operation, is obtained only at the expense of reduced transmission at other frequencies. Any appreciable degree of impedance match at frequency ranges where impedance match is not required will detract from the quality of impedance match possible in the desired operating band.

Although Fano² states the general theoretical limitations on the design of lossless impedance-matching networks for arbitrary loads, the problem of practical, optimum design of impedance-matching networks has been solved only for relatively simple cases. Discussions of various aspects of this problem will be found in Refs. 3 to 9. A case of considerable practical importance for many microwave applications is the case where the load to be matched may be represented over the frequency range of interest by a single reactive element and a resistor, or by a single resonator and a resistor. Matching networks for these cases can be designed from low-pass prototypes of the form shown in Fig. 18-5, where the specification of the load (or source) circuit to be matched in

the actual microwave circuit has been transformed to a specification of the quantity $1/(\omega'_1 g_1 g_0)$ for the prototype. Green^{7,8} has presented some very useful data that apply to this problem. He has presented closed-form equations for the coupling coefficients for Tchebyscheff and maximally flat filters of this type,^{7,8} and has presented charts⁸ of the coupling coefficients vs decrement for circuits of this form which give minimum reflection loss in the pass band for the given decrement.* His charts cover the cases of Tchebyscheff circuits having 2, 3, or 4 reactive elements. Barton⁹ has independently prepared equivalent charts, and also includes charts for maximally flat impedance-matching networks.

Using Green's closed-form equations for Tchebyscheff-filter coupling coefficients, element values were computed on this project for optimum prototype matching networks of the form shown in Fig. 18-5. The charts plotted from these values are presented in Section B, and their use is discussed there.

B. ELEMENT VALUES FOR IMPEDANCE-MATCHING NETWORKS GIVING MINIMUM REFLECTION

The networks referred to herein are of the form shown in Fig. 18-5. However, since the network is reciprocal, the roles of g_0 and g_{n+1} as belonging to the generator and the load, respectively, may be reversed. The impedance-matching problem to be considered is that where the decrement

$$\delta = \frac{1}{\omega'_1 g_1 g_0} \quad (30-1)$$

has been fixed by the load (or source) impedance that is to be matched, and it is desired to find a network of the form shown in Fig. 18-5 which will maximize power transmission in the frequency range from $\omega' = 0$ to $\omega' = \omega'_1$.

It is convenient to discuss the performance of impedance-matching networks in terms of their available power loss, which is defined as

$$L_A = 10 \log_{10} (P_{av, \text{avail}}/P_L) \text{ decibels} \quad (30-2)$$

* In the notation of Fig. 18-5, the decrement is $1/(\omega'_1 g_1 g_0)$. The definition of coupling coefficient as used here will be given in Section C.

where P_{avail} is the available power of the generator, and P_L is the power absorbed by the load. Available power loss is a more convenient quantity than, say, insertion loss, since available power loss is a direct index of the circuit's ability to transfer power, and is independent of the relative magnitude of the source and load impedance. Insertion loss values are dependent on the termination ratios so that for a given power transfer, the insertion loss may have most any value, depending on the relative size of the source and load impedance.

Figure 30-1 shows a typical available power loss characteristic for the impedance-matching networks under consideration. The element values of the networks discussed in this section are specified so that for the given decrement, δ , the maximum pass-band loss, $(L_A)_{max}$, will be as small as possible. Under these conditions, we are not free to choose $[(L_A)_{max} - (L_A)_{min}]$, and we must take whatever value for this quantity that comes out. Figure 30-2 shows a plot of $(L_A)_{max}$ vs δ for matching networks having $n = 1, 2, 3$, and 4 reactive elements, while Fig. 30-3 shows the corresponding Tchebyscheff-ripple values $[(L_A)_{max} - (L_A)_{min}]$.

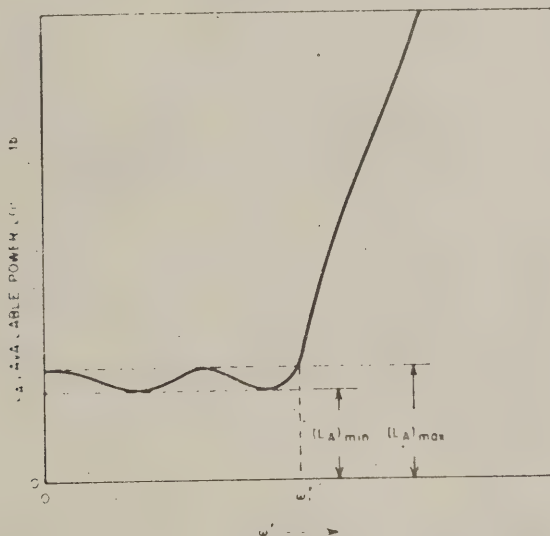
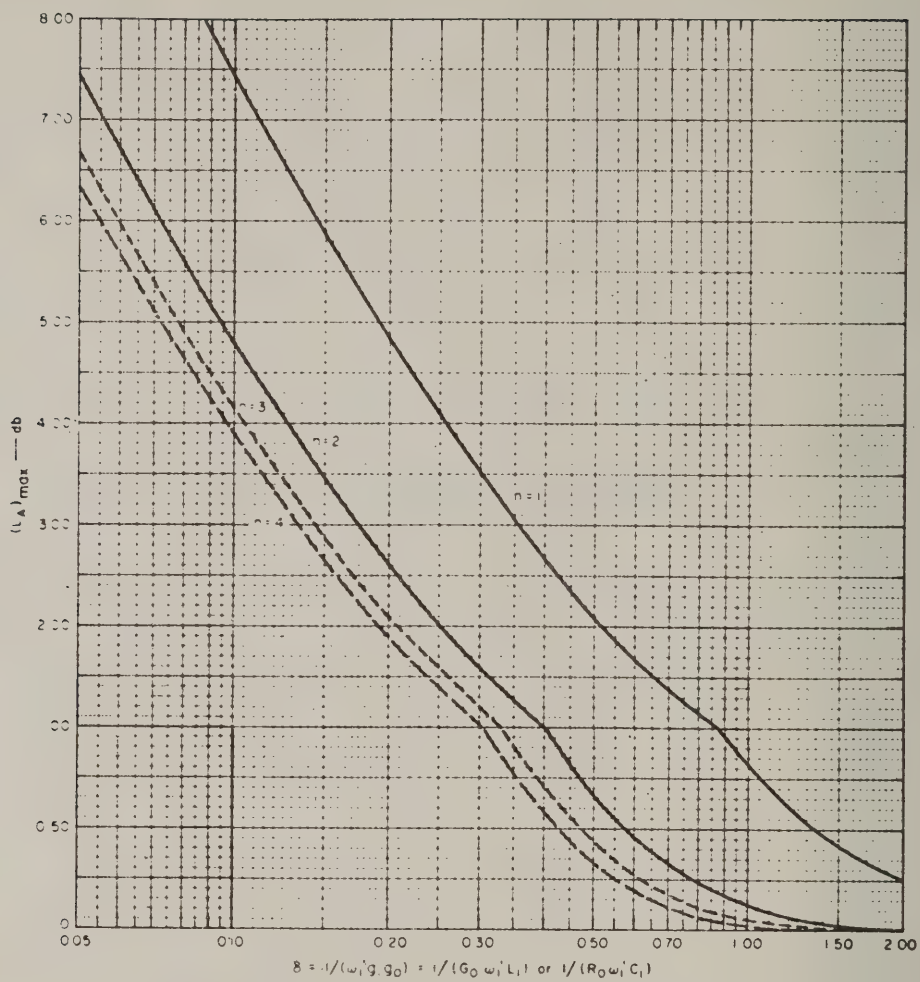


FIG. 30-1

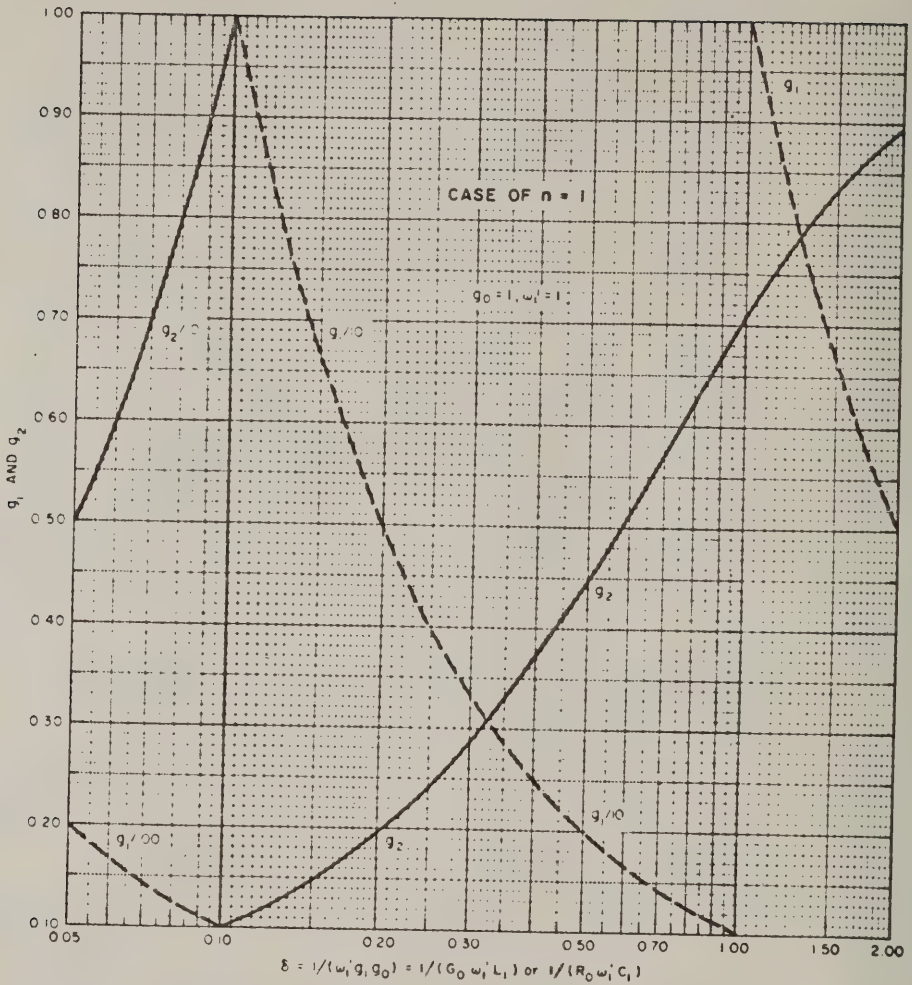
DEFINITION OF $(L_A)_{max}$ AND $(L_A)_{min}$ FOR TCHEBYSCHIEFF
IMPEDANCE MATCHING NETWORKS DISCUSSED HEREIN



9-2326-322

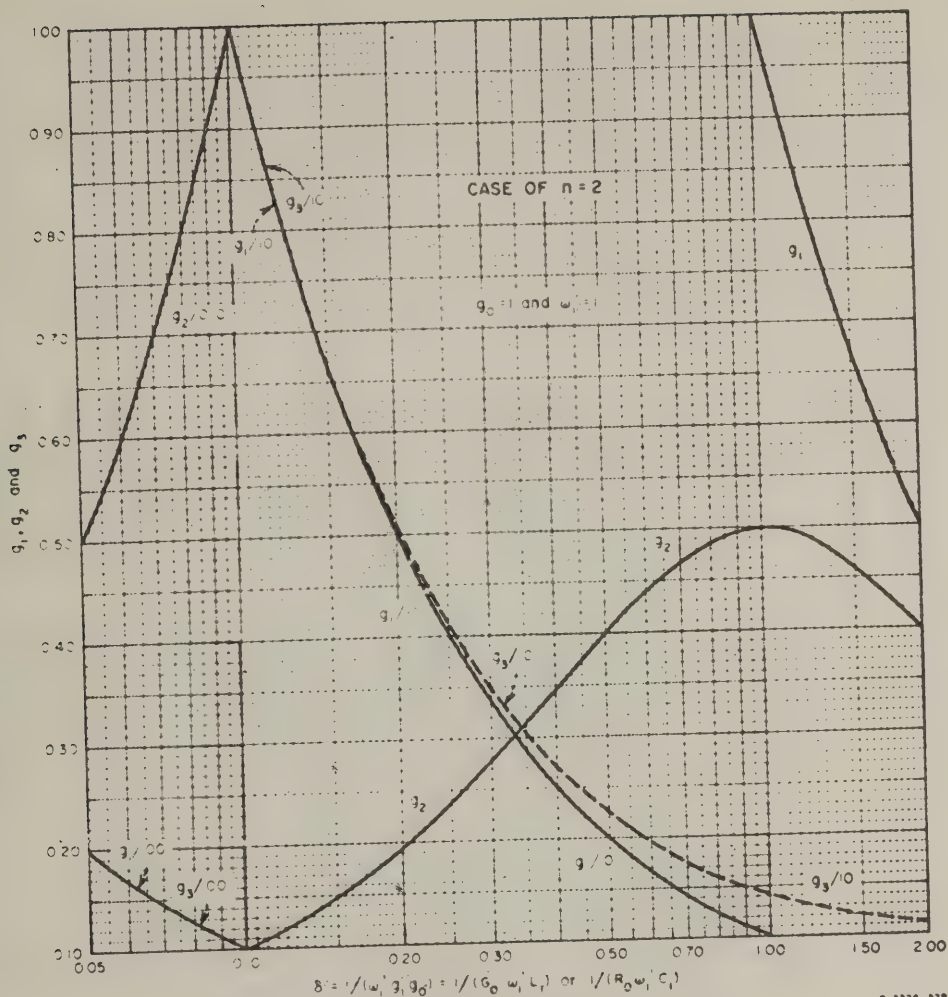
FIG. 30-2

$(L_A)_{\max}$ VS δ FOR THE IMPEDANCE MATCHING NETWORKS WHOSE ELEMENT VALUES ARE GIVEN IN FIGS 30-4(a), (b), (c), (d)



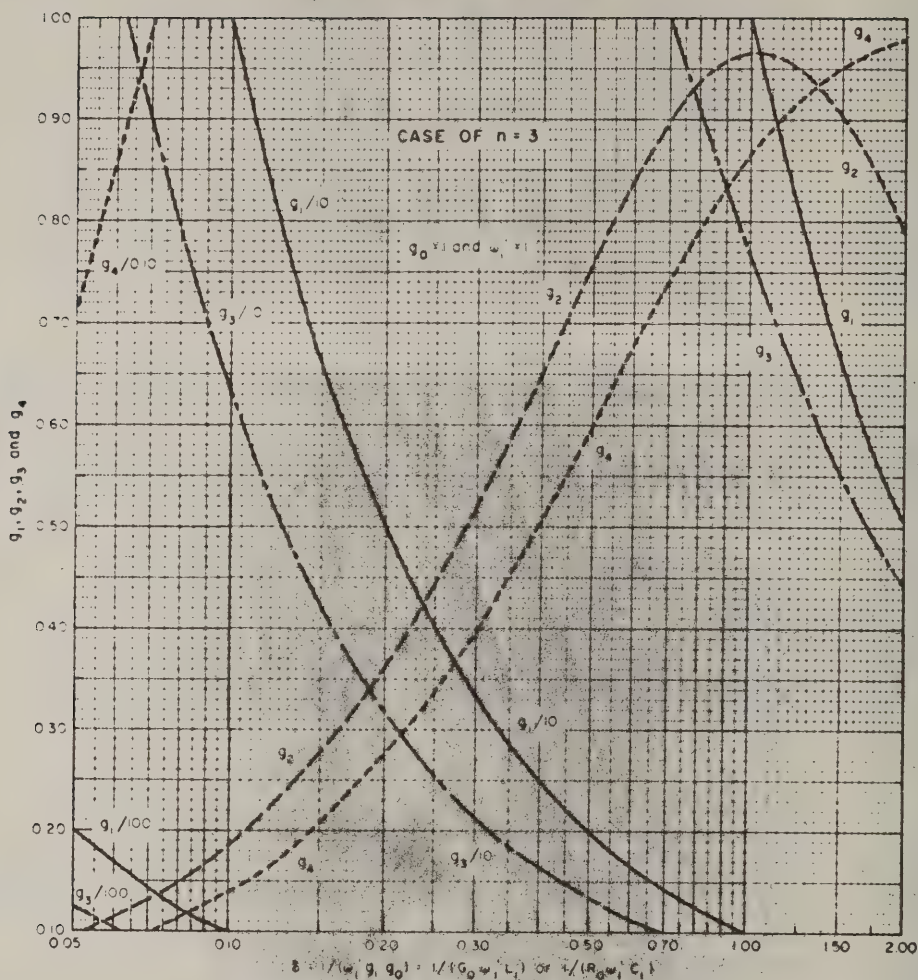
0-2326-926

FIG. 30-4(a)
ELEMENT VALUES VS δ FOR TCHEBYSCHOFF IMPEDANCE MATCHING NETWORKS
WHICH MINIMIZE $(L_A)_{\max}$



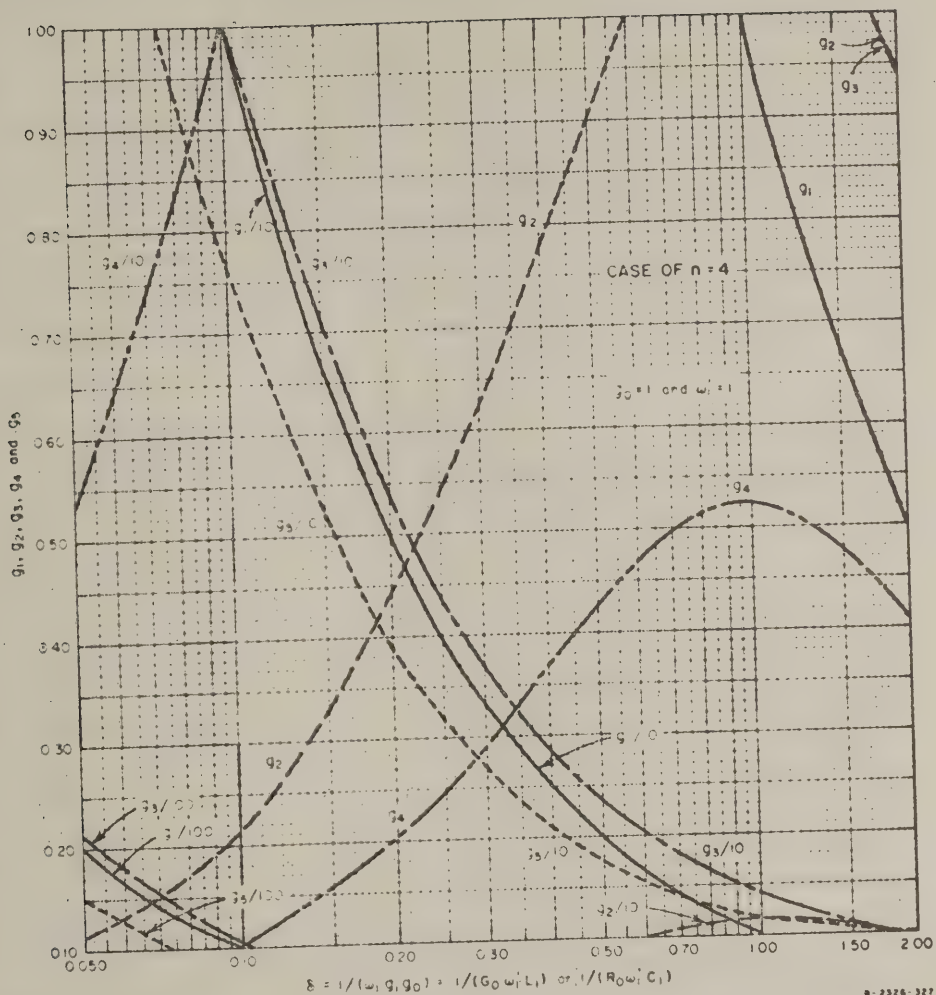
B-2326-329

FIG. 30-4(b)
ELEMENT VALUES VS δ FOR TCHEBYSCHIEFF IMPEDANCE MATCHING NETWORKS
WHICH MINIMIZE $(L_A)_{\max}$



8-2326-328

FIG. 30-4(c)
ELEMENT VALUES VS δ FOR TCHEBYSCHIEFF IMPEDANCE MATCHING NETWORKS
WHICH MINIMIZE $(LA)_{max}$



D-2326-327

FIG. 30-4(d)

ELEMENT VALUES VS δ FOR CHEBYSCHIEFF IMPEDANCE MATCHING NETWORKS
WHICH MINIMIZE $(L_A)_{\max}$

where γ_g , Ω_1 , and ℓ_1 are as defined in Fig. 29-1, and the subscript p refers to the pump-circuit filter. By Eq. (29-36) we then obtain for the decrement

$$\delta = \frac{R_g^p}{\alpha_1^p \omega_p} \quad (30-4)$$

where, as is discussed in Chapter 29, α_1^p is the *slope parameter* (see Sec. C of Chapter 29 for definition of this parameter) of the diode resonator at its pump frequency resonance, R_g^p is the effective resistance in series with the diode resonator at its pump-frequency resonance, and ω_p is the fractional operating bandwidth required for the pump circuit.

Let us now consider the upper-sideband up-converter example discussed in Section H of Chapter 29. In that example $(\Omega_1 \ell_1 / \gamma_g)_p = 7.1$, so that $\delta = 1/7.1 = 0.141$. In Section H of Chapter 29 it was computed that if a pump filter with $n = 3$ resonators is used and a 0.5-db Tchebyscheff ripple is desired, then $A = 0.49$ in Eq. (29-43) and $(L_A)_{\text{min}} = 3.1$ db. For $\delta = 0.141$, we see from Fig. 30-2 that for $n = 3$, $(L_A)_{\text{min}}$ is about 3.1 and from Fig. 30-3 the Tchebyscheff ripple is 0.48 db. Thus the 0.5-db ripple originally asked for was nearly the value for minimum loss. By Fig. 30-4(c) for $\delta = 0.141$, the values $g_1/10 = 0.71$, $g_2 = 0.26$, $g_3/10 = 0.45$, and $g_4 = 0.195$ are obtained from the chart. Thus the prototype element values are $g_0 = 1$, $g_1 = 7.1$, $g_2 = 0.26$, $g_3 = 4.5$, and $g_4 = 0.195$. In terms of the element value definition in Fig. 29-1, the elements are $\gamma_g = 1/g_0 = 1$, $\ell_1 = g_1 = 7.1$, $c_2 = g_2 = 0.26$, $\ell_3 = g_3 = 4.5$, and $\gamma_L = 1/g_4 = 5.13$. If the pump filter were to be realized in ladder form, the reactance or susceptance slope parameters could be calculated from these element values and the data in Fig. 29-3. In most cases, however, it will be more practical to realize the filter in direct-coupled filter form as suggested in Section D of Chapter 29. (See also discussion of direct-coupled filters in Chapter 15.) Direct-coupled resonator filter realization is a convenient form for filters of this relatively narrow bandwidth (about 6 percent), and provides means for accommodating any desired internal resistance level for the pump signal generator.

In the example from Section H of Chapter 29, the diode resonator with reactance slope parameter $\alpha_1^p = 430$ ohms and with series resistance $R_g^p = 3.86$ ohms was fixed, and the additional two resonators to make up a three-resonator pump circuit were added to improve the transmission into

the pump resonator over the required fractional bandwidth, $w_p = 0.0638$. It is interesting to note how much improvement in performance is gained by introducing the two additional resonators.

Let us first suppose that the pump generator is inductively coupled to the pump resonator so as to give unity VSWR at the pump channel midband frequency, f_0^p . Computations show that under this condition the available power loss at the edges of the pump frequency band would be 11.3 db. Thus, L_A varies across the band from 0 db at midband to 11.3 db at the band edges, an entirely intolerable situation for the application discussed in Chapter 29. However, even when using only a single resonator, the situation need not be this bad. In this situation the decrement is still $\delta = 0.141$, as discussed above, and by Fig. 30-2 we see that the optimum single-resonator (i.e., $n = 1$) design would reduce $(L_A)_{\max}$ from 11.3 db to 6.1 db while by Fig. 30-3 $[(L_A)_{\max} - (L_A)_{\min}]$ is reduced from 11.3 db to about 2.4 db. This substantial improvement can be achieved simply by tightening the coupling to the pump generator so that at resonance the pump circuit VSWR is $(\text{VSWR}) = g_0/g_2 = 1/0.14 = 7.1$ [See Fig. 30-4(a)].

As seen from the preceding, the "optimum" single-resonator adjustment gives much better results than does the case where one demands perfect power transfer at f_0^p . However, for the application discussed in Chapter 29, the optimum, single-resonator results would not be good enough. But, adding two additional resonators permits reducing $(L_A)_{\max}$ from 6.1 db to 3.1 db, while reducing $[(L_A)_{\max} - (L_A)_{\min}]$ from 2.4 db to 0.48 db. These latter values should be satisfactory for the application under consideration.

In the impedance-matching problem just discussed, the load consisted of a resistor in series with a resonator which was tuned to the center frequency of the desired operating band. In general, of course, the load to be matched will not necessarily have such resonance properties or may be resonant but not at the desired frequency. In such cases it should be ascertained, either by examination of the load-circuit diagram or by measurement of the load impedance vs frequency, which combination of a resistor and one or two reactive elements the load resembles most closely in the operating band of interest. If the load impedance can be approximated reasonably well in the band of interest by, say, the impedance of a resistor and a capacitor in parallel, then a parallel inductive element

should be added to bring the load into resonance at the midband frequency of the desired operating band. Then from the equivalent susceptance slope parameter b (see Section C of Chapter 19) for the resonance, the equivalent load conductance G , and the desired fractional bandwidth w , the decrement is computed in the fashion dual to that in Eq. (30-4) i.e.,

$$\delta = \frac{1}{\omega_1 g_1 g_0} = \frac{G}{bw} \quad (30-5)$$

The element values for a suitable low-pass prototype can then be obtained from the charts in this chapter. It is anticipated that the general use of these methods for design of microwave impedance-matching structures will be treated in more detail in the course of the new Signal Corps contract which is scheduled to follow the present one.

The prototype element values given herein can, of course, also be used for the design of impedance-matching networks for low-pass filters. However, true low-pass impedance-matching networks (and also high-pass matching networks) have the difficulty that it is not possible to achieve impedance transformations in the circuit. Thus, the generator internal resistance and the resistor in the load must be related in size just as the g_0 and g_{n+1} values in the charts indicate. The reason for this is easily seen; in the case of a low-pass filter the available power loss at DC is determined solely by the ratio of generator to load resistance. In the case of band-pass filters it is always possible to introduce impedance-level transformation within the filter structure so that the generator and load resistance levels can be established independently (see, for example, the direct-coupled filters discussed in Chapter 15).

For the case of loads that cannot be resonated so as to look like a single resonator plus a resistor within the frequency band of interest, more complicated design techniques will be necessary if precise design is desired. However, even in cases where the load impedance to be matched gyrates too much to be representable in the form expressly treated herein, these procedures may still be useful for improving the match to the load. To do this, the real and imaginary parts of the actual load impedance are replaced by real and imaginary parts of a form that can be treated by the methods of this chapter, where the new real and imaginary parts have median characteristics with respect to the actual load impedance characteristic.

In the preceding discussion, it was said that the networks whose element values are given in the charts give the minimum value of $(L_A)_{\dots}$ for the given decrement. Perhaps it should be added that a somewhat smaller value of $(L_A)_{\dots}$ should be possible for a given number of elements if networks are used which incorporate resonant branches which introduce poles of attenuation at various finite frequencies in the stop bands. The improvement would result from the somewhat sharper cutoff of such filters. However, the use of such networks as filter prototypes would complicate the design problem considerably, and the improvement gained would probably not be very great.

A brief discussion of the equations from which the curves in Figs. 30-2 to 30-4(d) were computed will be found in Section D.

C. IMPEDANCE-MATCHING NETWORK PROTOTYPES WITH A SPECIFIED PASS-BAND TCHEBYSCHIEFF RIPPLE

The networks discussed in the preceding section were specified so that $(L_A)_{\dots}$ was to be as small as possible. Under that condition, it was necessary to accept whatever pass-band Tchebyscheff ripple the charts might call for in the case of any given design. Alternatively, we may specify the pass-band Tchebyscheff ripple and accept whatever value of $(L_A)_{\dots}$ may result. Since in some cases keeping the pass-band attenuation constant may be the major consideration, computation of prototype matching network element values for a specified Tchebyscheff ripple will be briefly outlined.

In a manner similar to that discussed in Section F of Chapter 29, first compute

$$d = \sinh \left(\frac{\sinh^{-1} \sqrt{\frac{1}{H-1}}}{n} \right) \quad (30-6)$$

where

$$H = \text{antilog}_{10} \frac{(\text{db Tchebyscheff ripple})}{10} \quad (30-7)$$

and n is the number of reactive elements in the low-pass prototype. Table 29-1 shows values for d for $n = 2$ to 6 for 0.2, 0.5, and 1.0 db ripple.

Next compute

$$e = d - \frac{2}{\delta} \sin\left(\frac{\pi}{2n}\right) \quad (30-8)$$

where

$$\delta = \frac{1}{(\omega_1' g_1 g_0)}$$

as before. Using Fig. 29-10 or Ref. 4, determine $U_n(d)$ and $U_n(e)$ for the given value of n , and compute

$$|\rho|_{\dots} = \frac{U_n(e)}{U_n(d)} \quad (30-9)$$

Then the $(L_A)_{\dots}$ value that must be accepted is

$$(L_A)_{\dots} = 10 \log_{10} \frac{1}{1 - |\rho|_{\dots}^2} \quad (30-10)$$

Figure 30-5 shows a plot of $(L_A)_{\dots}$ vs δ for various values of n and various amounts of Tchebyscheff ripple amplitude $[(L_A)_{\dots} - (L_A)_{\text{min}}]$. Suppose that $\delta = 0.10$ and 0.10 db ripple is desired. This chart shows that $(L_A)_{\dots}$ will then be 5.9 db. By Figs. 30-2 and 30-3 it is seen that for the same δ , when $(L_A)_{\dots}$ is minimized, $(L_A)_{\dots} = 4.8$ db while the ripple is 0.98 db. Thus, the price for reducing the ripple from 0.98 db to 0.10 db is an increase in $(L_A)_{\dots}$ of about 1.1 db.

Green's work^{7,8} appears to provide the easiest means for determining the element values. Using his equations altered to the notation of this chapter, we obtain

$$D = \frac{\sinh d}{\delta \sin\left(\frac{\pi}{2n}\right)} - 1 = \frac{g_0 g_1}{g_{n+1} g_n} \quad (30-11)$$

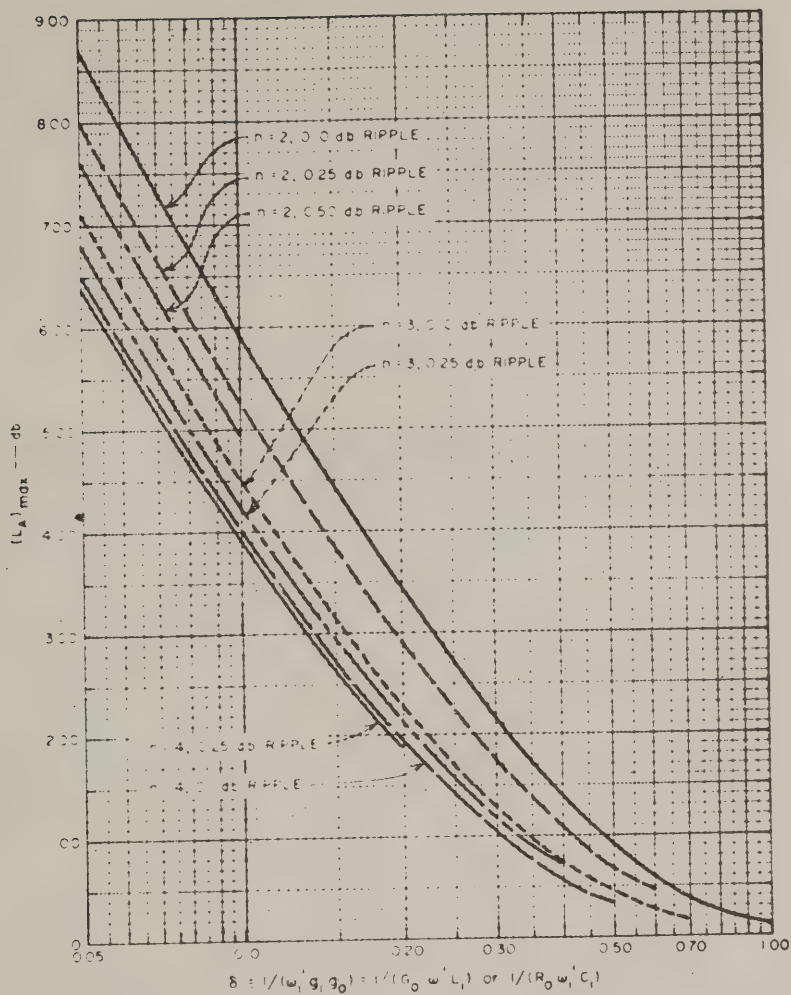


FIG. 30-5
 $(L_A)_{\max}$ VS δ FOR IMPEDANCE MATCHING NETWORKS HAVING A SPECIFIED
 CHEBYSCHIEFF RIPPLE (SEE SEC. C)

where the g_j 's are as defined in Fig. 18-5. The element values are then computed by use of the equations

$$g_1 = \frac{1}{\delta \omega'_1 g_0} \quad (30-12)$$

$$g_j \Big|_{j=2 \text{ to } n} = \frac{1}{g_{j-1} k_{j-1,j}^2 (\omega'_1)^2} \quad (30-13)$$

$$g_{n+1} = \frac{1}{D \delta g_n \omega'_1} \quad (30-14)$$

where the $k_{j-1,j}$ are coupling coefficients to be evaluated as shown below.

Green's equations for the $k_{j-1,j}$ are^{7,8}

$$\underline{n = 2}$$

$$k_{12} = \sqrt{\frac{1 + (1 + D^2) \delta^2}{2}} \quad (30-15)$$

$$\underline{n = 3}$$

$$k_{12} = \sqrt{\frac{3}{8} \left[1 + \left(1 + \frac{D^2}{3} \right) \delta^2 \right]} \quad (30-16)$$

$$k_{23} = \sqrt{\frac{3}{8} \left[1 + \left(\frac{1}{3} + D^2 \right) \delta^2 \right]} \quad (30-17)$$

$$\underline{n = 4}$$

$$k_{12} = \sqrt{\frac{1}{2\sqrt{2}} \left[1 + \left(1 + \frac{8D^2}{\alpha^4} \right) \delta^2 \right]} \quad (30-18)$$

$$k_{23} = \sqrt{\frac{2}{\alpha^2} \left[1 + \frac{2}{\alpha^2} \left(1 + D^2 \right) \delta^2 \right]} \quad (30-19)$$

$$k_{34} = \sqrt{\frac{1}{2\sqrt{2}} \left[1 + \left(\frac{8}{\alpha^4} + D^2 \right) \delta^2 \right]} \quad (30-20)$$

where

$$\alpha^2 = 2(2 + \sqrt{2}) = 6.83$$

For n Arbitrary

$$k_{r,r+1} = \sqrt{\frac{\sin^2 r\theta \cos^2 r\theta + (\cos^2 r\theta + D^2 \sin^2 r\theta)(\sin^2 \theta) \delta^2}{\sin(2r-1)\theta \sin(2r+1)\theta}} \quad (30-21)$$

where

$$\theta = 2\pi/n$$

It is usually convenient to normalize the prototype design so that $g_0 = 1$ and $\omega'_1 = 1$.

D. COMPUTATION OF ELEMENT VALUES THAT MINIMIZE $(L_A)_{\dots}$

The element values for the prototype matching networks discussed in Section B and plotted in Fig. 30-4(a), (b), (c), (d) could have been obtained using Green's charts⁸ of coupling coefficients and D values along with Eqs. (30-12) to (30-14). However, in order to ensure high accuracy, to add the $n = 1$ case, and to cover a somewhat wider range of decrements than was treated by Green, it was decided to carry out the computations from the beginning. The procedure used was that described below.

Fano² has shown that, for low-pass networks of the type under consideration, $(L_A)_{\dots}$ will be as small as possible if

$$\frac{\tanh na}{\cosh a} = \frac{\tanh nb}{\cosh b} \quad (30-22)$$

where

$$a = \sinh^{-1} d \quad (30-23)$$

$$b = \sinh^{-1} e \quad (30-24)$$

and d and e are as indicated in Eqs. (30-6) and (30-8). By Eqs. (30-23), (30-24) and (30-8),

$$b = \sinh^{-1} \left[\sinh a - 2\delta \sin \frac{\pi}{2n} \right] \quad (30-25)$$

A computer program was set up to find values of a and b that satisfy Eq. (30-22) under the constraint given by Eq. (30-25). From these a and b values for various δ , d and e values were obtained by $d = \sinh(a)$ and $e = \sinh(b)$. When values of d and e had been obtained for various δ , the element values for the networks were computed as indicated in Section C.

The data for the charts in Fig. 30-2 were obtained by using the values of a and b vs δ obtained above, computing²

$$|\rho|_{\dots} = \frac{\cosh nb}{\cosh na} \quad (30-26)$$

and then computing $(L_A)_{\dots}$ by use of Eq. (30-10). The data in Fig. 30-3 were obtained by use of Eqs. (30-23), (30-6) and (30-7).

